CARDIFF UNIVERSITY
PRIFYSGOL CAERDYDD

19th International Conference on Microwave and High-Frequency Applications

AMPERE 2023

11-14 September 2023
Cardiff, United Kingdom

DOI: 10.5281/zenodo.10125116

Conference Proceedings

Welcome letter from the AMPERE chairs

Dear Colleagues,

On behalf of the AMPERE 2023 Organising Committee and Scientific Committee, we are honoured and delighted to present the proceedings of the 19th International Conference on Microwave and High Frequency Applications, held in Cardiff, UK 11-14 September 2023.

AMPERE 2023 was attended by more than 170 delegates, from over 25 different countries and marked a triumphant return to in-person AMPERE events after the very successful virtual conference organised by RISE in Gothenburg in 2021.

AMPERE has been an important organisation for the promotion of microwave and RF applications for almost 40 years. It remains a focus of emerging scientific and industrial research in Europe and around the world. The conference it runs every two years has become one of the most important international events dedicated to microwave and radiofrequency power systems, science, technology and applications. The conference provides an excellent forum for researchers and engineers from academia and industry to exchange innovative ideas, network, discuss collaborations and to meet with international experts in a wide variety of specialties at both scientific and industrial scale.

The AMPERE 2023 programme consisted of a short course, modelling workshop and over 130 talks. The main themes of the technical programme included important emerging applications in sustainability and decarbonisation, with talks representative of the broad scope of the AMPERE community. Attendees were treated to a range of excellent talks in plasma processing, biomass and waste processing, chemistry/biochemistry applications, design of applicators and components and industrial scale up, modelling, measurements and metrology, food processing and biological applications.

Cardiff is the capital city of Wales and has a rich cultural heritage that we were delighted to share, with an event at the historic Coal Exchange, including an astonishing and very moving performance by the Welsh National Opera (please do visit them and support them if you have the chance!), followed by our gala dinner in the beautiful surroundings of the National Museum of Wales.

Special recognition should go to the Local Organising Committee members who all worked extremely hard to create a successful conference. Many thanks also to all attendees who made this event a joy to host.

We hope to see you at the next AMPERE.

Daniel Slocombe and Adrian Porch

Cardiff, UK, October 2023

Daniel Slocombe

Adrian Porch

Contents

Chemistry, Biochemistry and Processing

Energy and Environmental Applications

Plasma Phenomena and Processing

Industry Focus

Industrial Equipment and Scale-Up

Design of Applicators and Components

Materials Properties and Interaction

Medical and Biological Applications

Modelling and Numerical Techniques

Measurements and Metrology

Plenary Speakers

Professor D. Michael P. Mingos FRS

Michael Mingos is a pioneer of microwave chemistry. He is an Emeritus Professor of Chemistry at the University of Oxford and holds Honorary Fellowships at Keble College and St Edmund Hall, where he was Principal for 10 years.

https://en.wikipedia.org/wiki/Michael_Mingos

Professor Neil Alford

Neil Alford has published groundbreaking work on microwave materials, including the discovery of the room temperature MASER. He has served as Head of the Department of Materials at Imperial College London, Vice-Dean (Research) in the Faculty of Engineering, Acting Vice-Provost for Research and until 2022, the Associate Provost for Academic Planning.

https://www.imperial.ac.uk/people/n.alford

Professor Satoshi Horikoshi

Satoshi Horikoshi is a leader in the field of microwave chemistry and processing of materials, in manufacturing, environmental and life sciences. He is a professor in the Faculty of Science and Technology at Sophia University.

https://researchmap.jp/19711020?lang=en

Professor Steve C. Cripps

Steve Cripps is a recognised authority on microwave power amplifier design. He is a distinguished research professor at Cardiff University and a member of the Centre for High Frequency Engineering.

https://www.cardiff.ac.uk/people/view/364356-cripps-steve

Professor Duncan Gregory

Duncan Gregory has pioneered microwave synthesis and high temperature microwave applications. He is the WestCHEM chair of inorganic materials at the University of Glasgow.

https://www.gla.ac.uk/schools/chemistry/staff/duncangregory/

Dr A C Metaxas

A C (Ricky) Metaxas co-authored Industrial Microwave Heating, a book which is regarded as the “Bible” for researchers working in the field of Microwave Heating. He is a Life Fellow at St John’s College, Cambridge, and is a founding member and former president of AMPERE.

https://www.joh.cam.ac.uk/dr-ac-ricky-metaxas

John F Gerling

John Gerling is a leading industrialist and has more than 35 years experience in microwave heating technologies for consumer, commercial, industrial and scientific applications. He is the president of the International Microwave Power Institute (IMPI)

http://www.jfgerling.com/index.html

Development of the Chemical Applications of Microwave Dielectric Heating at the End of the Last Century

D. M. P. Mingos[1]

[1]*Inorganic Chemistry Laboratory, University of Oxford, Oxford OX1 3QR, UK*
Michael.mingos@seh.ox.ac.uk

Keywords: chemical synthesis, temperature measurement, containing flammable materials, metal powders, catalysis.

Although the widespread use of microwave dielectric heating in the food industry can be traced back to the 1950s its applications in chemistry and material science laboratories was delayed until 1980s, when it started to be used in analytical laboratories to accelerate the digestion of insoluble samples by aqueous inorganic acids prior to atomic absorption spectroscopic analysis. These analytical applications were facilitated by the development of Teflon pressure containers which could be inserted into microwave ovens operating at 2.45GHz which could attain temperatures above 250°C and pressures of 80 atmos [1]. The nuclear industry also explored the possibility of using microwave dielectric heating to incorporate radioactive waste materials with long half-lives into glass blocks which could withstand degradation when stored underground for hundreds of years. This emerged from the observation that solid uranium oxides had high loss tangents at 2.45GHz and experienced high heating rates (10-20°C/s) [2]. In 1986 the first detailed studies of microwave dielectric heating for accelerating the synthesis of organic compounds were reported by Gedye *et al* [3] and Giguere, Majetich *et al* [4]. The great potential of this technique was quickly appreciated by organic chemists in both university and pharmaceutical laboratories, who recognised that if you wish to screen hundreds of related drug molecules then reducing the time taken for their synthesis by several orders of magnitude made both economic and scientific sense.

I had been trained in synthetic organometallic chemistry at Sussex University by Professor Joseph Chatt and as an independent academic my main research interests since the 1970s had centred around the synthesis of cluster compounds of the platinum metals and gold and the study of co-ordination compounds, containing ambivalent ligands such as NO and SO_2. In 1988 David Baghurst joined me at Oxford University and I suggested we explore the possibility of extending these microwave studies to inorganic chemistry. Since Oxford also had a strong tradition in solid state chemistry and John Goodenough had hired me I encouraged David not to limit his research to solution chemistry, but also given the previous work in nuclear laboratories, also explore potential applications in the solid state. Our initial papers in the late 1980s showed that the microwave technique did indeed accelerate the synthesis of organometallic and co-ordination compounds in organic solvents and also demonstrated that it could be applied to the intercalation of molecules in layered inorganic materials [5-8]. The successful synthesis of a wide range of mixed metal oxides confirmed the wide possible applications of microwave dielectric heating for the synthesis of new materials [9] and we also reported the microwave synthesis of high temperature superconductors, which were attracting great interest in the 1980s [10] as a result of the Nobel Prize winning research of the IBM Group in Zurich.

At this stage I had very limited knowledge regarding the interaction of microwave radiation with dielectric materials, although as a research student I had measured the dipole moments of some coordination compounds of iridium [11]. von Hippel's classical books and compilations of dielectric data published in the 1950s [12] and A.C. Metaxas and R.T. Meredith's "Industrial Microwave Heating" published in 1983 [13] guided our initial experiments and exposed enormous gaps in our knowledge of the fundamental principles. Furthermore, although von Hippel had tabulated the relevant dielectric parameters necessary for understanding the heating characteristics of cooking ingredients such as meats, flour, vegetables and oils and their variation with their water content it did not give much relevant data for common solvents and reagents used in modern chemistry. It became apparent that if microwave dielectric heating was to evolve from a promising novelty into a scientifically based reliable tool for synthetic chemistry, then the following issues needed to be satisfactorily addressed:

1. The relationships between the dielectric properties of common reagents and their heating rates at commercially available microwave frequencies. This required the publication of a database of dielectric parameters which defined the loss tangents for solvents commonly used in organic and inorganic chemistry. These broad trends in the parameters for homologous series of commonly used organic solvents should be interpreted in a way which emphasised their relationship to molecular properties which chemists could appreciate and interpret.
2. The development of accurate and reliable measurement of the temperature and pressure in the reaction vessel whilst the reaction proceeded was an immediate and important problem which needed to be solved.
3. It was also necessary to establish whether the efficient conversion of microwave energy resulted in significant and persistent temperature variations within the vessel and whether significant hot-spot formed and persisted when solutions and solid-state mixtures were heated with microwaves.

4. Chemists needed to develop containers and protocols to contain the volatile and flammable organic solvents safely in a microwave cavity and thereby prevent fires or explosions from harming research workers.
5. Could the different dielectric properties of inorganic substances and materials be used to selectively heat a certain component of a chemical reaction?
6. Could the transparency of a compound in the microwave region be exploited to undertake novel purifications processes or chemical reactions?

In the subsequent 15 years my group sought to address this wish list and those which were realised were communicated in 50 papers and reviews. Our interesting journey included equal measures of successes and failures will be described in more detail in my introductory talk [14-17].

References

[1] H.M. Kingston and L.B. Jassie, "Introduction to Microwave Sample Preparation" , Washington, United States, American Chemical Society , 1988.
[2] D.M.P. Mingos, Microwaves in Chemical Synthesis", Chemistry Industry,5 96-599,1994.
[3] R. Gedye, F. Smith, K. Westway, H. Ali, L. Balderisa, L. Laberge and J. Rousell, "The Use of Microwave Ovens for Rapid Organic Synthesis ", Tetrahedron Lett., 27, 279-282, 1986.
[4] R.J. Giguerre, T.I. Bray, S.N. Duncan and G. Magetich, "Application of Commercial Microwave Ovens to Organic Synthesis", Tetrahedron Lett., 27, 4945-4958, 1986.
[5] D.R. Baghurst, D.M.P. Mingos and M.L Watson, "Application of Microwave Dielectric Loss Heating Effects for the Rapid and Convenient Synthesis of Organometallic Compounds", J. Organometal. Chem., 1989, Vol. 368, C43-44, 1989.
[6] D.R. Baghurst and D.M.P. Mingos, "Design and Application of a Reflux Modification for the Synthesis of Organometallic Compounds using Microwave Dielectric Loss Heating Effects", J. Organometal. Chem.,, 384, C57-60, 1990.
[7] D.M.P. Mingos and D.L. Greene, "Application of Microwave Dielectric Loss Heating Effects for the Rapid and Convenient Synthesis of Ruthenium(II) Polypyridyl Complexes", Trans. Met. Chem., 16, 71-2, 1991.
[8] K. Chatakondu, M.L.H. Green, S.M. Reynolds and D.M.P. Mingos, "Application of Dielectric Loss Heating Effects for the Rapid and Convenient Synthesis of Intercalation Compounds", J.C.S.Chem.Commun., 1515-1517, 1989.
[9] D.R. Baghurst and D.M.P. Mingos, "Applications of Microwave Heating Techniques for the Synthesis of Solid-state Inorganic Compounds", J.C.S. Chem. Commun., 829-830, 1988.
[10] D.R. Baghurst, A.M. Chippindale and D.M.P. Mingos, "Microwave Syntheses for Superconducting Cerarnics", Nature, 332, 311, 1988.
[11] P. Debye, "Polar Molecules", New York, United States, Chemical Catalogue, 1929.
[12] A.R. von Hippel, "Dielectric Materials and Applications", Boston United States, MIT Press, 1954.
[13] A.C. Metaxis and R.J. Meredith, "Industrial Microwave Heating", London, United Kingdom, Peter Peregrines Press, 1983.
[14] C. Gabriel, S. Gabriel, E. Grant, B. J. Halstead and D.M.P. Mingos, "Dielectric Parameters Relevant to Microwave Dielectric Heating", Chem. Soc. Rev., 1998, 27, 213-223.
[15] Zhang, X., Lee, C.S-M., Mingos, D.M.P. and Hayward, D.O., " Effects of Microwave Dielectric Heating on Heterogeneous Catalysis", Catal. Lett., 88, 33 -38, 2003.
[16] A.G. Whittaker and D.M.P. Mingos, "Microwave Assisted Solid State Reactions Involving Metal Powders and Gases", J. C. S. Dalton Trans., 2541-2543; 1993; 2751-2752, 1992.
[17] D.R. Baghurst and D.M.P. Mingos, "Applications of Microwave Dielectric Heating Effects to Synthetic Problems in Chemistry, Chemical Society Reviews, 20, 1-47, 1991.

From Ultra-Low Dielectric Loss to Room Temperature MASERs

N. Alford[1]

[1]*Imperial College London, South Kensington Campus, London, UK*
n.alford@imperial.ac.uk

Microwave dielectric materials were first reported in the 1930s and took a long time to be used successfully in filters. In this talk we tell the story of the quest for extremely low loss (the tan δ) in oxides and specifically methods to overcome the dielectric limit. We do this using a Bragg reflector (whose layers are aperiodic in thickness - a bit like a Russian Doll or Matryoshka) to reach remarkably high values of $Q=0.6x10^6$ at 30GHz [1]. This result suggested that it might be possible to reach the threshold for masing and produce a solid-state room temperature maser (**M**icrowave **A**mplification by **S**timulated **E**mission of **R**adiation) and indeed we demonstrated that in P-terphenyl doped with pentacene when located inside a very high Q sapphire resonator maser action can be observed in pulsed mode. This was the first time a solid-state maser had been demonstrated at room temperature and in the earth's magnetic field [2]. The next step was to achieve continuous maser action and this was achieved in diamond containing nitrogen vacancy defects – the first demonstration of continuous masing at room temperature [3]. In this talk we discuss the conditions for continuous wave masing – the gain medium, the dielectric permittivity and dielectric loss of the resonator, the Purcell factor – and how the interplay of all these must be balanced carefully in order to breach the threshold for masing [4]. Finally, we discuss progress towards miniaturisation and potential applications.

References

[1] Better than Bragg: Optimizing the quality factor of resonators with aperiodic dielectric reflectors Breeze Jonathan; Oxborrow Mark; Alford Neil McN APPLIED PHYSICS LETTERS Volume: 99 Issue: 11 Number: 113515 DOI: 10.1063/1.3639271 SEP 12 2011

[2] Room Temperature Maser nature11339 Mark Oxborrow, Jonathan Breeze and Neil Alford NATURE, 16 August 2012 DOI 10.1038/ (2012)

[3] Continuous-wave room-temperature diamond maser Jonathan Breeze, Enrico Salvadori, Juna Sathian, Neil Alford and Christopher Kay. Nature 555, pages 493–496 (22 March 2018) doi:10.1038/nature25970

[4] Exploring the Spin Dynamics of a Room-Temperature Diamond Maser using an Extended rate Equation Model Yongqiang Wen, Philip L.Diggle, Neil McN. Alford, and Daan M. Arroo arXiv preprint arXiv:2304.03217

A Review of Product Development Activity for Solid State RF Cooking

J. F. Gerling[1]

[1]*Gerling Consulting, Inc., 12150 Calle Uvas, Gilroy, California, USA*
john@jfgerling.com

Keywords: microwave, microwave oven, solid state RF, microwave cooking, patents

Early Development Activities

The benefits of solid state radio frequency (SSRF) technology as an alternate to magnetrons for cooking were recognized as early as 1969 when Westinghouse Electric Corporation filed the first known US patent describing the use of "a plurality of solid state oscillators" to provide uniform distribution of energy [1]. Since then and until recently several more patents were issued, including to major appliance manufacturers Matsushita (Panasonic) and Whirlpool, for various methods and apparatus employing SSRF technology for microwave ovens [2].

Not surprisingly, none of the early inventions resulted in introduction of a commercially available product. Midea (China) announced in 2012 the availability of the world's first SSRF microwave oven [3], although apparently this claim was premature as no such product was ever available for sale to consumers. NPX later announced "Sage," a uniquely designed compact SSRF cooker that again never made it to market [4].

First Product Launches

Arguably, the main reason for the long wait to see these products on store shelves has been cost. While a 1 kW magnetron operating at 2450 MHz costs as little as €10 (in volume), the cost of the equivalent for SSRF devices is at least two orders of magnitude greater. Undaunted by these figures, two companies have taken a leap of faith by introducing products for commercial sale. The Miele (Germany) Dialog oven targeted to the high-end consumer market and ITW (USA) Ibex oven for commercial food service were priced at roughly €7200 [5] and €17000 [6], respectively.

Fig. 1. Miele Dialog (left) and ITW Ibex (right) solid state microwave ovens.

Fulfilling the promise to deliver superior cooking requires more than SSRF technology alone. An important technique that enables SSRF technology to improve microwave cooking is cavity sensing and algorithms [7]. By implementing closed-loop feedback the oven controls can adjust frequency, phase, and amplitude to optimize field distribution and heating uniformity. Goji Research (Israel) has developed and patented technologies based on closed-loop control algorithms that combine information about RF parameters collected every two seconds with a priori data about food characteristics [8]. Current versions of the Miele and ITW ovens operate using licensed Goji technologies. Others are also developing technologies for adaptive control of solid state microwave ovens, including both Miele and ITW [9,10] and NXP (The Netherlands) [11].

Although the technique can be applied to any food cooked in a microwave oven, the food characteristic data must be present for the control algorithm to be properly executed. Otherwise, random meals not already programmed into the oven controls may not be cooked any better than in a conventional microwave oven. This limited versatility may hinder acceptance of the technology by consumers, while technology licensing costs may deter the adoption of SSRF technology by other microwave oven manufacturers. An alternate approach to proprietary control methodologies is a combination of open-source standards for characterizing the foods to be cooked and non-proprietary methods for controlling the oven based on those characteristics. Both food producers and appliance manufactures may then be more inclined to pursue markets enabled by SSRF technology.

Ongoing Cost Reduction

While making the solid state microwave oven more versatile can significantly improve market acceptance, cost remains a major hurdle to market penetration (Figure 2). System architectures utilizing solid state power amplifier (SSPA) modules, coaxial cables, and connectorized antennas are not likely to ever achieve cost reduction targets. An alternate lower cost architecture described in a Miele patent application [12] integrates a waveguide launch structure with a SSPA pallet and antenna (Figure 3).

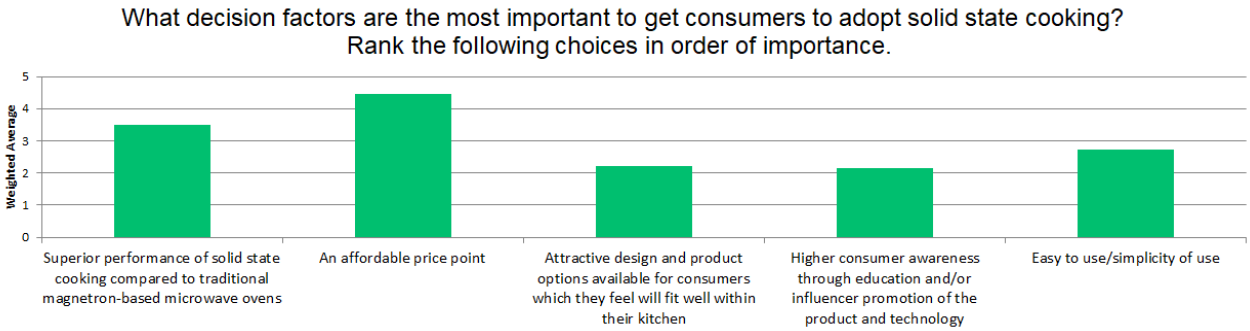

Fig. 2. Partial results from a recent survey of microwave heating technologists conducted by IMPI.

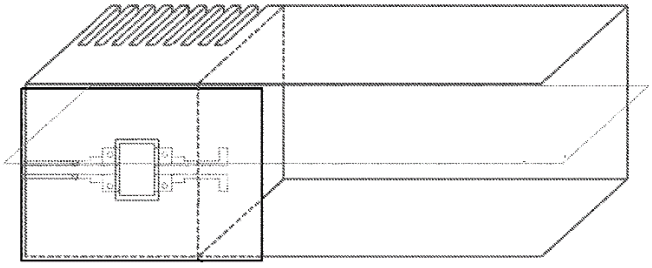

Fig. 3. Section view of a launch waveguide with integrated SSPA pallet and antenna [12].

It is worth noting that other major manufacturers of microwave foods and appliances are actively developing solid state RF cooking technologies. Whirlpool (USA) has been securing patents for the past twenty years, most recently in 2021 for a low cost method to deliver microwave energy into a cavity from a solid state RF amplifier [13], while Nestlé (Switzerland) more recently has been developing food packaging methods specifically intended for use in a solid state microwave oven [14]. Nestlé is also developing methodologies for multi-channel SSRF technology [15].

Conclusion

The previously mentioned SSRF cooking survey found that 70% of respondents believe SSRF cooking may be widely available within the next 2-5 years. It seems reasonable to conclude that these activities are indicators of confidence that SSRF-based microwave cooking may soon achieve economic viability and market acceptance.

References

[1] B. R. McAvoy, *Solid State Microwave Oven*, U.S. Patent 3 557 333, issued January 19, 1971.
[2] E. Schwartz, *Historical Notes on Solid-State Microwave Heating*, AMPERE Newsletter, issue 89, July 2016.
[3] X. Tang, *Midea Innovation: World's First Solid State RF Microwave Oven*, PR Newswire, June 21, 2012.
[4] J. F. Gerling, *Recent Developments in Solid-State Microwave Heating*, AMPERE Newsletter, issue 89, July 2016.
[5] M. Wolf, *Miele Shipping the Dialog, Their Oven With Solid State Cooking Tech, to 20 Countries*, The Spoon, January 28, 2020.
[6] iFoodEquipment.ca storefront website, Hobart IBEX High Speed Oven, July 19, 2023.
[7] R. Wesson, *RF Solid State Cooking White Paper*, Ampleon, 2016.
[8] B. Manz, *RF Energy is Finally Cooking*, Microwaves & RF (mwrf.com), December 18, 2017.
[9] H. Nelson, et al, *Method for Operating a Cooking Appliance, and Cooking Appliance*, U.S. Patent Application 20220283135, published September 8, 2022.
[10] M. Carcano, M. Sclocchi, *Method for Managing a Microwave Heating Device and Microwave Heating Device*, U.S. Patent 11 032 878, June 8, 2021.
[11] M. Ma, et al, *Establishing RF Excitation Signal Parameters in a Solid-State Heating Apparatus*, U.S. Patent 11 224 102, January 11, 2022.
[12] T. Wixworth, A. Kersting, *Device for Generating and Transmitting High-Frequency Waves*, U.S. patent application 20180343711, published November 29, 2018.
[13] N. Roumpedaki, F. Giordano, *Intermediate Transition Between an Antenna and a Coplanar Waveguide Transmission Line of a Solid State Amplifier*, U.S. Patent 11 122 653, September 14, 2021.
[14] S. Dhawan, et al, *Reusable Microwave Vessel*, U.S. Patent 11 412 583, August 9, 2022.

Scaling-Up Dielectric Processes for Industrial Decarbonisation – Microwaves in Green Steel

R. S. E. Bell[1], M. J. G. Sinclair[1]

[1]*C-Tech Innovation Ltd, Capenhurst Technology Park, Chester, UK*
Rob.Bell@CTechInnovation.com

Keywords: microwave, scale up, industrial decarbonisation.

The transition to a decarbonised economy demands a far greater role for electrification in high temperature industrial processes. The use of electricity also provides the opportunity to consider energy transfer and a optimisation to deliver efficient, cost effective processes. Previous work at C-Tech Innovation Ltd has demonstrated the advantage of hybrid microwave furnace technology in a range of high temperature processes [1,2,3]. The hybrid microwave approach uses radiant heating elements to provide the majority of thermal input and control the temperature, with application of dielectric fields to assist processing of the materials.

This work presents the laboratory and process development steps undertaken to address the challenge of applying this technology to a pilot scale continuous process using hydrogen for the direct reduction of iron ore.

Steelmaking is one of the largest contributors to worldwide industrial carbon dioxide emissions. Almost all primary iron production uses fossil fuels for the conversion of iron ore, with approximately 70% produced via the blast furnace route, using coke/coal, and the remainder via direct reduction with natural gas [4].

The reduction of iron ore with hydrogen results in the formation of water instead of carbon dioxide as the by-product, which is a huge advantage from the perspective of net zero manufacturing. However, changing from carbon as both fuel and reductant, results in the reaction being endothermic and therefore additional heat input is required during the reaction in order to maintain reaction kinetics [5,6]. Additionally replacing a cheap energy source such as coal requires additional efforts to reduce energy usage in order to keep costs as low as possible.

In lab scale studies it was identified that the application of a 2.45 GHz field promoted the initial reduction reaction rate by up to 50%, and this enhancement demonstrates the potential of microwave assistance to reduction of iron ore at an industrial scale. The development of the laboratory scale Hybrid Kiln (Figure 1) to study the effect of microwave fields on the hydrogen direct reduction of hematite (Fe2O3) was key to the understanding of the interplay between temperature, field effects and reaction rates achieved.

The data and process understanding generated was then applied to the development of a 5 metre long hybrid rotary kiln to allow material processing and testing at tonne scale (Figure 2).

The development of the prototype rotary kiln, and the engineering approach demonstrated, show that microwave assisted processes are a promising solution for industry. The rate improvements along with potential energy savings makes this an attractive solution for the electrification of industrial processes.

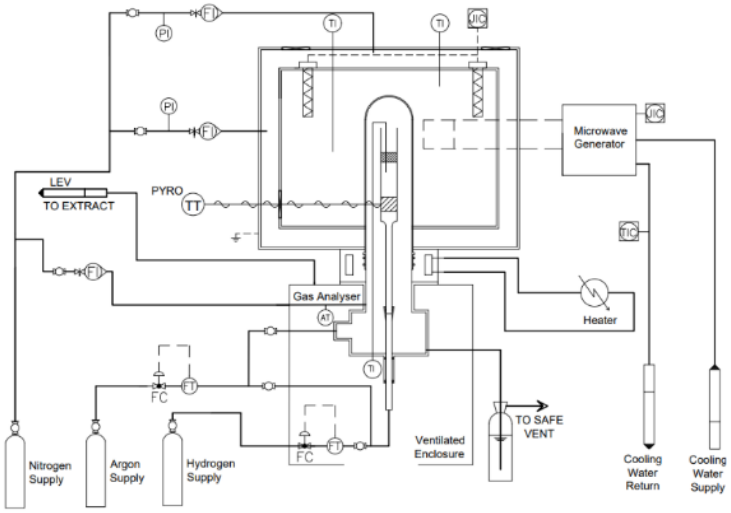

Fig. 1. P&ID for lab scale Microwave hybrid kiln

Fig. 2. Pilot Scale Microwave hybrid rotary kiln for reduction of iron ore.

References

[1] Rowley, A.T., Wroe, R., Vazques-Navarro, D. et al. Microwave-assisted oxygenation of melt-processed bulk YBa2Cu3O7-δ ceramics. Journal of Materials Science 32, 4541–4547 (1997).
[2] Wroe, R., Rowley, A.T. Evidence for a non-thermal microwave effect in the sintering of partially stabilized zirconia. Journal of Materials Science 31, 2019–2026 (1996). https://doi.org/10.1007/BF00356621
[3] John Marsh; Ruth Wroe UK Patent GB 2 435 649 A 2007
[4] Holappa, L. A General Vision for Reduction of Energy Consumption and CO2 Emissions from the Steel Industry. *Metals (Basel)* **2020**, *10*, 1117, doi:10.3390/met10091117
[5] Spreitzer, D.; Schenk, J. Reduction of Iron Oxides with Hydrogen—A Review. Steel Res Int 2019, 90, 1900108, doi:10.1002/srin.201900108.
[6] Otto, A.; Robinius, M.; Grube, T.; Schiebahn, S.; Praktiknjo, A.; Stolten, D. Power-to-Steel: Reducing CO2 through the Integration of Renewable Energy and Hydrogen into the German Steel Industry. *Energies (Basel)* **2017**, *10*, 451, doi:10.3390/en10040451

Breaking out of the 50 Ohm Straightjacket: RF Power Amplifier Design for Industrial and Biological Applications

S. C. Cripps[1]

[1]*School of Engineering, Cardiff University, UK*
CrippsSC@cardiff.ac.uk

Design techniques for RF power amplifiers have been the subject of many papers, articles, application notes, and books, over many years. But almost all of this work has been aimed at applications in mobile communications and military ECM systems, where a 50 Ohm source and load is specified over the required operating frequency bandwidth. As such, commercial products are also designed and specified to perform to full specification only with 50 Ohm source and load terminations. Conversely, most industrial heating and chemical or biological microwave exposure systems present a target impedance to the RF source that can be anywhere on the Smith Chart and which can move significantly during the exposure. From an RFPA designer's viewpoint, there is an irony, given that an RF power transistor itself does not work optimally, or even anywhere close, with a 50 Ohm load.

This talk will examine possibilities for designing RFPAs in a less ironic manner for these applications.

AMPERE the story thus far

A. C. Metaxas[1]

[1]*Life Fellow, St John's College, Cambridge, England, UK.*
acm33@cam.ac.uk

Keywords: microwave, radiofrequency, genesis of AMPERE

In this talk I will look back at my involvement with RF and microwave heating, describe the birth of our association and outline my vision for AMPERE's next stage of development and future challenges.

My earliest recollection with the topic of RF and Microwaves goes back to 1972 when I was first employed by the Electricity Council Research Centre (ECRC) at Capenhurst, Cheshire, as a Research Officer within the Electrophysics Group. ECRC was part of the Electricity Supply Industry (ESI) with its headquarters in London which included generation and utilisation. My first assignment was to devise a method for measuring the dielectric properties of paper and board. Lots of troubleshooting followed in industry attempting to install and test RF and microwave drying prototypes.

Before I discuss the genesis of AMPERE it is perhaps important to stress that the history of RF and microwave heating in the UK, and indeed in Europe, was intimately connected with the Power Utilities and the ESI. In the UK at the time the Electricity Council (EC) in London had overall control with the Central Electricity Generating Board (CEGB) being responsible for generation and distribution and the Area Boards (closely liaising with ECRC) being primarily responsible for utilisation and for meeting the needs of industrial, commercial and domestic customers.

It is important to stress that the 1970s was the decade which highlighted the problems associated with diminishing fossil fuels and the need to look for alternative techniques for carrying out many processes in industry. Equivalent centres to ECRC in Europe included Laborelec in Belgium, KEMA in Holland, Les Renardieres in France and of course the Union International d' Electrothermie (UIE).

The first encounter I had with fellow scientists and engineers across the 'pond' involved a conference on RF and microwave heating organized at the University of Loughborough by Harry Barber, who had a long association with IMPI (International Microwave Power Institute) in the USA. Up to that time IMPI organized an annual conference held alternately in Canada and the USA and it was deemed useful to include Europe on a three year cycle, so in 1970 the first IMPI-European conference was held in the Hague, which was followed in 1973, 1976 and 1979 with subsequent meetings in the series held at Loughborough, Leuven (Belgium) and in Monaco respectively.

Alas, I did not attend the 1979 conference in Monaco, which turned out to be the last European-IMPI collaborative meeting. Also, like myself, many of my European colleagues could not attend the annual IMPI meetings in Canada or the USA because of the lack of funding. In fact, the birth of AMPERE can be traced following my move to Cambridge University Engineering Department (CUED). "Go and teach the bright young undergraduates all about electroheat and stress the importance of electricity in industrial processing" was my Director's comment after I had agreed to a period of 18 months secondment. I hasten to add that the 18-month stint became "a permanent stint" as I am still in Cambridge after 41 years. Given the energy crisis of the 1970's, during my first lecture on Energy to second year engineers at Cambridge I discussed the well-known Hubbert bell-shaped curve. M K Hubbert, a Shell geophysicist, published a paper in 1956 on Nuclear Energy and Fossil Fuels, which in essence stated that the amount of oil in the ground in any geographical region is finite and although following its discovery the rate of production increases eventually it reaches a peak and then it starts to decline. That was meant to shock the undergraduates forcing them to think of electrical techniques! Shortly after my move to Cambridge, I set up the Electricity Utilisation Group, my Research Group at CUED, in order to expand my ideas about electroheat, which of course included RF and microwaves. Prompted by my inability to attend any IMPI meetings, I started thinking seriously of resurrecting the notion of a conference in Europe on this topic. This idea culminated a conference at St John's College in 1986, which is now regarded as the first in the series of AMPERE conferences on Microwave and High Frequency Heating although at the time the name AMPERE had not been suggested.

I will conclude with the formation of AMPERE, its subsequent biennial conferences in Europe, its establishment as a non-profit organisation based in France and our link between the World Congresses which have now morphed into the Global Conference Microwave Energy Applications (GCMEA).

Reference

[1] AC Metaxas, The origins of AMPERE and personal recollections of our field of activity, AMPERE Newsletter, Issue 100, 15 Nov 2019

Microwave Synthesis of Inorganic Materials; Insight and Advances

D. H. Gregory[1]

[1]*University of Glasgow, School of Chemistry, Joseph Black Building, Glasgow G12 8QQ, UK*
Duncan.Gregory@glasgow.ac.uk

Keywords: Synthesis, carbides, alloys, *in-situ* characterisation, plasmas

Energy efficiency, sustainability and economic viability have become priorities in the materials manufacturing sector. Conventional synthesis of solid-state materials is time- and energy-intensive, often requiring high temperatures and complex procedures. Microwave (MW) processing is a viable alternative that addresses these challenges while providing the opportunity to access new and metastable materials and to understand the interaction of solids with electromagnetic fields.

Carbon-containing materials are attractive candidates for MW synthesis on account of the high dielectric loss tangent exhibited by the element at MW frequencies, resulting in rapid temperature increases during MW heating. Reaction times can be orders of magnitude shorter than seen conventionally. As potential products of such reactions, carbides possess high melting points, hardness, fracture toughness, compressive strength and chemical resistance, finding application as cutting tools and ceramics. Recently carbides have also found uses in catalysis. We will describe the synthesis of WC, Mo_2C, SiC and ternary carbides using both multimode and single mode MW systems and demonstrate how synthetic and reactor parameters can be exploited to control microstructure [1-7].

MW synthesis and processing is not restricted to carbides only, however and recent work at Glasgow has demonstrated how nanostructured alloys can be fabricated under relatively low power MW conditions *via* metal plasma synthesis – so called Metal Induced Microwave Plasma (MIMP) reactions (Fig. 1). The nano-alloys (such as Laves phases M_2X; M=metal, X=main group metalloid) can be used as functional materials themselves or used as precursors in dealloying reactions to form nanoporous metals or semiconductors (for use as electrodes in metal ion batteries, for example) [8-12].

Ex-situ analysis allows characterisation MW-synthesised materials, but gives little insight into reaction mechanisms. This prompted us to investigate *in-situ* studies of MW synthesis in the solid state. Bespoke MW reactors have been developed for use at neutron sources (such as ISIS at the Rutherford Appleton Laboratory, UK) to enable the study of MW reactions *in-situ* via time-resolved neutron powder diffraction. We will present details of the development of our reactors and some preliminary results.

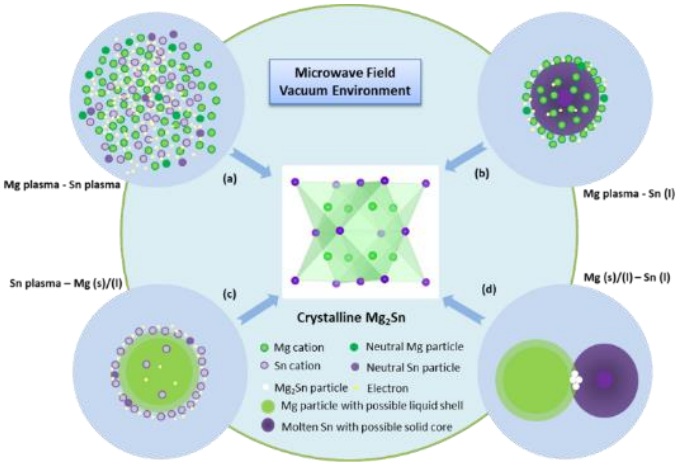

Fig. 1. Schematic of the possible reaction mechanisms in the MIMP synthesis of the Laves phase, Mg_2Sn

References

[1] S. R. Vallance, S. Kingman and D. H. Gregory, "Ultra-rapid Materials Processing: Synthesis of Tungsten Carbide, WC, in Sub-minute Timescales" *Adv. Mater.*, **19**, 138-142, 2007.
[2] S. R. Vallance, S. Kingman and D. H. Gregory "Ultra-rapid Processing of Refractory Carbides; 20 s Synthesis of Molybdenum Carbide, Mo_2C.", *Chem. Commun.*, 742-744, 2007.
[3] S. R. Vallance, D. M. Round, C. Ritter, E. J. Cussen, S. Kingman and D. H. Gregory "Ultra-rapid Microwave Synthesis of Superconducting Refractory Carbides.", *Adv. Mater.*, **21** ,4502-4504, 2009.
[4] L. Carassiti, A. Jones, P. Harrison, P. S. Dobson, S. Kingman, I. MacLaren and D. H. Gregory "Ultra-rapid, Sustainable and Selective Synthesis of Silicon Carbide Powders and Nanomaterials *via* Microwave Heating.", *Energy Env. Sci.*, **4**, 1503 – 1510, 2011.

[5] S. R. Vallance, H. J. Kitchen, C. Ritter, S. Kingman, G. Dimitrakis and D. H. Gregory, "Probing the microwave interaction mechanisms and reaction pathways in the energy-efficient, ultra-rapid synthesis of tungsten carbide." *Green Chem.*, **14**, 2184-2192, 2012.

[6] H. J. Kitchen, S. R. Vallance, J. L. Kennedy, N. Tapia-Ruiz, L. Carassiti, A. Harrison, A. G. Whittaker, T. D. Drysdale, S. W. Kingman and D. H. Gregory "Modern Microwave Methods in Solid State Inorganic Materials Chemistry; From Fundamentals to Manufacturing.", *Chem. Rev.*, **114**, 1170−1206, 2014.

[7] J. L. Kennedy, T. D. Drysdale, D. H. Gregory, "Rapid, Energy-efficient Synthesis of the Layered Carbide, Al_4C_3." *Green Chem.*, **17**, 285-290, 2015.

[8] Z. Fan, M. D. Cappelluti and D. H. Gregory, "Ultra-fast, Energy-efficient Synthesis of Intermetallics; Microwave-Induced Metal Plasma (MIMP) Synthesis of Mg_2Sn" *ACS Sustainable Chem. Eng.*, **7**, 19686-19698, 2019.

[9] Z. Fan, G. Baranovas, H. A. Yu, R. Szczęsny, W-R. Liu and D. H. Gregory, "Ultra-rapid Synthesis of the $MgCu_2$ and Mg_2Cu Laves Phases and Their Facile Conversion to Nanostructured Copper with Controllable Porosity; an Energy-efficient, Reversible Process" *Green Chem.*, **23**, 6936 – 6944, 2021.

[10] Z. Fan, H.-N. Ho, R. Szczęsny, W.-R. Liu and D. H. Gregory, "Rapid, Energy-Efficient and Pseudomorphic Microwave-Induced-Metal-Plasma (MIMP) Synthesis of Mg_2Si and Mg_2Ge", *CrystEngComm*, **24**, 5801 - 5809, 2022.

[11] Z. Fan, S. C. Stevenson, A. Mungall, A. Nishio, R. Szczęsny, Y.-G. Lin, M. Chen, W.-R. Liu, S. Okada and D. H. Gregory, "Hierarchical Nanoporous Ge Anodes for Lithium-ion Batteries via Plasma-phase-fabricated Mg_2Ge" *Mater. Adv.*, **3**, 8512 - 8521, 2022.

[12] Z. Fan, W-R. Liu, L. Sun, A. Nishio, R. Szczesny, Y-G. Lin, S. Okada and D.H. Gregory, "Carbon-free Conversion of SiO_2 to Si via Ultra-Rapid Alloy Formation: Towards the Sustainable Fabrication of Nanoporous Si for Lithium Ion Batteries" *ACS Appl. Mater. Interfaces*, **15**, 36076-36085, 2023.

Development of Applications for Hydrogen Energy, Recycling, Food and Bioactivity Based on the Techniques Learned in Microwave Chemistry

S. Horikoshi[1]

[1]*Sophia University, Department of Materials and Life Sciences, Faculty of Science and Technology*
7-1 Kioicho, Chiyodaku, Tokyo 102-8554, Japan
horikosi@sophia.ac.jp

Keywords: microwave, hydrogen energy, waste plastics, biology, bioactivity, food science

Microwave chemistry started in the late 1980s, and the number of research reports has increased since 2000. The microwaves afford a novel promising technology to achieve process escalation owing to rapid, volumetric, and selective heating by microwaves as opposed to conventional heating. These unique abilities of microwave heating have been summarized as Green Chemistry processes. Moreover, the possibility of scale-up of some reactions has also been examined and a scaled-up reactor design has also been reported. Such developments deepened the understanding of microwave irradiation equipment for chemists and made them imagine their own ideas. Along with this, a connection is being made from microwave chemistry to "***microwave science***". In this trend of the times, we are making connections to hydrogen energy, recycling, food science and bioactivity based on microwave chemistry, and we will introduce this point.

Two papers published in 1989 proposed a novel methodological concept in carrying out in organic syntheses [1, 2]. This novel methodology, which can best be described from the old adage ***learn from the old, but know the new*** involved the use of a microwave domestic oven as the heat source in carrying out chemical syntheses. Soon thereafter, there was considerable interest from the chemistry community in the use of microwave energy as an alternative heating method because of some advantages this novel technology offered over conventional heating methods. Currently, the use of microwaves as a heating source to conduct chemical reactions is no longer unusual.

On the other hand, the development of microwave chemistry is linked to the development of microwave equipment. When heating food in a microwave oven, even if the temperature is uneven or does not reach the desired temperature, you can enjoy a satisfying meal by applying further microwave irradiation. On the other hand, what about chemical reactions? If the micro irradiation was insufficient, the sample would not reach the desired reaction temperature, the temperature would overshoot, and the heating would often be uneven. This will not satisfy chemists. In other words, precise microwave control is necessary for chemical reactions. Indeed, after using domestic microwave ovens in the early years of research into microwave chemistry, microwave equipment with user interfaces became available that could automatically control both the temperature and the microwaves regarding frequency range and output power. Users with scarce knowledge of the physical manifestations of electromagnetic waves and custom-made microwave equipment now easily perform chemical syntheses with modern microwave equipment in a manner that parallels the use of a domestic microwave oven.

Apart from that, some chemical reactions have also been reported that cannot be achieved with thermal energy on microwave chemistry. Although these are very attractive research reports, it is difficult to logically understand this phenomenon that cannot be achieved with heat because it requires creative cross-disciplinary consideration. To solve this new phenomenon, many researchers have modified microwave irradiation equipment and investigated it from multiple angles. Due to this background, various new ideas of equipment were announced, which led to significant advances in the engineering of microwave irradiation. Recently, semiconductor microwave generators have become available at low cost, making it possible to perform digital control such as precise frequency control, phase control, and power control of microwaves, opening a new door in the field of "***microwave science***". In particular, the development of microwave engineering cultivated through microwave chemistry is about to open new possibilities in the fields of energy, environment, biology, bioactivity, and food science. In this presentation, we will introduce the possibilities of exploratory research into these possibilities using the author's research as an example.

Approximately 87 million tons of hydrogen were produced worldwide in 2020, with about 30–50% of the production being used for petroleum refining, and the rest used mainly as a basic petrochemical raw material to produce ammonia (Haber process) and methanol (reduction of CO), as well as a fuel in the transportation sector. Important to note, however, most hydrogen produced (~95%) originates from fossil fuels by steam reforming of natural gas (6% of global CH_4) and other light hydrocarbons, together with partial oxidation of methane, coal gasification (2% of global coal), biomass gasification and electrolysis of water. However, the classical steam reforming process with fossil fuels is undesirable as CO_2 is generated (about 830 million tons of carbon dioxide per year) along with the evolution of hydrogen. On the other

hand, generation of hydrogen gas from the direct decomposition of water (water splitting) can be achieved electrically by electrolysis, thermally by thermolysis, and by photolysis using electromagnetic waves, all of which have been investigated for some time. Yet these technologies have not attracted industrial usage because of their relative inefficiencies. Nonetheless, hydrogen is an attractive energy vector that is likely to replace fossil fuels in the near-to-medium term as it avoids the formation of greenhouse gases. We were researched hydrogen gas production by decomposing seawater using microwave absorption heating element (MAHE) as a novel method of obtaining hydrogen. In early research, we reported that hydrogen generation can be achieved quite efficiently from seawater and contaminated waters at low temperatures using a microwave-driven hydrogen production (MDHP) process and waste activated carbon as the microwave absorption heating element (MAHE). However, the problem with this method is that activated carbon (a heat source from the microwaves) is used in the decomposition of water in which the quantity of activated carbon continues to decrease in parallel with the evolution of hydrogen. This problem has been resolved in this study by using magnetite as a novel MAHE component at low temperatures; the energy-saving thermochemical steam reforming reaction was performed with a mixed water/ethanol solution, for which results showed a maximum hydrogen generation yield somewhat greater than 80%. No hydrogen evolved in the thermochemical steam reforming process upon heating the magnetite at 350 °C in a conventional electric furnace, in contrast to the case where hydrogen was generated in yields greater than 40% by heating at 350 °C with microwaves.

Plastics are a typical chemical substance that has made our lives easier. However, the long-term stability of chemical structures of plastics has made post-use processing difficult. For example, in Japan, which has a small land area, more than 50% of waste plastics are treated by thermal recycling, and thermal energy is recovered by burning them. However, since this recycling method produces CO_2 gas, it cannot be sustained from the viewpoint of global warming. Furthermore, although chemical recycling is the most noticeable recycling method, it is not a major recycling process due to its difficulty and process complexity. Pyrolysis is known as one of the most feasible ways to convert waste plastic into chemical materials easily. However, in general, pyrolysis requires a large amount of energy to break down polymers, and the use of energy-efficient heat sources is essential to build a novel recycling process. Additionally, when waste plastic is thermally decomposed by conventional heating, polyaromatic hydrocarbons such as tar and char are usually generated, and resources cannot be obtained.

In the midst of these social problems, we examined the thermal decomposition of waste plastic with MAHE. Polyethylene (PE) was used as model waste plastic, as they have a large amount of production and waste. When microwave heating was performed for 3 min using 7 mg of carbon materials with respect to 70 mg of polyethylene pellets, a gas containing ethylene as a main component was obtained with a gas yield of 84% (**Fig. 1**). Immediately after irradiation with microwaves, the temperature of the sample increased significantly and reached over 1000 °C in a few sec. Microwave heating creates this kind of fast pyrolysis, which is characterized by a microscopic high-temperature field (hot spot) of more than 1500 °C. Upon observing the inside of the reactor after 3 minutes of microwave irradiation, polyethylene is decomposed to the extent that it cannot be visually confirmed after microwave heating. on the other hand, the presence of tar could not be confirmed.

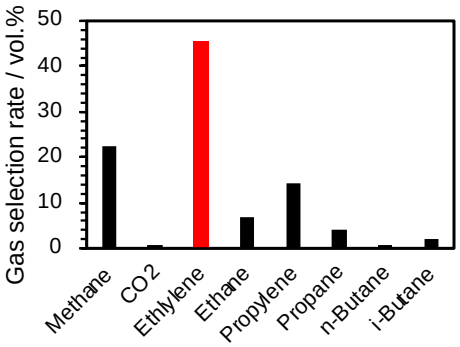

Fig. 1. Gas selection rate of microwave pyrolysis of polyethylene

To evaluate the practicality of the microwave recycling method developed in this research, we thermally decomposed the waste plastics in municipal solid waste collected in Tokyo and evaluated it. After 4 min of microwave heating, the gasification rate was 53%, and the main component of the generated gas was ethylene, so it was expected that the main component of the waste plastic was polyethylene. Even if actual waste plastics are used, monomerization can be achieved in a sufficiently short time. It is believed that further optimization will establish a more perfect chemical recycling method. It was also demonstrated that the pyrolysis of municipal waste can be performed. In addition, it was suggested that it is a sustainable method with little environmental impact that emits almost no carbon dioxide.

Food loss is a problem all over the world, and it is related to SDGs Goal12: Responsible Production and Consumption. Global food loss amounts to about 1/3 of all food production, or about 13 billion tons. Because approximately 800 million people around the world suffer from hunger, this indicates that the problem of hunger can be greatly improved if

appropriate food distribution and consumption are carried out. As a solution to this problem, it is required to freeze food. However, this is not the solution. Although it is possible to freeze food in freshly prepared form, the technology to defrost it to freshly prepared form in a short period of time is very difficult. Microwave heating is expected to heat food to the core, but it is still not possible to maintain quality. Additionally, thawing raw fish or raw vegetables in a very short period can lead to cell rupture. We proposed a new device that uses a semiconductor microwave generators and steam to make it impossible to distinguish between freshly prepared and frozen foods. These heat sources have proven to be able to defrost various types of frozen foods in a very short time while compensating for each other's shortcomings and are already being used in food stores and restaurants.

When using microwaves for living organisms or cells, it is necessary to control the microwaves so that they do not generate heat and do not have weak fluctuations. We will introduce these in the presentation.

References

[1] Gedye, R., Smith, F., Westaway, K., Ali, H., Baldisera, L., Laberge, L., Rousell, J., Tetrahedron Lett. 27, 279–282 (1986).
[2] Giguere, R. J., Bray, T. L., Duncan, S. M., Majetich, G., Tetrahedron Lett. 27, 4945–4948 (1986).

Biomass and Waste Applications

Enhancing the Recycling of Steelmaking by-products by Applying an Innovative Microwave Energy

M. Omran[1], T. Fabritius[1], S. Wölfelschneider[2], H. Schmid[3], M. Häuselmann[4], L. Gronen[5], A. Morillon[5], R. Pietruck[2], D. Adolphy[2]

[1]*Oulun Yliopisto, Process Metallurgy Research Group, Faculty of Technology, University of Oulu, Oulu, Finland*
[2]*VDEh Betriebsforschungsinstitut GmbH, Resource Technology Feedstock, Düsseldorf, Germany*
[3]*voestalpine Stahl GmbH, Research and Development, Linz, Austria*
[4]*K1-MET GmbH, Resources and Recycling, Leoben, Austria*
[5]*FEhS – Institut für Baustoff-Forschung e.V., Secondary Raw Materials / Slag Metallurgy, Duisburg, Germany*
mamdouh.omran@oulu.fi

Keywords: microwave treatment, magnetic properties, dielectric properties, intergranular cracks, steelmaking wastes.

Steel industries generate large streams of by-product wastes annually. The European environmental regulations force the metal industry to take major steps towards efficient recycling of by-product wastes and prohibit the landfilling of wastes. In this work, we propose a method, based on microwave heating, for recycling steelmaking wastes. This will lead to increased electrification of metallurgical processes and reduce greenhouse gas emissions according to the EU Green Deal vision. In this study, microwave energy was applied for the recovery valuable metals from electric arc furnace (EAF) dust and basic oxygen furnace (BOF) slag.

The results indicated that microwave energy improves the recycling of EAF dust. Furthermore, it is observed, that the microwave pre-treatment improves the liberation and grindability of BOF slag through the formation of intergranular cracks on the grain boundaries. This work also found that microwave irradiation under ambient air atmosphere leads to an additional oxidation of wustite in the solid slag. This results in an increased magnetic susceptibility, enhancing the magnetic separation efficiency in comparison to untreated reference samples. Based on this work, more detailed studies are needed to overcome the challenges facing upgrading microwave processes to industrial scale i.e., dielectric properties of slag, design of microwave applicator, and how microwave energy is delivered to the applicator.

Microwave pre-treatment is applied to enhance liberation and magnetic separation of minerals in order to increase efficiency of steelmaking by-product recycling. By using microwave treatment intergranular fractures are generated due to the difference in the absorption of microwave energy, thermal expansion and the dielectric properties of minerals [1, 2]. Microwave radiation has also a significant effect on the magnetic properties of iron bearing minerals while heating up through the formation of new and more magnetic phases that facilitate their separation from non-magnetic minerals [3].

To improve the recovery of valuable metals from BOF slag it is subjected to microwave irradiation (Fig. 1). The cracks are formed due to the thermal stress, induced by the selective heating of the slag, as Fe bearing phases, unlike calcium silicate phases, absorb the microwave irradiation [4]. The microwave pre-treated material is then ground in order to liberate the mineral phases before being subjected to magnetic separation, as the Fe bearing phases show magnetic susceptibility [5]. Dry magnetic separation methods (DMS) are employed.

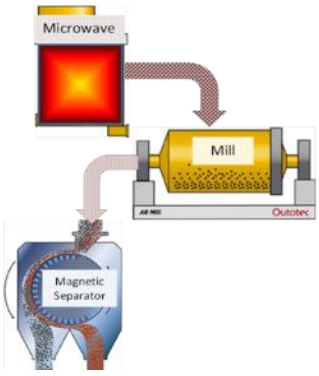

Fig. 1. Experimental flowsheet

Microwave treatment is tested in batch and continuous operation. For batch operation a multi-mode microwave chamber oven, with a 4 kW output power and 2.45 GHz frequency magnetron is used. Samples weighing 1.2 kg are irradiated for 7 and 10 min respectively. For continuous operation of a microwave oven a custom-built device is required. The device features an inclined rotary tube of 70 mm diameter, which transports the slag through the TAIKOTM resonance cavity applicator (up to 30 kW at 915 MHz). Throughputs of 10 kg/h were reached. Both microwave irradiation methods result in a rapid heating of the slag. For batch operation, the bulk temperature of the sample reaches temperatures above 800 °C in five minutes and in continuous operation these temperatures are reached almost instantaneously (less than 30 seconds).

This rapid heating leads to thermal stress in the slag, since only the Fe bearing phases selectively absorb the microwave radiation and neighbouring crystals are heated only by subsequent conductive heat transfer [4]. The thermal stress leads to cracks within the slag structure, as depicted in Fig. 2.

The results indicated that microwave irradiation improved the grindability of the slag. The kinetic grinding test showed that the work index reduces from 27.3 kWh/t for untreated slag to about 7 kWh/t after microwave irradiation. In addition, microwave irradiation had a positive effect on the magnetic mass yield, as it increases by up to 30 %.

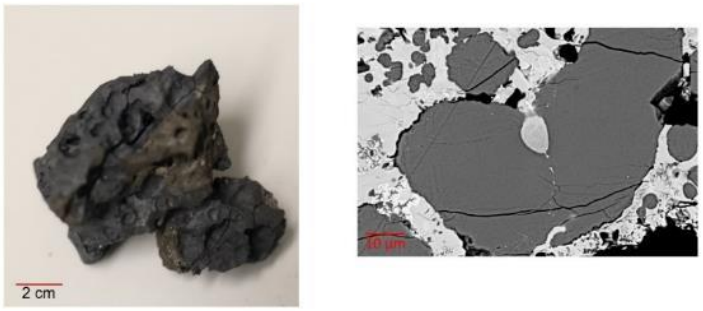

Fig. 2. Optical and SEM images of BOF slag treated at 4 kW microwave power at 2.45 GHz.

References

[1] M. Omran, T. Fabritius, R. Mattila, Thermally assisted liberation of high phosphorus oolitic iron ore: A comparison between microwave and conventional furnaces, Powder Technology 269 (2015): 7-14.
[2] M. Omran, T. Fabritius, A. Mahdy, N. Abd-Elkhalek, S. Gornostayev, Improvement of phosphorus removal from iron ore using combined microwave pretreatment and ultrasonic treatment, Separation and Purification Technology 156 (2015): 724-737.
[3] M. Omran, T. Fabritius, M. El-Aref, N. Abd-Elkhalek, A. Mahdy, Effect of microwave pre-treatment on the magnetic properties of iron ore and its implications on magnetic separation, Separation and Purification Technology 136 (2014): 223-232.
[4] K. Morita, M. Guo, Y. Miyazaki, N. Sano, (2001). The Heating Characteristics of CaO-SiO2-FetO System Slags under Microwave Irradiation. ISIJ International, 41(7) (2001) 716–721.
[5] H. Kubo, K. Matsubae-Yokoyama, T. Nagasaka, (Magnetic separation of phosphorus enriched phase from multiphase dephosphorization slag. ISIJ International, 50(1) (2010) 59–64.

Influence of Microwave Activation Time on CO_2 Uptake Capacity of PET-Derived Adsorbents

E. Dan[1], C. Fernández Martín[1, 3], A. Mccue[2], D. Dionisi[1]

[1]*School of Engineering, University of Aberdeen, AB24 3UE, Aberdeen, UK*
[2]*Department of Chemistry, University of Aberdeen, AB24 3UE, Aberdeen, UK*
[3]*Centre for Energy Transition, King's College, University of Aberdeen, Aberdeen AB24 3UE, UK*
cfmartin@abdn.ac.uk

Keywords: PET, microwave, activated carbon, carbon capture, activation

Microwave-assisted chemical activation (MCA) of char to produce activated carbon (AC) is a way to save energy and lower the overall cost of producing ACs for carbon capture. The high temperature (typically 700ºC) and long duration (2 h) of activation required to produce ACs with significant CO_2 uptake [1] account for most of the increase in energy cost. In MCA, chars are activated at a lower temperature (300–400ºC), in less than 30 min, resulting in ACs with comparable or even higher CO_2 uptake capacities than ACs obtained by conventional activation [1]. These results make the MCA route outstandingly more energy efficient.

There is however need for a more sustainable AC precursors and further investigation on the microwave-assisted AC production parameters that would result in ACs with higher CO_2 uptake, but with the least energy input. Shorter activation times are seen as a good strategy to reduce the amount of energy needed to make ACs [2]. Therefore, the present study assesses the influence of microwave activation time on the CO_2 uptake capacity of an alkaline-impregnated, thermally generated polyethylene terephthalate (PET) char.

Herein, PET waste was carbonized at 600ºC for 1 h in a vertical tubular furnace (VTF) under nitrogen flow (100 mLmin^{-1}). The char was impregnated with KOH at a low KOH:char ratio of 1:1, oven-dried at 105ºC for 12 h, and activated via microwave at 400ºC with varying activation time of 3 to 35 min. Carbon yield, dynamic CO_2 uptake at 298 K, and maximum equilibrium CO_2 uptake at 273 K for the ACs are presented in Fig. 1. The result shows that a shorter activation time of 5 min leads to an AC with optimal yield and CO_2 uptake compared to a longer activation time (15, 25, 35 min). Furthermore, the total CO_2 adsorbed over ten adsorption–desorption cycles was measured. The results indicate that the adsorbents were highly stable after ten repetitive CO_2 adsorption-desorption cycles. Char activated for 5 min showed the highest total CO_2 uptake (16.69 mmol/g) with a stable working capacity of 1.67 mmol/g, whereas the lowest uptake (11.79 mmol/g) was displayed by the one activated for 35 min with a stable working capacity of 1.17 mmol/g. The CO_2 uptake showed by the ACs produced in this work is higher than that of commercial AC Norit R2030CO2, and many published ACs used in CO_2 adsorption [3].

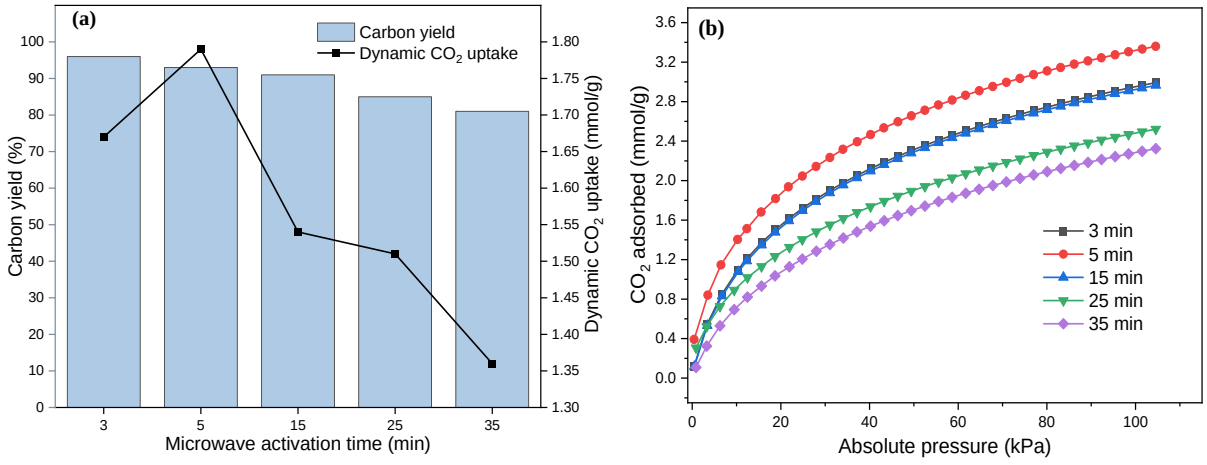

Fig. 1. (a) Correlation between microwave activation time with carbon yield and dynamic uptake, (b) CO_2 isotherm at 273 K for PET-derived ACs

References

[1] G. Duran-Jimenez, L. A. Stevens, E. T. Kostas, J. P. Robinson, and E. R. Binner, "Rapid, simple and sustainable synthesis of ultra-microporous carbons with high performance in CO_2 uptake, via microwave heating," *Chemical Engineering Jour.*, vol. 388, pp. 1-13, Feb. 2020.

[2] H. Ma, O, D. Zhou, Z. Hashisho, S. Wang, H. Chen, H. Wang, and M. J. Lashaki, "Microporous activated carbon from pinewood and wheat straw by microwave-assisted KOH treatment for the adsorption of toluene and acetone vapour," *RSC Adv.*, vol. 5, pp. 36051-36058, Jan.

2015.

[3] A. Mukherjee, J. A. Okolie, A. Abdelrasoul, C. Niu, and A. K. Dalai, "Review of post-combustion carbon dioxide capture technologies using activated carbon," *Jour. of Env. Sci*., vol. 83, pp. 46-63, Mar. 2019.

Appetite Enhancement of *Galleria Mellonella L.* (Honey Worms) for Carbon Recycling of Plastics using Weak Microwaves

R. Murata[1], S. Horikoshi[1]

[1]*Sophia University, Department of Materials and Life Sciences, Faculty of Science and Technology*
7-1 Kioicho, Chiyodaku, Tokyo 102-8554, Japan
horikosi@sophia.ac.jp

Keywords: plastic, food, microwave, *Galleria mellonella,* electromagnetic effect(s)

We propose carbon recycling by using bugs and plastics. Efficiency is a problem in the process of growing insects feeding on plastic, which is the key item of this method. Therefore, we succeeded in slowing the growth of insects under low temperature and improving their appetite by microwave irradiation. We hypothesized that this effect was due to the microscopic thermal and electromagnetic effects of microwaves.

Plastic was first synthesized in the United States in 1907. Since then, it has been used as an important material to support our daily lives. However, since its raw materials are derived from crude oil, the problem of end-of-life waste and use of plastic became a global issue. Among general-purpose plastics, polystyrene (PS) and polyethylene (PE) are produced at a rate of more than 100 million tons per year in terms of function and price. Nevertheless, shortly after being used, they become waste. Therefore, it has a negative impact on the global environment and living organisms. Recently, it has been reported that the larvae of the wax worm (*Galleria mellonella*), a well-known beekeeping pest, can biodegrade PS and PE [1].

From the 1940s to the 1950s, the effects of microwaves on living organisms were debated, mainly divided into thermal effects and non-thermal effects. However, the distinction between the two has been unclear. For the negative non-thermal effects, in 1998, as an example of the non-thermal effects of microwaves on proteins, thermophilic and thermostable enzymes, S-adenosylhomocysteine hydrolase and 5'-methylthioadenosine phosphorylase, were irradiated with microwaves at 10.4 GHz. It has been reported to cause non-thermal inactivation [2].

On the other hand, in 2015, our research is one of the few reporting positive non-thermal effects of microwaves. We have succeeded in immediately evolving the growth rate of plants by irradiating them with very weak microwaves for 15 sec for the seed or the first true leaf. This effect makes it clear that plants induce heat stress tolerance and drought stress tolerance, which makes it possible to grow even in high temperature and low water soil. In addition, insect repellent effect and size control can be achieved.

The world population continues to increase year by year, and it is said that the world population will reach 9.1 billion in 2050, and the global demand for meat will increase by about 200 million tons [3]. However, as the world's livestock population increases, so does the demand for its feed. Since FAO (Food and Agriculture Organization of the United Nations) published the report "Edible insects: Future prospects for food and feed security" [4] in 2013, the use of insects as food and feed has attracted attention. The main factors are that insects are high in protein, can be reared in small spaces, and can feed on low-grade organic waste.

Our strategy for this research is to propose a carbon cycle model for plastics, insects, and humans. First, by eating plastic waste, the carbon in the plastic waste becomes the insect's body. In addition, waste plastics can be used as a food resource for these insects. As the next stage, we will use the insects that have consumed plastic as feed for livestock, transferring carbon from insects to livestock. After that, carbon is taken into humans by using the livestock as human food. As a result, we aim to find a method of carbon conversion of plastics into food for humans via insects and livestock. This can method is a novel example of “Bio-recycling”.

The problem with this bio-recycling, however, is that insects do not eat enough of the plastic. Therefore, by irradiating insects with weak microwaves, we aimed to induce a microwave non-thermal effect (electromagnetic wave effect) and increase the amount of plastic that insects eat.

In a temperature-controlled microwave irradiation chamber with semiconductor microwave generator, honey worm larvae (*Galleria mellonella L.*; 1600 ± 100 mg body weight) were irradiated with microwaves at a constant output. Moreover, the effect of microwave irradiation on the biodegradation of polyethylene foam (PE) and polystyrene foam (PS) in the honey worms was examined based on the amount of PE and PS in the honey worms. The effect of microwave irradiation was studied. The experiment was monitored for 18 days, and the body temperature of the honey worms was measured using a fiber-optic thermometer.

When foamed plastic and honey worms were placed in a container and continuously irradiated with 5 W microwaves, we confirmed that the biodegradation rate of PE and PS increased by 3.5% and 5.5%, respectively, compared to the unirradiated plastic. Our expectations were higher, therefore, another device was devised to increase the honey worms' appetite. By making the honey worm rearing environment harsher, we expected non-thermal activation of honey worms by microwaves. Low temperatures slow honey worm growth significantly and helps prolong their lives, while also reduceing appetite. However, by irradiating the worms with microwaves, their appetite is increased while reducing the growth rate.

Environmental conditions for honey worm growth was strictly fixed at 10°C and irradiated with microwaves at 20 W. While little decrease in mass of PE and PS was observed in the unirradiated honey worms, eating progressed in the microwave-irradiated honey worms (Fig. 1). Microwave irradiation also succeeded in suppressing metamorphosis into pupae. In other words, we were able to reduce the growth rate. When the body temperature of the honey worms was measured, only a 1.4°C temperature increase was observed compared to the initial body temperature of 10.7°C (under 20 W microwave irradiation). This result suggests that microwaves affected the honey worms as electromagnetic energy rather than thermal energy.

We proposed the mechanism of appetite enhancement by microwave irradiation as follows. The effect of microwaves on ion channels in endocrine and locomotor organs improved the fluidity of metabolic and motor processes that had been reduced by the low temperature.

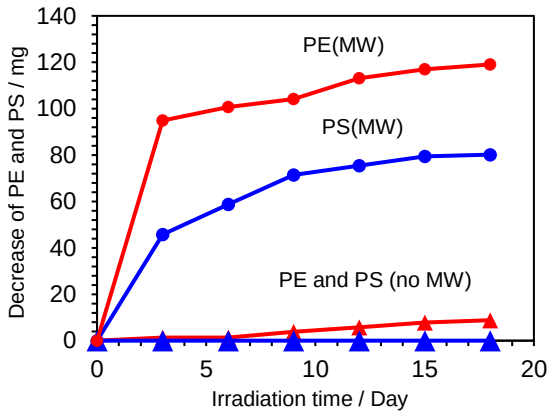

Fig. 1. Amount of plastic eaten by honey worms: foamed polyethylene (PE) and foamed polystyrene (PS)

Since honey worms are poikilotherms, their body temperature depends on their external temperature at low temperatures. Therefore, hypothermic honey worms were prevented from metamorphosing into pupae by inhibiting neuronal hormonal control processes leading to metamorphosis, and by inhibiting temperature-sensitive endocrine organs involved in metabolism and locomotion, plastic crushing was inhibited.

However, the local thermal effect of microwaves acted on the endocrine and locomotory organs and improved the fluidity of metabolic and motor processes, which had declined at low temperatures. We hypothesized that microwaves stimulated appetite by altering the thresholds required to excite action potentials of transmembrane ion channels in the axons of neural networks.

By combining microwave irradiation and low temperature conditions, we succeeded in promoting plastic biodegradation while inhibiting metamorphosis of *Galleria mellonella* into pupae. Furthermore, we suggested the possibility of adapting the optimum conditions of microwave irradiation to lead to a method that can induce and nurture insects. We were able to establish the key technology of the carbon recycling method using living organisms.

References

[1] Y. Lou, P. Ekaterina, S.-S. Yang, B. Lu, B. Liu, N. Ren, P. F-X Corvini, D. Xing, Y. Lou, "Biodegradation of Polyethylene and Polystyrene by Greater Wax Moth Larvae (*Galleria mellonella L.*) and the Effect of Co-diet Supplementation on the Core Gut Microbiome" *Environ. Sci. Technol.*, **54** (2020) 2821.
[2] M. Porcelli, G. Cacciapuoti, S. Fusco, R. Massa, G. d'Ambrosio, C. Bertoldo, M. De Rosa, V. Zappia, Non-thermal effects of microwaves on proteins: thermophilic enzymes as model system, *FEBS Lett.*, **402** (1997): 102.
[3] United nations, Population division of the Department of Economic and Social Affairs of the United Nations Secretariat, 2007.
[4] FAO, Edible insects: Future prospects for food and feed security, 2013.

Efficient Microwave and Radifrequency-Assisted Extraction of Sulfated Polysaccharides from *Ulva* Seaweed

K. Matsuzaki[1], S. Tsubaki[1], N. Igura[1], M. Hiraoka[2]

[1]*Graduate School of Bioresource and Bioenvironmental Sciences, Kyushu University, Fukuoka, 819-0395, Japan*
[2]*Usa Marine Biological Institute, Kochi University, Kochi, 781-1164, Japan*
stsubaki@agr.kyushu-u.ac.jp

Keywords: seaweed biomass, microwave-assisted extraction, sulfated polysaccharide, ulvan

Seaweeds are so-called “blue carbons” which absorb and store CO_2 as useful biomolecules. In particular, *Ulva* seaweeds grow rapidly due to eutrophication in coastal waters due to their high CO_2 fixation capacity. In particular, *Ulva meridionalis* grows up to 4.1 times its mass in a day [1]. Ulva contains a large amount of sulfated polysaccharide called ulvan as a functional component [2]. *Ulva meridionalis* can rapidly synthesize ulvan through its vigorous photosynthesis and carbon fixation [3]. Conventional ulvan extraction requires 1-3 hours with chelating agents [2]. Microwaves selectively heat intra- and inter-cellular layers, thus, promoting the diffusion of the encapsulated compounds within the cells [4]. We have previously reported that microwave-hydrothermal extraction effectively improves the efficiency of extracting ulvan polysaccharides [5]. Herein, we report the effects of extraction conditions such as solid-liquid ratio and frequency (2.45 GHz and 200 MHz) on the extraction of ulvan from *U. meridionalis*.

The extraction was performed using a multi-mode 2.45 GHz microwave oven and closed reactor by changing the heating temperature from 100 ºC to 180 ºC. The maximum yield was reached at 160°C in just 10 minutes of microwave irradiation. However, sugar browning occurred above 160ºC, and the yield decreased significantly. By changing the solid-liquid ratio (0.1 g, 0.5 g, 1.0 g, 1.5 g, 2.0 g, 2.5 g, and 3.0 g in 20 mL), the maximum ulvan yield was obtained at 1.0 g/20 mL, and the yield decreased remarkably at higher solid fractions. From the FT-IR spectra of the extracted polysaccharide, the stretching vibration of S=O was confirmed at 1256 cm^{-1}, indicating that the sulfated ulvan was extracted. In addition, size exclusion chromatography revealed that the molecular weight decreased as the extraction temperature increased. The extracted polysaccharides were decomposed due to autohydrolysis at higher extraction temperatures. Since the molecular weight changes depending on the extraction temperature, the viscosity of the extract can be controlled by microwave conditions.

Next, we investigated the effect of the 200 MHz radio frequency using a parallel-plate type reactor. From the dielectric property measurement of ulvan extract using the coaxial probe method, significant conduction loss was observed in the radio frequency band, which can be attributed to the vibrations of ulvan anions and their cations [6]. Moreover, the conduction loss became prominent at elevated temperatures due to increased ion mobility at higher temperatures. Then, we compared the amount of ulvan extraction by 200 MHz radiofrequency and 2.45 GHz microwaves. The higher sugar yield was achieved by 2.45 GHz, but the glucose content was also high, indicating that 2.45 GHz facilitates the extraction of intracellular starch concomitantly with intercellular ulvan. On the other hand, less glucose yield was observed by 200 MHz suggesting that radiofrequency facilitates more selective extraction of ulvan than 2.45 GHz microwaves.

References

[1] M. Hiraoka, Y. Kinoshita, M. Higa, S. Tsubaki, A. P. Monotilla, A. Onda, A. Dan, “Fourfold daily growth rate in multicellular marine alga *Ulva meridionalis*”, *Sci. Rep*. 10, 12606, 2020.
[2] M. Lahaye, A. Robic, “Structure and functional properties of ulvan, a polysaccharide from green seaweeds”, *Biomacromolecules*, 8, 6, 1765–1774, 2007.
[3] S. Tsubaki, H. Nishimura, T. Imai, A. Onda, M. Hiraoka, “Probing rapid carbon fixation in fast-growing seaweed *Ulva meridionalis* using stable isotope ^{13}C-labelling”, *Sci. Rep*. 10, 20399, 2020.
[4] A. Taqi, E. Facrcot, J. P. Robinson, E. R. Binner, “Understanding microwave heating in biomass-solvent systems”, *Chem. Eng. J*. 393, 124741 2020.
[5] S. Tsubaki, K. Oono, M. Hiraoka, A. Onda, T. Mitani, “Microwave-assisted hydrothermal extraction of sulfated polysaccharides from *Ulva* spp. and *Monostroma latissimum*”, *Food Chem.* 210, 311-316, 2016.
[6] S. Tsubaki, M. Hiraoka, S. Hadano, H. Nishimura, K. Kashimura, T. Mitani, “Functional group dependent dielectric properties of sulfated hydrocolloids extracted from green macroalgal biomass”, *Carbohydr. Polym.* 107, 17, 192-197, 2014.

In-Situ Analysis of Microwave-Boosted Catalytic Pyrolysis of Lignocellulosic Biomass

S. Tsubaki[1], J. Fukushima[2], M. Nishioka[3], H. Einaga[4], T. Sugiyama[5], W.-J. Chun[6], K. Kimijima [7], M. Kimura[7], Y. Wada[8], M. Yasuda[9]

[1]*Graduate School of Bioresource and Bioenvironmental Sciences, Kyushu University, Fukuoka, 819-0395, Japan*
[2]*Department of Applied Chemistry, Graduate School of Engineering, Tohoku University, Sendai, 980-8579, Japan*
[3]*Minamo, Sendai, 983-8551, Japan*
[4]*Department of Advanced Materials Science and Engineering, Kyushu University, Fukuoka, 816-8580, Japan*
[5]*Research Center for Synchrotron Light Applications, Kyushu University, Fukuoka, 816-8580, Japan*
[6]*Graduate School of Arts and Sciences, International Christian University, Tokyo, 181-8585, Japan*
[7]*Institute of Materials Structure Science, High Energy Accelerator Research Organization, Tsukuba, 305-0801, Japan*
[8]*International Research Frontiers Initiative, Tokyo Institute of Technology, Tokyo, 226-8503, Japan*
[9]*Department of Applied Chemistry, Graduate School of Engineering, Osaka University, Osaka, 565-0871, Japan*
stsubaki@agr.kyushu-u.ac.jp

Keywords: catalytic pyrolysis, microwaves, lignocellulosic biomass, in-situ XAFS, in-situ XRD

Due to the depletion of petroleum resources, lignocellulosic biomass is an expected carbon resource to produce essential chemical products since biomass can convert CO_2 into biopolymers. In addition, efficient use of electricity from renewable energy such as solar and wind power is desired to achieve carbon neutrality of the various chemical processes [1]. Microwaves are one of the key technologies to convert electricity into heat by directly supplying energy to materials. Therefore, microwave energy can be effectively applied to converting electrical energy into useful chemicals derived from biomass. Microwave pyrolysis has been widely studied since microwaves rapidly heat biomass which can promote pyrolysis [2]. Highly sharp microwaves by semiconductor generators enable ultra-rapid heating of biomass without using microwave-absorbing heat carriers such as carbon and SiC [3]. More recently, microwave catalytic pyrolysis have been further applied to hydrogen production from plastics [4]. In addition, microwaves have been considered to generate local hot spots on supported metal nanoparticles. The existence of a local hot spot on platinum nanoparticles has been demonstrated by using microwave in-situ X-ray absorption fine structure (XAFS) [5,6]. Direct energy supplied to the metal nanoparticles can enhance catalytic reactions. In this study, microwaves are used to boost the pyrolysis of lignocellulose as well as the catalytic conversion of pyrolyzate by using Ni/SiO_2-Al_2O_3 catalysts. We have also demonstrated the formation of a local high-temperature field on Ni nanoparticles using "*in situ*" observation methods such as XAFS and XRD.

Rapid pyrolysis of cellulose with Ni/SiO_2-Al_2O_3 catalyst (65 wt%) was performed using a single-mode (TM_{010}-mode) applicator equipped with a frequency auto-tracking semiconductor microwave generator. Rapid heating of cellulose at 4987°C/min occurred when no catalyst was added. The rapid temperature increase is attributed to the thermal runaway during the exothermic decomposition of cellulose. On the other hand, the heating rate decreased to 241°C/min with the addition of Ni/SiO_2-Al_2O_3 catalyst. The TG-DTA analysis suggested that the catalytic pyrolysis of cellulose by Ni/ SiO_2-Al_2O_3 is an endothermic reaction. The hydrogen generation rate with Ni/SiO_2-Al_2O_3 catalyst reached 7 times that without a catalyst and doubled with the conventional heating using TG-DTA (heating rate; 50°C/min). In addition, TG-DTA required a reaction temperature of 400-500°C, whereas with the use of microwaves the required reaction temperature fell to 330°C. This is attributed to the formation of the local high temperature of the Ni nanoparticles on the catalyst due to microwave heating, thus, facilitating the endothermic hydrogen evolution reaction from biomass at the Ni/SiO_2-Al_2O_3 catalyst at an apparently low reaction temperature. We have also applied this catalytic reaction system to bamboo as real lignocellulosic biomass. In this case, the temperature reached 600°C with a maximum heating rate of 400°C/min at 40 W. The hydrogen production rate by microwaves was five times higher than that of TG-DTA (50°C/min), demonstrating the high effectiveness of this process.

Then, we estimated the local temperature of the supported Ni nanoparticle during microwave irradiation using in-situ XAFS. The peak intensity derived from the 1st coordination shell of Ni-Ni of Ni/Al_2O_3 catalyst (5 wt%) decreased as the heating temperature increased. The temperature-dependent Debye-Waller factor was calculated from the FT-EXAFS spectra (Ni-K edge). We converted the Debye-Waller factor into temperature using the values obtained by conventional heating (electric furnace) as a calibration curve. The temperature difference between the bulk temperature measured by thermography and the local temperature of Ni nanoparticles observed by in-situ XAFS reached 60–80 °C, demonstrating the local high

temperature at the reaction field around the Ni nanoparticles. Next, we used in-situ XRD to characterize the structural change of the Ni/SiO_2-Al_2O_3 catalyst (65 wt%) under microwaves and compared with the conventional heating using an image furnace (heating rate; 100°C/min). Extensive sintering of Ni particles occurred by microwave heating at 350-400 °C. On the other hand, no remarkable sintering of Ni occurred by conventional heating, even at 1000°C with the peak intensity derived from the Ni nanoparticles gradually decreasing with increasing temperature due to thermal vibration. From the microwave in-situ XAFS and XRD measurements, we demonstrated that a local high-temperature field was generated in the supported Ni nanoparticles by microwave irradiation.

We conclude that microwaves particularly enhance the pyrolysis of lignocellulose by a thermal runaway. In addition, microwaves facilitated the endothermic formation of hydrogen at the Ni/SiO_2-Al_2O_3 catalyst, which is attributed to the formation of local high temperatures at the Ni nanoparticles.

References

[1] K.M van Geem, V.V. Galvita, G.B. Marin, "Making chemicals with electricity", *Science*, vol. 364, pp. 6442, 2019.
[2] R. Luque, J. A. Menéndez, A. Arenillas, J. Cot, "Microwave-assisted pyrolysis of biomass feedstocks: the way forward?", *Energy Environ. Sci.*, 5, 5481-5488, 2012.
[3] S. Tsubaki, Y. Nakasako, N. Ohara, M. Nishioka, S. Fujii, Y. Wada, "Ultra-fast pyrolysis of lignocellulose using highly tuned microwaves: synergistic effect of a cylindrical cavity resonator and a frequency-auto-tracking solid-state microwave generator", *Green Chem.*, vol. 22, pp. 342-351 2020.
[4] X. Jie, W. Li, D. Slocombe, Y. Gao, I. Banerjee, S. Gonzalez-Cortes, B. Yao, H. AlMegren, S. Alshihri, J. Dilworth, J. Thomas, T. Xiao, P. Edwards, "Microwave-initiated catalytic deconstruction of plastic waste into hydrogen and high-value carbons", Nature Catal., vol 3, pp. 902–912, 2020.
[5] T. Ano, S. Tsubaki, A. Liu, M. Matsuhisa, S. Fujii, K. Motokura, W.-J. Chun, Y. Wada, "Probing the temperature of supported platinum nanoparticles under microwave irradiation by in situ and operando XAFS" *Commun. Chem.*, vol 8, 86, 2020.
[6] T. Ano, S. Tsubaki, S. Fujii, Y. Wada, "Designing local microwave heating of metal nanoparticles/metal oxide substrate composites" *J. Phys. Chem. C*, vol 125, 43, pp. 23720–23728, 2021.

Investigation on the Mechanism of Microwave Discharge in Root Vegetables

R. Ito[1], S. Horikoshi[1]

[1]*Sophia University, Department of Materials and Life Sciences, Faculty of Science and Technology*
7-1 Kioicho, Chiyodaku, Tokyo 102-8554, Japan
horikosi@sophia.ac.jp

Keywords: microwave discharge, carrot, root vegetable, fibrovascular bundle

The microwave heating, drying, and sterilization of food is widely used in industrial applications. Although microwave heating has many advantages, it also has its issues. One of them is microwave discharges. If microwave discharge occurs, it leads to deterioration of food quality. The purpose of this study was to systematize the electric discharge phenomenon from root vegetables caused by microwaves and to elucidate the principles. Experiments using carrots as a model food confirmed that sliced carrots easily generate microwave discharges, suggesting that the structure of root vegetables and the ions contained in them are related to the generation of microwave discharges.

The use of microwave heating in the food field has a wide range of industrial applications, including heating, drying, and sterilization, and its features have advantages that differ from those using infrared heating or hot air heating. For example, in the drying field, microwave heating can achieve (1) short heating time, (2) uniform drying, (3) high quality without damaging the flavor and color of the material, and (4) internal sterilization. On the other hand, when microwave irradiation is used on highly conductive materials, such as metals, caution must be exercised because microwave-induced electrical discharges can occur. Such microwave discharge phenomenon can also occur from food. For example, when two grapes are heated side by side inside a microwave oven, microwave discharge occurs between them [1]. This study suggests that grape size and microwave wavelength are important factors in triggering the discharge. However, reproducibility is low and other factors may be involved.

On the other hand, when cubes of carrots are heated in a microwave oven, the corners of the carrots may be discharged by microwaves, and it is common knowledge in the food industry that the carrots are carbonized by this phenomenon. This microwave discharge is probably due to the so-called "edge effect," in which electrons are concentrated in the corners of carrots and microwave discharge occurs. However, we also know that in many cases, even if a thin needle is microwaved in a microwave oven, no microwave discharge occurs. In other words, the edge effect does not always occur. Then why do microwave discharges occur? In particular, we are interested in why microwave discharge occurring from dielectrics such as food. The microwave-induced discharge in food products varies greatly depending on the atmospheric conditions (pressure, temperature (refrigeration), shape, size) and the gap between food products, so it is expected that microwaves cause the microwave discharge for specific situations. While there are advantages of microwaves as described above, the generation of such microwave discharges causes deterioration of food quality, which is a problem of microwave use in industry, and necessary to clarify the principle to improve the process. Furthermore, the elucidation of the principle will contribute to the development of microwave chemistry and material processing. The objective of this study is to systematize and clarify the principles of microwave-induced discharge phenomena, focusing on root vegetables among other foods.

The microwave irradiation apparatus used was a multimode microwave chemical synthesis equipment (EYELA MW0-1000) manufactured by Tokyo Rika Kikai Co. Ltd. Carrots (carrot; Daucus carota subsp.) were edible (five-sun carrots; grown in Chiba Prefecture) and formed into various shapes (stick, cube, round slice, semicircle, quarter slice, ring and center) using a design knife, and one piece of the carrot was subjected to continuous microwave irradiation (Fig. 1).

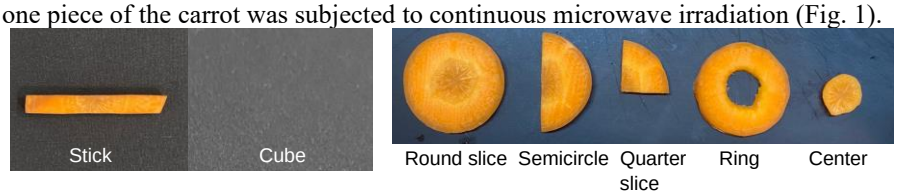

Fig. 1. Photos of carrots of various shapes used in the experiment.

The microwave discharge on the carrot surface was determined visually or by video camera (4K) observation. SEM and optical microscopy observations of the carrots after the microwave discharges were also conducted to confirm the changes to the microstructure after the microwave discharges. In addition, temperature distribution was measured using a thermographic camera to observe partial temperature changes in carrots during microwave heating and microwave discharge. The dielectric factor at 2.45 GHz was also measured using a network analyzer to investigate the interaction between microwaves and carrots.

Microwave irradiation of various shapes of carrots revealed that microwave discharges were generated not only from stick- and cube-shaped carrots (with corners), but also from round slices of carrots (without corners). It was also found that large plasma discharges were generated from the round slices of carrots. Microwave heating in the vicinity of the conduit selectively raised the temperature (Fig. 2a), and high-speed video recording showed continuous microwave discharges from the conduit (Fig. 2b), which eventually led to the confirmation of plasma generation (Fig. 2c). We hypothesized that the microscopic structure of the conduit, ionic components in the conduit, and carbonized portions of the conduit all contributed to the rapid microwave heating. In addition, carbonization progresses when microwave discharges occur, and observation of this carbonization with an optical microscope revealed that it changes into a fibrous structure. These factors were considered to have caused the microwave discharges.

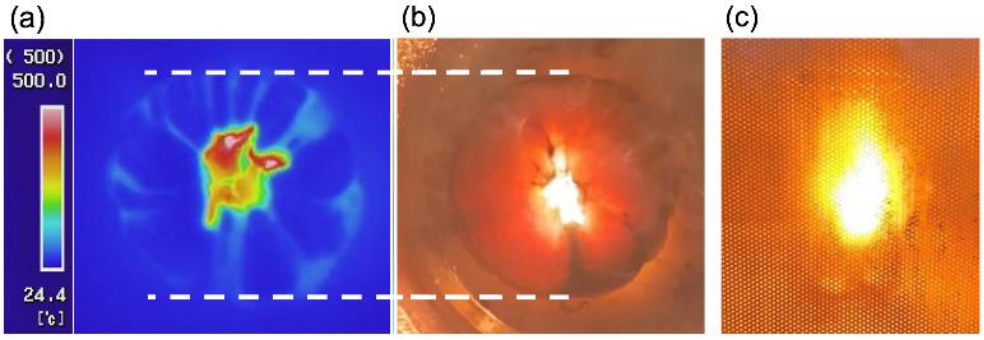

Fig. 2. Photographs of temperature change and microwave discharge generation by microwave irradiation of round sliced carrots: (a) Thermography image of temperature change in cross section, (b) microwave discharge generation from the center of cross section, (c) photograph of plasma taken from outside the applicator.

On the other hand, no microwave discharge was observed from semicircle and quarter slice carrots, suggesting that although ducts are associated with microwave discharge, they are not the only condition for the occurrence of microwave discharges. Similar experiments were conducted with other root vegetables such as burdock root and radish. Microwave discharges and plasma were observed from these root crops as well, but the mechanism of microwave discharge formation was found to be different from that of carrots. Therefore, we hypothesized that chemical components specific to carrots, such as β-carotene, were not involved in the formation of microwave discharges and plasma. We also hypothesized that the length of the microwave wavelength was not involved in the generation of microwave discharges, based on the difference in the diameter of the ring slices.

We measured the dielectric factor at each position of the sliced carrot and found that the dielectric loss in the center was higher than that in the outer circle (Table 1). As a reason for this, we predicted that the inner core of the carrot increased the dielectric loss. Furthermore, our results show when the carbonized part of a carrot is exposed to microwaves, it generates a large-scale plasma. This plasma is only generated in the carbonized part that previously experienced microwave discharge and not in the rest of the carrot. Additionally, when the carbonized part is exposed to microwaves again, it immediately undergoes microwave discharge, further indicating its relationship to the generation of large-scale plasma.

Table 1. Dielectric factors (relative permittivity (ε_r'), dielectric loss (ε_r''), tan δ) of round sliced carrot with and without microwave discharges occurrence.

	Position	εr′	εr″	tan δ
before microwave irradiation	Center	67.7	21.1	0.31
	Outside	63.9	15.0	0.23
after microwave discharges	Center	35.4	28.3	0.80
	Outside	40.0	14.2	0.36

We found that some microwave discharges generated from carrots by microwaves originate from the corners and others from the vicinity of the inner core. We also found that when a micro-carbonized area is generated by the microwave discharges, it leads to the generation of plasma from this starting point.

References

[1] H. K. Khattak, P. Bianucci, A. D. Slepkov, "Linking plasma formation in grapes to microwave resonances of aqueous dimers" *PNAS*, **2019**, *116*, 4000−4005.

Comparative Study Between Different Methods for Hydroxyapatite Valorisation from Solid Food Waste

M. Patrascu[1], C. Marculescu[1]

[1]*Power Engineering Faculty, POLITEHNICA University of Bucharest, Romania*
marianapat29@hotmail.com

Keywords: microwave, solid food waste, solid state microwave generator, convective heating, hydroxyapatite, food -waste technology

The aim of this study is to investigate the performance of microwave heating at both industrial frequencies of 2450 MHz and 915 MHz for the treatment of solid food waste from fast food restaurants for its valorisation in view of producing valuable chemicals. The core of the research is based on the comparative study of three reactors, namely NABERTHERM tubular reactor with convective heating (CH), and two batch microwave reactors supplied by solid state microwave generators operating at 2450 MHz and 915 MHz, for the production of hydroxyapatite (HA) from chicken bones (CB).

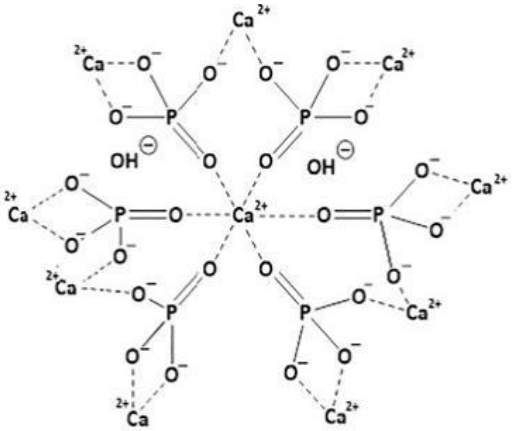

Fig. 1. Hydroxyapatite (HA) structure

The chicken bones were firstly cleaned using ultrasounds in the presence of H_2O_2 35%. In the second step CB were embrittled with ultrasounds in the presence of lipase and protease enzymes.

After the above pretreatment, the CB underwent the thermal treatment. The thermal treatment consisted of calcination at three different temperatures, i.e. 250 °C, 350 °C and 450 °C, with a heating rate of 10 °C/min under a 4 hour holding time in the CH reactor while under microwave field the heating rate was 5° C/min. The calcined samples were milled into fine powder for characterization by FTIR, SEM and BET analysis.

Future research will be focused on the development of new applications of the obtained HA as a platform for natural co-crystals for veterinary uses.

Acknowledgement
Funding provided through Romania's PNRR/2022/C9/MCID/I8 Component C9. Support for the private sector, research, development and innovation, "I8. Development of a program to attract highly specialised human resources from abroad in research, development and innovation activities", Contract no. 760094/2023.

References

[1] Soo-Ling Beea, M. Mariattia, N. Ahmada, B. H. Yahayab, Z. A. Abdul Hamid,'' Effect of the calcination temperature on the properties of natural hydroxyapatite derived from chicken bone wastes'', in Materials Today: Proceedings 16, (2019) 1876–1885.
[2] Vinay Kumar, Neha Sharma, Mridul Umesh, Manickam Selvaraj, Badria M. Al-Shehri, Pritha Chakraborty, Lucky Duhan, Shivali Sharma, Ritu Pasrija, Mukesh Kumar Awasthi, Siva Ramakrishna Lakkaboyana, Rodrigo Andlerl, Amit Bhatnagar, Subhrangsu Sundar Maitra, '' Emerging challenges for the agro-industrial food waste utilization: A review on food waste biorefinery'', Bioresource Technology 362 (2022) 127790.
[3] Arul Jayanthi Antonisamy, Sivasankari Marimuthu, Sankar Malayandi, Karthikeyan Rajendran, Yuan-Chung Lin, Gangadhar Andaluri, Siew Ling Lee, Vinoth Kumar Ponnusamy, '' Sustainable approaches on industrial food wastes to value-added products – A review on extraction methods, characterizations, and its biomedical applications'', Environmental Research 217 (2023) 114758.
[4] Marilena Radoiu, Ariel Mello, '' Technical advances, berrieres, and solutions in microwave – assisted technology for industrial processing'', in Chemical Engineering Research and Design 181, (2022), 331 – 342.
[5] Mário Andrean Macedo Castro, Thayane Oliveira Portela, Gricirene S. Correa, Marcelo Moizinho Oliveira, José Hilton Gomes Rangel b, Samuel Filgueiras Rodrigues, José Manuel Rivas Mercury, '' nthesis of hydroxyapatite by hydrothermal and microwave irradiation methods from biogenic calcium source varying pH and synthesis time'', Boletín de la sociedad española de cerámica y vidrio 61 (2022) 35–41.

Microwave Dielectric Properties of Biomass in Combustion and Pyrolysis Environment

A. A. Salema[1], J. Mouris[2], R. Hutcheon[2]

[1]*School of Engineering, Monash University Malaysia, Jalan Lagoon Selatan, Bandar Sunway 47500, Selangor Darul Ehsan, Malaysia*
[2]*Microwave Properties North, Deep River, Ontario K0J 1P0, Canada*
arshad.salema@monash.edu

Keywords: biomass, dielectric properties, microwave, combustion, pyrolysis

In recent years, microwave (MW) heating has become one of the emerging technologies to valorise the biomass materials specifically for thermo-chemical processes (pyrolysis and gasification). Several biomass materials such as oil palm shell [1], empty fruit bunch [2], rice husk [3], wood [4] and others [5-7] have been processed using MW technology. Most of these research works are conducted under an inert environment or using a pyrolysis process. Very recently, some limited work on biomass gasification [8] and combustion [9] under microwave irradiation have been published. The change in process or gas environment (air/oxygen or nitrogen) will impact the interaction of biomass with microwaves as well as its dielectric properties. The comparison of microwave dielectric properties of biomass under oxygen/air and nitrogen environment has not been reported yet in the literature. That provides some crucial information such as the change in MW absorption characteristics of the material during processing, the penetration depth, and how well the material will absorb or reflect MW energy at particular temperatures. Dielectric properties are also considered as the most important factors for designing large-scale MW systems [10], and lack of proper understanding about the dielectric properties may hinder the development of MW technology [6].

Therefore, this research work reveals the microwave dielectric characterization of oil palm biomass during the combustion process and compares with the pyrolysis process. The dielectric properties (dielectric constant (ε), and loss factor (LF)) were measured during heating process from room temperature to ~700 °C and at two industrial frequencies (912 and 2450 MHz). The loss tangent (LT) and penetration depth (PD) were calculated based on the measured dielectric properties data.

The oil palm shell (OPS) and empty fruit bunch (EFB) biomass samples were pulverized to particle size of ~ 100-600 μ m and the dielectric measurements were done on pelletized (formed by uniaxial pressing at ~130 MPa in a die lined with tungsten carbide) samples. The dielectric properties were measured during combustion (air) and pyrolysis (nitrogen) using the cavity perturbation technique developed by Microwave Properties North, Canada [11] and the details are provided by previous articles [12]. The cavity perturbation system measures between 400-3000 MHz and has a temperature range up to 1400 °C. The size of the sample is small (~0.1 cm^3), and is sensitive enough for low-loss material such as biomass. Unlike the pyrolysis process, miniature material (ash) was left after the combustion process.

The values of ε for EFB and OPS had similar profiles (Fig. 1) when the temperature was increased from room to 700 °C. The value of ε varied between 2.5 to 4. A peak was observed around 175 °C (just after the drying stage) indicating the MW response to the degrading structure and the mobile ions created during the initial combustion and pyrolysis reaction. A significant drop (~60 to 65 %) in the ε was observed in the temperature region from 175 °C to 500 °C. The values of ε almost plateaued beyond 500 °C up to 700 °C, with a slight increase at 550 °C. The EFB ash formed at 700 °C showed the highest ε, followed by OPS. The profiles (Fig. 1) of LF were almost similar to those of ε except that of the EFB. OPS showed two peaks at 200 and 325 °C, respectively, while the EFB sample depicted two peaks at 200 and 175 °C, respectively after the drying stage and at 275 and 400 °C, respectively during combustion. This result almost agrees with the derivative thermogravimetric (DTG) curves (in Fig. 1) that typically shows two peaks for biomass combustion. The ε and LF did not show a strong dependency on frequency during the combustion process.

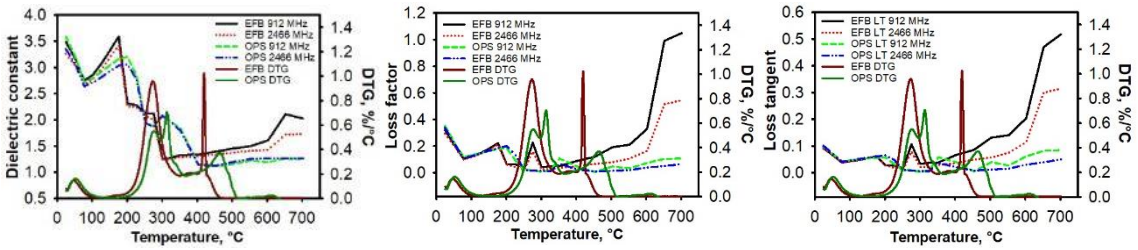

Fig. 1. Dielectric constant and loss factor of biomass at different frequencies in combustion environment.

The profiles of the ε and LF agreed well with previous studies [13-15] from room temperature to 300 °C in drying and to some extent in combustion region. However, it was completely different during char and ash formation stage (Fig. 1). The decrease in dielectric properties between 200 °C and 450 °C during the combustion can be attributed to the loss of molecules from the biomass due to decomposition of lignocellulosic matter. Basically, at this stage depolymerization occurs in the structure of the biomass material at elevated temperature. At this temperature, the volatile contents are released and the biomass shrinks significantly due to weight loss (about 60 to 80%). This results in the change of material density.

The dielectric properties in the char and/or ash formation (450 to 700 °C) during combustion were completely different from that of the pyrolysis process (Fig. 3). The ε and LF remained almost constant between 350 °C and 700 °C during the combustion process, while it drastically increased during this temperature rise in the pyrolysis process. It seems that the 'effective conductivity' of the samples were lost during the combustion process either due to complete loss of material or change in the chemical properties of the ash material. Unlike the biochar produced during pyrolysis which showed an increase in loss tangent beyond 450 °C, the loss tangent for ash material formed during combustion showed very minimal increase. OPS ash depicted highest dielectric constant, relatively smaller penetration depth at two well-known industrial used frequencies (912 MHz and 2466 MHz). Besides this, loss factor, loss tangent and penetration depth did not show any particular trend for these frequencies. This was due to very little sample mass remaining at the end of the combustion process.

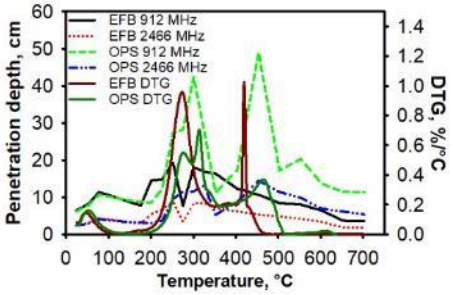

Fig. 2. Microwave penetration depth in the biomass sample at different frequencies in combustion environment.

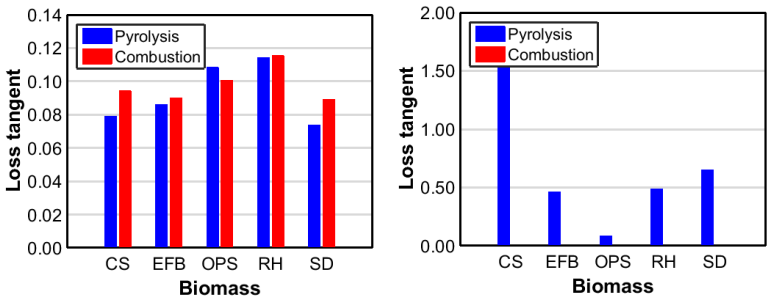

Fig. 3. Loss tangent of biomass in combustion and pyrolysis environments (24 °C and 2540 MHz)

References

[1] A.A. Salema, F.N. Ani, "Microwave-assisted pyrolysis of oil palm shell biomass using an overhead stirrer," J Anal Appl Pyrolysis, vol. 96, pp. 162-72, 2012.
[2] A.A. Salema, F.N. Ani, "Pyrolysis of oil palm empty fruit bunch biomass pellets using multimode microwave irradiation," Bioresour Technol., vol. 125, pp. 102-107, 2012.
[3] Y.F. Huang, W.H. Kuan, S.L. Lo, C.F. Lin, "Hydrogen-rich fuel gas from rice straw via microwave-induced pyrolysis," Bioresour Technol., vol. 101(6), pp. 1968-1973, 2010.
[4] J.P. Robinson, S.W. Kingman, R. Barranco, C.E. Snape, H. Al-Sayegh, "Microwave pyrolysis of wood pellets," Ind. Eng. Chem. Res., vol. 49(2), pp. 459-463, 2009.
[5] X. Ren, M.S. Ghazani, H. Zhu, W. Ao, H. Zhang, E. Moreside, J. Zhu, P. Yang, N. Zhong, and X. Bi, "Challenges and opportunities in microwave-assisted catalytic pyrolysis of biomass: A review," Applied Energy, vol. 315, pp. 118970, 2022.
[6] I.J. Siddique, A.A. Salema, E. Antunes, and R. Vinu, "Technical challenges in scaling up the microwave technology for biomass processing," Renewable and Sustainable Energy Reviews, vol. 153, pp.111767, 2022.
[7] A. Suresh, A. Alagusundaram, P.S. Kumar, D.V.N. Vo, F.C. Christopher, B. Balaji, V. Viswanathan, and S. Sankar, "Microwave pyrolysis of coal, biomass and plastic waste: a review," Environmental Chemistry Letters, vol. 19, pp. 3609-3629, 2021.
[8] C. Ke, C. Shi, Y. Zhang, M. Guang, and B. Li, "Energy conversion performances during biomass air gasification process under microwave irradiation," International Journal of Hydrogen Energy, vol. 47(74), pp. 31833-31842, 2022.
[9] S. Sathish, R. Nirmala, H.Y. Kim, and R. Navamathavan, "Deriving activated carbon using microwave combustion technique and its energy storage applications: a topical review," Carbon Letters, vol. 32(5), pp. 1151-1171, 2022.
[10] M. Al-Harahsheh S. Kingman, A. Saeid, J. Robinson, G. Dimitrakis, and H. Alnawafleh, "Dielectric properties of Jordanian oil shales," Fuel Proc Tech vol. 90(10), pp. 1259-1264, 2009.
[11] R. Hutcheon, M.D. Jong, F. Adams, G. Wood, J. McGregor, and B. Smith, "A System for Rapid Measurements of RF and Microwave Properties Up to 1400° C. Part 2: Description of Apparatus, Data Collection Techniques and Measurements on Selected Materials," Journal of Microwave Power and Electromagnetic Energy, vol. 27(2), pp. 93-102, 1992.
[12] A.A. Salema, F.N. Ani, J. Mouris, and R. Hutcheon, "Microwave dielectric properties of Malaysian palm oil and agricultural industrial biomass and biochar during pyrolysis process," Fuel Processing Technology, vol. 166, pp. 164-173, 2017.
[13] F. Motasemi, M.T. Afzal, A.A. Salema, J. Mouris, and R.M. Hutcheon, "Microwave dielectric characterization of switchgrass for bioenergy and biofuel," Fuel, vol. 124, pp. 151-157, 2014.

[14] F. Motasemi, A.A. Salema, and M.T. Afzal, "Dielectric characterization of corn stover for microwave processing technology," Fuel Processing Technology, vol. 131, pp. 370-375, 2015.
[15] H.H. Sait, and A.A. Salema, "Microwave dielectric characterization of Saudi Arabian date palm biomass during pyrolysis and at industrial frequencies," Fuel, vol. 161, pp. 239-247, 2015.

Microwave-Assisted Biomass Pyrolysis for the Obtention of High-Porosity Biochar

J. Navarro-Sánchez[1], P. Díaz[1], A. M. López-Buendía[1], L. S. Esteban[2], M. E. Borjabad[2], R. Ramos[2]

[1]*CEINNMAT, INNCEINNMAT SL. C/ Catedrático Escardino 9, 46980 Paterna, Valencia, Spain*
[2]*CEDER-CIEMAT, Autovia A-15, salida 56, 42290 Lubia, Soria, Spain*
jose.navarro@ceinnmat.com

Keywords: microwave, biomass, pyrolysis, biochar, porosity

Pyrolysis occurring in the absence of oxygen is one of the most promising thermal treatments for transforming biomass wastes into valuable products, such as biochar and energy dense, uniform and easily transportable fuel [1]. However, such treatments are very energy demanding, as the complex structure and diversity of the biomass residues requires very high processing temperatures. In this sense, microwave heating is a promising alternative to the pyrolysis by conventional heating approaches as it is able to conduct energy to materials with higher heating rates and higher energy efficiencies [2].

Biomass pyrolysis products used to be a biochar, a condensable tar and a bio-oil, whose proportion and quality strongly depends on the processing conditions [3]. In this work, we have focused on biochar properties developing some experiments to evaluate the influence of material conditioning, process variables and microwave parameters on the final quality of the biochar. In fact, the more appealing property of biochar is porosity, thus microwaves can be applied to reduce the bioavailability of pollutants, especially heavy metals, in soil. This will help tackle the issues of climate change by sequestering carbon and depleting fossil fuels via bio-oil and syngas production [4].

More specifically, the key operating parameters that have been explored are initial moisture content of the samples, microwave power, temperature and heating rate, and initial sweep gas flow rate/residence time. To sum up, it has been demonstrated that the microwave pyrolysis systems allow fast heating rates and minimization of thermal gradients in the material optimising the production of a porous and homogeneous biochar displaying 150 m^2/g of Brunauer-Emmett-Teller (BET) surface area (Figure 1).

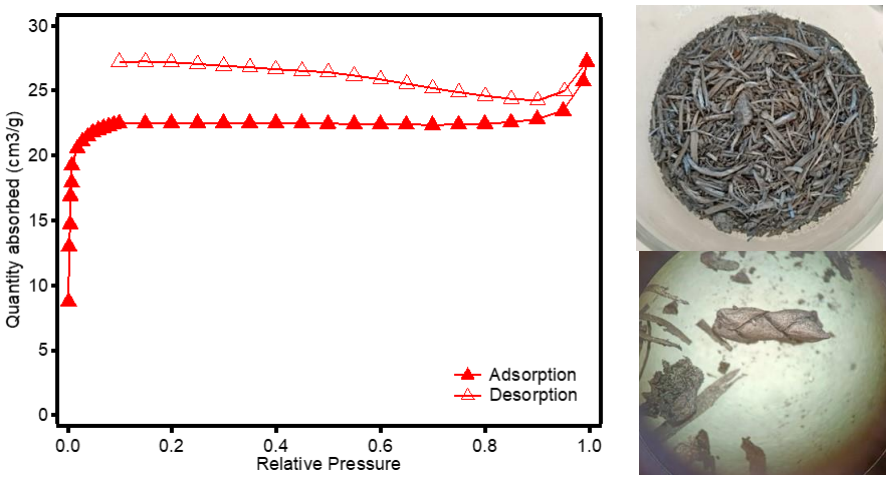

Fig. 1. N_2 porosity graph (left) and biochar production (right).

References

[1] Wystalska, K. & Kwarciak-Kozłowska, A. The Effect of Biodegradable Waste Pyrolysis Temperatures on Selected Biochar Properties. Materials 14, 1644 (2021).
[2] Bartoli, M., Rosi, L., Giovannelli, A., Frediani, P. & Frediani, M. Characterization of bio-oil and bio-char produced by low-temperature microwave-assisted pyrolysis of olive pruning residue using various absorbers. Waste Manag. Res. 38, 213–225 (2020).
[3] Ethaib, S., Omar, R., Kamal, S. M. M., Awang Biak, D. R. & Zubaidi, S. L. Microwave-Assisted Pyrolysis of Biomass Waste: A Mini Review. Processes 8, 1190 (2020).
[4] Oliveira, F. R. et al. Environmental application of biochar: Current status and perspectives. Bioresour. Technol. 246, 110–122 (2017).
[5] Lv, P. et al. Investigation into the interaction of biomass waste with industrial solid waste during co-pyrolysis and the synergetic effect of its char gasification. Biomass Bioenergy 159, 106414 (2022).

Microwave-Assisted Pyrolysis of Cellulose for Wide-Band Microwave Absorption under a Double-Layer Design

Y. Zhou[1]

[1]*College of Electronics and Information Engineering, Sichuan University, #29 Wangjiang Road, Chengdu, China*
ypzhou11@scu.edu.cn

Keywords: microwave-assisted pyrolysis, cellulose carbon, multi-layer microwave absorption

With the rapid development of microwave technology and the widespread application of wireless communication devices, the problems of electromagnetic interference (EMI) and EM radiation on human life have dramatically increased. Hence, the development of microwave absorption materials (MAMs) with good absorption capability, light weight, wide efficient absorption bandwidth (EAB), is imminent.

In this work, cellulose is annealed in a tube furnace at 800 ℃ and 900 ℃ to yield cellulose carbon (CC), designated as CC-800 and CC-900, respectively. Further, the CC-900 sample is irradiated by microwave in a ridge waveguide at 400 ℃ for 5 min to yield the sample CC-900-MW400. The CC-800 sample was mixed with paraffin at a weight ratio of 1:9, and pressed into a ring with Φ out = 7.00 mm, Φ in = 3.04 mm, yielding the sample CC-800-10%. Similarly, CC-900 and CC-900-MW400 was mixed with paraffin at a weight ratio of 3:7 respectively and pressed into the ring (designated as CC-900-30% and CC-900-MW400-30%, respectively) for EM parameter measurement which was conducted on an Agilent E8363C vector network analyser equipped with a coaxial transmission line. By comparing the EM parameter characterization of CC-900-30% and CC-900-MW400-30% shown in Figure 1, it can be seen that microwave irradiation enhances the parameters of the permittivity of the CC-900 sample, especially the imaginary part which is very beneficial for microwave attenuation. Finally, a double-layer microwave absorption material with CC-800-10% as the upper layer and CC-900-MW400-30% as the bottom layer is developed (shown in Figure 2), exhibiting an EAB of 11.0 GHz when the upper layer is 2.68 mm thick and the bottom layer is 1.72 mm thick.

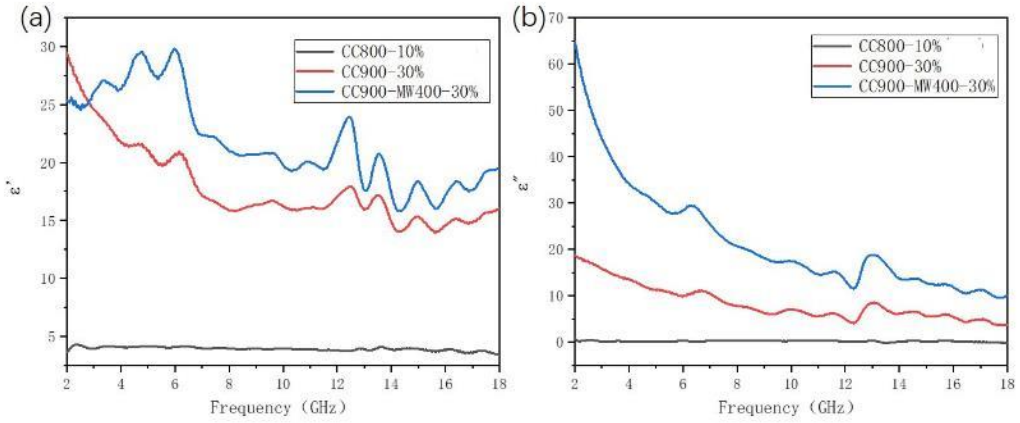

Fig. 1. The permittivity parameters of the CC-800-10%, CC-900-30%, and CC-900-MW400-30% samples showing (a) real part of the permittivity and (b) imaginary part against frequency

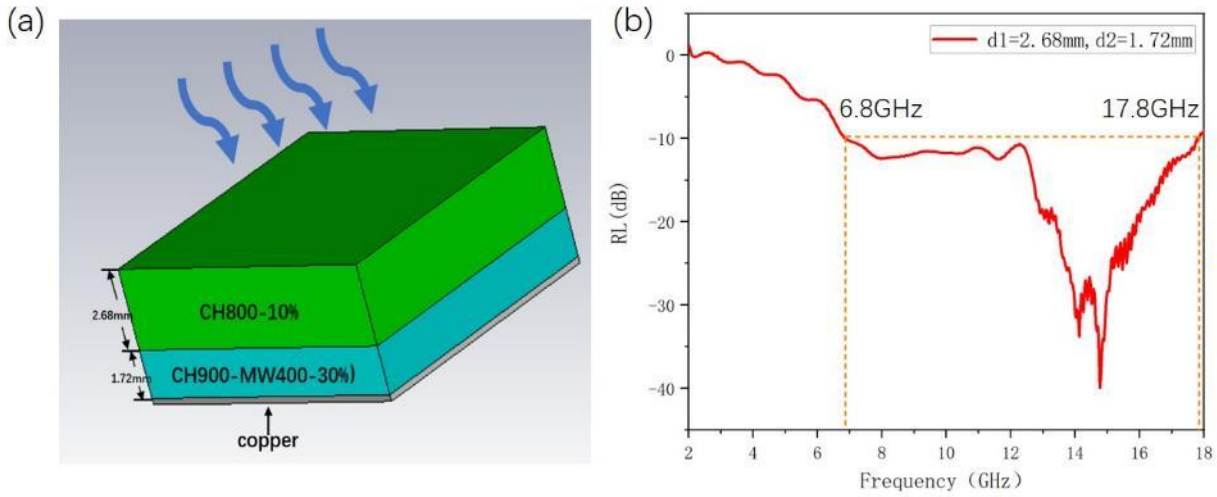

Fig. 2. (a) The double-layer model and (b) its microwave absorption performance.

Microwave Pyrolysis of Mixed Hydrocarbon Waxes and Polyolefin Plastic Waste to Produce a Linear Alpha Olefins

V. A. Bolotov[1], V. N. Parmon[1]

[1]*Federal Research Center Boreskov Institute of Catalysis, Lavrentiev Ave. 5, Novosibirsk, Russia*
bolotov@catalysis.ru

Keywords: microwave, pyrolysis, paraffin wax, polyolefin plastic waste, linear alpha olefins

Approximately 350 million tons of polymer materials are produced worldwide every year including more than 200 million tons of packages and short-lived items to be transformed immediately to solid municipal waste. Polymers are practically non-biodegradable that makes them, when placed on waste disposal sites, environmentally harmful. At present, no more than 10 % of plastic wastes are treated using mainly thermomechanical methods. These are energy-intensive processes, while the number of processing cycles is limited (no more than 2–3 cycles).

An alternative way for plastic waste management is thermal cracking to produce various fuels (coke, liquid hydrocarbon and gaseous fuels) or valuable petrochemicals including initial monomers. It should be noted that thermal cracking (pyrolysis) does not require costly procedures for crude pretreatment such as purification of polymers containing nitrogen, sulfur, phosphorus and chlorine compounds which may poison catalysts at later treatment stages.

Among the main disadvantages of thermal cracking are high energy consumption and the necessity of the further upgrading of the products obtained. Microwave (MW) heating of the reaction mixture can be considered as a promising method for depolymerization of plastic waste. Effective heat energy supply to the reactants is characteristic of the MW heating that provides acceleration of the depolymerization process and, therefore, reduces overall cost of the process.

There are a number of problems with MW heating for processing of polyolefins (PE and PP) because of considerable temperature nonuniformity in the reactor. This is due to the necessary introduction of special additives (MW absorbers) to the polymer (which are MW-nonabsorbent) in order to effectively transform MW energy for heating reactants. In thermocatalytic cracking, polyolefins are predominantly in the form of melts where heat and mass transfer processes are hampered. This causes emerging points of local overheating, the process becomes uncontrolled, and carbonization products predominate.

A nontraditional approach is suggested for overcoming the problems. The approach was developed [1] and tested in the processes of thermodecomposition of high-molecular hydrocarbons (linear C_{16+} paraffins, fuel oil, vacuum residue). This is a liquid-phase process when a three-phase 'solid catalyst – gas – liquid phase' system is formed owing to the selective MW heating. If so, the transformation products with the composition atypical of the traditional (uniform) heating of the catalytic system can be formed and stabilized. As a result, kinetic control is allowed during the catalytic process. More specifically, primary products of thermocatalytic transformations on the catalyst surface can be 'quenched' rapidly during their diffusion into the bulk of colder reaction mixture around the catalyst. For example, we observed selective formation of linear alpha olefins (LAO) during the MW pyrolysis of C_{16+} n-alkanes [2].

For the liquid-phase process of MW pyrolysis of plastic waste, pre-dissolution of polyolefins in hydrocarbon media (paraffins, naphthenes, arens) is necessary [3]. The use of solvents with contents of paraffins results in an increase in the yield of linear alpha olefins; naphthene- and arene-based solvents do not suffer from cracking and can be repeatedly used.

This work presents the results obtained during studies of MW pyrolysis of LLDPE solutions (packaging film, 4-15 wt.%) in paraffin wax and vacuum gasoil (VGO). Granules of silicon carbide (SiC, fraction 1-1.4 mm) were used as MW absorbers at the ratio mixture:SiC = 10:1. The MW pyrolysis was carried out using a lab scale set up (power up to 450 W) based on a rectangular single-mode cavity with high Q-factor (~6000), which is excited by oscillation mode TE_{102}. The MW lab scale set up used for the experimental studies consisted of a solid-state generator (Sairem, operating frequency 2450 ± 50 MHz,) and cavity-reactor [4]; pyrolysis was studied using a semi-batch quartz reactor (volume V=10 ml.). GCxGC-MS chromatography was used to analyzing liquid products. Typical composition of the liquid (condensed) products is given in Tables 1 and 2.

Table 1. Composition of liquid products of MW pyrolysis of mixed VGO and LLDPE (4 wt.%).

Boiling point data (wt.%)	n-Alkane	Cycloalkane	Aromatics	Isoalkane	LAO	Other Alkene	Alkadiene
Gasoline (IBP < 200° C)	0.50	2.27	14.93	0.00	23.51	19.68	7.81
Diesel (200-350° C)	1.02	1.27	3.69	0.33	1.98	1.66	1.78

VGO (350-500° C)	5.20	1.85	3.46	5.64	0.48	1.14	1.44
Residual (>500°C)	0.09	0.14	0.00	0.14	0.00	0.00	0.00
Total	6.80	5.53	22.08	6.11	25.98	22.48	11.02

Table 2. Composition of liquid product of MW pyrolysis of mixed paraffin wax and LLDPE (4 wt.%).

Boiling point date (wt.%)	n-Alkane	Cycloalkane	Aromatics	Isoalkane	LAO	Other Alkene	Alkadiene
Gasoline (IBP < 200° C)	1.24	3.43	2.30	0.00	48.89	2.16	8.90
Diesel (200-350° C)	1.73	1.77	1.04	0.00	15.10	1.04	4.82
VGO (350-500° C)	4.34	0.57	0.04	1.07	0.96	0.33	0.21
Residual (>500°C)	0.01	0.01	0.00	0.03	0.00	0.00	0.00
Total	7.33	5.78	3.38	1.11	64.95	3.53	13.93

The data obtained was used for assessment of the possibilities of scaling-up the MW pyrolysis process. With this aim in view, we developed a chemical reactor – MW applicator (volume V=1000 ml.) with combined component heating using the electrical and MW energy and heat and gas insulation from peripheral devices. Possibilities of heat and MW energy supply (power up to 5 kW) was provided. The applicator was a cylindrical stainless-steel resonator excited by oscillation mode TE_{115}. It contains two sections of a circular waveguide connected by a flexible waveguide (sylphon). The first section is short - circuited by a conducting plate, a waveguide MW input is mounted on the second one. Tuning of the resonance frequency in the range of 2450 ± 15 MHz and heat insulation from the peripheral devices is provided by the sylphon, the gas insulation by a radiotechnical mica partition mounted in front of sylphon in the resonator. A quartz glass setting disk placed directly against the shortening plate. The disk is mounted so that the first maximum of the electric field is near the disk surface. The additional heat energy supply through the cavity walls by electrical heating elements mounted above the first waveguide section was provided.

MW pyrolysis of mixed paraffin wax and LLDPE (15 wt.%) was achieved. Granules of silicon carbide (15 g SiC, fraction 1-1.25 mm) were used as MW absorbers at the ratio mixture:SiC = 30:1. The following results were obtained: conversion 27.9%, selectivity LAO – 67.8%. Process parameters: 180 min., T = 380° C , MW power P=500 ± 50 W. Qualitative and quantitative analysis of gaseous and liquid products and cracking residue was conducted. The data obtained was used for calculating the mass balance of MW pyrolysis (Fig. 1).

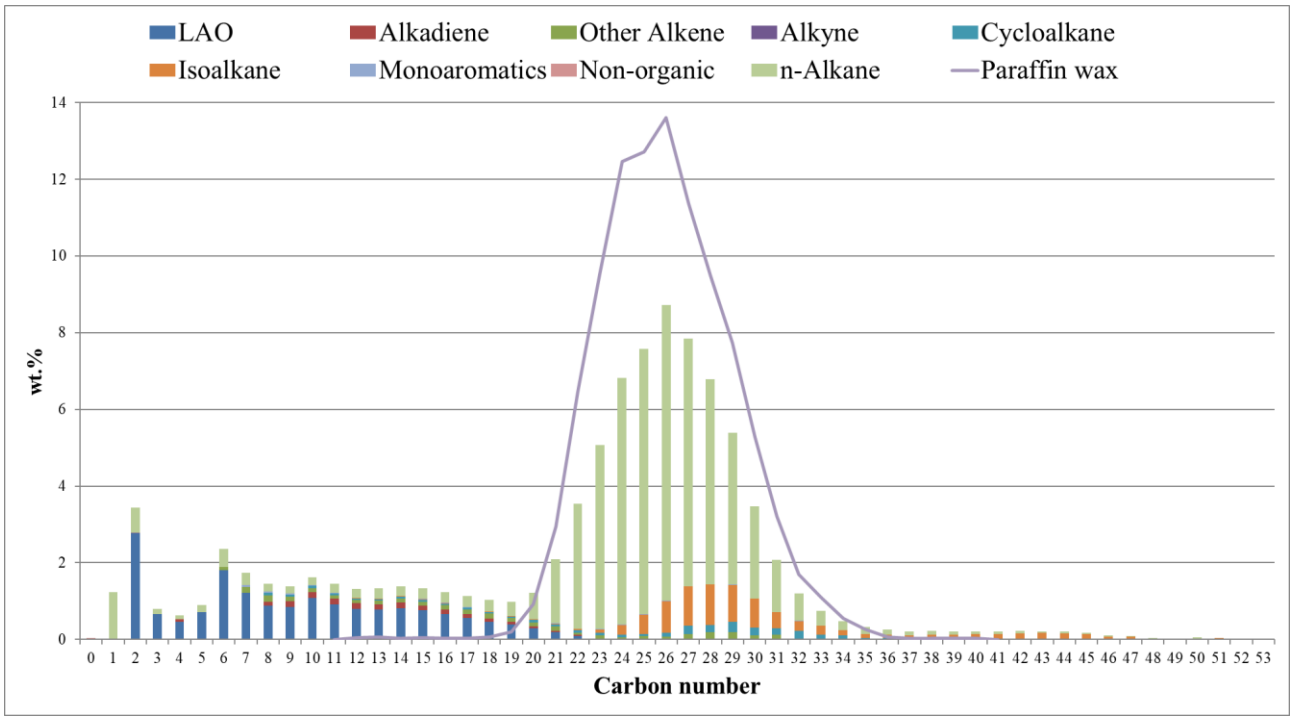

Fig. 1. Mass balance of MW pyrolysis of mixed paraffin wax and LLDPE (15 wt.%).

The research was supported by RSF (project No. 17-73-30032, https://rscf.ru/en/project/17-73-30032/)

References

[1] V.A. Bolotov, E.I. Udalov, V.N. Parmon, Y.Y. Tanashev, Y.D. Chernousov "Pyrolysis of Heavy Hydrocarbons Under Microwave Heating of Catalysts and Adsorbents", Journal of Microwave Power and Electromagnetic Energy, vol 1, pp. 39–46, 2012.

[2] V.A. Bolotov, S.F. Tikhov, K.R. Valeev, V.T. Shamirzaev, V.N. Parmon "Selective formation of linear alpha-olefins via microwave catalytic cracking of straight-chain alkanes", in Proc. 17th International Conference on Microwave and High Frequency Heating, 2019. p.464.
[3] M.L. Gringolts, K.I. Dement'ev, K.M. Kadiev, et al. "Chemical Conversion of Polymer Wastes into Motor Fuels and Petrochemical Raw Materials (A Review)", Pet. Chem., vol. 60, pp.751–761, 2020.
[4] Yu. D. Chernousov, et al. "An Apparatus for Performing Chemical Reactions under Microwave Heating of Reagents", Instruments and Experimental Techniques, vol.2, pp.289–294, 2019.

Chemistry, Biochemistry and Processing

Asymmetric-Propagation-Waveguide-Based High-Efficiency Microwave Heating System

H. Zhu[1]

[1]*College of Electronic and Information Engineering, Sichuan University, No.24 South Section 1, Yihuan Road, Chengadu 610065, China*
hczhu@scu.edu.cn

Keywords: microwave heating, meta-surface, asymmetric propagation, high-efficiency, continuous flow.

Microwave heating is a widely used technique in the chemical industry, but its efficiency is limited by the varying dielectric parameters of different chemical reactions. To address this challenge, we propose an asymmetric propagation waveguide based on gradient index metasurfaces (GIMs) for efficient microwave heating. We introduce the principle of asymmetric propagation and demonstrate its realization in both rectangular and circular waveguides. GIMs are then achieved using fluted and tapered mediums based on the principle of equivalent permittivity, enabling efficient microwave transmission in one direction at the working frequency. Finally, we design a continuous flow reactor based on the asymmetric propagation waveguide, which allows for high-efficiency heating of a wide range of dielectric fluids and various chemical reactions. Our proposed microwave heating system offers a new approach to overcoming the limitations of traditional heating methods and provides a promising solution for enhancing microwave heating efficiency in the chemical industry.

Fig. 1 demonstrates asymmetric propagation using GIMs on a 2D plane, which is applied to WR430 and C25 waveguides shown in Fig. 2 and Fig. 3. Microwaves transmit in only one direction, reducing waveguide loss and improving heating efficiency for different chemical reactions and dielectric fluids.

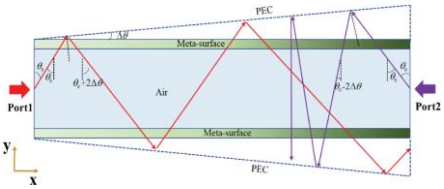

Fig. 1. Propagation path of electromagnetic wave on 2-D metasurface[1].

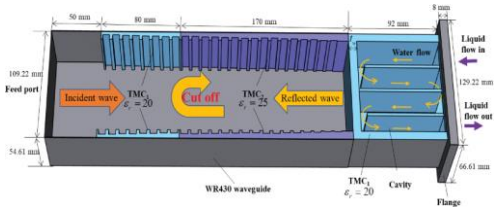

Fig. 2. MR430 waveguide microwave continuous-flow heating 3-D geometry model[1]

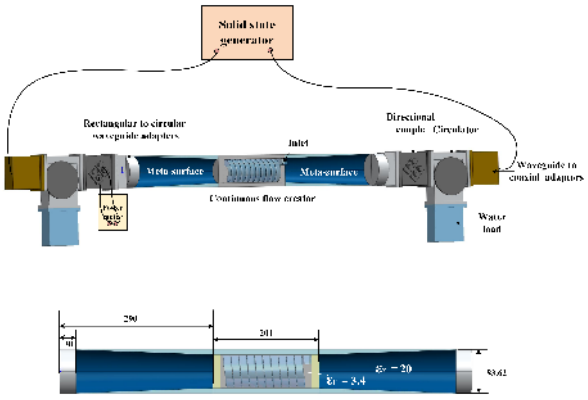

Fig. 3. C25 waveguide microwave continuous-flow heating 3-D geometry model

The heating efficiency of two microwave systems based on asymmetric waveguides for ethanol solutions of different volume ratios is demonstrated in Fig. 4 and Fig. 5, highlighting good energy utilization and confirming the feasibility of the proposed microwave heating system.

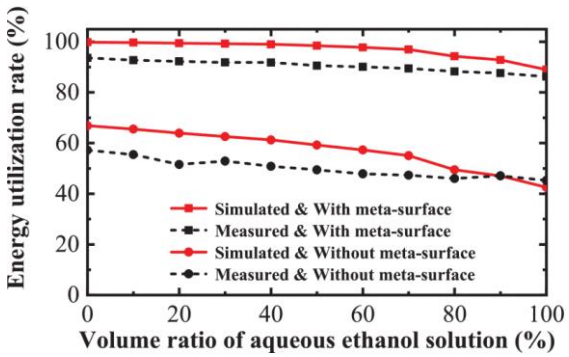

Fig. 4. Energy utilization of microwave heating of aqueous ethanol solution with different volume ratios (WR430)[1]

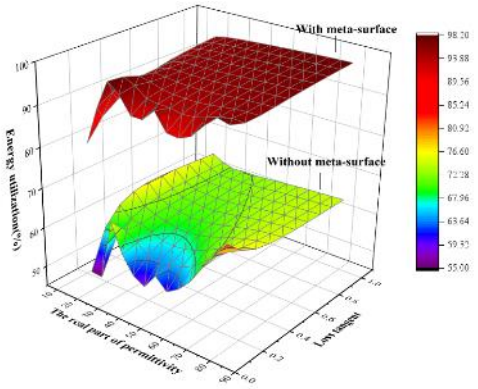

Fig. 5. Energy utilization of microwave heating of aqueous ethanol solution with different volume ratios (C25)

References

[1] Yang F, Zhu H, Yang Y, et al. High-Efficiency Continuous-Flow Microwave Heating System Based on Asymmetric Propagation Waveguide[J]. IEEE Transactions on Microwave Theory and Techniques, 2021, 70(3): 1920-1931.

Green Chemistry Protocols for the Synthesis of Some New Scaffolds of Isoxazolidine & Isoxazoline Derivatives via 1,3-Dipolar Cycloaddition Reaction and Potential Biological Activities of the Cycloadducts

B. Chakraborty[1]

[1]*Organic Chemistry Laboratory, Sikkim Government College (Renamed as Nar Bahadur Bhandari Government College), Tadong, Gangtok, Sikkim – 737102, India*
bhaskargtk@yahoo.com

Keywords: nitrone, cycloaddition reaction, solid phase synthesis, green chemistry protocol applications, biological activities

One of the excellent examples of spin trapping reagents is nitrones which play a fundamental role in the synthesis of five-membered heterocyclic ring compounds (commonly called isoxazolidine and isoxazoline derivatives) via 1,3-dipolar cycloaddition reactions, which are an integral part of many natural products. The medicinal activities of these heterocyclic compounds are of tremendous interest to synthetic organic chemists as they have been found to exhibit antibacterial, anticonvulsant, antibiotic, antituberculer, antifungal and anticancer activities. Except green chemistry methodologies, the majority of the reported procedures for the synthesis of isoxazolidine and isoxazoline derivatives require drastic experimental conditions like high temperature and long reaction times. In addition, these reactions are found to suffer from selectivity and also there are possibilities of poor yields as well as development of side products. A majority of these conventional procedures for the synthesis of isoxazolidine and isoxazoline derivatives are replaced successfully nowadays with the inception of green chemistry procedures like solvent free reactions (solid phase reaction), reactions conducted "in water" & "on water", microwave induced reactions and many more techniques. In the present work, few excellent examples based on stereoselective 1,3-Dipolar cycloaddition reactions using green chemistry protocols have been reported. These include "Ball-Milling techniques" and "Microwave Induced reactions" (MWI). Both the methodologies have been compared and found to have good to excellent yields, minimum reaction time, fast & simple isolation of products, environment friendly reaction conditions and stereoselectivities in the reported reactions which will certainly attract researchers working in this domain.

A scheme for synthesis of new isoxazolidine & isoxazoline derivatives following green chemistry methodology reported from our laboratory may be represented as below in Figure 1.

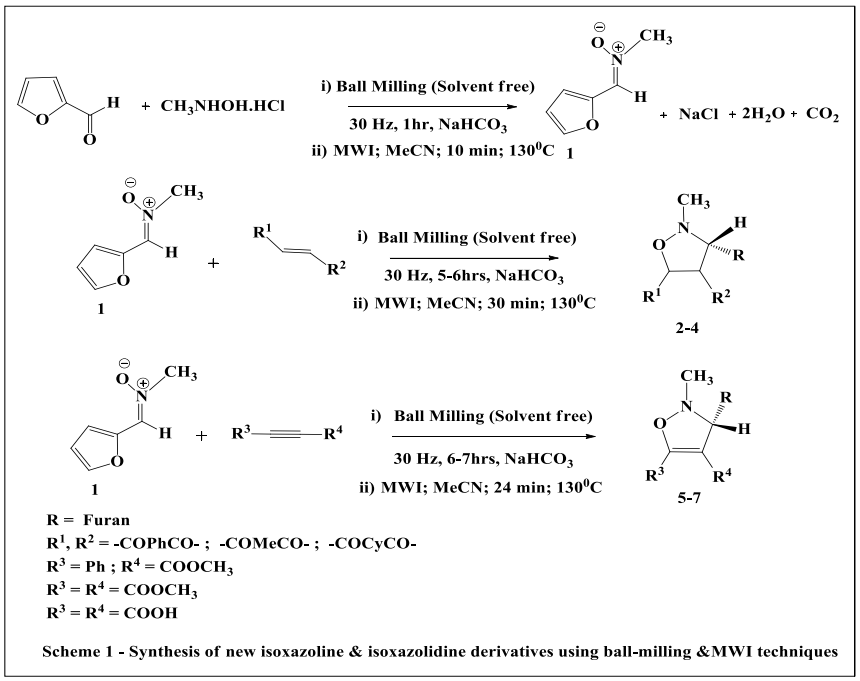

Fig. 1. Scheme for synthesis of new isoxazolidine & isoxazoline derivatives

References

[1] Chakraborty. B & Roy*, M.N, *ACS-Omega (American Chemical Society)*, **2022**, *7*, 4457-4470
[2] Tian, L. ; Liu, M ; Lei, X. ; Rao, W. ; Liao, L. Progress in Natural Science : Materials International **2022**, *32 (6)*, 665-673.
[3] Chakraborty, B & Chettri, E, *Results in Chemistry.* **2021,** 2, 10037-10043

[4] Chakraborty, B, *J. Heterocyclic. Chem.* **2020,** 57, 477-485
[5] Chakraborty, B. *J. Heterocyclic. Chem.* **2019,** 56, 3414-3422
[6] Chakraborty, B. ; Chettri, E. *J. Heterocyclic. Chem.* **2018**, *55*, 1157-1165
[7] Chakraborty, B.; Chettri M.S; Chettri E. *J.Heterocyc*lic Chem. **2017**, *54*, 110-120
[8] Chakraborty, B.; Chettri, M.S; Luitel, G.P. *J.Heterocyc*lic *Chem.* **2017**, *54*, 1611-1618
[9] Chakraborty, B.; Samanta, A.; Luitel, G.P.; Rai, N.; Mitra, D. *J.Heterocyc*lic *Chem.* **2016**, *53*, 1222-1230
[10] Chakraborty, B.; Luitel, G.P. *J.Heterocyc*lic *Chem.* **2015**, *52*, 726-731
[11] Chakraborty, B.; Sharma, P.K.; Kafley, S. *Green Chem Lett. & Rev*. **2013**, *6 (2)*, 141-147
[12] Chakraborty, B.; Luitel G P, *Tetrahedron Lett*, **2013**, *54*, 765
[13] Chakraborty, B.; Sharma C D, *Tetrahedron Lett*, **2013**, *54*, 5532
[14] Loupy, A.; Caldron, O.; Periz, E. *Tetrahedron*, **2006**, 62, 2616-2621.
[15] Etiemey, J. P.; Lidstrom, P. *Microwave assisted organic synthesis* (Blackwell Publishing), **2005**
[16] Padwa, A.; Pearson, W.H. Synthetic Application of 1,3- Dipolar Cycloaddition Chemistry toward Heterocycles and Natural Products; Wiley-New Jersey, **2003**.
[17] Kobayashi , S.; Jørgensen, K. A. *Cycloaddition Reactions in Organic Synthesis*; Wiley-VCH:Weimheim, **2002**.

Rapid Synthesis of High Entropy Oxides via Microwave Processing

J. Fukushima[1], T. Sekiguchi[1], S. Iwashita[1], H. Takizawa[1]

[1]*Department of Applied Chemistry, Graduate school of Engineering, Tohoku University, 6-6-07, Aoba Aramaki, Sendai, Miyagi 980-8579, Japan*
jun.fukushima.d5@tohoku.ac.jp

Keywords: microwave, solid state synthesis, spinel, high entropy oxides

Microwave processing has been used in the synthesis of ceramic materials, and examples of high-speed synthesis have been reported. For example, R. Roy et al. reported ultrafast synthesis of $BaTiO_3$, completing the synthesis of single-phase tetragonal $BaTiO_3$ even with a total synthesis time of 12 minutes [1].

Microwave processing can also be applied to the synthesis of high-entropy ceramics. High-entropy materials were initially reported as high-entropy alloys (HEA) and their nitrides. Currently, various systems of ceramics such as carbides and oxides (HEO) have been reported. Thus, high-entropy materials are defined as multicomponent materials consisting of a solid solution of equimolar elements. Among them, high-entropy oxides were reported by Rost [2]. HEOs with various crystal structures have been reported, including rock salt [2], perovskite [3], and spinel [4]. Among them, high-entropy spinel is expected to be applied as a catalytic material [5] and magnetic material [6]. Although there are only a few examples of microwave-assisted synthesis of HEO, it is reported that a single-phase spinel structure $(Co_{0.2}Cr_{0.2}Fe_{0.2}Mn_{0.2}Ni_{0.2})_3O_4$ high-entropy oxide was synthesized via a polymer precursor method by microwave processing [7]. In addition, HEO (Mg, Cu, Ni, Co, Zn)O nanoparticles were synthesized using an ultrafast high-efficiency low-temperature green method[8]. These methods were liquid-phase synthesis. On the other hand, as D. Agrawal's paper [1] suggests rapid synthesis of ceramics can be achieved via solid state synthesis. In this study, we attempted to synthesize high-entropy ceramics through microwave solid state synthesis.

Oxide powder was weighed to obtain the equimolar ratio of cations. After grinding and mixing in a mortar, 0.15 g of the powder was weighed. The powder was filled into a ⌀10 mm quartz test tube, and microwaves were irradiated at the position in the single-mode cavity which had the maximum electric field (Fig. 1). A semiconductor oscillator was used, and the maximum output power was 120W. The obtained samples were analysed by XRD measurement.

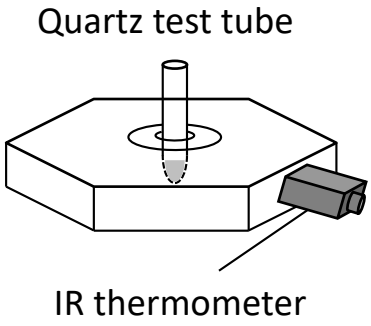

Fig. 1. Experimental setup

Cations of Cr, Fe, Mg, Mn and Ni were selected for synthesizing $(Cr,Fe,Mg,Mn,Ni)_3O_4$ spinel, and the mixed powder was irradiated with microwaves. Figure 2 shows the XRD results of the raw materials, and the sample synthesized at 960 °C for 300 s. The post-synthesized sample was not included the peaks of the raw materials, and three peaks appeared. These peaks were atypical of a high-entropy spinel [9]. In previous studies, when the rock salt and spinel phases are mixed, the sample includes two peaks at 37° and 43°. From the XRD peaks of the post-synthesis sample, the intensity of 37° peak was small, making it difficult to determine the peak splitting. On the other hand, the 43° peak was clearly a single peak. Thus, a single spinel-type high entropy ceramic of $(Cr,Fe,Mg,Mn,Ni)_3O_4$ was synthesized by microwave processing. The synthesis of high-entropy ceramics was achieved by microwave processing in less than 1000 °C for 300 s, whereas the conventional heating process requires rapid cooling after holding at 1000 °C for 20 h. The microwave heating is considered to have been advantageous for the synthesis of HEO because the atmosphere was at room temperature, resulting in rapid cooling.

Cations of Co, Cr, Fe, Mg, and Ni were selected for synthesizing $(Co,Cr,Fe,Mg,Ni)_3O_4$ spinel, and the mixed powder was irradiated with microwaves. Figure 3 shows the XRD results of the raw materials, and the sample synthesized at 960 °C for 300 s. The post-synthesized sample was not included the peaks of the raw materials. Similar to the results $(Cr,Fe,Mg,Mn,Ni)_3O_4$ case, intensity of the peak at 37° was small and peak splitting was difficult to determine. On the other hand, the 43° peak consisted of two peaks, and this shows the sample consisted of rock salt and spinel phase. Thus, the 43° peak was split even under conditions that the single-phase $(Cr,Fe,Mg,Mn,Ni)_3O_4$ was obtained. As well as $(Co,Cr,Fe,Mg,Ni)_3O_4$ case, The post-synthesized sample with cations of Co, Cr, Fe, Mg, Mn, Ni also consisted of spinel and rock-salt phases. These results suggested that a single-phase spinel synthesis is difficult when Co_3O_4 was used, but the reason is under investigation.

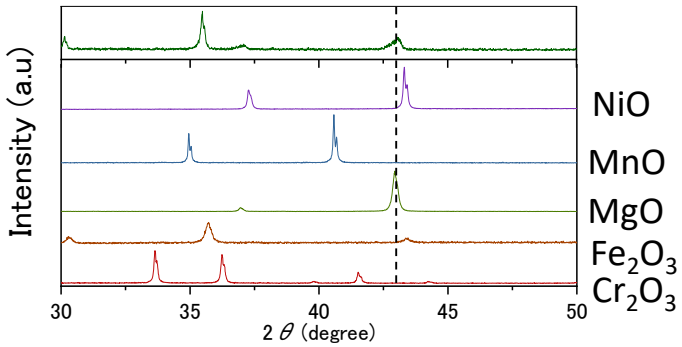

Fig. 2. XRD results of the raw materials, and the sample synthesized at 960 °C for 300 s.

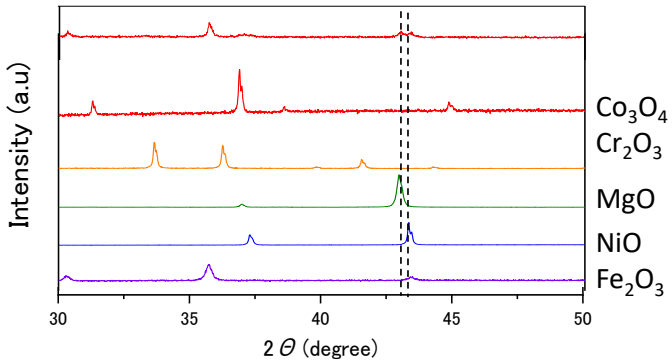

Fig. 3. XRD results of the raw materials, and the sample synthesized at 960 °C for 300 s.

References

[1] D. Agrawal, "Microwave processing of ceramics", *Current Opinion in Solid State and Materials Science*, **3**, (5), (1998),
[2] C.M. Rost, E. Sachet, T. Borman, A. Moballegh, E.C. Dickey, D. Hou, J.L. Jones, S. Curtarolo, J.-P. Maria, "Entropy-stabilized oxides", *Nature. Commun.* **6** (2015) 8485.
[3] A. Sarkar, R. Djenadic, D. Wang, C. Hein, R. Kautenburger, O. Clemens, H. Hahn, Rare earth and transition metal based entropy stabilised perovskite type oxides, *J. Eur. Ceram. Soc.* **38** (2018) 2318–2327.
[4] J. Dąbrowa, M. Stygar, A. Mikuła, A. Knapik, K. Mroczka, W. Tejchman, M. Danielewski, M. Martin, "Synthesis and microstructure of the $(Co,Cr,Fe,Mn,Ni)_3O_4$ high entropy oxide characterized by spinel structure", *Mater. Lett.* **216** (2018) 32–36.
[5] Hao Chen, Jie Fu, Pengfei Zhang, Honggen Peng, Carter W. Abney, Kecheng Jie, Xiaoming Liu, Miaofang Chi and Sheng Dai, "Entropy-stabilized metal oxide solid solutions as CO oxidation catalysts with high-temperature stability", *J. Mater. Chem. A.* 6 (2018) 11129–11133.
[6] J. Cieslak, M. Reissner, K. Berent, J. Dabrowa, M. Stygar, M. Mozdzierz, M. Zajusz, "Magnetic properties and ionic distribution in high entropy spinels studied by Mössbauer and ab initio methods", *Acta Mater.* **206** (2021) 116600.
[7] André L.F. Cardosoa, Claudia P.F. Perdomoa, Beatriz G. Foschiani, Julia A. Xaraba, Fabio L. Zabotto, and Rodolfo F.K. Gunnewiek, "Microwave Synthesis of Nanostructured High Entropy Spinel", http://dx.doi.org/10.2139/ssrn.4235110
[8] Mehdi Kheradmandfard, Hossein Minouei, Nikolai Tsvetkov, Ali Kasebi Vayghan, Seyed Farshid Kashani-Bozorg, Gihwan Kim, Sun Ig Hong, and Dae-Eun Kim, "Ultrafast green microwave-assisted synthesis of high-entropy oxide nanoparticles for Li-ion battery applications", *Materials Chemistry and Physics*, **262**, (2021), 124265
[9] Mirosław Stygar, Juliusz Dąbrowa, Maciej Moździerz, Marek Zajusz, Wojciech Skubida, Krzysztof Mroczka, Katarzyna Berent, Konrad Świerczek, and Marek Danielewski, "Formation and properties of high entropy oxides in Co-Cr-Fe-Mg-Mn-Ni-O system: Novel $(Cr,Fe,Mg,Mn,Ni)_3O_4$ and $(Co,Cr,Fe,Mg,Mn)_3O_4$ high entropy spinels", *Journal of the European Ceramic Society*, **40**, (4) (2020) 1644-1650.

How Microwaves Impact the ZSM5 Zeolite Production

R. B do Nascimento[1], M. A. Testa[1], L. A. Jermolovicius[2], E. R. de Castro[1], E. V. S. Pouzada[1]

[1]IMT - Instituto Mauá de Tecnologia, Praça Mauá, 1 - São Caetano do Sul, Brazil
[2]retired from IMT, now with LARJ Consultores Associados, Al. Terracota, 21, cj. 518 - São Caetano do Sul, Brazil
renatab@maua.br, profacidinha@gmail.com, luizalberto@larj.com.br, renatocastro@maua.br, epouzada@maua.br

Keywords: microwave process intensification, microwave industrial application, zeolite synthesis, ZSM5 zeolite.

This work deals with the microwave intensification of hydrothermal process for ZSM5 zeolite production. This process has two groups of procedures. The first one is a chemical process which begins with the ZSM5 zeolite precursor being synthesized from silica, sodium hydroxide, sodium aluminate, and tetra propylammonium bromide; it is finished with an endothermic high-pressure crystallization [1, 2]. The produced gel is dried and calcinated to its final form in the second procedure. All these operations are laborious tasks including energy and time consumption operations.

ZSM5 crystals were synthesized by an usual hydrothermal crystallization batch. This product was divided in two portions in order to compare results obtained by conventional drying and by microwave-assisted drying; both were followed by calcination operations. The conventional drying was done in accordance with the state of the art [1] in an electrical drying oven (1100 W, 220 V) at 105 ºC for 24 hours, and in an electrical muffle (4000 W, 220 V) at 500 ºC for 24 hours. The microwave-assisted drying was done in a microwave dryer (2.45 GHz with adjustable power up to 3 kW) with continuous measurements of the sample mass and the microwave incident and reflected power levels. Calcination operation used a hybrid microwave furnace (up to 1100 ºC, 2.45 GHz microwave adjustable power up to 3 kW) with a silicon carbide susceptor; continuous sample mass and microwave power level measurements were taken as before. Microwave-assisted tests were done until constant weight of sample in analysis were obtained; results are shown in Table 1. For both operations, the time elapsed to finalize the microwave-assisted operation was smaller than the conventional procedure.

Table 1. Processing time for ZSM-5 samples.

Operation	Time for electrical conventional process (min)	Time for microwave-assisted process (min)
Drying	1440	18
Calcination	1440	8
Total	2880	26

The structural characterization of the synthesized zeolites was done by X-ray diffraction (DRX) and scanning electron microscopy (SEM). Both samples have spectra compatible with zeolite ZSM-5 pattern [1]. However, the SEM microphotographs show a little difference between samples. The crystals produced with microwave-assisted drying and calcination show spherical crystals with a smooth surface; conventional processing samples have sharp surfaces (Fig. 1). As long as both samples were prepared by the same hydrothermal batch, it is plausible that microwaves had some influence on finishing the ZSM-5 zeolite. The reduction of drying time under microwave irradiation is well known [3-6], but the observed phenomena of crystal surface distortion is not usually reported. There are few references of ceramics synthesis [7,8] pointing out crystal structure changes due to microwaves.

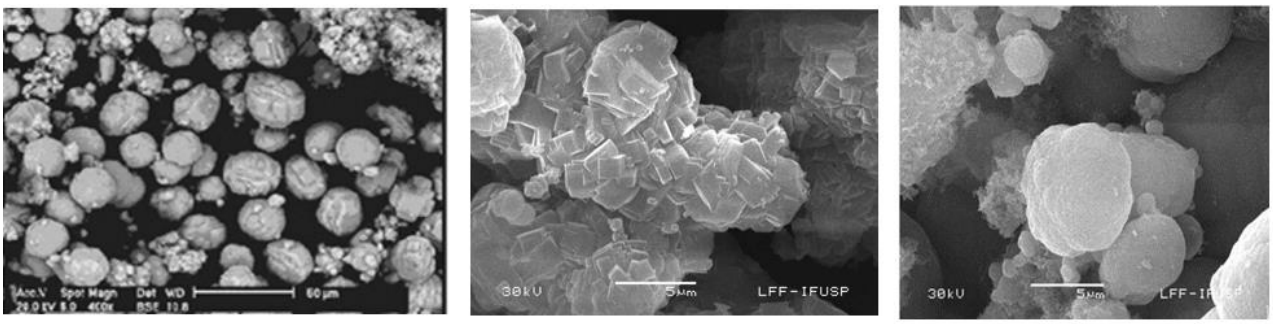

A: Standard ZSM-5

B: ZSM-5 by conventional process (drying/calcination)

C: ZSM-5 by microwave assisted process (drying/calcination)

Fig. 1. Comparison of dried/calcinated ZSM-5 crystals obtained by conventional and microwave-assisted processes.

References

[1] S. Mintova, Ed., *Verified Synthesis of Zeolitic Materials*, 3rd ed., Synthesis Commission of the International Zeolite Association, 2016.
[2] S. M. Auerbach, K. A. Carrado and P, K, Dutta, Eds., *Handbook of Zeolite Science and Technology*, USA, Marcel Dekker, 2003.
[3] A. C. Metaxas, and R. J. Meredith, *Industrial Microwave Heating*, England, Peter Peregrinus, 1993.
[4] A. S. Mujumbar, Ed., *Handbook of Industrial Drying*, 3rd ed., USA, CRC, 2006.
[5] H. Li, Z. Zhao, C. Xiouras, G. D. Stefanidis, X. Li, and X. Gao, "Fundamentals and Applications of Microwave Heating to Chemicals Separation Processes", Renewable and Sustainable Energy Reviews, 114, pp. 1-16, 2019.
[6] L. A. Jermolovicius, J. T. Senise and R. B. do Nascimento, "Microwave Drying of Zinc Sulfate", in Proc. International Microwave and Optoelectronics Conference – IMOC, Salvador, BR, 2007.
[7] G. Yang, H. Ji, H. Liu, B. Qian and X. Jiang, "Crystal Structure and Electrochemical Performance of Li3V2(PO4)3 Synthesized by Microwave Solid-state Synthesis Route", Electrochimica Acta, 55, pp. 3669-3681, 2010.
[8] A. A. Stanislavov, L. B. Sukhodub, L. F. Sukhodub, and V. N. Kuznetsov, "The Influence of Ultrasound and Microwave Irradiation on the Crystal Structure of Hydroxyapatite During Synthesis", in Proc. 6th International Conference on Nanomaterials Application and Properties, USA, 2016.

Investigation on Application to Anti-Discharge Solid Catalytic Reaction Using Variable Frequency Microwave Heating (VFM)

H. Mura[1], S. Horikoshi[1]

[1]*Sophia University, Department of Materials and Life Sciences, Faculty of Science and Technology*
7-1 Kioicho, Chiyodaku, Tokyo 102-8554, Japan
horikosi@sophia.ac.jp

Keywords: microwave, variable frequency microwave (VFM), standing wave, *E*-field intensity

This research consists of two stages. The first is the evaluation of the characteristics of the VFM device. By sweeping the frequency at high speed, the heating apparatus with variable frequency microwave (VFM) evens out the distribution of the electromagnetic field inside the cavity and suppresses the generation of standing waves theoretically. In this experiment, the distribution of the actual *E*-field is measured by using a photoelectric field sensor to examine properties. For comparison, it also measures *E*-field intensity of fixed frequency microwave (FFM) in conventional microwave heating. VFM irradiation shows a smaller bias of *E*-field intensity distribution and a higher *E*-field intensity than FFM irradiation. To confirm the result with heating of materials, we experiment with heating the heptane solution mixed with activated carbon. Comparing a rate of temperature increase, FFM irradiation is significantly smaller than VFM despite the same input energy amount. Furthermore, observation of sample after heating can show that activated carbon particles connect together and adhere in FFM irradiation. In addition, this advantageous situation was examined in the next stage of organic synthesis using solid catalysts, and we have confirmed that anti-discharge solid catalytic reaction can be achieved.

Microwave heating of materials can cause non-uniform temperature distribution in the samples and electrical discharge because bias of *E*-field intensity distribution due to standing waves specific to electromagnetic waves. To solve this problem, we have used a turntable that changes the sample position in the cavity and mode stirrer that changes the direction of microwave irradiation. However, the purpose of such mechanical solutions is the prevention of bias of *E*-field intensity distribution to sample from occurring temporarily, they are not fundamental solutions.

Following the VFM technology developed in 1991 at the Oak Ridge National Laboratories [1, 2], the present study used a bandwidth of frequencies from 5.85 to 6.65 GHz that were rapidly swept in a continuous sawtooth manner to be supplied to the cavity. The bandwidth was divided into 4096 discrete frequencies that were provided every 0.1 sec, such that the residence time for any of the 4096 frequency standing wave patterns was 25 μs, which rapidly changed with the sweeping frequency. This rapid sweep approach provided not only a uniform microwave field over the entire process volume, but also eliminated charge build-up on a metallic surface, thereby suppressing arcing and discharge phenomena. In this study, we compared the *E*-field intensity distribution inside the microwave irradiated cavity under VFM and FFM irradiation. Furthermore, the conventional microwave with chemical equipment using a magnetron was also compared [3].
Moreover, we examined the possibility of suppressing such arc discharges using the VFM methodology. After several experiments, conditions were selected that could easily generate arc discharges (hot spots) at a low fixed microwave power in combination with nonpolar solvents and activated carbon in model reactions. Explicitly, we examined the synthesis of 4-methylbiphenyl (and biphenyl as a by-product) via the Suzuki–Miyaura cross-coupling and homocoupling reactions in the nonpolar solvent toluene in the presence of Pd/AC catalyst particulates. Our clear objectives were to determine the yields of products and/or by-products formed by the VFM technology vis-à-vis the FFM approach and the conventional oil bath methodology.

The high-speed sweeping of the microwave frequency was achieved using a Lambda Technologies Inc. VariWave system with variable frequency microwaves (5.85 to 6.65 GHz; maximum power at 180 W), also, to confirme actual heating of materials, activated carbon particles 1.5 g as catalyst heat source were added to heptane solution 5.0 mL and heated by microwave. The 4-methylbiphenyl (4MBP) was synthesised in toluene solvent with Pd catalyst deposits on activated carbon particulates (Pd/AC).

We measured *E*-field intensity distribution with microwave irradiation sweeping from 5.85 to 6.65 GHz in 0.1 sec intervals (Fig. 1a). For comparison, we also measure *E*-field intensity of FFM (5.85 GHz) (Fig. 1b). VFM irradiation shows a smaller bias of *E*-field intensity distribution and a higher *E*-field intensity than FFM irradiation. Differences of more than 1 kVm^{-1} were observed in several locations in FFM.

Furthermore, measurements were made under different conditions. When the range of sweeping frequency was from 5.85 to 6.25 GHz or from 5.85 to 6.05 GHz, the bias of *E*-field intensity distribution was smaller over a wider frequency range. Changing the rate of frequency sweeping from 0.1 sec to 3.0 sec in the 5.85 to 6.65 GHz range resulted in a larger bias of *E*-field intensity distribution. Consequently, it is not just a matter of sweeping the frequency, but the range and rate of sweeping frequency is also important.

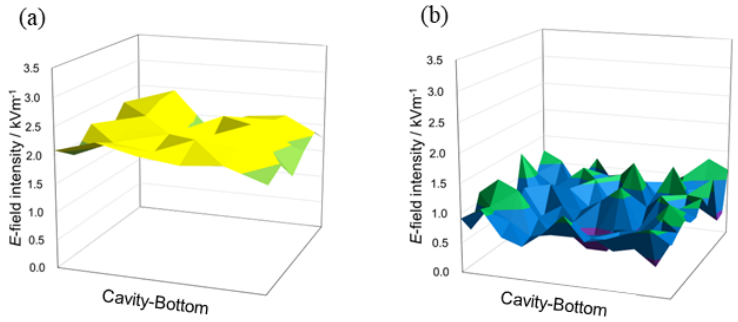

Fig. 1. *E*-field intensity distribution of (a) VFM (5.85 ~ 6.65 GHz) and FFM (5.85 GHz) at 7 cm height from bottom of the cavity

The mixed solutions of activated carbon particles and heptane were heated by VFM and FFM irradiation to examine characteristics of heating materials in VFM irradiation from the heating behaviour of activated carbon. At VFM, the temperature increased by 26.1 ℃ while at FFM, the temperature increased by 17.3 ℃ despite the same input microwave power. It seems to depend on *E*-field intensity. Furthermore, observation of sample after heating could show that activated carbon particles connected together and adhered in FFM irradiation. According to the previous study, it is inferred that activated carbon particles polarize and connect together and adhere by electrostatic attractive force. For this reason, during VFM activated carbon particles don't connect together and adhere due to uniform *E*-field intensity distribution. In contrast, during FFM activated carbon particles connect together and adhere according to high *E*-field intensity position.

The characteristics of variable frequency microwaves (VFM: 5.85 GHz to 6.65 GHz; fixed power, 6 W) and fixed frequency microwaves (FFM: 5.85 GHz and 6.65 GHz; fixed power, 6 W) were examined from the viewpoint of a chemical reaction that employed Pd particles supported on activated carbon particulates (Pd/AC) as the solid catalyst. The chemical yield of 4-methylbiphenyl produced with the VFM microwaves was 49% for a reaction time of 60 min, in contrast to a chemical yield of only 8% and 5%, respectively, for 4MBP when using FFM microwaves at a frequency of 5.85 and 6.65 GHz, also for a reaction time of 60 min. The heating time to reach an internal temperature of 100 °C was 15 sec with the VFM microwaves, while with the FFM (5.85 GHz) microwaves, the heating time to reach 100 °C was somewhat longer (135 sec). Whether VFM or FFM microwaves were used, the temperatures of the reactions oscillated within the range 98 ± 7 °C for a reaction time of 60 min. Differences in VFM and FFM rates were negligible and thus had little effect on the chemical yields. The synthesis yield of 4-methylbiphenyl from the oil bath heating method using the same reaction vessel was 17% [3].

VFM irradiation produced uniform *E*-field intensity distribution. The use of the VFM technology within a microwave heating and microwave chemistry scenario displays some specific advantages that include, among others, (i) uniform heating, (ii) arc-free processing, (iii) prevention of agglomeration of activated carbon particles, (iv) significant controllability, (v) higher coupling efficiency, and not least (vi) the ability to choose a "specific" frequency or frequency bands suitable for applications. Clearly then, the active use of metal-based catalytic particulates in microwave-assisted chemistry requires awareness and acquaintance of innovative technologies to avoid the deleterious arc discharges, to enhance chemical yields of products, and to minimize or altogether prevent possible mishaps. The VFM technology is one such novel approach that should prove advantageous in many respects in microwave chemistry.

References

[1] D. W. Bible, R. J. Lauf, "Variable frequency microwave furnace system" US Patent applied for on 14 November 1991. US Patent No. US5321222A, 14 June 1994.
[2] R. Lauf, D. W. Bible, A. C. Johnson, C. Everleigh, "2 to 8 GHz broadband microwave heating systems" *Microw. J.* **1993**, *36*, 34.
[3] S. Horikoshi, Y. Arai, I. Ahmad, C. DeCamillis, K. Hicks, B. Schauer, N. Serpone, "Application of variable frequency microwaves in microwave-assisted chemistry: relevance and suppression of arc discharges on conductive catalysts" Catalysts 2020, 10, 777.

Auto-Frequency Tuning Single-Mode Microwave Flow Chemistry for Synthesis of Functional Materials and Pharmaceutical Cores

J. P. Barham[1]

[1]*Institute of Organic Chemistry, University of Regensburg, Regensburg, Germany*
Joshua-Philip.Barham@chemie.uni-regensburg.de

Keywords: microwave, flow, single-mode, radio-frequency heating, solid state oscillator, organic synthesis

Microwave (MW) heating benefits organic synthesis by affording higher product yields in shorter time periods than conventional heating (CH), yet it suffers from poor scalability and is limited to polar solvents in typical batch mode reactors [1,2]. An auto-frequency tunable microwave (AFT MW) continuous flow (CF) reactor has been developed and used to compensate for changes in the microwave absorption properties (pemittivity, ε) with changing temperature 'on the fly',[1,2,3] affording excellent temperature and process control [4,5]. Herein, applications of this reactor from our research group will be presented toward the scalable organic synthesis of high value molecules such as pharmaceutical cores,[6] functional photovoltaic materials [7] and ionic liquids [8]. In particular, comparisons will be drawn between AFT MW heating and CH heating in flow, and where the use of this AFT MW CF reactor has expediated reaction optimization [9].

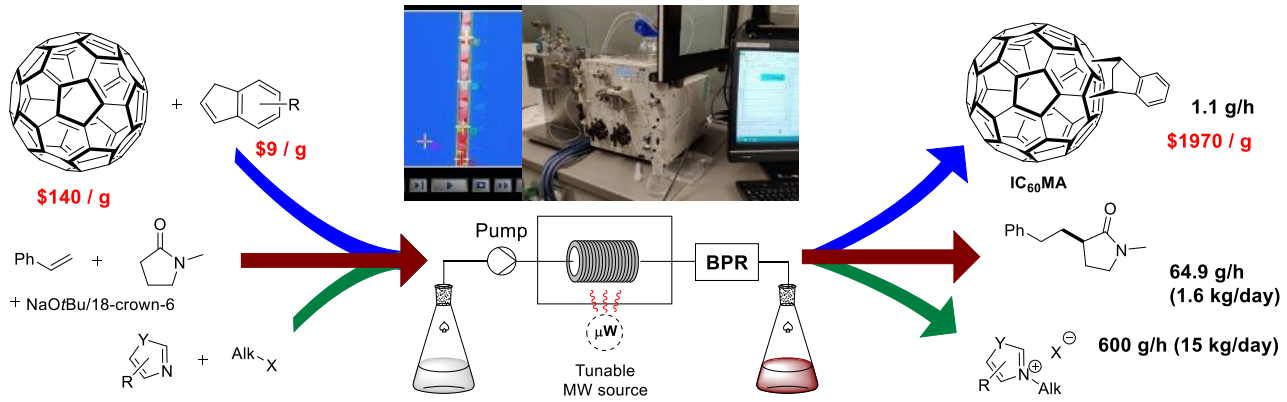

Fig. 1. An auto-frequency tuning microwave flow reactor as a robust, scalable tool for organic synthesis.

References

[1] D. Stuerga, *Microwaves in Organic Synthesis*, 2nd ed., Wiley-VCH, 2006.
[2] E. Grant and B. J. Halstead, "Dielectric parameters relevant to microwave dielectric heating" *Chem. Soc. Rev.* vol. 27, pp. 213-224, 1998.
[3] S. Chandrasekaran, S. Ramanathan, T. Basak, "Microwave material processing – a review," *AIChE J.* vol. 58, pp. 330-363, Aug. 2012.
[4] J. P. Barham, E. Koyama, Y. Norikane, N. Ohneda, and T. Yoshimura, "Microwave Flow: A Perspective on Reactor and Microwave Configurations and the Emergence of Tunable Single-Mode Heating Toward Large-Scale Applications," *Chem. Rec.* vol. 19, pp. 188-203, Jan. 2019.
[5] E. Koyama, N. Ito, J. Sugiyama, J. P. Barham, Y. Norikane, R. Azumi, N. Ohneda, Y. Ohno, T. Yoshimura, H. Odajima, and T. Okamoto, "A continuous-flow resonator-type microwave reactor for high-efficiency organic synthesis and Claisen rearrangement as a model reaction," *J. Flow. Chem.* vol. 8, pp. 147-156, Nov. 2018.
[6] J. P. Barham, S. Tamaoki, H. Egami, N. Ohneda, T. Okamoto, H. Odajima, and Y. Hamashima, "*C*-alkylation of *N*-alkylamindes with styrenes in air and scale-up using a microwave flow reactor," *Org. Biomol. Chem.* vol. 16, pp. 7568-7573, Sep. 2018.
[7] J. P. Barham, S. Tanaka, E. Koyama, N. Ohneda, T. Okamoto, H. Odajima, J. Sugiyama, and Y. Norikane, "Selective, Scalable Synthesis of C_{60}-Fullerene/Indene Monoadducts Using a Microwave Flow Applicator," *J. Org. Chem.* vol. 83, pp. 4348-4354, Apr. 2018.
[8] M. Domański, J, Žurauskas, and J.P. Barham, "Tunable Microwave Flow System for Scalable Synthesis of Alkyl Imidazolium-type Ionic Liquids," *Org. Process Res. Dev.*, vol. 26, pp. 2498-2509, Jul. 2022.
[9] J. P. Barham, E. Koyama, J. Sugiyama, Y. Norikane, H. Egami, and Y. Hamashima, "High Efficiency Microwave Flow Chemistry Toward Synthesis of Functional Materials and Pharmaceutical Cores," AMPERE 2019, Editorial Universitat Politecnica de Valencia, pp. 409-417, Sep. 2019.

Microwave-Assisted Chemical Vapor Infiltration Processing of SiC/SiC Composites Aided by Multiport-Multifrequency Solid-State Sources Excitation

R. D'Ambrosio[1], A. Cintio[1], M. Mallah[2], S. Probst[2], A. Lazzeri[3], G. Annino[1]

[1]*Istituto per i Processi Chimico-Fisici, CNR-IPCF, Via G. Moruzzi 1, 56124 Pisa, Italy*
[2]*Fricke und Mallah Microwave Technology GmbH, Werner-Nordmeyer-Str. 25, 31226 Peine, Germany*
[3]*Department of Civil and Industrial Engineering, University of Pisa, Via Diotisalvi, 2, 56122 Pisa, Italy*
roberto.dambrosio@pi.ipcf.cnr.it

Keywords: microwave-assisted processes, solid-state sources, multi-frequency microwaves, multiphysics modelling, chemical vapor infiltration

Silicon Carbide fiber-reinforced Silicon Carbide Ceramic Matrix Composites (SiC/SiC CMCs) are promising candidates for several high-temperature applications in strategic industrial sectors such as energy and aerospace. However, due to their high production cost (up to thousands of €/kg), new and more efficient processing technologies are actively investigated to develop simpler, more economical and efficient approaches to yield rapid and complete densification of these materials.

The application of microwave-assisted heating in Chemical Vapor Infiltration (MW-CVI) processes is an attractive approach due to the peculiar volumetric heating mechanism which releases energy selectively in the sample thanks to its dielectric absorption. The subsequent inverse temperature profile allows for an inside-out SiC matrix densification pattern avoiding the premature surface pore occlusion due to crusting and reducing the total processing times by about one order of magnitude. First activities, confirming the potential of this technology, were carried out at an innovative MW-CVI pilot plant based on an overmoded resonant applicator allowing for a multiport excitation by three magnetron sources operating around the 2450 MHz ISM band [1]. The design of this pilot plant resulted in a robust MW-assisted reactor, where SiC/SiC composites can be quickly heated to infiltration temperatures of about 900 – 1000 °C with reproducible operating conditions, reduced processing times and high chemical reaction efficiencies [2].

Nevertheless, a common limit of MW-CVI with samples larger than the electromagnetic wavelength, is the limited uniformity of the heating pattern resulting in localized infiltration of the SiC matrix. Furthermore, the efficient application of a multiport configuration was highly limited by the usage of magnetron-based MW sources which are prone to several drawbacks, mostly related to the incoherent nature of their electromagnetic emission, which cannot be controlled in phase and frequency.

An important step ahead in the development of efficient MW-CVI processing has been carried out by implementing an agile multi-frequency excitation of the reactor. This opportunity was made possible by the use of coherent MW solid-state sources while exploiting the multiport design of the MW-CVI reactor in Pisa, in the framework of the European CEM-WAVE project [3]. The combined use of different microwave frequencies, and so of different electromagnetic modes in the reactor, enables a significant improvement in the heating uniformity, and in general in the tailoring of the temperature pattern, of relatively large samples. This contribution will illustrate the results obtained by MW heating trials on 10 x 10 x 0,3 cm^3 SiC/SiC preforms, based on three solid-state generators delivering 2 kW of MW power each in the whole 2400 – 2500 MHz ISM band.

In particular, this contribution will discuss the choice of the most suited operating frequency combinations, both in terms of energy efficiency and heating uniformity, identified by rigorous multiphysics numerical modelling of the loaded cavity. An example of the typical numerical results of the multiport-multifrequency excitation obtained by using the software COMSOL 6.0 is shown in Fig. 1, together with the related experimental results. [4]. The numerical results agreed quite well with the experimental temperature patterns, confirming an increased temperature uniformity in the SiC/SiC sample with respect to the single port excitation cases.

The obtained results will be discussed in terms of energy efficiency, taking into account the power losses due to the power reflected on each excitation channel, as well as the cross-coupling between channels and the power dissipation in the walls of the reactor. Finally, multiport-multifrequency heating trials at the infiltration pressure of about 50 mbar will be presented, emphasizing the benefits of the more uniform distribution of the electromagnetic fields on the plasma occurrence at the typical overall employed power of 3 kW.

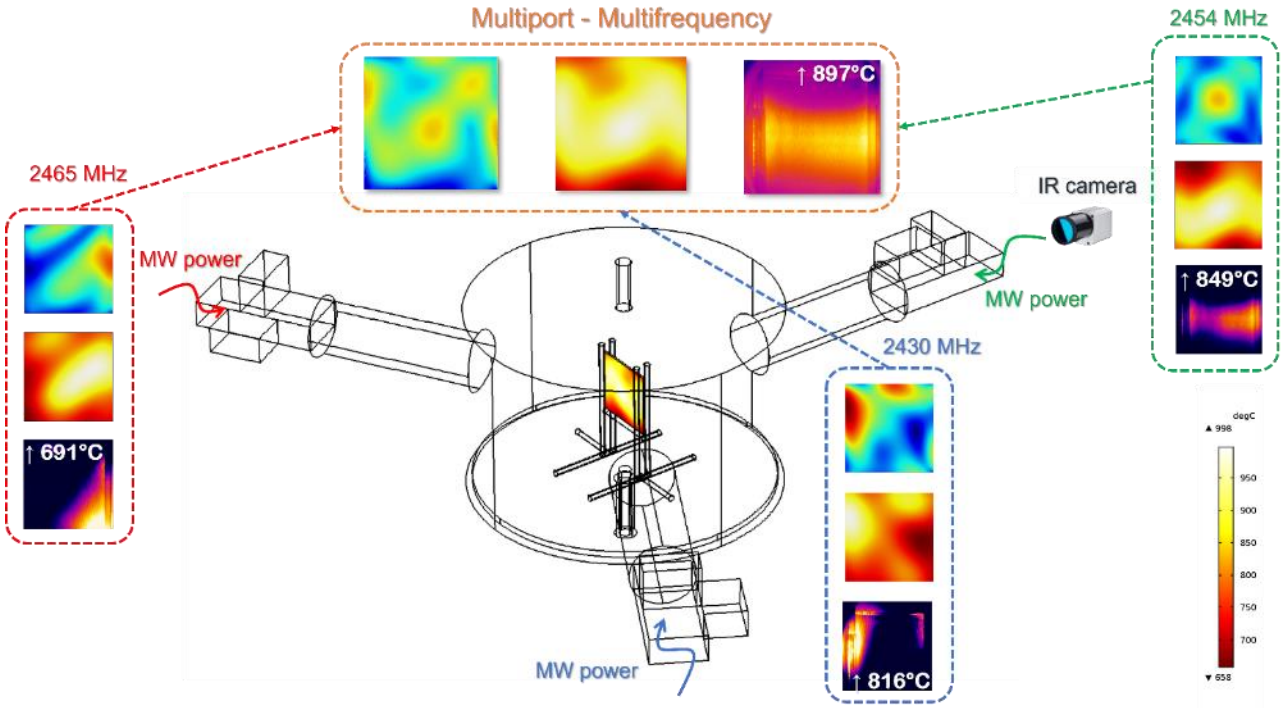

Fig. 1. MW-CVI reactor configuration scheme; Single-port vs multiport-multifrequency insets showing the calculated norm of the electric field and temperature distribution on the SiC/SiC sample along with the experimental frontal temperature profiles (max T highlighted) obtained by an IR camera.

References

[1] R. D'Ambrosio, A. Cintio, A. Lazzeri, G. Annino, Design of an Overmoded Resonant Cavity-based Reactor for Ceramic Matrix Composites Production, Chem. Eng. J. 405 (2021). https://doi.org/10.1016/j.cej.2020.126609.
[2] R. D'Ambrosio, L. Aliotta, V. Gigante, M.B. Coltelli, G. Annino, A. Lazzeri, Design of a pilot-scale microwave heated chemical vapor infiltration plant: An innovative approach, J. Eur. Ceram. Soc. 41 (2021) 3019–3029. https://doi.org/10.1016/j.jeurceramsoc.2020.05.073.
[3] Novel Ceramic Matrix Composites produced with Microwave-assisted Chemical Vapor Infiltration for energy intensive industries, (2020). https://www.cem-wave.eu/.
[4] COMSOL Multiphysics, https://www.comsol.it/.

Synthesis of Alkyl Imidazolium-Type Ionic Liquids in an Auto-Frequency Tuning Single-Mode Microwave Flow Reactor

M. Domański[1], J. Žurauskas[1], J. P. Barham[1]

[1]*Institute of Organic Chemistry, University of Regensburg, Regensburg, Germany*
michal.domanski@chemie.uni-regensburg.de

Keywords: microwave chemistry, flow chemistry, ionic liquids, imidazolium salts, microwave flow reactor, impedance matching, auto-frequency tuning

We demonstrate the potential of a commercial single-mode continuous flow microwave (MW) reactor fitted with an auto-frequency tunable solid-state oscillator as an efficient platform to synthesize alkyl imidazolium salts (Fig. 1.) [1].

Batch synthesis of imidazolium-based ionic liquids under conventional heating takes hours or even days. The rapid acceleration of the process was observed first by Westman [2] achieving alkylation within minutes of microwave irradiation. Surprisingly, the continuous synthesis in a MW flow reactor was under-reported despite the increasing popularity of microwave systems in organic chemistry laboratories. Erdmenger and coworkers [3] passed a mixture of n-butyl chloride and N-methylimidazole through a flow cell within a commercial MW reactor; however, the process has issues due to pumping difficulties arising from the high viscosity of ionic liquid (IL) products and phase separation during the reaction. We have decided to explore this method using the MW flow reactor with a single-mode resonator cavity from SAIDA FDS.

The key challenges for the microwave-assisted continuous flow synthesis of imidazolium salts in a single-mode resonant cavity are coming from the dramatic change of physical and dielectric properties of the mixture with the progress of the reaction. Moderately polar, aprotic reactants merge into an ionic and very viscous product that is not miscible with the starting haloalkane resulting in a complex and dynamic fluid system within the resonant cavity. To the rescue comes the auto-frequency tuning of the solid-state oscillator. The automatic feedback mechanism allows adjusting irradiation to maintain resonance, sustaining the electromagnetic standing wave focused on the reaction mixture. The use of simple borosilicate helical glass tubes allows for the reactor volume adjustment by selecting the geometry and internal diameter despite fixed cavity dimensions. The behavior of the mixture varies depending on the flow velocity revealing the influence of fluid dynamics phenomena in a transiently multi-phasic system during the reaction.

Under low flow rates and CSTR-type conditions, constant power operation was most suitable, affording alkylimidazolium salts in up to 97% yields and up to 139 g h^{-1} productivity with only <40 W input power. Primary alkyl bromides, iodides, sulfonate esters, and activated chlorides were all suitable to deliver products in high yields and short residence times (< 3 min). Introduction of β-branched groups is possible in compromised yields. Under high flow rates and plug-flow-type conditions, the auto temperature control mode offered excellent control and delivered selected products in high productivity (up to 91% yield, 600 g h^{-1}, 62.5 kg h^{-1} L^{-1}). After a simple workup, products can be afforded in high purity (>99%) and can be fully decolorized by a standard filtration procedure for liquids or by recrystallization for solids. Depending on the purpose, this highly productive method could prove to be useful for intensive applications of ILs such as their use as solvents.

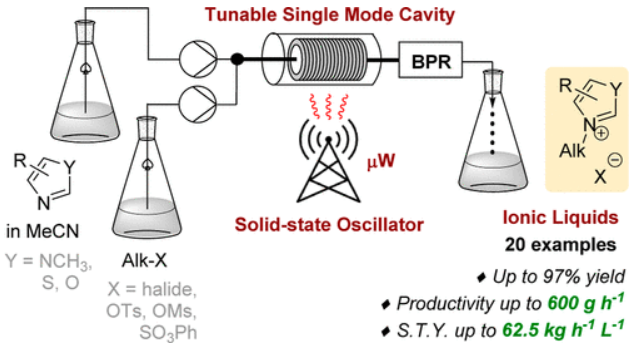

Fig. 2. General scheme of the method.

References

[1] M. Domański, J, Žurauskas, and J.P. Barham, "Tunable Microwave Flow System for Scalable Synthesis of Alkyl Imidazolium-type Ionic Liquids," Org. Process Res. Dev., vol. 26, pp. 2498-2509, Jul. 2022.
[2] J. Westman, "Preparation and use of ionic liquids in microwave assisted chemical transformations", World Patent 2000072956 A1, Jul. 12, 2000.
[3] T. Erdmenger, R. M. Paulus, R. Hoogenboom and U. S. Schubert, "Scaling-up the Synthesis of 1-Butyl-3-methylimidazolium Chloride under Microwave Irradiation", Aust. J. Chem., vol. 61, pp.197–203, Mar. 2008.

In-Situ Complete Monitoring of a MW Calcination: Dielectric Properties and Gas Evolution

E. Paradisi[1], P. J. Plaza-Gonzalez[2], G. Baldi[3], J. M. Catalá-Civera[2], P. Veronesi[1], C. Leonelli[1]

[1]*Department of Engineering "Enzo Ferrari", University of Modena and Reggio Emilia, Via P. Vivarelli 10, 41125 Modena, Italy*
[2]*Microwave Division (DiMaS), ITACA Research Institute, Universitat Politècnica de València, Camino de Vera, 46022, Valencia, Spain*
[3]*Ce.Ri.Col. Colorobbia Research Centre, Colorobbia Consulting S.R.L., Via Pietramarina, 123, 50053, Sovigliana-Vinci (Fi), Italy*
cristina.leonelli@unimore.it

Keywords: nanosized titania, dielectric properties, in-situ monitoring, cavity perturbation method, thermal analysis

Microwave (MW) calcination is extremely efficient when MW absorption of the material occurs during irradiation, and it is even more efficient when combustion synthesis is ignited. Yet, at these high temperatures the measurement of the dielectric properties of the sample undergoing calcination is very difficult to perform. This contribution presents a complete investigation of a complex calcination process for the preparation of N-doped TiO_2 nano-powders where the cavity perturbation method (CPM) has been used to determine the in-situ MW absorption of the precursor compound from room temperature to 800°C. In this method, a sample of N-doped TiO_2 containing also NH_4Cl and citrate derivatives that arise from its synthesis is placed inside a quartz vial of approximately 15 mm height and 9.8 mm diameter. The latter is introduced in a cylindrical cavity where microwave heating and simultaneous measuring of dielectric properties is feasible with two different sources without interferences [1]. The temperature of the sample is measured by an external IR pyrometer pointing to the surface of the quartz vial to track the variation of the loss factor with temperature. As another useful tool to study high-temperature processes, a simultaneous thermo-gravimetric and differential scanning calorimetry Netzsch STA 449F3 apparatuses operating with conventional resistance heating were combined with a Bruker FT-IR spectrometer to perform evolved gas analysis on titania precursors was performed. These data are combined with the dielectric behaviour observed in the MW cavity in Fig. 1.

The DSC curve (Fig. 1a) shows two main endothermic peaks at about 100°C and 221°C and three main exothermic peaks: 317.9, 494.8, and 592°C. All these peaks, except the last one, are associated with weight loss. The first two endothermic peaks correspond to water loss and to citrate decarboxylation occurring simultaneously with NH_4Cl decomposition [2]. The first two exothermic peaks correspond to further citrate derivatives decomposition, while the last one is probably due to the anatase-rutile transformation [3]. Weight loss is accompanied by a drastic volume reduction: such a change in the sample's geometry affects the EMW absorption as well as the changes its chemical composition. The curve of the loss factor shows higher values below 250°C and above 400°C (Fig. 1b), and lower values between 250°C and 400°C. This means that, if we combine these results with the previous ones, MW absorption is higher during the first decarboxylation and NH_4Cl decomposition, and also later, when TiO_2 crystallizes into the rutile form. Therefore, the lowest MW absorption is observed in the temperature range 250-400°C, where combustion occurs.

Results indicate that after a first non-combustive decomposition, the EMW absorption decreases, so hybrid heating is needed to reach the desired calcination temperature of 375-400°C. During MW calcination it is crucial to know at which temperatures electromagnetic energy is better adsorbed by the sample thus to modulate MW power during the process for energy optimization and fine tuning of material's properties.

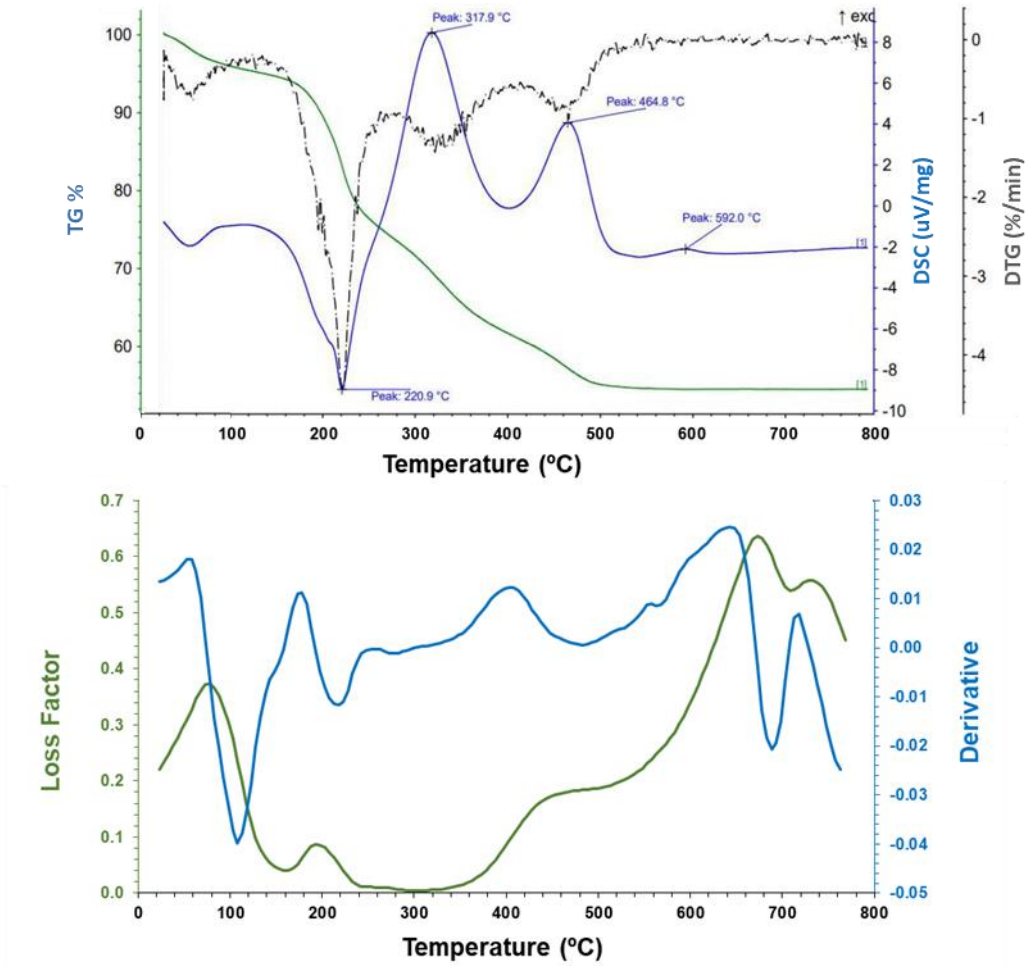

Fig. 1. (a) TGA/DSC curve for the N-doped TiO_2 precursor between r.t. and 800°C: TGA (green curve), first derivative DTG (dashed black), and DSC (blue). (b) Loss factor (green) and its derivative (blue) in the same temperature range.

References

[1] J.M. Catalá-Civera, A.J. Canós, P. Plaza-González, J.D. Gutiérrez, B. García-Baños, and F.L. Peñaranda-Foix, "Dynamic measurement of dielectric properties of materials at high temperature during microwave heating in a dual mode cylindrical cavity", *IEEE Trans. Microw. Theory Tech*. Vol. 63, issue 9, pp. 2905–2914. Sept. 2015.

[2] K. Van Werde, D. Mondelaers, G. Vanhoyland, D. Nelis, M.K. Van Bael, J. Mullens, L.C. Van Poucke, B. Van Der Veken, H.O. Desseyn, "Thermal decomposition of the ammonium zinc acetate citrate precursor for aqueous chemical solution deposition of ZnO", *J. Mater. Sci.* vol. 37, pp. 81-88, Jan. 2002.

[3] X. Wen, S. Zhao, S. Asuha, 2019. "Preparation of nitrogen-doped mesoporous TiO_2/RGO composites and its application to visible light-assisted photocatalytic degradation", *J. Nanomater.* article n°. 6467107, Oct. 2019.

[4] E. Paradisi, P.J. Plaza-Gonzàlez, G. Baldi, Josè M. Català-Civera, and C. Leonelli, "On the use of microwaves during combustion/calcination of N-doped TiO_2 precursor: An EMW absorption study combined with TGA-DSC-FTIR results", *Mater. Lett.* Vol. 338, article n°. 133975, Jan. 2023.

Theoretical and Experimental Study on Microwave Hyperpolarization Heating Effect

K. Huang[1], H. Shi[1], Q. Xiao[1]

[1]*College of Electronics and Information Engineering, Sichuan University, Chengdu 610065, China*
kmhuang@scu.edu.cn

Keywords: microwave heating, incoherent microwaves, molecular dynamics (MD) simulation, microwave hyperpolarization

It was found that the heating efficiency of a combination of multiple microwave sources was higher than that of a single microwave source. To study this phenomenon in detail, we have specially designed a set of equipment. The equipment was composed of two crossed rectangular waveguides, which can provide incoherent microwaves power from two independent sources. A visual depiction is shown in Fig. 1. Five common polar solvents, EtOH (ethanol), AcOH (acetic acid), H_2O (water), DMSO (dimethyl sulfoxide), and DMF (dimethyl dormamide) were selected to investigate this phenomenon. The measured heating profiles are presented in Fig. 2. Notably, the temperature of the five selected samples under irradiation of incoherent microwave sources rises faster than that of one microwave source with the same total power. Since macroscopical theory cannot explain this effect, molecular dynamics (MD) simulation was carried out to explore the mechanism of this effect on the molecular level. The results of MD simulation show that the temperature rise of the incoherent microwave sources is faster than that of one microwave source.

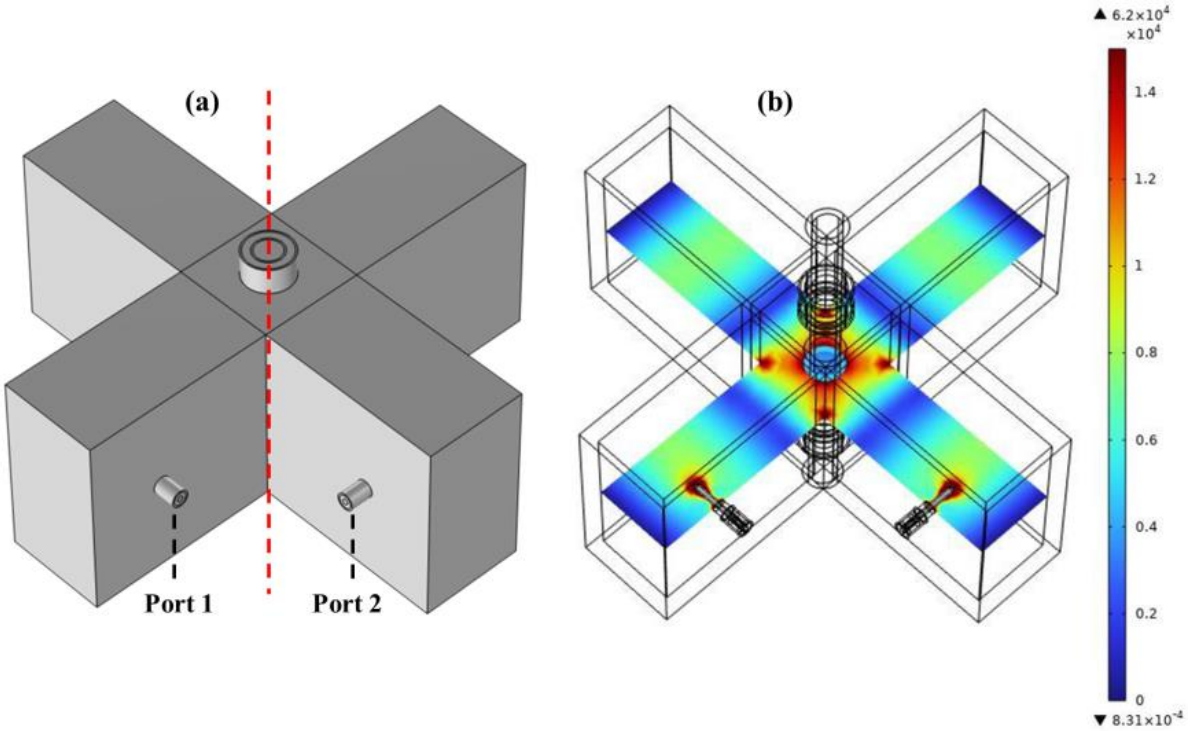

Fig. 1. Orthogonal waveguide device showing (a) diagram of model and (b) diagram of internal electric field distribution.

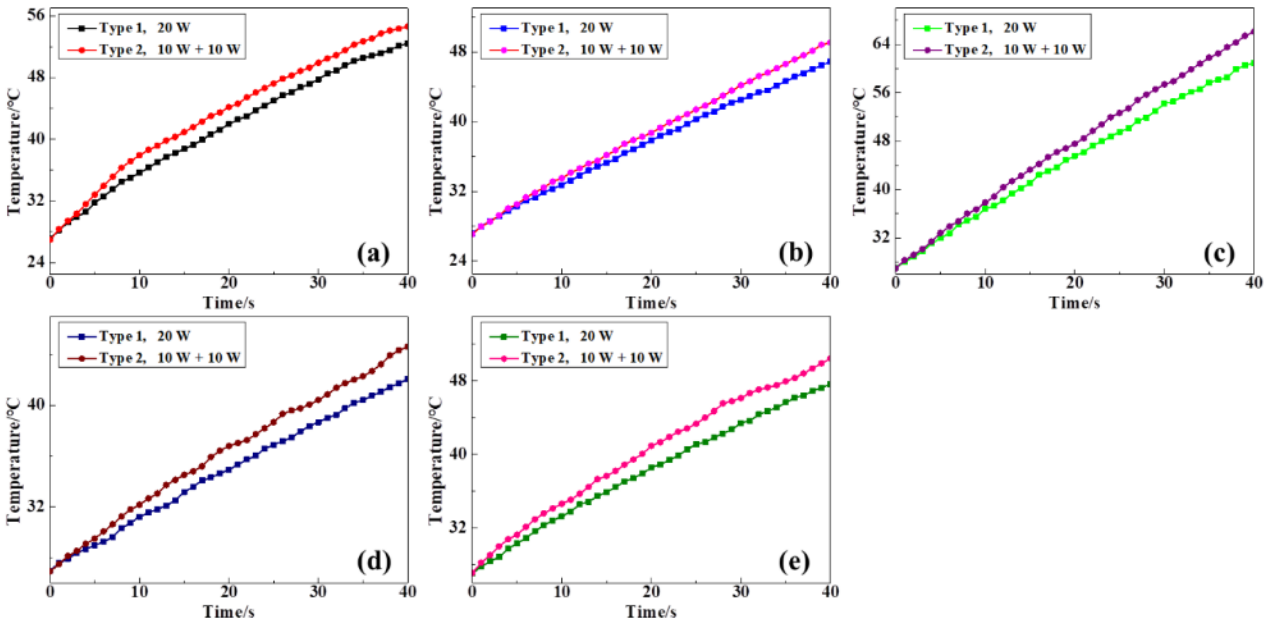

Fig. 2. The heating profiles of (a) EtOH, (b) AcOH, (c) DMSO, (d) H2O, and (e) DMF in response to both heating types.

The rotation autocorrelation function curves of the multipolarized microwave electric field decay faster, indicating that the molecules in the samples are rotating more frequently to align with the changing polarization directions. This increased rotational motion is caused by the microwave hyperpolarization effect, which results in higher heating efficiency due to incoherent microwave sources. This study has answered the long-standing question of whether to use a single high-power microwave source or a combination of several low-power microwave sources in engineering applications.

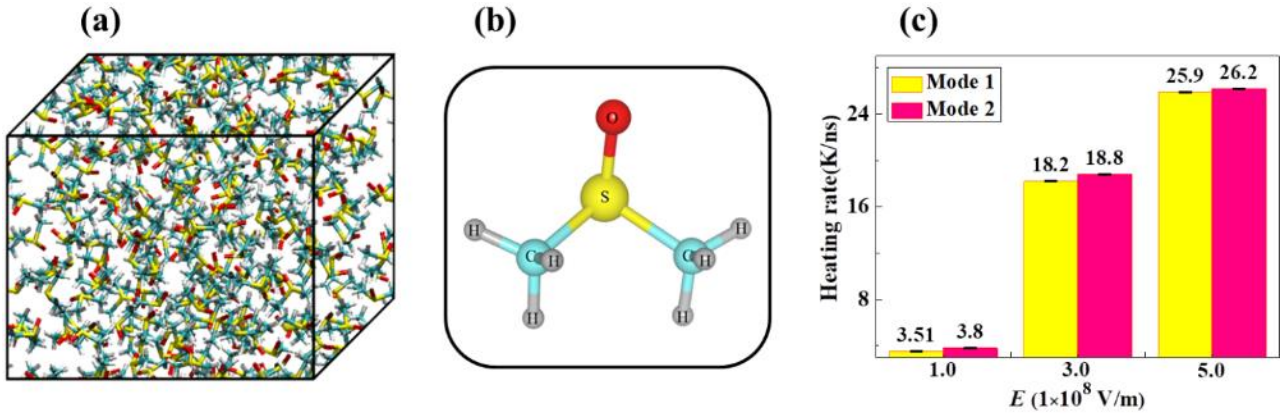

Fig. 3. Simulation results of DMSO. (a) Snapshot of the simulation box with 300 DMSO molecules, (b) structure of DMSO molecule and (c) the heating rates of two heating modes with three given electric field intensities of 1×10^8, 3×10^8 and 5×10^8 V/m, respectively.

An Overview of Microwave Characterization of Nanoparticle-Protein Corona

U. Singh[1], S. D. Krishnananda[2], R. Adelung[2]

[1]*Department of Physics & Computer Science, Dayalbagh Educational Institute, Dayalbagh, Agra, India*
[2]*Institute of Material Science, University of Kiel, Kiel, Germany*
ksdaya@dei.ac.in

Keywords: microwave, radiofrequency, dielectric resonators, power applications, plasmas

Nanoparticles (NP), when in contact with biological fluids, adsorb proteins due to their high level of surface free energy. The proteins that are adsorbed on the surface of nanoparticles form the so-called 'protein corona' [1].

Lately, the functional specificity of proteins in nanoparticle coronas has become a major concern [2]. Though nanoparticles have proved to be efficient target-specific drug carriers [3], the high surface energy of nanoparticles leads to changes in the functional specificity of the proteins leading to concerns about biological hazards [4]. The therapeutic efficacy of nanoparticles and the biodistribution and bioavailability of a drug depends on the nanoparticle-protein interaction in addition to local and structural parameters. Spectroscopic methods have been reported to be efficient in analyzing the temporal studies of the interaction patterns [5]. It is important to understand how nanocarriers interact with their biological surroundings. Importantly, can nanoparticle morphology and shape conserve proteins' functionality in-vivo? This understanding can facilitate the translation of nanomedicine into clinical applications.

The work presented here investigates the effect of the morphology of nanoparticles on the functional specificity of proteins. For this ZnO, spherical and tetrapodal structures were made to interact with insulin. Changes in functional specificity were studied by measuring dipole moment and electrical permittivity. Morphology and shape can affect the interaction mechanism of NP and proteins. This study clearly shows that ZnO tetrapodal structures preserve the spatial distribution of charge on insulin. The effect of papain in defragmenting protein is visible through an increase in the mechanical frequency.

From the present study, it is concluded that shape and surface morphology can affect the conformation of the protein. Tetrapodal ZnO structures were able to preserve the polarity and spatial distribution of the surface charge of insulin and therefore can be effective nanocarriers for insulin.

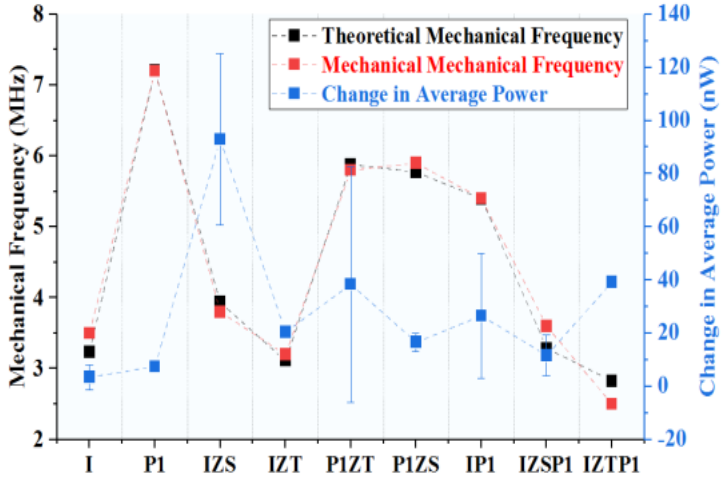

Fig. 1. Effect of morphologically different nanoparticles of ZnO on the mechanical vibrational frequencies of protein insulin (I) and its interaction with spherical ZnO (IZS) and tetrapodal ZnO (IZT)

References

[1] Kokkinopoulou, M., Simon, J., Landfester, K., Mailänder, V., & Lieberwirth, I. (2017). Visualization of the protein corona: towards a biomolecular understanding of nanoparticle-cell-interactions. Nanoscale, 9(25), 8858-8870.
[2] Klein, J. (2007). Probing the interactions of proteins and nanoparticles. Proceedings of the National Academy of Sciences, 104(7), 2029-2030.
[3] Bharali, D. J., Klejbor, I., Stachowiak, E. K., Dutta, P., Roy, I., Kaur, N., ... & Stachowiak, M. K. (2005). Organically modified silica nanoparticles: a nonviral vector for in vivo gene delivery and expression in the brain. Proceedings of the National Academy of Sciences, 102(32), 11539-11544.
[4] Nel, A., Xia, T., Madler, L., & Li, N. (2006). Toxic potential of materials at the nanolevel. science, 311(5761), 622-627.
[5] Li, L., Mu, Q., Zhang, B., & Yan, B. (2010). Analytical strategies for detecting nanoparticle–protein interactions. Analyst, 135(7), 1519-1530.
[6] Singh, U., Saifi, Z., Kumar, M., Reimers, A., Krishnananda, S. D., Adelung, R., & Baum, M. (2021). Role of structural specificity of ZnO particles in preserving functionality of proteins in their corona. Scientific Reports, 11(1), 1-9

Chemical Kinetics of the Microwave Effect on the Base Hydrolysis Reaction Rate of Benzyl Isobutyrate

R. Baba[1], S. Ohuchi[2]

[1]*Graduate School of Computer Science and Systems Engineering, Kyushu Institute of Technology, 680-4 Kawazu, Iizuka, Japan*
[2]*Department of Bioscience and Bioinformatics, Kyushu Institute of Technology, 680-4 Kawazu, Iizuka, Japan*
ohuchi@bio.kyutech.ac.jp

Keywords: Arrhenius equation, chemical kinetics, Eyring equation, microwave-assisted chemistry

The research on microwave-assisted chemistry is receiving increasing attention in the interdisciplinary fields of chemistry and electrodynamics. This is because a variety of beneficial effects on chemical reactions by using microwave energy have been reported. Some examples of these effects are, shortening of reaction time, improvement of reaction yield, improvement of reaction specificity, and improvement of reaction selectivity [1]. In addition, many experimental results on Arrhenius plots of chemical reactions under microwave irradiation have been reported. Changes in the slopes and/or intercepts of the Arrhenius plots depending on the presence or absence of microwave irradiation have been confirmed. For example, in the field of inorganic chemistry, regarding the Boudouard reaction [2] which is the reduction reaction of carbon dioxide to carbon monoxide, in the field of organic chemistry, regarding the dehydration reaction of xylose to furfural [3], in the field of polymer chemistry, regarding the ring-opening polymerization reaction of ε-caprolactone [4], and in the field of biocatalytic chemistry, regarding the synthesis reaction of alkyl benzoate esters by immobilized lipase enzymes [5]. These Arrhenius plots on microwave irradiation conditions are very linear, changing only the slopes and/or intercepts.

Since the linearity of Arrhenius plots does not depend on the presence or absence of microwave irradiation for a wide variety of chemical reactions, it can be said that Arrhenius plot and the Arrhenius equation on microwave irradiation condition can be extended empirically as (1) and (2)

$$\ln k_{\mathrm{MW}} = \ln A + \ln C_S - C_H \frac{E_\mathrm{a}}{R}\frac{1}{T} \tag{1}$$

$$k_{\mathrm{MW}} = C_S A \exp\left(-C_H \frac{E_\mathrm{a}}{RT}\right), \tag{2}$$

where T is the absolute temperature of chemical reaction system, R is the gas constant, E_a is the activation energy of the target chemical reaction, A is the pre-exponential factor of the target chemical reaction, k_{MW} is the reaction rate constant under microwave irradiation, and C_H and C_S are the correction coefficients for the Arrhenius plots of chemical reactions under microwave irradiation. Changes in slopes and intercepts of Arrhenius plots are generally interpreted to be due to formation of favorable polarization of substrate and increase in collision frequency under microwave irradiation, that is, changes in the activation energy E_a and pre-exponential factor A [6]. On the other hands, according to the transition state theory, C_H and C_S are expected to affect activation enthalpy ($\Delta H^{\circ\ddagger}$) and activation entropy ($\Delta S^{\circ\ddagger}$) of target reaction, respectively. For this reason, C_H and C_S are referred to as "enthalpic effect coefficient" and "entropic effect coefficient," respectively, in this study.

In this study, the hydrolysis reaction of benzyl isobutyrate by base-catalyzed conditions was carried out under single-mode traveling microwave irradiation and non-irradiation. According to the comparison based on the results of the chemical kinetic analysis, the microwave effect was quantified as C_H and C_S by using (1).

In experiment, 15 mM benzyl isobutyrate (BIB, >98.0%, Tokyo Chemical Industry Co., Ltd.) was hydrolyzed by 22.5 mM sodium hydroxide (NaOH, >96.0%, Wako Pure Chemical Industries, Ltd.) in dimethyl sulfoxide (DMSO, >99.0%, FUJIFILM Wako Pure Chemical Corporation) as a highly-microwave-absorbent solvent (dielectric loss $\varepsilon'' > 14$ [7]). After adding 4 M NaOH aqueous solution to DMSO in the inner tube of a double-tube test tube so that the reaction system solution involved BIB becomes 10 mL in total, this solution was set in TE_{10}-mode traveling microwave irradiator (IMCR-25003B, 2450 ± 30 MHz, J-Science Lab Co., Ltd.) and kept stirring by using a magnetic stirrer (ST-10, KENIS LIMITED). The solution temperatures were kept on the target reaction temperatures (40, 50, 60°C) by thermal transmission using kerosene as a low-microwave-absorbent refrigerant ($\varepsilon'' < 1$ [7]) flowing in the outer tube of a double-tube test tube using a pump (SL-03K, ELEPON E.C.A.P. Corporation). By changing the temperature of the water bath (AB-1600, ATTO Corporation) for the refrigerant, the target reaction temperature were maintained during non-irradiation or irradiation (50 W) with microwaves. After the solution reached the target reaction temperature, BIB was added to the solution so that the reaction system solution becomes 10 mL in total. Because the volume of BIB was much less than total volume of the reaction system, the system temperature was almost unchanged after adding BIB.

The temporal changes in BIB concentration during the hydrolysis reaction were measured by using HPLC system (pump: LC-10AD, SHIMADZU CORPORATION, and DP-8020; Tosoh Corporation, detector: UV-8020, Tosoh Corporation; column: TSKgel ODS-100V 5µm (0021455), Tosoh Corporation). The reaction rate constant was analysed as a second-order reaction by using (3)

$$kt = \frac{1}{[\mathrm{BIB}]_0 - [\mathrm{NaOH}]_0} \ln \frac{[\mathrm{BIB}][\mathrm{NaOH}]_0}{[\mathrm{BIB}]_0([\mathrm{NaOH}]_0 + [\mathrm{BIB}] - [\mathrm{BIB}]_0)} \quad (3)$$

where t is the reaction time, [X] is the concentration of chemical species X at t, $[X]_0$ is the initial value of [X], and k is the reaction rate constant on non-irradiation or irradiation with microwaves. E_a and A of this reaction were determined from the slope and intercept of the Arrhenius plot in the non-irradiation condition. C_H and C_S were quantified as by comparing the slope and intercept of the Arrhenius plots of non-irradiation and microwave irradiation conditions.

The Arrhenius plots of the hydrolysis reaction of BIB are shown in Fig. 1. Regarding Arrhenius plots in Fig. 1, the coefficients of determination are 0.993 for non-irradiation and 0.996 for microwave irradiation. Therefore, it can be said that the chemical kinetic analysis of the microwave effect on the reaction rate by (1) is proper due to these very high linearities. According to the Arrhenius plot on the non-irradiation condition, E_a is 8.08×10^4 and A is 7.62×10^{11}.

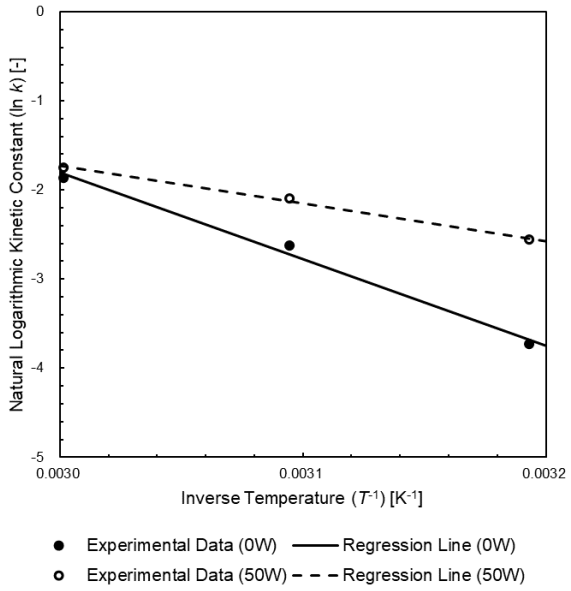

Fig. 1. Arrhenius plots of base hydrolysis reaction of benzyl isobutyrate under microwave non-irradiation and irradiation condition.

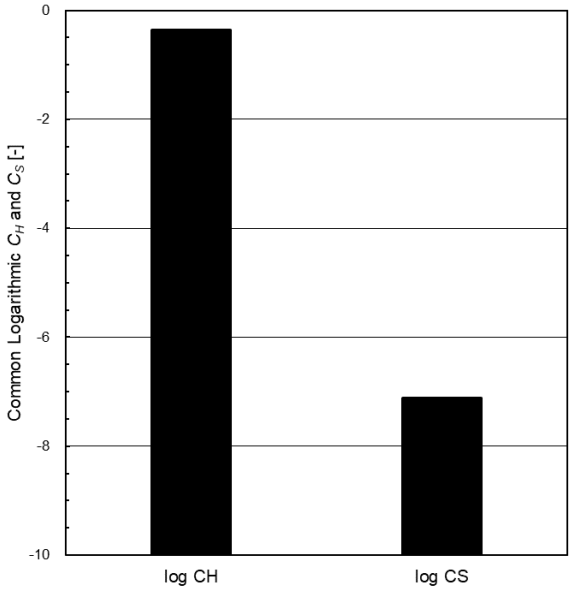

Fig. 2. C_H and C_S as microwave effect on base hydrolysis reaction of benzyl isobutyrate quantified based on extended Arrhenius equation.

By comparing the slope and intercept of the Arrhenius plots on the non-irradiation and microwave irradiation conditions, C_H and C_S quantified and shown in Fig. 2. These coefficients are shown as common logarithmic values in Fig. 2 due to the difference in scale. According to (2), it is expected that this difference was caused from what is C_S is directly multiplied by A, whereas C_H is multiplied by E_a inside the exponential function. In fact, C_H and exp C_S are 0.435 and 1.000, respectively, so it seems that their scales are almost equal.

Acknowledgement

This work was supported by JST SPRING, Grant Number JPMJSP2154.

References

[1] A. R. Yadav and S. K. Mohite, "A Brief Review: Microwave Chemistry and its Applications," Res. J. Pharma. Dosage Forms and Tech., vol. 12, no. 3, pp. 191–197, Aug. 2020. (DOI: 10.5958/0975-4377.2020.00033.6)
[2] J. Hunt, A. Ferrari, A. Lita, M. Crosswhite, B. Ashley, and A. E. Stiegman, "Microwave-Specific Enhancement of the Carbon-Carbon Dioxide (Boudouard) Reaction," J. Phys. Chem. C, vol. 117, no. 51, pp. 26871–26880, Oct. 2013. (DOI: 10.1021/jp4076965)
[3] L. Ricciardi, W. Verboom, J.-P. Lange, and J. Huskens, "Local Overheating Explains the Rate Enhancement of Xylose Dehydration under Microwave Heating," ACS Sustainable Chem. Eng., vol. 7, no. 16, pp. 14273–14279, Jul. 2019. (DOI: 10.1021/acssuschemeng.9b03580)
[4] S. Yamada, A. Takasu, and K. Kawamura, "The Effect of Microwave Irradiation on the Kinetics and Activation Thermodynamics of Ring-Opening Polymerization of ε-Caprolactone," J. Polym. Sci. Part A: Polym. Chem., vol. 51, no. 17, pp. 3732–3739, Jun. 2013. (DOI: 10.1002/pola.26776)
[5] S. D. Shinde and G. D. Yadav, "Microwave Irradiated Immobilized Lipase Catalyzed Synthesis of Alkyl Benzoate Esters by Transesterification: Mechanism and Kinetic Modeling," Ind. Eng. Chem. Res., vol. 53, no. 21, pp. 8706–8713, Apr. 2014. (DOI: 10.1021/ie4040972)
[6] L. Perreux and A. Loupy, "A tentative rationalization of microwave effects in organic synthesis according to the reaction medium, and mechanistic considerations," Tetrahedron, vol. 57, no. 45, pp. 9199–9223, Nov. 2001. (DOI: 10.1016/S0040-4020(01)00905-X)
[7] B. L. Hayes, Microwave Synthesis: Chemistry at the Speed of Light, Matthews, NC, USA: CEM Publishing, 2002. (ISBN: 978-0-97222290-7)

Microwave-Assisted Synthesis of ZnS:Mn Nanowires for Photocatalytic Applications

K. Matras-Postolek[1], A. Szymska[1], B. Szreniawa[1], A. Żaba[1], X. Zhang[1]

[1]Faculty of Chemical Engineering and Technology, Cracow University of Technology, Warszawska 24 St, 31-155, Krakow, Poland.
k.matras@pk.edu.pl

Keywords: organic dyes, photocatalysis, ZnS, doping, nanowires

Semiconducting materials including zinc sulfide (ZnS) nanowires represent a promising candidate in many fields, including optoelectronics and photocatalysis because of their advantages such as excellent optical properties, chemical stability and an easy-scalable simple synthesis method [1,2]. In this work, an energy-friendly microwave-assisted synthesis was used to develop the single-step, solvothermal process for the growth of ZnS:Mn and undoped nanocrystals (NCs) in the forms of nanowires. As stabilizer, two short amines were used; ethylenediamine and hydrazine. ZnS nanowires doped with Mn atoms show absorbance in UV and in the visible region of the spectrum. The photocatalytic degradation of rhodamine B in the presence of ZnS:Mn nanocrystals illuminated with a UV lamp has been comprehensively studied. The effect of Mn doping and the presence of a nanocrystal stabilizer on the degradation process was determined. It was proven that the efficiency of a photocatalytic degradation process was strongly affected by two factors: the concentration of Mn^{2+} atoms in the ZnS nanowires and the surface stabilizer [3].

References

[1] Zhang, S.-Y.; Regulacio, M.D.; Han, M.-Y. Self-assembly of colloidal one-dimensional nanocrystals. Chem. Soc. Rev. 2014, 43, 2301–2323, doi:10.1039/c3cs60397k.
[2] Efros, A.L.; Brus, L.E. Nanocrystal Quantum Dots: From Discovery to Modern Development. ACS Nano 2021, 15, 6192–6210, doi:10.1021/acsnano.1c01399.
[3] A. Żaba, S. Sovinska, T. Kirish, A. Węgrzynowicz, K. Matras-Postołek, Photodegradation Process of Organic Dyes in the Presence of a Manganese-Doped Zinc Sulfide Nanowire Photocatalyst, Materials (Basel). 2021, 14(19), 5840, doi: 10.3390/ma14195840
[4] Matras-Postołek, K.; Żaba, A.; Nowak, E.; Dąbczyński, P.; Rysz, J.; Sanetra, J. Formation and characterization of one-dimensional ZnS nanowires for ZnS/P3HT hybrid polymer solar cells with improved efficiency. Appl. Surf. Sci. 2018, 451, 180–190.
[5] Park, S.; An, S.; Mun, Y.; Lee, C. UV-activated gas sensing properties of ZnS nanorods functionalized with Pd. Curr. Appl. Phys. 2014, 14, S57–S62, doi:10.1016/j.cap.2013.11.041.

Sustainable Waste Plastic Management: Exploring the Feasibility of Microwave-Induced Chemical Recycling

S. Horikoshi[1], A. Sawai[1]

[1]*Sophia University, Department of Materials and Life Sciences, Faculty of Science and Technology*
7-1 Kioicho, Chiyodaku, Tokyo 102-8554, Japan
horikosi@sophia.ac.jp

Keywords: microwave, waste plastics, chemical recycling, pyrolysis

Plastics are typical chemical products that have made our lives comfortable, but waste plastics can have negative environmental impacts. Recently, the development of chemical recycling of waste plastics through pyrolysis has received much attention. However, it has been difficult to directly degrade plastics to monomers using energy-efficient heat sources. In this work, the chemical recycling of waste plastics can be achieved using microwaves and microwave absorption heating element (MAHE). Direct monomerization of high-density polyethylene (HDPE) was achieved through pyrolysis at around 1000 °C. After investigating various microwave devices and reactors for scale-up, a continuous two-stage pyrolysis system consisting of an electric furnace and a single-mode microwave was found to be an efficient method for decomposition. The microwave pyrolysis method was also applicable for other general plastics and actual waste plastics in Tokyo.

The long-term stability of chemical structures of plastics has made post-use processing difficult. For example, in Japan, which has a small land area, more than 50% of waste plastics are treated by thermal recycling, and thermal energy is recovered by burning them. However, since this recycling method produces CO_2 gas, it cannot be sustained from the viewpoint of global warming. Furthermore, although chemical recycling is the most noticeable recycling method, it is not a major recycling process due to its difficulty and process complexity.

Pyrolysis is known as one of the most feasible ways to convert waste plastic into chemical materials easily. However, in general, pyrolysis requires a large amount of energy to break down polymers, and the use of energy-efficient heat sources is essential to build a novel recycling process. Additionally, when waste plastic is thermally decomposed by conventional heating, polyaromatic hydrocarbons such as tar and char are usually generated, and resources cannot be obtained.

Therefore, we decided to mix the waste plastic with MAHE as a thermal filler and challenged to thermally decompose. Polyethylene (PE) and polypropylene (PP) were used as model waste plastic, as they have a large amount of production and waste [1]. Due to the transparency of these plastics to microwaves, pyrolysis does not proceed under microwave irradiation, we investigated the possibility of using a heating element that absorbs various microwaves as MAHE. The carbon material showed good performance, so this material and plastic were blended and used as a sample. In this novel pyrolysis method, a gas containing a monomer as the main component was obtained as a decomposition product from polyethylene and polypropylene.

In this presentation, three items are proposed: (i) optimization of MAHE material types, physical properties, and mixing conditions with plastics, (ii) a mechanism of pyrolytic recycling of polyethylene (PE) as model plastics and (iii) an investigation into a scale-up using actual waste plastics.

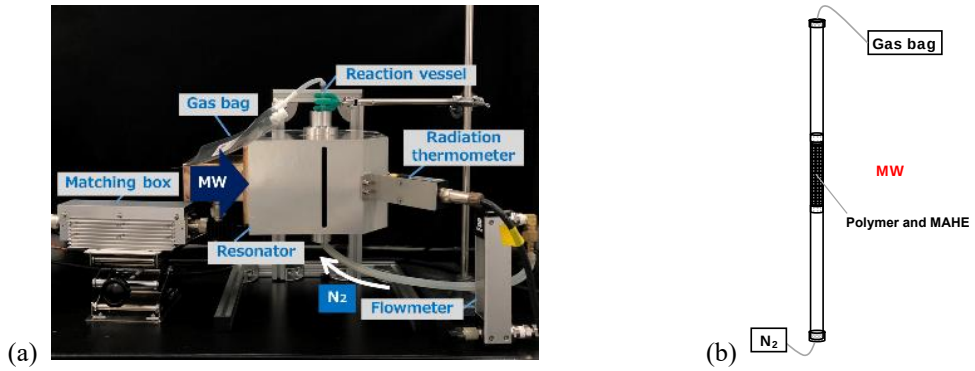

Fig. 1. (a) Picture of microwave single-mode pyrolysis equipment with semiconductor generator and (b) schematic of reactor with packed model polymer waste and microwave absorption heating element (MAHE).

An experiment was conducted using a single-mode applicator connected to a semiconductor-microwave generator to clarify the characteristics of the recycling of plastics by microwave flash heating (Fig. 1a). The sample temperature was monitored using an infrared thermometer (~2100 °C) as infrared radiation transmits through quartz. A material containing a mixture of

carbon material and model plastic pellets was enclosed in a synthetic quartz pipe flow reactor and irradiated with microwaves under nitrogen gas flow conditions (Fig. 1b). The reaction vessel was installed at the maximum position of the electric field (*E*-field) in the single-mode applicator and continuously irradiated with microwaves. The gas discharged from the reactor together with nitrogen carrier gas was collected by gas bag and subsequently analyzed by gas chromatography to quantify various decomposition gases.

When microwave heating was performed for 3 min using 7 mg of carbon materials with respect to 70 mg of polyethylene pellets, a gas containing ethylene as a main component was obtained with a gas yield of 84% (Fig. 2). Immediately after irradiation with microwaves, the temperature of the sample increased significantly and reached over 1000 °C in a few seconds. Microwave heating creates this kind of fast pyrolysis, which is characterized by a microscopic high-temperature field (hot spot) of more than 1500 °C [2]. Upon observing the inside of the reactor after 3 minutes of microwave irradiation, polyethylene is decomposed to the extent that it cannot be visually confirmed after microwave heating. On the other hand, the presence of tar could not be confirmed.

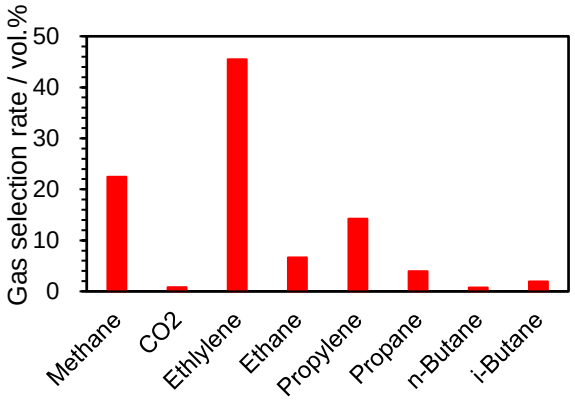

Fig. 2. Gas selection rate of microwave pyrolysis of polyethylene

After observing successful decomposition of polyethylene using microwave irradiation and carbon materials, decomposition of polypropylene was also attempted using the same method. The microwave pyrolysis provided a gas yield of 82.7% and was able to obtain propylene with high yield and high selectivity. These results demonstrate the potential of microwave-assisted pyrolysis as an efficient method for chemical recycling of waste plastics.

In order to evaluate the practicality of the microwave recycling method developed in this research, we thermally decomposed the waste plastics in municipal solid waste collected in Tokyo and evaluated it. Note that the samples for this experiment were obtained from a waste treatment plant meaning there is a mix of different plastics and other non-plastic waste. A waste plastic sheet (0.5 g) and MAHE were mixed, and it was packed in the quartz pipe flow reactor.

After 4 min of microwave heating, the gasification rate was 53%, and the main component of the generated gas was ethylene, so it was expected that the main component of the waste plastic was polyethylene. Even if actual waste plastics are used, monomerization can be achieved in a sufficiently short time. It is believed that further optimization will establish a more perfect chemical recycling method.

In the thermal decomposition of polyethylene and polypropylene through microwave heating, the plastic was decomposed into a monomer-based gas in high yield. The microwave heating enables chemical recycling of plastics, which is difficult with normal heating, and a gas containing a monomer as a main component can be obtained in an energy-effective manner. It was also demonstrated that the pyrolysis of municipal waste can be performed. In addition, it was suggested that it is a sustainable method with little environmental impact that emits almost no carbon dioxide.

References

[1] Ministry of the Environment in Japan "*Toward the situation surrounding plastics and the construction of a resource recycling system*", 2019.
[2] S. Horikoshi, A. Osawa, M. Abe, N. Serpone "On the generation of hot-spots by microwave electric and magnetic fields and their impact on a microwave-assisted heterogeneous reaction in the presence of metallic pd nanoparticles on an activated carbon support" *J. Phys. Chem. C*, 115 (2011) 23030–23035.

Energy and Environmental Applications

Multiphysics Study of CO_2-free Hydrogen Production Using Electromagnetic Radiation

M. Salakhi[1], M. Thomson[1]

[1]*Department of Mechanical & Industrial Engineering, University of Toronto; Toronto, Ontario, Canada.*
murray.thomson@utoronto.ca.

Keywords: hydrogen**,** microwave, volumetric heating, electric field distribution, power density

The burning of fossil fuels is the largest contributor to the significant levels of CO_2 emissions that drive climate change and global warming. This alarming increase in CO_2 concentrations is the result of the high energy demand and is accelerating the pace of climate change. However, hydrogen presents a renewable and carbon-free energy alternative that is utilized in various industrial sectors, such as oil refineries, chemical production, steelmaking, and power generation [1]. It plays a critical role in the transition to a net-zero emissions future by 2050 [2]. By embracing hydrogen as a vector for energy supply, we can work towards a cleaner and more sustainable future. Currently, only 0.5 Mtonnes/year is provided by clean technologies of hydrogen production, while the global demand for hydrogen is 70 Mtonnes/year. Thus, it is imperative to explore CO_2-free technologies for hydrogen production [3]. Despite the increasing interest in green hydrogen production, this method is highly energy intensive and not scalable enough to meet the demand. Alternatively, methane pyrolysis can produce hydrogen without direct CO_2 emissions and with modest energy inputs, making it a potential stepping stone from fossil fuels to renewable energies [4].

Microwave heating is considered a rapid and energy-efficient method of adding the required energy for methane pyrolysis. [5]. Unlike traditional heating methods, microwaves only heat the material, not the surrounding environment, thereby minimizing energy losses due to conduction, convection, and radiation. In this study, we introduce a novel approach to producing CO_2-free hydrogen through non-plasma methane pyrolysis using microwaves and carbon particles in a fluidized bed. Under microwave irradiation, carbon particles heat up in a bubbling fluidized bed and create a conducive environment for methane to decompose into hydrogen and solid carbon in an endothermic reaction as in (1)[6].

$$\mathrm{CH_4(g)} + \Delta \mathrm{H^\circ} = 74.52\ \mathrm{kJ/mol} \rightarrow \mathrm{C(s)} + 2\mathrm{H_2(g)} \qquad (1)$$

While there have been many experimental studies, numerical simulations of microwave-driven chemical conversion processes have received far less attention. The current study aims to develop a multiphysics model for CO_2-free hydrogen production using microwaves. This model can be a valuable tool to ameliorate our current understanding of the electromagnetic field, fluidization, and chemical reaction roles in clean hydrogen production systems. The development of a comprehensive computational model for microwave-driven methane pyrolysis in a fluidized bed reactor requires a simultaneous combination of detailed reaction kinetics, fluid dynamics, particle dynamics, population balance model, and electromagnetic model as shown in Fig. 1. This requires coupling three governing equations, namely, Navier-Stokes, Euler, and Maxwell equations. One important aspect of the electromagnetic field in our process is volumetric heating. The power density can be calculated using (2) as below:

$$P_{microwave} = 2\pi f \varepsilon_0 \varepsilon'' |E|^2 \qquad (2)$$

Where P is the power density, f is the microwave frequency, ε_0 is the vacuum permittivity, ε'' is the dielectric loss factor, and $|E|$ is the root mean square value of the electric field. As a first objective, a uniform electric field distribution is assumed. Then, the microwave power absorption within the particles is used as a heat source in the energy equation of each particle as follows in (3):

$$m_p c_p \frac{dT_p}{dt} = \dot{q} + P_{microwave} . v_p \qquad (3)$$

where m_p is the mass of a particle, c_p is the heat capacity, T_p is the particle temperature, v_p is the particle volume, and $\dot{q}$ is the other heat sources such as conduction and convection.

The results of adding microwave heating energy to particles' energy equation have been displayed in Fig. 2. As shown, the continuous increase in the particle temperature indicates the successful implementation of a uniform electromagnetic field. Moreover, gas temperature increases as it interacts with the particles absorbing microwave heating energy, indicating a prominent convective heat transfer between particles and gas. This could eventually provide a very hot medium for gas to decompose into its elements. Fig. 2 clearly demonstrates that microwave energy is first absorbed by particles, converted to heat, and then dissipated as convective heat to the gas.

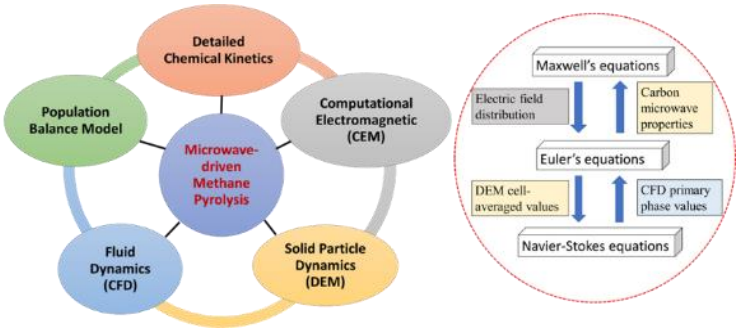

Fig. 3. Multiphysics study of CO_2-free hydrogen production via microwave-driven methane pyrolysis

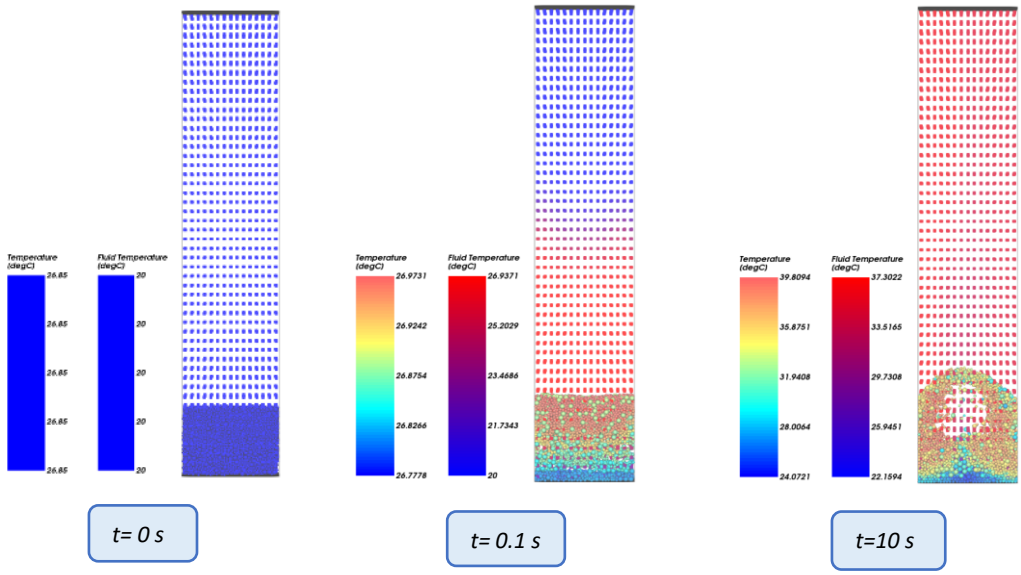

Fig. 4. Particle and gas temperature increase due to microwave heating energy absorption for three different time levels.

References

[1] Schneider S, Bajohr S, Graf F, Kolb T. State of the Art of Hydrogen Production via Pyrolysis of Natural Gas. ChemBioEng Rev 2020;7:150–8. https://doi.org/10.1002/cben.202000014.
[2] IEA. Global hydrogen demand by sector in the Net Zero Scenario, 2020-2030. Paris: n.d.
[3] Yang X, Nielsen CP, Song S, McElroy MB. Breaking the hard-to-abate bottleneck in China's path to carbon neutrality with clean hydrogen. Nat Energy 2022;7:955–65. https://doi.org/10.1038/s41560-022-01114-6.
[4] Sánchez-Bastardo N, Schlögl R, Ruland H. Methane Pyrolysis for Zero-Emission Hydrogen Production: A Potential Bridge Technology from Fossil Fuels to a Renewable and Sustainable Hydrogen Economy. Ind Eng Chem Res 2021;60:11855–81. https://doi.org/10.1021/acs.iecr.1c01679.
[5] Sun J, Wang W, Yue Q. Review on microwave-matter interaction fundamentals and efficient microwave-associated heating strategies. Materials (Basel) 2016;9. https://doi.org/10.3390/ma9040231.
[6] Vashisth A, Upama ST, Anas M, Oh JH, Patil N, Green MJ. Radio frequency heating and material processing using carbon susceptors. Nanoscale Adv 2021;3:5255–64. https://doi.org/10.1039/d1na00217a.

Hydrogen Production via Microwave-Induced Water Splitting at Low Temperature

A. Domínguez-Saldaña[1], L. Navarrete[1], M. Balaguer[1], B. García[2], D. Catalán[1], J. Santos-Blasco[1], P. Plaza-González[2], J. M. Catalá-Civera[2], J. M. Serra[1]

[1]Chemical Technology Institute (Universitat Politècnica de València –CSIC), Av. Los Naranjos, s/n, 46022 Valencia, Spain
[2]Institute of Information and Communication Technologies (Universitat Politècnica de València), Camí de Vera, s/n, 46022 Valencia, Spain.
adomsal@itq.upv.es

Keywords: microwave radiation, green hydrogen, ceramic materials, power applications, energy efficiency.

Nowadays, hydrogen is being used as an energetic vector for saving excess renewable energy. The most used techniques to generate hydrogen are thermochemical loopings [1], electrolysers [2], and hydrocarbon reforming [3]. However, all these techniques have several drawbacks, namely the high temperatures needed, the use of sophisticated machinery and the long operation times required for the hydrogen production.

Recently, the possibility to generate green hydrogen using electric energy, as microwave radiation, has been reported. This process uses metallic oxides as catalysts, e.g., CeO_2, and it occurs in a reactor at temperatures lower than 400ºC in less than five minutes (compared to more than 1000ºC in thermosolar technologies).

The hydrogen production mechanism happens in two steps. First, the material is irradiated with a microwave electromagnetic field, producing the reduction of the material with the concomitant release of oxygen (Fig. 1).

This radiation is able to stabilize a higher amount of oxygen vacancies in the fluorite structure at lower temperatures than the conventional radiative processes. When the microwaves are turned off in the presence of water, the material splits the H_2O molecule, therefore liberating a stream of molecular hydrogen and filling its oxygen vacancies. One example of this process is ceria-based materials.

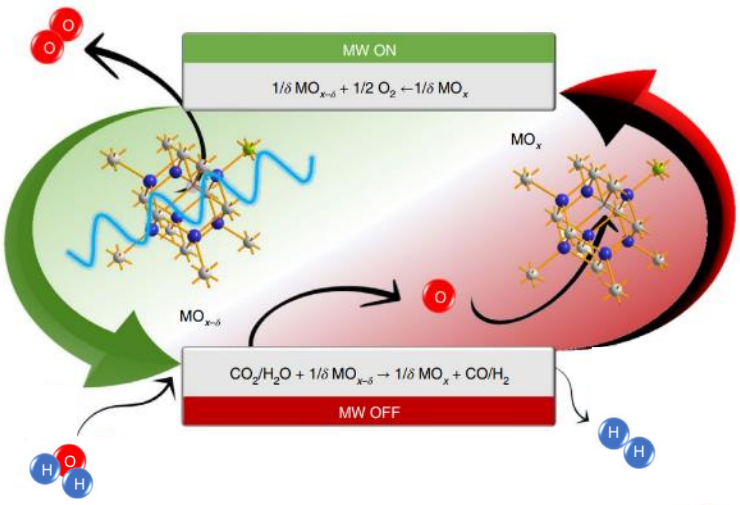

Fig. 1. Mechanism of microwave assisted water splitting process in a material with fluorite structure

The application of an external E-field transforms both the material's oxygen substoichiometry (δ) and charge carrier mobility, leading to the formation of oxygen vacancies and localized electronic charge carriers (polarons) per pair of reduced ceria atoms, accompanied by an increase in the electrical conductivity of the material [4]. This type of conductivity is not typical for ceria-type materials, which exhibit pure oxygen ion conductivity increase with the temperature [5]-[6].

In this work, we have synthesized and characterized a set of doped ceria, in order to study how the electromagnetic field interacts with the material, leading to material reduction. For this purpose, optical techniques and dielectric measurements have been used to monitor the process at each step.

Finally, to increase the amount of hydrogen produced, the influence of the dopant introduced in the ionic lattice has been studied with its ability to produce oxygen.

References

[1] Ran, J., Zhang, J., Yu, J., Jaroniec, M. & Qiao, S. Z. Chem. Soc. Rev. 43 (2014) 7787–7812.
[2] Vøllestad, E., Strandbakke, R., Tarach, M. et al. Nat. Mater. 18 (2019) 752–759.
[3] Sengodan, S., Lan, R., Humphreys, J., Du. et al. Renew. Sust. Ener. Rev. 82 (2018) 761-780.
[4] Serra, J. M., Borrás-Morell, J. F., García-Baños, et al. (2020). Nat. Energy. 5 (2020) 910-919.
[5] Balaguer, M., Solis, C., & Serra, J. M. J. Phys. Chem. 116 (2012) 7975-7982.
[6] Navarrete, L., Balaguer, M., Vert, V. B. et al. (2017). Fuel Cells. 17 (2017) 100-107.

Development of Sustainable Adsorbents for Post Combustion Carbon Capture: Conventional vs. Microwave-Assisted Activation

S. Biti[1], C. Fernández Martín[1, 3], A. Mccue[2], I. Graça[1], D. Dionisi[1]

[1]*School of Engineering, University of Aberdeen, AB24 3UE, Aberdeen, UK*
[2]*Department of Chemistry, University of Aberdeen, AB24 3UE, Aberdeen, UK*
[3]*Centre for Energy Transition, King's College, University of Aberdeen, Aberdeen AB24 3UE, UK*
cfmartin@abdn.ac.uk

Keywords: activated carbon, carbon capture, microwave susceptors, microwave activation, microwave heating

Post-combustion carbon capture has emerged as a key technology for the abatement of CO_2 emissions, for securing global net zero emissions, in line with Paris Agreement targets [1], a sentiment echoed notably at key UN Climate Change Conferences such as COP26 (2021) and COP27 (2022). Activated carbons (ACs) are promising, low-cost materials for post combustion CO_2 capture, which in being produced from renewable waste sources, can provide additional benefit to the circular economy [2]. Capitalising on this promising means of sustainable carbon capture requires an efficient AC production process. Microwave heating has thus emerged as a prospective alternative to conventional heating methods that rely on convective/conductive heating mechanisms during AC production [3].
This study investigates the development of cellulose-based sorbents for carbon capture, using both conventional and microwave heating.

Raw microcrystalline (μ) and alpha cellulose (α) were selected as the renewable feedstocks and were first converted to biochars by slow pyrolysis at 500°C. The next step in the process (converting biochars into ACs via activation) was used for comparison between conventional and microwave heating. Biochars were converted to ACs by CO_2 activation (20 ml/min) in a tubular furnace (600°C) and in a laboratory bench-scale microwave at lower temperature (400°C). For microwave activation, commercial and granular AC, Norit R2030CO2, referred to as Norit R, was mixed with the biochars prior microwave activation (1:4 weight ratio of biochar to Norit R) to improve heating.

For both methods of activation, ACs of 20 and 30% burn-off were produced. Key characterisation procedures adopted included the determination of their textural properties characterised from the measured N_2 (-196°C) and CO_2 (0°C) adsorption isotherms. Furthermore, their maximum CO_2 adsorption/desorption capacity under dynamic conditions and their cyclic adsorption-desorption behaviour, completed across 10 cycles, were measured in a Thermogravimetric Analyser (TGA). Finally, a dielectric kit for vials developed by the Microwave Division of the ITACA Institute (Polytechnic University of Valencia, Spain), was used to determine dielectric properties of the samples.

The reduced activation temperature under microwave-assisted heating was driven by the modest dielectric response of the biochars, detailed in Table 1. The loss tangent of the biochars produced at 500°C (*tan δ*: 0.01-0.02) are even inferior to that of the raw cellulose feedstocks (*tan δ*: 0.06-0.09), which justified the use of a microwave susceptor during their microwave-assisted activation. The greater loss tangent of Norit R (*tan δ* = 0.57*)* allowed for the sustained activation of the biochars at 400°C.

Table 1. Dielectric properties of cellulosic feedstocks, biochar and commercial AC Norit R, measured at 25 °C

Sample	ε'^{a}	ε''^{b}	$tan\delta^{c}$
μ	1.50	0.09	0.05
α	1.54	0.06	0.04
μ-Char	1.41	0.01	0.01
α-Char	1.44	0.03	0.02
Norit R	16.47	9.38	0.57

[a]Dielectric constant [b]Loss factor [c]Loss tangent

Table 2 details the calculated textural properties from isotherm data along with the average adsorption capacity per cycle of adsorption for the sorbents. Conventionally activated carbons are denoted with 'C', whilst microwave-activated AC are denoted as 'M'. The number following these letters represents that activation temperature (4 = 400°C; 6 = 600°C). The nomenclature is concluded with a percentage representing the amount of sorbent burned off during activation.

Most notably, micropore (W_0) and total pore volume (W_T) calculations revealed both methods of activation to produce highly microporous sorbents (W_0/W_T > 0.90), which is desirable for post combustion CO_2 capture. For both conventional and microwave prepared ACs, CO_2 adsorption capacity increased with increasing activation burn-off. This finding was identified as correspondent to greater development of the textural properties with increasing burn-off, specifically narrower average micropore width (L_0).

All sorbents also displayed substantial cyclic adsorption capacities, as shown in Figure 1, and stability after cycles with minimal fluctuation in these capacities observed (± 2%) across 10 cycles, and capability to fully desorb CO_2. From Table 2 it is observed that at equivalent burn-offs, microwave-prepared ACs exhibited greater CO_2 adsorption capacities than both the commercial Norit R and the conventionally prepared ACs, despite these ones being produced at an activation temperature 200°C lower than the conventional materials. This is indicative of interfacial heating and conductive heating effects in the assisted-microwave heating method contributing to improved textural properties development at lower temperatures, compared to conventional furnace heating.

The microwave-prepared ACs μ-M4-20% and μ-M4-30% are the ACs which showed the highest CO_2 adsorption capacities amongst all sorbents produced (1.64 and 1.73 mmol/g, respectively), and yet capacity was greater than that displayed by Norit R (1.58 mmol/g), which is a commercial AC formulated specifically for CO_2 capture. Accordingly, these two microwave-prepared ACs show outstanding potential to be effective adsorbents for post combustion carbon capture at a commercial standard, with the additional advantage of circularity as they were produced from cellulose.

Overall, this study identified an efficient, moderate-temperature route for developing sustainable sorbents for post combustion carbon capture. Their competitive CO_2 adsorption capacity compared to a commercial CO_2-capturing sorbent justifies their further development for use in post combustion capture applications.

Table 2. Textural properties for sorbents calculated from N_2 (a-e) and CO_2 (f-g) isotherms.

Sample	S_{BET}[a] (m^2/g)	W_T[b] (cm^3/g)	W_0[c] (cm^3/g)	D[d] (nm)	L_0[e] (nm)	$W_{0,ultra}$[f] (cm^3/g)	$L_{0,ultra}$[g] (nm)	$Q_{av,ads}$[h] (mmol/g)
μ-Char	403	0.18	0.17	1.82	1.46	0.18	0.63	0.90
μ-C6-20%	443	0.20	0.19	1.80	0.72	0.23	0.61	1.32
μ-C6-30%	487	0.21	0.20	1.72	0.63	0.27	0.59	1.58
μ-M4-20%	434	0.20	0.20	1.75	0.84	0.25	0.60	1.64
μ-M4-30%	510	0.21	0.21	1.80	0.72	0.25	0.59	1.73
α-Char	254	0.12	0.10	1.87	2.22	0.16	0.64	0.57
α-C6-20%	385	0.17	0.16	1.85	0.75	0.22	0.63	1.35
α-C6-30%	464	0.21	0.19	1.70	0.71	0.22	0.62	1.44
α-M4-20%	456	0.19	0.18	1.75	0.90	0.22	0.60	1.46
α-M4-30%	463	0.22	0.20	1.82	0.91	0.23	0.59	1.50
Norit R	870	0.62	0.37	0.60	2.84	1.41	0.26	1.58

[a]Specific surface area; [b]Total pore volume; [c]Total micropore volume; [d]Average pore diameter; [e]Average micropore width; [f]Ultramicropore volume; [g]Average ultramicropore width [h]Average CO_2 adsorbed per cycle

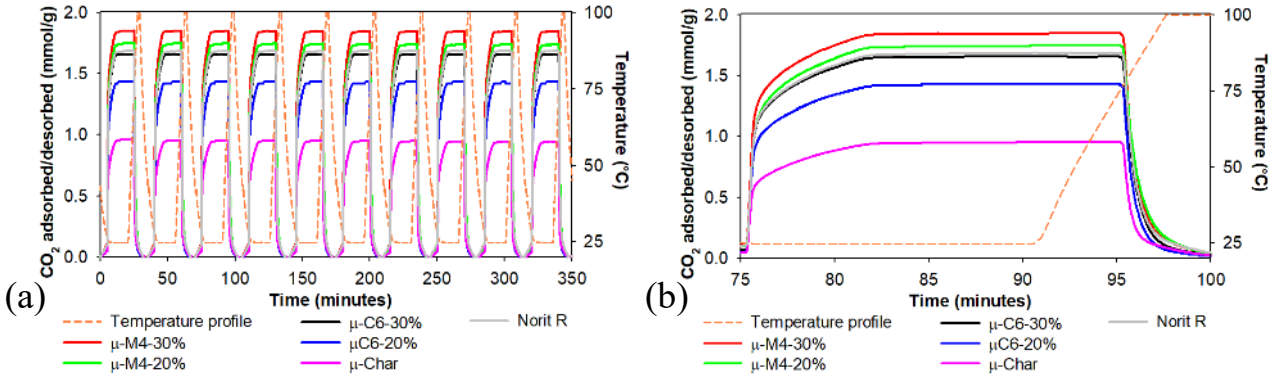

Fig. 1. Dynamic CO_2 adsorption-desorption cycles and TGA temperature profiles for microcrystalline cellulose sorbents over (a) 10 cycles (b) A single cycle (cycle no.3)

References

[1] C. Greig, S. Uden, The value of CCUS in transitions to net-zero emissions, The Electricity Journal. 34 (2021) 107004. https://doi.org/10.1016/J.TEJ.2021.107004.
[2] K. Malini, D. Selvakumar, N.S. Kumar, Activated carbon from biomass: Preparation, factors improving basicity and surface properties for enhanced CO_2 capture capacity – A review, Journal of CO_2 Utilization. 67 (2023) 102318. https://doi.org/10.1016/J.JCOU.2022.102318.
[3] M.A.A. Zaini, M.J. Kamaruddin, Critical issues in microwave-assisted activated carbon preparation, J Anal Appl Pyrolysis. 101 (2013) 238–241. https://doi.org/10.1016/j.jaap.2013.02.003.

Investigation into Microwave-Metal Discharge during Microwave Machining of Stainless Steel

A. Singh[1], A. K. Sharma[1]

[1]*Indian Institute of Technology Roorkee, Roorkee, Uttarakhand, India*
aks@me.iitr.ac.in

Keywords: microwave-metal (MW-m) discharge, microwave machining, delay, spark, arc

Microwave-metal discharge is a complex and inadequately understood electrical phenomenon observed during the interaction of microwaves with sharp metallic and some semiconductive and carbonaceous materials [1]. Microwave machining of non-metallic [2][3][4] and metallic [5][6] materials with microwave-metal discharge have been explored in limited studies. Moreover, the characteristics of microwave-metal discharge during microwave machining of metallic materials have rarely been investigated.

This work investigates microwave machining under the tool-work gap of 0.0–1.0 mm between the pointed thoriated tungsten tool (diameter: 1.6 mm) and stainless steel sheet (thickness: 1.0 mm) inside a customized microwave applicator operating under atmospheric conditions at 2.7 kW and 2.45 GHz frequency. The activities in the machining zone were recorded by a camera (fps: 26). Microwave-metal discharge was not triggered during tool-work contact since contact prevented charge concentration at the pointed tool by leaking charge into the electrically conductive work. Consequently, leakage inhibited the intensified electric field at the pointed tool needed for triggering discharge. Microwave-metal discharge was generated after a delay (of the order of seconds) when microwave power was switched on. The delay is attributed to the joule heating of the tool facilitating the excitation of electrons required for the discharge initiation. On average, delay decreased with reducing tool-work gap since shorter gap required lower breakdown voltage.

The tendency of sparking and arcing after the delay increased with decreasing tool-work gap. The short-lived (of the order of a fraction of a second) sparks abruptly initiated, grew and collapsed (Fig. 1(a)–(h)). Despite its ephemeral nature, sparks generated an infinitesimal crater (Fig. 1(i)). The long-lived arc initiated similarly, but the arc area kept pulsating (Fig. 2(a)–(p)) before collapsing when the power was switched off. The pulsation was due to the alternating nature of the microwave. The arc generated a considerably broader and deeper crater (Fig. 2(q)). In both cases, the crater diameter is considerably smaller than the average spark and arc diameter. Effects of tool-work gap on machining characteristics are also analyzed. This study will help advance the understanding of versatile microwave machining process based on microwave-metal discharge.

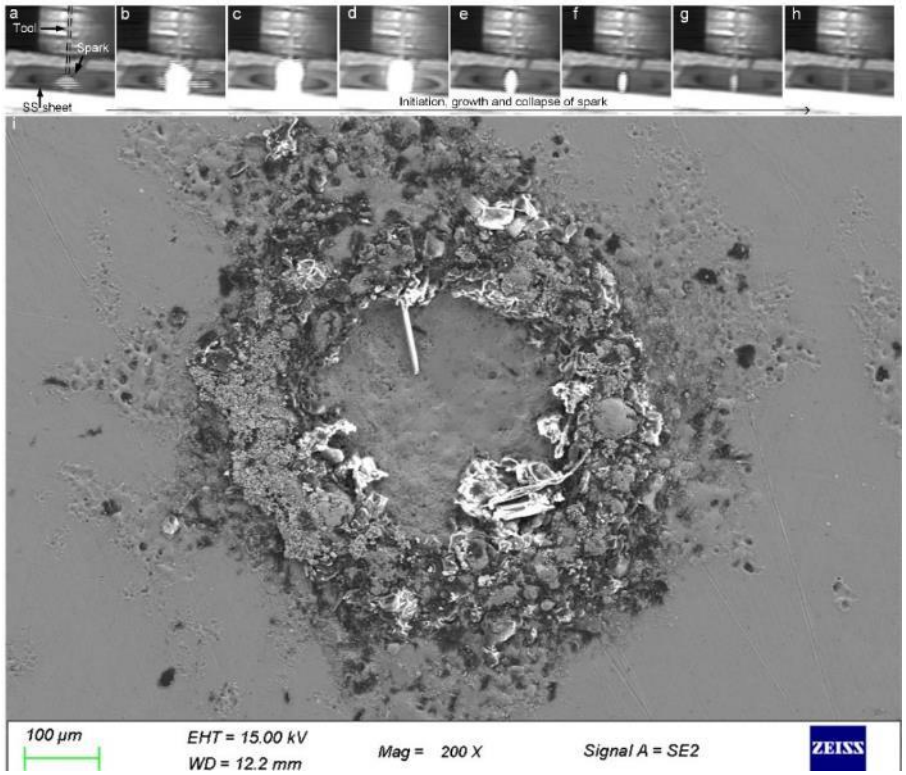

Fig. 1. (a)–(h) Microwave-metal discharge-induced spark and (i) corresponding crater under 0.1 mm tool-work gap

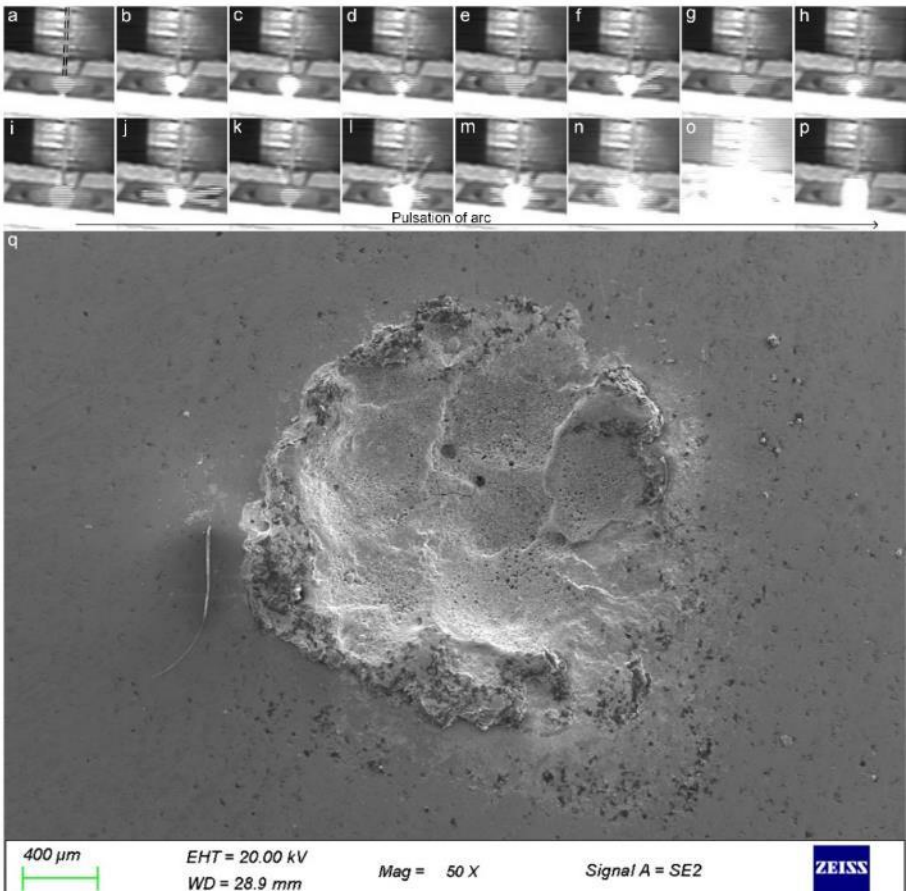

Fig. 2. (a)–(p) Microwave-metal discharge-induced arc and (q) corresponding crater under 0.2 mm tool-work gap

References

[1] Sun, J., Wang, W., Yue, Q., Ma, C., Zhang, J., Zhao, X. and Song, Z., 2016. Review on microwave–metal discharges and their applications in energy and industrial processes. Applied Energy, 175, pp.141-157.
[2] Lautre, N.K., Sharma, A.K., Kumar, P. and Das, S., 2015. A photoelasticity approach for characterization of defects in microwave drilling of soda lime glass. Journal of Materials Processing Technology, 225, pp.151-161.
[3] Lautre, N.K., Sharma, A.K., Kumar, P. and Das, S., 2018. Experimental evaluation of a microwave drilling process in Perspex. Journal of Testing and Evaluation.
[4] Kumar, G., Mishra, R.R. and Sharma, A.K., 2021. On defect minimization during microwave drilling of borosilicate glass at 2.45 GHz using flowing dielectric and optimized input power. Journal of Thermal Science and Engineering Applications, 13(3).
[5] Singh, A. and Sharma, A.K., 2020. On microwave drilling of metal-based materials at 2.45 GHz. Applied Physics A, 126(10), p.822.
[6] Gupta, P., Singh, A., Sharma, A.K. and Singh, I., 2023. Influence of liquid dielectric medium on microwave-metal discharge-based drilling of AISI 304 stainless steel. Applied Physics A, 129(2), p.150.

A 5.8 GHz Phased-Array Antenna Design for Weed Control Purpose

A. Omrani[1], G. Link[1], J. Jelonnek[1,2]

[1]*IHM, Karlsruhe Institute of Technology, Karlsruhe, Germany*
[2]*IHE, Karlsruhe Institute of Technology, Karlsruhe, Germany*
adel.hamzekalaei@kit.edu

Keywords: phased-array antenna, slotted waveguide antenna, power applications

In farming production, weeds compete with crops for sunlight, space, nutrients, water, and CO_2 and can significantly impact crop products worldwide. Dense weed growth can make harvesting very difficult and reduce it significantly. Even though an estimated 3 billion kg of pesticides are currently applied worldwide, it is estimated that 37 % of global crop production is still lost. 13 % of this is due to insects, 12 % to plant pathogens, and 12 % to weeds [1]. Weed control by microwaves is an environmentally friendly method for replacing chemical and pesticide methods respectively, which are no longer acceptable from an ecological point-of-view [2, 3].

A slotted waveguide phased array antenna operating at 5.8 GHz is designed to provide the maximum electric field strength at the reactive near-field region of the phased array for weed control purposes. Delivering the maximum possible electromagnetic (EM) power at the expected area of the weed demands a near-field focused (NFF) phased array antenna. In this manuscript, the conventional phase shift between the elements of the phased array is applied to achieve the maximum electric field at the near field area. A slotted waveguide (SWA) phased array antenna has been designed to demonstrate the feasibility of weed control using the phased array antenna in the near-field region. It is shown that the SWA (i) is appropriate for high-power applications, (ii) enables the fabrication of the phased array with a low number of elements, and (iii) provides the required focused area in both longitudinal and lateral directions. Due to the distribution of the slots in the longitudinal direction, the radiation pattern in the H-plane is already focused and in the E-plane it is not. Also, by controlling the number of slots, the size of the focal point in this direction can be adjusted. Needless to say, additional antennas are not required in this direction, which reduces the costs and complexity of the phased array antenna and overall system. By increasing the number of antennas, a focus on the E-plane is achieved.

Fig. 1 give the schematic of the single SWA (a) and proposed phased array antenna (b), which operates at 5.8 GHz. The dimension of the cross-section of the waveguide is 40.4 mm x 9.8 mm. Each SWA contains 10 slots with a length of 22.4 mm and a width of 4 mm. For ease of fabrication, the slots are slightly curved. The center distance of the slots to the sidewall is 11 mm. The center-to-center distance of two slots in the longitudinal direction is 32 mm. The distance between the last slots to the short wall is 10 mm. The simulated return loss of the designed SWA is depicted in Fig. 1 (c) in the ISM frequency band.

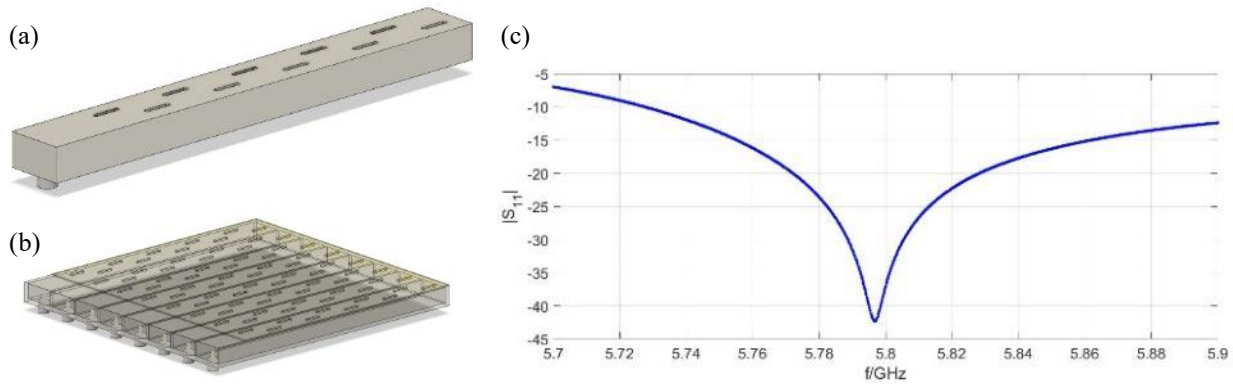

Fig. 1. Schematic of the SWA antenna (a) top view, (b) phased array and its simulated return loss (c).

A full wave simulation using commercial CST Studio Suite is used to obtain the electromagnetic field distribution in the domain of interest. It should be noted, the input power of the phased-array antenna is 400 W (50 W for each element). Fig. 2 (a) represents the electric field distribution when the far-field assumption is used to shape the phase distribution of the radiating elements. For a better comparison, the electric field distribution versus the axial distance of the antenna is plotted in Fig. 2 (b). As can be understood from this figure, the maximum electric field is occurring in the radiative near-field range of the phased array.

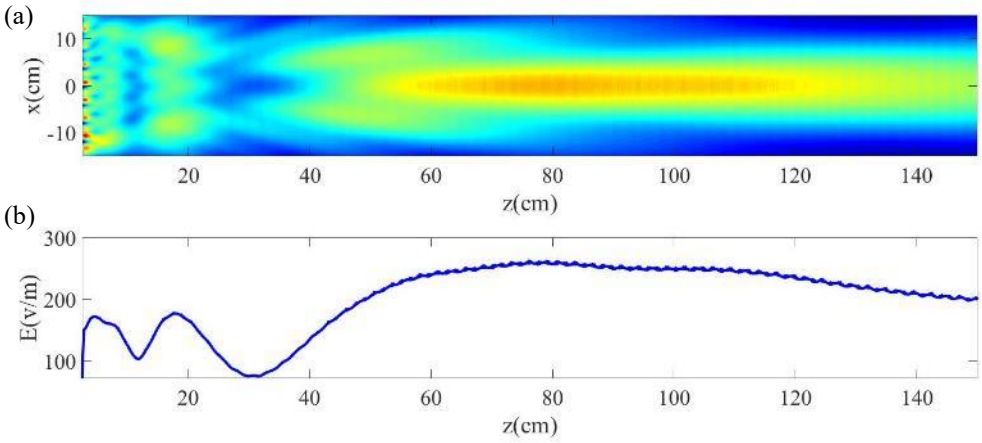

Fig. 2. (a) Electric field distribution in the radiative near field, (b) Electric field profile in z-direction in the E-plane.

To obtain the steering of the designed phased-array antenna in the near-filed range, the different phase shift is applied to the elements of the phased-array antenna, and the 3 dB electric field distribution is plotted in a domain of $[x \times y] = [100 \times 100]\ cm$.

The phased array antenna is positioned at the center of the plane, i.e. $(x, y) = (0\ cm, 0\ cm)$. Furthermore, it assumed the crop region's length is $10\ cm$, it starts from $x = 17.5\ cm$ to $x = 27.5\ cm$. Hence, the phase-array antenna should be able to span the crop region. The steering performance is shown in Fig. 3. The crop region is shown by white lines and each cell is $5\ cm \times 5\ cm$. As can be perceived from Fig. 3, a focus on the electric field distribution using the current design of the phased array can be provided at the pre-obtained location of the weed.

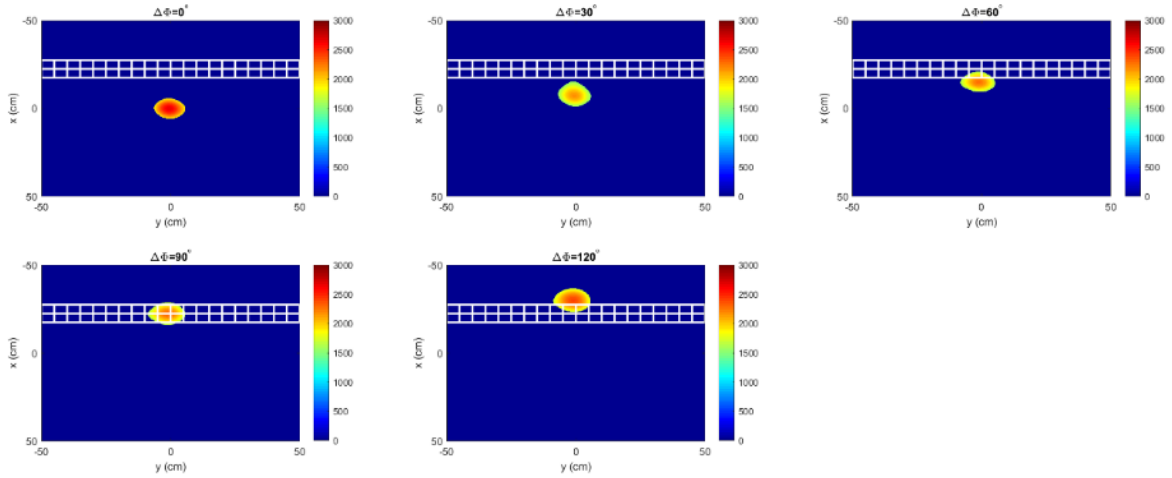

Fig. 3. Steering for different phase-shift and the electric field strength in the focused array at $z = 70\ cm$.

Moreover, it's worth mentioning the effect of the soil is not considered in the current simulations. By considering the effect of the soil, the steering doesn't change. However, the electric field strength would increase in the location of the weed due to the reflection from the soil. It may increase the field strength at the position of the weed. Furthermore, in the next studies, it will be shown how to increase the electromagnetic field strength at a closer range to the phased-array antenna using the time-reversal technique.

Acknowledgement

This Project is supported by the Federal Ministry for Economic Affairs and Climate Action (BMWK) on the basis of a decision by the German Bundestag. (project number KK5431301DF1)

References

[1] D. Pimentel, *Pest management in agriculture. In D. Pimentel (Ed.), Techniques for Reducing Pesticide Use: Environmental and Economic Benefits.* John Wiley & Sons, 1997.
[2] G. Brodie, M. V. Jacob, and P. Farrell, *Microwave and Radio-Frequency Technologies in Agriculture*. Warsaw, Poland: De Gruyter Open Poland, 2016.
[3] G. Brodie, Y. Pchelnikov, and G. Torgovnikov, "Development of microwave slow-wave comb applicators for soil treatment at frequencies 2.45 and 0.922 ghz (theory, design, and experimental study)," *Agriculture*, vol. 10, no. 12, 2020.

Experimental Study of a Microwave Methane Plasma for Hydrogen and Carbon Production

A. Martin Ortega[1], A. Hleli[1], M. Castelain[1], M. Radoiu[2], T. Belmonte[3], C. Noel[3]

[1]*SAKOWIN, Technopôle de l'Arbois, Aix-en-Provence, France*
[2]*Microwave Technologies Consulting, Rillieux-la-Pape, Lyon, France*
[3]*Université de Lorraine, CNRS, IJL, F-54000, Nancy, France*
alvaro@sakowin.com

Keywords: microwaves, plasma, hydrogen, methane decomposition, optical emission spectroscopy

Hydrogen gas is being promoted as a CO_2-free alternative to burning fossil fuels, whose use as energy source needs to be severely curtailed in view of minimizing the effects on climate change **Error! Reference source not found.**. Hydrogen gas is produced t hrough three main processes: steam reforming **Error! Reference source not found.**, water electrolysis **Error! Reference source not found.**,**Error! Reference source not found.**, and methane and/or other hydrocarbons decomposition **Error! Reference source not found.**. Steam reforming also generates CO_2 and as such, it is not seen as an environmentally acceptable source of CO_2-free energy. Water electrolysis, on the other hand, consumes a large amount of energy and requires a significant footprint for the process to become cost-effective. Direct decomposition of methane into hydrogen gas and solid carbon requires significantly less energy and does not emit CO_2. This process, known as methane pyrolysis, is achieved at high enough temperatures; however, it has not been deployed industrially so far.

Approaches based on different plasma technologies have offered new opportunities to industrially develop and deploy the plasma decomposition of methane (plasmalysis), with focus on either the produced solid carbon **Error! Reference source n ot found.** or on the hydrogen gas **Error! Reference source not found.**. The main advantages of using a plasma to achieve methane decomposition are the direct transfer of energy from the electric or electromagnetic system to the gas/plasma, the increased reactivity of the system due to electron collisions (ionization and excitation processes) and the access to energy levels inaccessible from simple heating. SAKOWIN develops a plasmalysis system based on microwave excited plasma, which allows very fast on/off cycles, removes the need for electrodes and allows for independent and fast control of process parameters, such as gas flow and microwave power delivered to the gas. A first prototype operating at 2.45 GHz and 6 kW of microwave power was used for the scope of the present work.

In this paper, we present the study of a nitrogen-methane microwave-excited plasma at atmospheric pressure using optical emission spectroscopy (OES). OES enables the temperature measurement of different probes, notably blackbody temperature, rotational temperature and vibrational temperature. A continuous spectrum dominates light emission at high methane concentration, being emitted possibly from carbon particles formed into the plasma. Fitting this continuous emission to a blackbody spectrum gives a temperature that corresponds to that of carbon particles; in turn, we can approximate it to the gas temperature in the regions where these carbon particles are present. Light emission spectra from CN and C_2 bands can be simulated to obtain rotational temperatures for these probes. The thus-determined temperatures are different between CN and C_2 bands, while being significantly higher than those obtained from blackbody radiation. There were no significant emissions from H_2 bands or from atomic H lines for any of the tested conditions, despite H_2 being detected at the outlet of the system by micro-gas chromatography (µGC) measurements. No NH bands were detected for any of the tested conditions, nor was NH_3 detected by µGC at the outlet of the system. The main products of the reaction were hydrogen, solid carbon and acetylene; small amounts of HCN and traces of higher hydrocarbons (C_3-C_6) by-products were also identified in the gas phase via µGC.

The results obtained by OES measurements provide an insight of the energy distribution across different species and energy levels, including intermediate molecules produced during the microwave plasmalysis of methane in nitrogen. These results will be further used for testing and validation of a model of the plasmalysis of methane currently under development at SAKOWIN. Equally important, the results are used for the optimization of SAKOWIN's commercial products at 2.45 GHz and 915 MHz, the latter with microwave power levels up to 100 kW.

References

[1] IPCC, 2021: "Climate Change 2021: The Physical Science Basis. Contribution of Working Group I to the Sixth Assessment Report of the Intergovernmental Panel on Climate Change". *Cambridge University Press, Cambridge, United Kingdom and New York,* NY, USA, 2391 pp
[2] Doan Pham Mihn, Tan Ji Siang, Dai-Viet N. Vo, C. Ridart, A. Nzihou and D. Grousset, "Chapter 4 - Hydrogen Production From Biogas Reforming: An Overview of Steam Reforming, Dry Reforming, Dual Reforming, and Tri-Reforming of Methane", Hydrogen Supply Chains, Academic Press, 2018, 111-166
[3] H. Zhang, G. Lin and Jincan Chen, "Evaluation and calculation on the efficiency of a water electrolysis system for hydrogen production", *Int. J. of Hydrogen Energy*, vol. 35 (20), 2010,10851-10858
[4] S. Shiva Kumar and V. Himabindu, "Hydrogen production by PEM water electrolysis – A review", *Mat. Science for Energy Tech.*, vol. 2 (3), 2019, 442-454

[5] H. F. Abbas and W.M.A. Wan Daud, "Hydrogen production by methane decomposition: A review", *Int. J. of Hydrogen Energy*, vol. 35 (3), 2010, 1160-1190
[6] L. Fulcheri, V.-J. Rohani, E. Wyse, N. Hardman and E. Dames, "An energy-efficient plasma methane pyrolysis process for high yields of carbon black and hydrogen", *Int. J. of Hydrogen Energy*, vol. 48 (8), 2023, 2920-2928,
[7] T. Boutot, J. Bullerwell, Z. Liu, W. Niu, T.K. Whidden and & Y. Yang, "Hydrogen and nanostructured carbon by plasma decomposition of natural gas", *ECS Transactions*, vol. 16 (50), 155.
[8] T. Belmonte, C. Noël, T. Gries, J. Martin and G. Henrion, "Theoretical background of optical emission spectroscopy for analysis of atmospheric pressure plasmas", *Plasma Sources Sci. and Tech.*, vol. 24 (6), 2015, 064003

Microwave Activation of Clays for Cement Industry in DESTINY Project

A. M. López-Buendía[1], E. Brau[1], J. C. Martínez[2], B. Łysiak[2], B. García-Baños[3]

[1]*CEINNMAT, INNCEINNMAT, SL. C. Agustin Escardino, 9. Paterna-Valencia, Spain*
[2]*CEMEX Innovation Holding AG, General-guisan-strasse 6,6300 Zug, Switzerland*
[3]*Universitat Politècnica de València, Camino De Vera, s/n. 46022 Valencia, Spain*
angel.lopez@ceinnmat.com

Keywords: microwave, calcined clays, dielectric properties, cement, pozzolan

Calcined clays have received significant attention in the cement industry to replace parts of the clinker content as supplementary cementitious materials (SCM) [1] and hydraulic lime because they exhibit pozzolanic activity [2]. The activation of clays using microwave energy has shown a good performance as pozzolanic materials for the cement industry with singular behaviour of activation and pozzolanic performance. Previous experiences using microwave activation of clays demonstrated the reactivity in alkaline solution [3], suggesting the behaviour with cement mortar or concrete.

Selected clays containing kaolinite were analysed by dielectric thermal analysis during microwave heating (MWDETA) to determine the dielectric constant (ε’) and loss factor (ε”) along the temperature of process. Mineralogical analysis of clay minerals and associated minerals were made using X-ray powder diffraction (XRD), complementing the transformation with thermogravimetry analysis (TGA).

Microwave energy is used to heat the clay mineral up to temperature of stability that, once achieved, leads to an endothermal reaction of dehydroxylation, where the hydroxides (OH^-) are liberated from the interlayered structure of the kaolinite and transformed into metakaolinite, also known as pop metakaolin.

An explanation of the process was done so that, under microwave energy, the transformation of dehydroxilation occurs suddenly due to the fast absorption of the unstable interlayered hydroxide bounds, with subsequent intercrystalline explosions drawn by the sublimation of the hydroxides. These expansions generate micro structural packages with coexistence of kaolinite and metakaolinite. Under conventional heating, dehydroxilation is markedly radial from the outer to the inner part of the kaolinite crystal.

After microwave treatment under different conditions, the characterisation was done using a mechanical test of pozzolanity on mortar bars with a partial substitution of clinker by microwave activated clays. To evaluate the effect of the microwave activation compared with thermal activation of clays, tests were done to samples with the conventional thermal activation procedure preparing clays in a furnace at 850ºC for 2 hours, as well as untreated clays.

Results show that some microwave treatments had an optimum mechanical performance using 200ºC below the required temperature in the conventional process, with residence times 30 times faster. These results show that the microwave activation is a very promising technology that is under implementation in the industry.

The trials performed during DESTINY project [4] demonstrated the applicability of the technology of microwave activation for kaolinite rich clays. New research and innovation activities are planned to generalize the technology for families of clays and to a higher scale of production.

References

[1] M Schneider, M Romer, M Tschudin, H Bolio. Sustainable cement production—present and future. Cement and Concrete Research. 2011;41(7):642-50.
[2] R Fernandez, F Martirena, KL Scrivener. The origin of the pozzolanic activity of calcined clay minerals: A comparison between kaolinite, illite and montmorillonite. Cement and Concrete Research. 2011;41(1):113-22.
[3] A.M. López-Buendía, J. Bastida, M.M Urquiola, B. García Baños, J.M. Catalá-Civera. Industrial microwave process for pozzolanic pop metakaolin and calcined clays. XVI International Clay Conference (ICC2017), Vol. 7, p. 490,, Granada (Spain), 2017
[4] DESTINY (H2020-NMBP-SPIRE-2018) GA n° 820783. Development of an Efficient Microwave System for Material Transformation in energy INtensive processes for an improved Yield.

Removal of Petroleum Hydrocarbon from Solid Materials using Microwave Processing

D. Tang'an[1], J. Robinson[1], M. Adam[1], E. Binner[1]

[1]*University of Nottingham, Department of Chemical and Environmental Engineering, University Park Campus, Nottingham, NG7 2RD, United Kingdom.*
Diret.Tang'an@nottingham.ac.uk

Keywords: microwave processing technology, land contamination, total petroleum hydrocarbon (TPH), remediation.

The rise in the world's energy demand has led to an increase in oil and gas exploitation and exploration activities. During these processes, spillages from crude oil and its refined products occur resulting in major environmental problems such as land pollution. Total Petroleum Hydrocarbon (TPH) is identified as a key land contaminant from these spillages that has led to the destruction of flora and posed severe health risks to human inhabitants [1, 2]. This research explores the viability of microwave processing technology for the removal of TPH from contaminated solid materials such as soil.

In this work, heavy oil-contaminated solids (road planings and filter cake samples) were collected from the UK and used for this study. These samples were characterised for dielectric properties, moisture, and oil contents and then subjected to microwave heating at 2.45 GHz using specific energies ranging from 0.4 – 4 kJ/g (see Table 1 and Fig. 1). Oil removal of >85 wt.% and ≥90 wt.% was achieved in road planings and filter cake samples respectively in ≤ 6.5 minutes. The power density was identified as the important parameter that drives oil removal from these solid materials. As power density increased, a corresponding increase in oil removal was observed [3, 4]. This remediation technology demonstrates high potential for the decontamination of these solids over a short residence time which would consume less energy and hence reduce the overall remediation cost compared with conventional heating.

Table 1. Oil and moisture contents of contaminated solids (wet basis)

Solid material	Oil content %(w/w)	Moisture content %(v/m)
Road planings	2.9 ± 0.14	7.3 ± 0.45
Filter cake	10.4 ± 0.15	52.1 ± 0.36

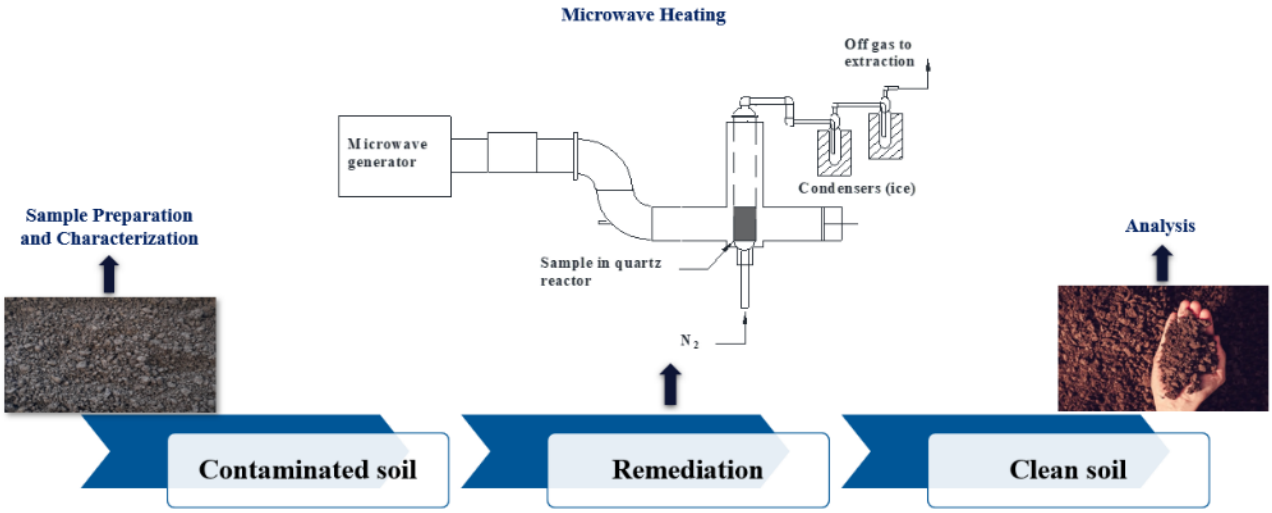

Fig. 1. Overview of methodology

References

[1] C. B. Chikere, I. J. Mordi, B. O. Chikere, R. Selvarajan, T. O. Ashafa and C. C. Obieze, "Comparative metagenomics and functional profiling of crude oil-polluted soils in Bodo West Community, Ogoni, with other sites of varying pollution history," Annals of Microbiology, vol. 69, pp. 495-513, 2019.

[2] K. Sam, F. Coulon and G. Prpich, "Management of petroleum hydrocarbon contaminated sites in Nigeria: Current challenges and future direction," Land use policy, vol. 64, pp. 133-144, 2017.

[3] J. Robinson, E. Binner, A. Saeid, M. Al-Harahsheh and S. Kingman, "Microwave processing of oil sands and contribution of clay minerals," Fuel, vol. 135, pp. 153-161, 2014.

[4] A. Buttress, E. Binner, C. Yi, P. Palade, J. Robinson and S. Kingman, "Development and evaluation of a continuous microwave processing system for hydrocarbon removal from solids," Chemical engineering journal, vol. 283, pp. 215-222, 2016.

Highly Selective Microwave Destruction of Plastic to Produce Hydrogen Gas

M. Nelson[1], A. Morgan[1], X. Jie[2], P. Edwards[2], D. Slocombe[1]

[1]*Centre for High Frequency Engineering, Cardiff University, Cardiff, UK*
[2]*Inorganic Chemistry Laboratory, University of Oxford, Oxford, UK*
NelsonMJ@cardiff.ac.uk

Keywords: microwave catalysis, plastic degradation, hydrogen production, resonant cavity heating, magnetic field

Abstract

Microwave resonant cavity heating has been used to heat materials both rapidly and selectively. Many studies investigating microwave heating utilise subject materials' dielectric characteristics to heat primarily using the electric field. Recent work has also effectively demonstrated using microwave heating of a catalyst substance to produce high-purity hydrogen from the degradation of hydrocarbon sources such as liquid alkanes [1][2] and powdered plastic [3-5]. Two major environmental problems that need to be urgently addressed are the massive amounts of plastic waste produced and the release of greenhouse gases such as carbon dioxide into the atmosphere. This work tackles these issues by investigating highly selective heating of plastic waste to degrade it into high-purity hydrogen that can be used to generate clean energy in fuel cells and other valuable products such as carbon nanotubes (CNTs), while minimising the volume of undesirable products like carbon dioxide.

Work by Jie et al. (2020) [3] has demonstrated a one-step process for the destruction of plastic into hydrogen and CNTs. Published results show a 650 ml volume of produced gases over only 90 seconds, with more than 80% of that volume being hydrogen (Fig. 1a.). Samples used in Jie et al. [3] were irradiated under 1000 W in the centre of a TM_{010} resonant cavity, being exposed to the region with the greatest electric field strength. This work instead focuses on a region within a TM_{010} cavity that experiences the greatest magnetic field strength. As fewer materials will be strongly heated by a microwave magnetic field, this allows for greater heating selectivity and increased efficiency as less power will be absorbed by the plastic sample. The resulting process will be more robust to the presence of any contaminants or other materials such as water. Using a target input power to the cavity of only 50 W, multiple samples of 0.1 g and 0.4 g of magnetite (Fe_3O_4) have been heated to over 700 °C in 120 seconds (Fig. 1b.). With a target power of 41.5 W, consistent heating to over 800 °C of samples of 0.1 g of magnetite has also been achieved. Further aims of this work include the testing of different iron-based materials as catalysts, such as pure iron nanopowders, and to experiment with different catalyst-plastic mixing ratios to produce the greatest proportion of hydrogen.

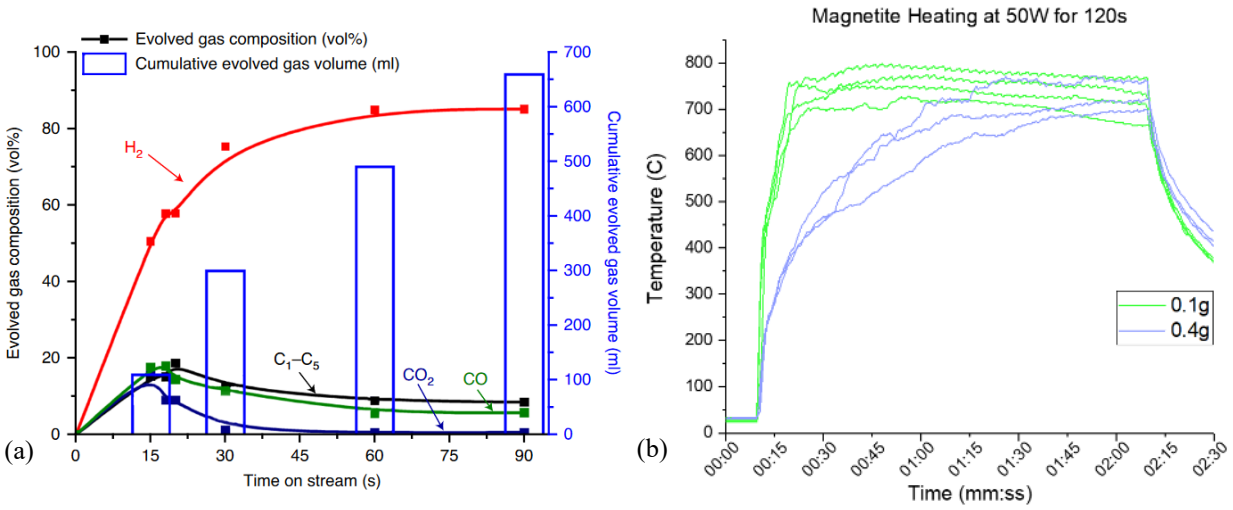

Fig. 1. (a) A time-on-stream analysis that shows gas evolution as a function of the time of the microwave-initiated decomposition of 0.4 g HDPE using 0.4 g of FeAlOx catalyst from Jie X. et al. (2020) and **(b)** A temperature-time plot of samples of Fe_3O_4 with masses of 0.1g and 0.4g in a TM_{010} cavity subject to a target power of 50 W for 120s

The selectivity of the magnetic-microwave heating process has been demonstrated using layers of magnetite and haematite (Fe_2O_3) and IR imagery. Shown in Figure 2 are samples of these iron oxide powders layered inside the quartz sample tubes after microwave irradiation of 30 W for 60 seconds. These images show a stark difference in reaction to the microwave radiation as in both cases the magnetite portions heat to greater temperatures than the haematite. As with tests performed on individual powder samples the magnetite increased in temperature rapidly, while the haematite increased more slowly. Some of the heating of haematite in these images can be attributed to conduction from the much hotter magnetite powder.

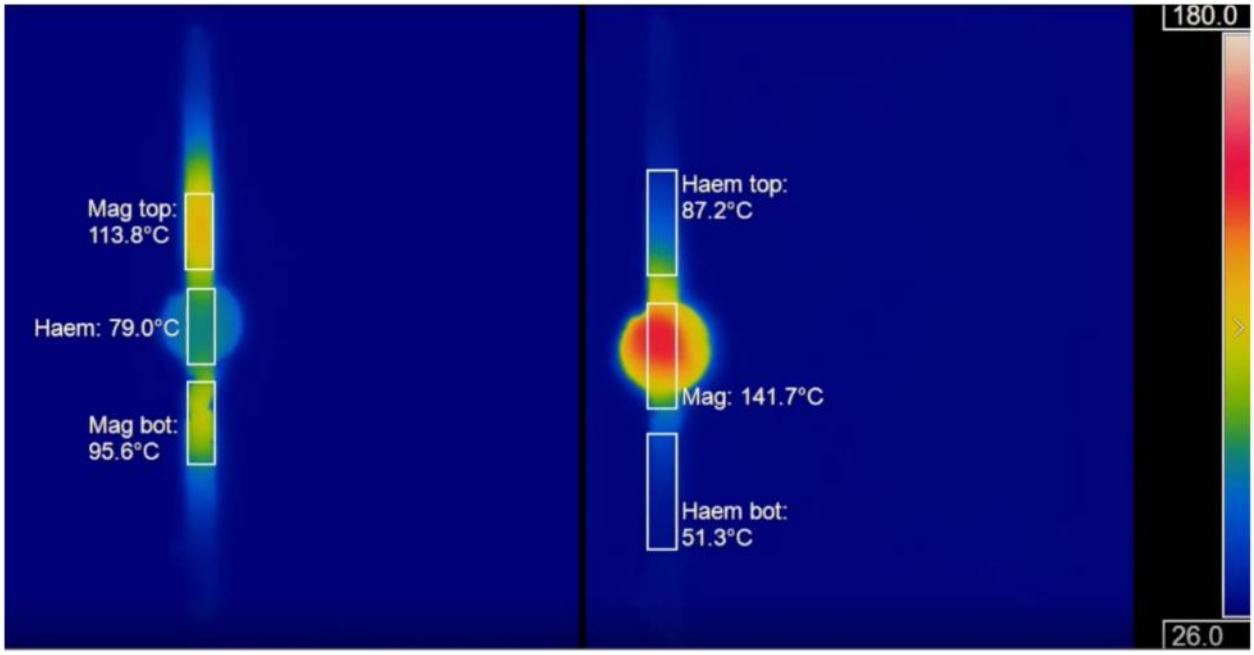

Fig. 2. Images taken from IR video of layered heating showing on the left **(a)** a Magnetite-Haematite-Magnetite sample and on the right **(b)** a Haematite-Magnetite-Haematite sample.

Introduction

Plastics

Plastics are a type of material which are popular in a wide variety of applications due to their versatile properties such as mechanical strength, flexibility, low weight and durability. Their broad applicability means they have been produced in tremendous quantities and unfortunately, a significant proportion of all produced plastics end up as environmental pollutants [6-8]. Plastic production exceeds 400 million tonnes annually and the cumulative plastic production since 1950 is greater than the population of all humans on Earth [9][10]. This is shown in Figure 3.

As a result of massive plastic production, there are billions of tonnes of plastic waste throughout the environment. Estimates suggest that as of 2015, 2.5 billion tonnes of plastic were still in use, while 6.3 billion tonnes accumulated as waste. Of this cumulative waste, 12.5% was incinerated, 9.5% recycled and the remaining 78% was discarded as waste [9]. This waste represents almost 5 billion tonnes of plastic, and this has certainly increased in the last eight years.

There are many different types of plastic and some of the most common include polyethylene (PE) which can be a high-density type (HDPE) or low-density (LDPE), polyethylene terephthalate (PET), polypropylene (PP), polystyrene (PS) and polyvinyl chloride (PVC). The largest sector for plastic production is packaging. In 2017, the production of packaging plastics was almost equivalent to the next three largest sectors put together (Building and Construction, Textiles, Consumer Products) [9]. This sector is dominated by PET, PE and PP and has the shortest useful lifespan for the plastics before they get discarded meaning these plastic types are some of the most prevalent in landfills and floating ocean garbage patches. Chemically, these materials mostly consist of hydrogen and carbon atoms, and sometimes other elements such as oxygen or chlorine. PE and PP have simpler chemical structures than PET. PE is formed of repeating chains of carbon atoms, each attached to two hydrogen atoms (ethylene), with the formula $(C_2H_2)_n$. PP is similar but consists of repeating propene chains, giving it an additional methyl group (CH_3) attached to every other carbon atom. It has the formula $(C_3H_6)_n$. The structure of

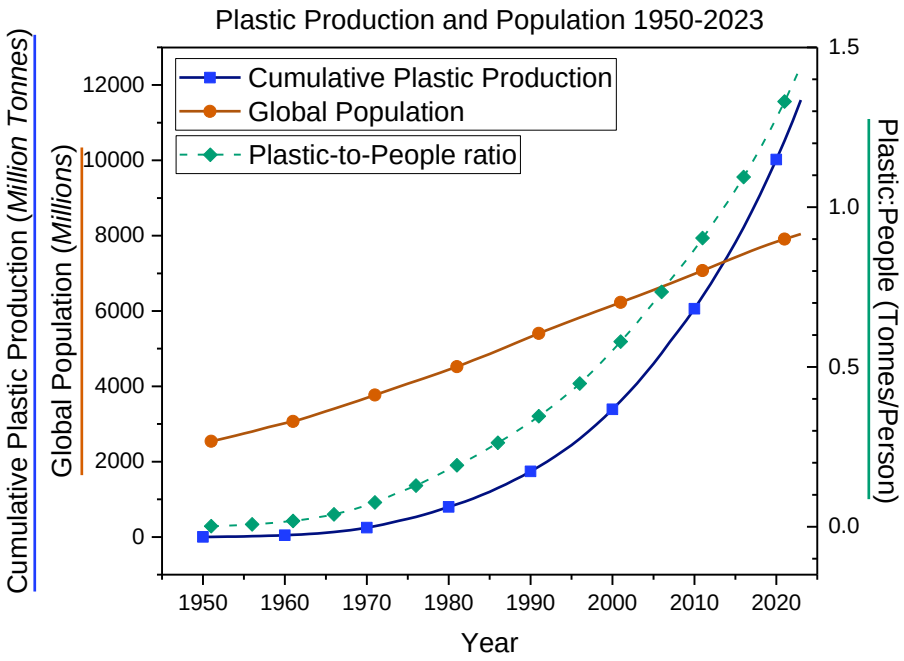

Fig. 5. Plastic production, population and ratio of tonnes of plastic to people (1950-2023)

PET is a little more complex as it contains a benzene ring with oxygen atoms adjoining either side (terephthalate) and additional oxygen and hydrogen atoms. The formula of PET is $(C_{10}H_8O_4)_n$. The structures of these polymers are shown in Figure 4.

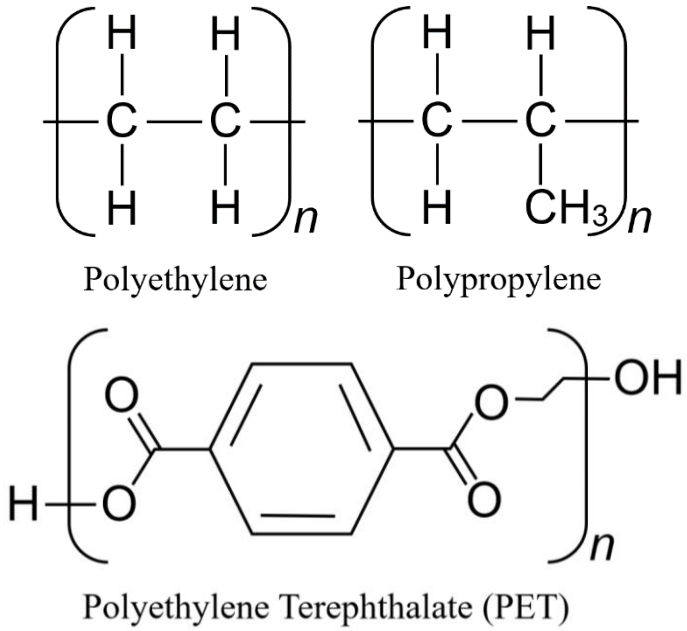

Fig. 4. Chemical structures of common polymers polyethylene, polypropylene and polyethylene terephthalate

Hydrogen

As the amount of plastic increases, so does the climate emergency and the demand for environmentally-friendly energy generation sources. The demand for energy, much like plastics, is higher than ever before and continues to increase. Most of the world's energy still comes from greenhouse-gas-emitting sources; coal, oil and natural gas [11]. Renewable energy generation is increasing, seeing the greatest use across Europe, North, South and Central America and in the Asia-Pacific region. However, carbon emissions are still too great to meet key targets concerning climate change, such as the Paris Agreement [12].

The necessity for greater investment and more innovation in low-carbon and carbon-neutral energy generation sources is obvious. Hydrogen as a fuel is excellent as it has incredible energy density, much higher than that of common fossil fuels. Hydrogen contains approximately 120 MJ/kg while natural gas has 54 MJ/kg, petrol 47 MJ/kg and coal has less than 35 MJ/kg [13-16]. As hydrogen is a chemically simple fuel the only products from a fuel cell are water, heat and electricity.

Hydrogen fuel seems like an incredibly promising alternative to fossil fuel systems but one of the greatest obstacles to large-scale implementation is initial generation of the hydrogen.

As their name suggests, fossil fuels exist as the remains of ancient organisms below Earth's surface in the form of oils and gases. These are energy reserves that only require extraction (and sometimes refinement) to produce large amounts of energy with well-established processes and infrastructure. Hydrogen acquisition is not as simple. Most hydrogen is generated rather than extracted and the vast majority of the generation is from fossil fuel sources [17]. The primary stream of hydrogen generation is methane steam reforming and a subsequent water-gas shift reaction (known as grey hydrogen). Other methods include steam reforming with carbon capture (blue hydrogen), electrolysis of water using renewables (green hydrogen), and gasification of coal (black/brown hydrogen). Most of the methods for hydrogen generation produce significant amounts of greenhouse gases as by-products and tend to require large amounts of energy to accomplish.

Microwaves

Microwaves (MW) are a type of electromagnetic radiation like radio waves, x-rays or visible light. They have a frequency range higher than radio waves but lower than infrared light in the range 300 MHz to 300 GHZ. Microwave heating has been used domestically and industrially for many decades and is well established as having certain advantages over conventional heating methods. Microwave heating is rapid, volumetric, selective, non-contact and penetrative [18]. These advantages lead to other benefits depending on application such as reduced processing times, greater product yields and better overall energy efficiency.

One of the most important attributes on microwave heating for this work is the selectivity of heating. Using conventional heating methods such as conduction or convection typically involves heating materials which are not intended. This can include the air inside a reaction vessel or the vessel itself. Heating these things is representative of wasted energy and is typically undesirable. Microwaves heat materials by interacting directly with them and causing changes which induce heating within the material. This is the basic operating principle of domestic microwave ovens which heat food by heating the water content. Water molecules are polar, meaning that they are electrically asymmetrical having a positive and negative "end". This polarity means the molecule reacts to an external electric field as the charged ends attempt to align with the opposite charges of the field. This causes molecules to rotate and if an alternating field with sufficient frequency is used the molecular friction dissipates energy as heat [19]. This is an example of dielectric heating.

Dielectric heating is a selective process as materials like water will heat well but materials like quartz are effectively transparent to microwaves and therefore do not absorb microwave energy. The list of materials able to be heated via dielectric heating is still long, so one method of increasing selectivity further is to instead use the microwave magnetic field to induce material heating. Far fewer materials can be heated by magnetic field interactions. For example, while water is strongly heated by electric field fluctuations it has no magnetic properties and thus the magnetic field fluctuations will have no impact on it. Primarily using the magnetic field for material heating allows greater control over the reaction as the vast majority of absorbed energy will be absorbed by a suitably chosen magnetically stimulated catalyst.

Motivation

This work aims to simultaneously address plastic waste removal and provide a new stream of low-carbon hydrogen generation. This will be achieved with rapid highly selective microwave magnetic heating of catalyst materials to subsequently heat plastic material and promote degradation into pure hydrogen and carbon products.

As PE has one of the simplest polymer structures and is one of the most common waste plastics it was chosen to begin experiments. This will be mixed with iron-based catalyst materials that are commonly available at economical prices and can be rapidly heated by exposure to magnetic fields. The rapid and highly selective heating will lead to rapid heating of the plastic and subsequent degradation into high-purity hydrogen, solid carbon materials and small amounts of hydrocarbon gases [1-3].

Methodology

This work uses a microwave resonant cavity operating in the TM_{010} mode at a frequency of 2.343 GHz. The cylindrical cavity has an internal height h of 4.0 cm and radius a of 4.9 cm. The TM_{010} mode was chosen for its simplicity and symmetry as the magnetic field only has one half-wavelength that exists radially within the cavity. This produces a predictable distribution that shows concentric rings of similar magnetic field strength with a minimum at the centre and a maximum approximately 77% of the radial distance from the centre. In this cavity the magnetic field maximum exists at approximately 3.8 cm from the centre of the cavity. The distribution of the magnetic field in the TM_{010} mode is shown in Figure 5; the lower

end of the data range has been slightly shortened to increase the contrast in the areas of highest field strength, especially near the edge of the cavity where a decrease is visible.

Many other works using the TM_{010} mode or cavities in general for material heating typically use the electric field and

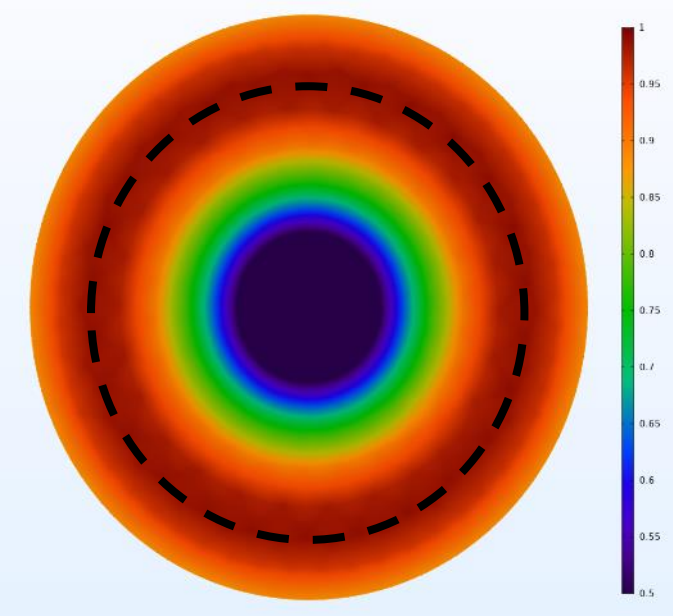

Fig. 5. Normalised magnetic field distribution of the TM010 resonant mode in a cylindrical cavity of radius 4.9 cm at a frequency of 2.343 GHz. The visible range has been modified slightly to make the regions of high field strength more apparent. The dashed line shows the region of highest field strength within the cavity, approximately 1.1 cm from the cavity's external wall.

materials with appropriate dielectric loss tangent [1-3]. A similar circular symmetrical pattern exists in the TM_{010} mode for the electric field, with a maximum at the centre of the cylinder reducing to zero field at the cavity walls.

Microwaves are introduced into the cavity using a portable microwave applicator (PMA). The PMA is a custom-built construction using a number of off-the-shelf components connected to generate a microwave output. It consists of a signal generator, an amplifier with attached heat sink followed by a circulator connected to both a directional coupler and an attenuator with 50 Ω termination, acting as an isolator. The PMA is controlled through USB connection to a computer and the output calibrated with an external attenuator and power meter. The PMA is much smaller than typical microwave generators or applicators, which often use magnetrons. It weighs only a few kilograms and sits on a tray with approximate dimensions 60 × 30 cm so it is conveniently portable.

Materials

The catalyst used for this work was powdered iron oxide (II,III) (Fe_3O_4) (Sigma-Aldrich, CAS:1317-61-9) commonly known as magnetite. The powder has a purity of 95% and average particle size <5 µm. Magnetite was chosen as a catalyst material due to its strong ferromagnetic properties and relatively low cost as a common metal oxide. Other magnetically-stimulated catalyst options include metals such as manganese, molybdenum and nickel which are significantly more expensive than iron.

Other Equipment

As well as the PMA and materials listed two infrared pyrometers were used to obtain temperature data. These are a Micro-Epsilon CT-SF22 (-30 °C to 975 °C) referred to as the "low range pyrometer" (LR) and a Micro-Epsilon CTM-3CF75H3 (250 °C to 1800 °C) referred to as the "high range pyrometer" (HR). A Kern PKS 360-3 was used to weigh all samples with resolution of 1 mg.

Experimental Procedure

The output of the PMA is initially connected to an attenuator and power meter to calibrate. Once calibrated the output can be connected to the cavity input. Once connected, the frequency and coupling strength of the system are altered by adjusting the physical position of the cavity input barrel through rotation and moving in or out of the cavity. With an empty quartz sample tube in the cavity a suitable coupling strength exceeding 20 dB is achieved and the input is secured in place. Normally the coupling strength is closer to 25 dB. The frequency of the empty cavity is then recorded in the control software.

Samples are weighed into the quartz sample tubes (typical outer diameter (OD) 8 mm and inner diameter (ID) 6 mm) and the tube with the sample is returned to the cavity. The coupling can then be adjusted again if required and the loaded frequency is saved into the software. The MW application parameters are now set. These include the target power output of the PMA, heating duration and frequency sweeping. Typically, the settings consisted of a target power of 38-45 W for a duration of 120 s with frequency sweeps every 2.5 seconds to continually find the optimum frequency for power delivery.

The pyrometers had two possible locations to be mounted to view the sample; one above the sample looking directly at its surface from around 60 mm away or one viewing from a small hole in the cavity's side 15 mm away from the quartz tube wall, which is 1 mm thick. Upon power application the pyrometers collect temperature data for each cycle. Usually 4 or 5 samples were heated separately before the coupling would be readjusted.

Results

Samples of magnetite with mass of 0.1 g were loaded into quartz sample tubes with outer diameter 8 mm and inner diameter 6 mm. The tubes have one closed rounded end and the other end is open to room temperature and atmospheric pressure. Samples were subjected to a target output power from the PMA of 41.5 W for 120 s with the high range pyrometer viewing the sample from the side and the low range pyrometer viewing the sample from above.

The recorded temperature data of three representative samples is shown in Figure 6 with the average of all curves also shown. There is little variation between the readings from both pyrometers suggesting the temperature reading is accurate and reliable. The temperature rises rapidly from room temperature (approx. 25 °C) to 800 °C in just over 21 seconds. This is characteristic of the vast majority of the recorded temperature curves as they show rapid heating in the first 10-20 seconds of microwave application. The temperature remains relatively stable throughout the remainder of the heating cycle, the average here lying between 812 and 836 °C for 90 seconds.

The strong agreement between both sets of recorded data suggests the pyrometer spot sizes are suitable for viewing the samples. If a spot size is too large it can record data from outside the sample including the quartz tube walls or reflections from the internal cavity walls. In this case the low range pyrometer has a spot size of about 7 mm and the high range pyrometer has a spot size of about 6 mm. Viewing from above, the low range pyrometer will also be collecting infrared data from some of the quartz tube walls, but assuming the pyrometer is positioned correctly about 73.5 % of its view will be

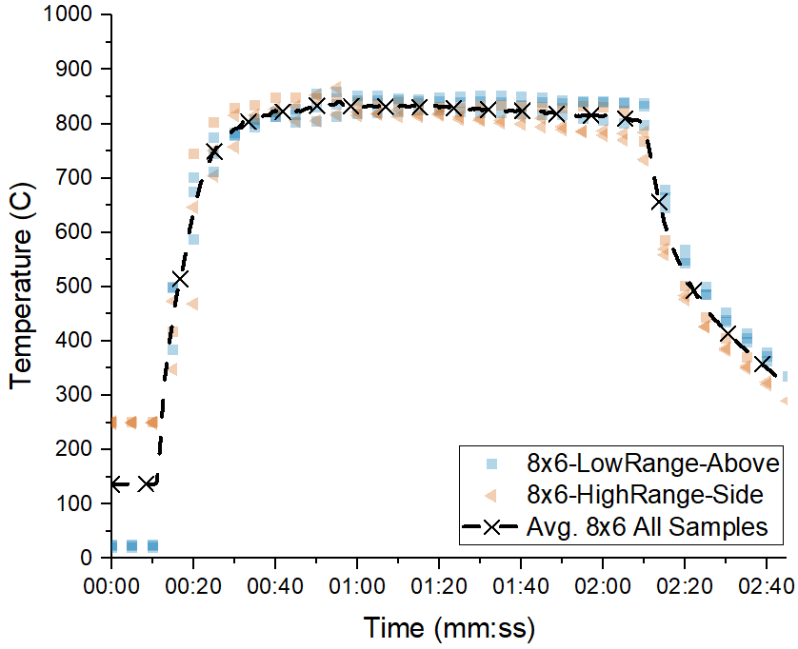

Fig. 6. Recorded temperature of samples of 0.1g of magnetite, target power 41.5 W, 120 s using two pyrometers. The average of all samples is shown by the dashed black line.

occupied by the sample surface. The high range pyrometer positioned from the side has a cross-sectional view of the sample which is rectangular rather than circular. The width of the sample here is the same as the internal diameter of the sample tube, 6 mm, which is the same as the approximate spot size, meaning the pyrometer's view can consist entirely of the sample. Even if the pyrometer is slightly misaligned there will be a minimal area of quartz tube being viewed. It is also worth noting that pyrometers viewing from the side receive infrared radiation from the sample through the sample tube wall (thickness 1 mm on all tubes).

Shown in Figure 7 is the same temperature data from the 3 samples shown in Figure 6 with the recorded absorbed power of each heating cycle overlaid. This shows the absorbed power exhibits a similar pattern to the temperature, although inversely, as it begins relatively high, some reaching over 28 W in the initial rapid heating stage and then decays to a relatively steady level. With these three samples the recorded absorbed power plateaus around 17-18 W. The higher levels of absorbed power do correlate to higher recorded sample temperatures as can be seen in Figure 7. The red triangular data points of sample C show slightly higher temperatures in agreement with the higher power levels, whereas the green square data points of sample A show the lowest temperatures and lowest absorbed power levels of these three samples.

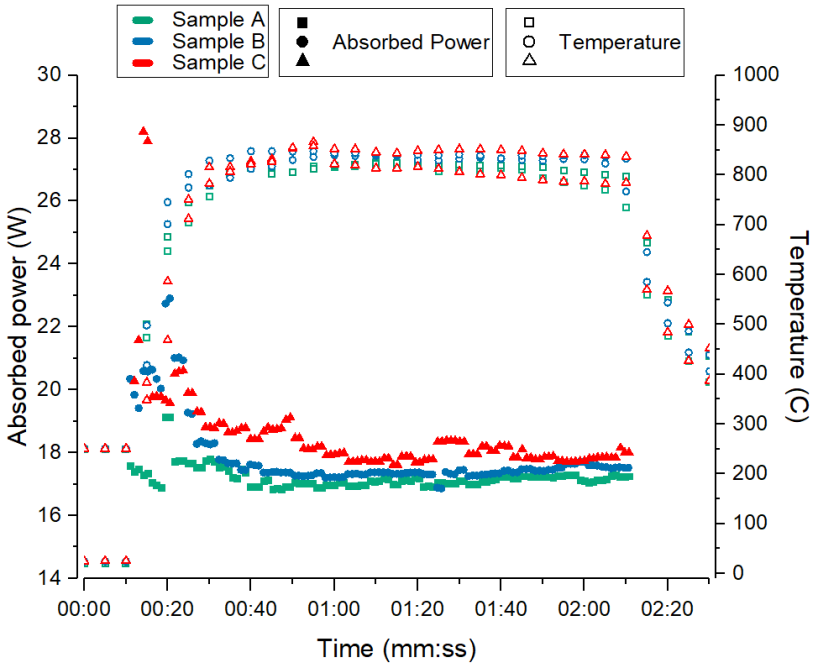

Fig. 7. Temperature profiles and recorded absorbed power of three representative samples.

Conclusion and Future Work

The consistent heating of small mass samples of magnetite has been demonstrated. Consistent heating above 800 °C has been achieved with target output power from a microwave applicator of only 41.5 W while using primarily an area of strong magnetic field rather than electric field. This is a promising result for future work including a powdered plastic component to rapidly and effectively generate gaseous products while using a relatively low input power level.

Using two pyrometers with different spot sizes at different distances has further illuminated the need to be consistent and careful when using them to record temperature data. Their spot sizes must be taken into account relative to the physical size of the sample under measurement in the future and ensure the pyrometer vision is as much as possible covered only by the intended sample.

The next major milestone of this work is to use a mixture of PE with catalyst powder and subject that to MW heating. Given the achieved temperatures in this work it is believed that plastic degradation into hydrogen-rich gaseous products will be possible with low masses (<0.5 g). Adjustments may have to be made concerning the input power level for larger masses. Any gaseous products will be collected and analysed via gas chromatography to determine the constituent products and their proportions. Further testing will include the analysis of produced gases at different points through the heating cycle, varied proportions of catalyst and plastic in each sample, varied masses of sample, and the reusability of the catalyst powders.

References

[1] X. Jie et al., 'On the performance optimisation of Fe catalysts in the microwave - assisted H2 production by the dehydrogenation of hexadecane', Catalysis Today, vol. 317. Elsevier BV, pp. 29–35, Nov. 2018. doi: 10.1016/j.cattod.2018.03.036.
[2] X. Jie et al., 'Rapid Production of High-Purity Hydrogen Fuel through Microwave-Promoted Deep Catalytic Dehydrogenation of Liquid Alkanes with Abundant Metals', Angewandte Chemie International Edition, vol. 56, no. 34. Wiley, pp. 10170–10173, May 23, 2017. doi: 10.1002/anie.201703489.
[3] X. Jie et al., 'Microwave-initiated catalytic deconstruction of plastic waste into hydrogen and high-value carbons', Nature Catalysis, vol. 3, no. 11. Springer Science and Business Media LLC, pp. 902–912, Oct. 12, 2020. doi: 10.1038/s41929-020-00518-5..
[4] L. Yao et al., 'Microwave-assisted decomposition of waste plastic over Fe/FeAl2O4 to produce hydrogen and carbon nanotubes', Journal of Analytical and Applied Pyrolysis, vol. 165. Elsevier BV, p. 105577, Aug. 2022. doi: 10.1016/j.jaap.2022.105577.R. E. Sorace, V. S. Reinhardt, and S. A. Vaughn, "High-speed digital-to-RF converter," U.S. Patent 5 668 842, Sep. 16, 1997.
[5] S. Papari, H. Bamdad, and F. Berruti, 'Pyrolytic Conversion of Plastic Waste to Value-Added Products and Fuels: A Review', Materials, vol. 14, no. 10. MDPI AG, p. 2586, May 16, 2021. doi: 10.3390/ma14102586.

[6] Vegter et al., "Global research priorities to mitigate plastic pollution impacts on marine wildlife," *Endangered Species Research*, vol. 25, no. 3, pp. 225–247, Oct. 2014, doi: https://doi.org/10.3354/esr00623.
[7] F. M. Windsor et al., "A catchment-scale perspective of plastic pollution," *Global Change Biology*, vol. 25, no. 4, pp. 1207–1221, Feb. 2019, doi: https://doi.org/10.1111/gcb.14572.
[8] D. Ita-Nagy, I. Vázquez-Rowe, and R. Kahhat, "Developing a methodology to quantify mismanaged plastic waste entering the ocean in coastal countries," *Journal of Industrial Ecology*, vol. 26, no. 6, pp. 2108–2122, Dec. 2022, doi: https://doi.org/10.1111/jiec.13349.
[9] R. Geyer, J. R. Jambeck, and K. L. Law, "Production, use, and fate of all plastics ever made," *Science Advances*, vol. 3, no. 7, Jul. 2017, doi: https://doi.org/10.1126/sciadv.1700782.
[10] OECD, "Plastics use in 2019," *OECD Environment Statistics*, Nov. 2017, doi: https://doi.org/10.1787/efff24eb-en.
[11] Energy Institute, "Statistical Review of World Energy," 72nd edition. 2023. Available at: https://www.energyinst.org/statistical-review
[12] United Nations Framework Convention on Climate Change, "THE PARIS AGREEMENT," 2016. Available at: https://unfccc.int/sites/default/files/resource/parisagreement_publication.pdf
[13] College of the Desert, "Hydrogen Properties," Rev. 0, Dec. 2001. Available at: https://www.energy.gov/sites/prod/files/2014/03/f12/fcm01r0.pdf
[14] Envestra, "About Natural Gas, Reference Guides," Oct. 2008. http://www.natural-gas.com.au/about/references.html (Archived)
[15] IOR Energy, "Engineering Conversion Factors - Fuel Energy Densities," Aug. 2010. http://www.ior.com.au/ecflist.html (Archived)
[16] J. Fisher, "Energy Density of Coal - The Physics Factbook," *hypertextbook.com*, 2003. Available at: https://hypertextbook.com/facts/2003/JuliyaFisher.shtml
[17] R. Rapier, "Life Cycle Emissions of Hydrogen," *The Fourth Generation*, Jun. 25, 2020. Available at: https://4thgeneration.energy/life-cycles-emissions-of-hydrogen/
[18] T. Santos, M. A. Valente, J. Monteiro, J. Sousa, and L. C. Costa, "Electromagnetic and thermal history during microwave heating," *Applied Thermal Engineering*, vol. 31, no. 16, pp. 3255–3261, Nov. 2011, doi: https://doi.org/10.1016/j.applthermaleng.2011.06.006.
[19] E. T. Thostenson and T. W. Chou, "Microwave processing: fundamentals and applications," *Composites Part A: Applied Science and Manufacturing*, vol. 30, no. 9, pp. 1055–1071, Sep. 1999, doi: https://doi.org/10.1016/s1359-835x(99)00020-2.

Simultaneous Global Climate Change "Heat Waves" and Microwave and Radio-Wave from Solar Flares

S. Yanagida[1], T. Matsumura[2]

[1]*Osaka University, ISIR, Ibaraki, Osaka, Japan*
[2]*Minerva Light Laboratory, Kyoto, Japan*
yanangida@mls.eng.osaka-u.ac.jp

Keywords: greenhouse gas, global warming, far-infrared, thermo-upconversion, molecular modelling, Nobeyama Radio Polarimeters,

Nobeyama Radio Polarimeters of Japan are observing the sun at multiple frequencies in the microwave range. The Sun emits a range of frequencies including far-infrared (500-0 cm^{-1}, 10 THz~GHz~radio wave) energy [1]. Water (H_2O), which is a liquid, nickel oxide (NiO) and iron oxide (FeO), which are solids, are instantly heated up by microwave irradiation. These facts are explained by the strong absorption of H_2O, NiO, and FeO in both infrared (4000-500 cm^{-1}) and the far-infrared (500-0 cm^{-1}, 10 THz~GHz~radio wave) regions. i.e., thermo-upconversion of absorbed far-infrared energy to infrared energy leads to the thermal effect by emission of infrared energy [2][3]. We are now anxious that some environmental activists in major industrialized nations are actively arguing that global warming and climate change are caused by carbon dioxide emitted as a result of human activity. Theoretical verification by DFT/MM (density function theory/molecular mechanics) will be attempted to determine whether carbon dioxide (CO_2) and water (both in gaseous state) are warmed by thermo-upconversion of solar far-infrared ray energy. Further, we attempt DFT/MM-based verification of the solar far-infrared heating of sea water and silica (SiO_2).

First, in order to verify whether CO_2 in the atmosphere is a greenhouse gas, we used the van der Waals aggregate of [$(CO_2)_3$] as a CO_2 gas model in dry state and [CO_2 (H_2O) $_2$] as CO_2 gas model in humid atmosphere. Their DFT/MM-based, i.e., theoretical IR/FIR spectra for [$(CO_2)_3$] and [CO_2 (H_2O) $_2$] are obtained (Fig. 1, Fig. 2). The formation of [$(CO_2)_3$] and [CO_2 (H_2O) $_2$] were found to have heat of formation of -2.90 and -6.90 kcal/mol, respectively. The exothermic heat of formation implies their favourable formation.

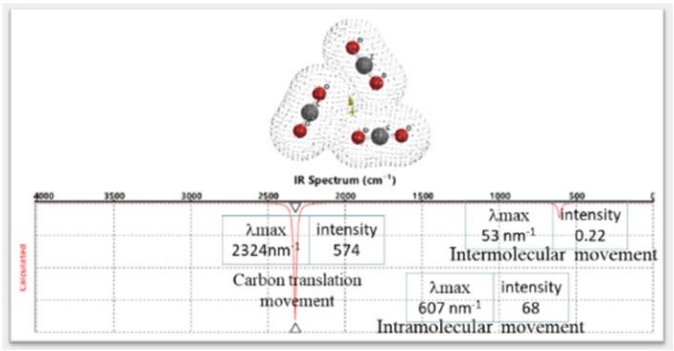

Fig. 1. Atmospheric carbon dioxide model [$(CO_2)_3$]. Heat of formation = -2.90 kcal/mol, dipole moment = 0.01 debeye

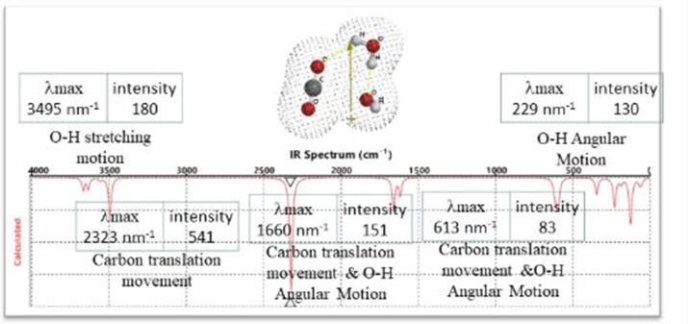

Fig. 2. Atmospheric carbon dioxide model [$CO_2(H_2O)_2$]. Heat of formation = -6.90 kcal/mol, dipole moment = 3.33 debeye

Interestingly, [$(CO_2)_3$] was found to have small peaks in the 500~0 cm^{-1} microwave~radiowave (MWRW) region, which are ascribed to CO_2 intermolecular motion-based absorptions. On the other hand, [$CO_2(H_2O)_2$] has many similar absorption peaks with high intensity in the same region, which are ascribed to intermolecular H_2O movement. This verifies that CO_2 in

high humidity conditions can be a greenhouse gas. However, the maximum concentration of CO_2 in atmosphere is about 500 ppm, and it is unlikely that it causes climate change on a global scale.

The ocean atomosphere is in a state close to saturated vapor pressure. Seawater has a salinity of 3.4%. Fig. 3 shows the theoretical IR/FIR analysis of the equilibrium geometry of the trimer model of gaseous H_2O [trigonal symmetry $(H_2O)_3$] having low dipole moment. Fig. 4 shows the analysis of the liquid state H_2O trimer model [facial symmetry $(H_2O)_3$] having high diple moment. Absorption due to intermolecular movement between these water molecules was verified in 500~0 cm^{-1} MWRW region, and it was confirmed that water molecules absorb MWRW region rays (500~0 cm^{-1}) by aggregation with hydrogen bonds. The movement between these water molecules is interestingly visualized in the DFT/MM determined IR/FIR spectrum. The intermolecular motion supports the collision mechanism proposed for microwave thermal effect [4].

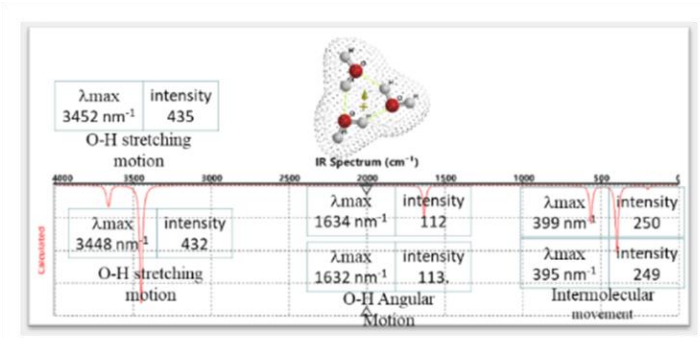

Fig. 3. Water model in gaseous state [trigonal symmetry $(H_2O)_3$]. Heat of formation = -19.90 kcal/mol, dipole moment = 0.01 debeye

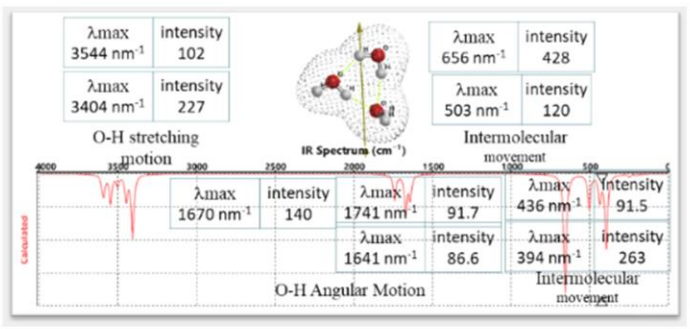

Fig. 4. Water model in liquid state [facial symmetry $(H_2O)_3$]. Heat of formation = -23.40 kcal/mol, dipole moment = 44.0 debeye

Fig. 5 was obtained by DFT/MM of salt water model [$NaCl(H_2O)_2$]. Many low-intensity absorptions in FIR are confirmed and assigned as due to intermolecular movement between Na^+, Cl^- and H_2O. It was understood that aqueous NaCl solution absorbs MWRW region rays effectively by association of NaCl and H_2O molecules. This verification explains that the radiant heat from the ocean is suppressed by greenhouse gas effect of water vapor molecules over the oceans. On the oceans, minimizing large temperature changes between day and night, and between summer and winter should contribute to control of global climate change.

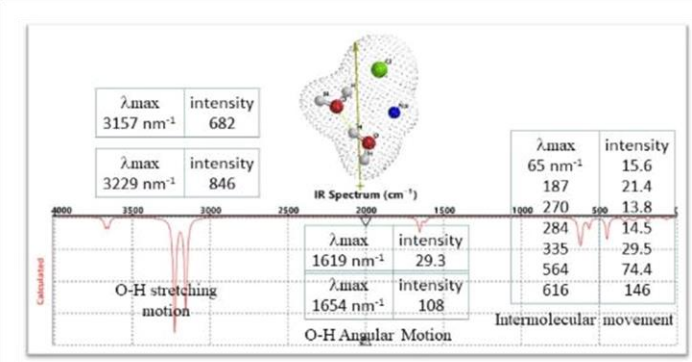

Fig. 5. Sea water model in liquid state [$NaCl(H_2O)_2$]. Heat of formation = -41.40 kcal/mol, dipole moment = 6.95 debeye

Figure 6 shows the theoretical IR/FIR analysis for an amorphous silica model [$(SiO_2)_3$]. It is verified that the absorption intensities in the IR and MWRW region (500~0 cm^{-1}) of the silica model [$(SiO_2)_3$] are much stronger than any of the aqueous solution models. This verifies that silica-based materials are warmed effectively depending on the intensity of solar

MWRW rays just as the silica that makes up the desert heats up during the day, MWRW energy, has excellent linearity, so we understood that the thermal upconversion mechanism works effectively on silica in the earth's crust to heat and keep it warm as reported recently [5].

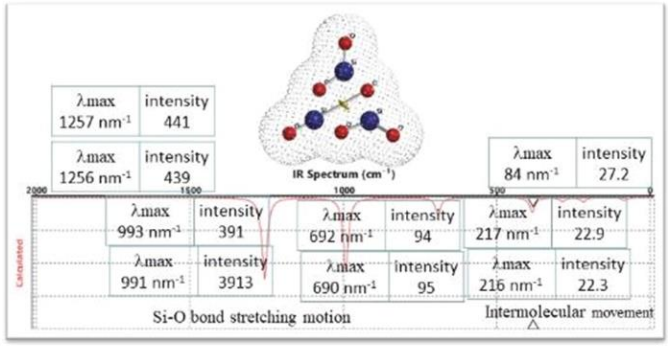

Fig. 6. Land silica model [$(SiO_2)_3$]. Heat of formation = -186.0 kcal/mol, dipole moment = 0.10 debeye

Solar flares occur during periods of high solar activity. It is thought that far-infrared energy will increase when a solar flare occurs. The occurrence of solar flares raises the temperature of ocean waters, the oceanic atmosphere, and silica on land by several degrees. Carbon dioxide is by no means the cause of climate change, and solar changing far-infrared radiation causes climate change.

References

[1] NAOJ Nobeyama Radio Observatory, About Nobeyama. Available from: https://www.nro.nao.ac.jp/en/public/teles.html#rp
[2] S. Yanagida and T. Matsumura, Computational Verification of Heating Mechanisms at Radio and Microwave Frequencies Using Density Functional Theory, AMPERE Newsletter Issue 95, March 12, 2018
[3] S. Yanagida and T. Matsumura, Quantum chemistry molecular modeling for radio-frequency and microwave-frequency thermo-upconversion heating of metal oxides of NiO and Fe_2O_3, Conference: **Ampere** 2019, DOI: 10.4995/AMPERE2019.2019.10234
[4] IMPI home page. Available from: https://impi.org/members-only/
[5] Michael Green et al, Light: Science & Applications (2018) 7:87 Official journal of the CIOMP 2047-7538,DOI 10.1038/s41377-018-0088- Doped, conductive SiO_2 nanoparticles for large microwave absorption
[6] Michael Green et al, Light: Science & Applications (2018) 7:87 Official journal of the CIOMP 2047-7538,DOI 10.1038/s41377-018-0088- Doped, conductive SiO_2 nanoparticles for large microwave absorption

Recycling of Polyethylene Terephthalate (PET) under Microwave Irradiation

D. Bogdal[1], A. Prociak[1], K. Balazinski[1], B. Kwasek[1]

[1]*Department of Chemical Engineering and Technology, Cracow University of Technology, Warszawska Street 24, 31-155 Krakow, Poland*
pcbogdal@cyf-kr.edu.pl

Keywords: microwave, plastics, PET, recycling

Due to its good heat resistance and dimensional stability, poly(ethylene terephthalate) (PET) is suitable for, among other applications, the production of high-demand parts. It is a very good material for sliding and abrasion applications, showing a low sliding coefficient and high dynamic load. As a result, it is possible to reduce the necessary drive power in the devices, avoid stick-slip behavior and significantly extend the service life of the parts used. It is used for the production of slats and slide bearings, guides and gears.

Due to the large volume of waste and resistance to atmospheric and biological factors, PET is perceived as a burdensome material. Therefore, PET recycling plays a significant role in waste removal. Chemical recycling consists of complete depolymerization of PET to low-molecular starting compounds or partial depolymerization to oligomers.

This presentation covers a short review on the depolymerization of post-consumer PET under microwave irradiation from lab to industrial scale.

Examples of our investigations will be shown in which the reaction of glycolysis of PET was carried out under microwave conditions. The appropriate amount of PET flakes, diethylene glycol and a catalyst (tetrabutyl orthotitanate) were added to a round bottom flask of 500 ml, which was then placed in a microwave reactor at reflux. The reaction is carried out in an atmosphere of inert gas - argon. A programmed heating cycle with the power of 360 W and the minimum and maximum temperature of 198 and 201 °C, respectively was employed. The reactions were carried out and one of the parameters was changed: the weight ratio of diethylene glycol to PET, the amount of catalyst and reaction time. Reaction of the PET glycolysis gave liquid products of high viscosity and deep green color. The resulting products were characterized by determining hydroxyl number (L_{OH}), and molecular weights by means of gel permeation chromatography (GPC).

References

[1] D. Bogdał, Polymer chemistry under action of microwaves. *Microwaves in Organic Synthesis*, A. de la Hoz, A. Loupy (Eds), III ed., Wiley-VCH, 2012, 1039-1058.

Plasma Phenomena and Processing

Al-Sc Alloy Production using Metal Ion Plasma

S. Fujii[1], J. Fukushima[2], Y. Okawa[3], T. Miyazawa[3]

[1]*Toyohashi University of Technology, 1-1 Tempaku-cho, Toyohashi, Aichi, Japan*
[2]*Tohoku University, 6-6-07 Aoba, Aramaki, Sendai, Miyagi, Japan*
[3]*Furuya Metal Co. Ltd., 1915 Morisoejima, Chikusei, Ibaraki, Japan*
fujii@ee.tut.ac.jp

Keywords: microwave, radiofrequency, metal ion plasma

In chemical reactions involving microwave irradiation, a local concentration of electric and magnetic fields between particles, such as catalysts and powders, increases the reaction rate and lowers the reaction temperature of the reduction [1, 2]. Plasma is thought to be easily generated by the concentration of electric and magnetic fields between solid particles. In high-temperature reactions between individual particles, these plasmas are directly involved in the chemical reaction and accelerate the reaction at a temperature that is reported to be lower than the reduction temperature with normal heating. The temperature of the reduction of copper oxide by carbon was determined from thermogravimetric measurements, and a lower reduction temperature was observed, indicating that the Ar plasma contributed to the reaction [3]. We demonstrated the reduction of scandium oxide and vanadium oxide at temperatures below 700 °C using a multimode applicator with Mg as the reductant. During these reductions, a decrease in the reaction temperature was observed, and the Mg ions acted as reducing agents in the microwave-assisted process [4, 5]. In addition, a method has been proposed to directly excite plasma without gases for reducing agents such as Mg and Ca using a microwave cavity in the TM110 mode [6].

The experimental setup is illustrated in Fig. 1. In the microwave resonator section, a cylindrical cavity (φ = 110 mm) in the TM110 mode at 2.45 GHz generating a high magnetic field was used as the Mg ion plasma source, and a Mg ribbon was used as the Mg source. The reduction reaction was performed at 660 °C by induction heating. Mg plasma was generated in this apparatus; three pellets were heated to about 650 °C for approximately 30 min while Mg plasma was generated. The XRD patterns of the pellets are shown below. All three pellets were successfully purified to Al_3Sc with an addition ratio of approximately 60%.

This experiment confirms that Mg ions contribute to a lowering of the temperature of the reduction reaction. The generation of Mg plasma by microwaves and the heating of the reaction zone by RF bands are expected to make the system larger than when using microwaves alone.

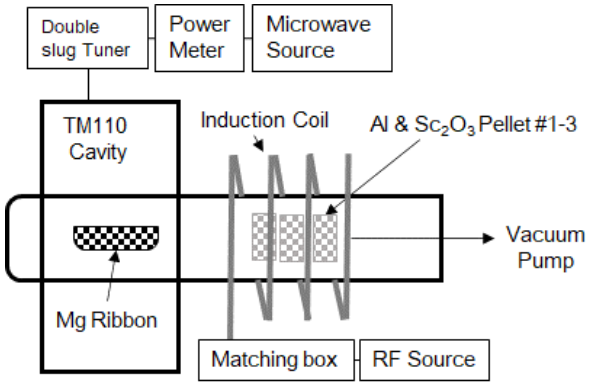

Fig. 1. Experimental apparatus for plasma generation and chemical reaction using a TM110 mode microwave

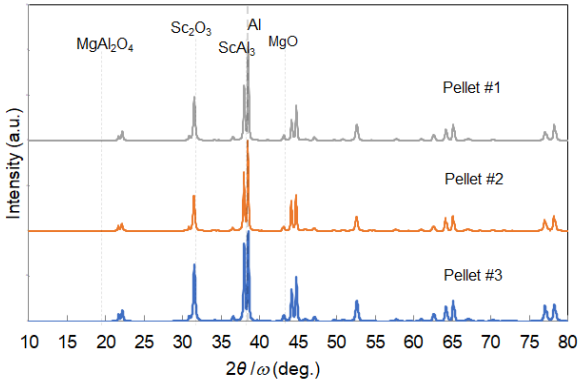

Fig. 2.XRD pattern of the mixture of residues and products of the reaction.

References

[1] N. Haneishi, S. Tsubaki, M. M. Maitani, E. Suzuki, S. Fujii, and Y. Wada, "Electromagnetic and Heat-Transfer Simulation of the Catalytic Dehydrogenation of Ethylbenzene under Microwave Irradiation," *Ind. Eng. Chem. Res.*, vol. 56, no. 27, pp. 7685-7692, 2017.

[2] S. Tsubaki, T. Matsuzawa, E. Suzuki, S. Fujii, and Y. Wada, "Operando Raman Spectroscopy of the Microwave-Enhanced Catalytic Dehydration of 2-Propanol by WO_3," *Ind. Eng. Chem. Res.*, vol. 59, no. 5, pp. 1781-1788, 2020.

[3] S. Fujii, M. Yamamoto, T. Matsuzawa, S. Fujii, M. Nishioka, and Y. Wada, "Reduction of Metal Oxides using Thermogravimetry Under Microwave Irradiation," *AIP Adv.*, vol. 11, pp. 065207, 2021.

[4] S. Fujii, E. Suzuki, N. Inazu, S. Tsubaki, J. Fukushima, H. Takizawa, and Y. Wada, "Microwave Irradiation Process for Al–Sc Alloy Production," *Sci. Rep.*, vol. 10, pp. 2689, 2020.

[5] N. Inazu, E. Suzuki, S. Fujii, S. Tsubaki, and Y. Wada, "A Facile Formation of Vanadium(0) by the Reduction of Vanadium Pentoxide Pelletized with Magnesium Oxide Enabled by Microwave Irradiation," *Chemistry Select*, vol. 5, pp. 2949, 2020.

[6] S. Fujii and J. Fukushima, "Metal Ion Plasma Generation under Strong Magnetic Field in Microwave Resonator," *AIP Adv.*, vol. 13, pp. 015320, 2023.

On Ejected Tungsten Oxide Nanoparticles during Microwave-Metal Discharge

P. Gupta[1], A. K. Sharma[1], I. Singh[1]

[1]*Department of Mechanical and Industrial Engineering, Indian Institute of Technology Roorkee, Roorkee–247667, Uttarakhand, India*
aks@me.iitr.ac.in

Keywords: microwave-metal discharge, nanoparticles, tungsten oxide, dusty plasma

Microwave-induced metallic discharge has secured considerable attention in recent times owing to its remarkable heating capabilities. Consequently, material processing techniques such as pyrolysis, pollutant removal, sintering, material synthesis, etc., are increasingly being performed using microwave-metal discharge phenomenon [1]. The present work is concerned with the ejection of tungsten oxide nanoparticles by direct oxidation of solid tungsten electrodes in an atmospheric air medium. Nanometric tungsten oxide is utilized in a variety of applications, such as energy storage devices, catalysis, biomedicine, and wastewater treatments [2]. The high temperature of the discharge exhibits the oxidation of tungsten metal. The oxide vapours, in the form of fine powder, get deposited on the substrates placed above and beneath the electrode as shown in Fig. 1(a). The optical emission spectroscopy (OES) of the dusty plasma formed (Fig. 1(b)) is majorly composed of WI spectral lines, which are attributed to the oxidation of the tungsten metal. The obtained powder was characterized for investigation of morphological, structural, and compositional properties. Transmission electron microscopy reveals the occurrence of particles in different geometries, such as spherical, hexagonal, and rectangular, with sizes ranging from 12 nm to 68 nm (Fig. 1(c)). Powder X-ray diffraction spectrum as shown in Fig. 1(d) affirms the crystallinity of the powder with a monoclinic phase. The broadened peaks in the diffraction pattern were indicative of the existence of particles in the nanoscale regime.

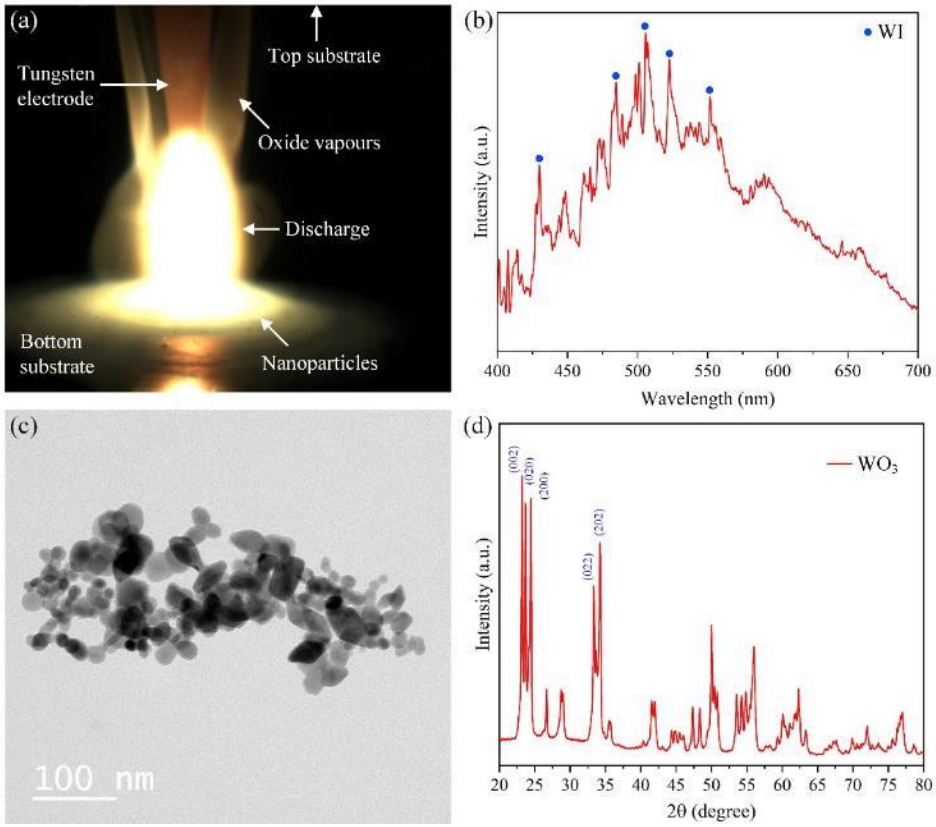

Fig. 1. (a) Nanoparticles ejected during discharge formation (b) OES of discharge plasma (c) TEM micrograph of the nanoparticles (d) XRD spectrum of the nanoparticles.

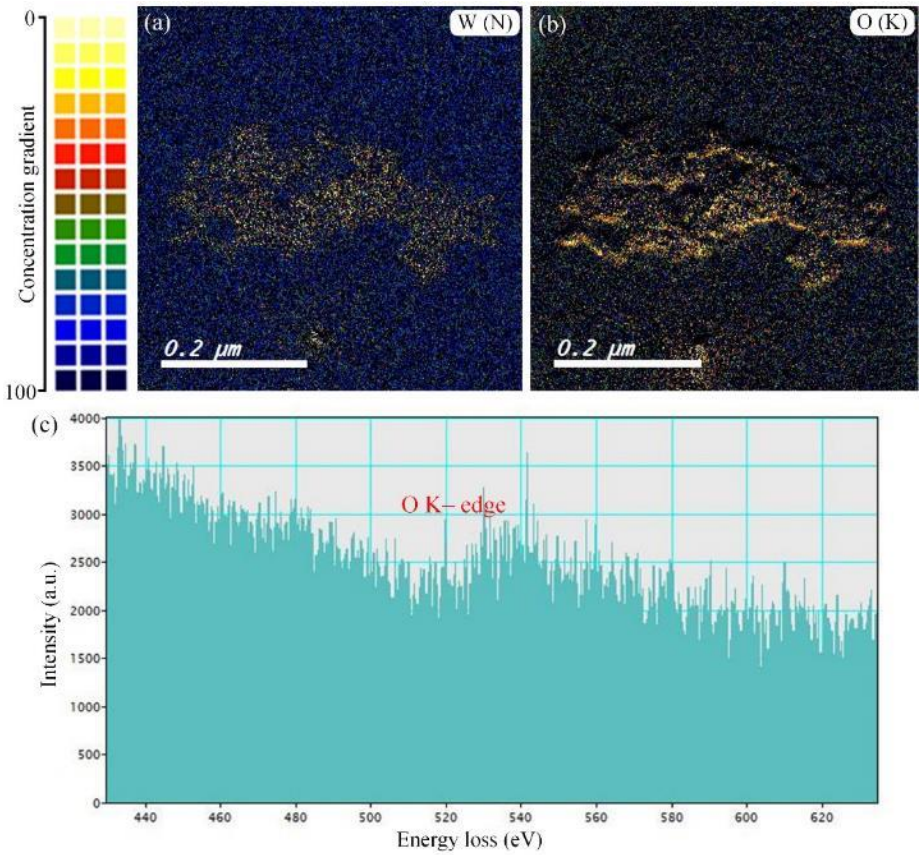

Fig. 2. EFTEM micrograph showing individual mapping for (a) tungsten and (b) oxygen. (c) EELS showing O-K edge of tungsten oxide nanoparticles.

The chemical concentration of the generated nanoparticles was examined using energy-filtered TEM (EFTEM) imaging which depicts the mapping of W and O elements corresponding to N and K energy shells, respectively (Fig. 2(a and b). In addition, electron energy loss spectrum (EELS) as illustrated in Fig. 2© shows a saw tooth-like O–K edge around ~532 eV, which may be attributed to the transition of electrons to the unoccupied bound states, which produces fine structures in the edge [3].

The methodology proposed here may be exploited for the facile and economical production of various metal oxide nanoparticles.

The authors acknowledge the funding provided by Science and Engineering Research Board (SERB), New Delhi, India under the grant no. CRG/2018/004305.

References

[1] Sun, J., Wang, W., Yue, Q., Ma, C., Zhang, J., Zhao, X. and Song, Z., 2016. Review on microwave–metal discharges and their applications in energy and industrial processes. *Applied Energy*, *175*, pp.141-157.

[2] Puzyn, T., Rasulev, B., Gajewicz, A., Hu, X., Dasari, T.P., Michalkova, A., Hwang, H.M., Toropov, A., Leszczynska, D. and Leszczynski, J., 2011. Using nano-QSAR to predict the cytotoxicity of metal oxide nanoparticles. *Nature nanotechnology*, *6*(3), pp.175-178.

[3] Ahmadi, M. and Guinel, M.J.F., 2014. Synthesis and characterization of tungstite ($WO_3 \cdot H_2O$) nanoleaves and nanoribbons. *Acta materialia*, *69*, pp.203-209.

A Low Power Self-Ignited Microwave Room-Temperature Air Plasma Jet at Atmospheric Pressure

L. Wu[1], X. Zhang[1], T. Liu[1], J. Tao[2], K. Huang[1]

[1]*Institute of Applied Electromagnetics, College of Electronics and Information Engineering, Sichuan University, 610065, P. R. China.*
[2]*LAPLACE (Laboratoire Plasma et Conversion d'Energie), INPT- ENSEEIHT, University of Toulouse, 31071, France*
wuli1307@scu.edu.cn

Keywords: microwave air plasma, atmospheric pressure, self-ignited plasma, low ignited power.

In the past few decades, atmospheric pressure plasma jets have received considerable attention due to their widespread application in diverse fields. Helium and argon are preferred as carrier gases due to their low breakdown powers and consequent low gas temperatures. However, the utilization of these noble gases makes the plasma system more expensive and less portable. As a freely available resource, air attracts more and more attention because air plasma not only overcomes the above mentioned limitations, but also has a larger variety of active particles, offering greater benefits in medical treatment. In view of this situation, this paper proposes a portable low power room temperature atmospheric air plasma driven by continuous 2.45 GHz microwave power. The device is capable of self-exciting air plasma with only 50 W of microwave input power. Its sustaining power is as low as 10 W and the gas temperature of plasma flame could be reduced to around 30℃. Spectroscopic measurements show stronger $OH(A^2\Sigma^+ \rightarrow X^2\Pi)$ bands at 306 nm-310 nm, oxygen atomic lines O^I (3p5P → 3s5S) at 777.1 nm and O^I (3p3P → 3s3S) at 844.6 nm. $NO-\gamma\left(A^2\Sigma^+ \rightarrow X^2\Pi_r\right)$ from 200 nm to 300 nm is also detected in this air plasma jet. This portable air plasma offers great potential for air plasma applications in the biomedical fields.

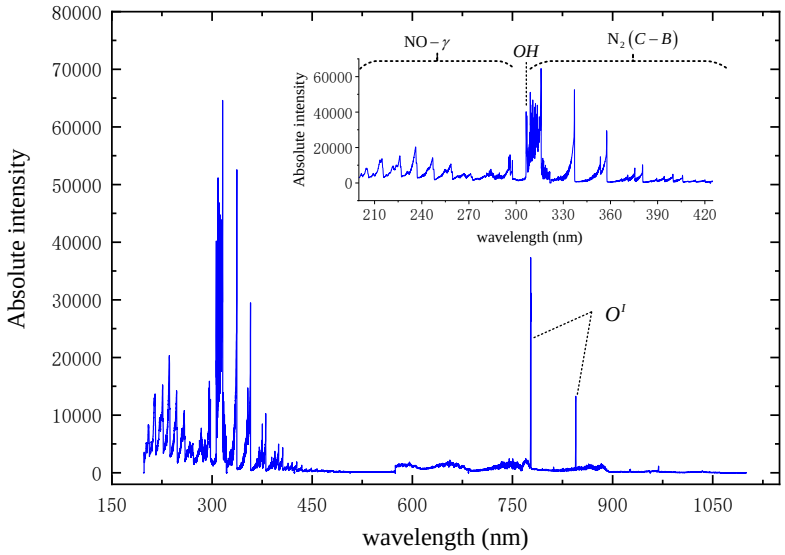

Fig. 1. Emission spectrum of air plasma (input power:70W, gasflow:10L/min)

Conversion of CO_2 in Atmospheric Plasma Sustained in a Surfaguide with Ultra-fast Microwave Pulsations

S. Soldatov[1], L. Silberer[1], G. Link[1], A. Navarrete[2], R. Dittmeyer[2], J. Jelonnek[1,3]

[1]IHM, [2]IMVT,[3]IHE, Karlsruhe Institute of Technology (KIT), 76131, Karlsruhe, Germany
sergey.soldatov@kit.edu

Keywords: CO_2 conversion, microwave plasma, pulsed microwave, energy efficiency

The increasing availability of renewable sources of electrical energy based on wind and solar power, paves the way for a gradual replacement of fossil fuels and the decarbonization of the industry. Yet, the intermittency of those sources necessitates the development of technologies capable of storing excess energy produced during one period for use it in another [1]. Utilizing surplus electrical energy for synthesizing liquid fuels is the energy storage method with the largest storage capacities and longest storage times as compared to other energy storage technologies such as flywheels, batteries, or compressed air storage [2]. One of the most promising pathways is the endothermic reduction of carbon dioxide (1), captured from industrial exhausts, which also could help to mitigate the greenhouse effect on the Earth [3].

$$CO_2(g) \rightarrow CO(g) + 1/2\ O_2(g) + 283\ kJ/mol \qquad (1)$$

The activation and deactivation of conventional chemical reactors are often too slow to follow the natural fluctuations of wind and solar energy. Plasma-based reactors allow the process to be switched on or off almost instantly and are therefore well suited to the intermittent availability of electricity [4]. Among various plasma-based reactors, microwave plasma reactors have so far demonstrated the highest efficiency (over 80%) for the conversion of CO_2 to CO at low pressure conditions [5, 6]. Atmospheric plasma systems are more robust and cheaper as compared to vacuum based systems, therefore they are much more appropriate for industrial applications and future large-scale CO_2 conversion technologies. Yet, the efficiency of the process deteriorates with as the pressure increases, because a large part of the supplied energy is wasted by excessive heating of the gas. A promising solution has been found in our recent experiments with a compact coaxial atmospheric plasma-torch by supplying microwave energy in short pulses rather than continuously [7]. It was shown that pulsations with durations of several microseconds and a duty cycle of about 0.25 promote the conversion and efficiency of the CO_2 splitting by a factor of 2. Moreover, the effective control of gas temperature by manipulating pulsation parameters was demonstrated [7, 8].

In this work, we investigate the possibility to control the gas temperature of atmospheric CO_2 plasma with ultrafast pulsations of microwave in a surfaguide [9] microwave reactor (Fig. 1). Moreover, the conversion and efficiency of the process (see (1)) are studied both in pulsed and continuous wave (CW) plasmas.

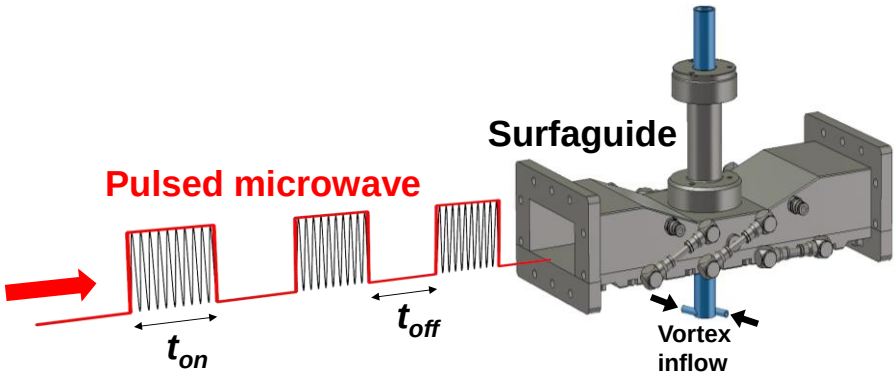

Fig. 1. Sketch of surfaguide reactor fed with pulsed microwave.

In our experiments presented here, an advanced microwave generator based on a solid-state amplifier is utilized. It enables an ultra-fast modulation of the output power and achieves a peak power (P_{peak}) of up to 8 kW. The generator has an independent control for pulse time (t_{on}) and inter-pulse time (t_{off}) in the range of 50 ns to 100 µs and frequency in the range of 2.4-2.5 GHz. The rise and fall times of a pulse are shorter than 20 ns.

An ignition system is realized with a microdischarge triggered by applying a high DC voltage to electrodes on the outer surface of the reactor quartz tube. A plasma ignited first in argon gas at a supplied CW microwave power of > 1.8 kW, and thereafter argon is replaced with CO_2 gas. To control the input CO_2 flow and the concentration of the products the gas massflow controller and the gas analyser (CO, CO_2, O_2, H_2, CH_4) are installed. The scheme of the experiment is shown in Fig. 2. To monitor the absorbed microwave power in the reactor the bi-directional coupler and pulsed power meters are

utilized. The vibrational and rotational temperatures of plasma were estimated with an optical emission spectroscopy (OES) system and with consequtive fitting of aquired spectra with MassiveOES [10, 11] software. Emitted light is collected with a collimator aimed to the center of the reactor (Fig. 2). Reactor tube is made of quartz and has inner / outer diameter of 16 / 20 mm.

For 15 slm inflow of CO_2, we have compared the efficency and conversion of the process when the plasma is sustained with continuous wave (CW) microwave against pulsed microwave. The t_{on} time was varied from 0.5 to 7.5 microseconds and the duty cycle (DC) was varied from 0.2 to 0.9. For characterization of the mean energy spent per molecule of reactant the specific energy input (SEI) term is used, which is defined as follows:

$$SEI = \frac{\overline{P_{abs}} \cdot V_m}{v_{inp} \cdot N_A} \qquad (2)$$

where, v_{inp} is the CO_2 gas inflow and $\overline{P_{abs}}$ is the mean absorbed microwave power in the system, V_m is the molar gas volume set to 24.47 l/mol and N_A is the Avogadro constant. For the pulsed regime, the mean absorbed power is given by $\overline{P_{abs}} = P_{abs} \cdot DC$. The duty cyle is defined by $DC = t_{on}/(t_{on} + t_{off})$. Therefore, SEI depends on t_{on} and t_{off} times. It was found that the longer t_{on} times and DC of about 0.5 (SEI≈2 eV/molecule) provide the most efficient scenarios for this configuration (see Fig. 2). Additionally, all pulsed scenarios with t_{on}>4 µs show higher CO_2 conversion rates as compared to CW plasma scenario for the given inflow rate of 15 slm.

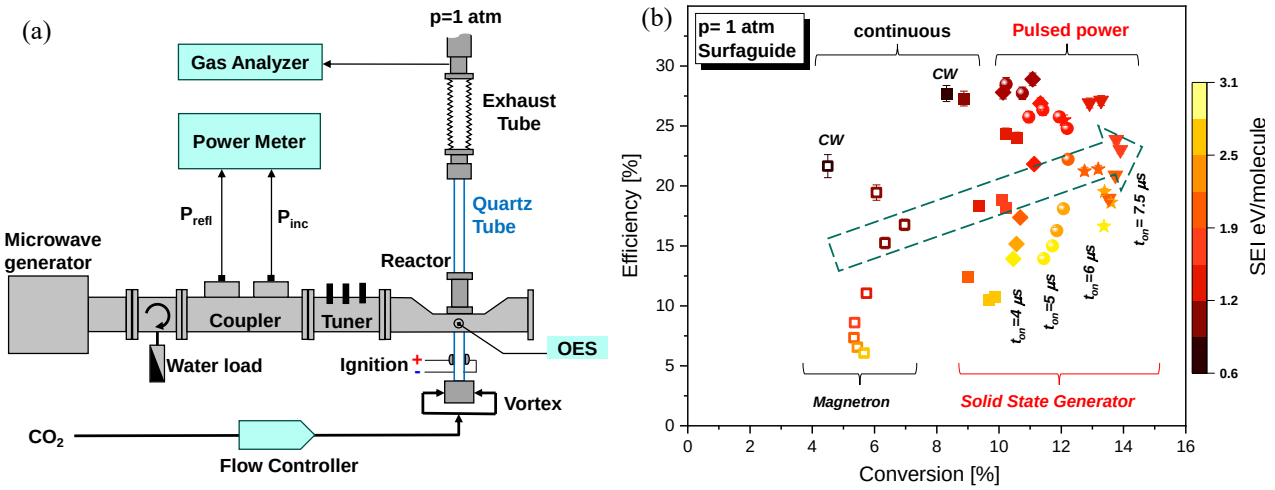

Fig. 2. (a) scheme of experiment. (b) Comparison of efficiency and conversion for magnetron microwave source against solid-state microwave source for CW and pulsed scenarios for 15 slm CO_2 flow rate. The corresponding Specific Energy Input (SEI) is color coded.

References

[1] IEA (2019), More of a good thing – is surplus renewable electricity an opportunity for early decarbonisation? IEA, Paris https://www.iea.org/commentaries/more-of-a-good-thing-is-surplus-renewable-electricity-an-opportunity-for-early-decarbonisation
[2] Schaaf, Tanja, Grünig, Jochen, Schuster, Markus Roman, Rothenfluh, Tobias, Orth, Andreas, Methanation of CO_2 - storage of renewable energy in a gas distribution system. *Energ Sustain Soc* **4**, 2 (2014). https://doi.org/10.1186/s13705-014-0029-1
[3] Navarrete, A.; Centi, G.; Bogaerts, A.; Martin, A.; York, A.; Stefanidis, G. D. Harvesting Renewable Energy for Carbon Dioxide Catalysis. *Energy Technol-Ger* **2017**, *5*, 796. DOI: 10.1002/ente.201600609
[4] Martens, J. A.; Bogaerts, A.; De Kimpe, N.; Jacobs, P. A.; Marin, G. B.; Rabaey, K.; Saeys, M.; Verhelst, S. The Chemical Route to a Carbon Dioxide Neutral World. *ChemSusChem* **2017**, 10, 1039. DOI: 10.1002/cssc.201601051
[5] Fridman, A. Plasma chemistry; *Cambridge University Press*, **2008**, https://doi.org/10.1017/CBO9780511546075
[6] Snoeckx, R.; Bogaerts, A. Plasma technology - a novel solution for CO2 conversion? *Chem. Soc. Rev.* **2017**, 46, 5805, https://doi.org/10.1039/C6CS00066E
[7] Sergey Soldatov, Guido Link, Lucas Silberer, Clara Marie Schmedt, Emile Carbone, Federico D'Isa, John Jelonnek, Roland Dittmeyer, and Alexander Navarrete, ACS Energy Lett. **2021**, 6, 124−130, https://doi.org/10.1021/acsenergylett.0c01983
[8] S. Soldatov, E. Carbone, A. Kuhn, G. Link, J. Jelonnek, R. Dittmeyer, A. Navarrete, Efficiency of a compact CO2 coaxial plasma torch driven by ultrafast microwave power pulsing: Stability and plasma gas flow dynamics, Journal of CO2 Utilization, Volume 58, 2022, 101916, https://doi.org/10.1016/j.jcou.2022.101916
[9] Moisan, Michel; Nowakowska, Helena (2018): Plasma Sources Sci. Technol. 27 073001, https://doi.org/10.1088/1361-6595/aac528
[10] Voráč, J.; Synek, P.; Potočňáková, L.; Hnilica, J.; Kudrle, V., *Plasma Sources Science and Technology* **2017,** *26* (2), 025010, https://doi.org/10.1088/1361-6595/aa51f0 .
[11] Voráč, J.; Synek, P.; Procházka, V.; Hoder, T., *Journal of Physics D: Applied Physics* **2017,** *50* (29), 294002, DOI:10.1088/1361-6463/aa7570

Physical and Numerical Investigation of Dielectrophoresis Behaviour of Atmospheric Pressure Plasma Jet

Y. Yu[1,2], K. Huang[1], L. Wu[1], Q. Chen[3], N. Shinohara[2]

[1]*College of Electronic and Information Engineering, Sichuan University, Chengdu 610065, P. R. China.*
[2]*Research Institute of Sustainable Humanosphere, Kyoto University, Uji 610-0011, Japan*
[3]*Institute of Electronic Engineering, China Academy of Engineering Physics, Mianyang 621999, P. R. China*
ytyu_academic@126.com

Keywords: dielectrophoresis behaviour, atmospheric pressure plasma jet, plasma control, microwave plasma, numerical investigation

This paper presents a study on the dielectrophoresis behaviours of an atmospheric pressure plasma jet (APPJ) subjected to an external electrostatic field between a pair of parallel electrode plates with DC voltages. The findings reveal that the plasma jet consistently deflects towards the electrode plate with an electrostatic potential, irrespective of the direction of the applied field, with the negative potential inducing a greater deflection compared to the positive potential. To further investigate these phenomena, an equivalent model is developed, where the plasma jet is proposed to be modelled as particles with permittivity and conductivity, based on its dielectric properties and motion characteristics. The numerical model exhibits short calculation times and demonstrates good agreement between simulation results and experimental observations, validating its accuracy. Through simulation, the dielectrophoretic force produced by the non-uniform electric field on the plasma is confirmed as the primary mechanism driving the observed experimental phenomena of APPJ. This work contributes to a deeper understanding of the collective effect of the plasma jet and provides an effective and efficient method for predicting the motion trajectory of the plasma jet, as well as guidelines for controlling plasma using external non-uniform electric fields.

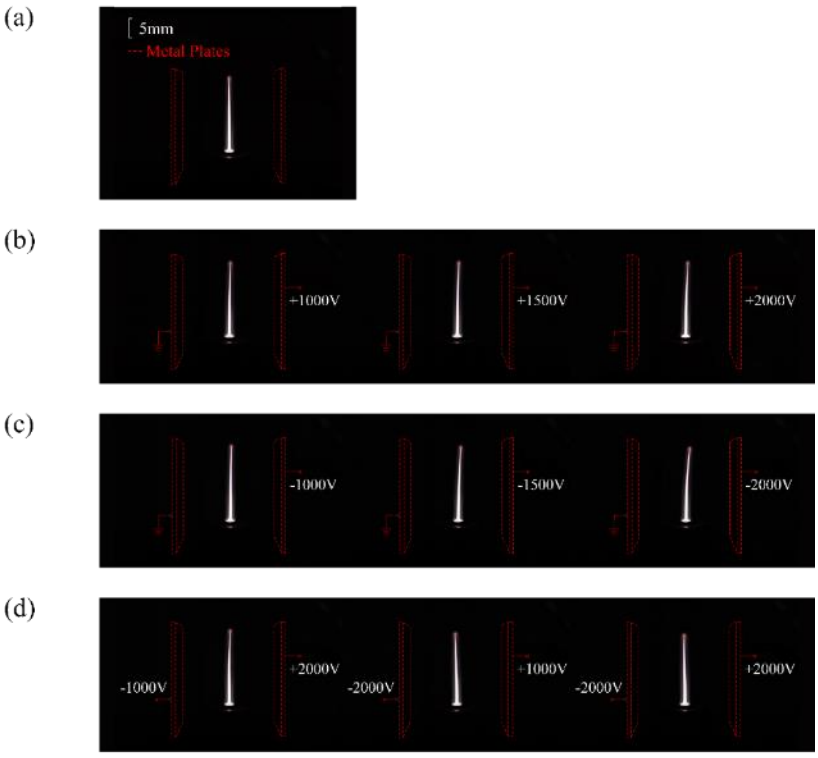

Fig. 1. Optical imagery of the influence of nearby electrode plates supplied with different DC voltages on 2.45 GHz microwave-induced APPJ. (a) Without external DC voltage. (b) With external DC positive voltages. (c) With external DC negative voltages. (d) With external DC negative and positive voltages.

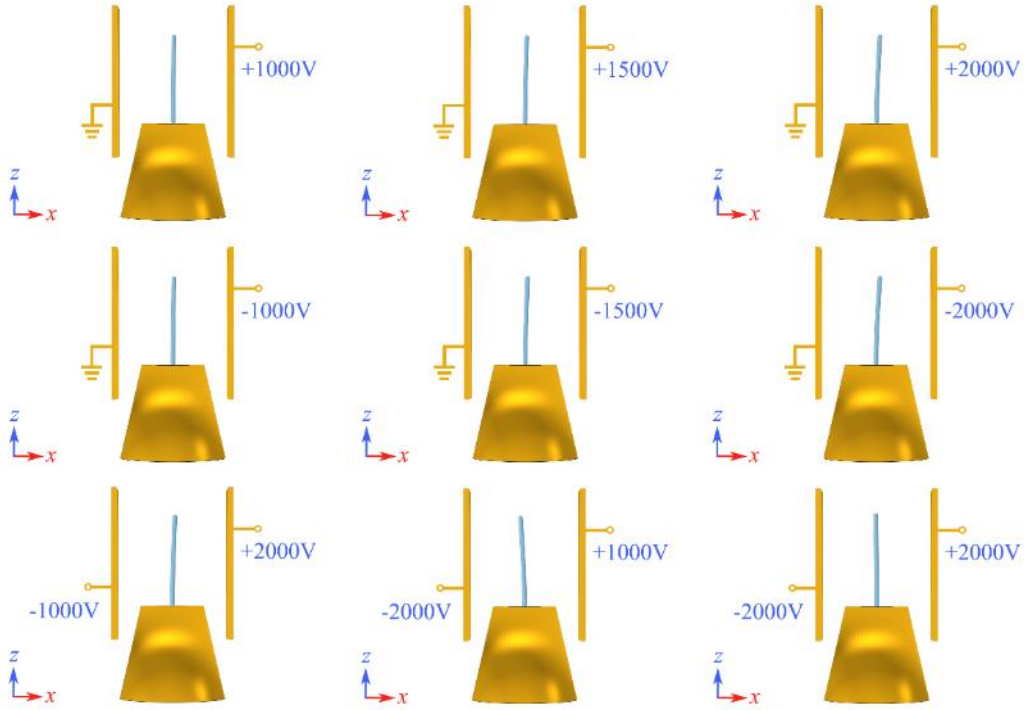

Fig. 2. Simulated results of the motion trajectory of the APPJ near the electrode plates supplied with different DC voltages.

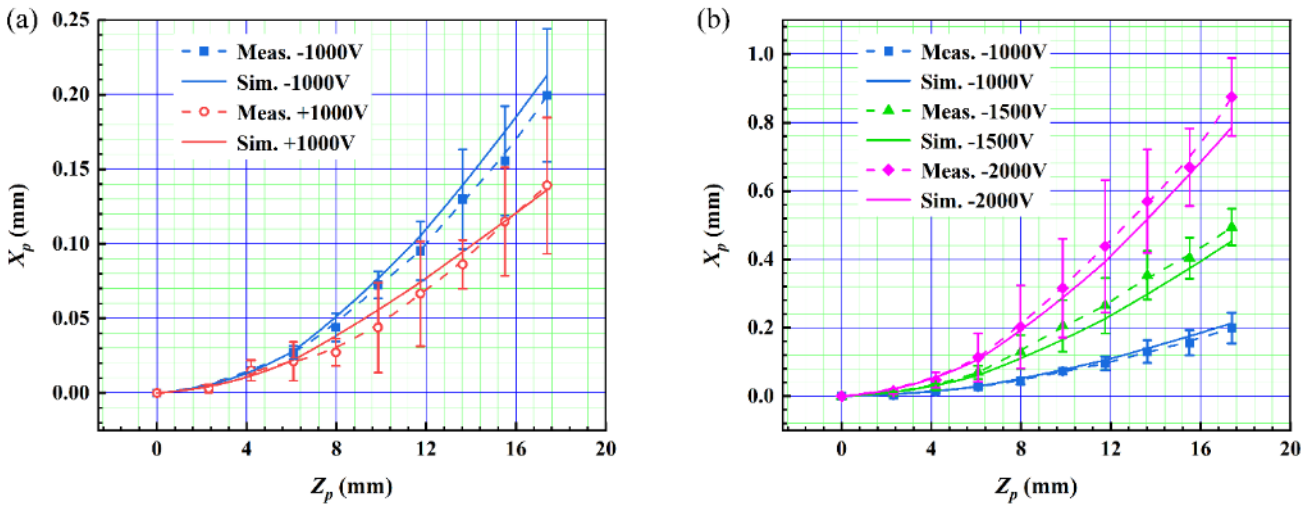

Fig. 3. Comparison of the simulated results and experimental data of the motion coordinate of plasma. The left electrode plate is grounded, and the right electrode plate is connected to the DC voltage source. X_p and Z_p are the X coordinate and Z coordinate of the plasma, respectively. (a) Comparison of different voltage polarities at the same amplitude. (b) Comparison of different voltages at the same polarity. Data are connected by Bezier curves. Error bars represent the standard deviation of the measurements.

A Novel Self-Excited Atmospheric Pressure Microwave Plasma Jet using Rectangular Coaxial Line

N. Zhong[1], K. Huang[1]

[1]*College of Electronic and Information Engineering, Sichuan University, Chengdu 610065, China. zhongny29@163.com*

Keywords: atmospheric pressure plasma jet, self-excited, water vapor, room temperature

Since the gas temperature of low-temperature atmospheric pressure microwave plasma jet (LT-APMPJ) is close to room temperature, it can hardly cause significant thermal damage to the human body. In addition, due to the presence of some highly oxidising particles, such as OH and oxygen active particles, LT-APMPJ has been used in sterilisation, wound healing, cosmetics, and so on. However, it is more difficult to excite plasma at atmospheric pressure than at low pressure. It is usually necessary to insert a metal tip into the high electric field region inside the device in order to excite the plasma.

This work reports a self-excited LT-APMPJ using a rectangular coaxial waveguide, which is designed based on the advantages of microstrip split-ring resonator (MSRR) and coaxial. The self-excited LT-APMPJ is simpler in structure and operation. Additionally, the experimental results show that when the working gas is argon, the APMPJ can be self-excited at an incident power of 20 W, and when the working gas is air, the lowest self-excited power is only 110 W. It also has higher electric field strength, electron temperature, electron density and gas temperature at the same microwave power. Besides, the gas temperature of the argon plasma jet is measured to be only 318 K at an incident power of 15 W, and the plasma jet can be touched by hand. Moreover, the air plasma jet can melt a copper wire at an incident power of 170 W. Finally, since hydroxyl (OH) radicals play an important role in the medical treatment of room-temperature plasma jets, the effect of adding a small amount of water vapour on the relative density of OH in the plasma jet is investigated, and the emission intensity of the OH line is tested by spectrometer. It is found that a small amount of water vapour can greatly increase the OH content. However, the flow rate of water vapour cannot be too large, or it will destroy the stability of the plasma jet.

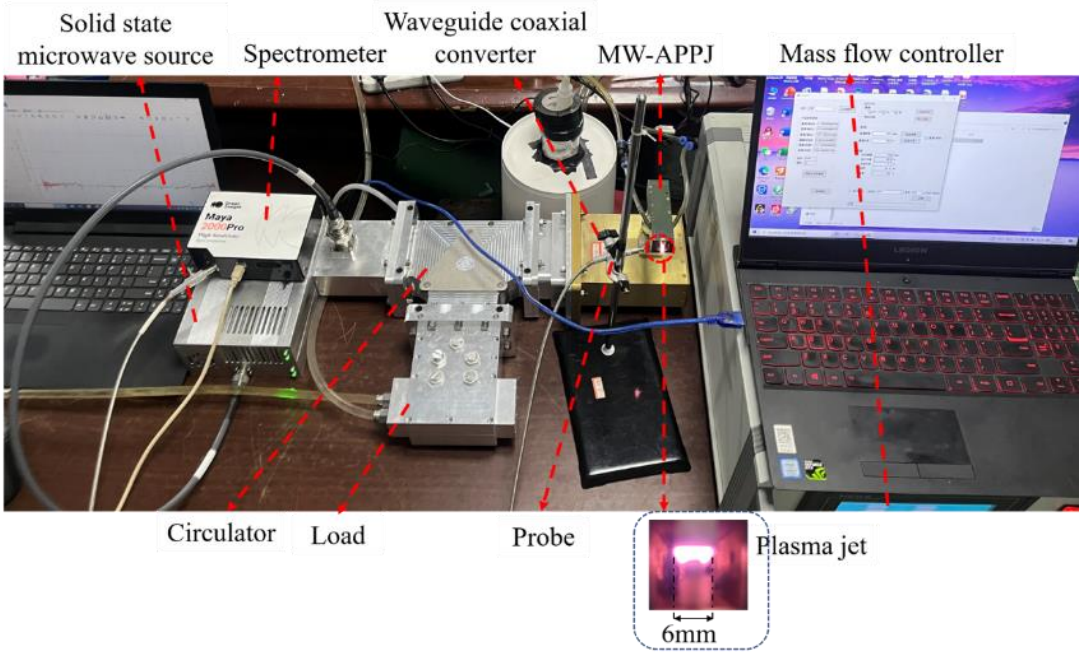

Fig. 1. The entire experimental system; the plasma jet reaches stability.

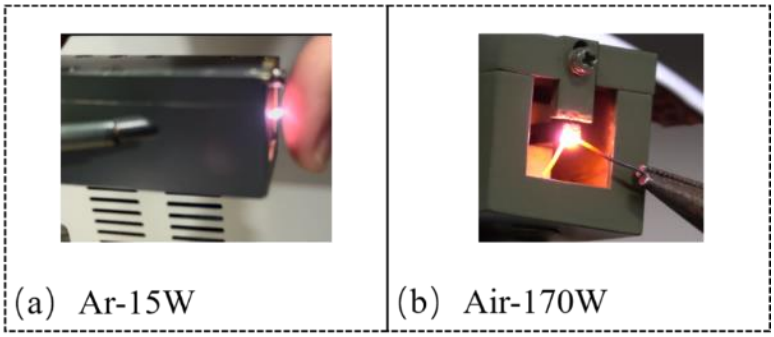

Fig. 2. Images of plasma jets. (a) Argon plasma at 15 W microwave power. (b) Air plasma at 170W microwave power.

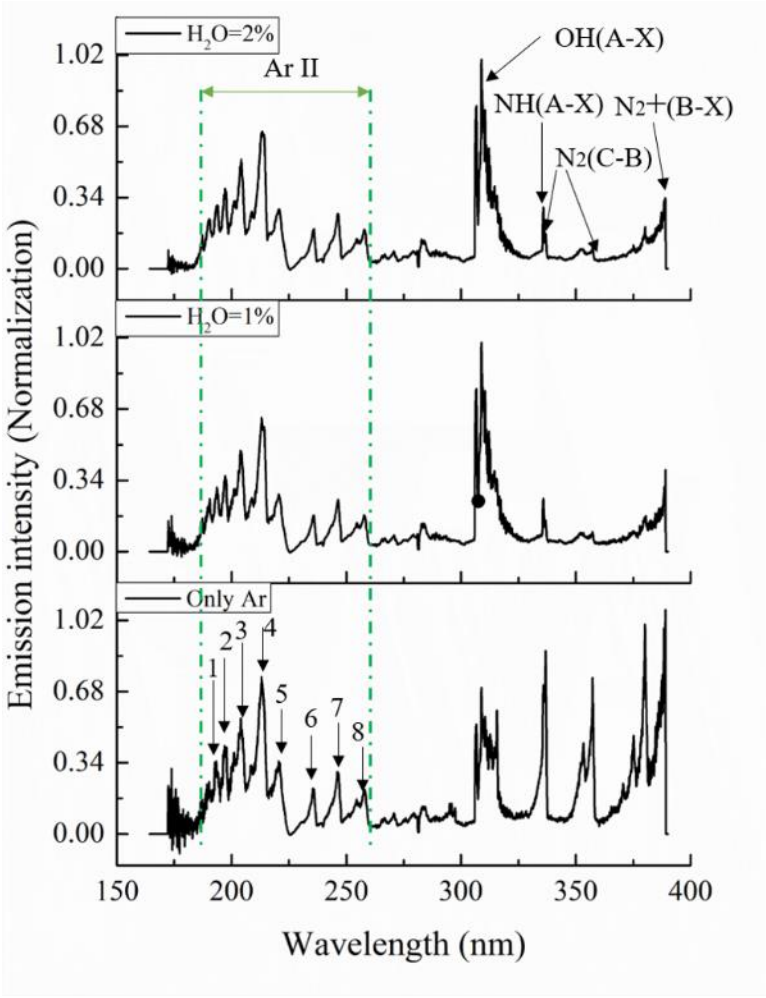

Fig. 3. Variation of emission spectra of plasma at different water vapour flow rates for the same argon flow rate.

References

[1] G. Fridman, A. D. Brooks, M. Balasubramanian, A. Fridman, A. Gutsol, V. N. Vasilets, H. Ayan, G. Friedman, "Comparison of Direct and Indirect Effects of Non-Thermal Atmospheric-Pressure Plasma on Bacteria," *Plasma Processes and Polymers*, vol. 3, pp. 370-375, May. 2007.

[2] Z. Liu, W. C. Zhang, J. W. Tao, L. Wu, K. M. Huang, "A microwave-induced room-temperature atmospheric-pressure plasma jet," *IEEE Transactions on Plasma Science*, vol. 47, pp. 1749-1753, APR. 2019.

[3] F. Iza, J. Hopwood, "Split-ring resonator microplasma: Microwave model, plasma impedance and power efficiency," *Plasma Sources Science and Technology*, vol. 14, pp. 397-406, MAY. 2005.

Nano-Porous Adhesion Layer for Sustainable Joining of Metal-Polymer-Hybrids

R. Emmerich[1], R. Dreher[1], J. Steffens[1], H. Werner[2]

[1]*Fraunhofer Institute Chemical Technology, J.-v.-Fraunhofer Str.7, Pfinztal, Germany*
[2]*Karlsruhe Institute of Technologie (KIT), Institute for Applied Materials – Materials Science and Engineering, Engelbert-Arnold-Straße 4, Karlsruhe, Germany*
Rudolf.emmerich@ict.fraunhofer.de

Keywords: microwave, plasma-enhanced chemical vapor deposition, nano-porous, adhesion layer, hybrid material

Metal-polymer hybrids are becoming more important mostly because of sustainability and cost reasons, but joining the material remains challenging. The nano-porous adhesion layer deposited with microwave plasma-enhanced chemical vapor deposition (MW-PECVD) on metal surfaces represents a possibility to join metals and polymers in a sustainable and cost-effective way with industrial processes. Joined hybrids are characterized by excellent adhesion.

Using materials where they are best suited due to their properties means a more sustainable use of resources. Polymer-metal hybrid materials are characterized, e.g. by weight savings, increased structural rigidity, realization of complex geometries, multi-functionality, integration of several process steps in one operation, less material usage, lower costs etc. The quality of the bond determines the performance of the entire component. Metal-polymer hybrid materials are joined often by adhesive bonding or by pre-treatment of the metal surface by mechanical or chemical structuring. The major disadvantage of adhesive bonded joints is that adhesion promoters and adhesives comprise more than 90% of the environmental impact of the bonding process [1] and recycling of the plastic-metal hybrid materials is hardly possible. During mechanical pre-treatment, the surface is roughened but the generated pores do not have undercuts, which limits the achievable adhesion. Laser-generated structures in the metal increase the adhesion, but the process speed is low with high heat impact in the metal. Chemical etching is very polluting and limited to aluminum.

For the deposition of coating, a linearly extended low-pressure plasma source was used (Fig. 1). The plasma is excited by microwaves at a frequency of 2.45 GHz. The plasma-line produces an axially homogeneous plasma around a quartz tube that is mounted through a vacuum chamber. Our set-up has eight plasma-lines arranged next to each other in a vacuum chamber with a length of 100 cm and a width of 60 cm. The microwaves are fed into the reactor from both sides by 8 continuous-wave (CW) magnetrons with 4 kW of pulse power / 2 kW each. Details regarding the electron density and temperature measured and the homogeneity of the plasma are given elsewhere e.g. [2].

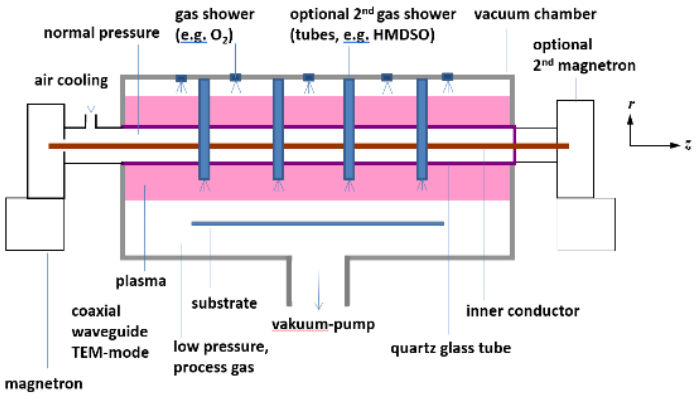

Fig. 1. Schematic view of the plasma-line

To overcome the restriction of bonding metal to polymer we are developing a SiOx-like nano-porous adhesion layer deposited with MW-PECVD [3]. Hexamethyldisiloxane (HMDSO) as precursor and oxygen as working gas are introduced in gaseous form into the plasma chamber. The molecules of the gases are excited by the plasma and react chemically, with the solid reaction products forming layers on the substrate.

$$(CH)_3Si\text{-}O\text{-}Si(CH)_3\ (g) + n\ O_2\ (g) + \text{Plasma energy} \rightarrow x\ SiO_2\ (s) + y\ H_2O\ (g) + z\ CO_2\ (g) \qquad (1)$$

By varying the plasma parameters (working pressure, microwave power, gas flow, etc.), the glass-like layer can also be deposited porously. The porous structure forms independently of the substrate material and adheres very well to metal, glass, ceramic and very many polymer surfaces. Figure 2 shows a scanning electron image of the porous layer. The porous layer grows in a columnar shape, with individual columns having a spacing in the nanometer range. The individual columns also

have a porous structure. Adhesion is created by the liquid polymer infiltrating the pores and causing mechanical interlocking at the undercuts of the layer as it solidifies. This nano-porous layer is also ideally suited for bonding plastic-metal components.

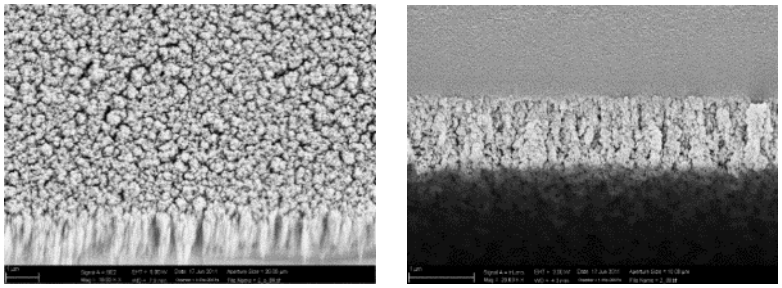

Fig. 2. SEM image top view and breaking edge (rotated 180°)

Aluminium (5754) and stainless steel (V2A) plates (width 150 mm, length 350 mm, thickness 2 mm) were coated with the nano-porous adhesion layer. The working pressure was 0.55 mbar, HMDSO-flow 630 SCCM and O_2-flow 8 SLM, deposition time 12 s. The plasma is generated with microwaves of 8 times 4kW pulse by a pulse-pause-ratio of 1:1. The coated metal plates were placed in a mould and covered with 6 layers of carbon fibre (quasi-isotropic). Liquid polyurethanes (PU) was applied to the top of the dry fibre, and compressed in a press, which pushes the resin primarily into the fabric and into the pores of the adhesion layer. The liquid resin infiltrates the nano-pores and after solidification (curing) the undercuts form an interlocked form fit.

The metal-polymer joints were tested by tensile shear edge test and the fracture surface examined by electron microscopy (SEM). An overview of the shear strength at the adhesion layer of the tested samples are summarized in Table 1.

Table 1. Results of the shear edge test.

Sample name	Reference	Alu 5754	V2A
Shear strength [MPa]	3.23	31.4	28.8
Standard deviation	--	4,5	9.29

The tested fracture surfaces of the tested samples were examined by SEM. The images are presented in Table 2 and the fracture pattern evaluated.

Table 2. Fracture pattern after shear edge tests

Reference	Alu5754	V2A
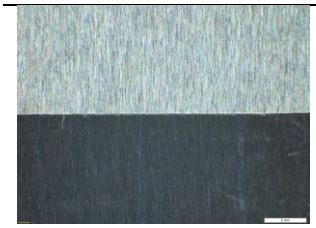	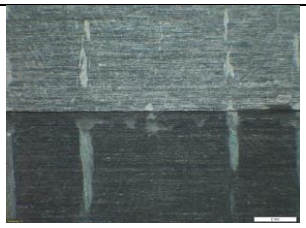	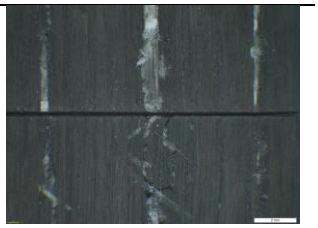
Purely adhesive failure	Near cohesive failure	Purely cohesive failure

Our study shows that with the nano-porous adhesive layer, excellent bonding can be achieved between aluminium or steel and PU, which fail almost cohesively. Hybrid materials are manufactured directly in a pressing process. Therefore, the nano-porous adhesive layer represents a sustainable and cost-effective alternative to joining metals with polymer. Further work is needed to further optimise this process for PU and extend it to other polymers.

The work received funding from the German Federal Ministry of Education and Research (No. 03INT614AB)

References

[1] C. Favi, F. Moroni, A. Lutey, N. Rodriguez: 29th CIRP Life Cycle Engineering 105 (2022) 565-570
[2] K.- D. Nauenburg, M. Oberberg, R. Dreher, R. Emmerich, PSE 2022, Erfurt
[3] R. Dreher, R. Emmerich, DE 10 2011 086 399 B4

Localized Microwave-Heating (LMH) and Direct-Current (DC) Synergy – Hybrid DC-LMH Intensification in Metal and Plasma

E. Jerby[1], Y. Shoshani[1]

[1]*Faculty of Engineering, Tel Aviv University, Ramat Aviv 6997801, Israel*
jerby@eng.tau.ac.il

Keywords: localized microwave-heating, microwave drill, additive manufacturing, dusty plasmas, thermite

Localized microwave-heating (LMH) and related studies conducted at Tel-Aviv University (TAU) in the last two decades have yielded conceptual, experimental and theoretical contributions, including microwave drilling and cutting [1], hotspot formation and thermal-runaway instabilities [2], basalt melting [3], LMH of metal powders for 3D-printing [4], thermite ignition in air and underwater [5, 6], and dusty-plasma ejection in forms of fire-columns and fireballs [7, 8]. Our recent finding of the DC-LMH synergy in metals [9] and plasmas [10] is introduced in this paper.

We have recently found that adding a relatively small direct-current (DC) to LMH may catalyze a hotspot effect in iron bulk, up to a local melting temperature (and even further to ablation and dusty-plasma ejection) [9]. This combined DC-LMH effect is demonstrated for instance by cutting an 8-mm$^{\varnothing}$ iron rebar (made of carbon-steel) without any susceptor added. Such a deep melting effect, as shown in Fig. 1, is not feasible otherwise in these conditions, neither solely by microwaves nor by only DC. This synergistic effect is attributed to a combined thermal skin evolution, which jointly forms a hotspot in a mutually intensified thermal-runaway instability, and inherently deepens the microwave penetration into the iron bulk.

The DC-LMH effect in metals is hypothesized here as conceptually illustrated in Fig. 1d [9]. In this scheme, a bulk of metal with a temperature-dependent electric conductivity is subjected to both microwave irradiation and a DC flow (I_{DC}) across it. The microwave is guided by a perpendicular electrode towards the metal plate (as in the microwave drill [1]). In this scenario, neither the DC alone nor the sole microwave irradiation (in equivalent power levels) may heat up the metal bulk. However, by combining the two, the heat energy dissipated in the EM skin region is diffused into the bulk beyond the skin depth, and further reduces its electric conductivity. Therefore, the initial microwave heating confined within the EM skin depth creates a deeper thermal resistive layer for the DC, due to the elevated resistivity of the hotter metal region. The deeper resistive layer, broadened beyond the EM skin-depth, absorbs more of the DC power and hence expedites the further expansion of this layer. The DC Joule heating is dissipated deeper than the EM skin, and further raises the temperature therein (which enables a deeper penetration of the microwave heating and hence a hotspot formation by a synergic DC-LMH thermal-runaway instability). This synergistic effect may intensify the combined heating process in a positive-feedback fashion, namely by a joint thermal-runaway instability, and hence forming a molten hotspot deeper in the metal bulk.

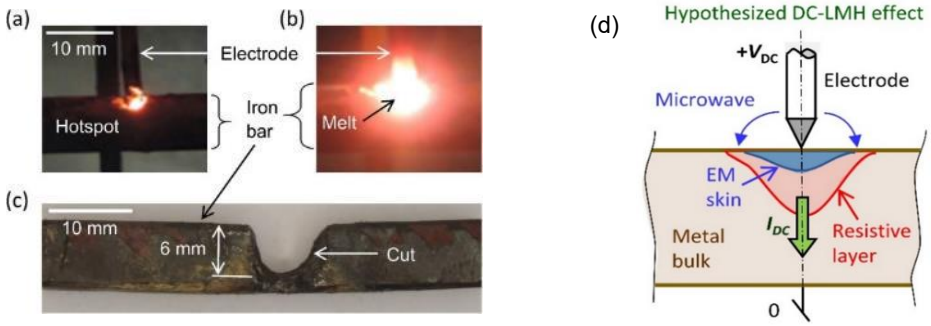

Fig. 1. DC-LMH example of iron melting and cutting [9]: (a) The hotspot formation by DC-LMH in the iron rebar; (b) the deeper melting obtained, and (c) a cut performed by DC-LMH in the iron rebar. (d) The hypothesized DC-LMH interaction in metal bulks.

DC-LMH synergy is also obtained in dusty-plasma ejection, e.g. from basalt [10]. In this experiment, after the initial stage of LMH ignition, the plasma is gradually transferred to a form of a stably sustained, long-lived fire-pillar, solely maintained by the DC supply. A stepwise transitional process was applied in order to initiate a steady column, as shown in Fig. 2 (Left) [10]. First, (i) a hotspot is formed by an LMH thermal-runaway effect, and the inner basalt core is molten. Then, (ii) the hotspot is further intensified by applying a DC current (by an electrode) to the conducting molten channel formed inside the isolating solid substrate. Once the DC channel is established, (iii) a plasma column is ejected from the molten hotspot to the air atmosphere, and the electrode is lifted upwards whereas the dusty-plasma section interacts with the microwave irradiation and closes the DC-circuit loop. Finally, (iv) the microwave is turned off, leaving a stable DC current in the serial circuit.

This LMH ignition process is intended to create a self-sustained, steady dusty-plasma column, in the form of a fire-pillar, solely maintained by the DC supply.

We have studied this finding with respect to two different themes [10]. One refers to material-processing aspects of rocks and minerals using microwave-assisted techniques. The other theme is related to the resemblance of microwave-excited fireballs to rare ball-lightning (BL) phenomena (also associated with volcanic eruptions). The known resemblance between microwave-excited plasmoids and BL phenomena is further confirmed here by the LMH-to-DC transition effect since DC sources are readily available in nature, as provided for instance by charged clouds with similar electric-field intensities (in the range $>10^3$ V/m), as illustrated in Fig. 2 (Right) [10]. The LMH-to-DC-transition applied here may provide a more comprehensive analogy between laboratory observations and natural phenomena (compared to sole RF models) and it may suggest a merge of internal- and external-energy BL theories (possibly with another localized heating source as a starter).

The DC-LMH synergy, and the research outcomes of its further investigations, may lead to a new paradigm of more efficient hybrid thermal processes of various materials, in solid, powder, and plasma phases.

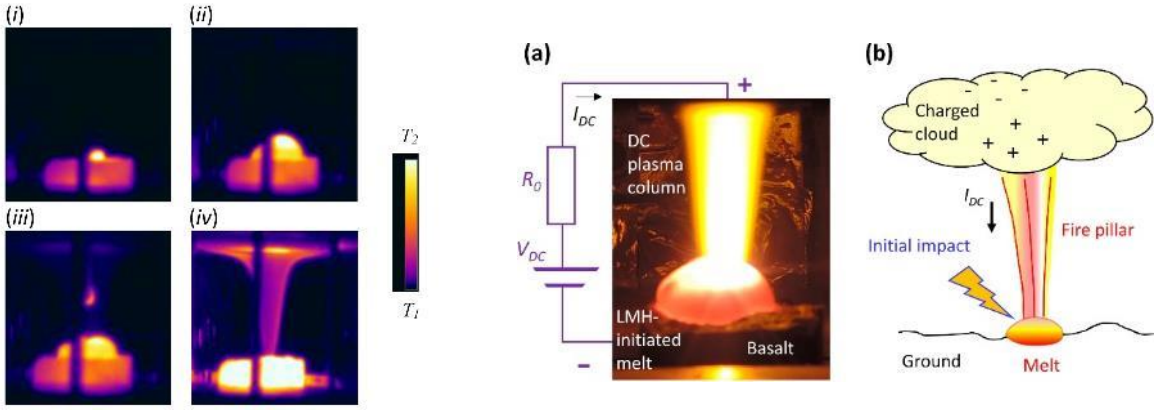

Fig. 2. (Left) Thermal images of the four LMH-to-DC stages of plasma column formation from basalt [10]. (Right) The analogy between (a) the experimental, DC-sustained dusty-plasma column emitted from basalt (initially melted in an LMH-to-DC transition), and (b) a natural, fire-pillar-like lightning, sustained between an electrically-charged cloud and a melt on the ground (caused for instance by a normal-lightning impact which may create a ball lightning).

References

[1] E. Jerby, V. Dikhtyar, O. Actushev, and U. Grosglick, "The microwave drill," *Science*, Vol. 298, pp. 587-589, Oct. 18, 2002.
[2] Y. Alpert and E. Jerby, "Coupled thermal-electromagnetic model for microwave heating of temperature-dependent dielectric media," *IEEE Trans. Plasma Science*, Vol. 27, pp. 555-562, 1999; See also E. Jerby, "Localized microwave-heating intensification – A 1-D model and potential applications," *Chemical Engineering and Processes (CEP)*, Vol. 122, pp. 331-338, 2017.
[3] E. Jerby and Y. Shoshani, "Localized microwave-heating (LMH) of basalt – Lava, dusty-plasma, and ball-lightning ejection by a "miniature volcano"," *Scientific Reports*, Art. No. 12954, 2019.
[4] E. Jerby, Y. Meir, A. Salzberg, E. Aharoni, A. Levy, J. Planta Torralba, and B. Cavallini, "Incremental metal-powder solidification by localized microwave-heating and its potential for additive manufacturing", *Additive Manufacturing*, Vol. 6, pp. 53–66, 2015
[5] Y. Meir and E. Jerby, "Thermite-powder ignition by electrically-coupled localized microwaves," *Combustion and Flame*, Vol. 159, pp. 2474–2479, 2012.
[6] Y. Meir and E. Jerby, "Underwater microwave ignition of hydrophobic thermite powder enabled by the bubble-marble effect," *Applied Physics Letters*, Vol. 107, 054101, 2015.
[7] V. Dikhtyar and E. Jerby, "Fireball ejection from a molten hot-spot to air by localized microwaves," *Physical Review Letters*, Vol. 96, No. 045002, 2006.
[8] E. Jerby, "Microwave-generated fireballs," *Encyclopaedia of Plasma Technology*, Taylor and Francis, 2017, pp. 819-832.
[9] Y. Shoshani, and E. Jerby, "Local melting and cutting of iron bulks by a synergic microwave-DC thermal skin effect," *Applied Physics Letters*, Vol. 118, Art. No. 194102, 2021.
[10] Y. Shoshani and E. Jerby, "Microwave-ignited DC-plasma ejection from basalt: Powder-generation and lightning-like effects," *Applied Physics Letters*, Vol. 120, 264101, 2022.

Industry Focus

Biogas Catalytic Decomposition under 915 MHz Microwaves - EU Project TITAN

M. Radoiu[1], A. Mello[1]

[1]*Microwave Technologies Consulting, Axel'One 5, av. G. Berger, 69100 Villeurbanne, France*
mradoiu@microwavetechs.com

Keywords: microwave, fluidised bed, hydrogen, carbon, biogas

For the last 10 years or so, renewable energy sources have been the main focus of research to decrease CO_2 production, this being a central goal of the Paris Agreement [1]. While these energy sources are widely accepted as the future for clean electricity production, certain limitations hamper the possibility of directly using their energy, namely, intermittency and hard storability. To address these issues, hydrogen has been proposed as a form of clean energy. At present many studies are focused on obtaining the so-called green hydrogen from water electrolysis using renewable electricity sources however, this method is recognised as being both electricity and capital cost intensive [2,3].

An alternative technology for hydrogen production is based on methane pyrolysis – in this method there are no CO_2 emissions, and the electricity input is much less than for water electrolysis.

EU funded Project TITAN [4] - Direct biogas conversion to green H_2 and carbon materials by scalable microwave hea**T**ed catalyt**I**c reac**T**or for soil **A**mendment and silico**N** carbide production – addresses the direct conversion of biogas (~50-60% CO_2 and 40-50% CH_4) via dry reforming + water shift reaction into valuable carbon materials and a H_2 rich stream using a 915 MHz heated fluidised bed catalytic reactor – equations (1) and (2). A schematic of TITAN's concept is shown in Fig. 1.

$$2CH_4 + CO_2 \rightarrow 4H_2 + C + 2CO \quad (1)$$

$$2CH_4 + 2H_2O \rightarrow 6H_2 + C + CO \quad (2)$$

Due to the strong endothermic effect of above reactions, an effective energy supply to the reaction zone is crucial for both H_2 production but also for maintaining a longer lifetime and performance of the catalyst. The main advantage of the proposed microwave-assisted processing is that microwaves are delivered straight to the catalyst particles.

Within the framework of a circular economy concept, the valorisation of the produced carbon materials will be studied for two applications, namely *i)* agriculture soil amendment and *ii)* production of SiC materials. The long-term storage of the carbon species and their impact on soil organisms and soil properties when released into agricultural soils will be studied.

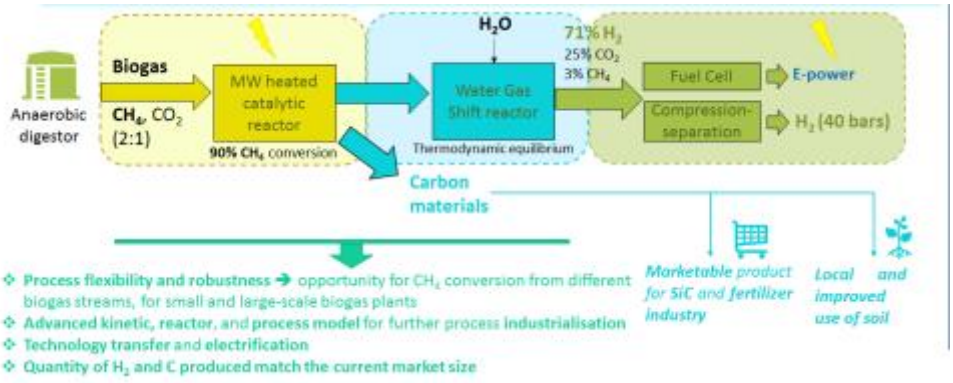

Fig. 1. TITAN concept for the conversion of biogas using 915 MHz microwave-assisted catalytic processing

Acknowledgements

Funded by the European Union. Views and opinions expressed are however those of the authors only and do not necessarily reflect those of the European Union or the European Climate, Infrastructure and Environment Executive Agency (CINEA). Neither the European Union nor the granting authority can be held responsible for them.

Funded by the European Union

titan
microwave biogas cracking

References

[1] R. Falkner, "The Paris Agreement and the new logic of international climate politics", *International Affairs*, 92 (5). pp. 1107-1125, 2016
[2] S.K. Shiva, V. Himabindu, "Hydrogen production by PEM water electrolysis – a review", *Mater. Sci. Energy Technol.*, vol. 2, pp. 442-454, 2019.
[3] P. Nikolaidis, A. Poullikkas, "A comparative overview of hydrogen production processes", *Renew Sustain. Energy* rev., vol. 67, pp. 597-611, 2017
[4] European Commission. Funding & tender opportunities, available from: https://ec.europa.eu/info/funding-tenders/opportunities/portal/screen

Microwave Assisted CO_2 Desorption from Solvent Flowing into Hollow Fiber Membrane

A. Hajj[1,3], E. Savary[3], T. Hauviller[2], S. Curet[2], P. Pré[1]

[1]*IMT Atlantique, GEPEA, UMR CNRS 6144, 44307 Nantes, France*
[2]*Oniris, Nantes Université, CNRS, GEPEA, UMR 6144, F-44000 Nantes, France*
[3]*SAIREM, 82, Rue Elisée Reclus, 69150 Decines Charpieu, France*
ali.hajj2@imt-atlantique.fr

Keywords: EM modelling, separation process, CO_2 capture

Chemical absorption is considered as one of the most mature technologies for carbon capture from flue gases, it is composed of the absorption stage where CO_2 is dissolved chemically into the solvent and the desorption stage where the latter is regenerated at high temperatures. Despite its technological maturity it suffers from several drawbacks most noticeably the large equipment footprint and the high operating cost of the desorption stage [1]. This is presented by the intensive steam consumption that provides heat for the desorption reaction of CO_2 and acts as a sweeping gas. Lately, application of microwave technology (MW) to chemical absorption has been receiving increasing attention from the scientific community owing to increased operational flexibility, small footprint, and most notably its intensification potential [2]–[4]. Successful scale-up of the process depends on the choice of the gas-liquid contactor. Hollow fiber membrane modules, which consist of a bundle of porous polymer membrane capillaries can be used in MW assisted CO_2 desorption due to their inertness to MW irradiation. In addition, they provide a further potential for process intensification thanks to their high surface area compared to packed columns [5]–[7]. This original research aims at studying the potential of MW technology for chemical desorption of CO_2, while using hollow fiber membrane modules as a contactor.

The MW assisted regeneration of the solvent was first studied at a single fiber scale in order to examine the effect of the local temperature and concentration distributions between the gas and the liquid phases on the desorption rates. To this end, a single hollow fiber was placed parallel to the E-field in a single mode TE_{10} 2450 MHz microwave cavity as shown in Figure 1. A CO_2-rich solvent was introduced into the fiber submitted to variable MW powers. The released CO_2 crossing the gas-permeable porous membrane fiber was swept by a N_2 flow on the annular side. Experimental campaigns were performed by varying the solvent flow rates to reach similar hydrodynamic conditions to that in the membrane module. The initial CO_2 loading was varied over the range representative of operating conditions of a stripping column, whilst the MW power was controlled to achieve different outlet liquid temperatures. Impedance matching between the cavity and the waveguide was performed through a sliding short circuit to achieve acceptable levels of microwave reflected power.

Considering the complexity of the involved coupled physical and chemical phenomena, a progressive step-by-step approach was applied relying on the development of a numerical model using Comsol® Multiphysics 6.0 software. The electromagnetic propagation was first simulated in order to describe the E-field propagation throughout the MW cavity, as well as the S11 spectrum for microwave reflected power. The latter was compared to data obtained by vector network analyzer measurements. Afterwards heat transfer and fluid mechanics were considered and the direct coupling with electromagnetic phenomena generates spatial temperature maps. The temperature varies radially depending on the flow regime, and axially along the fiber depending on the residence time in the microwave cavity. Once the temperature profiles could be computed, mass transfer and reaction phenomena were incorporated to predict the CO_2 desorption rates associated with the obtained local temperature variations.

The MW-assisted CO_2 desorption was investigated experimentally on the scale of a single hollow fiber to validate a model simulating desorption rates function of different operating parameters. Future challenges will focus on upscaling the modelling approach from the scale of a single fiber to that of a membrane module containing a bundle of fibers. An experimental set-up was designed to test the regeneration process at the prototype scale, using either MW irradiation for solvent pre-heating or directly into the membrane contactor. Such tests should illuminate the potential of MW technology for this application.

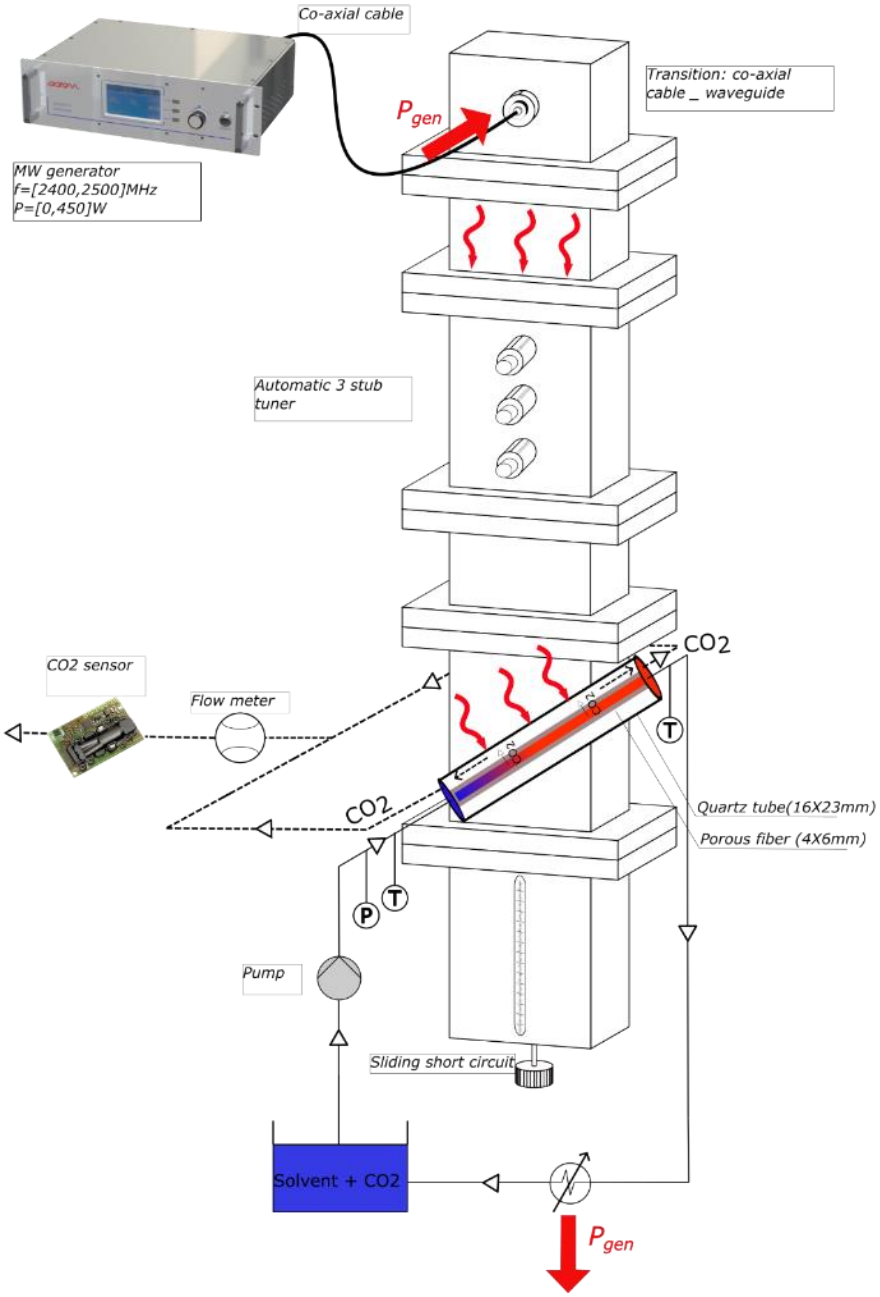

Fig. 1. MW assisted regeneration of CO2 rich solvents at the scale of a single hollow fiber.

References

[1] S. Ziaii, G. T. Rochelle, and T. F. Edgar, "Dynamic Modeling to Minimize Energy Use for CO 2 Capture in Power Plants by Aqueous Monoethanolamine," *Ind. Eng. Chem. Res.*, vol. 48, no. 13, pp. 6105–6111, Jul. 2009, doi: 10.1021/ie801385q.
[2] F. Bougie and X. Fan, "Analysis of the Regeneration of Monoethanolamine Aqueous Solutions by Microwave Irradiation," *Energy Procedia*, vol. 142, pp. 3661–3666, Dec. 2017, doi: 10.1016/j.egypro.2017.12.259.
[3] Z. Ji, J. Wang, D. Hou, Z. Yin, and Z. Luan, "Effect of microwave irradiation on vacuum membrane distillation," *J. Membr. Sci.*, vol. 429, pp. 473–479, Feb. 2013, doi: 10.1016/j.memsci.2012.11.041.
[4] S. J. McGurk, C. F. Martín, S. Brandani, M. B. Sweatman, and X. Fan, "Microwave swing regeneration of aqueous monoethanolamine for post-combustion CO 2 capture," *Appl. Energy*, vol. 192, pp. 126–133, Apr. 2017, doi: 10.1016/j.apenergy.2017.02.012.
[5] H. Kreulen, C. A. Smolders, G. F. Versteeg, and W. P. M. van Swaaij, "Microporous hollow fibre membrane modules as gas-liquid contactors. Part 1. Physical mass transfer processes," *J. Membr. Sci.*, vol. 78, no. 3, pp. 197–216, Apr. 1993, doi: 10.1016/0376-7388(93)80001-E.
[6] N. Nishikawa *et al.*, "CO2 removal by hollow-fiber gas-liquid contactor," *Energy Convers. Manag.*, vol. 36, no. 6–9, pp. 415–418, Jun. 1995, doi: 10.1016/0196-8904(95)00033-A.
[7] M. Vogt, R. Goldschmidt, D. Bathen, B. Epp, and H. Fahlenkamp, "Comparison of membrane contactor and structured packings for CO2 absorption," *Energy Procedia*, vol. 4, pp. 1471–1477, Jan. 2011, doi: 10.1016/j.egypro.2011.02.013.

Application of Microwave Energy in the Drying Process of Selected Insect Larvae

J. Majerska[1], M. Nowakowski[1], A. Zimmer[2], M. Wilk[3], R. Parosa[1]

[1]*Promis–Tech sp. z o. o., ul. Danuty Siedzikowny 14, 51-214 Wroclaw, Poland*
[2]*Wroclaw University of Environmental and Life Sciences, Institute of Agricultural Engineering, ul. Chelmonskiego 37a, 51-630 Wroclaw, Poland*
[3]*Faculty of Biology and Animal Science, University of Environmental and Life Sciences, ul. Chełmonskiego 38c, 51-630 Wroclaw, Poland*

Keywords: microwave drying, wave reflection, heat pump, larvae, protein

Abstract
In the present study, the microwave drying processes of the larvae of the yellow mealworm (YMW) (*Tenebrio molitor*) and the black soldier fly (BSF) (Hermetia *illucens*) were investigated. Microwave drying (MW) (process parameters: 500-1000 W), microwave reduced pressure drying (MVD) (process parameters: 500-1000 W, 30-40 hPa), and microwave-convection drying using a heat pump (MW-HP) (process parameters: 500-1000 W, 50°C) and hot air convection drying (HACD) (process parameters: 50-100°C) were used as control processes. In the present study, the microwave power transmitted to the chamber, the drying temperature and time, the reflected wave during microwave (MW), microwave-vacuum drying (MVD) were determined, and the final quality of the product, assessed by physical and chemical analyses, i.e. moisture content, colour, protein and amino acid content, was examined. Based on the processes and analyses performed, the most favorable methods for drying larvae were selected and a concept for a dedicated industrial-scale larvae drying plant using microwave energy was developed. The use of microwaves in the drying process shortens its time, which has a positive effect on the parameters of the dried material, such as colour and protein content.

Introduction
Drying is one of the well-known methods of food preservation, during which the evaporation of water from the material can take place in several ways. One of the factors enabling effective dehydration of the material is microwave energy. Drying using electromagnetic field radiation allows heating the product in its entire volume, in the direction from the inner to the outer layers of the material, where the energy is rapidly conjugated with moisture, resulting in fast heating and drying of the material [1]. Reducing the drying process time improves the quality of the final product due to a shorter exposure to the drying agent, making microwave drying a promising food preservation technology compared to conventional methods of food dehydration [2,3]. In addition, in drying processes using microwaves, the issue of microwave reflection during the drying process is very important, as it directly affects the time of drying, quality of dried products and, most importantly, energy consumption [4,5,6].

The world's growing population is causing a relatively high burden on traditional food sources, mainly animal protein. This has prompted a search for alternative sources of protein, which can be the larvae of selected insects [7]. As a sustainable alterative for protein, larvae can also serve as additive due to their nutritional composition. It has been reported that black soldier fly larvae contain an average of 35-44% protein, and mealworm larvae between 50-57% protein [8,9]. Above all, this makes black soldier fly larvae, as well as mealworm larvae, a promising species for industrial production, which can be easily reared [10].

There are a limited amount of studies on reflected wave measurement for microwave drying of insect larvae, while to date there are no literature reports on black soldier fly larvae that use microwave drying to remove water from material [11,12]. In addition, the literature provides no information on the use of heat pumps in relation to the drying of insect larvae and their impact on the process and on energy consumption.

The aim of these studies is the optimisation of microwave transmission, including the selection of the methods of microwave introduction into the chamber and energy matching in the microwave transmission line. Additionally, the quality assessment of the drying of selected insect larvae obtained using microwaves was carried out at atmospheric pressure and reduced pressure. The applied drying methods were compared based on energy density to choose a drying method that represents a compromise between process power density and larvae quality. Measuring the reflection coefficient as a function of the relative humidity of the dried material allows obtaining data for the design of matching elements in transmission lines (tuners or matching apertures). As a result of these activities, a concept of a dedicated industrial-scale installation for drying larvae using microwave energy was developed.

Materials

The research utilised larvae of the yellow mealworm (YMW - Tenebrio molitor L.) and larvae of the black soldier fly (BSF - Hermetia illucens) obtained from a local breeder (PRS PROMAROL SP. Z O.O., Poland). The larvae were raised on "organic" food mixed with soil, following the European Union requirements for insect larvae farming practices, and under strict hygienic conditions in accordance with Hazard Analysis and Critical Control Points (HACCP) production procedures. The larvae were cleaned of substrate residues and subjected to planned drying processes. After drying, the larvae were ground and vacuum-packed into special bags, and then submitted for analysis. Figure 1 below presents the yellow mealworm larvae (Fig. 1a) and the black soldier fly larvae (Fig. 1b).

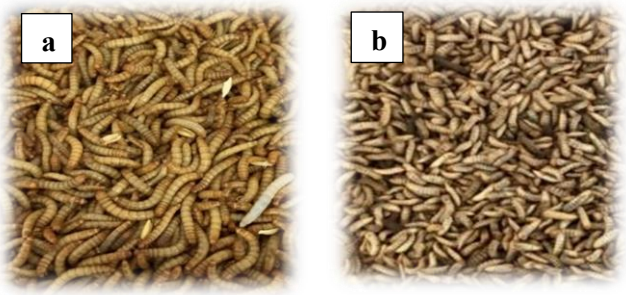

Fig. 1. a) - yellow mealworm (YMW) and b) - black soldier fly (BSF)

Methods - Drying

The initial moisture content of yellow mealworm larvae was MCi=60% (MCi - initial moisture content), and MCi=65% for black soldier fly larvae. For drying, larvae samples with a mass of m=200 g were prepared. Each drying process continued until a steady mass was achieved. Selected drying processes were conducted with two technological repetitions (n=2).

The drying processes were carried out using a convection-microwave-vacuum dryer (ZLP-2000, Promis-Tech sp. z o.o. (Fig. 2) in various operating modes, as illustrated in Figures Fig. 3, Fig. 4, Fig. 5, and Fig. 6.

For the insect larvae drying, hot air convective drying (HACD) was applied as the control process. The drying was performed in a convection-microwave mode (with microwaves turned off), as presented in Fig. 2. The convective drying process was conducted at temperatures ranging from 50 to 100°C.

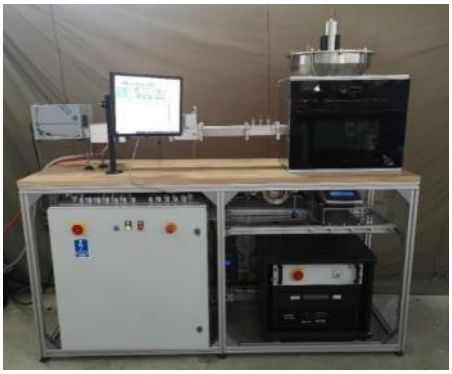

Fig. 2. Laboratory convective-microwave dryer ZLP-2000

The subsequent drying process utilised for water evaporation from yellow mealworm larvae and black soldier fly larvae was microwave drying (MWD) with power levels ranging from 1000 to 2000 W. The drying process was carried out in convection-microwave mode illustrated in Fig. 3.

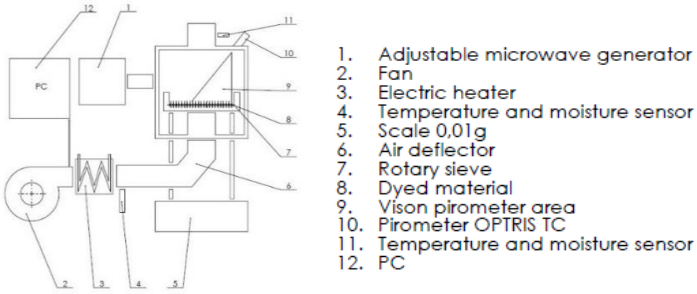

Fig. 3. Laboratory convective-microwave dryer ZLP-2000.

In the research, microwave-convection drying assisted by a heat pump (Beko, R-134a, 800 W, Turkey) was also employed, and its operating mode is illustrated in Figure 4. Throughout the process, the air temperature did not exceed 50°C, and the microwave power ranged from 1000 to 2000 W.

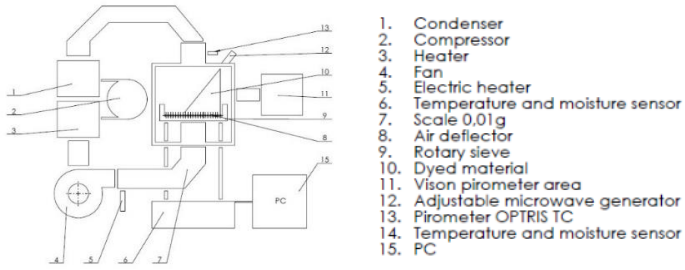

Fig. 4. Laboratory convective-microwave dryer ZLP-2000 with heat pump.

Microwave-vacuum drying (Fig. 5) was also utilised for drying yellow mealworm larvae (YMW) and black soldier fly larvae (BSF). The process was conducted within a microwave power range of 1000-2000 W and under a vacuum pressure of 30 hPa.

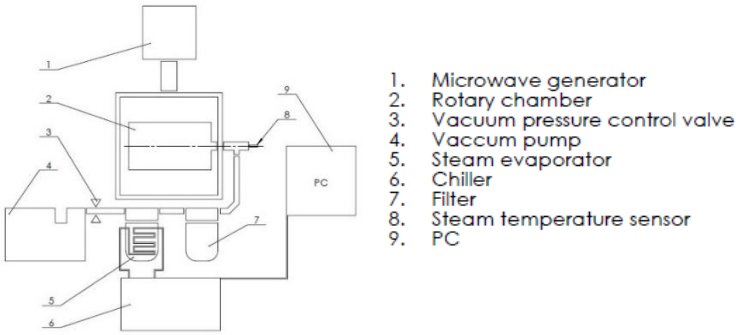

Fig. 5. Laboratory microwave-vacuum dryer ZLP-2000.

Reflection of the microwave power

The measurement of delivered and reflected power was carried out using a reflectometer (MUEGGE, type MM1010E-110AF, Germany). The measurement results were recorded every 3 minutes from the beginning to the end of the process. Using this data, the reflection coefficient modulus of the microwave wave was determined based on the following ratio (1). :

$$|\Gamma| = \frac{P_r}{P_0} \quad (1)$$

where P_r is reflected power and P_0 is power transmitted.

The conceptual diagram of the measurement setup for the reflected wave is shown below in Figure 6.

Based on the literature [13], it is known that various substances alter their dielectric parameters depending on humidity and temperature. In this article, this phenomenon is observed during the drying process.

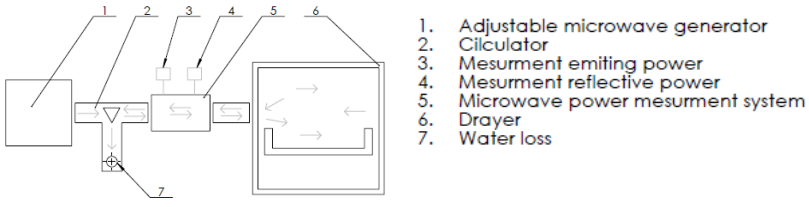

Fig. 6. Schematic of a setup for measuring reflected microwave power.

Energy consumption

Energy consumption was recorded using the control program of the dryer in CoDeSys (CODESYS GmbH, V2.3.9.61, 2020, Kempten, Germany). Furthermore, the energy consumption generated by the heat pump in the MW-HP process was measured using an electrical energy consumption meter (BLOW 72-020) and then combined with the energy consumption of the microwave-convection dryer recorded in the CoDeSys program.

Physico-chemical properties

The moisture content of the larvae was determined using a vacuum dryer SPT-200 (ZEAMiL, Horyzont, Kraków), where the samples were held at 80°C for 20 hours [14]. Water activity (aw) in the obtained dried samples was measured using the AQUA LAB DewPoint Water Activity Meter (Washington State, USA). The measurement of water activity at 25°C ± 2°C was conducted with two repetitions (n=2). Colour measurement of the dried larvae was performed using the Minolta CR-400 colourimeter (Osaka, Japan). The colour coordinates were determined in the CIE Lab* colour space, where L* represents brightness (0-100), a* represents the red-green axis, and b* represents the blue-yellow axis. The measurement was conducted using the D65 standard illuminant. Colour measurements were repeated 5 times (n=5).

The crude protein concentrations were analysed according to the AOAC standard procedures using the Kjeldahl method (section 954.01) with the use of FOSS Tecator 2300 Kjeltec Analyzer Unit (FOSS Tecator, Hoganas, AB, Sweden). Association of Official Analysis Chemists International (AOAC). Official Methods of Analysis of AOAC International. Association of Official Analysis Chemists International (2000).

Result and discussion

Reflection *– Hermetia illucens (BSF – black soldier fly)*

As part of the study, microwave drying with the assistance of hot air (500 W, 50°C; 1000 W, 100°C; 2.45 GHz) was performed, during which the complex reflection coefficient magnitude $|\Gamma|$ was measured. This coefficient represents the ratio of the reflected power from the drying chamber to the transmitted power, as shown in Figure 6. The measured complex reflection coefficient magnitude was plotted against the water content (relative humidity) in the dried sample, with moisture decreasing from 65% to 5%. The graph illustrates that the microwave reflection from the sample increases between a humidity of 65% and 50%, reaching a value of approximately $|\Gamma| = 0.25$. Subsequently, as the water content decreases from 50% to 35%, the microwave reflection coefficient also decreases to around 0.1. With a further reduction in sample moisture (from 25% to 5%), there is a dynamic increase in the reflection coefficient to values around $|\Gamma| = 0.4 – 0.6$, depending on the sample. Within this humidity range, there is a significant decline in the material's ability to absorb microwaves. Moreover, the high reflection coefficient indicates low process efficiency, especially within the 25% to 5% moisture range.

The primary factor causing material heating is microwave absorption by water molecules. In the final stages of drying, when the dried material contains very little water, the reflection coefficient increases significantly. Changes in the reflection coefficient in the relative humidity range of 20 - 60% are attributed to effects related to alterations in the distribution of the electromagnetic field within the drying chamber during the process, due to changes in the complex dielectric permittivity of the material.

During microwave drying assisted by a heat pump, the trends (Figure 7) and changes in the microwave reflection coefficient modulus are similar to those observed in the microwave drying process with convection. In the graph, it can be observed that microwave reflection increases at around 65% humidity up to a sample humidity of about 25-30%. Then, as the water content decreases from 50% to 35%, microwave reflection also drops, and the reflection coefficient modulus decreases to values around $|\Gamma| = 0.1 – 0.2$. With a reduction in sample moisture from 25% to 5%, there is a dynamic increase in the reflection coefficient to values around $|\Gamma| = 0.4 – 0.6$, depending on the sample. This phenomenon is also observed in the case of microwave drying assisted by convection. In the discussed drying process, the following factors [15] affect the reflection coefficient odulus: water content in the sample, sample temperature, and composition – the ratio between water, fat, and protein content in the sample.

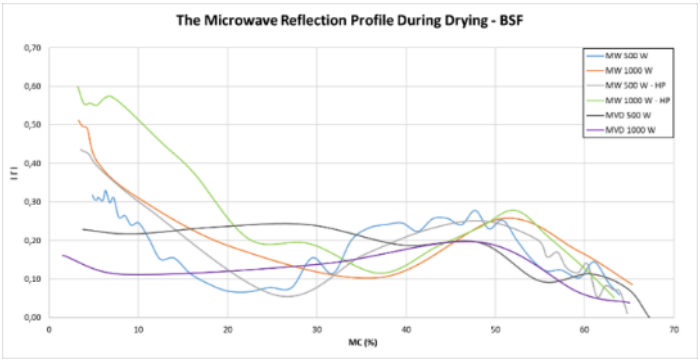

Fig. 7. Microwave reflection profile during selected methods of drying black soldier fly larvae 200g sample.

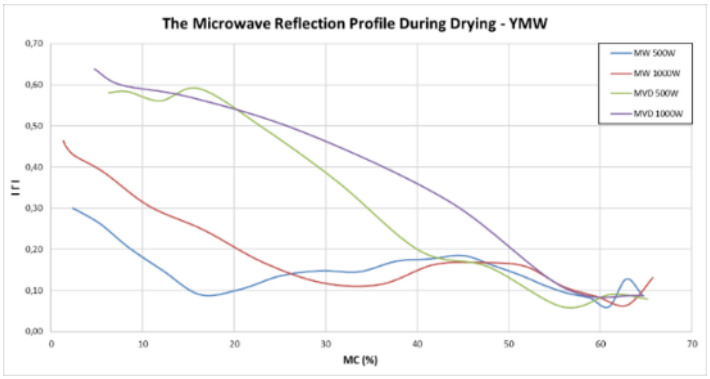

Fig. 8. Microwave reflection profile during selected methods of drying yellow mealworm larvae 200g sample.

The profiles of the reflection coefficient function with respect to the sample's water content differ between microwave drying assisted by hot air and microwave drying with the use of a heat pump. This variation may stem from the lower temperatures and slower heating rates during microwave and heat pump-assisted drying. It implies the existence of a relationship between the sample's temperature and the reflection coefficient value.

In the microwave-vacuum drying process (Fig. 7), the reflection coefficient values are lower than those in microwave drying and microwave drying with a heat pump. The reflection coefficient does not exceed $|\Gamma| = 0.25$. A comparable trend between the trials was not achieved; however, an increase in the reflection coefficient was observed from 0 to 0.2 as the water content decreased from 65% to 40%. Subsequently, the reflection coefficient value fluctuates within the range of $|\Gamma| = 0.2\text{-}0.1$ and is significantly lower than in microwave-convection processes. The tendency suggesting a sharp increase in reflection due to the decrease in water particles towards the end of the process is much less pronounced.

The profiles of the microwave reflection function with respect to the sample's water content differ between microwave-assisted drying and microwave drying with a heat pump. This variation may arise from lower temperatures and a slower heating rate in microwave drying with a heat pump. Additionally, this may indicate a dependence of the reflection coefficient value on the sample's temperature as well.

Relatively high reflection coefficient values in industrial drying installations lead to reduced energy efficiency (they are converted into waste heat from the process). This comparison suggests significant losses in the final stages of drying. This is an unnecessary cost that generates increased consumption of electrical energy. Test results indicate the need for dynamic tuning of microwave systems during batch drying processes. This will contribute to an increase of process efficiency and reduction of energy losses. In continuous mode in industrial installations, adjusting the equipment along the process, considering changes in the properties of the dried material, is recommended.

Reflection – *Tenebrio molitor (YMW – yellow mealworm)*
The measurement of microwave reflection in relation to yellow mealworm larvae (YMW) was conducted solely for the MW-CD and MVD drying processes. These processes for the drying of black soldier fly larvae (BSF) allowed achieving the smallest level of microwave reflection and relatively low energy consumption. As part of the study, microwave drying assisted by hot air (500 W, 100°C; 1000 W, 100°C; 2.45 GHz) was performed, during which the complex reflection coefficient magnitude $|\Gamma|$ was measured. This coefficient represents the ratio of the reflected power from the drying chamber to the transmitted power, as shown in Figure 7. The measured complex reflection coefficient magnitude was plotted against the water content (relative humidity) in the dried sample, with moisture decreasing from 65% to 5%. Similarly to the case of BSF, the graph illustrates that microwave reflection from the sample increases between a humidity of 65% and 50%, reaching a value of approximately 0.2. Subsequently, as the water content decreases from 50% to 35%, the microwave reflection coefficient also decreases to around 0.1. With a further reduction in sample moisture (from 25% to 5%), there is a dynamic increase in the reflection coefficient to values of 0.4-0.6, depending on the sample. Within this humidity range, there is a significant decline in the material's ability to absorb microwaves. Moreover, the high reflection coefficient indicates low process efficiency, especially within the 25% to 5% moisture range.

In the microwave-vacuum drying process (MVD500, MVD1000) (Fig. 8), the reflection coefficient increases quite proportionally with decreasing humidity. Trends similar to microwave-convection drying are not observed. The reflection coefficient value also significantly increased to around 0.6 at the end of the process.

In the discussed drying process, the following factors [15] affect the reflection coefficient magnitude: water content in the sample, sample temperature, and composition – the ratio between water, fat, and protein content in the sample.

Drying conditions and energy consumption
In Table 1 and Table 2, the drying process parameters for *Hermetia illucens* and *Tenebrio molitor* larvae are presented. For BSF larvae, it can be observed that increasing the drying temperature in HACD from 50 to 100°C resulted in a 20-fold

reduction in drying time and a 15-fold decrease in energy consumption for this process. In the case of MW drying, increasing the magnetron power from 500 to 1000 W led to a 30% increase in the maximum drying temperature for BSF larvae (106.8°C), a 5-fold reduction in drying time, and a 3-fold decrease in energy consumption. For YMW larvae during MW drying, no significant differences in drying time or energy consumption were observed with the increase in power from 500 to 1000 W. The use of a heat pump (HP) in MW drying of BSF larvae led to more than a 2-fold increase in drying time compared to MW drying without HP assistance, due to temperature limitations resulting from the properties of the heat pump's gas. This extension of drying times directly led to increased energy consumption. For YMW larvae, microwave drying assisted by a heat pump was performed only with the 1000 W power variant, and the drying time and energy consumption were reduced by at least 6 times compared to BSF larvae. The most advantageous drying method for both species of larvae, in terms of drying time and energy consumption, was microwave-vacuum drying (MVD). For BSF larvae, the maximum temperatures were nearly 90°C for MVD 500 W and almost 105°C for MVD 1000 W, whereas for YMW larvae, the temperatures for both power variants were around 60°C. Increasing the power from 500 W to 1000 W in MVD drying almost halved the process time for both species of larvae, and the energy consumption of the MVD processes was the lowest among the investigated drying methods, not exceeding 1.462 kWh.

Table 1. Drying conditions of black soldier fly larvae.

Type of Larvae	Methods of Drying	Drying Conditions			Energy Consumption (Kwh)
		MW Power (W)	Max. Temperature (°C)	Time Of Drying (Min)	
Black Soldier Fly (BSF)	HACD	(-)	50	1770	29.246
		(-)	100	88.5	2.262
	MW	500	77	117	3.606
		1000	106.8	22.5	1.221
	MW-HP	500	68.3	252.5	8.823
		1000	89.9	105	5.382
	MVD	500	89.5	27	1.237
		1000	103.65	14	0.850

Table 2. Drying conditions of yellow mealworm larvae.

Type of Larvae	Methods of Drying	Drying Conditions			Energy Consumption (kWh)
		MW Power (W)	Max. Temperature (°C)	Time of Drying (Min)	
Yellow Mealworm (YMW)	MW	500	97.10	20	0.940
		1000	102.50	15	0.912
	MW-HP	1000	86.00	40	1.836
	MVD	500	61.60	30	1.462
		1000	60.90	18	1.145

Physicochemical properties

The drying processes resulted in obtaining dried larvae from BSF with moisture content ranging from 3.08% (MVD1000 W) to 6.94% (HACD 50°C), and for YMW larvae from 3.19% (MVD 1000 W) to 6.01% (MW-HP 1000 W). Similar moisture values were obtained in other studies related to larvae drying [16]. For BSF larvae, increasing the drying air temperature from 50 to 100°C during convective drying (HACD) led to a two-fold reduction in moisture content. A similar trend is observed during microwave-convection drying (MW-CD), microwave-convection drying assisted by a heat pump (MW-HP), and microwave-vacuum drying (MVD), where increasing microwave power from 500 to 1000 W resulted in moisture reduction of 30%, 10%, and 20%, respectively. Such tendencies are also shown in studies on fruit and vegetable raw materials [14, 17]. The lowest average moisture content was achieved after microwave-vacuum drying (MVD) - 3.41% and MW-HP 3.35%, while the highest was obtained after HACD - 5.17%.

The range of water activity for dried *Hermetia ill*. (BSF) larvae spans from 0.3166 (MVD 1000 W) to 0.5760 (HACD 50°C). Similar tendencies regarding the influence of the drying method, temperature, and power were observed for water activity as in the case of moisture content analysis of larvae. This is confirmed by a high correlation coefficient of 0.93 for BSF. In relation to YMW larvae, water activity ranged from 0.3304 (MVD 1000 W) to 0.5470 (MW1000 W- HP), and the correlation coefficient between moisture content and water activity was 0.96. This indicates a very strong positive relationship between these two variables. In the context of moisture content and water activity, such a high correlation coefficient suggests that changes in one variable (e.g. moisture content) are strongly correlated with simultaneous changes in the other variable (e.g. water activity), as observed in many studies related to drying obtained from plant materials [18].

Table 3. Physico-chemical properties of black soldier fly larvae

Type of Larvae	Methods and Drying Parameters	Moisture Content (%)	Water Activity (-)	Colour			Crude Protein (%)
				*L**	*a**	*b**	
Black Soldier Fly (BSF)	HACD 50°C	6.94	0.5760	34.30	1.95	4.29	34.05
	HACD 100°C	3.40	0.4099	38.77	2.19	7.93	35.29
	MW 500W	4.83	0.5165	36.25	1.80	6.69	34.90
	MW 1000W	3.29	0.3756	45.85	2.25	13.59	35.31
	MW-HP 500W	3.52	0.3542	36.56	1.45	6.01	34.52
	MW-HP 1000W	3.18	0.3440	40.43	1.86	9.58	35.28
	MVD 500W	3.75	0.3577	42.51	2.21	10.35	35.72
	MVD 1000W	3.08	0.3166	46.72	2.39	12.33	35.60

Table 4. Physico-chemical properties of yellow mealworm larvae

Type of Larvae	Methods and Drying Parameters	Moisture Content (%)	Water Activity (-)	Colour			Crude Protein (%)
				*L**	*a**	*b**	
Yellow Mealworm (YMW)	MW 500W	5.22	0.5055	38.65	3.69	10.20	53.79
	MW 1000W	3.98	0.4472	40.04	4.06	11.60	57.35
	MW-HP 1000W	6.01	0.5470	37.94	3.77	10.52	53.73
	MVD 500W	6.30	0.5579	40.34	4.11	11.75	55.48
	MVD 1000W	3.19	0.3304	42.57	5.32	13.04	56.95

Microwave-vacuum drying (MVD) and microwave-convection drying (MW-CD) resulted in obtaining the brightest larvae due to their relatively short drying times, which limited the impact of drying factors. Additionally, the use of reduced pressure during microwave drying allowed obtaining an attractive product not only due to its colour but also a commercially viable structure. Results from other studies regarding colour measurement of BSF larvae obtained through infrared drying were similar to the results of this study only in relation to convective drying (HACD) [19]. The colour measurement of dried BSF larvae shows that the least favourable results were obtained after HACD at 50°C and after MW-HP at 50°C, which might be related to the relatively long drying time and exposure to oxidative conditions that caused darkening of the material. Prolonged drying time can lead to oxidation or other chemical reactions in the sample, which can impact colour changes. For instance, extended drying times of food can lead to pigment oxidation, altering its colour, which is not always a desirable outcome.

The protein content in BSF and YMW larvae after different drying processes is presented in Table 4. For BSF larvae, the average protein content was 35.09%, and for YMW larvae, it was 55.46%. For both species of larvae, an increase in temperature or microwave power led to an increase in protein content due to shorter drying times, resulting in shorter exposure to drying conditions. The highest protein contents for both BSF and YMW were obtained through the MVD and MW drying processes.

Conclusion

The present study confirms the existence of alterations in the dielectric properties of materials as their temperature and humidity levels vary. Additionally, a strong correlation with moisture content in the sample is observed towards the end of the drying stage. The application of microwaves in drying processes reduces drying times. Importantly, it does not degrade the sample; in fact, it has a positive impact on its quality, as evidenced by the product's colour and protein content.

The optimisation of microwave transmission involves introducing microwaves into the drying chamber using multiple generators with radiators placed on the chamber walls in a way that minimises microwave transmission between the generators (minimises coupling between generators). This is why radiators with a single polarisation of the electric field (vertical or horizontal) are used, and individual radiators are positioned so that adjacent radiators emit waves that are mutually perpendicular.

The results of the research are intended to serve as a basis for designing industrial-scale installations. The proposed energy matching system can be applied in an industrial pulse-fluidized bed dryer by distributing generators with radiators along the chamber and using appropriately matched elements in successive dryer zones.

It is worth making adjustments using tuning devices and determining similar trends, for example, when reflection is compensated at a specific intermediate moisture content (e.g., 50%). The curve's nature will likely be similar (a sharp increase in the reflection coefficient at low moisture content), but the overall energy input for drying would be lower.

In the current global context, minimising energy consumption is essential. Hence, it is crucial to the search for processes that combine various technologies to reduce energy consumption is crucial. Microwave-assisted drying can lead to energy savings in these processes due to shorter processing times, particularly in comparison to conventional drying methods or even freeze-drying, which can be time-consuming.

An example of microwave utilisation in industrial-scale larval drying is the developed pulsed fluidised bed dryer with a capacity of approximately 1000 kg/h, as shown in the image below (Fig. 9). This dryer is currently in the optimisation phase, incorporating findings from the described laboratory research.

Fig. 9. Industrial scale pulsed fluidised bed dryer.

References

[1] F. Hao, Y. Yun and J. Tang. Microwave Drying of Food and Agricultural Materials: Basics and Heat and Mass Transfer Modeling. Food Engineering Reviews, 2012, vol. 4, pp. 89–106. DOI: 4. 10.1007/s12393-012-9048-x .
[2] N. N. An, D. Li, LJ Wang and Y. Wang. Factors affecting energy efficiency of microwave drying of foods: an updated understanding. Critical Reviews in Food Science and Nutrition, 2022, vol. 22, pp: 1-16. DOI: 10.1080/10408398.2022.2124947.
[3] M. Zielińska. Microwave-assisted drying of blueberry (Vaccinium corymbosum L.) fruits: Drying kinetics, polyphenols, anthocyanins, antioxidant capacity, colour and texture. Food Chemistry, 2016, vol. 212, pp: 671-680. DOI: 10.1016/j.foodchem.2016.06.003.
[4] S. Lenaerts, M. Van Der Borght, A. Callens, L. Van Campenhout. Suitability of microwave drying for mealworms (Tenebrio molitor) as alternative to freeze drying: Impact on nutritional quality and colour. Food Chemistry, 2018, vol. 254, pp:129-136. DOI: 10.1016/j.foodchem.2018.02.006.
[5] L. De Martino, L. Caputo, G. Amato, M. Iannone, A. A..Barba, V. De Feo. Postharvest microwave drying of basil. Foods, 2022, vol. 11(7), pp:1029. DOI: 10.3390/foods11071029.
[6] M. T. Sebastian, M. A. S. Silva, A.S.B. Sombra. Measurement of microwave dielectric properties and factors affecting them. Dielectric Materials for Wireless Communication, 2017, pp: 11–47. ISBN-13: 978-0-08-045330-9. DOI:10.1016/b978-0-08-045330-9.00002-9.
[7] H. Wang, K.U. Rehman, X. Liu, Q. Yang, L. Zheng, W. Li, M. Cai, Q. Li, J. Zhang, Z. Yu. Insect biorefinery: a green approach for conversion of crop residues into biodiesel and protein. Biotechnol Biofuels, 2017, 10:304. DOI: 10.1186/s13068-017-0986-7.
[8] L. Zheng, Y. Hou, W. Li, S. Yang, Q. Li, Z. Yu. Biodiesel production from rice straw and restaurant waste employing black soldier fly assisted by microbes. Energy, 2012, 47(1):225–229.
[9] N. Krönckea, V. Böschenb, J. Woyzichovskia, S.Demtrödera, R. Benninga. Comparison of suitable drying processes for mealworms (Tenebrio molitor). Innovative Food Science and Emerging Technologies, 2018, 50: 20–25. DOI: 10.1016/j.ifset.2018.10.009.
[10] A. Osimani, C. Garofalo, V. Milanović, M. Taccari, F. Cardinali , L. Aquilanti, M. Pasquini, M. Mozzon, N. Raffaelli, S. Ruschioni, P. Riolo, N. Isidoro, F. Clementi. Insight into the proximate composition and microbial diversity of edible insects marketed inthe European Union. Eur Food Res Technol, 2017, 243:1157–1171.
[11] Ch. Monisha and M. Loganathan. Impact of drying methods on the physicochemical properties and nutritional composition of defatted black soldier fly (Hermetia illucens) pre-pupae flour. Journal of Food Processing and Preservation, 2021, vol. 46(1). DOI: 10.1111/jfpp.16184.
[12] P. da Silva, N. Ribeiro, M.N. Pinheiro, and R. Costa. Modelling Drying Kinetics of Black Soldier Fly (Hermetia Illucens, L.) Larvae. E3S Web of Conferences, 2019, vol. 128. DOI: 10.1051/e3sconf/201912809011.
[13] F. Zhang, D. Zhai, X. Shang, J. Chen, M. Liu, J. Peng. Electromagnetic wave absorbing performance of aspirin powder during 2450 MHz microwave drying. Drying Technology, 2021, 39(5), pp : 596-607. DOI: 10.1080/07373937.2019.1699567.
[14] M. Cano-Lamadrid, K. Lech, A. Michalska, M. Wasilewska, A. Figiel, A. Wojdyło, A. A.Carbonell-Barrachina. Influence of osmotic dehydration pre-treatment and combined drying method on physico-chemical and sensory properties of pomegranate arils, cultivar Mollar de Elche. Food Chemistry 232, 2017, 306–315. DOI: 10.1016/j.foodchem.2017.04.033\.
[15] M.S. Venkatesh, G.S.V. Raghavan. An Overview of Microwave Processing and Dielectric Properties of Agri-food Materials. Biosystems Engineering, 2004, vol. 88(1), pp: 1-18. DOI: 10.1016/j.biosystemseng.2004.01.007.
[16] I. Shorstkii, M. Comiotto Alles, O. Parniakov, S. Smetana, K. Aganovic, M. Sosnin, S. Toepfl, V. Heinz. Optimization of pulsed electric field assisted drying process of black soldier fly (Hermetia illucens) larvae. Drying Technology, 2022, 40(3), pp. 595-603, DOI: 10.1080/07373937.2020.1819825.
[17] A. Michalska, A. Wojdyło, G.P. Łysiak, K. Lech, A. Figiel. Functional relationships between phytochemicals and drying conditions during the processing of blackcurrant pomace into powders. Advanced Powder Technology, 2017, 28: 1340–1348. DOI: 10.1016/j.apt.2017.03.002.
[18] A. Michalska, A. Wojdyło, K. Lech, G.P. Łysiak, Figiel, A. Physicochemical properties of whole fruit plum powders obtained using different drying technologies. Food Chemistry, 2016, 207: 223–232. DOI: 10.1016/j.foodchem.2016.03.075.
[19] R. Bogusz, S. Smetana, A. Wiktor, O. Parniakov, K. Pobiega, K. Rybak, M. Nowacka. The selected quality aspects of infrared-dried black soldier fly (Hermetia illucens) and yellow mealworm (Tenebrio molitor) larvae pre-treated by pulsed electric field. Innovative Food Science and Emerging Technologies, 2022, vol. 80. DOI: 10.1016/j.ifset.2022.103085.

TransZeroWaste Project: Hot Microwave Pelletising Technology in the Upgrading of Low-Quality Iron Ores and Mill Scale with Low Carbon Technologies

M. Hubrich[1], K. Marx[1], A. M. Lopez-Buendia[2], E. Brau[2], S. Bethlehem-Seidel[3], L. Schmidt[4], B. García-Baños[5], J. M. Catalá-Civera[5]

[1]*BFI, VDEh-Betriebsforschungsinstitut GmbH, Sohnstraße 69, 40237 Düsseldorf, Germany*
[2]*CEINNMAT, INNCEINNMAT SL. Av. Catedratico Escardino, 9. 46980 Paterna- Valencia, Spain*
[3]*DILLINGER, AG der Dillinger Hüttenwerke, Postfach 1580, 66763 Dillingen/Saar, Germany*
[4]*K1-MET GmbH ,Franz-Josef-Straße 18 8700 Leoben, Austria*
[5]*Universitat Politècnica de València, Camino de Vera s/n, 46022 Valencia, Spain*
angel.lopez@ceinnmat.com

Keywords: microwave, iron ores, dielectric properties, microwave kiln

Growing demand for high quality iron ores and scrap as well as abandonment of carbon intensive sintering in the future require novel technological approaches for upgrading of low-grade iron ores and recycling of mill scale. TransZeroWaste will apply hydrometallurgy for mill scale de-oiling and use this and other iron-rich scrap equivalent to upgrade low-grade iron ores. For that, TransZeroWaste will develop low carbon technologies such as cold pelletising and briquetting, hot microwave pelletising, and magnet-supported hydrometallurgy. TransZeroWaste will serve as a vehicle for the transition of the European steel industry to the carbon free zero waste future.

Hot pelletisation with microwaves will be used for upgrading low-quality iron ores to increase the iron grade as new breakthrough technology for a low CO_2 material treatment. The method to upgrade iron ore of minor quality, as well for separation of interfering components as oil or zinc, is based on the new concept of treating granular feedstock for material transformation using microwave energy in cellular kilns. The system is conceived as modular units - material feeding + product microwave (MW) processing. Thus, the system is compatible and easy to integrate, which reduces the investment needed. The concept is indeed a paradigm change: it enables new small low-cost solutions to be integrated in large existing industrial processes for fast-track industrial implementation. The new system will be a clear opportunity to improve the current industrial heating processes by raising the energy efficiency, in particular for low production (downscaled) operations, since most of them are currently inefficient, expensive, and unfeasible for cost-effective production.

Microwave heating offers an efficient alternative to high-energy consumption conventional heating techniques, still common to a wide range of industrial manufacturing processes [1]. Hot pelletisation with microwaves of residuals was studied in the previous project DESTINY [2]. The scalability allows the use of all the power from the best available technology from microwave generators for easier implementation. Studies about materials and microwaves interaction at high temperatures have shown the advantages of modulating internal wavelength. This approach will allow raw materials to be efficiently heated. A new concept of electromagnetic field distribution is the base of a new concept of microwave applicator enabling the processing at higher volume adapting the feedstock speed with power and microwave tuning on real time and therefore better scalability for industrial application.

Total impact of TransZeroWaste will include upgrading of 27 million t/a materials with low carbon technologies and avoiding of corresponding sinter plant carbon footprint of 4,3 – 9,9 $MtCO_2$/a. TransZeroWaste will serve as a vehicle for the transition of the European steel industry to the carbon free zero waste future.

References

[1] J.P. Lampke, S. Silge: Agglomeration by pelletizing discs – an important process in times of rising worldwide demand for iron ore. AUFBEREITUNGS TECHNIK 49 (2008), Nr. 8
[2] DESTINY (H2020-NMBP-SPIRE-2018) GA n° 820783. Development of an Efficient Microwave System for Material Transformation in energy INtensive processes for an improved Yield.

On Evaluation of Microwave Oven Door Chokes

V. Bilik[1]

[1]*S-TEAM Lab, Strojnicka 29, Bratislava, Slovak Republic*
vladimir.bilik@s-team.sk

Keywords: microwave oven, door choke, microwave door seal

Introduction

A microwave oven door choke (also known as a door seal), is a noncontacting structure, integrated with the oven door, that prevents microwave radiation from escaping from the oven chamber through the gap between the door and the oven body. A complete development cycle of a door choke consists of essentially four steps: (a) design of the basic choke shape, (b) optimization of the choke dimensions using electromagnetic simulation, (c) prototyping and experimental evaluation of the choke performance, and, in the case of commercial ovens, (d) a certification process. As the certification process is expensive, one should be reasonably confident that the subjected structure will comply.

Because both simulation and measurement can produce vast amounts of data, difficulties may arise when trying to evaluate and compare performance of various choke modifications. A mere visual analysis is usually unable to discern differences and trends among designs with varying parameters. To deal with this situation, in this paper, we propose some data processing automation, along with a few simple criteria for choke quality. Before introducing them, we will discuss how the primary (source) data are obtained by both simulation and measurement.

The paper is organized as follows. Section **Error! Reference source not found.** explains the functional principle of m icrowave oven door chokes and introduces their basic variants. Section **Error! Reference source not found.** explains the effect of higher-order modes, which fundamentally affects choke performance. Section **Error! Reference source not found.** o utlines the modal analysis method of the electromagnetic simulation and argues why we chose it for choke design and optimization. Section **Error! Reference source not found.** presents a typical setup for choke isolation measurements and t ype of data obtained as a result of these measurements. The core Section **Error! Reference source not found.** introduces the quantities that we propose for the evaluation of door choke performance. Based on one of these proposed quantities, the leakage factor, Section **Error! Reference source not found.** attempts to predict the surface power density of the leaked r adiation in real device operation. Section **Error! Reference source not found.** illustrates an example of applying the outlined procedures on a real microwave oven. Finally, section **Error! Reference source not found.** summarizes the merits o f the proposed methodology.

Microwave Oven Door Choke

As a first approximation, a microwave oven door choke can be imagined as a band-stop (notch) filter that is cascaded between an input two-conductor transmission line TL1, fed from the waveguide WG1, representing the oven interior, and an output line TL2, open to the waveguide WG2, representing the oven surroundings (**Error! Reference source not found.a**). The f ilter has the form of a recess in the inner conductor block. The recess acts as a short-circuited transmission line (TL3) connected in series with the main line TL1 – TL2 (**Error! Reference source not found.b**). The length L_c of TL3 is one q uarter of the free-space wavelength at the design frequency f_d (for f_d = 2.45 GHz, L_c = 30.6 mm). The input impedance at f_d of such a short-circuited transmission line is infinite, which means that the signal flow between the oven interior and its surroundings is interrupted. In terms of scattering parameters, the transmission coefficient S_{21} is zero at f_d; the choke effectiveness gradually decreases as the operating frequency f departs from f_d.

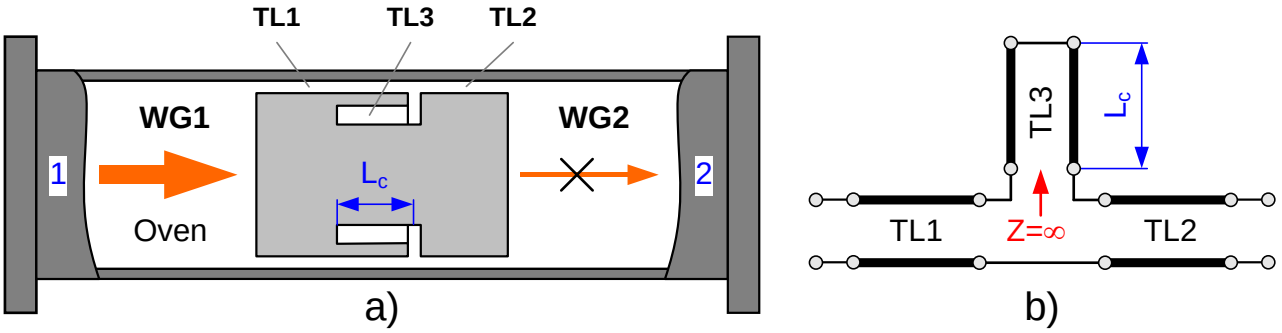

Fig. 1. a) Microwave oven door choke as a band-stop filter; b) choke equivalent circuit.

In electromagnetic modelling, the input waveguide WG1 has the same cross section as the oven chamber. The output waveguide WG2 can be larger. The choke created in this way will be referred to as a *plunger choke* (**Error! Reference s**

ource not found.a). The choke structure can also be relocated to the oven outer periphery: we shall refer to this modification as a *peripheral choke* (**Error! Reference source not found.b**), the type as a rule used in domestic ovens. To improve the c hoke efficiency, the two types can even be combined.

Higher-Order Modes and Slotted Choke

The simple explanation provided in Section **Error! Reference source not found.** was based on the implicit assumption that o nly a basic TEM wave exists in the choke structure, both in the door gap represented in **Error! Reference source not found.** by TL1 and TL2 as well as in the recess represented by TL3. This is not the case, which in fact fundamentally changes real choke behavior. The reason why higher-order modes can propagate is that the *door gap circumference* is an order of magnitude longer than the working wavelength $\lambda_d = c_0/f_d$, where c_0 is the speed of light. The same is true for the choke recess circumference. In such *oversized* transmission lines, a number of higher-order modes can propagate in addition to the basic TEM wave [1]. As an example, consider a commercial oven with chamber width a_1 = 445 mm, chamber height b_1 = 475 mm and door gap s = 5 mm (throughout in this paper, an oven with these dimensions will be used as an example). The mean gap circumference is $u = 2\,(a_1 + b_1) - 4\,s = 1820$ mm $\approx 15 \times \lambda_d$. In such a structure, 28 higher-order modes can propagate at 2.45 GHz, with guide wavelengths reaching from 123 mm to 356 mm. The choke, designed for the TEM wave, is generally inefficient for these modes. Higher-order modes can be quite efficiently excited at discrete frequencies, propagate unattenuated along the door block and radiate to the oven environment to cause leakage radiation resonant peaks, stubborn in the sense that no variation in the door structure dimensions is able to suppress them.

Analysis of the higher-order modes propagating in the band of interest identifies them as *TE modes*. Unlike the fundamental TEM wave, the surface currents of TE modes also have a transversal component, giving rise to currents circulating around the choke block. Osepchuk et al. [2] were first to realize that such transversal currents can be efficiently blocked by means of longitudinal slots mutually spaced by less than about $\lambda_d/4$ (neither the distance nor the slot width being critical), thus inventing a slotted or "serrated" microwave door choke [3]. By virtue of the slots, the original TE modes are distorted to become more TEM-like, including their wavelengths. Consequently, a choke designed for a TEM wave will also be operational for these waves. A more detailed analysis of modes that can exist in similar structures has been provided in [4]. The technique is better illustrated by a smaller structure [5] employing the same principle in a non-contacting waveguide sliding short (**Error! Reference source not found.**, where the interrupted surface currents J_s are illustrated by the orange d ashed arrows). The slotted choke can be alternatively viewed as a periodic structure in the circumferential direction with stopbands in the working frequency range, an approach used by its inventors [2].

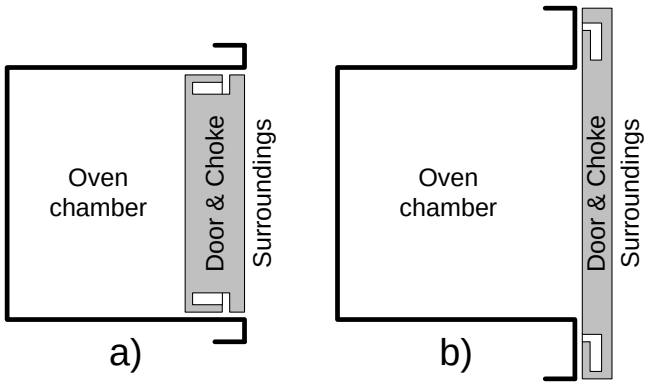

Fig. 2. Basic door choke types: a) plunger choke, b) peripheral choke.

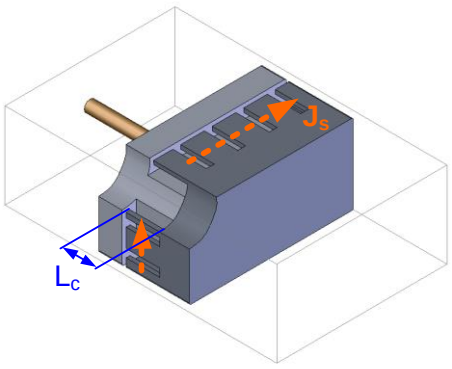

Fig. 3. Slotted choke in a non-contacting sliding short. Blocked surface currents illustrated by dashed arrows.

There are quite a number of patents and other publications, which are essentially modifications of the original Osepchuk's concept and can be found under keywords such as "microwave door choke" or "microwave door seal." However, there is no clear guidance regarding a practical choke design, which is more challenging due to the existence of various shapes and convolutions of the slotted "fingers," or presence of dielectric layers covering the structure, etc. Therefore, a choke design and optimization must rely on electromagnetic simulation and measurement.

Electromagnetic Simulation

The electromagnetic simulation method we adopted for the choke design is based on **Error! Reference source not found.**, w here an oven is modelled by a section of a rectangular waveguide WG1, excited at one end (Port 1) and terminated at the other end by the door structure under investigation. The exterior side of the door faces another, possibly larger, *output* waveguide WG2, representing the oven surroundings (Port 2). We borrowed this approach from [5].

Because of their oversized dimensions in relation to working wavelengths, both waveguides can support a considerable number of propagating modes. Any waves that can travel in such waveguides can be decomposed into a superposition of these modes. Each mode excited in WG1 can be, by virtue of the door structure, partially converted into any of the output

modes in WG2. The conversion factor for each such input-output combination is the transmission scattering coefficient $S_{21} = S_{2(y)1(x)}(f)$ where x identifies the input mode at Port 1 (excitation), and y identifies the output mode at Port 2 (response)[1]. These transmission coefficients are exactly the quantities that an electromagnetic simulator computes. The design idea is an attempt to sufficiently suppress the magnitudes of S_{21} for all possible input-output mode combinations in the band of interest. Then the choke will be effective for *any* field distribution in the input waveguide, representing the oven chamber. In this way, the choke can be designed irrespective of actual loading of the oven or arrangement for its excitation.

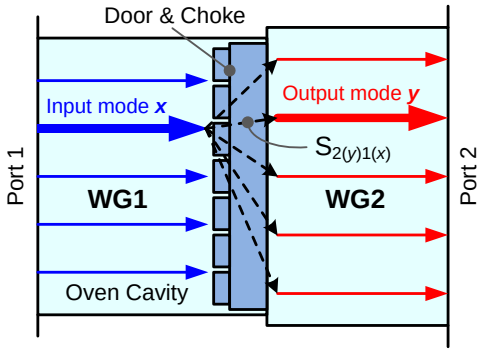

Fig. 4. Principle of the used electromagnetic simulation of a microwave door choke.

However, in practice, the number of the propagating modes can be prohibitively high. For instance, the waveguide with dimensions $a_1 = 445$ mm, $b_1 = 475$ mm of our example model from Section **Error! Reference source not found.** supports $N_x = 90$ propagating modes at 2.45 GHz. The output waveguide used in our model ($a_2 = 575$ mm, $b_2 = 605$ mm) supports $N_y = 132$ propagating modes. Therefore, in order to be completely rigorous, for every choke modification we should perform $N_x = 90$ simulation runs (each can take about 10 hours), resulting in total $N_s = N_x \times N_y = 11880$ simulation frequency responses $S_{21}(f)$ to be further evaluated, an unrealistic undertaking.

For these reasons, we considered only a limited number of the modes (typically $N_x = N_y = 12$, leading to $N_s = N_x \times N_y = 144$ responses) in the belief that the lowest-order modes have the most significant impact, and that those 144 responses constitute a statistically relevant ensemble. Even so, the simulation is quite time-consuming, which is a disadvantage of this method. The choke performance criteria will be derived from collections of responses such as this. To simplify the notation, a simulation provides an ensemble of $N_s = N_x \times N_y$ frequency responses $S_{21n}(f)$, $n = 1 \ldots N_s$, where N_x and N_y are the numbers of the considered input and output modes, respectively.

Isolation Measurement

A typical isolation measurement setup is shown in **Error! Reference source not found.a**, where a vector network analyzer (VNA) feeds the transmitting antenna (TX ant) located inside an oven under test. The receiving antenna (RX ant) is stepped at a number N_m of predetermined locations X_n, $n = 1 \ldots N_m$, along the door gap. For each position, the "max hold" transmission frequency response $S_{21}(f)$ is measured. An alternative to a VNA is to use a sweep generator and a spectrum analyzer in tracking mode, synchronized with the generator. Care should be taken to prevent any other leakage than the leakage through the door structure. In particular, the TX cable shield should be connected galvanically to the cavity wall as perfectly as possible: around the complete cable circumference, without any gaps. A good alternative is to feed the chamber using a magnetron antenna probe in place of the magnetron. For observing broadband behavior of the choke, the measurement frequency range should be sufficiently wide, e.g., 2.2 – 2.7 GHz. Frequency step should be sufficiently small, e.g., 500 kHz, to not miss narrow peaks in the response. Distance between neighboring measurement locations should be less than a half of the working wavelength.

Our measurement procedure is as follows:

- The calibrated measurement instrument is set to *Max Hold* mode.
- The sensing antenna is moved to a desired measurement location X_n.
- Continuous sweeping is started.
- To capture the maximum possible signal level, the sensing antenna is, while the sweeping is running, oriented in three mutually orthogonal directions or oriented randomly, allowing at least one complete sweep for each orientation. The process is continued until the displayed trace does not change anymore.
- The sweeping is stopped and the trace recorded. In this way, a measured trace $S_{21n}(f)$, associated with the antenna location X_n, is obtained.

The result of the whole procedure is, similarly to the simulation, an ensemble of frequency responses $S_{21n}(f)$, $n = 1 \ldots N_m$, although they are physically very different from the simulation responses discussed in Section **Error! Reference source n ot found.**. Typically, n is less than 100.

[1] This notation has been borrowed from the CST Studio Suite [8].

Choke Performance Criteria

Both electromagnetic simulation and measurement produce an ensemble of frequency responses

$$S_{21n}(f), \quad n = 1...N \tag{1}$$

The responses are, in fact, specified at discrete frequencies f_k, $k = 1\ldots N_f$, covering a frequency range of interest, where $f_{k+1} > f_k$. Although the physical meaning of both sets of responses is different, they can be subjected to the same procedures to arrive at the respective choke performance characteristics.

We propose the following design criteria: (a) MaxHold frequency response, (b) smoothed MaxHold response, (c) leakage factor, and, only for the measurement, (d) spatial leakage distribution.

MaxHold Frequency Response

The first step in constructing the performance characteristics is computing the overall "MaxHold" frequency response $E(f)$. It is defined as the upper envelope of all N agglomerated S_{21} responses, and represents the "worst case" scenario. For any frequency f, the MaxHold is defined as the maximum value of all the frequency response magnitudes $|S_{21n}(f)|$ at that frequency:

$$E(f) = \max\left\{ \left| S_{21n}(f) \right| \right\}_{n=1}^{N} \tag{2}$$

The MaxHold operation can be equivalently performed either in linear or logarithmic (dB) scale. If the individual frequency responses contain sharp resonant peaks, these peaks occur also in the MaxHold response.

Smoothed MaxHold

Smoothed MaxHold frequency response $H(f)$ characterizes a choke *wideband* performance, which is important for centering its band of operation while reducing the disturbing effect of resonant peaks very likely occurring in the MaxHold trace. The smoothed MaxHold is obtained by smoothing the *linear* MaxHold frequency response **Error! Reference source not found.**) as

$$H(f) = \mathrm{smoo}\left[E(f), \Delta f \right] \tag{3}$$

where smoo[$E(f)$, Δf] symbolizes a floating average of $E(f)$ over a specified subinterval Δf centered at f. For Δf we typically used 5% of the whole frequency range, i.e., Δf = 25 to 50 MHz for the 2.45-GHz band. The resulting curve can then be converted to dB as

$$H_{dB}(f) = 20\log\left[H(f) \right] \tag{4}$$

Note: Smoothing a logarithmic MaxHold envelope would lead to over-optimistic results, although the difference is usually insignificant (less than 1 dB).

Leakage Factor

The leakage factor is a quantity that characterizes a choke performance by a *single number*. We define it as the mean value of the *unsmoothed linear* MaxHold response in a specified (narrow) frequency interval $f_a \le f \le f_b$

$$L = \mathrm{avg}\left[E(f) \right]_{f=f_a}^{f_b} = \frac{1}{b-a+1} \sum_{k=a}^{b} E(f_k) \tag{5}$$

where avg[x] represents averaging over this interval. The rightmost expression is the implementation for a case of discrete frequencies, where $a < b$ are the indexes of f_a, and f_b, respectively. The averaging interval should best coincide with the working band of the studied oven (e.g., 2425 – 2475 MHz), or of the intended magnetron (e.g., 2460 ± 10 MHz). The resulting figure can then be converted to dB.

The leakage factor is a good criterion for comparing a multitude of chokes "at a glance." In the case of measurement, it can also be used for estimating the actual oven leaked radiation power density (see Section **Error! Reference source not found.**).

Spatial Leakage Distribution

Spatial leakage distribution is a function that expresses the dependence of the amount of leakage on the position X_n along the oven door gap (X_n, $n = 1\ldots N_m$, are the locations of the sensing antenna during the measurement). It cannot be defined for the kind of simulations described in Section **Error! Reference source not found.**; in the context of this paper, it is only meaningful for measured responses.

For each measured frequency response $S_{21n}(f)$, i.e., for each sensing antenna location X_n, the maximum transmission value $D(n)$ in a specified frequency range $f_a \le f \le f_b$ can be computed as

$$D(n) = \max\left[\left| S_{21n}(f) \right| \right]_{f=f_a}^{f_b} = \max\left[\left| S_{21n}(f_k) \right| \right]_{k=a}^{b} \tag{6}$$

As in the case of the leakage factor, the specified frequency range should best coincide with the working band of the oven or the used magnetron. Using linear or logarithmic scale is equivalent. Since the points X_n are normally arranged successively along a curve copying the door circumference, the figures $D(n)$ can be viewed as a tabulated function of position X_n and presented as a curve. This dependence is what we will refer to as the *spatial distribution of leakage transmission coefficient*. It is useful, for instance, for discovering the leakiest spots along the door (typically corners), or for detecting any door irregularities (local deformations). A curve like this can also be obtained in full-power (hot) leakage radiation power density measurement.

Relation to Compliance Testing

Compliance testing of microwave oven leakage essentially consists of searching for peak radiated power density at a 5-cm distance from an oven under test when the oven is powered by its own magnetron and specifically loaded. The limit value is 5 mW/cm^2 [7]. A possible measurement setup is shown in **Error! Reference source not found.b**.

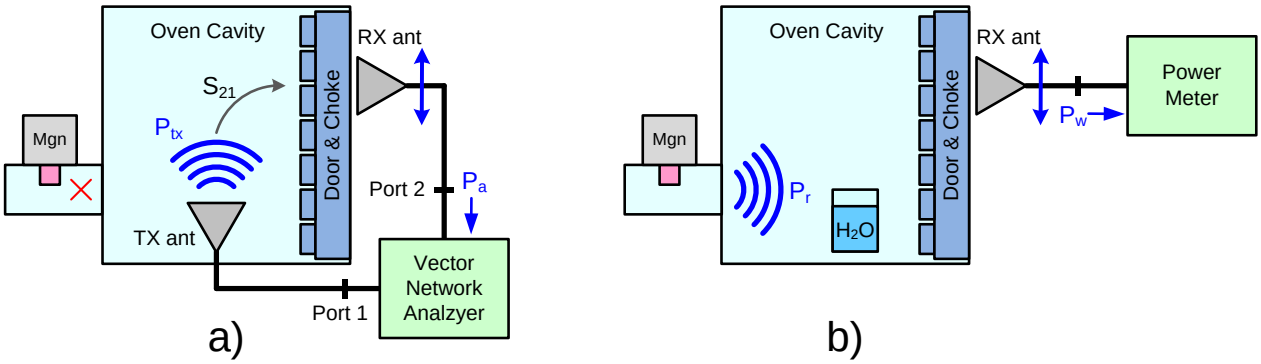

Fig. 5. a) Isolation measurement of a door choke. b) Measurement of oven leaked radiation power density.

The performance criteria proposed in Section **Error! Reference source not found.**, particularly the leakage factor L c omputed from the measured data, can be used for a rough estimation of the leakage power density to be expected in compliance tests. This is based on the argument that follows.

Ignoring subtleties (because accuracy within an order a few dB is not substantial in this process), we can maintain that, using the same sensing antenna, the relation P_w/P_r between the power P_r delivered into the cavity by the magnetron and the power P_w measured in **Error! Reference source not found.b** by the power meter is the same as the relation P_a/P_{tx} between the p ower P_{tx} injected into the cavity by the generator and the power P_a entering the VNA in the isolation measurement (**Error! Reference source not found.a**):

$$\frac{P_w}{P_r} = \frac{P_a}{P_{tx}} \qquad (7)$$

Power P_{tx} radiated into the cavity by a matched generator is

$$P_{tx} = P_g\left(1-|\Gamma_{tx}|^2\right) \qquad (8)$$

where P_g is the generator power deliverable to a matched load and Γ_{tx} is the transmitting antenna reflection coefficient. Power P_a entering the VNA is

$$P_a = P_g\,|S_{21}|^2 = P_g L^2 \qquad (9)$$

where $|S_{21}|$ is the generator-to-analyzer transmission coefficient modulus, for our purpose substituted by the leakage factor **Error! Reference source not found.**). Eliminating P_g, we have

(10)

The available power[2] P_{av} generated by the same sensing antenna, now employed in the "hot" setup according to **Error! R eference source not found.b**, is

$$P_{av} = SA_e \qquad (11)$$

where S is the wanted power density of the leaked radiation at the antenna location and A_e is the effective area of the sensing antenna [6].

The power P_w measured by the power meter is

[2] The available power of a source (in this case of the sensing antenna) with the reflection coefficient Γ_a is the real power absorbed in a *conjugated* load $\Gamma_L = \Gamma_a^*$.

$$P_w = P_{av}\left(1-|\Gamma_a|^2\right) = SA_e\left(1-|\Gamma_a|^2\right) \quad (12)$$

where Γ_a is the sensing antenna reflection coefficient (the power meter input is assumed matched). Inserting **Error! R eference source not found.**) and **Error! Reference source not found.**) into **Error! Reference source not found.**) and solving for S, we finally obtain

$$S = \frac{P_r L^2}{A_e\left(1-|\Gamma_a|^2\right)\left(1-|\Gamma_{tx}|^2\right)} \quad (13)$$

where:

- P_r is the power radiated into the cavity by the magnetron. The nominal magnetron power will serve well for this purpose.
- L is the oven leakage factor **Error! Reference source not found.**) obtained from the *measured* transmission c oefficients.
- A_e is the effective area of the sensing antenna. It is related with the antenna gain G by $A_e = \lambda^2 G/(4\pi)$. Usually, G is provided by the antenna supplier. If the antenna structure is known, the gain can also be obtained via electromagnetic simulation.
- Γ_a is the reflection coefficient of the sensing antenna.
- Γ_{tx} is the reflection coefficient of the transmitting antenna used in the isolation measurement.

Illustrative Example

As an example, we present selected results of simulation and measurement of an experimental commercial 2.45-GHz oven with chamber width a_1 = 445 mm and chamber height b_1 = 475 mm. The oven door can embed a modular choke having a plunger part and a peripheral part (**Error! Reference source not found.a**). Only the peripheral part was used for the results r eported here.

Simulation

We used CST Studio Suite [8] as the electromagnetic simulation tool. The model (**Error! Reference source not found.b**) i s parametrized by 48 variables, controlling all dimensions, material properties, and presence of features, such as of the plunger and peripheral choke components, a gasket (the magenta frame), or covering dialectic slabs. The input waveguide WG1 represents the oven chamber, the output waveguide WG2 represents the oven surroundings; its width and height are a_2 = 575 mm, b_2 = 605 mm. A detail of the choke is shown in **Error! Reference source not found.c**.

We found the time domain solver to be appropriate for the simulations. As explained in Section **Error! Reference source n ot found.**, we excited WG1 at Port 1 by N_x = 12 lowest-order modes, and for each of them observed the conversion factors (transmission scattering coefficients) S_{21} to all N_y = 12 lowest-order output modes in WG2. This resulted in an ensemble of $N_s = N_x \times N_y$ = 144 frequency responses $S_{21n}(f)$, $n = 1 \ldots N_s$. For this ensemble, we computed the choke performance characteristics according to Section **Error! Reference source not found.**. The results are summarized in **Error! Reference so urce not found.**. The gray area is an agglomeration of all 144 magnitude responses (in fact, many of them are below -100 dB). For illustration, one of the responses is highlighted green. As evident, the trace contains many resonant peaks. This makes the simulated time-domain response decay very slowly. For this reason, we truncated the time evolution to 140 ns. Due to this, the peaks in $|S_{21}|$ appear wider than they are in reality. The magnitudes remain correct.

The blue curve is the MaxHold frequency response, i.e., the upper envelope of all the individual responses. The red curve is the smoothed MaxHold response. The smoothing width was 25 MHz, i.e., 5% of the full simulation band. The smoothed response proves that the choke is tuned reasonably, if not ideally. The thick black line represents the obtained leakage factor

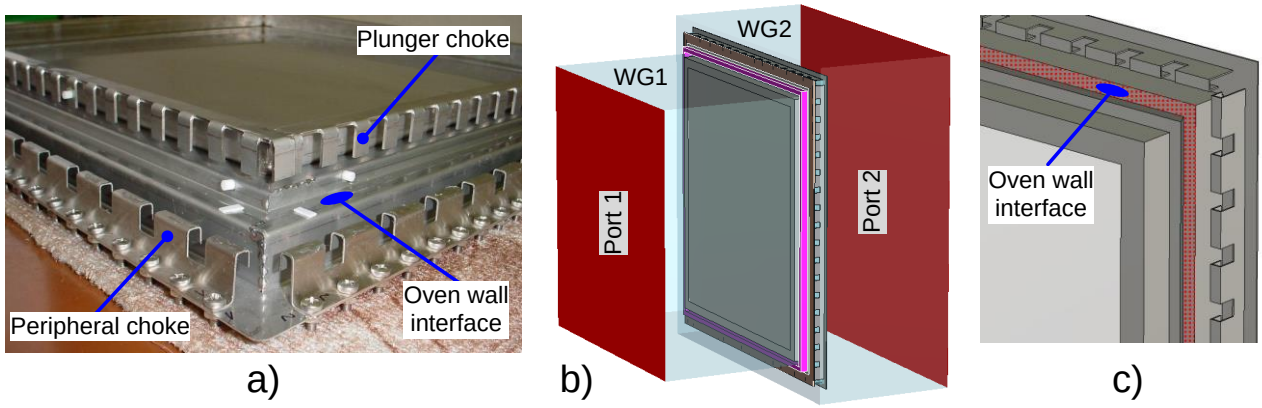

L = -56.3 dB for the band 2425 – 2475 MHz.

Fig. 6. a) Experimental combined choke. b) CST Microwave Studio model of the oven. The magenta frame is a silicone gasket. c) Detail of the door with only a peripheral choke.

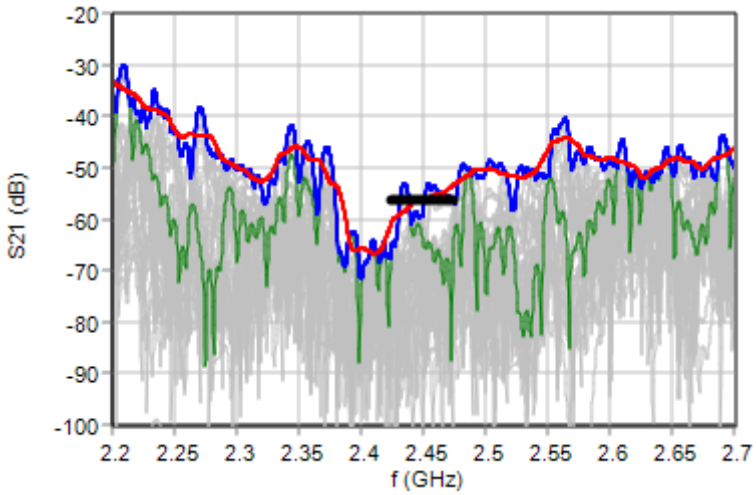

Fig. 7. Simulation results and derived quantities.

Measurement

We carried out the door choke isolation measurement according to Section **Error! Reference source not found.**, using the s etup shown in **Error! Reference source not found.a**. The VNA used was Agilent HP8753D with the *Max Hold* function turned on. The TX antenna was a commercial WLAN 2.45 GHz rod antenna, placed inside the oven and fed through the magnetron launcher structure. The oven was empty (not loaded by any amount of water). The measurement frequency range was 2.2 – 2.7 GHz, step 5 MHz (101 points). The sensing (RX) antenna was a thin rod tuned at 2.45 GHz (diameter 0.8 mm, length 30 mm) extending from the center conductor of an N-connector with a square 25.4-mm flange. (This was, in fact, a poor choice: the cable shield currents depend on where the cable is being held, which distorts the radiation pattern and affects the antenna reflection coefficient. In later experiments, we used a more suitable antenna).

The measurement was taken at 42 points around the door periphery, spaced horizontally about 53 mm and vertically about 50 mm. The location numbering started at the top left corner (looking from outside), increasing circumferentially in the clockwise direction.

The results of the S_{21} measurement and its post-processing are summarized in **Error! Reference source not found.**. The g ray area is an agglomeration of all 42 magnitude responses. One of them is highlighted in green. The jagged nature of the trace reveals that the frequency step should have been smaller (1 MHz or less) to appropriately cover the many resonant peaks present.

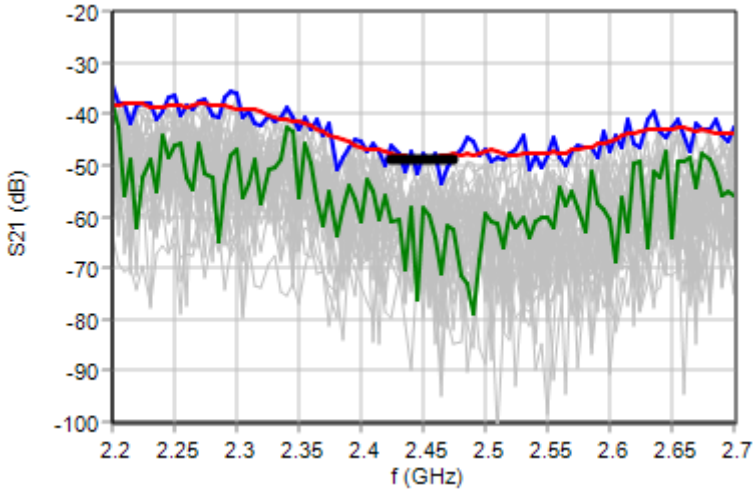

Fig. 8. Measurement results and derived quantities.

The blue curve is the MaxHold frequency response, i.e., the upper envelope of all individual traces. The red curve is the smoothed MaxHold response. The smoothing width was 25 MHz, i.e., 5% of the full measurement band. This response shows that the choke is well tuned but its isolation is not exceedingly good. The thick black line represents the leakage factor for the band 2425 – 2475 MHz, which is L = -48.9 dB. The difference from the simulation (7.4 dB) is rather high. In other experiments, we usually observed differences on the order of 3 dB. However, because of distinctly different nature of the two sets of the data, one should not expect that the respective leakage factors should agree.

Error! Reference source not found. shows the spatial distribution of the leakage transmission coefficient obtained from t he measured data. It proves that there is no spot with exceedingly high radiation. The peak value (location 12) is -46.1 dB, about 3 dB higher than the leakage factor (-48.9 dB).

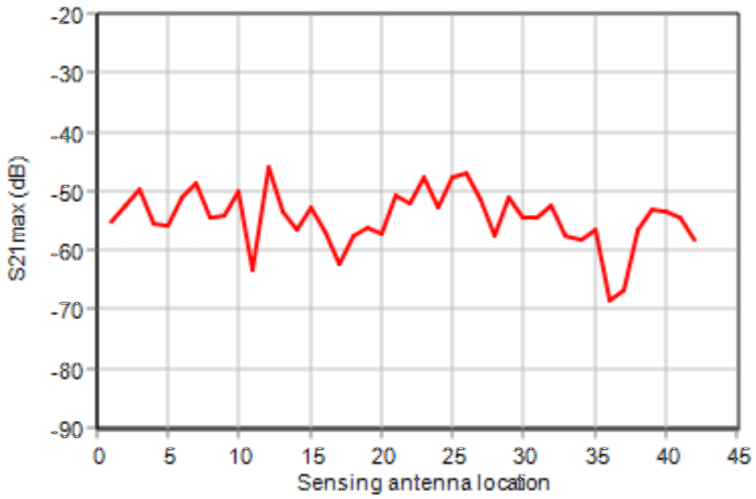

Fig. 9. Spatial distribution of leakage transmission coefficient.

Leakage Power Density

Using **Error! Reference source not found.**) with the leakage factor obtained for the measurement, we can compute the e xpected power density of the leaked radiation in a real oven operation. The leakage factor -48.9 dB must be converted to linear scale, resulting in $L = 0.00359$. The magnetron power was set to $P_r = 2$ kW because the experimental oven was supposed to be fed from two domestic oven magnetrons. The effective area A_e of the sensing antenna was estimated using several methods, such as electromagnetic simulation of its gain, or irradiating the antenna from an open WR340 waveguide at several distances (the E-field strength for this experiment was obtained by simulation). The final estimate, used in **Error! R eference source not found.**), was $A_e \approx 10$ cm^2. The reflection coefficients of both antennas were found to be $|\Gamma_{tx}| \approx |\Gamma_a| \approx 0.3 = -10.5$ dB.

The obtained leakage power density estimate was $S = 3.11$ mW/cm^2. The figure is below the permitted limit of 5 mW/cm^2, but the margin is too small (one should target values on the order of 0.5 mW/cm^2). This implies that this choke probably needs further development and more extensive experiments.

Conclusions

The choke performance criteria that we have proposed in this paper are useful in situations where simulation or measurement produce a large quantity of similar data, and it is difficult to assess the choke performance by their mere inspection.

Particularly large quantities of data are generated by electromagnetic simulation in the case of choke design principle outlined here, based on exciting the model structure by a number of input modes and computing how each of them is converted to a set of output modes. Large amounts of data are generated also by measurements.

The smoothed MaxHold response gives an indication of how well a choke is tuned in respect to the oven operation band. The leakage factor is a single-number characteristic good for quick comparison of various choke types and modifications. In the case of measurement, it can also be used for assessment of actual leakage power densities in a real oven operation or compliance testing.

References

[1] D. M. Pozar, *Microwave Engineering*, 4th Ed., New York: Wiley & Sons, 2012.
[2] J. M. Osepchuck, J. E. Simpson, and R. A. Foerstner, "Advances in choke design for microwave oven door seals," *Journal of Microwave Power*, vol. 8, no. 3, pp. 295-302, Nov. 1973.
[3] J. M. Osepchuck and J. E. Simpson, "Energy seal for high frequency energy apparatus," U. S. Patent 3 767 884, Oct. 23, 1973.
[4] V. Bilik and J. Bezek, "Analysis of modes in rectangular-waveguide noncontacting shorting plunger," in *Proc. GeMiC 2006*, Karlsruhe, Germany, 28-30 March 2006 (CD ROM).
[5] V. Bilik and J. Bezek, "Noncontacting R26-waveguide sliding short for industrial applications," in *Proc. 36th EuMC*, 2006, Manchester, UK, pp. 1032-1035.
[6] J. L. Volakis, Ed., *Antenna Engineering Handbook*, 4th Ed., New York: McGraw-Hill, 2007.
[7] *Household and similar electrical appliances - Safety - Part 2-25: Particular requirements for microwave ovens, including combination microwave ovens*, IEC Std. 60335-2-25:2020.
[8] Dassault Systems: CST Studio Suite, https://www.3ds.com/products-services/simulia/products/cst-studio-suite/.

Sustainable Applications of Microwave Plasma Sources

R. Mueller[1], K.-M. Baumgaertner[1], M. Dingeldein[1], J. Hofmann[1], J. Schneider[1]

[1]Muegge GmbH, Hochstrasse 4-6, D-64385 Reichelsheim (Odenwald), Germany
Robert.Mueller@muegge-gerling.com

Keywords: microwave plasma, atmospheric plasma, downstream plasma, renewable energies, energy saving, recycling, sustainability

Microwave plasma sources can be operated in a wide range of process parameters, providing high radical densities in non-equilibrium plasmas at low-pressure conditions, i.e., the co-occurrence of high-energy electrons and “cold” gas particles at temperatures well below 100 °C, and gas temperatures of several 1000s °C in the core of atmospheric pressure plasma sources (APS), respectively. Accordingly, microwave-excited plasmas are well suited for a large variety of industrial applications, particularly when sustainability is crucial.

Sustainability implies not only the use of renewable energies, but also saving of energy and resources as well as avoidance or even removal of greenhouse gases and pollutants. Microwave plasma from methane and other natural gases for production of hydrogen is a prominent example for resource-saving and sustainable applications. The process uses a microwave-assisted plasma source with up to 100 kW per unit (see Fig. 1). In an oxygen-free atmosphere, methane or similar hydrocarbons dissociate in the microwave plasma, the resulting radicals recombine to hydrogen and carbon-based products in high concentration and with high purity [1]. When powered by renewable electricity, hydrogen can be produced with extremely low carbon footprint. Depending on the process, plasma-based manufacturing reduces electricity per unit of hydrogen up to 70% compared to electrolysis [2].

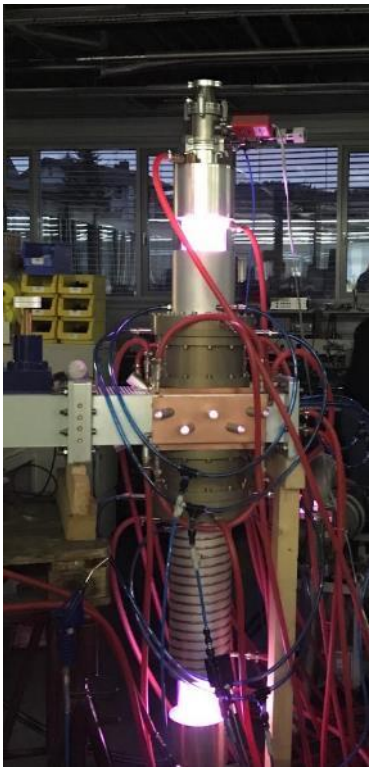

Fig. 1. 915 MHz plasma source in operation.

Recycling of water containing organic residues from industrial processes was demonstrated by application of a 2.45 GHz atmospheric pressure microwave plasma torch operated with pressurized air. Swirling of the pressurized air after admixture of the process water and subsequent injection via venturi nozzle into the plasma torch results in formation of tiny droplets of water in the pressurized airstream [4]. The smaller the droplets, the higher the probability of complete dissociation of the organic residues in the high-energy air plasma, where hydroxide and oxygen radicals convert organic residues into water vapor and carbon dioxide. After plasma processing, the water admixed to the pressurized airstream can be easily recaptured by quenching, which is shown in Fig. 2.

In a feasibility study, solutions of 16.81 g of acetic acid and of 8.74 g of ethanol, respectively, in 1 L of distilled water were used as substitutes of the organic residues to demonstrate the efficiency of atmospheric pressure microwave air plasma in

water recycling. Using a comparably low microwave power of 2 kW, the experimental results showed the reduction of ethanol by 92% and the removal of acetic acid by 88% [4].

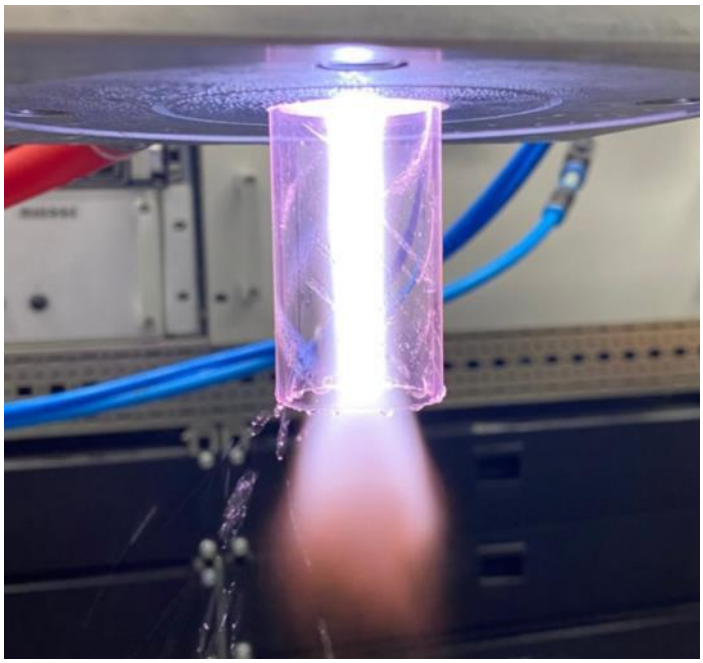

Fig. 2. Recovery of the water by quenching after cleaning from organic residues in a 2.45 GHz atmospheric pressure microwave plasma torch.

Microwave-assisted plasma conversion of methane and other hydrocarbons into hydrogen, and wastewater cleaning (containing organic residues from industrial processes) using APS improves different aspects of sustainability, i.e., use of renewable energies, saving of energy and resources as well as avoidance or even removal of greenhouse gases and pollutants. Based on the positive results, the ratio of microwave-assisted plasma applications in the Power-to-X industry is expected to rapidly increase, rendering these processes continuously more sustainable.

References

[1] N. Ashcraft, and R. Mueller, "Carbon-negative hydrogen production," Webinar, May 18, 2021. [Online]. Available: https://vimeo.com/552460925/2b13f3272f
[2] (2023) Technology overview webpage of Transform Materials. [Online]. Available: https://www.transformmaterials.com/technology-overview/
[3] R. Mueller, K.-M. Baumgaertner, M. Dingeldein, M. Gorath, J. Hofmann, A. Schulz, and M. Walker, "Atmospheric plasma source and downstream source: characteristics and industrial applications," invited talk, *Contributions to 56th Annual Microwave Power Symposium (IMPI 56),* Savannah, Georgia (USA), Jun. 14-16, 2022.
[4] N. Kaiser, "Behandlung von schwach kontaminierten Abwässern mittels Plasma-Technologie (Treatment of low-contaminated residual water using plasma technology)," Bachelor's Thesis, College of Technology "Georg Simon Ohm", Nuremberg (Germany), Aug. 4, 2021.

Microwave-Assisted Combustion of Biological Material

K.-M. Baumgaertner[1], M. Dingeldein[1], J. Schneider[1], A. C. Dorn[2]

[1]Muegge GmbH, Hochstrasse 4-6, D-64385 Reichelsheim (Odenwald), Germany
[2]Neo Joule B.V., Hofstraat 23, NL-6051 D Maasbracht, The Netherlands
Sales@muegge.de

Keywords: microwave-assisted combustion, microwave-assisted drying, microwave-assisted incineration, cremation.

Biological material contains a large amount of water which makes it difficult to reach the ignition temperature for combustion processes. Consequently, it is essential to remove or lower the amount of retained water and moisture from biological materials before combustion can be efficient. In a novel concept using microwave heating, the content of retained water and moisture of biological material is significantly reduced before increasing process temperature for efficient combustion.

The new microwave assisted combusting of biological material is performed in two steps. In the first step, the biological material is heated by microwaves to 100°C - 200°C. At this temperature, only minor degradation of the biological material occurs and retained water easily vaporizes. As a result, the moisture content of the biological material is reduced fast and efficiently. After the biological material is sufficiently dried, step 2 begins, and the microwave power is raised to reach temperatures significantly above 200°C where the biological material starts to incinerate (combustion step) [1].

Combustion tests of biological material using microwaves were performed in a large cylindrical barrel made of stainless steel. The front cover of the cylindrical barrel can be unlocked for loading and unloading. 915 MHz microwaves are injected into the cylindrical barrel by four ports. The ports allow optimization of microwave coupling into the cylindrical barrel, where the microwaves are directed on the biological material placed on a tray at the bottom of the cylinder. This configuration avoids cross coupling of microwaves from different ports as well as reflection of microwaves via adjacent ports or ports on opposite site. The design of the cylindrical barrel was developed by Neo Joule in cooperation with MUEGGE for the electromagnetic considerations for that design.

For the experiments, 14 kg of meat (size of a small pig) was used. 915 MHz microwaves from a single 100 kW microwave generator were distributed via power splitters to the four ports of the cylindrical barrel. The power splitters allow selection of the microwave power level at each port according to the shape of the biological material and its position inside the cylindrical barrel. The dielectric loss due to high water content of at least 50% - 70% accounts for microwaves not completely penetrating the biological material at the beginning of the drying phase. However, continuous evaporation of water will decrease the dielectric constant of the biological material, hence reducing its ability for microwave absorption. In order to maintain microwave absorption for heating and evaporation of water, microwave susceptor materials (e.g. tiles of silicon carbide) can be placed underneath the biological material at the bottom of the cylindrical barrel [1]. From the moment microwaves begin being absorbed by the susceptor material, microwave energy is transformed into thermal radiation, which applies additional heat to the biological material.

Continuous air flow through the cylindrical barrel guarantees the continuous removal of water vapor. The use of air or another oxygen-containing gas mixture is critical, as sufficient oxygen is the prerequisite for complete incineration of the dried biological material after reaching ignition temperature in the subsequent combustion step. In principle, microwave power can be significantly reduced during combustion, especially when the dried biological material is surrounded by combustible material (e.g. wooden container). Moreover, microwaves positively interact with emerging flames during incineration, which allows the reduction of microwave power as soon as the incineration of the biological material has started. In a microwave-assisted combustion test it was demonstrated that this novel concept is applicable for cremation to replace gas-powered cremators. The test object (14 kg of meat) was efficiently combusted using microwave power of 30 kW (20 minutes of drying), which was reduced to 15 kW in the subsequent combustion phase of 105 minutes, followed by 45 minutes of combustion without microwave energy [1].

The microwave-assisted combustion tests performed using a 100 kW microwave generator successfully showed shorter process time and improved energy efficiency compared to gas-powered systems. Having demonstrated its applicability in industrial processes, microwave-assisted combustion is currently qualified for processing hazardous biological waste and cremation of human or animal bodies.

References

[1] A. C. Dorn, and M. Costa, "Method for combustion of a biological material and a process for cremating a human or animal body or body part," International Patent Application WO 2022/081013 A1, Oct. 15, 2021.

Scaling Up Microwave-Driven Methane Pyrolysis

E. R. Bobicki[1], E. T. Furnell[1], J. F. Gerling[2]

[1]*Aurora Hydrogen, 16001 80 Ave NW, Edmonton, Canada*
[2]*Gerling Consulting, Inc., 12150 Calle Uvas, Gilroy, California, USA*
erin.bobicki@aurorahydrogen.com, *john@jfgerling.com*

Keywords: microwave, methane pyrolysis, fluidized bed

The global hydrogen market is expected to grow tenfold by 2050 as the world moves towards decarbonization of the energy sector and industrial processes. To date, hydrogen uses have been limited to a few applications, such as oil refining or chemical production. As the market grows, applications are expected to expand to, for example, heavy-haul fuelling, natural gas blending/replacement, or energy. Low-cost, distributed hydrogen production is required to enable new use cases; however, it does not yet exist. Aurora Hydrogen is developing a novel hydrogen production technology that produces hydrogen and solid carbon from natural gas via methane pyrolysis ($CH_4 \rightarrow H_2 + C$) without generating any CO_2 emissions or consuming water. Aurora's approach is to use microwave energy to directly heat the solid carbon product of the reaction in a fluidized bed reactor, the heat from which drives the methane pyrolysis reaction. The solid carbon product grows on the existing particles and hydrogen flows out the top of the reactor. Aurora Hydrogen has demonstrated the technology at the bench scale (1 kg-H_2/day) and is currently scaling-up the technology to an industrially relevant size.

A bench scale prototype of Aurora's process, capable of producing 1 kg-H_2/day, was constructed at the University of Toronto. The prototype consists of a 1-inch quartz tube serving as the fluidized bed reactor, positioned vertically inside a multimode microwave cavity (1 kW, 2.45 GHz) ("tube-in-box"). Seed carbon particles (activated carbon, 212 – 425 µm) are placed inside the quartz tube reactor and supported by a quartz fritted disk. Methane gas/nitrogen mixtures is introduced through the bottom of the reactor and serves both as the reactant and fluidizing gas. Fluidization ensures the particles are constantly mixed, preventing clogging and localized hotspots. Microwaves introduced into the cavity heat the fluidized carbon particles, modelled in Ansys HFSS 2023 (Fig. 1), which provides the temperatures necessary to convert methane to hydrogen. The product gas is filtered and analyzed by GC-TCD for hydrogen, methane, ethane, ethylene, acetylene, and nitrogen content.

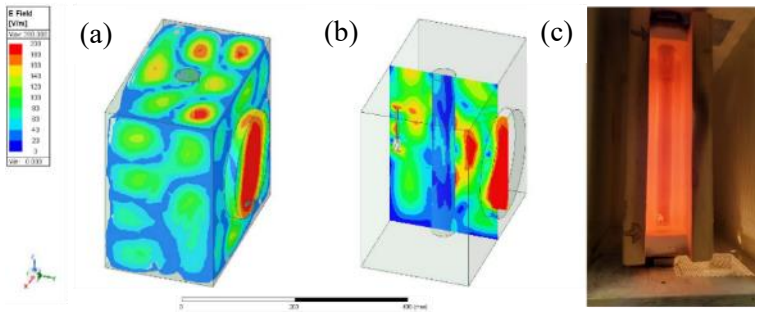

Fig. 1. Microwave field within the lab scale microwave set up: (a) Modal field distribution throughout the cavity, (b) cross section of the field to illustrate the field through the central carbon load, (c) photo of Aurora's 1 kW, 2.45 GHz prototype.

Cavity perturbation technique was used to assess the real and imaginary permittivity of the product carbon with increasing temperature at different microwave frequencies (Fig. 2). The carbon material is lossy and is an excellent microwave absorber, resulting in efficient, volumetric heating of the fluidized carbon.

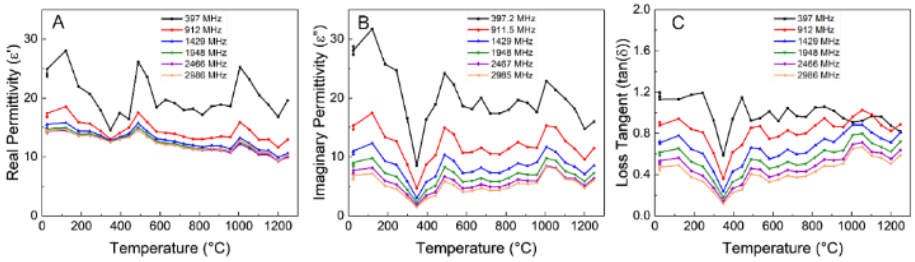

Fig. 2. (a) Real and (b) imaginary permittivities, and (c) calculated loss tangent of product carbon.

Bench scale testing has demonstrated a strong effect of temperature on conversion rate; methane conversion increases rapidly after approximately 950°C, reaching 90% conversion at 1216°C. Limitations of the prototype prevent testing of temperatures higher than 1250°C. Minor species, including ethane, ethylene and acetylene, form at approximately 820°C, increase with temperature to 1050°C, and diminish thereafter with almost no minor species observed at 1216°C.

Having successfully demonstrated the technology at the bench-scale, Aurora Hydrogen is building a 200 kg-H_2/day pilot plant in Fort Saskatchewan, Canada. The pilot will utilize a 75 kW, 915 MHz generator, and the fluidized bed reactor and the microwave cavity will be integrated into a single vessel (field modelled in Ansys HFSS 2023, Fig. 3). The operation of the pilot plant will depend heavily on the mixing within the fluidized bed to convert localized microwave heating to a nearly isothermal bed of carbon particles. Because the microwave absorptivity of the carbon is so high, the penetration depth into the carbon is limited.

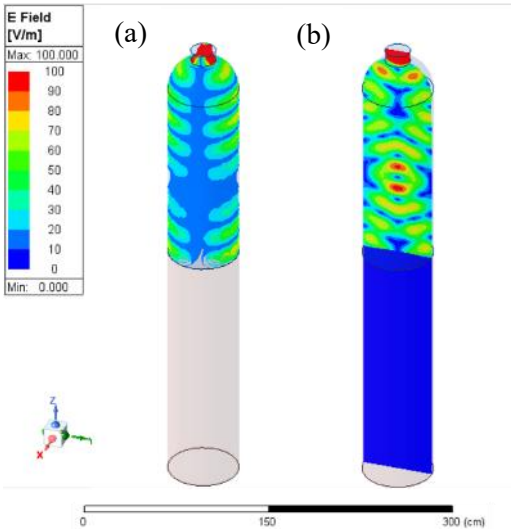

Fig. 3. Microwave field within the reactor: (a) Modal field distribution throughout the cavity, (b) cross section of the field

The transition from a tube-in-box design to an integrated reactor design has many challenges associated with the microwave cavity and waveguide design.

The temperature requirements for methane pyrolysis are high as the reaction relies on cleaving the carbon-hydrogen bonds in a reducing environment. The methane cracking reaction proceeds most efficiently at temperatures above 1000°C, leading to materials selection challenges. The following are the primary design criteria: 1) high temperature stability and strength, 2) high electrical conductivity to contain the microwave within the reaction chamber for safety reasons and to limit wasted microwave energy, 3) chemical resistance to contain the fluidized bed and chemical reaction. Current design involves a multilayered reaction vessel, as there is no one material which meets all criteria.

The reactor dimensions are largely dictated by the requirements of the fluidized bed. The seed carbon particles must be sufficiently fluidized to ensure good mixing and heat transfer. Fluidization must also be designed to limit slugging (i.e., gas bubbles become as large as the bed diameter) or gas by-passing (i.e., the gas moves through the bed without interacting with the carbon particles). Because the fluidizing gas is reacting, the gas properties change with respect to height within the reactor. The reaction efficiency may also affect the fluidization behaviour, depending on reaction conditions, and therefore the design must be robust to accommodate these changes.

There are significant design challenges regarding the placement of the microwave waveguide within the cavity. Ideal placement from a fluidized bed perspective would be near the base of the bed, to ensure heating is circulated upwards. However, there are significant challenges in sealing a microwave window within the bed including: differential thermal expansion, sealing materials, and heat resistances. Based on these challenges, it was determined that the microwave waveguide and window should be located outside of the carbon bed zone.

Finally, the handling of carbon solids has also been identified as a significant challenge. Materials behavior which governs the particulate solids flow will change over time, which may lead to solids handling issues. Solids handling is being carefully considered because it is a leading cause of failure for pilot projects involving particulate solids.

Although the plant in Fort Saskatchewan is a pilot, Aurora's technology can be deployed at a similar scale in a distributed manner, for example at small fueling stations or for niche industrial uses. Upon successful demonstration at 200 kg-H_2/day, Aurora will immediately scale-up to 2 tonne-H_2/day and larger to meet market demand.

Opportunities of Solid-State Microwave Technology: Thermodynamics, Kinetics and Optimization of the Applied Electric Field

A. Doroshenko[1]

[1]SAIREM, Décines-Charpieu, France

Keywords: microwave, solid-state generators, energy efficient, microwave power balance, no carbon process

Microwave (MW) heating is an alternative to traditional conventional processes, representing a different mechanism of heating [1, 2]. There are two different technologies for MW generation: magnetron and solid-state [3]. The solid-state technology has a set of advantages over the magnetron technology, including high accuracy of MW power control (1 W) and variable frequencies. Here we report the advantages of solid-state technologies for biomass-associated reactions.

All the experiments were done using the MicroChem system (SAIREM) with a possibility for an optimisation of the applied electric field (Figure 1), adjustment of MW frequencies between 2400-2500 MHz, and permanent estimations of the level of the absorbed MW power.

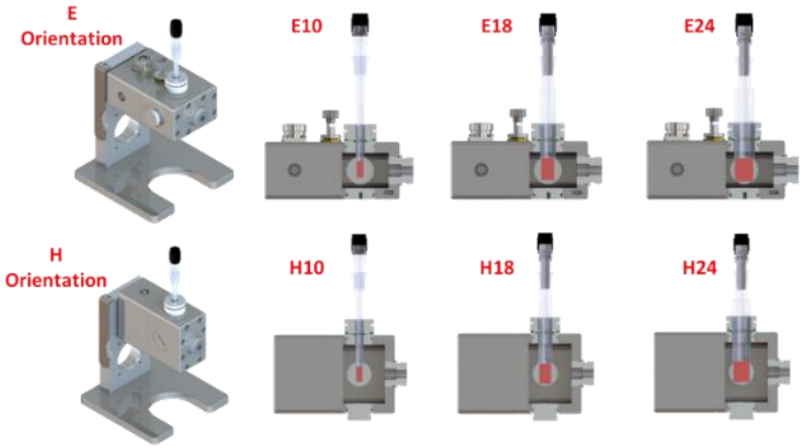

Fig. 1. E-orientation and H-orientation for parallel and perpendicular orientations of the applied electric field to the sample.

The main focus was dedicated to the values of absorbed power, monitored in real-time by MicroChem. Based on the example of extraction from grape seeds, it was shown that the control of the absorbed MW power substantially influences the repeatability of the experimental tests. The repeatability was substantially improved when absorbed power was used as a main controlling parameter instead of the forwarded power. The values of the absorbed power were used to estimate the energy consumption of the process (that can be directly applied to Life Cycle Assessment). Moreover, with the example of water, it was shown that the values of the absorbed power can be used to estimate the tangent loss of liquids during heating (Figure 2).

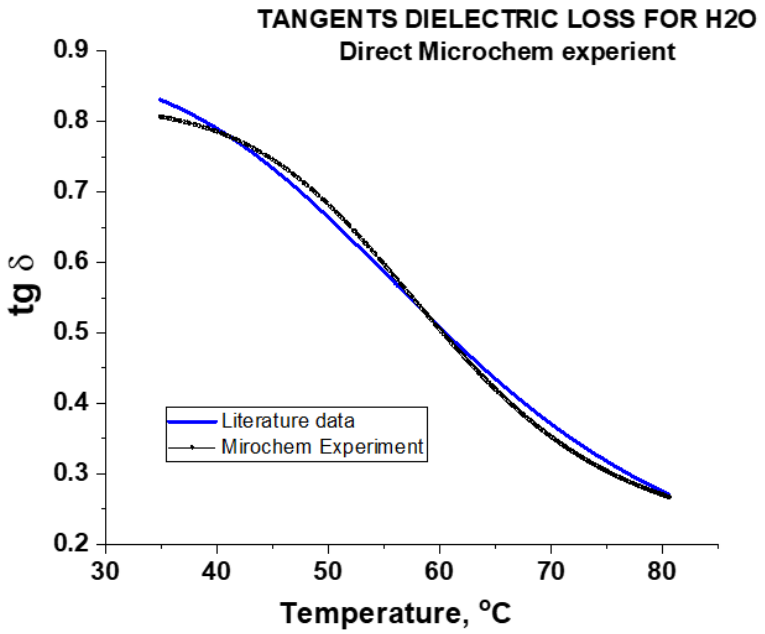

Fig. 2. A direct comparison of tangent loss between the literature data vs the calculated tg δ based on MicroChem measurements

The methodologies developed in SAIREM make it possible to estimate thermodynamic constants, including specific heat capacity, changes in enthalpy, and changes in entropy based on the measurements provided by MicroChem. The experimental error was below 5 % for ΔH and ΔS, while C_p was estimated with more than 1 % accuracy.

Finally, kinetics were calculated for the gelation of starch, giving the dependency of reaction rate depending on the generation degree just based on direct measurements provided by MicroChem.

Overall, the advanced features of solid-state technology make it possible to improve the repeatability of the results and highlight the effects of microwaving. MicroChem is a user-friendly study tool designed for research purposes and in combination with methodologies developed in SAIREM, it can be used for the estimation of energy consumption of the process, tangent loss, and thermodynamic and kinetics constants. These data can open an avenue to quickly optimise the processes, determine the effect of microwave heating and improve the understanding of chemical mechanisms.

References

[1] Singh, T. Christensen, C. Panoutsou, Policy review for biomass value chains in the European bioeconomy. Global Transitions, vol. 3, pp.13-42, 2021.
[2] N. Dutta, M. Usman, G. Luo, S. Zhang. An Insight into Valorization of Lignocellulosic Biomass by Optimization with the Combination of Hydrothermal (HT) and Biological Techniques: A Review. Sustain. Chem., vol. 3, pp. 35-55, 2022
[3] M. De Bruyn, V. Budarin, G. Sturn, G. Stefanidis, M. Radoiu, A. Stankiewicz, D. Macquarrie. Subtle Microwave-Induced Overheating Effects in an Industrial Demethylation Reaction and Their Direct Use in the Development of an Innovative Microwave Reactor. JACS, pp. 5431-5436, 2017

Industrial Equipment and Scale-Up

Real-Time Monitoring of Ground-Tire Rubber Microwave Devulcanization with Thermal and Electrochemical Sensors

R. Pérez-Campos[1], J. Fayos-Fernández[1], J. Monzó-Cabrera[1]

[1]*Grupo de Electromagnetismo y Materia, Universidad Politécnica de Cartagena, Plaza del Hospital 1, E-30202, Cartagena, Spain*
rafael.perez@upct.es

Keywords: microwave, dielectric properties, ground-tire rubber, devulcanization, electrochemical sensors

Nowadays, there is a major problem with rubber waste due to its widespread consumption. The recycling process is currently considered a much better solution than the energy recovery with combustion or landfill accumulation, which are not acceptable for the circular economy and the environment [1]. Hence, the most beneficial procedure for ground-tire rubber (GTR) to be rubber feedstock for the manufacturing industry is devulcanization [2].

The devulcanization process involves the selective scission of the sulphidic bonds that crosslink the rubber polymer during vulcanization. At the same time, the polymeric structure backbone must be preserved, which means that the carbon bonds must not be broken. Microwave technology seems a good approach to accomplishing that [3] due to the savings in processing time and energy consumption, as well as the simplicity with which control parameters like power level and treatment duration can be adjusted.

Thus far, rubber temperature has been deemed the primary indicator of whether the microwave devulcanization process was successful. Thus, rubber temperature has been the most employed parameter to control the process. Nevertheless, it is particularly challenging to construct a suitable temperature monitoring and control subsystem on a lab scale [4], requiring a methodology to assess the process during microwave treatment [3].

When waste rubber is microwave processed, several important chains are broken, thereby producing volatile organic compounds and volatile sulfur compounds (VSC) [5]. These sulfur gas by-products might be employed as control and monitoring variables, as stated in our previous work [6]. In this contribution, a modified conventional microwave oven was used to devulcanize GTR while its temperature and three VSC concentrations were monitored, as illustrated in Figure 1. The concentrations of VSC were monitored by means of electrochemical sensors, which are able to collect high-quality data on air pollutants [7].

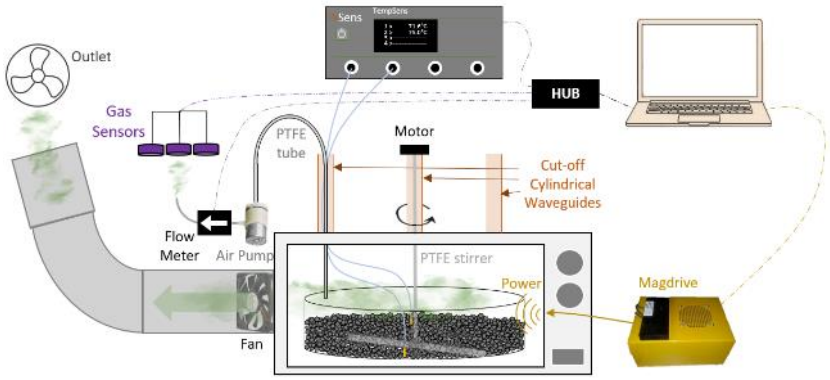

Fig. 10. Schematic diagram of the experimental setup

For all tests, constant microwave power was supplied to the magnetron. In some tests, only one power pulse was used, whereas various on-off pulses were used in other tests. The efficiency of the stirring system was evaluated by taking some thermal photographs of the treated GTR. The microwave-processed GTR was evaluated by determining the values of its mass loss (ML) and the variation of its electric permittivity, which is strongly related to its chemical composition and structure, as demonstrated in [8].

During the microwave processing, certain sulphidic bonds in the GTR are broken, resulting in the release of several types of gases and a consequent reduction in mass. The relationship between the total amount of monitored sulphur gas concentrations and the ML is depicted in Figure 2.

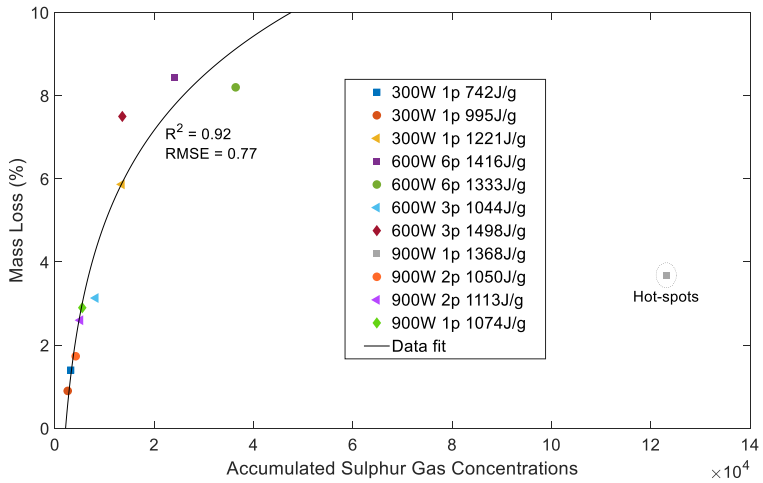

Fig. 11. ML evolution versus accumulated sulphur gas concentrations (ppm·s) for the different microwave energy levels

Figure 3 shows the relation between the ML and the dielectric properties, which are directly related to the chemical composition and structure of the GTR [8], for the microwave-processed GTR. The results indicate that, due to the release of gases, there is a ML in the rubber sample as well as a rise in both the dielectric constant and loss factor values.

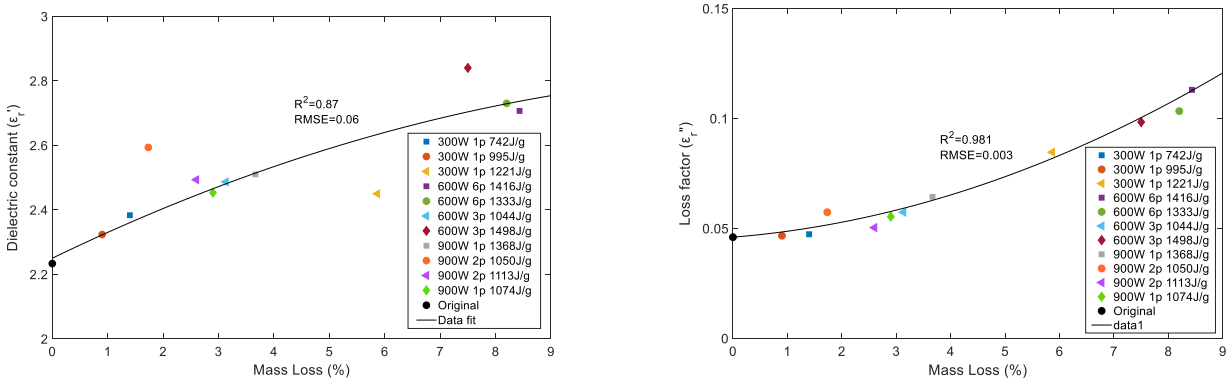

(a) (b)

Fig. 12. Permittivity evolution versus ML: (a) dielectric constant; (b) loss factor

The differences in permittivity values demonstrated that the microwave treatment modified the chemical structure. Some difficulties were found in adequately monitoring the MUT temperature. In addition, the recorded thermal images revealed that some hot-spots are generated during the microwave process. Both the energy thresholds and the sensible energy absorbed by the GTR seem to be mainly related to the stirrer efficiency. Finally, this paper demonstrates that monitoring the VSC time evolution can provide a reliable indication of ML and, consequently, devulcanization evolution even at non-uniform temperature conditions for GTR batches.

Additional results for the optimization of GTR devulcanizing control by monitoring the VSC will be presented at the conference.

References

[1] K. Formela, "Sustainable development of waste tires recycling technologies–recent advances, challenges and future trends", *Advanced industrial and engineering polymer research*, vol. 4, no. 3, pp. 209-222, 2021.
[2] L. Asaro, M. Gratton, S. Seghar, and N.A. Hocine, "Recycling of rubber wastes by devulcanization", *Resources, Conservation and Recycling*, vol. 133, pp. 250-262, 2018.
[3] K. Formela, A. Hejna, L. Zedler, Colom Fajula, X., and F.J. Cañavate Ávila, "Microwave treatment in waste rubber recycling–recent advances and limitations", *Express polymer letters*, vol. 13, no. 6, pp. 565-588, 2019.
[4] A. Bani, G. Polacco, and G. Gallone, "Microwave-induced devulcanization for poly (ethylene–propylene–diene) recycling", *Journal of Applied Polymer Science*, vol. 120, no. 5, pp. 2904-2911, 2011.
[5] M. Gągol, G. Boczkaj, J. Haponiuk, and K. Formela, "Investigation of volatile low molecular weight compounds formed during continuous reclaiming of ground tire rubber", *Polymer Degradation and Stability*, vol. 119, pp. 113-120, 2015.
[6] R. Pérez-Campos, J. Fayos-Fernández, J. Monzó-Cabrera, A. Díaz-Morcillo, A. Martínez-González, and A. Lozano-Guerrero, "Improved control on the microwave devulcanizing of ground tire rubber by means of sulphur gas sensors", in *Proc. AMPERE 2021*, pp. 146, 2021
[7] A. Samad, D.R. Obando Nuñez, G.C. Solis Castillo, B. Laquai, and U. Vogt, "Effect of relative humidity and air temperature on the results obtained from low-cost gas sensors for ambient air quality measurements", *Sensors*, vol. 20, no. 18, pp. 5175, 2020.
[8] R. Pérez-Campos, J. Fayos-Fernández, J. Monzó-Cabrera, F. Martín Salamanca, J. López Valentín, J.M. Catalá-Civera, P. Plaza-González, and J.R. Sánchez-Marín, "Dynamic Permittivity Measurement of Ground-Tire Rubber (GTR) during Microwave-Assisted Devulcanization", *Polymers*, vol. 14, no. 17, pp. 3543, 2022.

Generation of Uniform Power Density Distribution over a Large Area using OAM Modes

K. Suzuki[1], T. Mitani[1], N. Shinohara[1]

[1]*Research Institute for Sustainable Humanosphere, Kyoto University, Gokasho, Uji, Kyoto, Japan 611-0011*
kento_suzuki@rish.kyoto-u.ac.jp

Keywords: microwave heating, uniform power density, microstrip antenna, orbital angular momentum, uniform circular array

The objective of this study is to realize uniform microwave heating over a large area. Microwave heating is a technique that can heat objects from the inside, and has the characteristics of high energy efficiency and rapid heating. Because of these advantages, there are various applications in industrial processes such as sterilization and drying [1][2]. In addition, the promotion of chemical reactions and the generation of new materials using the non-thermal effects of microwave irradiation are also being studied [3]. In these applications, in order for the microwave effect to work over a large area, it is desirable to irradiate the microwaves with uniform intensity over a large area without irregularities. However, it is known that conventional heating devices using cavity resonators cannot generate a uniform power density distribution due to the nodes and antinodes of standing waves.

We aimed to generate a uniform power density distribution by an irradiation-type heating system using an array antenna. In a previous study, we proposed a new method for generating a uniform beam by using the irradiation pattern of the orbital angular momentum (OAM) modes of electromagnetic waves [4]. By using the circular ring irradiation patterns of the OAM modes and synthesizing the distributions of multiple modes, a uniform power density distribution was realized in the simulation. However, there was a problem of large unwanted radiation outside the heating area, and the uniform area was small. Therefore, we investigated the arrangement of antenna elements to reduce unwanted radiation and expand the uniform area.

In this study, we use a uniform circular array (UCA), which is a typical OAM mode-generating antenna [5][6]. The UCA has a structure in which antenna elements are arranged at equal intervals around the circumference. In order to solve the problem of unwanted radiation, we considered reducing the element spacing. For OAM mode generation using the UCA, it is known that the smaller the radius of the array, the more the sidelobes are suppressed [7]. In addition, it is expected that the main lobe angle for non-zero modes becomes larger, and the range of uniform power density distribution can be expanded. However, there is a possible effect of disturbing the radiation pattern due to mutual coupling between the elements by arranging the elements closer together. Therefore, we investigated the range in which uniformity of power density distribution can be maintained on the heating surface when the element spacing of the UCA is close.

Figure 1 shows the simulation model of the UCA. Square microstrip antennas were used as element antennas. The number of antenna elements was set to 10, considering the generation of modes 0, +1, and +2. When the element spacing s is changed in increments of 0.1 λ (λ : wavelength in free space), the minimum distance at which the element antennas can approach each other without overlapping is 0.5 λ . Therefore, the element spacing s was set to 0.5 λ , 0.6 λ , and λ . The power density distribution of each mode in a plane at z = 500 mm was simulated using CST Studio Suite 2022. Then, the intensities of the power density distributions for the three modes were added together at an appropriate ratio assuming the ratio of the irradiation time. The size of the uniform area was evaluated for the case of the ratio that maximized the uniform area. The uniform area was defined as the area where the power density is higher than 90% of the maximum value in the simulation range.

Figure 2 shows the results of adding the power density distributions for the three modes by the ratio which maximizes the uniform area. The distributions in Fig. 2 represent normalized values. Table 1 shows the size of the uniform area in the results of Fig. 2 at each element spacing. The size of the uniform area was increased by arranging the elements close together. This is because of the larger main lobe angle due to the larger array radius. However, when the element spacing was 0.5 λ , which is the minimum spacing, the shape of the uniform area was greatly distorted. This is due to the fact that using too small a spacing gap between the elements caused a strong effect of mutual coupling between the elements, and the symmetry of the circular distribution of OAM modes was distorted. These results indicate that it is effective to reduce the element spacing of the UCA within the range of small mutual coupling effects in order to expand the uniform area while maintaining the symmetrical heating range.

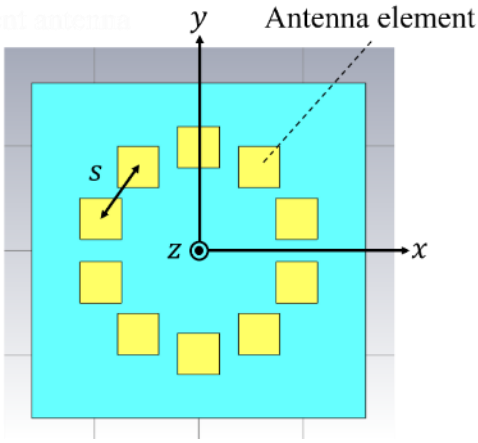

Fig. 1. Simulation model of a UCA.

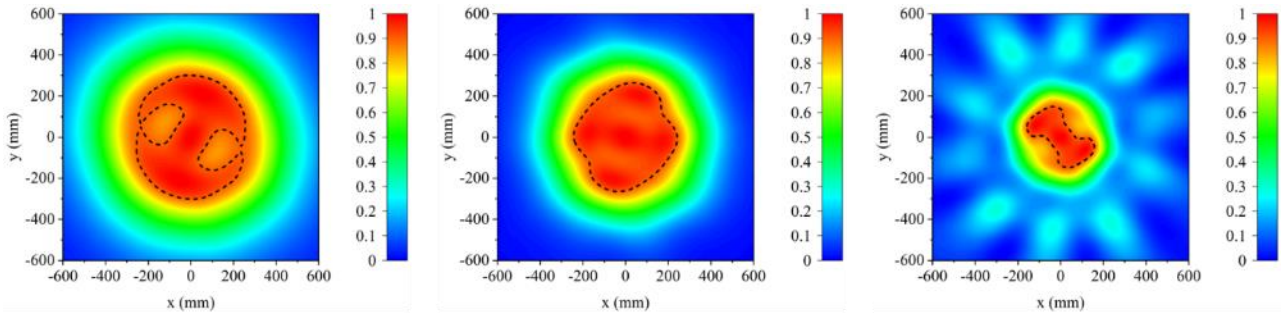

Fig. 2. Normalized results of the synthesized power density distribution at each element spacing (The dashed line indicates 90% contour of the maximum value). (a)$s = 0.5\lambda$; (b)$s = 0.6\lambda$; (c)$s = \lambda$.

Table 1. Results for the size of the uniform area at each element spacing.

s	Uniform area [mm^2]
0.5λ	2.032×10^5
0.6λ	1.802×10^5
λ	4.61×10^4

Acknowledgment
This work was supported by JSPS KAKENHI Grant Number JP21K04175.

References

[1] N. E. Bengtsson and T. Ohlsson, "Microwave heating in the food industry," in Proceedings of the IEEE, vol. 62, no. 1, pp. 44-55, Jan. 1974.
[2] L. Bandici, T. Leuca and S. Coman, "The use of microwave field energy in the drying process of wooden sticks," 2017 14th International Conference on Engineering of Modern Electric Systems (EMES), Oradea, Romania, 2017, pp. 95-98.
[3] D. Katovic, S. B. Vukusic, S. Hrabar and J. Bartolic, "Microwaves in Chemical Finishing of Textiles," 2005 18th International Conference on Applied Electromagnetics and Communications, Dubrovnik, Croatia, 2005, pp. 1-4.
[4] K. Suzuki, T. Mitani and N. Shinohara, "Feasibility Study of Uniform Microwave Heating by Switching OAM Modes," 2022 Asia-Pacific Microwave Conference (APMC), Yokohama, Japan, 2022, pp. 659-661.
[5] Y. Yuan, Z. Zhang, J. Cang, H. Wu and C. Zhong, "Capacity analysis of UCA-based OAM multiplexing communication system," 2015 International Conference on Wireless Communications & Signal Processing (WCSP), Nanjing, China, 2015, pp. 1-5.
[6] Z. Li, Y. Ohashi and K. Kasai, "A dual-channel wireless communication system by multiplexing twisted radio wave," 2014 44th European Microwave Conference, Rome, Italy, 2014, pp. 235-238.
[7] S. M. Mohammadi et al., "Orbital Angular Momentum in Radio—A System Study," in IEEE Transactions on Antennas and Propagation, vol. 58, no. 2, pp. 565-572, Feb. 2010.

Investigation of Refractory Materials for Glass Industry under Microwave Influence in the Temperature Range up to 800°C

V. Grimm[1], R. Behrend[1], H. Krause[1]

[1]*TU Bergakademie Freiberg, Institute of thermal engineering, Professorship of Gas and Heat systems, Gustav-Zeuner-Straße 7, 09599 Freiberg, Germany*
Valerie.Grimm@iwtt.tu-freiberg.de

Keywords: microwave, high temperatures, refractory materials

Abstract
The following paper presents the results of selected refractory linings for the glass industry. The materials HZFC, AZS, Mullite and Quarzal were investigated and an evaluation for use in microwave heated high temperature equipment was performed. For this purpose, the dielectric properties of the materials were determined up to a temperature of 900 °C. These results were subsequently validated under real conditions up to 800 °C.

Introduction

The relining of industrial furnaces with refractory linings is usually associated with high costs for new material and long downtimes. For this reason, an accurate prediction of the reactions of the refractory material to heating (microwaves) is of great importance.

From the investigations, it became clear that the behaviour under microwave influence varies from brick to brick. There are materials that absorb microwaves very well and others that have high transmission. More precise dependencies could not be defined exactly, especially for the inhomogeneous materials (which are used as standard) [1–7]. In this regard, further investigations were carried out in the field of dielectric properties. As part of the MiGWa project, a test facility for determining dielectric parameters was set up at the Institute of Thermal Engineering and Thermodynamics at the Freiberg University of Mining and Technology. The results obtained from this on the dielectric properties were then verified in a microwave transmission test system.

The dielectric properties of a material can not only give a rough estimate of its behaviour under microwave influence, but also serve for theoretical considerations such as simulations. This allows prior consideration of the behaviour of refractory materials under microwave influence in the context of certain general conditions.

Experimental set-up and execution

At the beginning, the samples were examined with regard to their dielectric properties. The measurement setup used for this purpose is shown in Fig. 1. It consists of a vector network analyzer, which is connected to the measuring waveguide by a coaxial connector. This is heated to the desired temperature by an external heater. For control purposes, a moving short is attached to the end of the waveguide. This is adjusted manually.

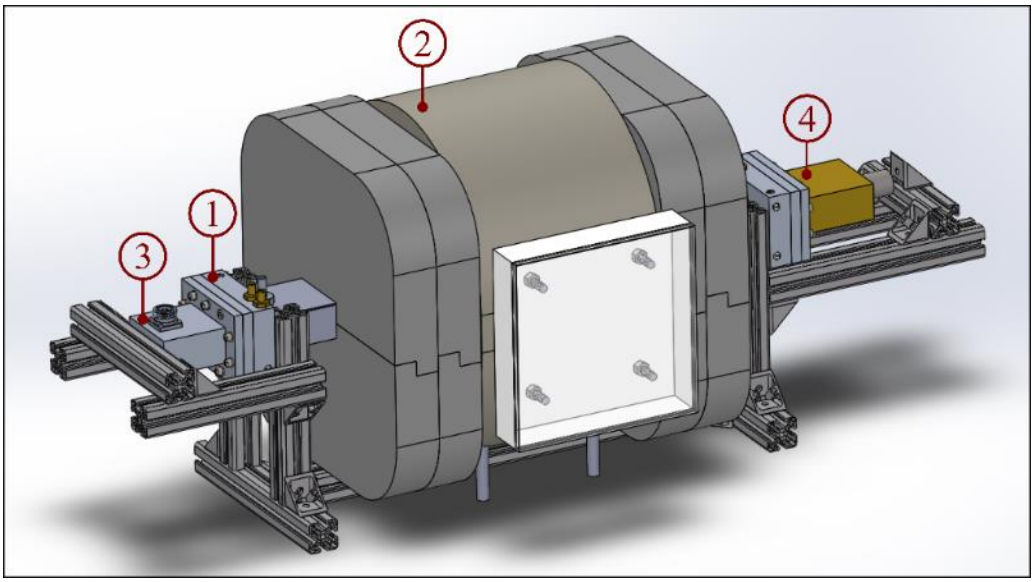

Fig. 6. Dielectric Properties Measurement System with (1) water cooling, (2) heater, (3) coax-waveguide-transition and (4) moving short

The samples were cut to a diameter of 35 mm and a height of 20 mm. These are positioned centrally in the waveguide. Temperatures from 25 °C (room temperature) to 900 °C are realized in the experiment. These temperature levels are approached from 200 °C in 50 K steps.

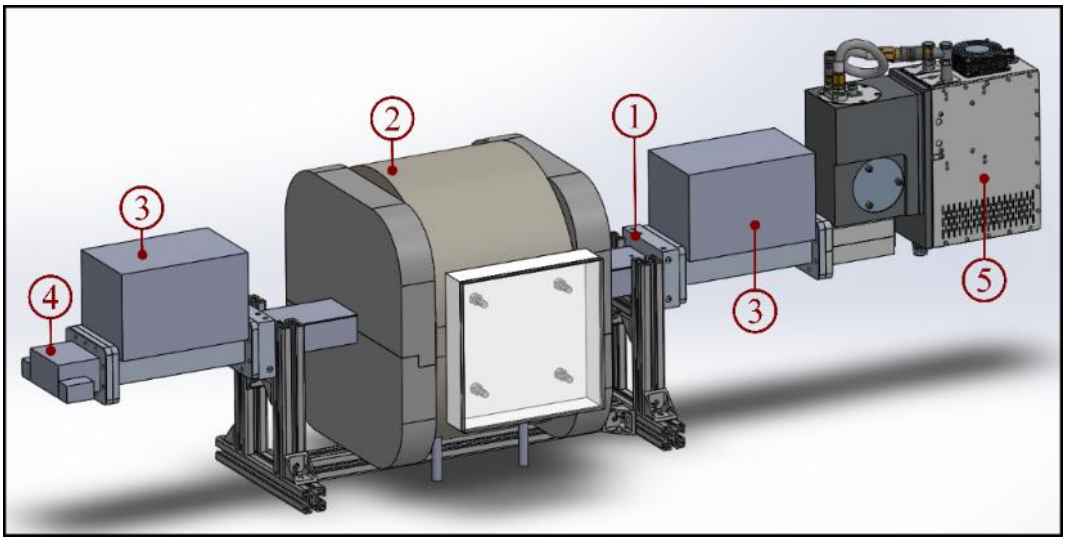

Fig. 7. Refractory test facility with (1) cavity, (2) heater, (3) 3-stub tuner with 6-port reflectometer, (4) water load and (5) magnetron

For the validation of the dielectric properties, a transmission measurement was performed (Fig. 7). The test system consists of a 3-kW magnetron as microwave sources. A 3-port reflectometer is installed in front of and behind the sample as the measuring device. In between, as in the dielectric measurement, is the measuring waveguide with external heating. A water load is integrated at the end of the setup. This is to prevent possible reflections that could influence the measurement result.

The samples used have a size of 40 mm × 40 mm × 84 mm. They are positioned centrally in the measuring waveguide. Temperatures from 25 °C to 800 °C were realized. From a temperature of 100 °C the measurements were carried out in 100 K steps.

Measurement results and evaluation

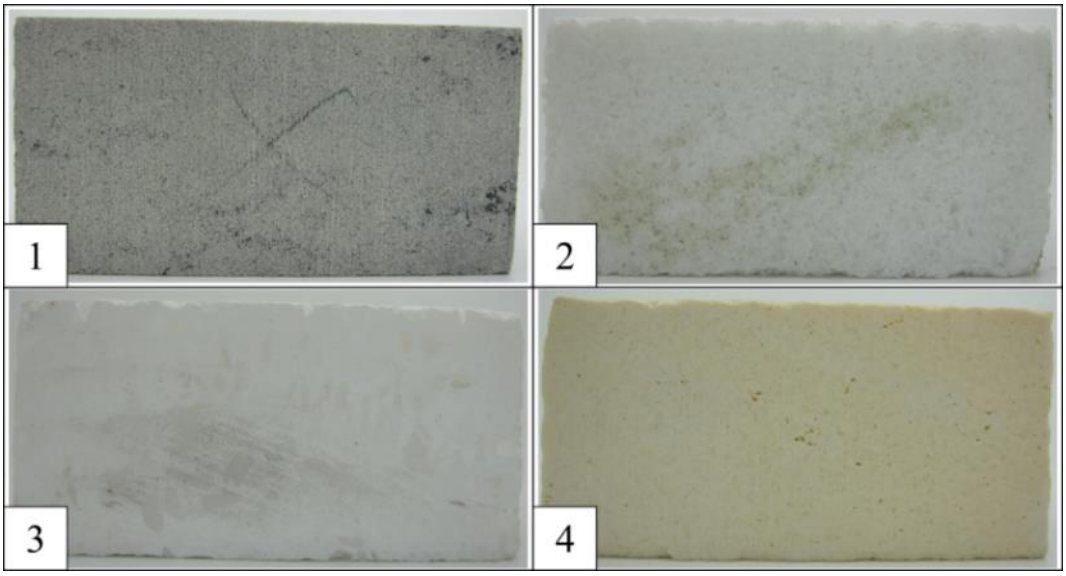

Fig. 8. Investigated refractory materials: (1) HZFC, (2) mullite (3) Quarzal and (4) AZS

Four refractory materials were considered in the investigations. Two fused cast materials (AZS and HZFC) and two sintered bricks (Quarzal and mullite). These bricks are standardly used in glass furnaces. Therefore, it is important to know how these materials behave under microwave influence. The initial condition is shown in **Error! Reference source not found.**.

Table 1. Density and composition of the refractory sample material

	Density $\left[\frac{kg}{dm^3}\right]$	Al_2O_3 [%]	ZrO_2 [%]	SiO_2 [%]	Fe_2O_3 [%]	Na_2O [%]
Quarzal	2.00	45.55	41.00	12.20	[-]	1.0
Mullite	2.55	0.80	94.50	4.00	[-]	0.40
AZS	3.98	[-]	[-]	99.60	[-]	[-]
HZFC	5.40	74.00	[-]	25.00	0.20	[-]

In order to determine whether a material is suitable for use under the influence of microwaves or not, the imaginary part of the relative permittivity plays a decisive role. This becomes clear from the formula for the power density [8], which gives an estimate of the absorption behaviour of a material. This is composed of the frequency f, the permittivity ε_o, the imaginary part of the relative permittivity ε_r'' and the electric field strength E.

$$p = 2 \cdot \pi \cdot f \cdot \varepsilon_o \cdot \varepsilon_r'' \cdot E^2 \qquad (1)$$

The first material studied was Quarzal (Fig. 4). This has a very low imaginary part of the relative permittivity (0.004 to 0.009), which increases slightly with higher temperature. The results could be confirmed by the transmission measurement. The material exhibits a high transmission of 95% and a very low absorption of 1% to 2%. The reflection is also very low, ranging from 3% to 4%. Because of the low values for the dielectric properties, a temperature dependence could not be determined under real conditions.

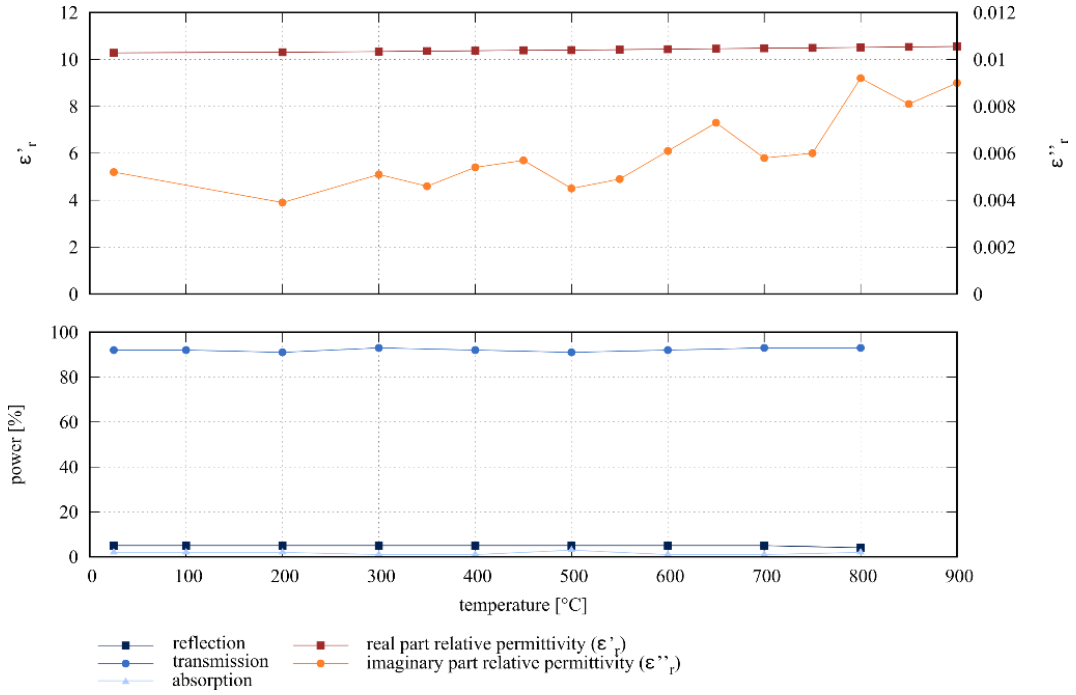

Fig. 9. (top) Dielectric properties of Quarzal from 25 °C to 900 °C, (bottom) relative reflected, transmitted and absorbed power of Quarzal from 25 °C to 800 °C and a power of 600 W

The second material investigated was mullite (Fig. 5). This material also exhibits a low imaginary part of relative permittivity of 0.01 to 0.03 up to a temperature of 600 °C. Thereafter, the value increases up to 0.15. This could be approximately confirmed in the tests under real conditions. Up to a temperature of 200 °C, there is an absorption of 5%. After that, the value increases continuously to 15% up to 600 °C and then increases further to 18%. At the same time, the reflection also increases and the transmission decrease significantly from 78% to 52%.

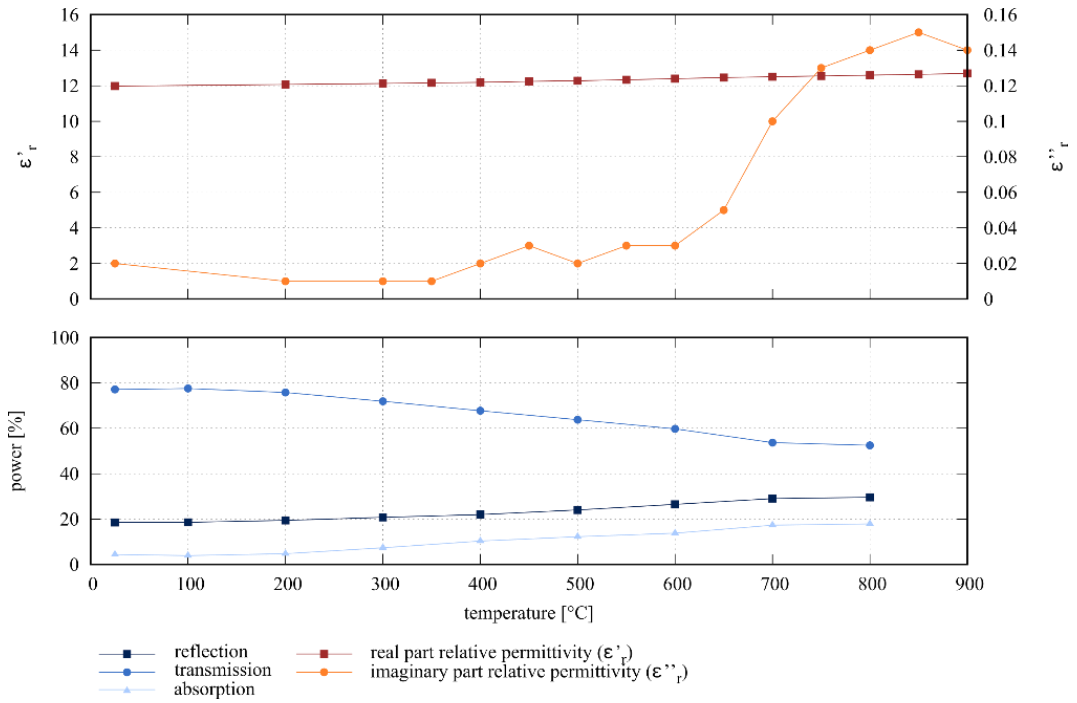

Fig. 10. (top) Dielectric properties of Mullite from 25 °C to 900 °C, (bottom) relative reflected, transmitted and absorbed power of Mullite from 25 °C to 800 °C and a power of 600 W

In contrast, two fused cast materials (AZS and HZFC) were investigated, which have a higher density compared to the sintered materials (Table 1). HZFC (Fig. 6), similar to mullite, has a low imaginary part of the relative permittivity of 0.02 to 0.07. It is surprising that the absorption is relatively high compared to mullite with 38% to 65%. A possible reason could be the high density of 5.40 kg/dm³, for mullite this is 2.55 kg/dm³. It is remarkable that HZFC has a high reflectance of up to 60%. The transmission, on the other hand, assumes a value of almost 0% at 200 °C.

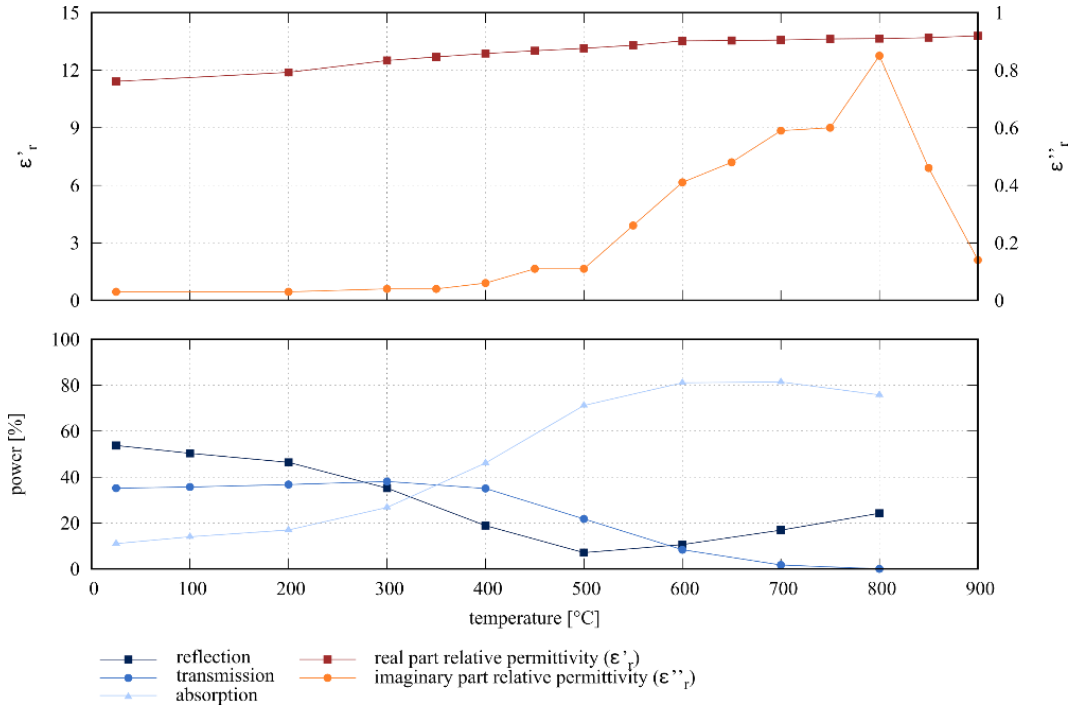

Fig. 11. (top) Dielectric properties of HZFC from 25 °C to 900 °C, (bottom) relative reflected, transmitted and absorbed power of HZFC from 25 °C to 800 °C and a power of 600 W

HZFC (Fig. 6), similar to mullite, has a low imaginary part of the relative permittivity of 0.02 to 0.07. It is surprising that the absorption is relatively high compared to mullite with 38% to 65%. A possible reason could be the high density of 5.40 kg/dm³, for mullite this is 2.55 kg/dm³. It is remarkable that HZFC has a high reflectance of up to 60%. The transmission, on the other hand, assumes a value of almost 0% at 200 °C.

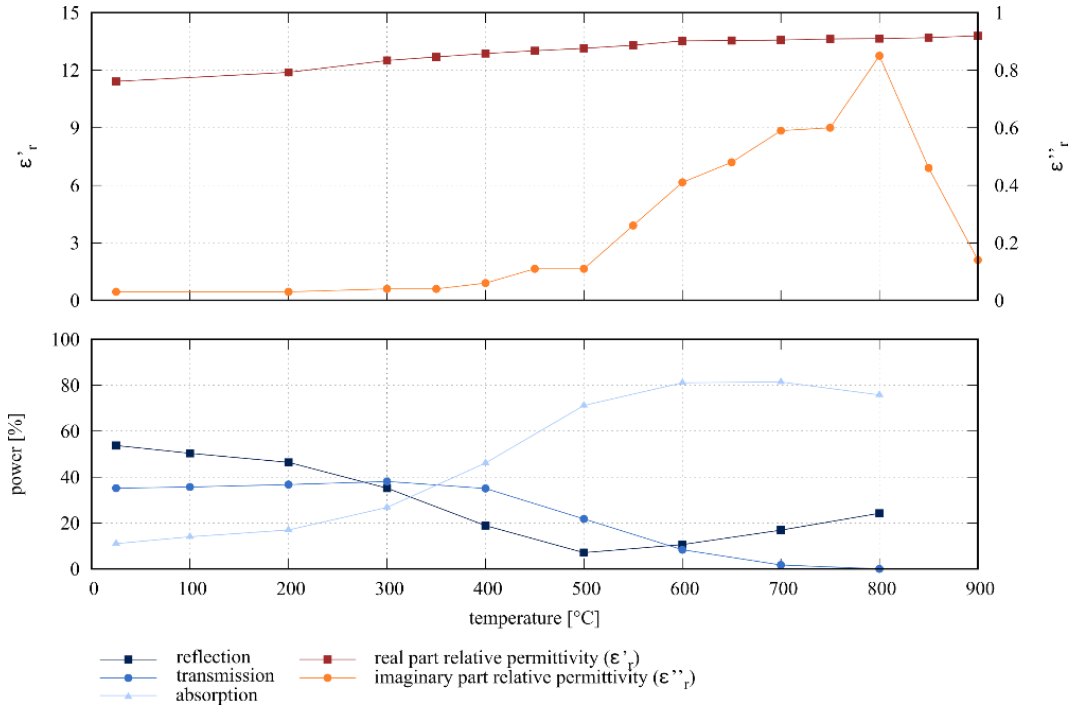

Fig. 12. (top) Dielectric properties of AZS from 25 °C to 900 °C, (bottom) relative reflected, transmitted and absorbed power of AZS from 25 °C to 800 °C and a power of 600 W

AZS has a high imaginary part relative permittivity compared to the other materials (Fig. 7). Up to 400 °C this is 0.05 and rises to 0.1 by 500 °C. Thereafter there is a high increase to 0.6 by 750 °C and at 800 °C there is a jump to 0.85 before the value drops again. The absorption also increases with increasing temperature. This already starts in the temperature range from 25 °C to 300 °C from 10% to 30%. This is followed by a larger increase up to 500 °C to 70% and reaches its maximum at 600 °C to 700 °C with 80%. The transmission has a value of 40% up to 300 °C before it continuously decreases and takes on a value of 0% up to 800 °C. The reflectance drops from 55% to 10% up to 500 °C and then starts to increase again continuously.

Conclusion

From the results it is clear that the measurement data from the dielectric measurement fundamentally agree with the tests under real conditions. There are certain deviations, which could be related to the inhomogeneity of the materials.

It can be seen that the fused cast materials (AZS and HZFC) with a high density also have a high to very high absorption. And would be well suited for use in the tub area. In contrast, the sintered materials (Quarzal and mullite) show good transmission and would be suitable in an area where high transmission of microwaves is required.

Acknowledgement

The authors would like to thank the German Federal Ministry of Education and Research as well as the European Union for funding the project “MiGWa” under grant agreement no. 01LJ2001B.

References

[1] W. B. Westphal, A. Sils: Dielectric Constant and Loss Data : Technical Report AFML-TR-72-39 (1972)
[2] Shang, Xiaobiao ; Di Zhai ; Zhang, Fucheng ; Wei, Cong ; Chen, Junruo ; Liu, Meihong ; Peng, Jinhui: Electromagnetic waves transmission performance of alumina refractory ceramics in 2.45 GHz microwave heating. In: Ceramics International (2019)
[3] Min Kyu Park ; Na Neul Kim ; Seung Su Baek ; Eul Son Kang ; Yong Kee Baek ; Do Kyung Kim: Dielectric properties of alumina ceramica in the microwave frequenzy at high tmperature : Solid State Phenomena, 2007
[4] Nelson, S. ; Lindroth, D. ; Blake, R.: Dielectric properties of selected minerals at 1 to 22 GHz (1989)
[5] A. Von Hippel: Dielectric Materials and Applications England (1954)
[6] Shang, Xiaobiao ; Di Zhai ; Liu, Meihong ; Chen, Junruo ; Zhang, Fucheng ; Wei, Cong ; Bai, Yongzhen ; Li, Guangchao: Dielectric properties and electromagnetic wave transmission performance of aluminium silicate fibreboard at 915 MHz and 2450 MHz. In: Ceramics International (2021)
[7] Di Zhai ; Zhang, Fucheng ; Wei, Cong ; Bai, Yongzhen ; Zhu, Liyue ; Li, Guangchao ; Shang, Xiaobiao ; Sun, Junfeng ; Chen, Junruo ; Liu, Meihong ; Peng, Jinhui ; Gu, Huabin: Dielectric properties and electromagnetic wave transmission performance of polycrystalline mullite fiberboard at 2.45 GHz. In: Ceramics International (2020)
[8] Meredith, Roger: Engineers' Handbook of Industrial Microwave Heating : Institution of Engineering and Technology, 1998

Homogeneous and Sustainable Microwave Heating of Glass Fiber

Y. Alekajbaf[1], D. Dancila[1, 2]

[1]*FREIA, Department of Physics and Astronomy, Uppsala University, Sweden*
[2]*Microwave Group, Department of Electrical Engineering, Uppsala University, Sweden*
yasin.alekajbaf@Physics.uu.se

Keywords: microwave, glass fiber, dielectric, power amplifier, heating

Glass fiber (GF) is widely used in aerospace and automotive industries due to advantages like low weight, low cost, and high mechanical performance. The heating process plays a key role in glass fiber manufacturing because it directly affects the properties of GF. A homogenous and controllable heating process can provide a GF with high mechanical performance. Convection heating is a common method in the GF heating process but consumes a large amount of energy and cost. Therefore, microwave-based heating methods as an attractive alternative are developed in this matter. Microwave heating methods reduce the time and energy required to reach the desired temperature for GF production. However, achieving homogeneous heating is the main challenge of microwave heating [1], [2].

In this paper, we present a hybrid microwave heating solution that provides satisfactory homogeneous heating while saving time and energy. In this method, we use a combination of two 250 Watt solid-state power amplifiers (SSPA) at 2.45 GHz and a convection heating source. According to Fig. 1, two SSPAs are used in both sides of a 1300 mm WR340 waveguide filled by GF (FR4) and a heat source is also placed around to decrease heating time.

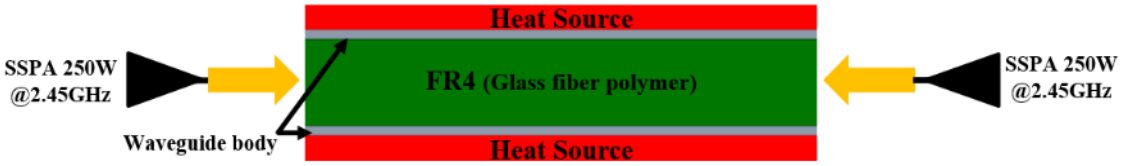

Fig. 1. Presented hybrid microwave heating structure

The heating behavior of the presented solution is simulated in Ansys Icepak software. Figure 2 illustrates the heat-up time comparison for convection heating, microwave-based heating, and the presented hybrid method. It can be seen that using the presented hybrid microwave heating method reduces the heat-up time of the sample (from 20 ˚C to 70 ˚C) to 10 minutes compared with the convection heating method at 30 minutes.

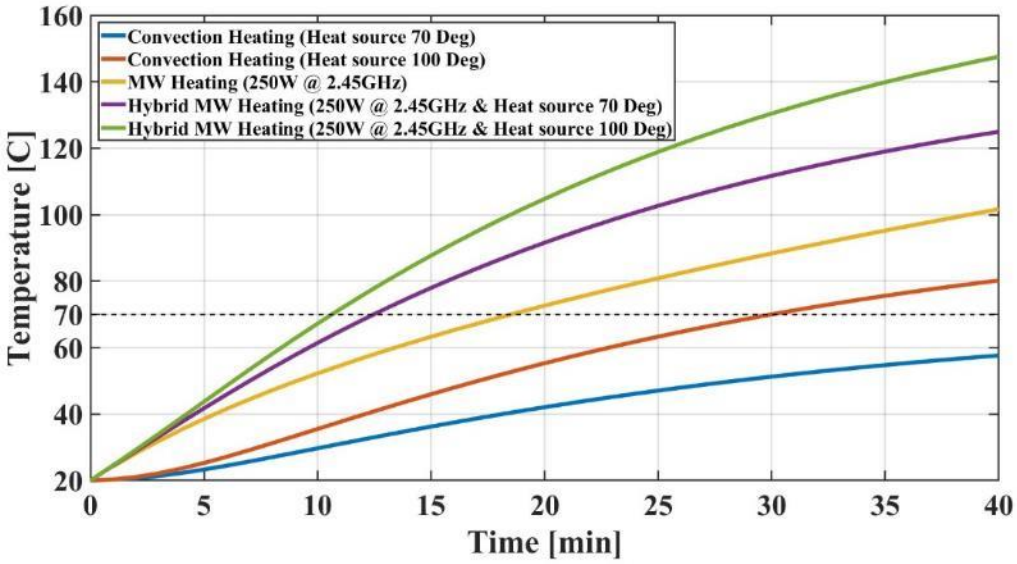

Fig. 2. Heat-up time at the center of GF for 1) convection heating 70˚C 2) convection heating 100˚C 3) microwave heating 250 W 4) hybrid microwave heating 250 W and 70˚C 5) hybrid microwave heating 250 W and 100˚C

Based on our application, 70˚C is assumed as the desired temperature in GF, so the temperature of the heat source is set to 100 ˚C. Figure 3 shows the temperature profile in GF, it can be seen that the heat is distributed homogenously inside GF.

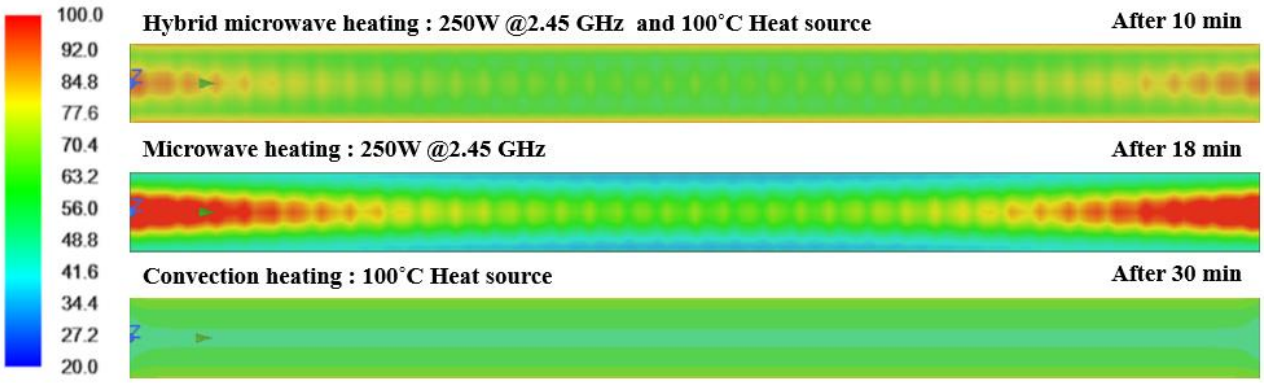

Fig. 3. Temperature distribution inside GF 1) hybrid microwave heating 250W and 100˚C 2) microwave heating 250W 3) convection heating 100˚C

References

[1] V. Tanrattanakul, and D. Jaroendee, "Comparison between microwave and thermal curing of glass fiber–epoxy composites: Effect of microwave-heating cycle on mechanical properties." *J. Appl. Polym. Sci.*, vol. 102, pp. 1059-1070, 2006. https://doi.org/10.1002/app.24245

[2] D. Teufl, S. Zaremba, "2.45 GHz Microwave Processing and Its Influence on Glass Fiber Reinforced Plastics." *Materials (Basel)*, vol. 11, no. 5, pp. 838, 2018. doi: 10.3390/ma11050838.

Microwave Modification of Softwood Round Timber for Preservative Treatment

G. Torgovnikov[1], P. Vinden[1], A. Leshchinskaya[2]

[1]*University of Melbourne, School of Agriculture, Food and Ecosystem Sciences,4 Water St.,Creswick, Victoria 3363, Australia*
[2]*Plekhanov Russian University of Economics. 36 Stremyannyy Pereulok,115093 Moscow, Russia*
grigori@unimelb.edu.au, pandsavinden@icloud.com, alixfl@mail.ru

Keywords: microwave applicator, microwave wood modification, preservative treatment, timber, cost

Abstract
The protection of wood from biological degrade is critical to increasing the service life of timber. Douglas fir (Pseudotsuga menziessi) and Radiata pine (Pinus radiata) heartwood have low permeability and are difficult to impregnate with preservatives. Microwave (MW) wood modification significantly increases wood permeability and improves preservative distribution and uptake. Experimental studies of microwave (MW) log modification and impregnation with preservatives demonstrated the effectiveness of the process. Main MW processing parameters have been determined. A cost analysis of MW conditioning of round timber indicates costs of AU$17–49/m^3 depending on electricity costs (in the range US$0.08 to 0.20$/kWh) and process requirements. These costs are acceptable for industry and provide good opportunities for commercialization of the new MW technology.

Introduction

The protection of wood from biological degrade is critical to increasing the service life of timber. The low permeability of many wood species causes problems during timber preservative treatment. Extreme difficulties take place in impregnating refractory timber species with preservatives and resins. Douglas fir (*Pseudotsuga menziessi*) and Radiata pine (*Pinus radiata*) heartwood have low permeability and are difficult to impregnate with preservatives. Therefore, it is essential for the timber industry to have a technology that can provide an increase in wood permeability. Intensive microwave (MW) wood processing provides a several thousand-fold increase in wood permeability in the radial, tangential and longitudinal directions [1]. It can be achieved in species previously found to be impermeable to liquids and gases. MW wood modification allows an improvement in the preservative treatment of posts and poles.

The practical application of microwaves to wood requires high intensity power, applied in short duration to provide the required degree of wood modification [2]. Raw material, whether round or sawn timber, can have large cross sections and a wide range of sizes. In some cases, it is necessary to modify the full cross section of timber. Research objectives in the present study include assessing the impact of MW processing of logs using a 300-kW microwave plant combined with a specialty MW applicator, studying the efficacy of the intense microwave energy on wood permeability and subsequent impregnation with preservatives, and assessing MW processing costs.

Material and methods

Material

Two species - Douglas fir and Radiata pine were used for experiments (Fig. 1). Twenty-nine green debarked Douglas fir logs with diameters ranging from 100 - 230 mm and 2.4-3.1 m in length were selected for this work. Percent wood moisture contents (MC) were found to range between 102-126% (average 122%) for sapwood and 38-47% (average 42%) for heartwood. The oven-dry density of the wood was in the range from 440-600 kg/m^3 (average 513 kg/m3) for sapwood and 350-560 kg/m^3 (average 480 kg/m^3) for heartwood.

Radiata pine peeler cores (cylindrical logs from central part of the tree stem) from plantation grown timber measuring 126-130 mm in diameter by 2600 mm long (280 logs) and 138 mm in diameter by 2600 mm long (29 logs) were used in experiments. Every log contained heartwood with different densities and moisture contents. Moisture content ranged from 18 to 36%. Oven dry density ranged from 373-468 kg/m^3 with an average of 426 kg/m^3.

Fig. 1. Douglas fir logs (left) and Radiata pine peeler cores (right).

Experimental plant

A 300 kW MW plant (frequency 0.922 GHz) was used for experiments (Fig. 2). The plant is capable of handling logs with diameters ranging from 100-300 mm and lengths of 4700 mm. The plant output was 0.5-2.5 m^3/hr, power was 30-300 kW, and feed speeds were up to 8.5 m/min.

Fig. 2. 300 kW MW experimental Plant for timber modification.

The key part of every MW plant is the applicator which must provide the required energy distribution within the timber. Applicator "350A" (Fig. 3) was used for round-wood processing. It has an aluminium cylindrical body (diameter 350 mm) and three radiator inlets (waveguides with open ends 60 × 200 mm) through which MW energy is supplied to the applicator. Vector electric field strength "E" orientation was parallel to wood grain.

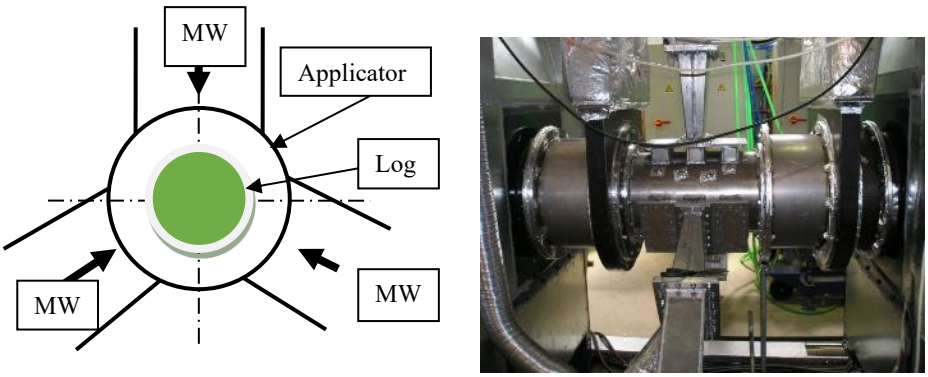

Fig. 3. Three port MW Applicator (350A) for wood modification.

MW power applied to the logs ranged from 90 to 150 kW measured by power meters during timber processing. The average MW intensity (flux) in the radiator cross section 60 × 200 mm ranged from 0.25-0.42 kW/cm^2. The required log speed was provided by a variable speed drive. Vapours released from the wood during modification were removed from the applicator using air flow with speed 10 m/sec at temperature 90-110ºC.

Experiment description

In these experiments the logs were conveyed via Applicator 350A. Logs were processed in the applicator using a MW power range of 90 – 150 kW. Speed for Douglas fir logs was 6-10 mm/sec and for Radiata pine peeler cores wasp 14-30 mm/sec. MW energy supplied to Douglas fir logs ranged from 150-200 kWh/m^3 and for Radiata peeler cores was 80-126 kWh/m^3.

After MW conditioning logs were pressure impregnated with water-based copper-chrome-arsenic (CCA) preservative using the following schedule: vacuum -85 kPa – 20 min, pressure 1300 kPa – 20 min, **and** final vacuum -85 kPa – 20 min. After MW processing and impregnation, the preservative distribution in the log cross sections and uptake were analysed. The

preservative distribution was determined by copper spot test reagent Chrome Azurol-S (CAS). The presence of copper was identified as a black or blue colouration on the cross section of logs.

Results and discussion

MW wood modification

During intensive MW processing the internal steam pressure ruptures ray cells and provides micro- and macro-voids in the radial-longitudinal planes. This structural wood modification increases wood permeability in the radial, tangential and longitudinal directions. After MW processing the logs had visible radial checks in heartwood and less visible checks in sapwood. Average wood moisture contents before and after MW log modification is presented in Table 1.

Table 1. Average moisture content (MC) of wood before and after MW modification.

Timber	Applied MW energy, kWh/m^3	MC before MW modification, %	MC after MW modification, %	MC loss, %
Douglas fir log	200	104	54	50
Sapwood		122	58	64
Heartwood		41	12	29
Radiata pine peeler core	90-110	22-30	10-11	12-19

Analyses of Douglas fir wood structure after MW modification identified that the wood was "over-modified". The logs had lost 50% of their original moisture content at applied energy 200 kWh/m^3. This is too high. Previous research with other species showed that required wood modification can be achieved at moisture losses of 25-35%**.** MW schedules for Douglas fir logs can be more moderate at lower energy consumption (e.g., 140-175 kWh/m^3). During MW modification the wood loses strength. Calculations of Douglas fir log bending strength (MOR) before and after MW modification, taking into consideration the width of the sapwood and different properties of heartwood and sapwood showed that, depending on degree of modification, the strength of MW treated logs reduces by 9 to 22%. Strength losses in this range can be acceptable in most cases.

The difference in modulus of elasticity and modulus of rupture of MW treated and non-MW treated Radiata peeler cores was not identified. Strength tests of 30 MW treated peeler cores with applied MW energy 110 kWh/m^3 showed the average log modulus of elasticity at MC = 21.7% was 6.6 GPa with a variation coefficient of 27.2%. The modulus of rupture was 31.9 MPa with a variation coefficient of 23.5%. The MW treated Radiata pine peeler cores can be rated grade F7 according to Australian Standard AS1720 (1997).

Log impregnation

After impregnation with CCA solution Douglas fir logs had uptakes ranging from 323-543 l/m^3 and an average of 439 l/m^3. Control samples had an average uptake of 93 l/m^3. MW modified logs had 4.7 times higher uptake compared to control samples. The higher uptake is evidence by the much higher permeability of Douglas fir wood after MW modification. Fig. 4 demonstrates that after MW modification it is possible to impregnate the full log cross section with water-based preservatives. Coloration of the log cross-sections indicates CCA distribution. There is virtually no penetration of preservative into the control samples.

Fig. 4. Solution distribution in Douglas fir log cross section after MW modification and impregnation (left photos) and controls (right photos).

The average CCA uptake of MW modified Radiata peeler cores was 326 l/m^3 with a coefficient of variation of 12.3%. For control logs CCA uptake was 35 l/m^3 with a coefficient of variation of 31.8%. The log uptake increases 9.3 times after MW processing. Thus MW modification provides very significant heartwood permeability increases. MW processing allows for the required preservative uptake and full cross section preservative distribution (Fig. 5).

Fig. 5. Solution distribution in Radiata peeler core cross section after MW modification and impregnation (left photos) and controls (right photos).

Increases in MW energy supplied to the peeler cores (from 90 to 110 kWh/m^3) did not show significant increase in CCA solution uptake or improvement in preservative distribution. This can be explained by the significant variability in wood moisture content, density and resin quantity in the wood. The minimum applied MW energy needed to provide full log cross section by water based preservative penetration is 90 kWh/m^3 applied at a frequency 0.922 GHz.

Costs of MW modification

An economic assessment of MW log conditioning has been completed with the aim of estimating specific production costs. This assessment has been based on technical data from experiments and world prices for equipment.

The economic assessments for microwave Douglas fir log and Radiata peeler core modification are given based on the following conditions:

1. Output 18,000 m^3/y (750 shifts per year, 6000 working hours per year), 3.0 m^3/h,
   12,000 m^3/y (500 shifts per year, 4000 working hours per year), 3.0 m^3/h.
2. Microwave conveyor plant at frequency 0.922 GHz for Douglas fir logs - MW power 400 kW, for Radiata peeler cores – 300 kW.
3. Microwave plant operates automatically.
4. Electric energy consumption for Douglas fir logs - 175 kWh/m^3, for Radiata peeler cores -110 kWh/m^3.
5. Electricity cost range from US$0.08/kWh to $0.20/kWh.
6. Cost of 400 kW microwave plant for Douglas fir logs - US$ 760,000; cost of 300 kW microwave plant for Radiata peeler cores - US$ 570,000.
7. Depreciation rate - 17%.

Fig. 6 provides specific costs for MW processing Douglas fir logs and Radiata peeler cores depending on plant output and electricity costs. The estimated specific costs include costs associated with capital, maintenance, magnetron replacement, and electricity costs. These costs do not include costs of mechanical installation, electrical connections, building, on costs (overheads) and taxes.

Electricity costs form the largest share of specific costs: for Douglas fir logs at electricity costs US$0.08-0.12$/kWh – 50-64% and at electricity costs US$0.16-0.20$/kWh – 67-78%;for Radiata peeler cores at electricity costs US$0.08-0.12$/kWh – 45-64% and at electricity costs US$0.16-0.20$/kWh – 62-75%.

A cost analysis of MW conditioning of Douglas fir logs indicates costs of approximately US$24 – 49/m^3 and Radiata peeler cores - US$17- 33/m^3 depending on electricity costs in the range US$0.08 to 0.20 $/kWh and process requirements. These costs are reasonable and acceptable for industry.

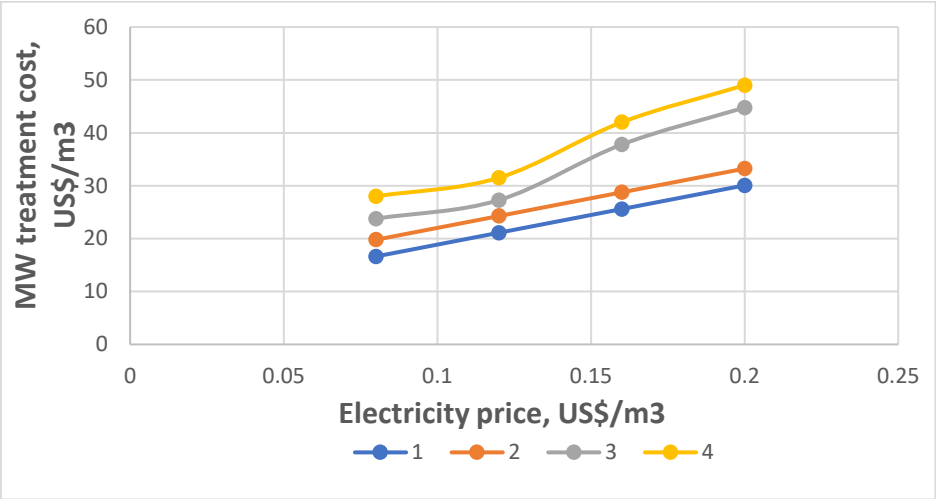

Fig. 6. MW log processing costs depending on plant output and electricity costs (frequency 0.922 GHz). 1- Radiata peeler cores, plant output18,000 m³/year, three working shifts per day; 2- Radiata peeler cores, plant output 12,000 m³/year, two working shifts per day; 3- Douglas fir logs, plant output 18,000 m³/year, three working shifts per day; 4 - Douglas fir logs, plant output 12,000 m³/year, two working shifts per day.

Conclusions

The MW modification of green Douglas fir logs provides an increase in wood permeability and facilitates full cross section impregnation with preservatives. MW modified logs had 4.7 times higher preservative uptake compared to control samples. MW modification reduces the strength of MW treated logs by 9 to 22% depending on the degree of modification.

The MW treatment increases heartwood Radiata pine permeability (based on uptake increase) for water based preservatives by 9.3 times and facilitates full cross-section preservative distribution. The difference in modulus of elasticity and modulus of rupture of MW treated and non-MW treated Radiata peeler cores was not identified.

Required microwave energy consumption for green Douglas fir log modification for preservative treatment is 140-175 kWh/m^3 at a frequency 0.922 GHz. The minimum applied MW energy needed to provide full Radiata peeler core cross section by water based preservative penetration is 90 kWh/m^3.

A cost analysis of MW conditioning of Douglas fir logs indicates costs of approximately US$24 – 49/m^3 and Radiata peeler cores - US$17- 33/m^3 depending on electricity costs in the range US$0.08 to 0.20$/kWh and process requirements. These costs are acceptable for industry and provide good opportunities for commercialization of the new MW technology.

References

[1] Vinden P., Romero J., Torgovnikov G. A method for increasing the permeability of wood, 2004, US Patent No 6,742,278.
[2] Torgovnikov G. and Vinden P. High intensity microwave wood modification for increasing permeability, Forest Product Journal vol 59, no 4, pp 84-92, 2009.

Electrification in Energy-Intensive Industries using Microwave Technology: A Case Study of the Successful DESTINY Project

B. García-Baños[1], A. M. López-Buendía[2], L. Guaita[3], P. Chiariotti[4], G. M. Revel[5], J. C. Martínez[6], J. L. Godes[7], K. Marks[8], L. Schmidt[9], D. M. Albuquerque[10], O. Centelles[11], D. Giannopoulos[12], K. Van Reusel[13]

[1]*ITACA Institute, Universitat Politècnica de València, Camino de Vera s/n, 46022 Valencia, Spain*
[2]*CEINNMAT, INNCEINNMAT, SL. C. Agustin Escardino, 9. Paterna-Valencia, Spain*
[3]*Keraben Grupo SA, Ctra. Valencia-Barcelona Km 44.3, 12520, Nules, Spain*
[4]*Dept. of Mechanical Eng., Politecnico di Milano, Via Giuseppe La Masa 1, 20156 Milano, Italy*
[5]*Dept. Indus. Eng. and Math. Sci., Univ. Polit. delle Marche, Via Brecce Bianche s/n, Ancona, Italy*
[6]*CEMEX Innovation Holding AG, General-guisan-strasse 6,6300 Zug, Switzerland*
[7]*Al-Farben S.A, Ptda. Torreta s/n, 12110, Alcora, Spain*
[8]*VDEH-Betriebsforschungsinstitut GmbH, Sohnstrasse 65, 40237, Dusseldorf, Germany*
[9]*K1-MET, Stahlstraße 14, 4020 Linz, Austria*
[10]*Instituto Superior Tecnico, Avenida Rovisco Pais 1, 1049-001, Lisboa, Portugal*
[11]*Chumillas Technology, Ctra. Onda, 2, 12540 Villarreal, Spain*
[12]*School of Mechanical Engineering, National Technical University of Athens, 15780 Athens, Greece*
[13]*LABORELEC, Rodestraat 125, 1630, Linkebeek, Belgium*
beagarba@upvnet.upv.es

Keywords: microwave heating, firing processes, industrial pilot plant, continuous processes

Manufacturing is a pivotal pillar of the European economy, contributing significantly to the region's Gross Domestic Product (GDP) with a value over € 6,553 billion and representing approximately 21% of the EU GDP. With the ongoing climate change legislation, fluctuating energy prices, and growing environmental consciousness, contemporary manufacturing must prioritize the incorporation of modern and renewable energy solutions while also emphasizing sustainability and eco-efficiency. These efforts are necessary to minimize the industry's carbon footprint and reduce its impact on the environment, while simultaneously ensuring its continued growth and competitiveness. Achieving further substantial energy reductions requires a targeted approach focusing on the most energy-intensive segments of the production chain, particularly the firing processes [1-3].

This work presents an innovative solution to perform eco-efficient firing processes based on a microwave applicator designed for high-temperature continuous material processing. It has been successfully applied to process materials from three sectors: Cement, Ceramics and Steel, in the frame of the European project DESTINY [4].

The key innovations of this development are described including the design of the kiln as a new modular and portable concept, the adaption of material formulation to optimize microwave absorption and the monitoring/control strategies implemented to increase the overall efficiency.

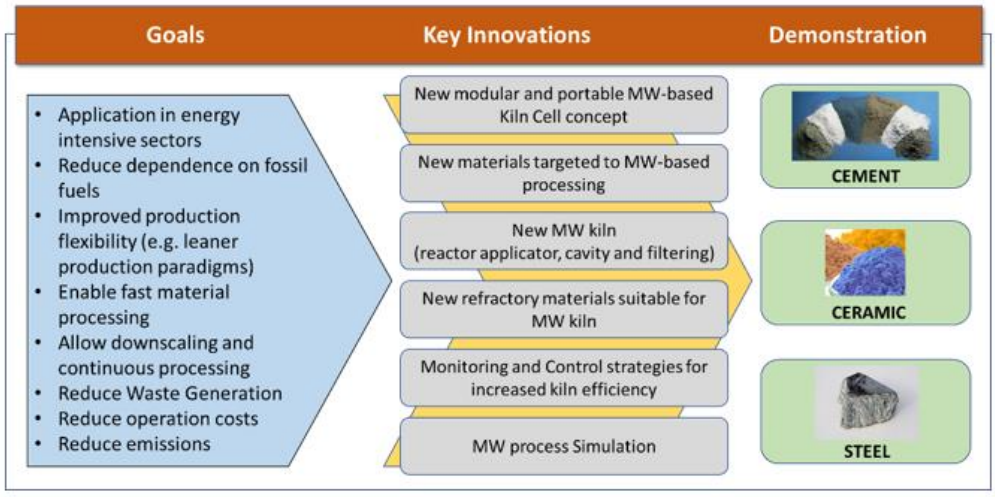

Fig. 1. Main goals, key innovations and addressed industrial sectors in DESTINY project.

The pilot plant performance has been evaluated with throughputs up to 45 Kg/h under operational conditions which are representative of a potential industrial application, resulting in significant energy savings. Studies of the system efficiency are presented for the different sectors, showing for example a heat demand of 450 KW/t in the case of clays for cement, which represents up to 35% energy savings with respect to conventional heating methods.

The present study has also covered the analysis of CO_2 emissions, OPEX, and CAPEX, to determine the technology's feasibility and environmental impact. A summary of the improvements is provided showcasing the potential of advanced microwave technology to drive sustainable industrialization and promote eco-efficient materials processing.

Acknowledgement
This research was funded by the European Union's Horizon 2020 research and innovation programme under grant agreement number 820783.

References

[1] United Nations (UN) (2015) Transforming our world: the 2030 agenda for sustainable development. [Online] Available: https://sustainabledevelopment.un.org/post2015/transformingourworld
[2] A.M. López-Buendía, B. García-Baños, J. Bastida, G. Llorens-Vallés, M. Urquiola, J.M. Catalá-Civera., "Microwave calcination of clays" in *3rd Global Congress on Microwave Energy Applications (GCMEA)*, 2016, pp. 145-149.
[3] M. Schneider, M. Romer, M. Tschudin, H. Bolio, "Sustainable cement production—present and future", *Cement and Concrete Research.* Vol. 41, No. 7, pp. 642-50, 2011.
[4] DESTINY (H2020-NMBP-SPIRE-2018) GA n° 820783. Development of an Efficient Microwave System for Material Transformation in energy INtensive processes for an improved Yield. [Online]. Available: https://www.destinyh2020andbeyond.eu/

Rapid Homogeneous Heating of SiC Based on Novel Solid-State Microwave Power Generators

V. Ramopoulos[1], G. Hintz[1]

[1]*TRUMPF Hüttinger, Germany*
vasileios.ramopoulos@trumpf.com

Keywords: microwave, SSPG, SiC, homogeneous heating

Nowadays, the heating of SiC wafers to very high temperatures of several hundred degrees represents a particularly energy-intensive and time-consuming task, mainly due to the low possible relative heating rates and the high requirements on temperature homogeneity. This motivates the investigation of new heating technologies that allow much higher heating rates and at the same time a well-controlled temperature distribution. In this context, microwave heating represents a promising technology due to its volumetric direct heating characteristics.

To investigate the heating behavior of SiC waver, the experimental setup shown in Fig. 1 is used. The basically consists of a TRUMPF Hüttinger's TruHeat MW 1000-0.3/2450 microwave generator directly connected in a TE111-mode microwave cavity. This field distribution allows a homogeneous heating of the used rectangular samples with an edge length of about 20 mm and a thickness of 0.35 mm. Furthermore, a pyrometer of type CS-LT15-SF is used for the temperature acquisition.

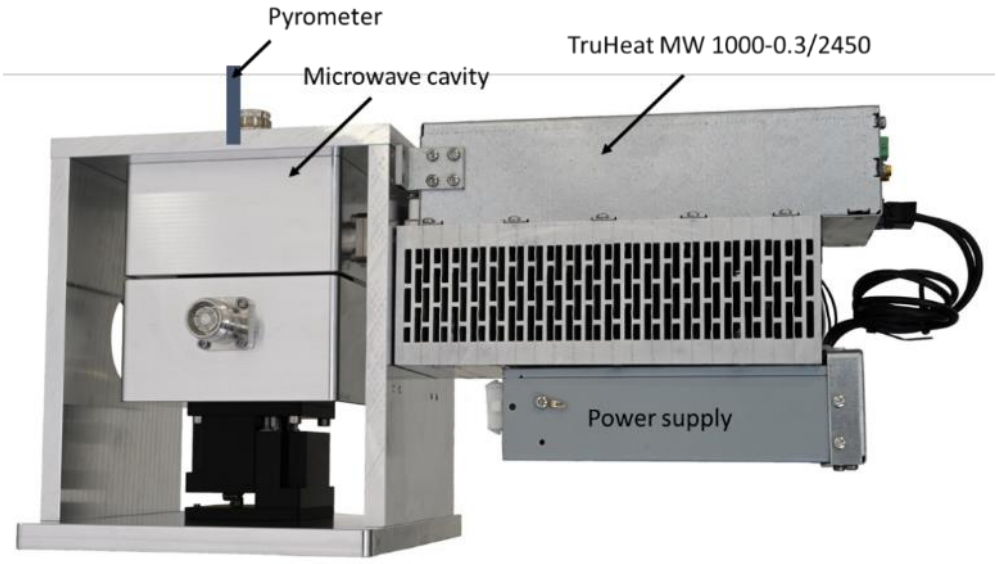

Fig. 1. Experimental setup consisting of TE111- mode cavity, TRUMPF Hüttinger's 300-Watt microwave amplifier and pyrometer.

Using a setup that is not optimized for this application, heating rates of well above 10 °C/sec at temperatures of a few hundred degrees were easily achieved. Furthermore, using the recorded reflection characteristics in combination with 3D full wave simulations, the dielectric material parameters of the SiC wafers used is recorded, which showed that the material can be heated simultaneously over the entire wafer thickness.

Since the potential feasibility of rapid heating of SiC wafers has been demonstrated, this application, like any microwave heating process in general, raises the question of future reproducible and reliable upscaling possibilities. In this context, TRUMPF Hüttinger's microwave generators of the TruHeat MW series are especially suitable due to their ability to switch between different frequencies within 1 ms. Thereby, the generator can independently sweep the entire ISM band between 2.4 and 2.5 GHz and identify all possible resonances within the MW applicator, with each resonance within a resonator being associated to a different field pattern/mode. Thus, by optimizing the combination of multiple field patterns (Fig. 2) a much higher field homogeneity over an area >> $\lambda/2$ can be achieved.

Since the TruHeat MW series is based on a highly modular design based on 300 W amplifier units in combination with suitable combiners, higher power classes of several kW can be realized to meet the requirements of each application.

Furthermore, TRUMPF Hüttinger's microwave generators feature a MTBF of > 100,000 hours stable output power compared to below 8,000 hours for conventional microwave sources (magnetrons) with creeping degradation of their output powers. These features ensure a reliable and stable process and, in combination with the modularity and suitably dimensioned redundant power, ensure an uninterrupted operation.

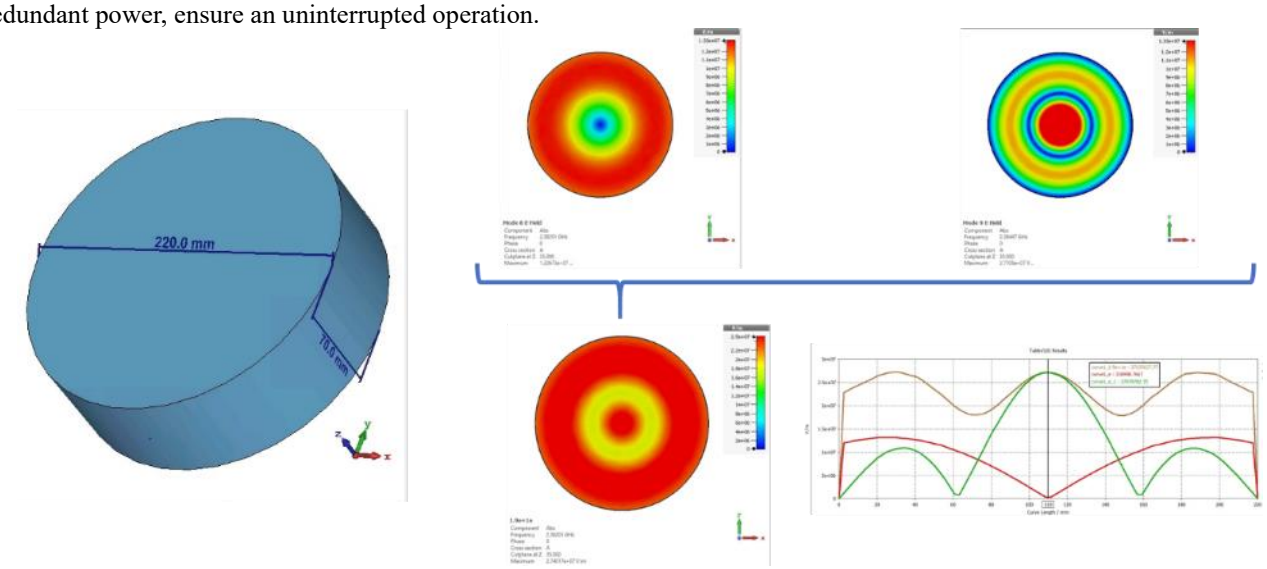

Fig. 2. Exemplary combination of two possible field distributions to achieve increased power distribution homogeneity. The colored images represent the electric field distribution in a cylindrical resonator and the diagram radial field strength distribution per mode (red and green curve) as well as the radial field distribution resulting from using them in combination (brown curve).

Design of Applicators and Components

Microwave Heating Applications of High-Power Coaxial-Cavity Stop-Band Filters

J. Monzó-Cabrera[1], A. Díaz-Morcillo[1], A. Martínez-González[1], A. Lozano-Guerrero[1], J. Fayos-Fernández[1], R. Pérez-Campos[1]

[1]Electromagnetics and Matter Group, Universidad Politécnica de Cartagena, Plaza del Hospital n.1, Cartagena, Spain
juan.monzo@upct.es

Keywords: microwave applicators, stop-band filters, mode stirrers, solid state generators, source decoupling

Introduction

Mode stirrers are a common method for ensuring uniformity in microwave applicators, and these stirrers occasionally need to be metallic due to mechanical constraints or chemical considerations. On the other hand, employing metallic mode-stirrers in high-power microwave cavities may cause unintended leakage or overheating; as a result, appropriate stop-band filters should be used to block microwaves from leaving the applicator [1-2].

On the other hand, the expanding usage of solid-state generators creates new opportunities for heating uniformity by integrating several frequencies, such as 915 MHz, 2.45 or 5.8 GHz, modes, and heating patterns, all within the same microwave cavity or applicator. However, this obviously calls for decoupling the generators, and as before, band-stop filters must be used at the relevant ISM frequencies [3–4].

High-power coaxial-cavity band-stop filters have additional applications in metrology, where they can be used to heat and measure material characteristics like permittivity, as shown in [5]. In this application, the coaxial-cavity filter would be used to detect a measurement mode while rejecting the mode used for microwave heating.

In this contribution, we suggest that all of these applications make use of the innovative high-power coaxial-cavity band-stop filters that were presented in [6]. We also provide various illustrations of how this new form of filter might be advantageous in microwave heating applications.

Foundations of high-power coaxial band-stop filters

A diagram of the coaxial band-stop filter is depicted in Figure 1. In order to incorporate a metallic axis for a mode stirrer, it can be seen that this sort of filter contains two coaxial ports and a coaxial cavity where the inner metal can rotate [6]. A potential design for the filter's size that would allow it to resonate at 2.45 GHz is shown in Table 1. These dimensions were obtained using the Interpolated Quasi-Newton optimization technique within the optimization tool of CST Studio Suite 2023. The objective of the optimization was to reduce the magnitude of S_{21} to zero at 2.45 GHz. The time-domain solver performed 808 evaluations throughout this optimization process.

Table 1. Optimized dimensions in cm for the coaxial-cavity resonator to provide a band-stop behaviour at the 2.45 GHz ISM band.

Dimension	Description	Value (cm)
a_1	Internal coaxial conductor radius	0.5
b_1	External coaxial conductor radius	1
L_2	Internal hight of the coaxial cavity (optimized)	1.6
b_2	Internal radio of the coaxial cavity (optimized)	5.133

The filter's S_{21} band-stop behavior for the dimensions specified in Table 2 is depicted in Figure 2, which shows how the coaxial cavity can attenuate signals by more than 20 dB in the 2.4–2.5 ISM band with a single cavity, and it can attenuate signals by 70 dB at 2.45 GHz.

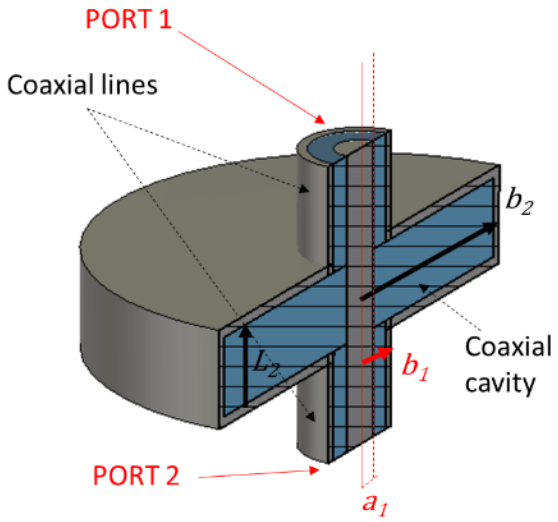

Fig. 1. Diagram of high-power coaxial-cavity band-stop filter.

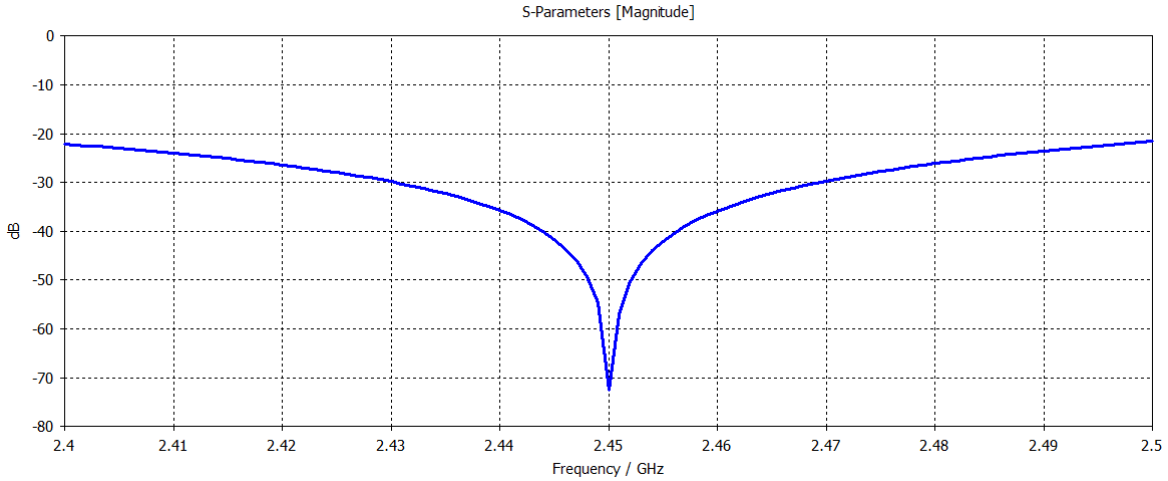

Fig. 2. $|S_{21}|$ behaviour of the high-power coaxial-cavity band-stop filter for dimensions shown in Table 1.

Figure 3 shows the electric field distribution within the filter at 2.45 GHz for a cross section including the coaxial propagation direction (above) and for a cross section perpendicular to that coaxial propagation direction (below). From the obtained results it can be observed that although a TEM mode is excited in port 1, a TM_{010} mode is excited in the coaxial cavity. Therefore, the electric field within the coaxial cavity is perpendicular to the TEM mode of the coaxial port. It can be observed that the electric field slightly couples with the TEM mode of port 2 due to the different polarization it has versus the TM_{010} resonating mode and, therefore, a high attenuation is produced between port 2 and 1.

Installation of metallic-axis mode stirrers

Figure 4 presents two simulation scenarios where a multimode microwave oven with inner dimensions equal to 41.2 cm × 41.2 cm × 21.2 cm is fed with a WR-340 waveguide installed at the central position on a lateral wall. The microwave oven has a simple metallic stirrer with a metallic shaft positioned at the centre of the upper wall of the applicator. A three-stage coaxial-cavity stop-band filter is used in the right scenario of Fig. 4 to reduce the leakage created by the stirrer coaxial line needed to introduce the stirrer shaft. Each stage of this coaxial filter has the same dimensions as the ones indicated in Table 1 for Figure 1. The three stages are concatenated by using coaxial lines with 4 mm length and the same dimensions as the ports in Figure 1 (with 50 Ω impedance). A 10 cm × 10 cm × 1 cm humid sand sample with a relative dielectric constant equal to 13 and a loss tangent equal to 0.29 is centred at the inner lower wall of the applicator. A coaxial port is included to calculate the S_{21} parameter regarding the WR-340 port and study the behaviour of the three-stage coaxial filter. The situation with no filter is also simulated for comparison purposes.

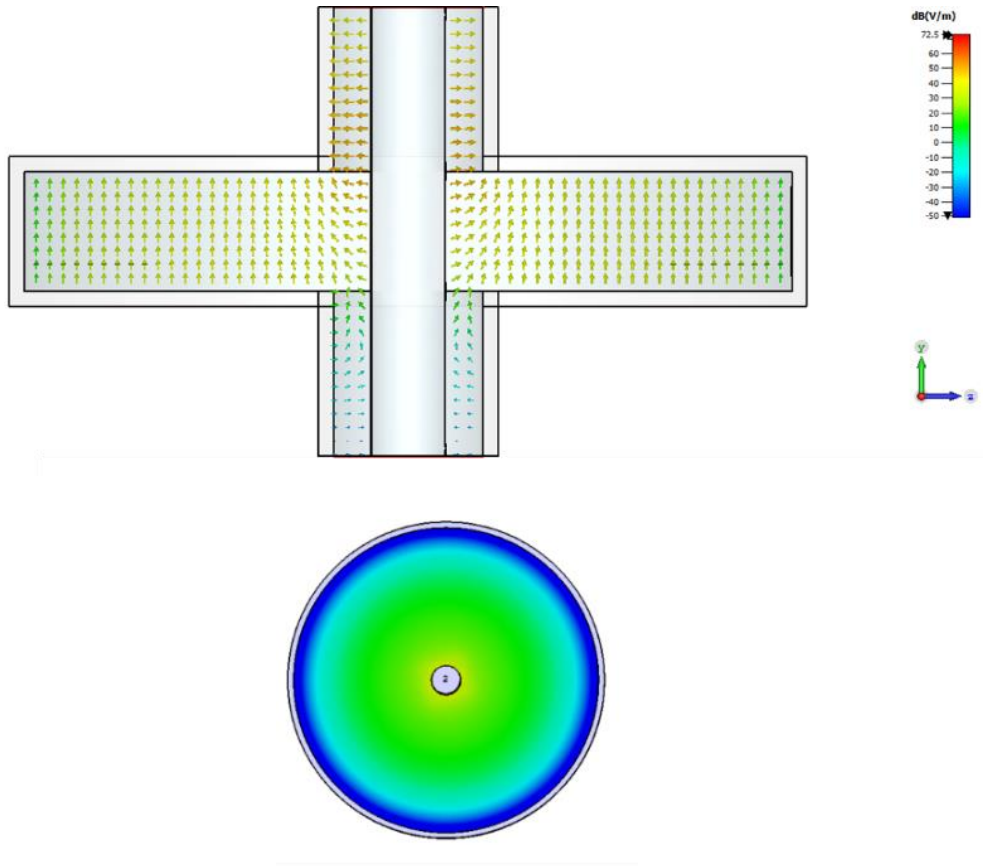

Fig. 3. Cross-section views for the electric field distribution in the high-power coaxial-cavity band-stop filter for dimensions shown in Table 1. Vectorial variation at the propagation direction (above) and variation of the magnitude with radius distance (below)

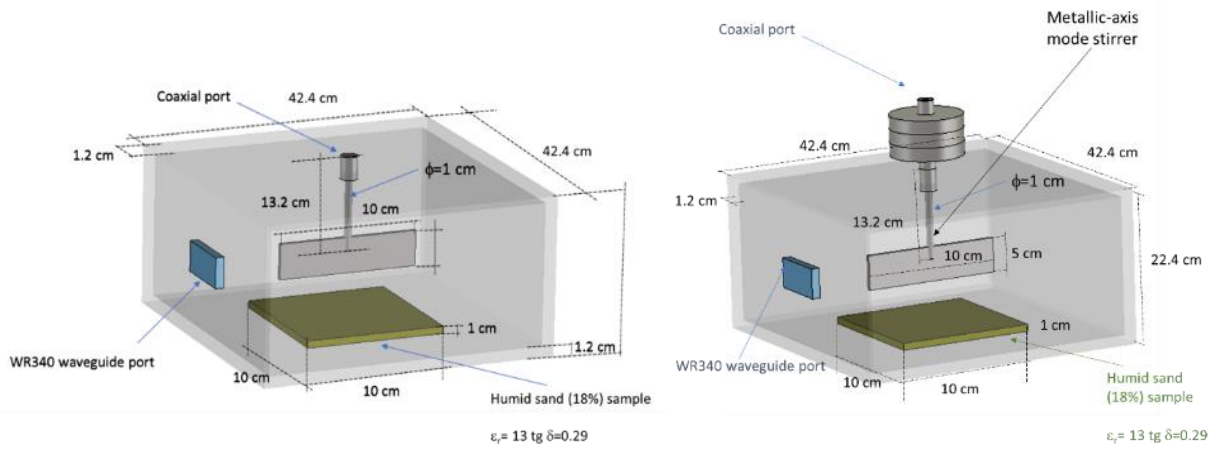

Fig.4. Structure for the introduction of a metallic-axis mode stirrer in a multimode microwave heating cavity without using a filter (left) and with a three-stage band-stop coaxial filter (right).

Figure 5 illustrates the power transfer from the WR-340 waveguide port to the coaxial port (S_{21}) as well as the reflection coefficient at that waveguide port (S_{11}), for both the scenario without (above) and with (below) the three-stage high-power coaxial filter. The results show that the waveguide port has good load matching for frequencies over 2.42 GHz and that, in the absence of a filter, the power loss from this port to the coaxial port is only about -10 dB for some frequencies. Accordingly, when no filter is used, 100 W could pass through this coaxial port when 1 kW is used in the waveguide port, leading to high leakage values or the overheating of the bearing balls that enable the mode stirrer to turn. However, an S_{21} with attenuation levels larger than 70 dB in the whole 2.45 GHz band is produced when the three-stage filter is used.

Therefore, the usage of this type of filter can be considered to introduce any device that uses a metallic axis with a high level of rejection for the 2.45 GHz ISM band. In comparison to the single-stage filter in Figure 1, the addition of multiple stages expands the stop-band and results in higher attenuation levels.

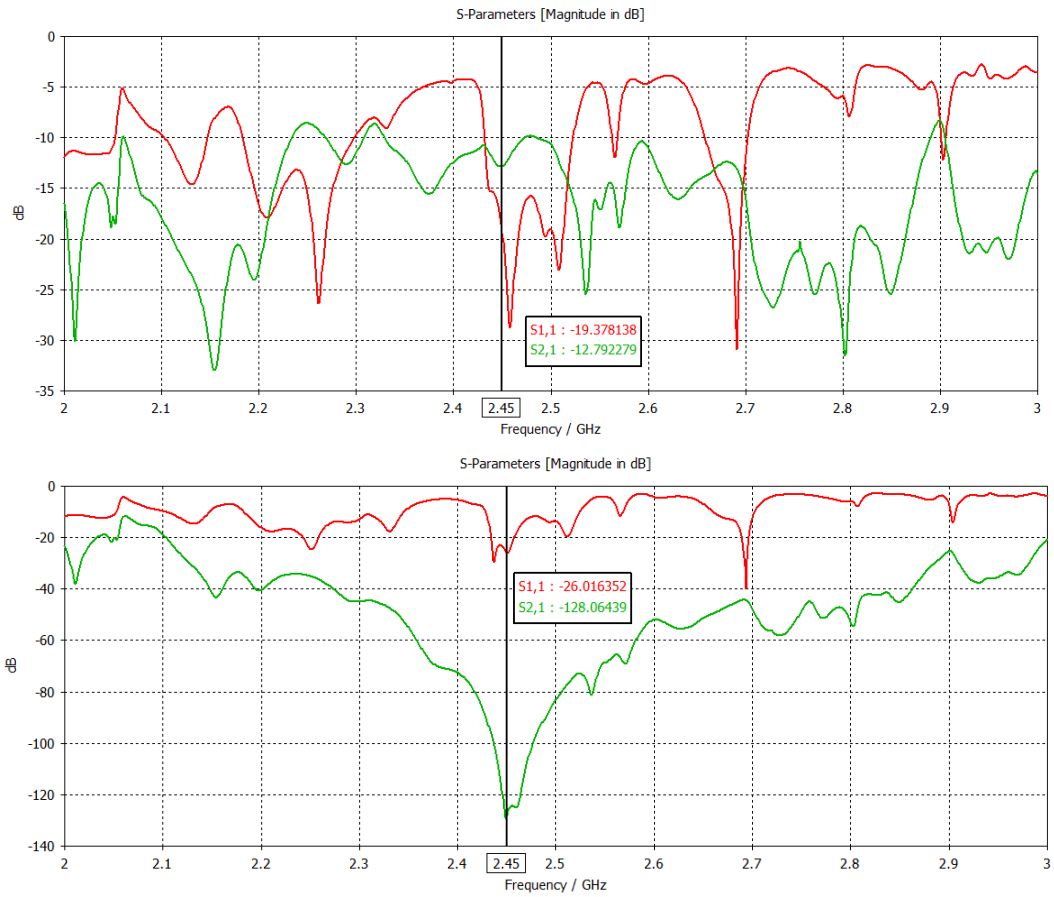

Fig. 5. Behaviour of the WR-340 port matching (S_{11}) and leakage estimation (S_{21}) without (above) and with (below) the three-stage high-power coaxial-cavity band-stop filter.

Other applications of coaxial-cavity stop-band filters

Figure 6 shows a possible application of this type of filters to simultaneously heat with solid-state generators at both 2.45 and 5.8 GHz without coupling the microwave sources. In this case, the higher-frequency solid-state generator can use a WR-159 waveguide to introduce the microwave energy in the cavity whereas the 2.45 GHz solid-state generator can irradiate the cavity through a coaxial-cavity band-stop filter centred at 5.8 GHz. In this way, the WR-159 waveguide would act as a cut-off waveguide for the 2.45 GHz electric fields, while the 5.8 GHz filter would decouple the 5.8 GHz power from the 2.45 GHz generator.

This same filtering scheme can also be used to irradiate and monitor the system behaviour at the same time with different frequencies. For instance, one could irradiate at 5.8 GHz with a microwave generator to heat the humid sand sample and sense through the coaxial filter and antenna the evolution of the reflection coefficient at the 2.45 GHz ISM band with a Vector Network Analyzer. The evolution of the reflection coefficient could be used to estimate the permittivity of the heated sample, its moisture content, or other magnitudes of interest.

Finally, this type of coaxial-cavity stop-band filter shown in figure 1 could be used for permittivity estimation due to its resonant behaviour. By filling the coaxial cavity with a dielectric material, the resonant frequency and Q-factor would be reduced, which in turn could be used for permittivity measurement. More research is envisaged in these directions to show the multiple applications of this type of resonant structure.

Conclusions

In this work, we have shown the foundations and some of the multiple applications of high-power coaxial-cavity stop-band filters initially presented in [6]. As can be deduced from the presented results, these filters can be very helpful in situations such as the usage of metallic stirrers, to decouple several solid-state generators working at different ISM frequencies or for low-signal measurements with simultaneous microwave heating processes. Permittivity estimation is also a possibility to explore due to the resonant nature of the coaxial cavities.

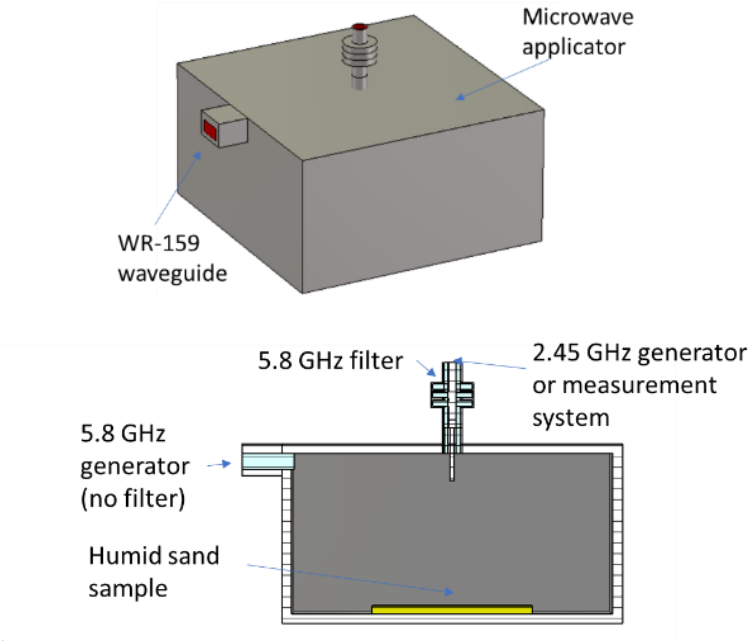

Fig. 6. Usage of several solid-state microwave generators with different ISM frequencies with very low coupling levels.

References

[1] P. Plaza-Gonzalez et al., Effect of mode-stirrer configurations on dielectric heating performance in multimode microwave applicators. IEEE Trans. Microw. Theory Tech. 2005, 53, 1699–1706.
[2] J. Monzó-Cabrera et al., Assessment of coaxial filters for the installation of metallic mode stirrers or turntables in multimode microwave ovens. In Proceedings of the 18th International Conference on Microwave and High Frequency Applications: AMPERE 2021,13–16 September 2021.
[3] V. V. Yakovlev, Effect of frequency alteration regimes on the heating patterns in a solid-state-fed microwave cavity, Journal of Microwave Power and Electromagnetic Energy, 2018, 52:1, 31-44.
[4] Ran Yang et al., Development of a complementary-frequency strategy to improve microwave heating of gellan gel in a solid-state system, Journal of Food Engineering, 2022, Vol. 314, 110763.
[5] Pérez-Campos, R. et al., Dynamic Permittivity Measurement of Ground-Tire Rubber (GTR) during Microwave-Assisted Devulcanization. Polymers 2022, 14, 3543.
[6] J. Monzo-Cabrera et al., A Novel Bandstop Filter Based on Two-Port Coaxial Cavities for the Installation of Metallic Mode Stirrers in Microwave Ovens, Electronics, 2022, 11, 1989.

Rectangular TE_{10} to Circular TE_{01} Converter for Microwave Heating Application

J. Tao[1], J.-P. Laviolette[2]

[1]*LAPLACE, Toulouse University, CNRS, INPT, UPS, Toulouse, France*
[2]*PYROWAVE Inc., Montreal, Canada*
tao@laplace.univ-tlse.fr

Keywords: mode converter, ridged waveguide, macro function, high power application

Circular waveguide modes with azimuthally symmetric electric fields find applications in a variety of systems such as electron cyclotron masers, gyrotrons, or linear colliders [1-6]. Their low wall loss is particularly appreciated in very high-power applications. Among these modes, the TE_{01} circular mode particularly attracts our attention because its lowest cutoff frequency exists between all low loss modes.

The practical use of this type of mode requires the development of mode converters starting from the rectangular TE_{10} mode or the coaxial TEM mode. We propose here a review of the mechanisms used in the development of converters whether by in-line coupling or by lateral coupling. A projection will be made in the main ISM frequencies used in microwave heating application in order to study the feasibility of each type of converter in this context.

Compared to the aforementioned applications, microwave heating uses much lower frequencies, which potentially poses the problem of converter size. The research of a compact structure becomes necessary, questioning the coupling mode usually used.

We will consider the design of this kind of converter as a macrofunction. In this device the introduction of some perturbation component leading the mode conversion but also the generation of a number of unwanted modes, since the circular TE_{01} mode is not the lowest one (Fig. 1). So, in this macrofunction all unwanted modes need to be minimized, as well as the return losses of the rectangular TE_{10} mode.

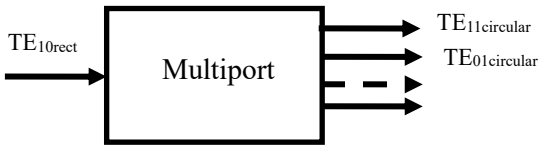

Fig. 1. Mode converter modelled by a microwave multiport

The ridged waveguide is widely used in the design of microwave filters and polarizers [7]. By inserting metallic ridges in a conventional rectangular TE_{10} to circular TE_{11} converter the electric field will be disturbed at several frequencies.

As can be observed in Fig. 2 at most frequencies in the working frequency band the output is mostly the circular TE_{11} mode at the frequency of 915 MHz. But for some specific frequencies there are different resonances depending the size, the position and the rotating angle of metallic ridges. For this testing structure with one pair of symmetric ridges positioned at 45 degrees from the vertical we have two resonances near 915 MHz. A very small increase of return losses occurs at 885 MHz but with a quasi TE_{01} field pattern. The other resonance at 934 MHz presents a peak of reflection; a great amount of TE_{01} mode can be observed. For this late case a small discontinuity placed very close to the ridged elements can be used to transform the rejection behavior to band pass behavior.

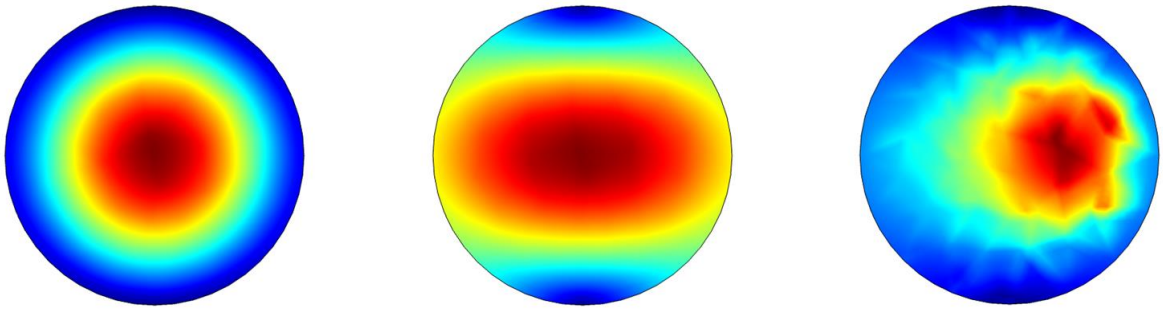

885 MHz 915 MHz 934 MHz

Fig. 2. Electric field at the output of a function of the permittivity for a dielectric bar

In the design procedure we will consider the transverse electric field at the output port referenced as $z_{ref,}$ shown in (1),

$$\vec{E}_t\left(\rho,\theta,z_{ref}\right)=\sum_{n=1}^{\infty}v_{TE}^{(n)}\left(z_{ref}\right)\vec{e}_{TE}^{\ (n)}\left(\rho,\theta,0\right)+\sum_{m=1}^{\infty}v_{TM}^{(m)}\left(z_{ref}\right)\vec{e}_{TM}^{\ (m)}\left(\rho,\theta,0\right) \qquad (1)$$

Here all circular TE and TM modes will be considered. For a given set of tuning parameters we can calculate the mode voltage $v^{(n)}$ and $v^{(m)}$ for all propagating modes (the others are negligible at a small distance from output plane).

Along with the input return losses an optimization design of the mode converter consists to minimize all coefficients except $v^{(2)}{}_{TE}$ corresponding to the circular TE_{01} mode, while $v^{(1)}{}_{TE}$ related to the circular TE_{11} mode must be very small.

References

[1] G. R. P. Marie, “Mode transforming waveguide transition,” U.S. Patent 2 859 412, Nov. 4, 1958.
[2] J. P. Tate, H. Guo, M. Naiman, L. Chen, and V. L. Granatstein, “Experimental proof-of-principle results on a mode-selective input coupler for gyrotron applications,” IEEE Trans. Microw. Theory Tech., vol. 42, no. 8, pp. 1910–1917, Aug. 1994.
[3] W. Wang, Y. Gong, G. Yu, L. Yue, and J. Sun, “Mode discriminator based on mode-selective coupling,” IEEE Trans. Microw. Theory Tech., vol. 51, no. 1, pp. 55–63, Jan. 2003.
[4] W. Lawson, M. R. Arjona, B. P. Hogan, and R. L. Ives, “The design of serpentine-mode converters for high-power microwave applications,” IEEE Trans. Microw. Theory Tech., vol. 48, no. 5, pp. 809–814, May 2000.
[5] T. H. Chang and C. F. Yu, “Polarization controllable TE mode converter,” Rev. Sci. Instrum., vol. 76, 074703, 2005.
[6] Z. Wu, X. Liao, K. Wang, M. Wang, Y. Pu, Y. Luo, "A Circular TE02 Mode Generator with High Purity for Gyro-TWT Study," IEEE Microw. Wirel. Compon. Lett. Vol. 30, pp.137–140, 2020,
[7] J.W. Tao, H. Baudrand, "Rigorous analysis of triple-ridge waveguides," Electronics Letters, Vol.24, pp.820-821, June 1988

A Monomode Microwave Rotary Kiln for High Temperature Applications

J. Vermeiren[1,2], V. Goovaerts[2], C. Groffils[2], J. Vleugels[1]

[1]*KU Leuven, Department of Materials Engineering, Kasteelpark Arenberg 44, 3001 Leuven, Belgium*
[2]*MEAM International, Centrum-Zuid 3060, 3530 Houthalen-Helchteren, Belgium*
jules.vermeiren@meam.be

Keywords: microwave, electrification, energy transition, rotary kiln, calcination, dehydration, sintering

In sectors like the cement and lime industry processes involving high temperatures like dehydration, calcination and sintering produce harmful emissions. Electrification of these heat treatments could lead to a reduction in CO_2, NO_x and SO_x emissions, as burning of fossil fuels would be avoided. Due to the volumetric heating, microwave (MW) technology may have the potential to electrify these processes in the most energy efficient way. In conventional cement kilns, for example, a flame temperature of ~2000°C is required to heat the reagents up to 1450°C via convection [1], whilst MW heating would occur directly in the product volume, without the need for higher temperatures in flames or heating elements. Published research on these topics is limited and often restricted to static sub-kg scale experiments in batch-type MW systems. To bridge the gap between laboratory and larger demonstrator installations, more knowledge is needed regarding the feasibility, controllability, reproducibility, etc. of high-temperature MW processes when carried out in a continuous rotary kiln type furnace.

In this work, a batch cylindrical monomode cavity (2.45 GHz) was converted to a continuous microwave rotary kiln for high-temperature dehydration, calcination and sintering treatments on a ~1 kg/h scale. The cylindrical resonant cavity, with adjustable cavity height, was equipped with top and bottom flanges with bearings to allow insertion of a rotating mullite tube (Figure 1). The reason for using a monomode resonance cavity was to benefit from multiple locations of high electric field (E-field) intensity (heating zones) along the length of the tube. Other systems, in which a tube is fitted through a simple waveguide, perpendicular to the wave propagation direction [2-4], only have a single heating zone and might require longer processing times or lower throughput volumes. Another reason for using a monomode cavity at resonance is the higher E-field intensity that can be reached, allowing direct MW heating of materials with less-favourable dielectric properties at low temperature, like limestone [5]. This differs from 'hybrid MW kilns', in which a susceptor is used to assist the heating via infrared radiation [6]. If needed, however, a susceptor can be incorporated in the current monomode system.

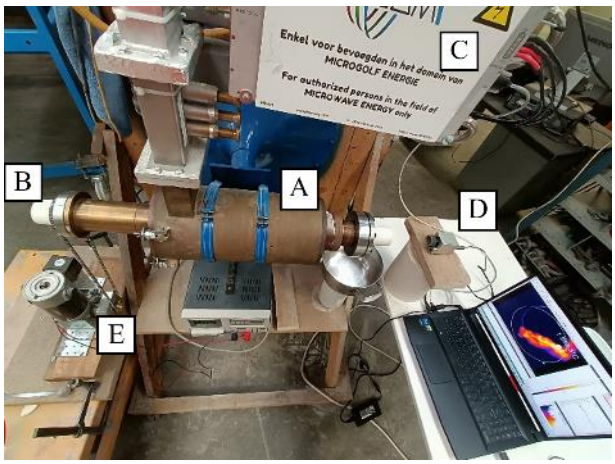

Fig. 1. Microwave rotary kiln setup, including the (a) cylindrical monomode cavity, (b) mullite tube, (c) solid state power source, (d) infrared camera and (e) chain drive for tube rotation.

The effects of the flanges, mullite tube, insulation material, etc. on the empty-cavity resonance E-field distribution was modelled using COMSOL Multiphysics software, and the predicted field distributions at resonance were experimentally verified using thin sheets of oily baking paper (Figure 2). Both the model and experiments verified the multiple-heating-zones concept. The model was successfully used to predict the thermal behaviour of a static load of polyamide powder.

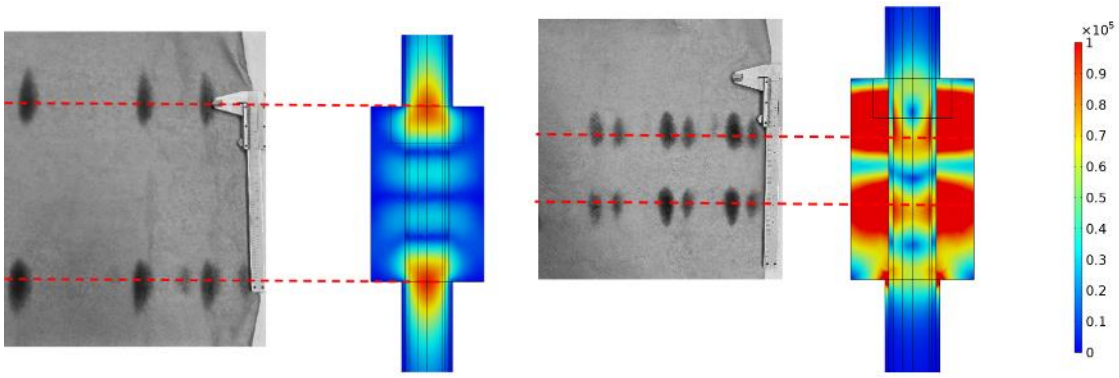

Fig. 2. Experimental validation of the modelled empty-cavity E-field distribution (V/m) at the two resonance cavity heights with thin sheets of oily baking paper. The modelled input power was 1 kW.

The high-temperature operation of the MW rotary kiln was positively validated for the calcination of dolomite and for the dehydration of hydrated cement paste (Figure 3), allowing the conversion of fine concrete waste into a recycled binder that can (partially) replace Portland cement in sustainable concrete [8, 9]. Plans for further validation experiments include calcination of limestones and clays.

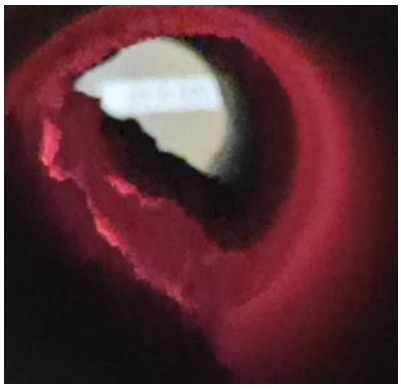

Fig. 3. Dehydration of hydrated cement paste in the MW rotary kiln at ~650°C.

References

[1] F. Schorcht, I. Kourti, B. M. Scalet, S. Roudier, and L. Delgado Sancho, *Best Available Techniques (BAT) Reference Document for the Production of Cement, Lime and Magnesium Oxide: Industrial Emissions Directive 2010/75/EU:(Integrated Pollution Prevention and Control). EUR 26129.* Publications Office of the European Union, JRC83006, Luxembourg, 2013.
[2] DAPhNE Project, *PROJECT FINAL REPORT: Adaptive production systems and measurement and control equipment for optimal energy consumption and near-to-zero emissions in manufacturing processes*. DAPhNE Project, 2015
[3] CEINNMAT, *Deliverable D3.6: Demo MW applicator validation*. DESTINY Project, 2021.
[4] CEINNMAT, *Deliverable 4.2: Optimization of BR microwave roasting and prototype furnace design*. RemovAl Project, 2021
[5] M. Fall, G. Esquenazi, S. Allan, H. Shulman, and Ceralink Inc., *Rapid Limestone Calcination Using Microwave Assist Technology*, in Proceedings ACEEE 2011 Summer Studies on Energy Efficiency in Industry, 2011.
[6] D. J. Hwang et al., *Characteristics of precipitated calcium carbonate by hydrothermal and carbonation processes with mega-crystalline calcite using rotary microwave kiln*, Journal of Industrial and Engineering Chemistry, vol. 20, no. 5, pp. 2727–2734, 2014.
[7] S. Real, A. Carriço, J. A. Bogas, and M. Guedes, *Influence of the treatment temperature on the microstructure and hydration behavior of thermoactivated recycled cement*, Materials (Basel)., vol. 13, no. 18, 2020.
[8] J. Wang, M. Mu, and Y. Liu, *Recycled cement*, Constr. Build. Mater., vol. 190, pp. 1124–1132, 2018

AMPERE 2023 - Survey of Low-Cost Matching-Networks for Radio-Frequency Heating of Structures with High Load-Resistance

R. Sallier[1,2], D. Schlayer[2], L. Nietner[1,2], B. Reimann[2]

[1]*Leipzig University of Applied Sciences, Karl-Liebknecht-Str. 132, 04277 Leipzig, Germany*
[2]*Advisory Council respectively member at FTZ e.V. Leipzig*
rene.sallier@htwk-leipzig.de, lutz.nietner@htwk-leipzig.de, bernd.reimann@htwk-leipzig.de

Keywords: radiofrequency, dielectric heating, matching-network, power applications

Abstract
Dielectric heating using RF-energy, in this case with the ISM-frequency of 13.56 MHz (**I**ndustrial, **S**cientific and **M**edical Band), is a good alternative to conventional techniques for heating and drying of many technical structures, as well as the chemical-free pest control in wood-based materials [1]. In order to achieve an adequate cost-benefit ratio such applications should be build with standard components like RF-generators typically realised with an internal resistance of 50 Ω. The substances in question of heating (e.g. wood, asphalt etc.) feature as dielectric load much higher effective resistances. Thus, there has to be matching network between generator and load together with reactive power compensation. This is the special problem regarding the fact that the load-resistances goes up to 10 kΩ. Additionally, the economic efficiency is highly dependent from the power efficiency of the matching network.

Objective is to develop a matching network featuring a transformation between high effective resistance load and generator by simultaneous compensation of reactive power and minimal power-losses in the matching network (see also [2]). The goal is to maximize the entry of active power in dielectric stuctures. In order to achieve the goal structures of matching networks featuring resonance-transformation were surveyed. In order to achieve the goal structures of matching networks featuring resonance-transformation were surveyed. The research was made theoretical and mathematical as well as in experimental setups and with a programmed calculation tool in addition with consideration of coil quality. Additionally, an experimental setup was built, featuring adjustable components using step-motors and a control facilitating a feedback control which detects the starting point of the match and adjusts the shift of the load-induced by heating in order to maintain the adjustment (see also [3]).

During the research, the electrophysical and technical limitations of different matching networks were investigated and demonstrated. For example, resonance transformation with two reactive components is limited by electrode design requirements, which requires intensive computational simulation and optimization.

This paper shows how cost-effective matching networks can be calculated and thus dimensioned and implemented. In the **Introduction** chapter, initial values regarding the load are presented and their determination from the point of view of power efficiency on condition that the matching network should be air-cooled. In the chapter **Fundamentals** two approaches to possible usable matching network structures via resonance transformation are presented. In the chapter **Design and calculation of the selected network structures** the theory of these matching networks is presented by an example. Finally, a summary and a conclusion are given in the chapter **Conclusion**.

Introduction

In order to delineate the individual system components for a dielectric heating system, a generally applicable modular structure was specified for a wide variety of applications. This structure basically includes an RF generator, a matching network (matchbox) and the RF-load. The structure is shown in Fig. 1. With this structure realized in the laboratory, analytical and experimental developments as well as investigations of network structures for impedance matching for the respective application fields considered are possible.

An RF-generator from the company Advanced Energy was used for the RF-generator module. This air-cooled RF-generator provides a maximum RF power of 1.5 kW. Different network structures were investigated for the matching network, which are explained in more detail in the Fundamentals chapter. In order to integrate different material types as RF-loads and to analyze the occurring impedances with regard to the matching possibility, different electrode configurations were used for the different applications such as wood and asphalt.

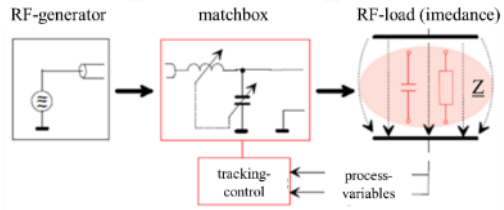

Fig. 1. Basic structure of the laboratory setup for dielectric heating of various applications.

For the applications heating of wood to control wood pests (circular electrode arrangement, left) and heating of asphalt slabs (single and double electrode configuration, center and right) is the electrode configurations showing in Fig. 2. For the applications heating of wood, a circular electrode configuration was used. For the applications heating of asphalt, a single plate capacitor arrangement was used on the one hand and a double electrode arrangement with ground plates on both sides on the other.

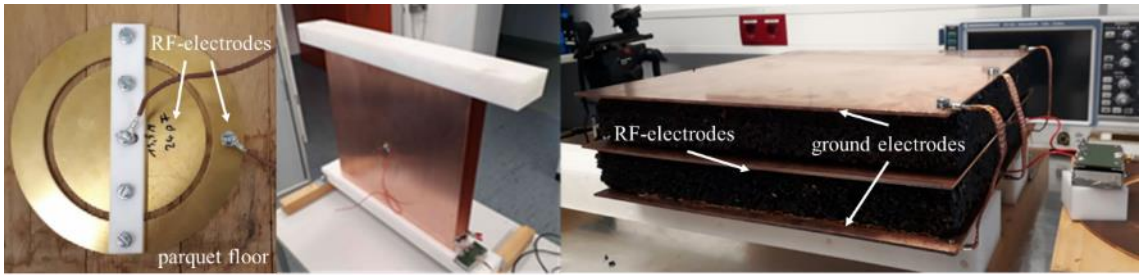

Fig. 2. Electrode configurations for dielectric heating for the applications wood (left) and asphalt(center and right).

Table 1 shows the electrical parameters of the respective applications measured with the aid of a VNA (Vector Network Analyzer).

Table 1. RF load-resistances of different applications wood and asphalt.

Application	Load-resistance range	Impedance value
Wood, moistened (after 1min)	>1 kΩ	$C_L = 21.0$ pF, $R_P \approx 5.7$ kΩ
Wood, dry	>10 kΩ	$C_L = 25.0$ pF, $R_P \approx 11$ kΩ
Asphalt, cold ($\vartheta = 22$ °C)	>10 kΩ	$C_L = 22.3$ pF, $R_P = 12.1$ kΩ

For the mentioned applications and their configured electrode systems (see Tab.1.) different network structures were investigated with the aim to develop a matching network which allows a transformation between load and generator with simultaneous compensation of the reactive power and minimal power losses in the matching network. This is presented in more detail in the Fundametals chapter.

Fundamentals

Basically, two network structures were investigated for matching the presented applications with respect to their impedance:

- resonance transformation with 2 reactive components
- resonance transformation with 3 reactive components

Resonance transformation with 2 reactive components

In resonance transformation, the real internal resistance R_i of a generator is transformed to another value of the real load-resistance by utilizing the voltage or current boost at the reactive elements L and C. The transformation is then applied to real components. The consideration is first done for ideal components and then for extended to real components.

Ideal components

Since $R_a > R_i$ is valid for the applications, an upward transformation must be realized. A possible network structure for upward transformation with 2 reactive components is shown in Fig. 3.

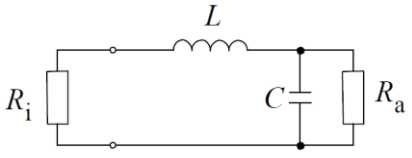

Fig. 3. Upward transformation $C||R_a$

Assuming ideal components for the resonance transformation with 2 reactive components, the equivalent circuit applies at the operating frequency:

$$R_i + j\omega L = R_a || \frac{1}{j\omega C} \qquad (1)$$

The circuit structure shown in Fig. 3 basically offers the advantage that the capacitance of the electrode configuration for dielectric heating can already be included in the necessary capacitance C for the resonance transformation.

With the approach from (1) according to the circuit in Fig. 3. after the conjugate complex expansion and the comparison of the real and imaginary parts, the required reactances can be calculated and with the given frequency can be calculated the corresponding values of the components:

$$X_C = \sqrt{\frac{R_i \cdot R_a^2}{R_a - R_i}} \text{ whereby } C = \frac{1}{j\omega X_C} \qquad (2)$$

and

$$X_L = \sqrt{R_i \cdot (R_a - R_i)} \text{ whereby } L = j\omega X_L. \qquad (3)$$

Using the normalization approach $n = \frac{R_a}{R_i}$, the following normalized equations are obtained:

$$\frac{C}{C_0} = \frac{\sqrt{n-1}}{n} \text{ with } C_0 = \frac{1}{\omega R_i} \qquad (4)$$

and

$$\frac{L}{L_0} = \sqrt{n-1} \text{ with } L_0 = \frac{R_i}{\omega} \qquad (5)$$

From these functions the necessary values for L and C can be calculated with variable load-resistance R_a and given internal resistance R_i at a fixed frequency ω. Fig. 4 shows the function curves $\frac{C}{C_0} = f(n)$ (left) and $\frac{L}{L_0} = f(n)$ (right) according to the normalized equations (4) and (5).

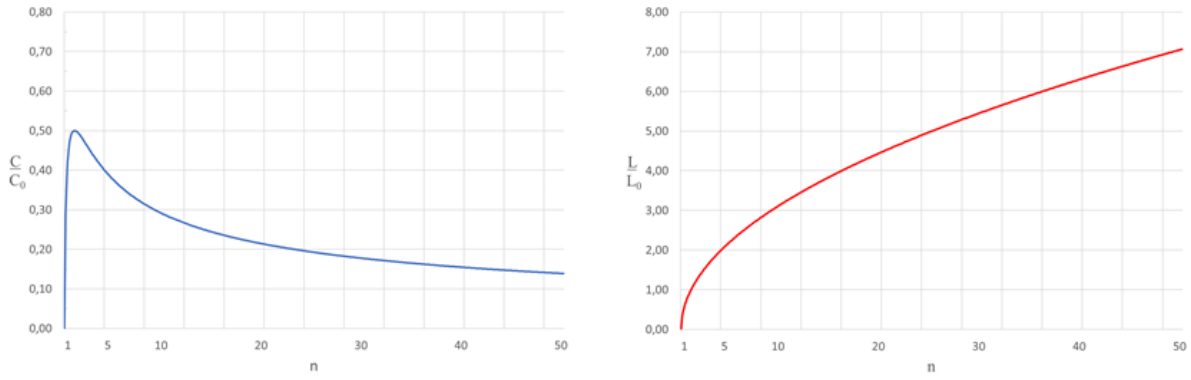

Fig. 4. Function curves $\frac{C}{C_0} = f(n)$ (left) and $\frac{L}{L_0} = f(n)$ (right) according to the normalized equations (4) and (5).

For values $n < 2$, the resonance transformation does not provide usable values, since the resonance becomes ineffective when $n = 1$ is matched. Furthermore, it can be seen from the normalized function curve $\frac{C}{C_0} = f(n)$ in Fig. 4. that for very high impedance loads (resistance and reactance respectively capacitance) the tuning range becomes very sensitive, since the ratio $\frac{C}{C_0}$ remains almost constant. This results in the basic equivalent circuit for a matching circuit with 2 reactive components (Fig. 5.). In the course of the heating process, a change of the capacitive and the ohmic component of the load-impedance is to be expected, so that the tuning condition to a $SWR = 1$ at the generator must be constantly readjusted via the variable quantities L and C.

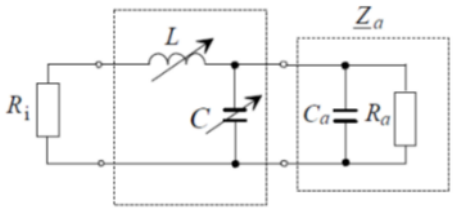

Fig. 5. Matching circuit by applying a resonance transformation with 2 reactances

Real components

The real components coil and capacitor cannot be manufactured loss-free. Furthermore it has to be considered practically that the resonance frequency of the used components should be sufficiently high compared to the operating frequency 13.56 MHz. Since the losses as well as the cutoff frequency of the components used depend essentially on the design of the components, these values can be determined by measurement and represented by means of a suitable equivalent circuit. For capacitors, the practical values of the achievable quality Q are about 1000 and more (e.g. for vacuum capacitors). For coils in the large range, values for the quality Q of 50 to 500 are achievable. In the literature [4], coil qualities up to about 1000 are mentioned for high-impedance circuits. The losses of the capacitors can therefore be neglected compared to the losses of the coil. Fig. 6. shows the circuit of the resonance transformation, extended by the series equivalent resistance of the coil.

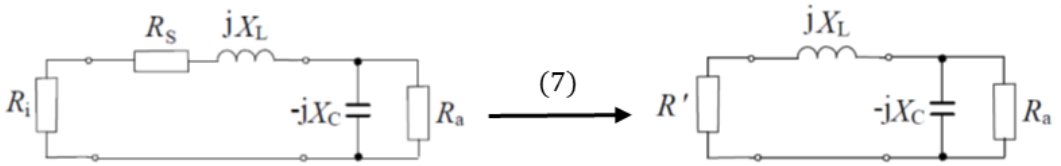

Fig. 6. Calculation for resonance transformation using the auxiliary quantity

The following relationship applies to the quality Q_L:

$$Q_L = \frac{X_L}{R_S} \qquad (6)$$

The series equivalent resistance R_S describes all acting ohmic losses of the real coil. To calculate the matching network for the upward transformation according to Fig. 6. applies:

$$R' = R_i - R_S \qquad (7)$$

By comparison according to equation (1) concerning the admittance $\underline{Y}_a$ of the parallel circuit with the equivalent series equivalent circuit and after the conjugate complex expansion, the following relationship arises:

$$\underline{Y}_a = \frac{1}{R_a} + j\frac{1}{X_C} = \frac{1}{\underline{Z}'} = \frac{1}{R'+jX_L} = \frac{R'}{R'^2+X_L^2} - j\frac{X_L}{R'^2+X_L^2} \qquad (8)$$

By comparing the real and imaginary parts, the required reactive components can be calculated. It applies:

$$\frac{1}{R_a} = \frac{R'}{R'^2+X_L^2} = \frac{R_i-R_S}{(R_i-R_S)^2+X_L^2} = \frac{R_i-d_L X_L}{(R_i-R_S)^2+X_L^2} \text{ mit } d_L = \frac{1}{Q_L} = \frac{R_S}{X_L} \qquad (9)$$

The loss factor of the real coil is describes through d_L. The conversion to X_L yields a quadratic equation:

$$X_L^2 + \left(\frac{(R_a-2R_i)d_L}{1+d_L^2}\right)X_L + \left(\frac{R_i^2-R_aR_i}{1+d_L^2}\right) = 0 \qquad (10)$$

If the loss factor d_L is substituted by the quality Q_L and the normalization $n = \frac{R_a}{R_i}$, the following applies:

$$X_L^2 + \left(\frac{R_i(n-2)Q_L}{1+Q_L^2}\right)X_L + \left(\frac{R_i^2(1-n)Q_L^2}{1+Q_L^2}\right) = 0 \qquad (11)$$

Since a quadratic equation results for the reactance of the coil, the reactance of the capacitor can only be calculated afterwards. The following applies to the reactance of the capacitor:

$$\frac{1}{X_C} = -\frac{X_L}{(R_i-d_L X_L)^2+X_L^2} \qquad (12)$$

Using the comparison $(R_i - d_L X_L)^2 + X_L^2 = R_a(R_i - d_L X_L)$, from equation (9), equation (12) holds:

$$\frac{1}{X_C} = -\frac{X_L}{R_a(R_i-d_L X_L)} \qquad (13)$$

After inserting the quality Q_L and the normalization $n = \frac{R_a}{R_i}$ is valid:

$$X_C = -nR_i\left(\frac{R_i}{X_L} - \frac{1}{Q_L}\right) \qquad (14)$$

Thus, if the coil quality is known, the matching network with 2 blind elements (reactive elements) can be designed accordingly for the upward transformation.

Resonance transformation with 3 reactive components (π-circuit respectively Collins filter)

In contrast to the resonance transformation with 2 reactive components, where the matching can only be achieved with a fixed assigned value pair L and C, the resonance transformation by means of 3 reactive components allows a degree of freedom for the choice of a reactive component, so that a further parameter must be specified. A matching circuit with 3 reactive components represents the classical low-pass filter in π- or T-replacement circuit. Since the electrode arrangement in dielectric heating is capacitive due to the system, the π-circuit is suitable, since the electrode capacitance is already included in the output capacitance C_a of the π-circuit.

Usually, an operating quality is specified for the π-circuit (two port network theory) for the direction of energy flow from the generator to the load. As the operating quality of the filter increases, the bandwidth of the two port network for the dimensioned frequency decreases and the resonance sharpness increases. Thus, the necessary voltage boost for a high-impedance terminating resistor R_a is achieved. Since the intended applications for dielectric heating work with only one frequency (working frequency of 13.56 MHz), a derivation can be simplified by introducing an auxiliary resistor (Fig. 7. left). For this purpose, the inductance L is split in the π-circuit and an auxiliary resistor R_i' is introduced, which forms the internal resistance for the transformation in the two subcircuits. This approach actually produces a downward transformation for the first subcircuit, i.e. $R_a' > R_i'$ must apply. The known generator internal resistance R_i of the π-output circuit becomes the upward transformed load-resistance R_a' of the first subcircuit. The potentials across the resistors R_i' are equal in both subcircuits, so that the auxiliary resistor can be eliminated again after the calculation and the two inductances are to be added ($L = L' + L''$). With this separation of the π-circuit into two transformation stages, the already known calculation principle of the transformation by means of 2 reactive components can be applied one after the other, as the following example will show, see Fig. 7.

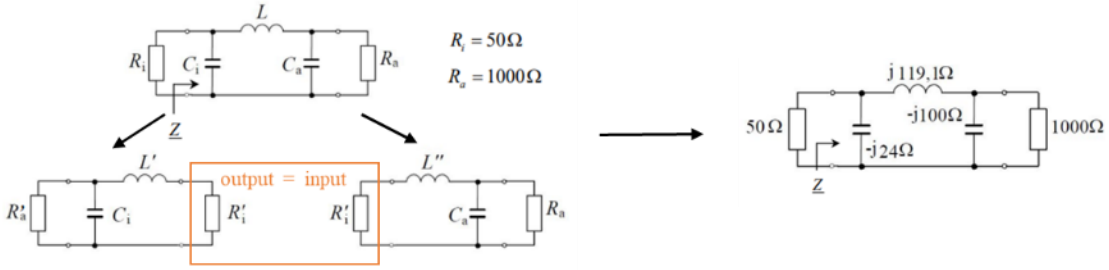

Fig. 7. Numerical example of resonance transformation by means of π-circuit.

$R_i' = 10\ \Omega$ chosen → $C_0 = \frac{1}{\omega R_i'} = 1174$ pF and $L_0 = \frac{R_i'}{\omega} = 117.4$ nH

$n = \frac{R_a'}{R_i'} = \frac{50\ \Omega}{10\ \Omega} = 5$ $\qquad$ $n = \frac{R_a}{R_i} = \frac{1000\ \Omega}{10\ \Omega} = 100$

Thus, according to equations (4) and (5):

$C_\mathrm{i} = C_0 \frac{\sqrt{n-1}}{n} = 488$ pF → $-jX_{C_\mathrm{i}} = -j24\ \Omega$ $\qquad$ $C_\mathrm{a} = C_0 \frac{\sqrt{n-1}}{n} = 116.8$ pF → $-jX_{C_\mathrm{a}} = -j100\ \Omega$

$L' = L_0\sqrt{n-1} = 234$ nH → $jX_{L'} = j20\ \Omega$ $\qquad$ $L'' = L_0\sqrt{n-1} = 1164$ nH → $jX_{L''} = j99\ \Omega$

With $L = L' + L'' = 1{,}4$ µH results $jX_L = jX_{L'} + jX_{L''} = j119\ \Omega$.

The level of the reactive currents is influenced by the choice of the auxiliary resistor and thus the resonance sharpness of the filter. If the load-impedance changes to higher electrode capacitances and a more highly resistive active component, the auxiliary resistor R_i' must be reduced. This causes the reactive currents to rise sharply, so that the power dissipation at the real coil also increases, which in turn reduces the efficiency of the matching circuit. Thus, the Collins filter must also be calculated taking into account the quality of the coil.

Design and calculation of the selected network structures (see Fundamentals)

For this detailed calculation a calculation routine has been developed, which calculates the values of the components. This calculation routine determines the output capacitance and the output resistance, see Introduction. Based on this, a calculation of the elements of the matching network with and without coil quality can be done, see Fundamentals.

The calculated values can then be used to perform an efficiency calculation. The efficiency is defined as the ratio of the converted active power P_a at the active resistor R_a to the delivered generator active power P_{Gen}. While the auxiliary resistance R_i' only represents a calculation aid and is not a real component, this does not apply to the coil quality Q_L. The efficiency of the matching depends on it. The efficiency of the matching network depends on it significantly. The higher the coil quality, the higher the efficiency of the overall system (see Fig. 8.). As can be clearly seen, however, improving the coil

quality from a value of approx. $Q_L = 150$ is only of limited use, since the curve asymptotically approaches a maximum value. This corresponds with the fact that "real" coils with a quality of greater than 150 are increasingly difficult to realize in this frequency range.

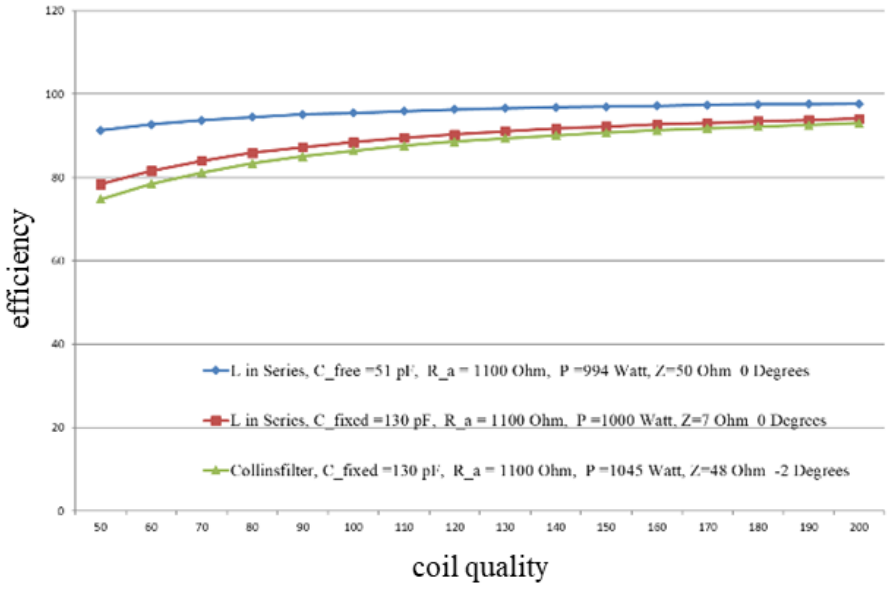

Fig. 8. Illustration of the efficiency as a function of the coil quality.

If an efficiency or the coil quality of the π-circuit is specified, the auxiliary resistance R_i' is no longer freely selectable. In this case, the auxiliary resistance is given by the ratio of R_a to C_a. It can be seen that for careful dimensioning of the π-circuit, it is essential to consider the efficiency of the matching circuit and sets limits to the practical application. If input powers greater than 1 kW are required, the efficiency of the matching circuit plays a decisive role, since the power dissipation of the coil must be dissipated by cooling. Power losses of a few 100 W can be dissipated by air cooling. For power losses above 1 kW, water cooling is required.

In order to introduce higher RF powers into the asphalt sample, the electrode configuration was changed - capacitive arrangement double electrodes for two asphalt samples, see Fig. 9. Here the electrode configuration was dimensions of electrodes 400 mm × 400 mm × 52 mm with 2 asphalt samples against inner electrode and outside 2 × ground electrode.

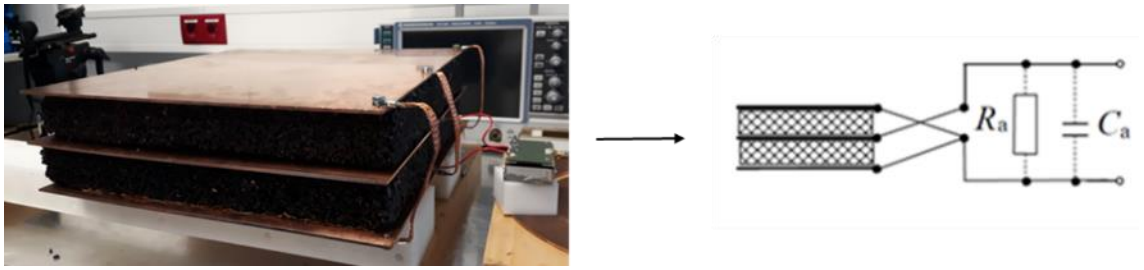

Fig. 9. Measuring arrangement and set-up for capacitive arrangement of double electrodes for two asphalt samples

Table 2. Measurement results of the measurement setup for a working frequency of 13.56 MHz.

Measurements (VNA)	Load-resistance range R_a	Impedance value C_a
1	1.9 kΩ	238 pF
2	1.4 kΩ	268 pF

The measured values of measurements 1 and 2 from Table 2 fluctuate due to slight changes in the laboratory setup. In addition, when the electrode plates are enlarged, the influence of the stray fields and thus the influence of the spatial conditions increases. However, due to the ground plates on both sides, the spatial stray fields decrease again. The arrangement can be driven asymmetrically. The ground connection should be guided symmetrically. The pairs of plates electrically form a parallel circuit, which leads to approximately doubling of the electrode capacitance and halving of the effective component. A π-circuit was used as the matching circuit. The following values were obtained with the developed calculation routine: $C_1 = 1300$ nF, $L = 0{,}58$ µH, $C_2 = 268$ pF

A $SWR = 1$ could be set by a slight readjustment. The control was done with $P_{Gen} = 200$ W. However, due to the high reactive currents ($I_{C_1} \approx 12$ A) the supply line heated up strongly (Fig. 10.).

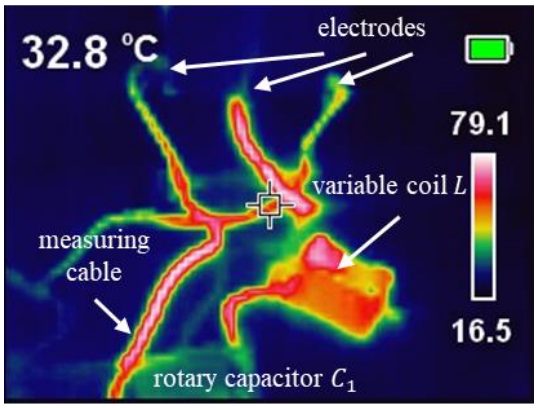

Fig. 10. Heating of the supply line of the measuring arrangement and measuring setup for the capacitive arrangement of double electrodes for two asphalt samples.

After adjustment, the tuning elements were re-measured and showed good agreement with the dimensioning specification from the calculation routine. The coil quality was nearly $Q_L = 120$, so that the circuit was first recalculated with ideal components (Fig. 11.).

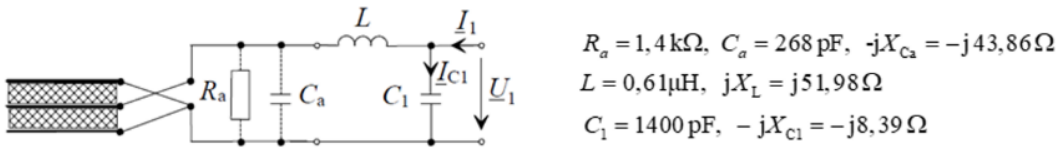

Fig. 11. Recalculation of the circuit with ideal components

The following values were obtained, see Table 3.

Table 3. Calculation of the values.

Element	Values
Input resistance	$\underline{Z}_1 = \underline{Z}_{c_1} \| \underline{Z}_L + \underline{Z}_a = 49.9\ \Omega\angle -0.15°$
Generator	$P_{Gen} = 200$ W, $R_i = 50\ \Omega$, $U_1 = 100$ V und $I_1 = 2$ A
Reactive current through C_1	$\underline{I}_{c_1} = \dfrac{\underline{U}_1}{\underline{Z}_{c_1}} = 11.9\ \mathrm{A}\angle 90°$
Reactive current through L	$\underline{I}_L = \dfrac{\underline{U}_1}{\underline{Z}_L + \underline{Z}_a} = 12\ \mathrm{A}\angle -80.5°$
Voltages	$\underline{U}_L = \underline{I}_L \underline{Z}_L = 625\ \mathrm{V}\angle 9.5°$ und $\underline{U}_a = \underline{I}_L \underline{Z}_a = 525\ \mathrm{V}\angle -169°$
Results	$P_{forward} = \dfrac{U_a^2}{R_a} = 196$ W

If the series loss resistance of the coil is calculated from the measured coil quality $Q_L = 120$, a value of $R_S = 0.43\ \Omega$ results. With the coil current, this results in a power loss of $P_{loss} = R_S I_L^2 = 62$ W. This value proves the strong heating of the coil and contradicts the calculated forward power $P_{forward} = 196$ W with ideal components. The quality or the converted power dissipation at the coil decisively determines the efficiency of the matching circuit and cannot be neglected. In principle, the objective is to minimize the reactive currents, but this imposes limits on the upward transformation. This coincides with the investigations on resonance transformation by means of 2 reactive components.

Conclusion

The possibility of realizing low-cost matching networks for dielectric heating applications of load structures with a high resistive component, represents an essential prerequisite for the use of a wide variety of dielectric heating applications. In this context, the influence of the load with high resistive components is considered difficult to evaluate. Thus, in addition to a suitable network structure with sensible dimensioning with respect to the objective of minimal reactive currents in the reactive elements, the electrode design with respect to the coupling into the load must also be taken into account. Here, a very good design possibility exists if the electrode design for coupling into the load can be included in the design of the matching network, see Fig. 5. If too high reactive currents place too great a thermal load on the matching network, a concept of cooling by means of fluids must be used instead of air cooling.

In summary, this paper shows that it is possible to design inexpensive matching networks according to the presented concept and at a fixed operating frequency (13.56 MHz). However, limits are also are shown with respect to the efficiency of such a

system. Basically is to be noted that from a very high ohmic component ($(> 10\ \mathrm{k}\Omega$) the efficiency of such a system decreases significantly due to the physical due to the physical interrelationships. Fig. 12. shows the structure of the controllable matching network (inner structure) can be seen (left, center). In the right picture of Fig. 12. the programmed surface is shown.

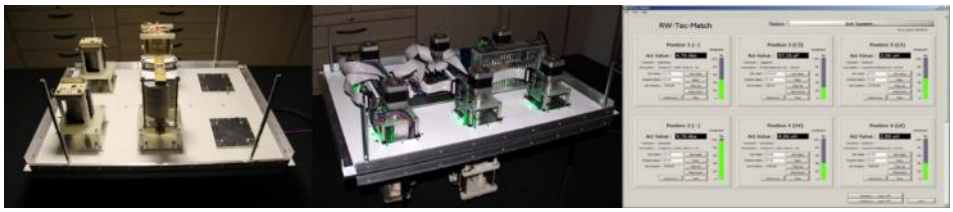

Fig. 12. Modular matching network with RF components (top left), actuators and electronics (top right) and corresponding user interface (bottom).

Acknowledgement
We, the authors of this paper, would like to thank our project partners in the research project [5] in which this work was embedded.

References

[1] Roland, U., F. Holzer et al., *COMPEL*, 2018, **37**, 1933-1942
[2] Laabs, Martin et al., "Anordnung zur Automatischen Impedanzanpassung", European Patent EP 3 767 829 A1, 20.1.2021
[3] Collins Kenneth et al., , "Using matching network to provide maximum power transfer detecting reflected power and varies impedance to adjust it through feedback," U.S. Patent 39287489, 11.08.1989
[4] Verfügung 76/2003. Allgemeinzuteilung von Frequenzen in den Frequenzteilbereichen gemäß Frequenzbereichszuweisungsplanverordnung (FreqBZPV), Teil B: Nutzungsbestimmungen (NB) D138 und D150 für die Nutzung durch die Allgemeinheit für ISM-Anwendungen. Bundesnetzagentur
[5] Schlayer, D., Sallier, R., Reimann, B., Pechan, T., Leichsenring, A., Holzer, F., Abschlussbericht zum Kooperationsprojekt zwischen Unternehmen und Forschungseinrichtungen (KF) im Rahmen des Programms „Zentrales Innovationsprogramm Mittelstand" (ZIM) des Bundesministeriums für Wirtschaft und Energie (BMWi): "Entwicklung und Realisierung eines anwendungsorientierten, modularen Radiowellen-Anpassnetzwerkes - RWTec-Match", 2023

Tunable Monopole Antennas for High-Power Applications in the ISM Bands

S. Soriano[1], P. Santón[2], R. de Los Reyes[3], E. de Los Reyes[1]

[1]*Universidad Politécnica de Valencia, Valencia, Spain*
[2]*pinkRF B.V., Nijmegen, Netherlands*
[3]*Microbiotech S.L, Vilamarxant, Spain*
sasogo@teleco.upv.es

Keywords: antennas, monopole, solid-state, microwave, ISM band, microwave heating

The current industry landscape demands a sustainable use of energy. This implies the importance of researching and developing technologies which can exploit the maximum supplied energy, that is to say, that are efficient and do not generate waste, complying in this way the Sustainable Development Goals of the United Nations and the European Union [1].

Microwave energy is important in this context. At the laboratory level, the effective use of microwave energy has been achieved in numerous applications such as synthesis, heating and drying, obtaining high efficiency and without producing emissions [2]. Nevertheless, their implementation at the industry level has a slower pace. Now, there are businesses dedicated to researching and developing industrial solutions through heating applications using microwaves. These microwave heating processes are typically powered by magnetrons in both industrial and commercial microwave ovens.

With the many advances in semiconductor technology in recent years, microwave heating techniques have evolved in terms of efficiency, stability, and handling of signal properties, thanks to solid-state generators [3]. The fact of including solid-state RF generators in microwave heating systems opens the door to studying and researching different designs, such as the integration of antennas typically used for applications in free space and use them as transmission wave ports in the cavity [2][4]. If successful, the possibility of introducing more of them forming an antenna array also exists.

Nowadays, the company Microbiotech S.L studies and develops projects with these kinds of new systems, and researches with different antennas to transmit energy to the product. Under this situation we work towards the development and design of a new monopole antennas capable of tuning in the ISM band. These antennas can correct or improve the adaptation of the system when it is affected by the environment of the cavity and the geometry or load properties, through a new degree of freedom provided by a cylindrical tuner element.

The properties of this antenna design are very interesting in the industrial environment. A promising approach is its use for the calibration of mass-produced equipment without the need to design and manufacture new antennas for each one of them. The manufacture of microwave heating equipment is very sensitive and irregularities may appear in its operation that must be corrected through calibration. In this way it is possible to provide quality and fluidity in the manufacture of this equipment, complying with the sustainability goal [1].

The antenna design is based on two types of coaxial connectors; an N connector which is able to support up to 500 watts, and 7/16 connector which is able to support up to 1000 Watts. For each connector type three antennas have been implemented at the frequencies of 433, 915 and 2450 MHz.

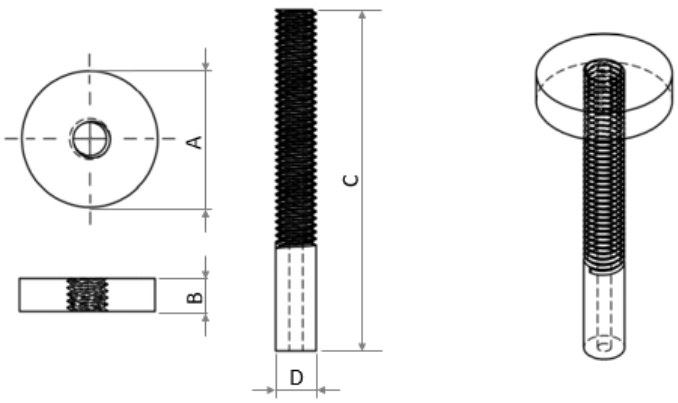

Fig. 1. Pieces, parameters and monopole antenna schematic representation

From Fig. 1, it is possible to appreciate the different parts of monopole antenna. The dimensions of each part of the antennas have been determined by the working frequency, pre-established design rules and computer simulations by HFSS (High Frequency Structure Simulator) software. The design process starts with computer modelling using HFSS and realising simulations first in free space and subsequently cavity conditions. The simulations are based on a wide study about the different parameters of the antenna (see Fig.1), and determining the proper dimensions of each parameter with the support of the reflection scattering parameters.

Focusing on the physical properties of the antenna, it is possible to differentiate two parts: the stick of antenna which has a thread along the body and the cylindrical piece with a central thread perforation which allows movement along of the stick and maintains both adequate position and physical contact between the pieces.

The cylindrical piece movement along the stick allows us to modify the antenna characteristic impedance and adapt it to the cavity-load impedance for transmitting the maximum power to the load.

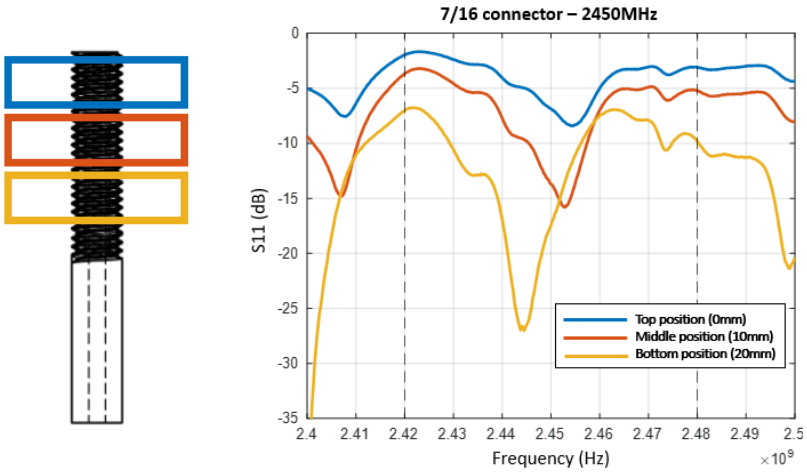

Fig. 2. Power transmitting variation in almonds load at 2450MHz

The first physical tests not in a simulation environment, have been realized on different cavities depending on working frequency. Products treated and used as load for checking the antenna's behaviour have been mainly water and almonds.

A 2450 MHz operation example can be observed in Fig. 2. This test was realized in a 500 x 600 x 570 mm aluminium cavity charged with a 310 x 240 x 40 mm rectangular tray containing 2.492 kg of almonds. The antenna, attached to a 7/16 coaxial connector, has a 30 mm height and 8 mm diameter for the stick, and 5 mm height and 20 mm diameter for the cylindrical element. Through a vector network analyser, the reflection scattering parameters are measured in three steps of 10 mm along the height of the cylindrical element, starting the process at the top part. The illustrated graphic in Fig. 2 shows an appreciable improvement in power transmission when the cylindrical element is displaced to the bottom part of the stick.

This result permits us to conclude that it is possible to add a regulator power element in the antenna design, allowing the design of standard microwave ovens with calibration capability to adapt to the properties of the load. This provides versatility in the manufacturing process and optimal use of energy.

References

[1] (2023) The United Nations website. [Online]. Available: https://www.un.org/sustainabledevelopment/
[2] M. W. Lorence, U. Erle and P. S. Pesheck, Development of packaging and products for use in microwave ovens. Elsevier, 2009.
[3] M. Mehdizadeh, Microwave/RF Applicators and Probes for Material Heating, Sensing, and Plasma Generation. Elsevier. 2015.
[4] L. F. Chen, C. K. Ong, C. P. Neo, V. V. Varadan and V. K. Varadan, Microwave electronics. National University of Singapore, Pennsylvania State University: John Wiley & Sons, Ltd., 2004.

Mitigation of Multipath Surface Waves Along the Air-Skin Interface for Microwave Breast Cancer Detection

C. J. Salomon[1], N. Petrovic[1], P. O. Risman[1]

[1]*School of Innovation, Design, and Engineering, Mälardalen University, Universitetsplan 1, Västerås, Sweden*
christoph.salomon@mdu.se

Keywords: surface waves, multi-path, microwave imaging, electromagnetic waves, magnetic near field, dielectric, breast cancer

Unwanted multi-path surface waves are a major problem in medical microwave imaging (MWI), introducing model errors and obscuring the response signal from a potential tumor or lesion one seeks to detect [1]. In multistatic imaging systems, surface waves traveling on the outline of the object under study (OUS, e.g., the female breast) might be wrongly interpreted as signals originating from the lesion when captured by a receiving antenna. This is amplified by the fact that such surface waves are usually less attenuated than the response originating from an inhomogeneity inside the OUS.

A common way to mitigate multi-path surface waves is to immerse antennas and the object under study (OUS, e.g., the female breast) into a lossy coupling liquid [2]. While these liquids attenuate unwanted stray signals, they also reduce the attenuation budget, i.e., the power loss tolerated by the hardware system to still ensure an adequate signal-to-noise ratio (SNR). To avoid the trade-off between attenuating disturbing and information-carrying signals, a new magnetic near field (MNF) concept has recently been proposed that allows for an efficient coupling of electromagnetic energy into the female breast, without the need for direct contact or a coupling liquid [3].

While this principle has shown promising results in overcoming reflections from the skin (another problem in dry measurement setups [4]), surface waves could still be observed in a simple numerical modelling scenario.

With this paper, we aim to quantify surface waves in a numerical simulation scenario by means of the total power balance in the simulations domain as illustrated in Fig. 1 (a) and to propose a method to physically reduce surface waves when applying the MNF principle with our proposed applicator.

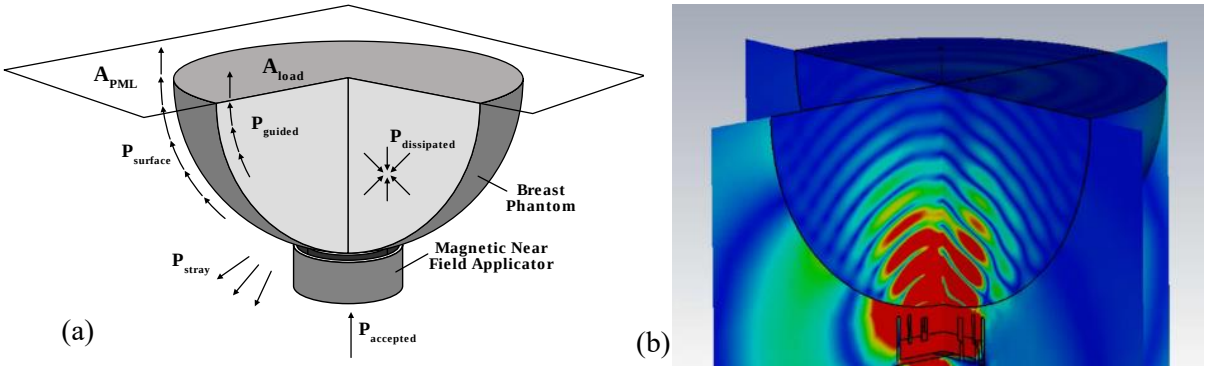

Fig. 1. (a) Power distribution in the simulation setup used to quantify multi-path surface waves along the outline of the homogeneous, hemispherical breast model. (b) Instantaneous electric field component inside the numerical simulation setup.

It is known that surface waves originate from first order interactions of the OUS surface with the perpendicular electric field component of the inbound electromagnetic wave [5]. While in the MNF principle ideally no electric field interacts with the load, residual electric energy protruding outside the applicator aperture leads to unwanted interactions with the breast surface. Confining the electric energy to the applicator aperture by introducing a suitable dielectric material in the applicator is expected to mitigate these effects which will be further investigated in this study.

The outcome of this study is to find a suitable dielectric material that can be used to increase the overall efficiency of energy transmission into the load while reducing stray signals and unwanted multi-path signals.

References

[1] P. M. Meaney, F. Shubitidze, M. W. Fanning, M. Kmiec, N. R. Epstein, and K. D. Paulsen, “Surface Wave Multipath Signals in Near-Field Microwave Imaging,” *International Journal of Biomedical Imaging*, Apr. 10, 2012.

[2] P. M. Meaney, C. J. Fox, S. D. Geimer, and K. D. Paulsen, "Electrical Characterization of Glycerin: Water Mixtures: Implications for Use as a Coupling Medium in Microwave Tomography," *IEEE Transactions on Microwave Theory and Techniques*, vol. 65, no. 5, pp. 1471–1478, May 2017.
[3] N. Petrović, Ch. Pichot, and P. O. Risman, "Further Developments of Applicator Concepts for Detection of Body Part Inhomogeneities," in *2019 IEEE Conference on Antenna Measurements Applications (CAMA)*, Oct. 2019, pp. 218–221.
[4] J. M. Felício, J. M. Bioucas-Dias, J. R. Costa, and C. A. Fernandes, "Microwave Breast Imaging Using a Dry Setup," *IEEE Transactions on Computational Imaging*, vol. 6, pp. 167–180, 2020.
[5] L. Sani *et al.*, "Novel microwave apparatus for breast lesions detection: Preliminary clinical results," *Biomedical Signal Processing and Control*, vol. 52, pp. 257–263, Jul. 2019.
D. A. Hill and J. R. Wait, "Excitation of the Zenneck surface wave by a vertical aperture," *Radio Science*, vol. 13, no. 6, pp. 969–977, 1978.

Materials Properties and Interaction

Microstructural Evolution in Gold Thin Films by Microwave Post-Annealing

N. Yoshikawa[1], T. Igarashi[2], Taguchi[3], A. Nagata[3], S. Komarov[1]

[1]Graduate School of Engineering, Tohoku University, 6-6-02, aza-Aoba, Aramaki, Aoba-ku, Sendai, Japan 980-8579
[2]Graduate Student at Tohoku Universiry, same address
3Undergraduate Student at Tohoku University, same address
yoshin55555@gmail.com

Keywords: microwave, gold thin film, post annealing, roughness reduction, microstructure

Abstract
In the manufacture of electronic devices, metal thin films are used as wiring (interconnect) materials, usually obtained by vapor deposition. It is preferable to deposit films at the lowest possible temperature to reduce thermal damage to the substrate. However, metal thin films deposited at low temperatures have fine crystal grains and poor conductivity, requiring post-annealing treatment. The authors investigated the rapid and selective heating of metal thin films using microwaves and performed a quantitative analysis of the changes in thin film roughness that occur during post-annealing. The microstructural evolution of Au thin films during post-annealing by microwave and electric furnace heating was compared. Wave number spectra of film surface roughness were analyzed to characterize the roughness variation with annealing.

Then, a simulation study was performed to interpret the experimental results on the roughness reduction of Au thin films by the two annealing methods. The simulation model of this study is based on one-dimensional capillary-driven surface diffusion with the inclusion of electromigration force due to microwave irradiation. It has been shown that the alternating microwave electric field does not completely cancel out the atomic migration due to the simultaneous capillary-driven (thermal) effects during the alternating period. However, it is not sufficient to explain the variation of the film profiles (the observed wavenumber spectra). In this study, the capillary model was applied to furnace annealing, and an anisotropic factor in atomic transport by electromigration was introduced in microwave annealing simulations. We were able to reproduce the profiles and spectral changes observed in the experiments using both annealing methods.

Introduction

Metal interconnects in the integrated circuits of electronic devices are in most cases fabricated as a form of thin films by vapor deposition methods. This process is called metallization. In these processes, low temperature deposition is preferred to reduce thermal damage to the substrates and other patterned circuit elements. However, low temperature deposition results in metal films with fine (nano) grains, so the electrical conductivity of the films is not always high enough for the interconnects [1].

Also, in the case of ceramic films, the low temperature deposited films have poor crystallinity and do not exhibit sufficient performance of the materials functions, such as ferroelectric and pyroelectric properties. In the case of Si, diffusion of implanted dopants in Si and stress relief are required.

To improve the electrical conductivity of metallic films, the crystallinity of ceramic films, and the dopant distribution in polysilicon, rapid thermal annealing (RTA) post-annealing techniques have been employed. One of the main methods is lamp annealing, although it has some drawbacks, such as the difficulty in selecting the wavelength of the lamp light and the limited heating depth on the film surfaces. Electric furnace annealing is the other conventional method, but it requires heating the whole atmosphere in the furnace chamber, which is not necessarily favourable from the point of view of energy saving, together with the necessity of controlling the sample transport time for continuous operation of annealing.

As a candidate method for the alternative processing of the post annealing, microwave heating is considered. This is because of microwave selective heating for the metal interconnects, ability of rapid heating and volumetric heating (as long as the film thickness is an order of the microwave skin depth δ (for normal metal, less or equal to micron meter, for example, Au δ = 0.97 μm at 5.8 GHz estimated by (1), assuming an electrical conductivity of Au film $\sigma_{Au} = 4.5 \times 10^7 [S \cdot m^{-1}]$.)).

$$\delta = \sqrt{\frac{2}{\sigma \mu \omega}} \qquad (1)$$

It has been shown that metal thin films can be heated very effectively in microwave magnetic field in a single mode microwave cavity even at low power input [2], while the substrate (such as SiO_2 or pure Si) is heated much less, and selective heating is achieved.

Microstructural changes of materials during RTA have been studied for a long time. The authors investigated the rapid and selective heating of metallic thin films using microwaves and performed a quantitative analysis of the changes in thin film roughness that occur during the post-annealing [3]. In this study, the film thickness profiles (surface roughness) measured by AFM (Atomic Force Microscope) are Fourier transformed to obtain the wave number (k) spectra. It is possible to determine at which wavenumbers (wavelengths) the roughness changes occur. This study is expected to contribute to provide fundamental information for the potential application of microwave to film annealing processes.

Next, in this study, in order to analyze the author's experimental results, a numerical simulation of the film roughness variation under the imposition of microwave alternating electric field is conducted. The simulation results will be compared with the previously reported observations. Basically, the simulation model is to analyze the roughness reduction phenomena caused by the capillary-driven surface diffusion, which had been proposed and discussed by Mullins and Herring [4,5] (M-H model).

In this study, a numerical simulation of the roughness reduction by applying the alternating electric field at microwave frequency is performed, whose model is based on the M-H model and with the inclusion of the electromigration effect. The effect of electromigration on the film profiles and wave number spectra of polycrystalline film roughness is discussed. An attempt is made to compare the simulation results between with the capillary driven roughness reduction (M-H model) for the furnace annealing case and the electromigration model with the microwave annealing experiments.

Experimental and Simulation method

Specimen

Thin Au films were deposited on SiO_2 substrates by direct current (DC) ion sputtering at room temperature. The SiO_2 substrate was cleaned in alcohol with an ultrasonic agitation prior to deposition. The coating apparatus is a sputter coater to prevent charging of specimens for SEM observation. In this study, Au was selected as the film material, because its oxidation can be neglected when heated in air and has less requirement in the storing the film specimens. SiO_2 substrate was chosen because it is a low-loss material and is almost transparent to microwave irradiation. The substrate thickness is 0.5mm. The films with a thickness of about 200~250nm were usually used for the post-annealing experiments. As will be mentioned later, the film thickness is less than the microwave skin depth, so the microwave is considered to penetrate the film, and the volumetric heating is achieved.

Microwave and conventional (electric furnace) heating

Microwave heating was performed using TE103 single-mode cavity at 5.8 GHz (max. power 150 W Fuji Denpa Koki, Ltd. GNU-300AA, Solid State Oscillation, Saitama, Japan) (Fig.1(a)). The specimen is placed at the maximum magnetic field position in the cavity, perpendicular to the direction of microwave magnetic field oscillation (Fig. 1(b)). The temperature measurement was conducted with a sapphire light pipe by PhotoriX optical system (Luxtron Co. Ltd., Santa Clara CA. USA). The emissivity of the specimen film was determined by calibration measurements, compared with a thermocouple reading in an electric furnace. An electric furnace with the SiC heating element was used.

Microstructural characterization and observation, numerical simulation

Microstructure of the as-deposited and post-annealed Au films were characterized using X-ray diffraction, FE-SEM and AFM. In this study, AFM had roles of the film characterization, not only for observing the film morphology but also for the film thickness profiles, which were obtained as the two-dimensional digital data. One-dimensional thickness profiles were obtained by line scanning. Within an observation area of 10 μm × 10 μm, line scanning data was obtained from the parallel four lines In order to characterize the film roughness, wave number spectra of the film profiles from Fourier transform (Fast Fourier Transform (FFT)) of the data were obtained by implementing Hamming window function. The details of the methods can be found in a reference [3]

Numerical simulation

In this study, we propose a continuum numerical model based on the Mullins-Herring model and consider the electromigration effects caused by microwave irradiation and analyze the experimental results of the post-annealing by electric furnace heating and microwave heating [6]. In this study, the fourth-order partial differential equation (2) for the time variation $h(x,t)$ (x: position, t: time) of the 1D film thickness distribution (several 100 nm, (experimental value)) for the capillary-driven surface diffusion model (Mullins model) is solved by the finite difference method (explicit solution), where the thickness distribution of 10 μm region was divided into 1024 meshes. The notations are as follows: D_s: surface diffusion coefficient [m^2/s], γ: surface tension [N/m], ν: number of atoms on the surface [m^{-2}], Ω: atomic volume [m^3], k_B: Boltzmann constant [J/K], T: temperature [K], representative length: x_0 [m]. The variation of $h(x)$ with annealing time was Fourier transformed to obtain a (spectral) distribution with wavenumber $k = 2\pi/\lambda$ (λ: wavelength [m]). On the other hand, the thickness change by including the effect of electromigration under microwave irradiation was solved in the same way using (3). Here, the effective charge q^* (literature value [7]) of Au was used for electromigration due to the application of an alternating electric field $E_S \cdot \sin\omega t$ at the microwave angular frequency ($\omega=2\pi f$, f=5.8 GHz). The time step in the unsteady calculation was set to be 1/10 of the microwave (5.8 GHz) alternating period. The details of the methods can be found in a reference [3].

$$\frac{\partial h}{\partial t} = -\frac{D_S \gamma \nu \Omega^2}{k_B T x_0^4} \cdot \frac{\partial^4 h}{\partial x^4} \quad (2) \qquad \frac{\partial h}{\partial t} = -\frac{D_S \gamma \nu \Omega^2}{k_B T x_0^4} \cdot \frac{\partial^4 h}{\partial x^4} - \frac{D_S E_S sin\omega t \cdot q^* \nu \Omega}{k_B T x_0^2} \cdot \frac{\partial^2 h}{\partial x^2} \quad (3)$$

Results and Discussions

Comparison of microstructure changes by microwave and furnace annealing

According to the SEM images of the as-deposited film shown in Fig. 1, the morphology shows an island-like state consisting of small grains that has a surface roughness with a scale of tens to hundred nanometres. Flatter surface would be available if other sputtering methods were used, such as a magnetron sputtering which provides higher energy to the depositing atoms.

Annealing causes the island crystals to bond together, forming a labyrinth-like structure. Below 750°C, it is obvious that the microwave annealed sample has a flatter surface than the electric furnace annealed sample. With increasing the annealing temperature, the structure becomes coarser and finally (above 850°C) the microstructure of both annealing methods became similar.

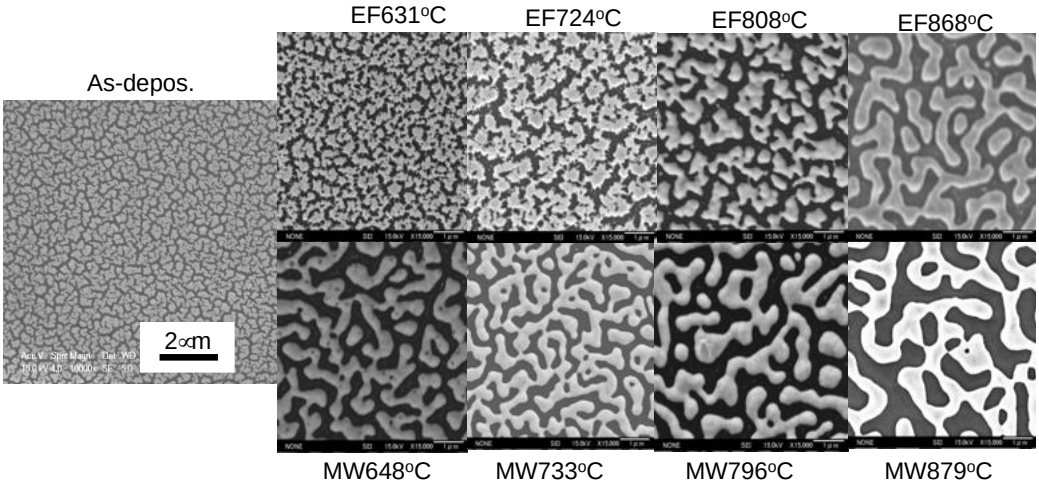

Fig. 1. SEM images of (left) as-deposited state, (upper) electric furnace (EF) annealed for 60 s and (lower) microwave (MW) annealed Au thin films at different temperatures.

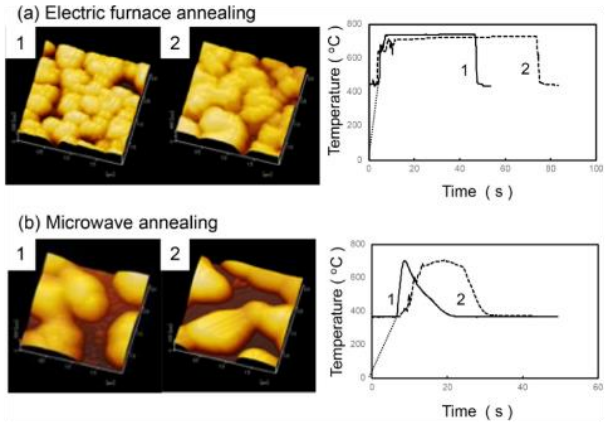

Fig. 2. AFM images of (a) electric furnace annealing and (b) microwave annealing of Au thin films. The corresponding heating curves are shown in the right images. [2]

AFM images of the annealed films for different heating times are shown in Fig. 2 together with their heating curves. The temperature below 400°C is shown with a dotted line in Fig. 2, because of the detection limit of the optical method. Coarsening of the microstructure was observed with increasing annealing time in the electric furnace annealing. However, the change in the microstructure became small after 60 seconds annealing in Fig. 2(a). Therefore, the furnace annealing images for 60 s are shown in Fig. 1.

On the other hand, microwave annealing did not show a clear temporal change between two runs (Fig. 2(b)). The heating curve of Fig. 2(b) has a temperature peak at the initial heating stage. In a single-mode cavity, it is not possible to keep the temperature constant without changing the microwave power, and it is necessary to perform impedance matching by manipulating a stub tuner. Therefore, we turned off the input power immediately after reaching the maximum temperature.

Spectrum analysis of film surface roughness

Spectral analysis of surface roughness is performed in order to characterize the differences between the two annealing methods. Fig. 3(a) shows the AFM image of the as-deposited film. The film surface profiles along the four scan lines (A, B, C, D) were obtained and digitally recorded. The profiles of the as-deposited film are Fourier-transformed and the film roughness spectra are shown in Fig. 3(b), the average of the spectrum for four scanning lines is shown at the bottom. The abscissa is a tentative wave number k' (k' corresponds to the general definition of wavenumber k, where $k = 2\pi/\lambda_{roughness}$: $\lambda_{roughness}$ is a wavelength of surface roughness)). k' = 10 corresponds to the bump wavelength of 1 μm, and indicates 10 waves within 10 μm.

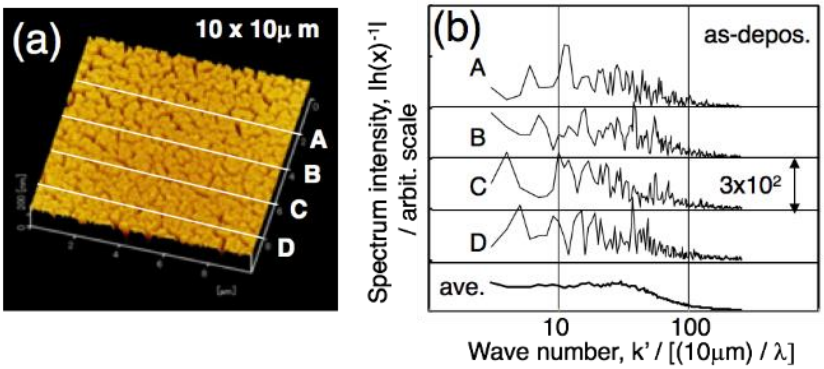

Fig. 3. (a) AFM image of as-deposited film indicating four scanning lines (A, B, C, D). (b) Wave number spectra obtained from the film surface profiles along four lines (A, B, C, D) in (a) and their average. [2]

In Fig. 4(a), the spectra of the films annealed at 720°C are shown, the intensity of the annealed films in high k' region ($20 \leq k' \leq 100$) became small compared to the as-deposited state (Fig 3(b)). Fig. 4(b) shows comparison for the spectra at different annealing temperatures. When annealed at 630(613)°C, the intensity of microwave annealing is obviously lower than that of furnace annealing, indicating the greater roughness reduction in this k'range. By annealing at 720°C, the spectra of both annealings became similar except for range of k'~20. This difference in the intensity corresponds to the difference in surface roughness of the SEM images in Fig. 2. On the other hand, in the low k' range, the spectrum intensity of microwave annealing became larger, and the difference from the furnace annealing is exaggerated. This tendency of larger intensity of microwave annealed film in lower k' range is mainly due to the preferential increase of the bump height. The reasons are discussed in terms of the surface tension [2].

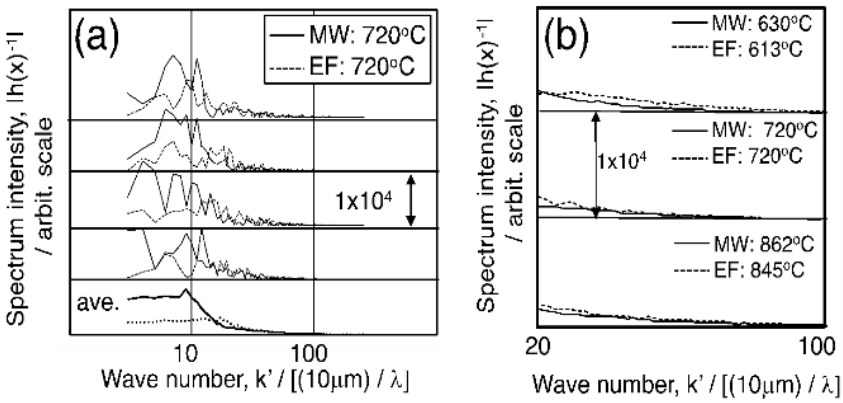

Fig. 4. Wave number spectra of films (a) annealed at 720°C, and (b) at different temperatures by the two annealing methods. [2]

Simulation of surface roughness reduction by annealing

Capillary model

Normalized spectrum of annealing for 60 s at 613°C in an electric furnace, (In this study, the intensities of wave number spectra were normalized with respect to their maximum values, and a comparison was made between the experimental and simulated ones).

The calculated spectra for different annealing times are shown in Fig. 5, where an as-deposited spectrum is included for comparison. The data shown for the as-deposited film profile are one of the four line scans in an AFM view that was input as the initial profile for the simulation. It was shown that the large wave number above $k' > 50$ was reduced by furnace annealing for 1min. However, if only the capillary model is simply applied to reproduce the spectrum by microwave annealing (for less than 500 ms), it is not possible to account for the resulting spectra (the roughness around k'~50 is more

reduced by microwave annealing as shown in Fig. 4(b). Therefore, in this study, a simulation model considering the effect of electromigration-driven surface diffusion was attempted.

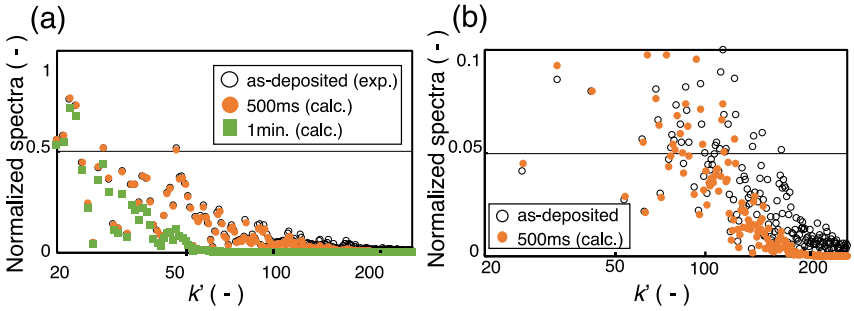

Fig. 5. Model simulation in comparison with experimental data of electric furnace annealing at 613°C for 60 s. [3] The magnitudes of the spectra are normalized. (a) Normalized spectra by capillary model simulation for 500 ms and 60 s. (b) Magnified spectra of (a) of as-deposited and capillary model for 500 ms.

Electromigration-driven model

In this study, the atomic transport by electromigration [8] was considered [9]. However, the transport distance was limited due to the alternating ***E***-field, which led to cancellation of the transport, although the occurrence of thermal diffusion during the half period of microwave field prevented complete cancellation [10].

In this study, an anisotropy in the atomic transport at the bump of the film surface due to the mutual directional relationship between the directions of the ***E***-field and the bump surface gradient was considered. In order to express this effect, a simple fitting parameter (f) is introduced, which has a meaning of the shadowing effects of the ***E***-field by the bumps, or a meaning of a difference in the probability of atomic transport according to the direction of the ***E***- field with respect to the surface gradient. In this study, the bulk ***E***-field value was simply used for the local field, as conducted in the other studies [9].

In the simulation, the gradient of the bump surface is first calculated and the f parameter is applied. (The value of f is predetermined for the simulation, $f = 1$: no difference in transport to either direction or complete cancellation, $f = 0$: no transport for an atom in position B). A considerable variation of the spectra is obtained by choosing different f values. Simulated spectra for $f = 0.9$ are shown as an example in Fig. 6.

The experimental profiles of the annealed films by both methods are also shown in Fig. 7. They do not starting from the same specimen and had different profiles in their as-deposited state (the shown profile positions of the film are rather arbitrary). However, experimental features of roughness reduction are almost predicted by simulations, such that the roughness of several hundred nanometre scales was less effectively reduced by (a) furnace annealing than by (b) microwave annealing, which corresponds to the better roughness reduction in the range of $k' = 20$~100 range. This tendency is consistent with the SEM and AFM surface morphologies of Fig. 2 in the previous study [6].

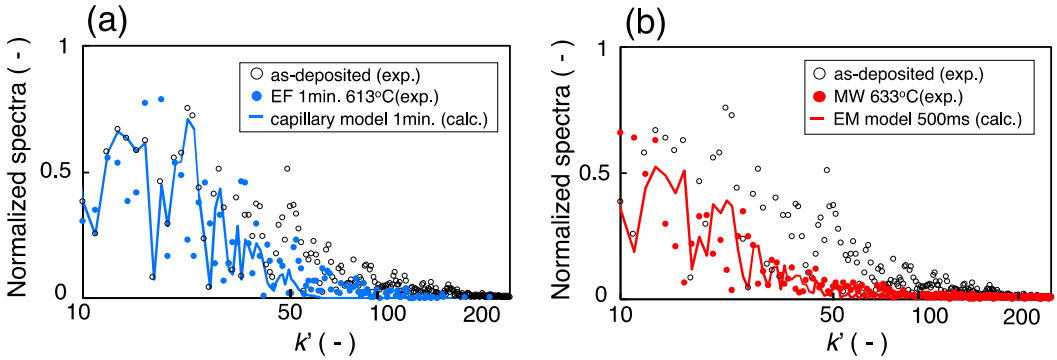

Fig. 6. Comparison between the simulated and experimental spectra (a) by capillary and (b) EM (+capillary) model, f =0.9). [3]

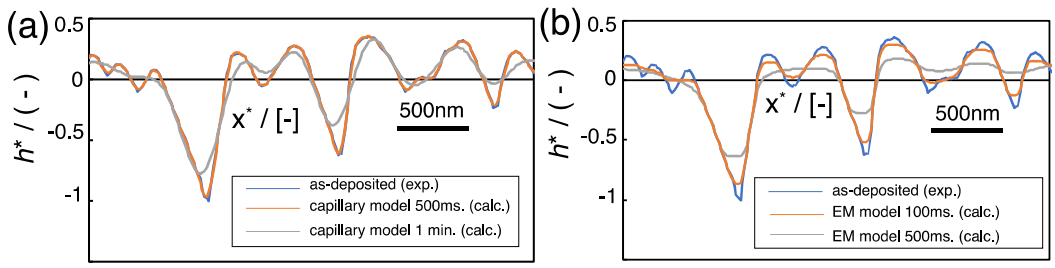

Fig. 7. Simulated variation of surface profiles after duration of time for the cases of (a) capillary model (furnace annealing) and (b) EM model (microwave annealing). [3]

Conclusion

In this study, the changes of microstructure and surface roughness of Au thin films annealed by microwave heating with variation of annealing time and temperature were investigated. They were also compared with annealing in an electric furnace.

Coarsening of the film microstructures was observed by both annealing methods as an increase of the annealing temperature. However, accelerated reduction of fine surface roughness (the high wave number region) was observed by microwave annealing at low temperature below 720°C. Variations in wave number spectra of surface roughness were observed and the roughness reduction process was discussed. The superposition of the electro-migration effect to the capillary driven surface diffusion was suggested for this interpretation.

It was not possible to explain the spectrum of short microwave annealing time (less than 500 ms) by capillary driven surface diffusion alone. To overcome the difficulties, an attempt was made to include the electromigration force. By introducing an anisotropy parameter of the atomic migration depending on the relative directions between the bump gradient and the E-field, the simulations reproduced the film profile and the wave number spectra to account for the variation of annealing conditions by both methods.

References

[1] S.P. Murarka, Multilevel interconnections for ULSI and GLSI era, Mater. Sci. Eng., **R19**, (1997) 87-151.
[2] Z. Cao, N. Yoshikawa and S. Taniguchi, Microwave Heating Behavior of Nanocrystalline Au Thin Films in Single Mode Cavity, J. Mater. Res., **24** (2009) 268-273.
[3] N.Yoshikawa, T.Igarashi, H.Taguchi, A.Nagata and S.Komarov, "Surface Roughness Variation and Microstructural Evolution of Au Thin Films in Rapid Annealing by Microwave and Electric Furnace Heating", Thin Solid Films, **713** (2020) 138352, 1-8.
[4] W.W.Mullins, Theory of Thermal Grooving, J. Appl. Phys., **28** (1957) 333-339.
[5] C. Herring, Effect of Change of Scale on Sintering Phenomena, J. Appl. Phys., **21** (1950) 301-303.
[6] N.Yoshikawa, T.Igarashi,"Simulation on surface roughness variation of Au thin films by microwave post annealing", Thin Solid Films, **737** (2021) 138939, 1-7.
[7] H.B.Huntington and A.R.Grone, Current-induced marker motion in gold wires, J. Phys. Chem. Solids, **20** (1961) 76-87.
[8] J.Lienig and M.Thiele, Fundamentals of Electromigration-Aware Integrated Circuit Design, Springer, Nature, Switzerland AG, 2018 pp.17, ISBN 978-3-319-73557-3.
[9] D. Maroudas, Dynamics of transgranular voids in metallic thin films under electromigration conditions, Appl. Phys. Lett., 67(1995) 798-800.
[10] J. Tao, M.W. Cheung and C.Hu, Metal electromigration damage healing under bidirectional current stress, IEEE Electron Device Lett., 14 (1993) 554-556.

Microwave Magnetic Loss Mechanism and Ferro-Magnetic Resonance Heating

N. Yoshikawa[1]

[1]*Graduate School of Engineering, Tohoku University, 6-6-02, aza-Aoba, Aramaki, Aoba-ku, Sendai, Japan 980-8579*
yoshin55555@gmail.com

Keywords: microwave, magnetic resonance, FMR, heating, magnetic loss, magnetic field

Abstract
It is known that the microwave energy absorption per unit volume of a material, P [W/m^3] is expressed by (1) in terms of the interaction with the microwave electric field ($\boldsymbol{E}$) and with the microwave magnetic field ($\boldsymbol{H}$). (ω: angular frequency, ε'': dielectric loss factor, μ'': magnetic loss factor, σ: electric conductivity)

$$P = (\omega \varepsilon'' |\boldsymbol{E}|^2 + \omega \mu'' |\boldsymbol{H}|^2 + \sigma |\boldsymbol{E}|^2)/2 \qquad (1)$$

The second term (magnetic loss) in (1) includes μ''. We have considered that a natural resonance in ferromagnetic materials is one of the phenomena leading to magnetic loss. Ferrites at high frequency applications encounter this phenomenon, which determines their limit in use.

The authors have attempted to heat ferro(ferri)magnetic samples by applying an external magnetic field and microwaves of several tens to several hundreds of watts to deliberately induce ferromagnetic resonance (FMR). Temperature increase was observed at the particular magnetic field value during increasing and decreasing magnetic field. We attributed it to the occurrence of FMR. We estimated the resonance field, taking into account the effect of demagnetization using Kittel's equation, and the experimental values are in agreement with the estimated ones.

It was also shown that the higher the initial temperature (initially the microwave power is applied and heated with zero external magnetic field), the lower the degree of temperature increase was obtained. This is due to the fact that as the temperature increases and approaches the Curie temperature, the magnetization decreases.

Introduction

The Poynting vector ($\boldsymbol{S} = \boldsymbol{E} \times \boldsymbol{H}$) is the microwave energy flux density, and by taking its divergence ($\nabla \cdot \boldsymbol{S}$) and substituting Maxwell's equation (Farady and Ampere's law), we can obtain the microwave energy absorption per unit volume of a material P [W/m^3], which is expressed by (1) in terms of the interaction with the microwave electric field ($\boldsymbol{E}$) and with the microwave magnetic field field ($\boldsymbol{H}$).

In a dielectric material such as water, the dielectric loss (in the first term on the right side of (1)) is caused by the alternating electric field ($\boldsymbol{E}$), where the dielectric constant (dielectric loss factor: ε'') is a physical property related. On the other hand, non-magnetic metals (ferromagnetic metals, as well) generate Joule heat due to the ohmic (conductive) loss caused by the induced current generated by the alternating magnetic field ($\boldsymbol{H}$). Therefore, it is often misunderstood as the magnetic loss expressed by the second term of (1). However, it must be expressed by the third term, which is related to the electric conductivity (σ). In (1), the electric field $\boldsymbol{E}$ in the third term corresponds to the induced current $\boldsymbol{J} = \sigma \boldsymbol{E}$.

The second term (magnetic loss) of (1) contains a magnetic permeability (permeability loss factor μ''). Let us examine the mechanism by which this is achieved. For example, it is well known that voltage transformers have two types of losses: copper loss and iron loss. Copper loss is the Joule heat loss due to the current flowing in the coil and corresponds to the third term in (1). On the other hand, iron loss is the loss due to AC magnetization in the iron core inside the coil. Ferromagnetic materials such as iron have spontaneous magnetization, which means that there are regions (magnetic domains) where the electron spins are aligned in the same direction. When the direction of magnetization is changed by an alternating magnetic field, the boundary of the magnetic domain (magnetic wall) moves, and its moving resistance becomes a loss and exhibits hysteresis in magnetization. The magnetic loss (the second term on the right side of (1)) could correspond to the iron loss (related to the electron spin). However, unlike AC at tens of Hz, the motion of the magnetic walls at microwave frequencies cannot keep up. Instead, there are several mechanisms related to magnetic losses in the microwave range.

It is well known that ferromagnetic materials can be well heated by microwaves. Our group has confirmed that they can be well heated especially in $\boldsymbol{H}$-field up to Curie temperature. The magnetic mechanism plays an important role in the microwave heating of ferromagnetic materials. On the other hand, the RF loss in a range of 10^8~10^9 Hz is a harmful phenomenon and must be avoided in the design of RF devices such as ferrite cores for high-frequency operation. This loss mechanism is

specifically known as natural resonance [1]. Natural resonance is due to the precession motion of the electron spin according to the internal field that exists in the ferromagnetic materials.

This is one of the mechanisms of magnetic loss and it is one of ferromagnetic resonance (FMR) phenomena. FMR is classified as electron spin resonance (ESR) which occurs in ferromagnetic materials. The frequency of the electromagnetic waves resonating with the internal magnetic field is approximately in the GHz band, and the frequency is distributed according to the distribution of the internal magnetic fields. On the other hand, even in (non-magnetic) materials such as paramagnetic materials, unpaired electrons cause ESR and absorb the energy, but their number (involved in the resonance) is overwhelmingly small, making it difficult to observe a temperature increase in the material.

Natural resonance occurs in the absence of a static external magnetic field. On the contrary, it is expected to be possible to induce FMR in ferromagnetic materials applying static external magnetic field and deliberately causing the FMR loss leading to heat. Namely, if natural resonance is one of the mechanisms responsible for microwave magnetic heating, it might be possible to expect the extra heat generation due to FMR and observe the temperature rise.

If the energy absorption at FMR is converted into heat, the pathway of FMR energy to heat (thermal energy) is the spin-lattice relaxation process. In this study, an attempt was made to observe the temperature change of Fe_3O_4 powder particles and Permalloy sheets. The authors attempted to heat ferromagnetic samples by applying an external magnetic field and microwaves of tens to hundreds of watts to deliberately induce FMR [2]. Temperature increase was observed at the particular magnetic field value during increasing and decreasing magnetic field. In this report, our recent experimental results or findings are presented.

Experimental

Specimen

The specimen used were Fe_3O_4 powder (4N in purity, 0.5 μm, Sigma-Aldrich) and Permalloy sheet (Ni+Co: 70~80%, Fe: 20~30%, Mo: 4%, C<0.08%, Mn<0.5%, 7 × 7 mm, thickness 10 μm, Nilaco, Tokyo, Japan). Their magnetic properties (hysteresis loop measurement) were performed using VSM (vibrating sample magnetometer).

Microwave heating apparatus with magnetic field imposition and methods

The specimens were placed in a flat-bottom silica glass tube container. The specimen container was placed in a 5.8 GHz TE103 microwave cavity at the $\boldsymbol{H}$-field maximum position and the magnetic field ($\boldsymbol{H}^{ext}$) was applied up to 0.45 T using an electromagnet that can control the rate of the increase and decrease of the external magnetic field.

The specimen temperature was measured optically using a sapphire light guide, and the powers of the traveling forward wave (P_f) and reflected wave (P_r) of the microwave were monitored. N_2 gas was flown downward onto the specimen surface and no heat insulating materials were placed above the specimens. In the series of experiments, the specimens were previously heated in microwave $\boldsymbol{H}$-field up to the predetermined temperature without imposition of $\boldsymbol{H}^{ext}$, then $\boldsymbol{H}^{ext}$ was imposed and its strength changed at a controlled rate. Data of the temperature variation with time were recorded digitally. Details of the experimental setup are shown in the previous paper [2].

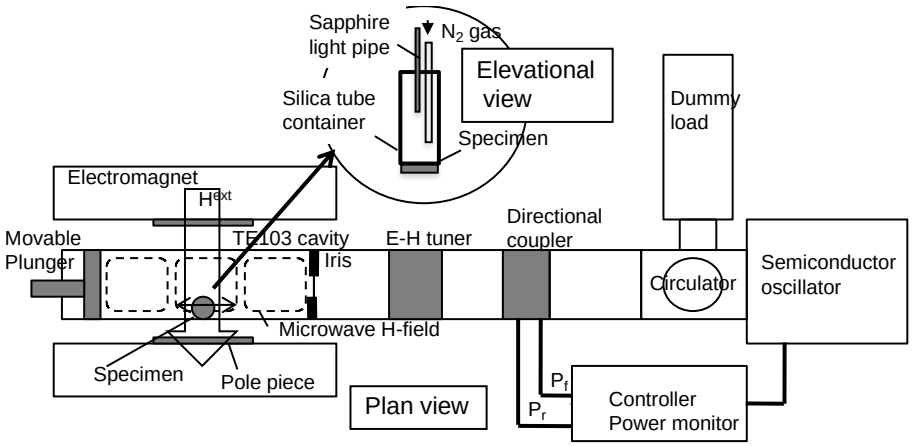

Fig. 1. Schematic illustration of apparatus. Specimen is placed in a cavity at maximal microwave magnetic field. (h_f : indicated by dotted line) and an external magnetic ($\boldsymbol{H}^{ext}$) is applied perpendicularly to h_f.

Results and Discussion

FMR heating characteristics

Curves of time variation of external magnetic field $\boldsymbol{H}^{ext}$, temperature and P_f, P_r are obtained for the of Fe_3O_4 powder particles and Permalloy sheet. They are shown in Fig. 2. As the external magnetic field is increased and then decreased, temperature peaks are observed twice. It can also be seen that the temperature peaks occur at almost the same magnetic field during the magnetisation up and down processes. The P_f is kept almost constant, but the P_r decreases a little at the position of the temperature peak, corresponding to the energy absorption. This was more pronounced in Fe_3O_4, but less so in Permalloy.

This increase in temperature could be due to the occurrence of FMR, but it is also possible that the smaller change in Pr is due to the fact that Permalloy is an alloy foil, and has a smaller volume compared to a lump of Fe_3O_4 powder. However, it should be noted that the degree of temperature increase (ΔT) in the Permalloy sheet is significant despite the larger surface area/volume ratio.

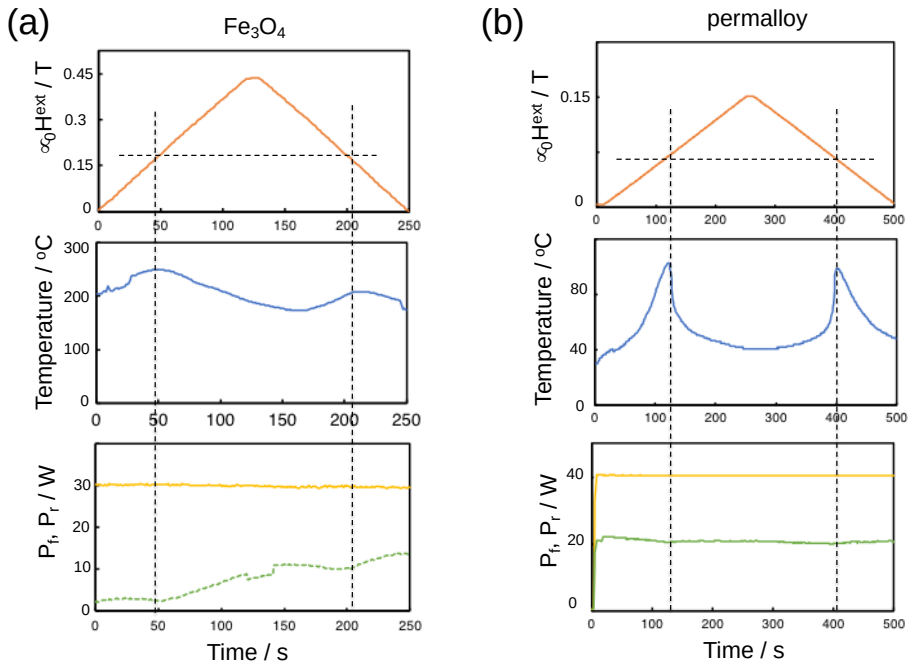

Fig. 2. Temporal variation of the externally imposed magnetic field, specimen temperature and P_f, P_r of (a) Fe_3O_4 powder particles and (b) Permalloy sheet.

Resonance field

The next step is to consider whether the value of the magnetic field at the time of the temperature peak can be considered to be equal to the FRM resonance magnetic field. The resonance magnetic field (H_r) of a ferromagnetic material is influenced by various factors such as the internal magnetic field and the demagnetization field, and it is predicted by Kittel's equation [3] as written by (2). The effect of the demagnetization field is considered to be more significant than the anisotropic magnetic field (H_A) for both materials, because they have cubic crystal structures, so the effect of the latter was ignored. Therefore, (3) was used to estimate H_r.

$$\omega_r = \gamma\sqrt{\left\{H_r + \frac{1}{\mu_0}(N_x - N_y)I_s + (H_{Ay} - H_{Ax})\right\}\left\{H_r + \frac{1}{\mu_0}(N_z - N_y)I_s + (H_{Ay} - H_{Az})\right\}} \qquad (2)$$

$$\approx \gamma\sqrt{\left\{H_r + \frac{1}{\mu_0}(N_x - N_y)I_s\right\}\left\{H_r + \frac{1}{\mu_0}(N_z - N_y)I_s\right\}} \qquad (3)$$

where, ω_r is the resonant (angular) frequency (2π x $5.8\text{x}10^9$[rad/s]), γ is a gyro magnetic ratio, μ_0 is a magnetic permeability of vacuum, N_i (i = x, y, z) are demagnetization factors for the coordinates shown in Fig. 3 and I_s is the saturated magnetization. For the Fe_3O_4 specimen, the particles have cubic (equiaxial) shapes as shown in Fig. 4. And because we neglected the crystalline anisotropic field, we assumed N_x=N_y=N_z. Therefore, we estimated H_r by (4). On the other hand, for the Permalloy sheet, since thickness is considerably small, we assumed N_x = N_y =0, N_z=1, and H_r was estimated using (5).

$$\omega_r = \gamma H_r \qquad (4), \qquad \omega_r = \gamma\sqrt{H_r\left(H_r + \frac{I_s}{\mu_0}\right)} \qquad (5)$$

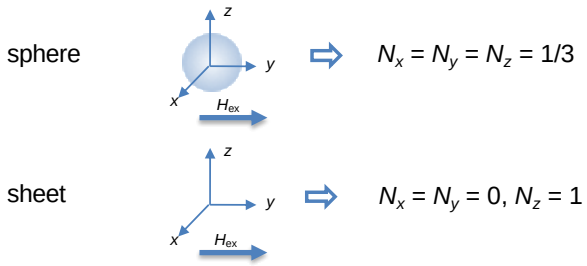

Fig. 3. Directions of magnetic field to the coordinates and demagnetization factors for specimens having spherical and sheet

Table 1. Summary of the measured (exp.) and estimated (calc.) H_r

	Fe_3O_4	Permalloy
I_s/T	0.52	0.65
μ_0 H_r (exp.) / T	~ 0.18	~ 0.07
μ_0 H_r (calc.) / T	0.21	0.06

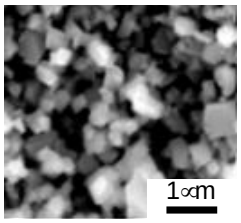

Fig. 4. SEM photograph of Fe_3O_4 powder.

The magnetic field of the temperature peaks and the estimated H_r values are listed in Table 1. Despite the rough assumptions, a reasonable agreement was obtained between the two. However, it is important to make a judgement on the relationship between the occurrence of FMR and the temperature rise by conducting the further experiments, that will be reported in the future.

In our previous study, it was shown that as the initial temperature (initial temperature by microwave heating when external magnetic field is not imposed.) increases, the resonance magnetic field H_r increases, as shown in Fig. 5. This is also expected from (5), because the value of I_s decreases to zero as the temperature increase approaches the Curie point (Fe_3O_4, 565°C)

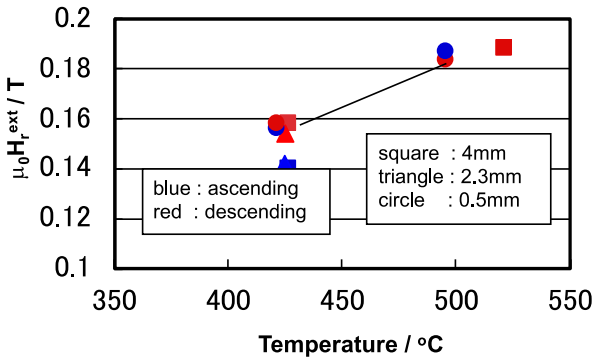

Fig. 5. Relationship between the initial temperature before imposition of external magnetic field and the degree of temperature rise upon resonance [2].

Heating mechanism

It is known that specimens absorb microwave energy by FMR, and the energy could either be consumed for re-emission as an electromagnetic wave [4] or contribute to some changes in microstructures, exciting reaction or magnetic transitions (although no reports found so far), but most likely the energy is converted into heat (lattice vibration). The FMR is the resonance of electron spin precession motion, but when it is converted into heat, there are some processes from the spin systems to that of the lattice.

First of all, FMR is a state where the unpaired electron spins (which contribute to ferromagnetism) precess uniformly around the (external) magnetic field direction under resonant conditions at the microwave frequency. Here, we consider the phase of electron spin motion in the specimen or take into account of the spin wave number. First, the spin motion starts from the uniform motion, as shown schematically in Fig. 6. In this case, the spin wave k number is 0, because the wavelength (λ =

$2\pi/k$) of microwave is large enough (an order of centimetres in vacuum), compared to the specimen scale. The process of FMR energy conversion into heat is via. spin wave to lattice vibration (magnon and phonon interaction: spin-lattice relaxation). Paths of the energy conversion are proposed and illustrated in Fig. 7 [5]. The spin wave number $k \sim 0$ motion caused by FMR increases the wave number by scattering with some inhomogeneities in the material (spin-spin relaxation) and changes into non-uniform motion, increasing the wave number and associating the lattice motion (spin-lattice interaction) (pathway 2). The uniform motion could also interact directly with the thermal magnon (pathway 1). Both paths dissipate microwave energy in the lattice. These paths have their own specific relaxation times. In the future study of the FMR heating experiments, it will be important to analyze the FMR energy absorption peak width and determine the degree of contribution of the two paths, and it will be fruitful to discuss the heating behaviour in terms of these processes.

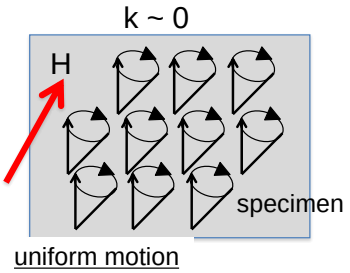

Fig. 6. Schematic illustration of the uniform precession motion of electron spins in FMR.

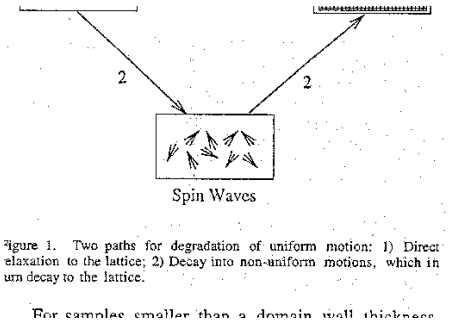

Figure 1. Two paths for degradation of uniform motion: 1) Direct relaxation to the lattice; 2) Decay into non-uniform motions, which in turn decay to the lattice.

For samples smaller than a domain wall thickness

Fig. 7. Proposed energy dissipation paths of magnetic resonance. [5]

Conclusion

Temperature increase (ΔT) was observed in Fe_3O_4 powder and Permalloy sheets under FMR conditions. And it was confirmed that the temperature peaks were observed almost at the same magnetic field both in increasing and decreasing stages.

The resonance filed H_r was estimated by Kittel's equation, considering the effect of demagnetization and the values of saturation magnetization measured. And they are consistent with the experimental data.

The values of ΔT decreased when the specimen temperature increases approaching to the Curie temperature. For this reason, the decrease of saturation magnetization (I_s) in approaching to T_c is pointed out. Mechanisms of microwave energy conversion to heat was discussed, and we concluded that occurrence of FMR is one of the magnetic loss mechanisms of microwave, which is expressed in the equation of the divergence of energy flux (Poynting vector).

References

[1] D.Polder and J.Smit, Rev. Modern Physics. **25** [1] (1953) 89-90.
[2] N.Yoshikawa and T.Kato, J.Phys. D, **43** (2010) 425403.
[3] C.Kittel, Phys. Rev., 73 [2] (1948) 155-161.
[4] A.Y.Tranenko, M.Mino, H.Yamazaki and V.L.Safonov, J.Phys.Soc.Jpn.,65[12](1996)4072-4075.
[5] H.Suhl, IEEE Trans. Mag. **34** [4] (1998) 1834-1838.

Electrical Conductivity Mechanisms of Glass-like Carbon

J. Stritt[1], J. A. Cuenca[1], E. L. H. Thomas[1], O. Williams[1]

[1]*School of Physics and Astronomy, Cardiff University, Cardiff CF24 3AA, Wales, UK*
strittj@cardiff.ac.uk

Keywords: dielectric spectroscopy, glass-like carbon, conductivity

Glass-like carbon can be briefly described as a macro-isotopic, non-planar form of non-graphitising carbon [1, 2]. In recent years, glass-like carbon has been synthesised through the pyrolysis of organic resins in the form of photoresists for further use in a variety of micro-electrical-mechanical systems (MEMS) [3,4]. Typically, resins are pyrolysed in inert atmospheres to temperatures exceeding 900°C in order to achieve a material with a suitably low resistivity. By understanding the pyrolysis-temperature dependant conductivity mechanisms in glass-like carbon, it is shown that the transition from high resistivity to the required electrical properties can be achieved at lower pyrolysis temperatures, thus improving the efficiency of glass-like carbon synthesis through pyrolysis.

In addition to favourable electrical properties, glass-like carbon's resilience to high temperature due to a high sublimation point (~3000°C) and non-graphitising structure, make it an ideal material for the fabrication of miniature black body emitters. Whilst previous studies have investigated various properties of glass-like carbon annealed at temperatures up to and exceeding 2500°C [5], a more comprehensive understanding of the development of glass-like carbons structure and the resulting conductivity mechanisms are paramount to understanding the behaviour of black body emitters fabricated from this material.

In this study, we explore the conductivity mechanisms in glass-like carbon synthesised from SU-8 3005 photoresist [3, 4] (a negative photoresist based on Bisphenol-A novolac resin) as a function of pyrolysis temperature. A variety of dielectric spectroscopic techniques are utilised, including broadband measurements using an open-ended coaxial probe (determined between 1kHz to 10GHz). and fixed-frequency resonance measurements using microwave cavity perturbation methods [6], to allow for a non-destructive and non-invasive measurement of complex permittivity and conductivity as a function of frequency. Analysis of microwave cavity perturbation measurements (Fig. 1) show a clear increase in the dielectric constant and loss factors of glass-like carbon's dielectric constants with an increase in pyrolysis temperature (Fig. 2).

By examining these properties, we are able to demonstrate how the development of an interconnected sp^2 carbon structure, allowing for long-range electrical transport, is dependent on pyrolysis temperature. These findings show that dielectric measurements (particularly microwave cavity perturbation) provide a simple and non-invasive means of determining successful glassy carbon pyrolysis, while the overall findings provide valuable insight into the electrical behaviour of glass-like carbon and have important implications for its potential applications in electronic devices.

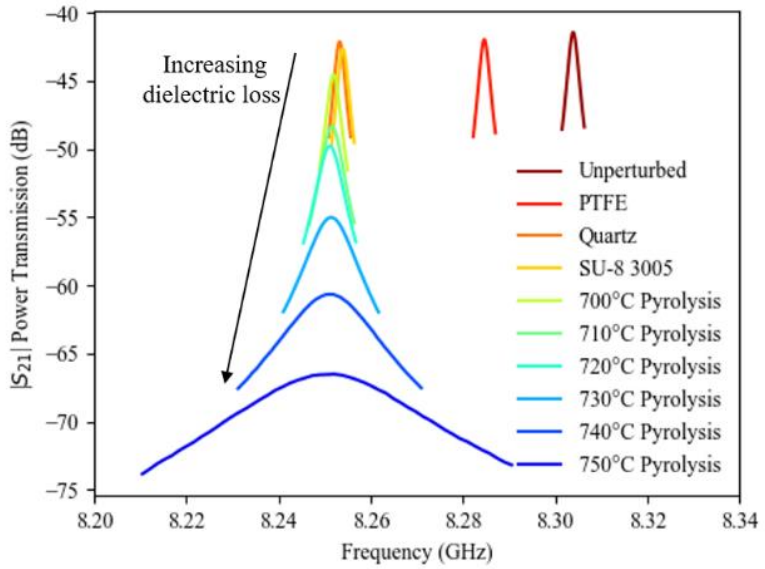

Fig. 1. Dielectric loss (measured using microwave cavity perturbation with a resonance peak at ~8.3GHz) increases as a result of increasing the maximum pyrolysis temperature of glass-like carbon (synthesised from SU-8 3005 spun onto quartz substrates), demonstrating the development of long-range electrical transport mechanisms.

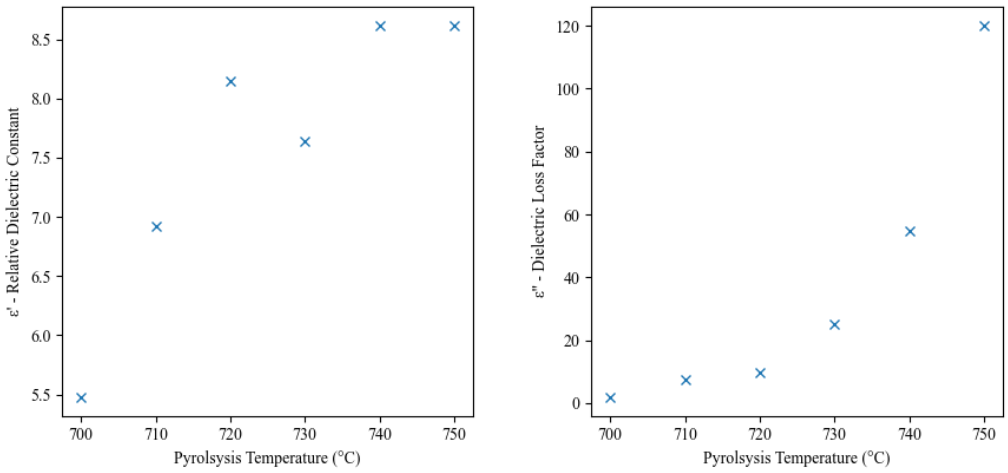

Fig. 2. Analysis of relative complex dielectric properties (as measured using microwave cavity perturbation method) to demonstrate the increase in both the real and imaginary parts of the relative complex dielectric constants.

References

[1] G. M. Jenkins and K. Kawamura. Structure of Glassy Carbon. Nature, 231(5299):175–176, May 1971.
[2] L. A. Pesin. Structure and properties of glass-like carbon. Journal of Materials Science, 37(1):1–28, 2002.
[3] Amit Singh, Jaishankar Jayaram, Marc Madou, and Sheikh Akbar. Pyrolysis of Negative Photoresists to Fabricate Carbon Structures for Microelectromechanical Systems and Electrochemical Applications. Journal of The Electrochemical Society, 149(3):E78, 2002.
[4] Rodrigo Martinez-Duarte. SU-8 Photolithography as a Toolbox for Carbon MEMS. Micromachines, 5(3):766–782, September 2014
[5] K. Jurkiewicz *et al.*, 'Evolution of glassy carbon under heat treatment: correlation structure–mechanical properties', *J Mater Sci*, vol. 53, no. 5, pp. 3509–3523, Mar. 2018
[6] J. A. Cuenca, E. Thomas, S. Mandal, O. Williams, and A. Porch, 'Microwave determination of sp2 carbon fraction in nanodiamond powders', *Carbon*, vol. 81, pp. 174–178, Jan. 2015

Exploring the Conductivity Enhancement in Solid State Ionic Materials under Microwave Irradiation

J. M. Catalá-Civera[1], B. García-Baños[1], J. D. Gutiérrez-Cano[1], J. R. Sánchez[1]

[1]*Instituto ITACA, Universitat Politècnica de València, Camino de Vera s/n, 46022, Valencia, Spain*
jmcatala@dcom.upv.es

Keywords: conductivity, dielectric properties, solid-state ionic materials, microwave cavity perturbation technique.

Over the past few years, the growing demand for energy has brought the advent of new materials with advanced properties, including the materials that generate, store and transport energy, along with innovative processing techniques such as radiofrequency, microwaves and solar energy. Among these techniques, electromagnetic radiation in the form of microwaves has gained significant attention for chemical synthesis as it offers an increased selectivity, higher product yield and a decrease in the reaction times and temperatures.

However, despite the numerous advantages of microwave processing, the effects and mechanisms of the microwave interaction with materials have not yet been fully clarified. Initially, the microwave interaction was considered to operate via two primary mechanisms, dipolar polarization and ionic conduction. However, it has been demonstrated that electromagnetic wave effects appear in chemical reactions when electrons are directly involved, and consequently, in chemical reactions progressing via electron transfer [1]. Therefore, the measurement of the conductivity enhancement during the application of microwave irradiation emerges as a core imprint of the electromagnetic nature of this electromagnetic wave effect.

The measurement of conductivity by microwave techniques was already reported in [2]. Most of these methods are based on the Microwave Cavity Perturbation Technique (MCPT) and allow the simultaneous measurement of the microwave permittivity and conductivity [3]. In a more recent paper, MCPT was applied to measure the temperature dependence and time evolution of dielectric properties and conductivity of materials simultaneous with the heating of the sample by high power microwaves [4].

In this work, we describe conductivity measurements of a selection of solid-state ionic materials, as well as the conductivity enhancement observed upon exposure to microwave irradiation. A comparative analysis is also conducted between the aforementioned materials and other materials that do not exhibit such alterations under similar conditions and/or conventional heating.

Figure 1 shows the Arrhenius plot of the conductivity during microwave and conventional heating of Ceria-oxide based samples. For example, the conductivity upon conventional heating of a sample of CGO follows an Arrhenius behavior characteristic of prevailing oxide-ion conduction. However, microwave heating emerges a distinct pattern and displays an abrupt increase in the conductivity.

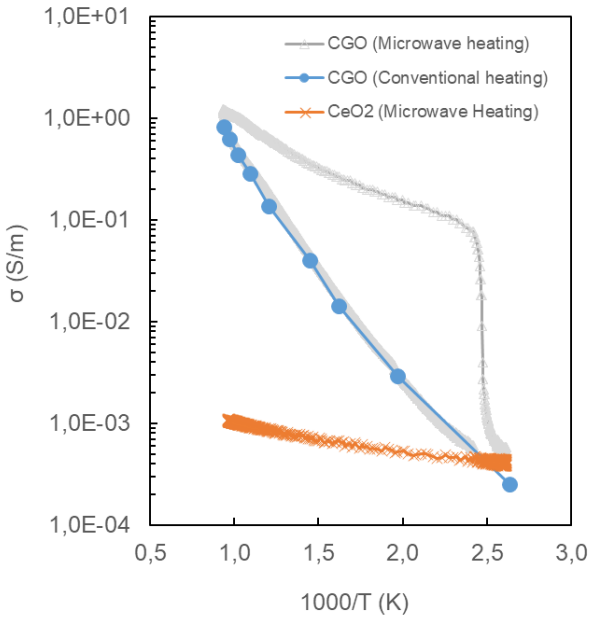

Fig. 1. Arrhenius plot of the conductivity during microwave and conventional heating of Ceria-oxide based samples.

References

[1] Horikoshi, S., Watanabe, T., Narita, A., Suzuki, Y., and Serpone, N., "The electromagnetic wave energy effect(s) in microwave–assisted organic syntheses (MAOS)," *Scientific Reports*, 2018, vol. 8, no 1, p. 5151.

[2] Hsieh, H., Goldey, J. M., and Brown, S. C., "A Resonant Cavity Study of Semiconductors," Journal of Applied Physics, 1954, vol. 25, no 3, p. 302-307.

[3] Krupka, J., "Contactless methods of conductivity and sheet resistance measurement for semiconductors, conductors and superconductors," *Measurement Science and Technology*, 2013, vol. 24, no 6, p. 062001.

[4] Catalá-Civera, J. M., Canós, A. J., Plaza-González, P., Gutiérrez, J. D., García-Baños, B., & Peñaranda-Foix, F. L., "Dynamic measurement of dielectric properties of materials at high temperature during microwave heating in a dual mode cylindrical cavity," *IEEE transactions on microwave theory and techniques*, 2015, vol. 63, no 9, p. 2905-2914.

Analysis of the Power Input for Crack-Free Drying of Green Bricks

V. Govindarasu[1], R. Wagner[1], M. Ganss[1], A. Tretau[1], N. Vorhauer-Huget[2], L. Briest[2]

[1]*Materials Research and Testing Institute at the Bauhaus-University Weimar, Coudraystr.9, 99423 Weimar, Germany*
[2]*Thermal Process Engineering, Otto von Guericke University Magdeburg, Magdeburg, Germany*
ralf.wagner@mfpa.de

Keywords: permittivity, green brick, shrinkage, temperature profile,

Introduction

The use of construction materials is essential in fulfilling the needs of modern urbanization and infrastructure development. However, it is important to note that the manufacturing and production of these materials emit greenhouse gases such as Carbon dioxide (CO_2), Methane (CH_4), and Nitrous oxide (N_2O) into the atmosphere and contribute to climate change. Among those various construction materials, the brick and tile industry are also responsible for a significant amount of greenhouse gas emissions, due to its conventional drying process that still relies on fossil fuel to fire the green bricks in kilns. In order to establish the drying of green bricks with microwave technologies in the production process, a crucial objective is to ensure the crack-free drying of these bricks, and it is necessary to meet the quality standard [1]. The occurrence of cracks mainly happens due to the shrinkage of clay materials when the drying process is too fast [2]. The findings from extensive research on intermittent microwave drying on bricks demonstrate the technical feasibility of this innovative technology in this domain when the microwave source is produced from renewable energy. In order to achieve crack-free drying of green brick, the process parameters must be studied and optimized. Therefore, in this work, the influence of intermittent power input on shrinkage, crack formation, and the drying process is investigated. Additionally, the temperature development within the test specimens is measured and studied.

Material and Methods

As an example, a Paving Clinker clay material with an initial moisture content of 20% is investigated for this work in order to study the drying process and identify the ideal energy input to achieve crack-free drying. The sample has a wide variety of minerals, with 65 % being layer silicate minerals that make the material moderately plastic, making it easy to shape. Freshly extruded and moist stored green products of paving clinker was used as sample material. Cylindrical samples were cut out of this material a diameter of about 38.8 mm and a height of 50.9 mm on average.

For the experiments, an ordinary household microwave oven was modified and equipped with a solid-state source with a frequency range of approximately 2.45 GHz and a maximum power output of 250 W. This made it possible to vary the power and the pulse length in the intermittent drying process. The microwave source is also equipped with a 100 W attenuator (frequency range: DC-3 GHz) to safeguard the microwave source from any reflected power from the microwave housing by diverting it to the attenuator, where it is converted into heat. A digital weighing balance is installed on the microwave housing and attached to the suspending sample holder inside the microwave-tight test chamber to record the sample's mass during the experiment. A small fan on the top right side of the oven housing was installed to remove the moisture air from the chamber to the outside. A very small optical camera from Rasberry Pi company was used to capture pictures of the sample. These pictures were utilized to study the relative shrinkage of the sample by using the two-point distance deformation method in GOM correlate software.

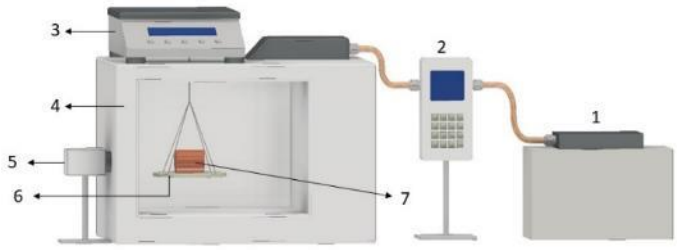

Fig. 1. Schematic diagram of the microwave drying system. 1. Microwave source, 2. Power meter, 3. Digital balance, 4. Microwave oven, 5. Optical camera, 6. Plastic tray, 7. Sample

A sensor made of optical fibre with polyimide coatings was utilized to measure the temperature profile of the sample. The fibre optic temperature measurements were performed with a single channel coherent frequency domain reflectometer type ODiSI B from LUNA (LUNA Innovations Incorporated, USA; distributed by Polytec GmbH, Germany) [3]. The temperature measurement is done with a spatial resolution of 0.65 mm, and the fibre optic sensor can measure temperatures up to 300 °C for extended periods. It measures around 2 m in length and has an inner diameter of 150 µm, which includes the coating.

The fiber end was meticulously prepared to avoid backscattering of light from its fractured surface. A Teflon tube with an inner diameter of 0.9 mm was inserted in the center of the sample along the radial axis to prevent any strain on the fiber optic sensor resulting from the sample's shrinkage during the drying process.

In this work, a series of ten experiments were conducted at room temperature and relative room humidity. All experiments were performed at a maximum power output (microwave source) of 150 W. To enable intermittent microwave drying, pre-programmed LabVIEW software controls the microwave source turning ON/OFF ratios, and it is also used to acquire data during the process. For a total of 30 seconds, considered one cycle, within this duration, the source was ON for a specific number of seconds and then OFF for another set of seconds. These ON/OFF ratios were varied for different experiments, and it was done to investigate the correlation between the mean power (P_{Mean}) and the presence of cracks in the samples and to study the drying process, shrinkage, and the influence of temperature.

Before starting the experiment, the sample parameters, such as diameter, height, and wet mass of the sample, were measured, and the sample was kept in the experimental chamber without rotation after placing the fiber optic sensor. Then the intermittent microwave drying tests started with the specified ON/OFF intervals. At the same time, the data acquisition system recorded the mass loss of the sample in the background. From the measured wet mass of the sample, moisture φ related to the dry mass was determined after the tests in the drying oven (1)

$$\varphi = \frac{m_{wet} - m_{dry}}{m_{dry}} \cdot 100 \qquad (1)$$

where m_{wet} and m_{dry} are the wet and dry mass of the sample. During the drying process, the moisture content of a substance gradually decreases over time. The drying rate, expressed as the percent of moisture evaporated over time, was determined by applying the formula in (2)

$$\dot{\varphi}_t = \frac{\varphi_t - \varphi_{t-\Delta t}}{\Delta t} \qquad (2)$$

where $\dot{\varphi}_t$ is the moisture content at any time t. The power emitted and the reflected power from the chamber was noted down during the experiment through the COMM-connect Power One directional RF Power Meter. From these values, the effective power P_{eff} was calculated using (3)

$$P_{eff} = P_{emi} - P_{ref} \qquad (3)$$

Where P_{emi} and P_{ref} are the emitted and reflected power in Watts, from this, the mean power at the beginning of the drying is calculated using (4)

$$P_{mean} = P_{eff} \cdot \frac{t_{on}}{t_{on} + t_{off}} \qquad (4)$$

The efficiency η of intermittent microwave drying refers to how effectively microwave energy is utilized to remove moisture from a material, and it was also calculated during the drying process as in (5)

$$\eta = \frac{P_{eff}}{P_{emi}} \qquad (5)$$

Results and Discussion

Moisture development

A graphical representation of how moisture changes over drying time with different levels of microwave energy input (mean power at the beginning) is illustrated in Figure 2. It shows that all samples have an initial moisture content of 20 % approximately. In order to meet industrial standards, brick samples must be dried to at least 3 % moisture content. The moisture curve demonstrates that samples exposed to high power, dry faster and reach the desired moisture content in less than 30 minutes. On the other hand, samples dried with low power takes nearly 2 hours to reach the same moisture level. This clearly indicates that the drying time is reduced in the high-power experiment, while in low-power experiment drying, the drying time is increased to achieve the desired moisture content.

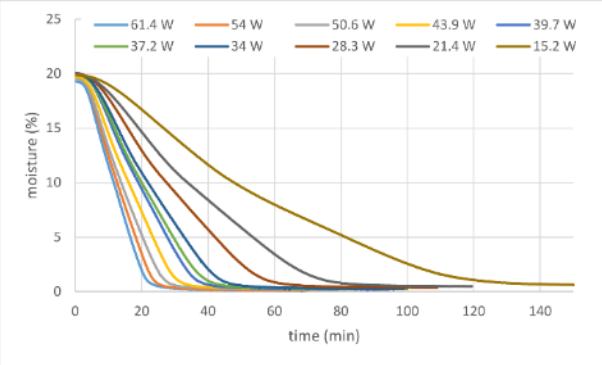

Fig. 2. Change in moisture over drying time with varying initial mean power levels

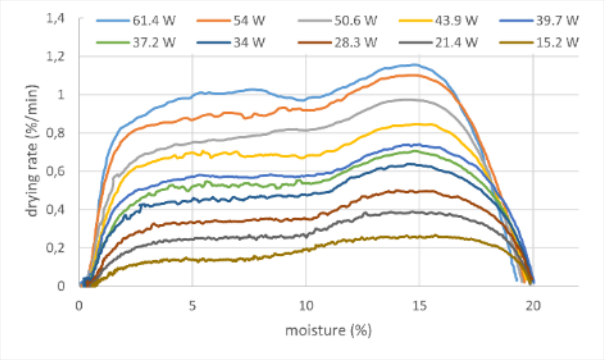

Fig. 3. Representation of drying rate over the moisture range with varying initial mean power levels.

From the moisture values over time, the drying rate is calculated and presented in Figure 3. It illustrates that samples dried with varying power inputs exhibit a similar pattern. The drying rate initially increased and reached its maximum, then decreased slightly to the moisture level of around 10 %. Further, it exhibits a constant trend until it reaches approximately 3 % of moisture, after which it decreases to the minimum. Notably, the maximum drying rate for different experiments with varying power inputs was achieved in the initial phase of the drying process. The sample dried with the high power (61.4 W) reached a maximum drying rate of 1.2 %/min, and the sample dried with the low power (15.2 W) attained a maximum drying rate of 0.25 %/min. Therefore, it clearly shows that the power input influences the drying rate, where the drying rate is high with high power, and the drying rate is low with low power.

Temperature profile

The temperature distribution within the sample's center along the radial axis was measured during the drying process for the medium power (39.7 W) experiment, and its significant insights are presented in Figure 4 at various time points. During the initial stage (t = 1 min, φ = 20 %), the heat is generated internally within the sample's core, owing to its distinctive feature of internal heating. Due to this, the temperature at the center rose to almost 60 °C in one minute. However, the temperature at the edges of the sample remained near room temperature. The maximum drying rate (t = 11.17 min, φ = 15 %) occurred with the resulting sample temperature of 100 °C, and the temperature distribution along the radial profile is more uniform. But still, the temperature is slightly high in the center of the sample. Then the temperature increases gradually (t = 19 min, φ = 10 %) and reaches the maximum temperature (t = 42.67 min, φ = 0.49 %). The temperature profile in this dry sample shows the highest values in the center and decreases towards the edges. The energy introduced into the sample by microwaves is released again as heat via the surface. Further drying almost no longer takes place. Moreover, it is essential to note that this sample dried without any cracks even though it reached the maximum temperature above 170 °C. Hence, it is evident that the occurrence of crack is not really based on temperature alone.

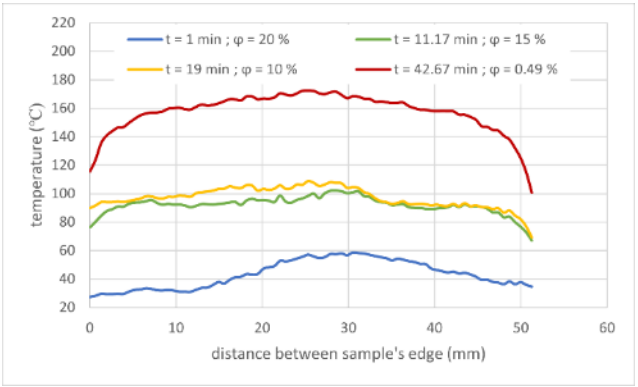

Fig. 4. Temperature distribution within the sample's center along the radial axis of

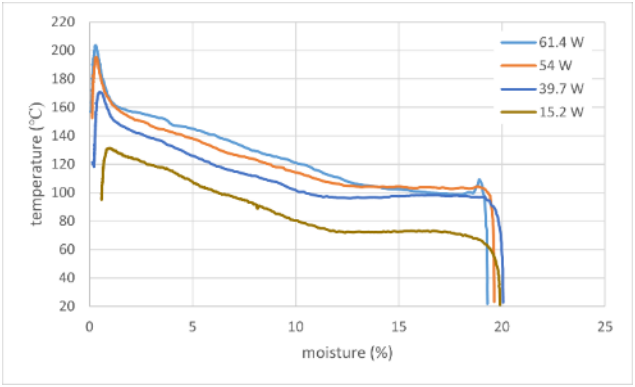

Fig. 5. Temperature development in the sample's core over the moisture range.

Additionally, the core temperature of the high, medium, and low power experiments was displayed in Figure 5 in relation to moisture. This graph depicts the various stages of temperature changes that occur during the drying process. Initially, the sample temperature increases and is stable over a specific moisture level, followed by a gradual rise to its maximum temperature, after which it begins to decrease. But the experiment which has the higher power input (61.4 W) differs from other medium and low energy input experiments because the sample temperature increases at the beginning and reaches 110 °C, but there is a slight drop to 100 °C, and its constant only over the short moisture range (until 15 %) then the temperature starts to increase gradually and reaches the maximum temperature of 200 °C and then it decreased. Meanwhile, the sample temperature for the medium and low-power experiments depicts a near-constant temperature until it reaches 10 % (approximately) after the initial phase. Afterward, it reached the maximum temperature of 170 °C and 130 °C, respectively, before decreasing. It is important to note that the samples are almost dry, with less than 3% moisture content, when the

temperature of the sample reaches its maximum. In summary, the sample dried with higher power experienced the highest maximum temperature, while the sample dried with low power achieved the lowest maximum temperature.

Shrinkage

During the drying process, moisture is removed from the sample, which causes the sample to shrink. Figure 6 displays the picture of the sample taken at the beginning (red circle) and end of the drying experiment (yellow circle), sample 1 dried with high power (61.4 W), and sample 10 dried with low power (15. 2 W). The pictures clearly show that Sample 1 experienced less shrinkage while sample 10 had more shrinkage after the drying process.

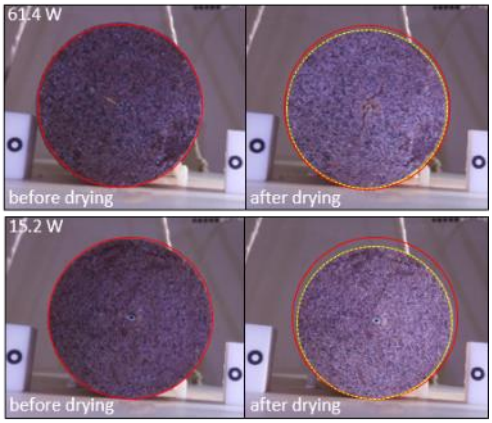

Fig. 6. Visual comparison of sample shrinkage before and after drying.

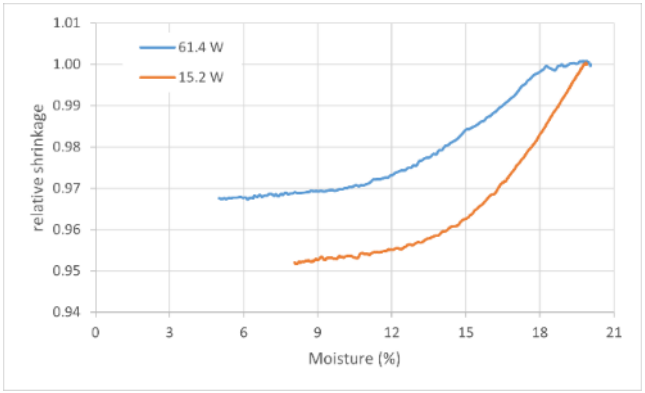

Fig. 7. Comparison of relative shrinkage between high and low power experiments.

Figure 7 presents the relative shrinkage of those samples plotted against the moisture. The relative shrinkage of sample 10 decreased from 1 to nearly 0.95, and sample 1 decreased from 1 to 0.97. Therefore, sample 10 has more relative shrinkage than sample 1 since it dried at low power. The relative shrinkage of sample 10 decreases gradually with the slower rate of moisture removal, which means that there is no such intense vapor pressure in the capillary that pulls the clay particles closer together over the drying time, which leads the sample to shrink more pronounced. However, the sample dried with the high power had no relative shrinkage at the very beginning of the experiment. In this stage, the sample temperature reaches the wet equilibrium and boiling temperature immediately and creates the liquid impulsion, which presses the liquid droplet to the surface (verified with the pictures taken during the drying process) and also creates intense vapor pressure in the capillary pores of the sample, counteracts the sample from the relative shrinkage that dries the sample with less shrinkage. To summarise, it is evident that the shrinkage behaviour of the clay sample is influenced by the power level at which microwave drying is carried out.

Optimal energy input

As mentioned before, we have examined samples with different power inputs and an initial moisture content of 20 %. Figure 8 depicts the maximum drying rate in correlation to the mean power, and it demonstrates a linear increase in the maximum drying rate as the mean power increases. It was observed that samples dried with a mean power exceeding 39.7 W exhibited cracks, whereas those dried below this threshold remained crack-free. Hence, for the 20 % initial moisture content, the nearest maximum power input (optimal energy input) to dry the sample without cracks is 39.7 W. Additionally, Figure 9 outlines the impact of different power inputs on sample dry densities. Dry densities show an exponential decline with increasing power inputs, eventually stabilizing after reaching 50.6 W. The low-power experiments yield higher dry densities due to increased shrinkage, whereas higher-power inputs result in reduced densities due to less shrinkage. However, it is known that samples getting cracks when it is subjected above the optimal energy input, as a consequence the dry densities tend to stabilize as crack forms. Finally, it has been revealed that increasing the power input further, does not lower the dry densities of these samples anymore.

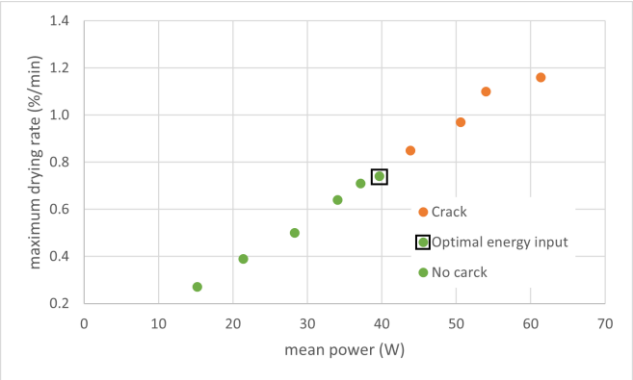

Fig. 8. Relationship between maximum drying rate and mean power for samples with 20 % initial moisture content

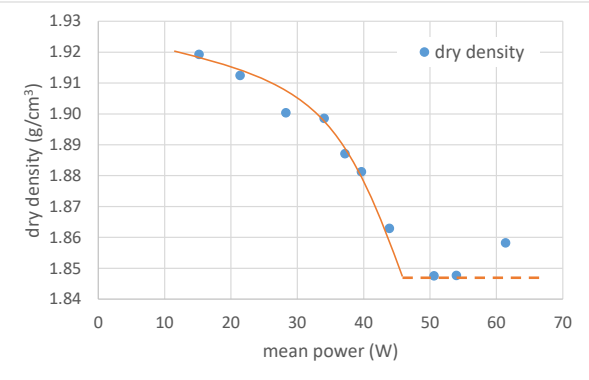

Fig. 9 Impact of mean power inputs on sample dry densities.

For the discussion of the drying process, the drying rate, core temperature, and efficiency of the crack-free sample are presented in relation to moisture in Figure 10. Starting at high moisture in the material, the temperature of the sample increases when microwave power is introduced into the sample chamber. During this initial phase of drying, the water molecules start to evaporate, then the drying rate increases and reaches its maximum value of 15 % (P1) whereas, the temperature inside the sample reaches 100 °C, and it tends to remain constant until the moisture is nearly 10 % (P2). As the drying progresses, its temperature increase, which further improves moisture removal and maintains a constant drying rate until 5 % of its moisture. The efficiency decreases at the beginning of the drying process. Later, with the increase of temperature, the loss factor of permittivity increases and thus the electrical energy is better absorbed by the sample. The efficiency increases again and reaches a maximum. With the dried sample and a moment of cooling, the dissipation factor decreases, less energy is coupled in and the temperature drops.

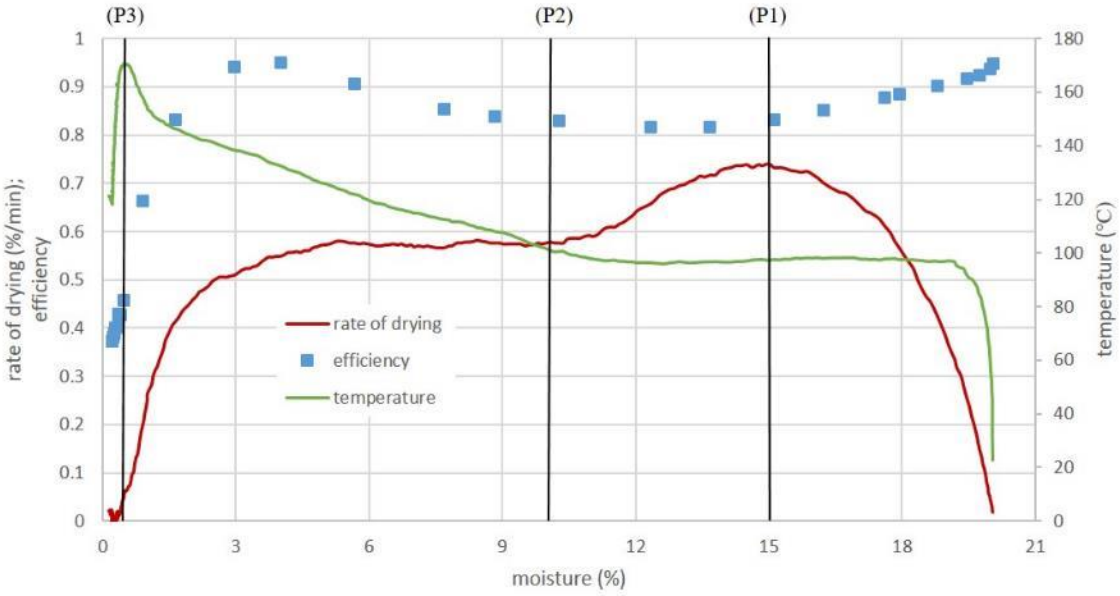

Fig. 10. Rate of drying, efficiency and temperature in the core of the cylindric sample

Therefore, the critical range for crack formation during drying is from the beginning until the sample reaches its maximum drying rate at point (P1). Hence, it is possible to increase the power input after reaching the critical range, which helps us to reduce the drying time further.

Conclusion

From the comparison of the experiments with different power inputs, a clear correlation between the amount of power and the internal temperature, as well as the maximum drying rate (at point P1), can be derived. From this, a limit value for the power input related to the amount of moisture at the beginning of drying can be determined. If the power input is above the limit value, cracks appear. Below the limit value, the sample dries without cracks. In the experiments, it was observed that the shrinkage between different samples depends on the power input. A higher power input leads to lower shrinkage, which results in lower density. The associated higher temperatures inside and the resulting higher partial pressure can explain this effect. The higher pressure inside counteracts shrinkage. The efficiency of the drying process decreases as drying progresses. The change in efficiency can be explained by the moisture and temperature dependence of the permittivity.

Acknowledgements

The research project was carried out in the framework of the industrial collective research program (IGF no. 20919 BG/2). It was supported by the Federal Ministry of Economics and Climate Protection of the Federal Republic of Germany (BMWi) through the AIF (German Federation of Industrial Research Associations eV) based on a decision taken by the German Bundestag.

References

[1] L. Briest, A. Tretau, R. Wagner, E. Tsotsas, N. Vorhauer (2022) “Microwave-assisted drying of clay roof tiles” *Drying Technology* vol. 40 (9)
[2] Y. Itaya, S. Uchiyama, S. Hatano, S. Mori, (2005) “Drying enhancement of clay slab by microwave heating” *Drying Technology* vol. 23(6), p. 1243-1255.
[3] D. Samiec *LAN Medium Access Control (MAC) and Physical Layer (PHY) Specification*, IEEE Std. 802.11, 1997.

Determination of the Permittivity of Clay to Explain Thermal Runaway during Microwave-Assisted Firing of Bricks

R. Wagner[1], M. Ganss[1], A. Tretau[1]

[1]*Materials Research and Testing Institute at the Bauhaus-University Weimar, Coudraystr.9, 99423 Weimar, Germany*
ralf.wagner@mfpa.de

Keywords: permittivity, clay, thermal runaway, resonator

Microwave technology could be an interesting method for electrified and energy-efficient firing of bricks. Compared to conventional heating, the heat is generated directly by absorption of the microwave radiation in the product. However, local discolouration, reduction nuclei due to microwave assisted firing are described in the literature [1, 2, 3]. In the case of silicate ceramic materials, the microwave-assisted firing can cause the temperature to rise locally very quickly and uncontrollably to a very high level. This effect is called 'thermal runaway' [4]. Figure 1 shows the results of a 'thermal runaway' illustrated by images from our own experiments. In these experiments, was used an illitic shale for paving clinker. The samples were cut out cylindrically from (in the brickworks) extruded green bricks.

Fig. 1. Pictures of thermal runaway in specimen with microwave-assisted firing. On the left with local discolouration and on the right with swelling and vitrification.

For the investigation of the thermal runaway effect, the permittivity was determined in a setup with a coaxial cavity resonator [5], frequency generator and detector. This type of resonator allows precise and reproducible positioning and measurements of larger specimens. The determination of permittivity with this measurement methodology has been discussed extensively and widely in the literature, with Flesoura et al. [6] and Hofele [7] in particular describing the high-temperature measurements. A calibration function is required to determine the complex permittivity from the resonance parameters resonance frequency and bandwidth. The calibration function was determined via a numerical simulation. For this purpose, the cavity resonator was constructed as a 3D FEM model in the Ansys HFSS software (Ansys, Inc., USA) and the interior tube was applied with a material of defined dielectric properties. The resonance parameters were determined from the simulated resonance curve for the idealised set-up. This allows calculating the functional relationship for the real or imaginary part of the permittivity. In order to deduce the local effect of the thermal runaway from the determined temperature-dependent permittivity, a sensor fibre was inserted in the radial axis of the cylinder to measure the linear temperature profile. This was used to measure the temperature development in the sample during the power input.

The dielectric properties of the above-mentioned clay material could be determined with the resonator set-up and a muffle furnace up to a sample temperature of about 900 °C. The values of the dielectric properties of the clay material are shown in Figure 2a for a frequency of 2450 MHz. Due to the drying of the samples, the permittivity drops significantly up to 110 °C. After that, the value of the complex permittivity is almost constant up to approx. 500 °C. At this temperature, a drop in the permittivity is observed. Above 750 °C, both the real and imaginary parts of the permittivity rise steeply.

During heating, the material undergoes various chemical processes. The individual effects can be derived from the DTG curve of the material. The DTA curve (Figure 2b) shows three endothermic peaks; (i) dehydration - physically bound water) at 90 - 130 °C, (ii) dehydration - interlayer water between 210 - 310 °C and (iii) dehydroxylation of the clay minerals between 450 - 750 °C. No structural change occurs. From approx. 800 °C, an amorphisation of the material takes place. Since various processes overlap, no significant changes in the mass are observed [8].

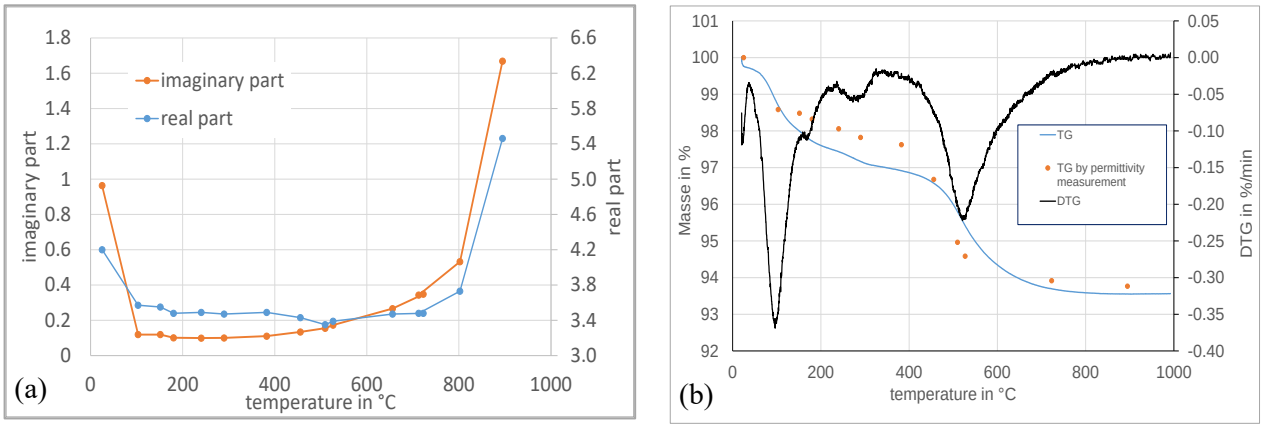

Fig. 2. (a) Temperature-dependent real and imaginary part of the permittivity. The samples had an initial moisture content of 1.4 %. (b) DTG curve and mass-loss curve as well as curve resulting from the permittivity measurement.

With the functional relationship between the temperature distribution from the fibre-optic measurements and the permittivity of the sample material, the imaginary part ε'' of the permittivity (loss factor) can be calculated. Figure 3 shows the local distribution of the imaginary part ε'' in the z-axis (sample height). Up to time t = 15.1 min, the loss factor ε'' varies only slightly over the profile. Thus, the spatial distribution of the energy input is essentially determined by the electric field. With increasing test duration, an inhomogeneous profile of the dissipation factor ε'' forms with higher values in the middle (approx. 10 to 30 mm). After a process time t = 29.85 min, the loss factor ε'' in the centre of the sample (h = 20 mm ± 8 mm) is clearly greater than 1. Thus, the energy input, which is directly proportional to the imaginary part, is increasingly concentrated in the centre of the sample. There, thermal runaway occurs with the undesirable effects described above.

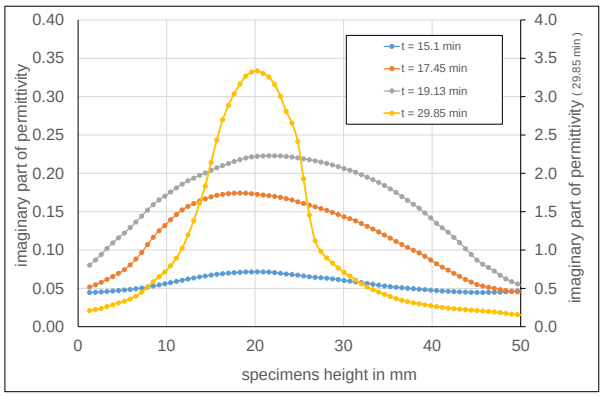

Fig. 3. Imaginary part of the permittivity in z-axis (specimen height). Remark: For better visualisation, a y-scale was included for the process time t = 29.85 min on the right side of the graphic chart.

The presented methodology for temperature-dependent permittivity determination, including a calibration by means of the simulation, is in principle suitable for any clay material. The temperature-dependent permittivities are material specific. Chemical reactions can be recognised in the real and imaginary part of the permittivity. The combination of spatially resolved temperatures with temperature-dependent permittivities allows for a detailed evaluation of the energy input by microwaves and the detection of 'thermal runaways' during microwave-assisted firing.

References

[1] S. Forouzan, (2020) "Mikrowellentechnik in der Baustoffherstellung - Erfahrungen und Potenziale." Available: https://www.transfer-und-innovation-ostbayern.de/fileadmin/Veranstaltungen/2020-09-29_TRIOKON_2020/Hub_Praesentationen/Forouzan_Mikrowellentechnik.pdf
[2] EUDP (2017) "Sustainable manufacture of brick and tiles with microwave energy" Final report 2017-12-14. Available: https://energiforskning.dk/sites/energiforskning.dk/files/slutrapporter/64013-0538_eudp_final_report_2017-12-14.pdf
[3] DTI (2017) "Microwave-assisted gas firing" *Ziegelindustrie International*, vol.6
[4] W. Xiaofeng (2002) "Experimental and Theoretical Study of Microwave Heating of Thermal Runaway Materials" Faculty of the Virginia Polytechnic Institute: Dissertation., Blacksburg, Virginia, USA
[5] K. Kupfer, G. Fuchs, R. Wagner, H. Kupfer, B. Müller, (2011) "Simulation of Resonator Sensors using HFSS" In: *Proc. 9th Int. Conf. on Electromagnetic Wave Interaction with Water and Moist Substances*, June 2011
[6] G. Flesoura, B. Garcia-Banos, J.M. Catala-Civera, J. Vleugels, Y. Pontikes (2019) "In-Situ Measurements of High-Temperature Dielectric Properties of Municipal Solid Waste Incinerator Bottom Ash." *Ceramics International* vol. 45, p.18751-18759
[7] J. Hofele, G. Link, J. Jelonnek (2022) "Reaction Kinetics and Process Model of the Polyacrylonitrile Fibers Stabilization Process Based on Dielectric Measurements." *Materials* 2022, vol. 15, p.1222, Available: https://doi.org/10.3390/ma15031222
[8] A. Schwarz-Tatarin (2009) Wirkmechanismen anorganischer Sekundärrohstoffe in silicatkeramischen Massen. Dissertation Bauhaus-Universität Weimar, June 2009

Enhancing the Efficiency of Industrial Microwave Firing Processes through In-Situ Monitoring of Dielectric Properties during Mineral Transformations

B. García-Baños[1], J. D. Gutiérrez-Cano[1], J. R. Sánchez[1], F. L. Peñaranda-Foix[1]

[1]*ITACA Institute, Universitat Politècnica de València, Camino de Vera s/n, 46022, Valencia, Spain*
beagarba@upvnet.upv.es

Keywords: dielectric properties, microwave heating, ceramic pigments, carbothermic reduction

In the fight against climate change, reducing the CO_2 footprint and improving resource efficiency are imperative goals for industries, particularly those that are energy-intensive, such as the ceramic and steel sectors. One promising solution that has garnered significant attention is the electrification of processes through use of microwave technology. This technology offers proven advantages, including shorter processing times, higher efficiencies, and compact device design. Furthermore, this approach aligns with sustainable practices by allowing for the use of renewable energy sources, rather than fossil fuels, to power the necessary electricity.

Concurrently with the development of microwave applicators for industrial use, there is a growing demand for analytical techniques that assist process designers in accurately defining process steps and conditions, thus optimizing the newly adopted microwave processes [1,2].

In this work, microwave dielectric thermal analysis (MW-DETA) [3] has been employed to identify material transformations in two microwave processes: the synthesis of ceramic pigments and the carbothermic reduction of iron-bearing wastes from the steel industry. Dielectric curves as a function of material temperature have been analysed providing valuable insights into reaction pathways, as well as the effects of varying operational parameters on the resulting reactions.

The analysis of dielectric data and its implications for the industrial processes is presented. In the case of ceramic pigment synthesis, the evaluation of dielectric curves has allowed the identification of the minimum temperature required for the reaction, the impact of ultra-fast heating rates, and the potential to simplify the composition of raw material mixtures.

For the microwave-driven carbothermic reduction of steel wastes, dielectric properties have shown clear disparities in reactions with respect to conventional heating methods. The work presents an analysis of dielectric properties as a function of density and carbon content leading to conclusions on how to optimize the microwave process. Furthermore, a parametric study of penetration depth as a function of temperature illustrated the best conditions for the upscaling towards a potential industrial process.

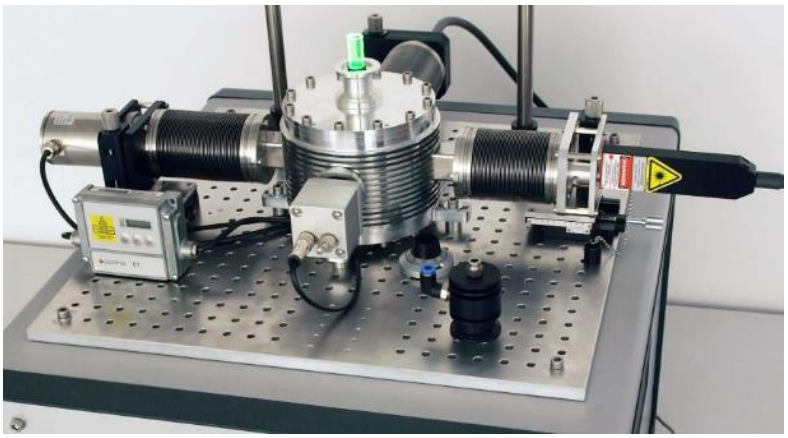

Fig. 1. Microwave equipment to perform dielectric thermal analysis (MW-DETA).

References

[1] P. Ramos, D. Albuquerque and J. Pereira. “Numerical simulation and optimization of the ceramic pigments production process using microwave heating”, *Chem. Eng. and Proc. – Proc. Intens.* 169, 108567, 2021.

[2] B. Garcia-Baños, J.M. Catalá-Civera, F.L. Peñaranda-Foix, P. Plaza-González and G. Llorens-Vallés, “In Situ Monitoring of Microwave Processing of Materials at High Temperatures through Dielectric Properties Measurement”, *Materials* 2016, 9(5), 349.

[3] J.M. Catala-Civera, A.J. Canós-Marín, P. Plaza-González, J.D. Gutiérrez Cano, B. García-Baños and F.L. Penaranda-Foix, “Dynamic Measurement of Dielectric Properties of Materials at High Temperature During Microwave Heating in a Dual Mode Cylindrical Cavity” *IEEE Trans. on Microw. Theory Techn.*, Vol. 63, pp. 2905-2914, 2015.

Highly Sensitive Gas Sorption Dielectric Measurements Using a Re-Entrant Microwave Cavity

M. Barter[1], Y. Chen[2], S. Yang[2], M. O. Jones[3,4], A. Porch[1]

[1]*Centre for High Frequency Engineering, School of Engineering, Cardiff University, UK*
[2]*School of Chemistry, University of Manchester, Manchester, UK*
[3]*ISIS Neutron and Muon Source, STFC Rutherford Appleton Laboratory, Didcot, UK*
[4]*University of St Andrews, St Andrews, Fife, UK*
BarterM@Cardiff.ac.uk

Keywords: microwave measurement, permittivity, re-entrant cavity resonator, gas sensing, material characterisation

Detection of the presence of gases is a challenging problem, especially with toxic gases like SO_2 that can have serious health implications down at single digit ppm levels [1]–[3]. One method of quantifying this is using a mesoporous material with the ability to absorb the required gas and measure changes in dielectric properties of the material as the gas is absorbed. Changes in resonant frequency of the cavity as the gas is absorbed by the material can be corelated to the amount of SO_2 present in the gas stream. We have also shown previously that microwave loss is a direct indicator of the dynamics of the sorbed species within the absorber matrix. This has been confirmed by simultaneous neutron diffraction measurements [4]–[6]. A standard cylindrical microwave cavity can be used to measure this with a high degree of success, however there is a lower limit on the gas concentration that can be detected and quantified.

This work investigates methods of quantifying SO_2 concentrations using microwave dielectric measurements. We propose the use of a cylindrical re-entrant cavity along with a suitable mesoporous material to detect and quantify the concentration of SO_2 present in a gas stream. As can be seen in Fig. 1, the electric field of a re-entrant cavity is confined to the bottom of the post in the centre of the cavity. The magnitude of this electric field remains approximately constant over the width of the post. If a sample of porous material is inserted under the post and a gas stream is passed over the sample, this will cause changes in the cavity's resonant frequency. Due to the high filling factor compared to a standard microwave cavity, this greatly enhances the sensitivity, which should allow for a lower limit of detection of SO_2 concentrations [7]. Fig. 2 shows a render of the re-entrant cavity design including a way of connecting a gas stream in and out of the cavity. Fig. 3 is an S_{21} response of the cavity showing the resonant frequency of the constructed microwave cavity of approx. 2.77 GHz and a Q factor of over 1200. This aluminium cavity has a height of 10 mm, cavity radius of 16 mm, post radius of 7.5 mm with a 1 mm gap at the bottom of the post.

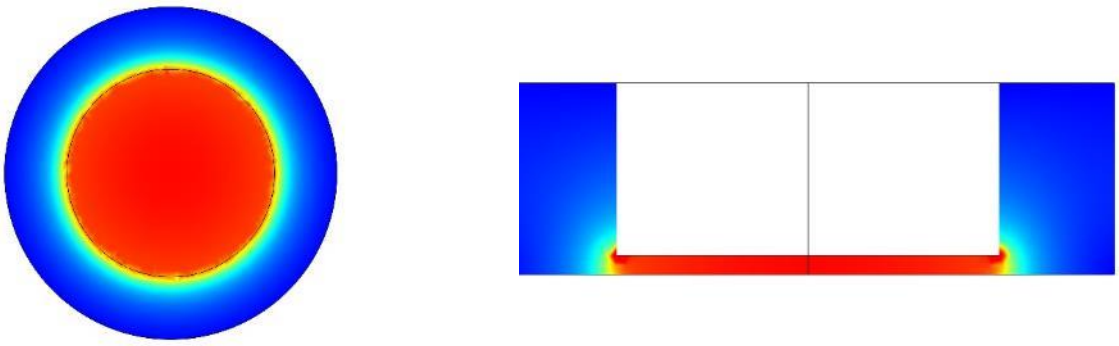

Fig. 1. COMSOL simulation of the electric field in cylindrical re-entrant cavity from top (left) and side (right) views.

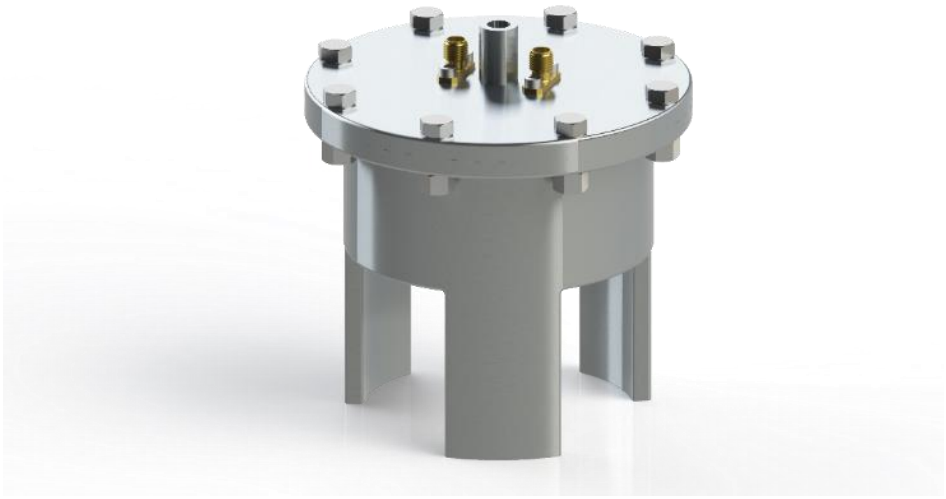

Fig. 2. Render of microwave cavity with gas tank.

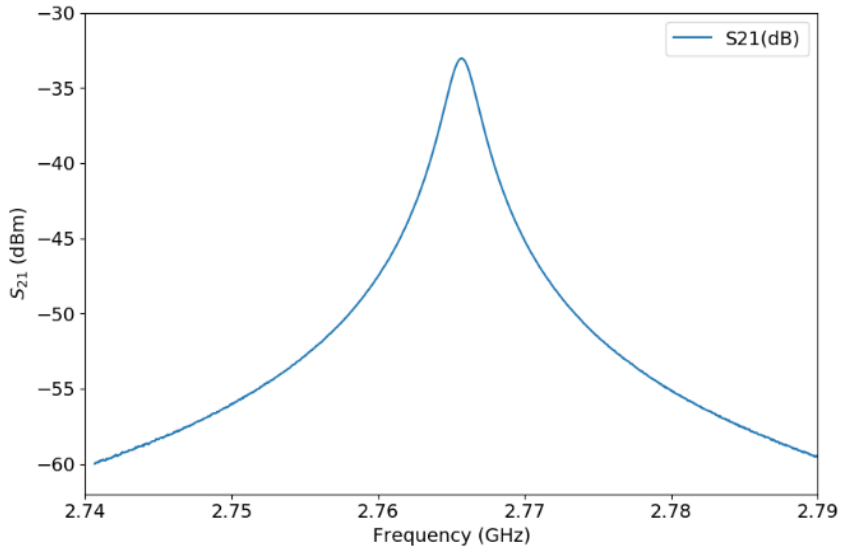

Fig. 3. S_{21} plot showing the resonant frequency of the TM_{010} mode of the constructed re-entrant cavity.

References

[1] N. Sun *et al.*, "Remobilization and bioavailability of polycyclic aromatic hydrocarbons from estuarine sediments under the effects of Nereis diversicolor bioturbation," *Environ. Pollut.*, vol. 242, pp. 931–937, 2018.
[2] J. Li *et al.*, "Major air pollutants and risk of COPD exacerbations: A systematic review and meta-analysis," *Int. J. COPD*, vol. 11, no. 1, pp. 3079–3091, 2016.
[3] J. A. Nadel, H. Salem, B. Tamplin, and Y. Tokiwa, "Mechanism of bronchoconstriction during inhalation of sulfur dioxide," *J. Appl. Physiol.*, vol. 20, no. 1, pp. 164–167, 1965.
[4] M. O. Jones, D. M. Royse, P. P. Edwards, and W. I. F. David, "The structure and desorption properties of the ammines of the group II halides," *Chem. Phys.*, vol. 427, pp. 38–43, 2013.
[5] M. Barter *et al.*, "Simultaneous neutron powder diffraction and microwave dielectric studies of ammonia absorption in metal-organic framework systems," *Phys. Chem. Chem. Phys.*, vol. 20, no. 15, pp. 10460–10469, 2018.
[6] M. Barter, G. Smith, S. Yang, M. Schröder, M. O. Jones, and A. Porch, "Simultaneous neutron powder diffraction and microwave characterisation at elevated temperatures," *Phys. Chem. Chem. Phys.*, vol. 23, no. 41, pp. 23602–23609, 2021.
[7] H. Hamzah, A. Abduljabar, J. Lees, and A. Porch, "A Compact Microwave Microfluidic Sensor Using a Re-Entrant Cavity," *Sensors*, vol. 18, no. 3, p. 910, 2018.

Study of Microwave Heating of Vacancy Induced 3C-SiC: A Molecular Dynamics Approach

T. L. Dora[1], R. R. Mishra[1]

[1]*Department of Mechanical Engineering, Birla Institute of Technology and Science Pilani, Pilani-333031, India.*
rraman.mishra@pilani.bits-pilani.ac.in

Keywords: 3C-SiC, vacancy defect, microwave heating, classical molecular dynamics, electric field strength, frequency

Microwave heating has gained significant attention due to its rapid, volumetric, and uniform heating capabilities. Extensive research has been carried out on the interaction between microwaves and various materials to comprehend the fundamental mechanisms and enhance the heating process. In recent times, silicon carbide (SiC) has gained significant attention as a potential material for various applications such as susceptor, electronic devices, nuclear reactors, and energy storage systems. However, the thermal and mechanical properties of SiC can be significantly affected by the presence of various defects like vacancy defect, interstitial defect etc. Recently, classical molecular dynamics (MDs) has been emerged as an effective tool to study the microwave irradiation of different material at molecular level. The present investigation utilizes molecular dynamics (MD) simulations to investigate the effects of microwave irradiation on vacancy-induced 3C-SiC under varying electric field strengths (0.1 and 0.5 V/Å) and frequencies (100 and 300 GHz).

To investigate the microwave heating effect of vacancy induced 3C-SiC, two sets of simulation systems were generated using the ATOMSK platform [1]. One set of system consist of 1% of Silicon (Si) vacancy whereas the other set includes 1% of carbon (C) vacancy. Both the system had dimension of 87.2×87.2×87.2 Å^3, with a lattice parameter 4.36 Å and consist of approximately 63,680 atoms. Periodic boundary conditions were employed in x, y and z-directions. Molecular simulations were carried out in an open-source Large Scale Atomic/Molecular Massively Parallel Simulator (LAMMPS) package [2] and post-processing of the simulation was performed using open visualisation tool (OVITO) [3]. The interactions between silicon (Si) and carbon (C) atoms were described using the Vashishta potential [4], which is a commonly utilized interatomic potential for simulating SiC materials. To begin with, both the systems were equilibrated in an NVT ensemble for 1.5 ns in order to reach a stable room temperature (300 K). Subsequently, the system was treated with microwave energy, by applying an external alternating electric field in x-direction in an NVE ensemble for 4.5 ns. The microwave field applied to the system can be expressed as [5]:

$$\vec{E} = \overrightarrow{e_x} E_n \sin(2\pi f t) \quad (1)$$

where, $\mathbf{E_n}$, $\overrightarrow{e_x}$, f and t are the electric field strength, direction of electric field, frequency of microwave and the elapsed time of microwave irradiation respectively. Different electric field strength (0.1 and 0.5 V/Å) and frequencies (100 and 300 GHz) were applied to examine the microwave effect in vacancy induced 3C-SiC.

From the results (Fig. 1), it was observed that, the evolution of temperature during microwave exposure in the case of C-vacancy induced 3C-SiC was more rapid than the Si-vacancy induced 3C-SiC. It was observed that the C-vacancy induced 3C-SiC reached the melting point of 3300 K in 3.84 ns at 0.5 V/Å and 300 GHz; whereas; for the same time the Si-vacancy induced 3C-SiC only attained a temperature of 1062 K at 0.5 V/Å and 300 GHz. The time taken by C-induced 3C-SiC to attain a temperature of 1062 K, was approximately 49.5% less than the Si-vacancy induced 3C-SiC. From the polyhedral template matching, for C-vacancy induced 3C-SiC, a reduction of 0.5% and 0.9% in hexagonal diamond and graphene structure was observed for 0.5 V/Å electric field strength and 300 GHz. In the meantime, the cubic diamond structure was increased by 1.1% compared to initial structure. On the other hand, a decrease of 0.2% graphene structure and an increase of 0.3% cubic diamond structure was observed in case of microwave irradiated Si-vacancy induced 3C-SiC while the other structure remained constant.

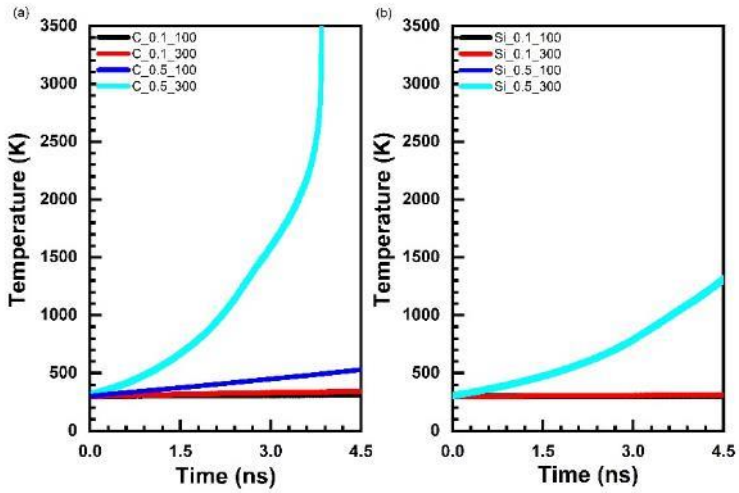

Fig. 1. Evolution of temperature during microwave heating of 3C-SiC having (a) C-vacancy and (b) Si-vacancy

References

[1] P. Hirel, Atomsk: A tool for manipulating and converting atomic data files, Comput. Phys. Commun. 197 (2015) 212–219. https://doi.org/10.1016/j.cpc.2015.07.012.

[2] A.P. Thompson, H.M. Aktulga, R. Berger, D.S. Bolintineanu, W.M. Brown, P.S. Crozier, P.J. in 't Veld, A. Kohlmeyer, S.G. Moore, T.D. Nguyen, R. Shan, M.J. Stevens, J. Tranchida, C. Trott, S.J. Plimpton, LAMMPS - a flexible simulation tool for particle-based materials modeling at the atomic, meso, and continuum scales, Comput. Phys. Commun. 271 (2022) 108171. https://doi.org/10.1016/j.cpc.2021.108171.

[3] A. Stukowski, Visualization and analysis of atomistic simulation data with OVITO – the Open Visualization Tool Visualization and analysis of atomistic simulation data with OVITO – the Open Visualization Tool, (2010). https://doi.org/10.1088/0965-0393/18/1/015012.

[4] P. Vashishta, R.K. Kalia, A. Nakano, J.P. Rino, Interaction potential for silicon carbide : A molecular dynamics study of elastic constants and vibrational density of states for crystalline and amorphous silicon carbide Interaction potential for silicon carbide : A molecular dynamics study of elastic c, J. Appl. Phys. Phys. 101 (2007) 1–12. https://doi.org/10.1063/1.2724570.

[5] T.L. Dora, A. Owhal, T. Roy, S.U. Belgamwar, S. Goel, H.Y. Nezhad, R.R. Mishra, Thermo-physical characteristics of 3C-SiC structure subjected to microwave exposure: A molecular dynamics study, Mater. Today Commun. 35 (2023) 105693. https://doi.org/10.1016/j.mtcomm.2023.105693.

Anisotropic Hexaferrite $BaFe_{12}O_{19}$ for Microstrip Devices of Microwave Electronics of the mm-Wavelength Range and Terahertz Electronics

V. G. Kostishin[1], S. V. Shcherbakov[2], A. G. Nalogin[2], A. A. Alekseev[2], A. Y. Mironovich[1], I. M. Isaev[1], A.V. Timofeev[1], G. A. Skorlupin[1]

[1]NUST MISIS, Leninsky Prospekt 4, building 1, Moscow, 119049, Russia
[2]JSC "NPP "Istok" named after Shokina", st. Vokzalnaya 2A, Fryazino, Moscow region, 141190, Russia
drvgkostishyn@mail.ru

Keywords: anisotropic hexaferrites, microwave electronics, terahertz electronics, degree of magnetic texture, ceramic technology, radiation thermal sintering technology, electromagnetic parameters

Anisotropic hexagonal ferrites $BaFe_{12}O_{19}$ in the form of plates and films are currently one of the most promising materials for the production of microwave electronic devices in the mm-wavelength range and terahertz electronics. In hexaferrites, it is possible to achieve the effect of self-displacement. This makes it possible to completely get rid of the external magnetic system or significantly reduce its dimensions. To achieve the self-bias effect, a high magnetocrystalline anisotropy or degree of magnetic texture is required. This can be realized in thin plates or films of hexagonal ferrites.

This paper presents the technological aspects of obtaining electromagnetic properties of polycrystalline plates and films of hexagonal ferrites $BaFe_{12}O_{19}$ with a high degree of magnetic texture for microstrip devices for microwave electronics in the mm-wavelength range and terahertz electronics. $BaFe_{12}O_{19}$ polycrystals were obtained using two technologies: (i) ceramic technology and (ii) radiation-thermal sintering technology [1]. Raw blanks for the two technologies were obtained by mixing high-purity oxides $BaCO_3$ and Fe_2O_3, followed by their grinding, ferritization and pressing in a magnetic field. Pressing of raw workpieces was carried out in the magnetic field with the intensity H = 10 kOe. The sintering of $BaFe_{12}O_{19}$ plates using technology (i) was carried out in thermal resistance furnaces, while using technology (ii) on the ILU-6 electron accelerator. The sintering temperature varied from 1200°C to 1400°C. The sintering time for technology (i) was 8-10 hours, for technology (ii) was 30-90 minutes. $BaFe_{12}O_{19}$ films were obtained by vacuum ion-beam sputtering. Argon was used as the working gas, which was fed into the chamber until the pressure of $5\text{-}7\cdot10^{-2}$ Pa was reached. The deposition was carried out using a Hall-type ion source with a hollow cathode cooled by water. The source voltage was 1.8–2.0 kV, and the current was 20–50 mA. Substrates based on Si and Al_2O_3 of different crystallographic orientations were used as substrates. Ti, TiO_2, Al_2O_3, Si_3N_4 layers and their modifications were used as buffer layers.

The samples were studied by X-ray diffraction and X-ray phase analysis, Mösbauer spectroscopy, and magnetometry. The degree of magnetic texture f (%) of the finished samples was estimated from the X-ray diffraction curves.

The research results showed that all the obtained samples are single-phase. Space group P63/mmc (No. 194) – hexaferrite. The maximum degree of magnetic texture of the obtained plates and films was f = 89–93%.

The paper also presents changes in the main magnetic and electromagnetic parameters of the synthesized anisotropic $BaFe_{12}O_{19}$ plates and films depending on the technological regimes.

Aspects of the practical use of the obtained results are discussed.

References

[1] V.G. Kostishin, V.V. Korovushkin, A.G. Nalogin, S.V. Shcherbakov, I.M. Isaev, A.A. Alekseev, A.Y. Mironovich, D.V. Salogub, "Features of the Magnetic Structure of $Y_3Fe_5O_{12}$ Polycrystals Synthesized by Radiation Thermal Sintering", Physics of the Solid State, 2020, vol. 62, No. 7, pp. 1156-1164.

Dielectric Properties of Common 3D Printed Materials at Microwave Frequencies

S. Hefford[1], A. Morgan[1], S. Hashimdeen[2], J. Cuenca[3]

[1]*Centre for High Frequency Engineering, School of Engineering, Cardiff University, Cardiff CF24 3AA, UK*
[2]*Wolfson Centre for Magnetics, School of Engineering, Cardiff University, Cardiff CF24 3AA, UK*
[3]*Condensed Matter and Photonics Group, School of Physics and Astronomy, Cardiff University, Cardiff CF24 3AA, UK*
heffordsj@cardiff.ac.uk

Keywords: microwave, radiofrequency, dielectric, 3D printing,

Over the past decade, 3D printing (3DP) has become extremely popular, giving the ability to produce complex structures at an economy and time scale which would otherwise be impossible using conventional methods. Within the context of microwave and radiofrequency applications, some prime examples of this include reflect arrays [1], as well as dielectric lenses [2,3], and broadband absorbers [4], to name a few. Despite the rapidly growing interest in utilising 3DP processes for microwave and radio applications, there has yet to be any significant work done on the characterisation of these materials, in terms of their dielectric (and magnetic) properties, at kHz - GHz frequencies. This information is crucial for the electromagnetic design of such components, critically, as the material properties of 3DP materials are often distinct from their bulk material counterparts, having been optimised for the 3DP process itself.

In this work we present preliminary results measuring the dielectric properties of three of the most common 3DP filament materials: acrylonitrile butadiene styrene (ABS), polylactic acid (PLA), and polyethylene terephthalate glycol (PETG), at frequencies up to 10 GHz using microwave cavity perturbation. The influence of pigmentation on dielectric properties, as well as the variation between different manufacturers, are also considered.

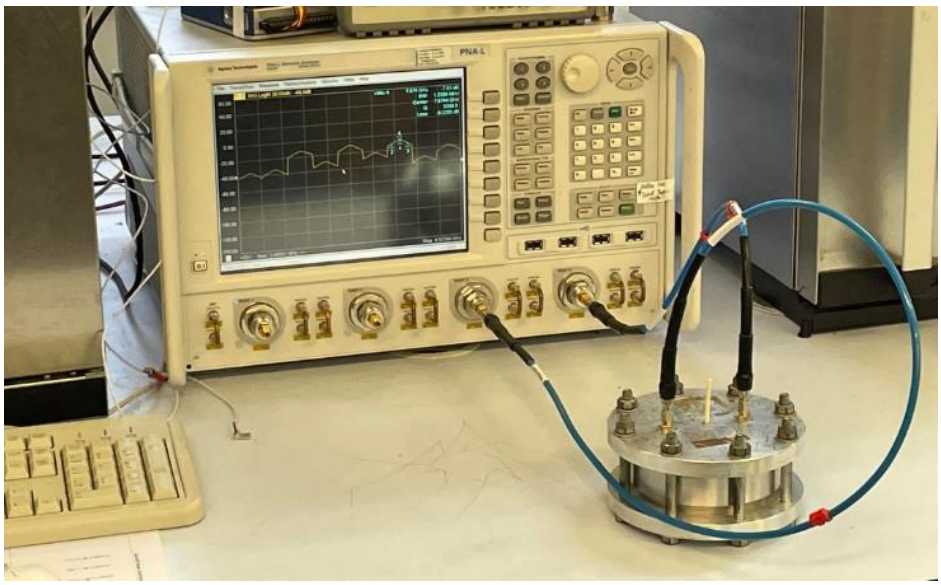

Fig. 1. Experimental setup.

Cylindrical samples of ABS, PLA, and PETG were produced by Fused-Deposition Modelling (FDM) and measured using a cylindrical microwave cavity resonator and vector network analyser (VNA) as shown in Fig. 1. Samples were printed flat to the build plate in order to minimise any depolarisation effects associated with the orientation of the layers themselves. Fig 2. shows a typical cavity perturbation result; the unloaded (empty) cavity resonance when perturbed by the sample undergoes a shift in resonant frequency (f_0) and a change in bandwidth (BW). The shift in f_0 is due to the real part of the sample permittivity, also known as the dielectric constant, while the change in BW is due to the imaginary component, which represents dielectric loss. Both quantities are evaluated using the microwave cavity perturbation equations [5]. A selection of results are given in Table 1.

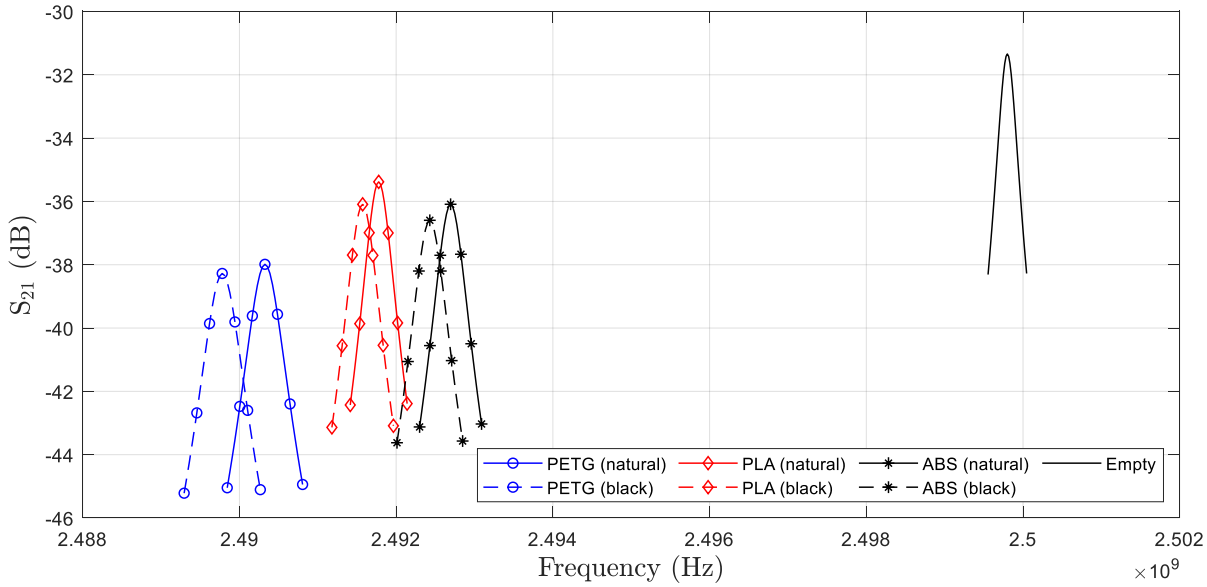

Fig. 2. Measured transmission (S_{21}) responses of TM_{010} resonant mode for PETG, PLA, and ABS samples.

Table 1. Dielectric Constant (Dk) and Dissipation Factor (Df) of PLA, PETG, and ABS 3DP Samples Measured by MCP.

Material	Colour	Dk (2.50 GHz)	Df (2.50 GHz)	Dk (5.73 GHz)	Df (5.73 GHz)	Dk (9.55 GHz)	Df (9.55 GHz)
PETG	Natural	3.09	8.11×10^{-3}	3.11	7.50×10^{-3}	3.11	7.20×10^{-3}
	Black	3.21	8.35×10^{-3}	3.24	7.86×10^{-3}	3.24	7.65×10^{-3}
	White	3.17	8.15×10^{-3}	3.20	7.56×10^{-3}	3.20	7.28×10^{-3}
PLA	Natural	2.77	4.41×10^{-3}	2.79	5.36×10^{-3}	2.80	6.04×10^{-3}
	Black	2.76	5.41×10^{-3}	2.76	6.46×10^{-3}	2.82	6.93×10^{-3}
	White	2.83	4.49×10^{-3}	2.85	5.44×10^{-3}	2.85	6.08×10^{-3}
ABS	Natural	2.61	6.16×10^{-3}	2.61	5.90×10^{-3}	2.63	5.66×10^{-3}
	Black	2.66	7.03×10^{-3}	2.65	6.74×10^{-3}	2.69	6.46×10^{-3}
	White	2.70	6.32×10^{-3}	2.70	5.99×10^{-3}	2.72	5.69×10^{-3}

References

[1] P. Nayeri et al., "3D Printed Dielectric Reflectarrays: Low-Cost High-Gain Antennas at Sub-Millimeter Waves," *IEEE Transactions on Antennas and Propagation*, vol. 62, no. 4, pp. 2000-2008, April 2014, doi: 10.1109/TAP.2014.2303195.

[2] Shiyu Zhang, "3D printed dielectric Fresnel lens," 2016 *10th European Conference on Antennas and Propagation (EuCAP)*, Davos, 2016, pp. 1-3, doi: 10.1109/EuCAP.2016.7481775.

[3] J. -M. Poyanco, F. Pizarro and E. Rajo-Iglesias, "3D-printed dielectric GRIN planar wideband lens antenna for 5G applications," 2021 *15th European Conference on Antennas and Propagation (EuCAP)*, Dusseldorf, Germany, 2021, pp. 1-4, doi: 10.23919/EuCAP51087.2021.9411342.

[4] K. G. Kjelgård, D. T. Wisland and T. S. Lande, "3D Printed Wideband Microwave Absorbers using Composite Graphite/PLA Filament," 2018 *48th European Microwave Conference (EuMC)*, Madrid, Spain, 2018, pp. 859-862, doi: 10.23919/EuMC.2018.8541699.

[5] J. A. Cuenca, E. Thomas, S. Mandal, O. Williams and A. Porch, "Investigating the Broadband Microwave Absorption of Nanodiamond Impurities," in *IEEE Transactions on Microwave Theory and Techniques*, vol. 63, no. 12, pp. 4110-4118, Dec. 2015, doi: 10.1109/TMTT.2015.2495156.

Advanced Material Sintering Using Adaptive Microwave Technique

Y. Alekajbaf[1], S. Murali[2], K. Pelckmans[1, 2], D. Pelikan[1], D. Dancila[1, 2, 3]

[1]*FREIA, Department of Physics and Astronomy, Uppsala University, Sweden*
[2]*Percy Roc AB, Uppsala, Sweden*
[3]*Microwave Group, Department of Electrical Engineering, Uppsala University, Sweden*
yasin.alekajbaf@Physics.uu.se

Keywords: microwave sintering, high entropy alloy, sodium-ion batteries, graphite, cavity resonator

Introduction

Microwave (MW) sintering is an innovative technique that is revolutionizing the way materials are processed, contributing to the fourth industrial revolution known as "Industry 4.0." By converting electromagnetic energy into thermal energy, this method facilitates the heating of materials through absorption and coupling of microwave energy. The result is a unique volumetric heating ability that leads to sintering of powder compacts with enhanced diffusion, short processing time, and reduced energy cost. This technology has enabled rapid heating of common metals and the fabrication of bulk amorphous alloys through microwave heating [1], [2]. In battery industry, improving battery performance necessitates the use of phase-pure materials, typically acquired through intricate techniques. Microwave processing is surfacing as an encouraging replacement, providing quick and even heating by transforming electromagnetic energy into heat. In contrast to traditional methods, microwaves have the ability to penetrate substances, leading to a decrease in processing time and an improvement in quality. The efficiency and distinct heating characteristics of this technology position it as a probable choice for commercial use in the coming years. It marks a substantial progression in the synthesis of materials, especially in areas like battery applications [3].

Sodium-ion batteries (SIBs) are seen as a potential substitute for lithium-ion batteries (LIBs) due to more abundant resources. The new SIB by CATL, designed for high-power stationary storage, has a lower energy density than most LIBs but addresses market needs by reducing reliance on scarce elements like lithium, cobalt, and nickel. The carbon-based anode in SIBs has a specific capacity that can be enhanced using alloy anodes from certain groups like silicon-germanium (Si-Ge) alloys. However, these alloy anodes can expand significantly during use, causing potential mechanical issues. A solution could be using amorphous nanocomposites or specific alloys to increase stability and handle the stresses of battery operation [4]-[8].

One of the most attractive advantages of microwave sintering is the adaptability of the system to change with the material properties with utilizing active feedback algorithms to maintain sintering temperatures and optimize the power within the resonator. The same machine can even be utilized to sinter different materials efficiently without significant reconfiguration, contributing to the flexibility and reproducibility that characterize modern manufacturing. Among its many applications are the development of high-entropy alloys for batteries, the achievement of compositional homogeneity, and the avoidance of conventional challenges such as slow processes and contamination. At its core, sintering is a heat treatment that compacts materials without melting them, and with microwave sintering, this process has become faster, more uniform, and more controlled, paving the way for future advancements in material science and engineering [4]-[8].

In this study, an optimized microwave sintering technique is presented using a TM010 microwave cavity resonator to precisely control the sintering of various materials. The high entropy alloys as a new attractive material in battery industry is sintered using presented system. To analyse the sintered alloy, X-ray and SEM analysis are used.

Experimental setup

The designed microwave sintering setup is illustrated in Fig. 1, operates within the 2.4 - 2.5 GHz ISM band. This system employs a TM010 cavity resonator, where materials for sintering are placed at the center and exposed to the maximum amplitude of the electric field. To control and optimize the process, a non-contact infrared pyrometer and a temperature sensor are utilized to measure the temperature within the cavity, as depicted in Fig. 1(a). These temperature readings are fed into a control algorithm managed by a microcontroller (Raspberry Pi), which is connected to a microwave signal generator (SG) capable of delivering up to 250 Watts using a Mini-circuit solid-state power amplifier. The control algorithm operates at the minimum resonance frequency of 2444 MHz and repeatedly tracks this frequency to maximize the microwave power absorbed by the target material. Using pyrometer measurements, the microwave power system is monitored and adjusted during operation. The implemented experimental setup is shown in Fig. 1(b).

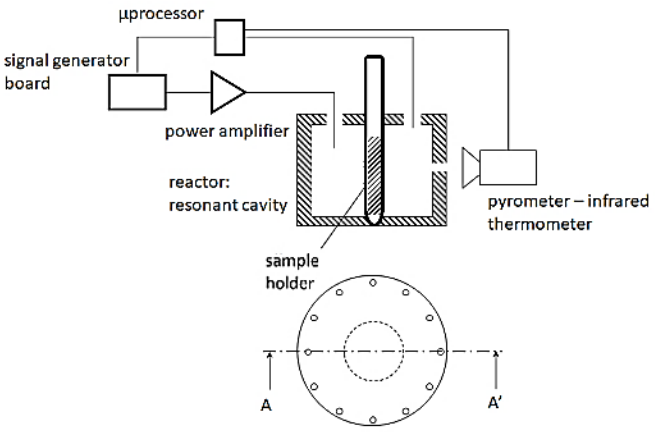

(a)

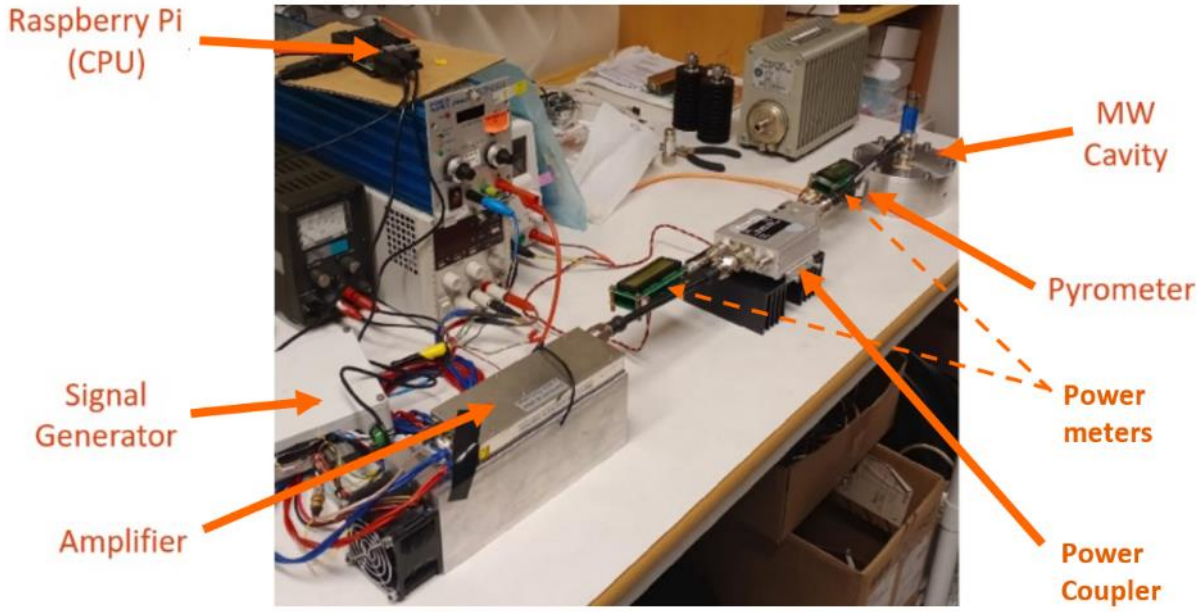

(b)

Fig. 1. (a) Proposed microwave-sintering setup. (b) Experimental setup.

Experimental tests and results

In this article, two different material samples have been used to investigate and test the introduced algorithm and system for microwave sintering. In the initial test, a graphite sample has been utilized for optimizing and evaluating the performance of the designed control algorithm. Subsequently, the microwave sintering process has been applied on an High entropy alloy (HEA) sample composed of the elements Si, Ge, and Cu, which is called A1 alloy for short. Then, the sintered alloy is examined through the characteristic analysis tests.

Initial microwave sintering test

In initial test, graphite powder is used as the target material due to its high thermal resistance. Approximately 500 mg of graphite powder is introduced into a quartz test tube that is placed inside the cavity as shown in Fig. 1(a). The Amplifier and SG that are controlled by the microprocessor runs a frequency sweep of the cavity to establish the maximum resonant frequency of target material based on the S11 measurements. The highest coupling for the material is initially established at 2.452 GHz as shown in Fig. 2. The algorithm now begins to deliver power into the cavity and follows the heat profile (HP) suggested for the target material. The HP suggests the algorithm to maintain 640°C across 5 mins, excluding ramp up and ramp down times. Fig. 3(a) highlights the performance of the algorithm in maintaining high temperatures. When we get to temperatures greater than 600°C we observe the graphite glowing within the cavity as observed in Fig. 3(b).

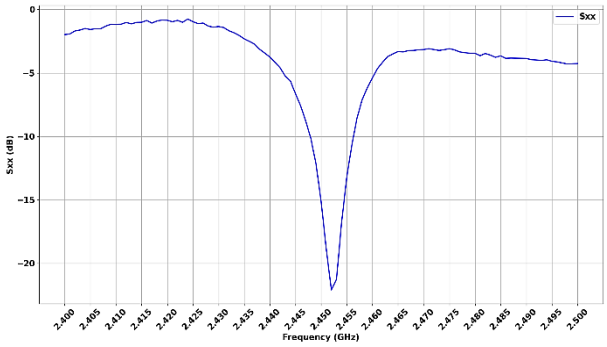

Fig. 2. Reflection coefficient S_{11}, obtained in real time, in a frequency sweep between 2.4 to 2.5 GHz directly from the amplifier reflected power sensor.

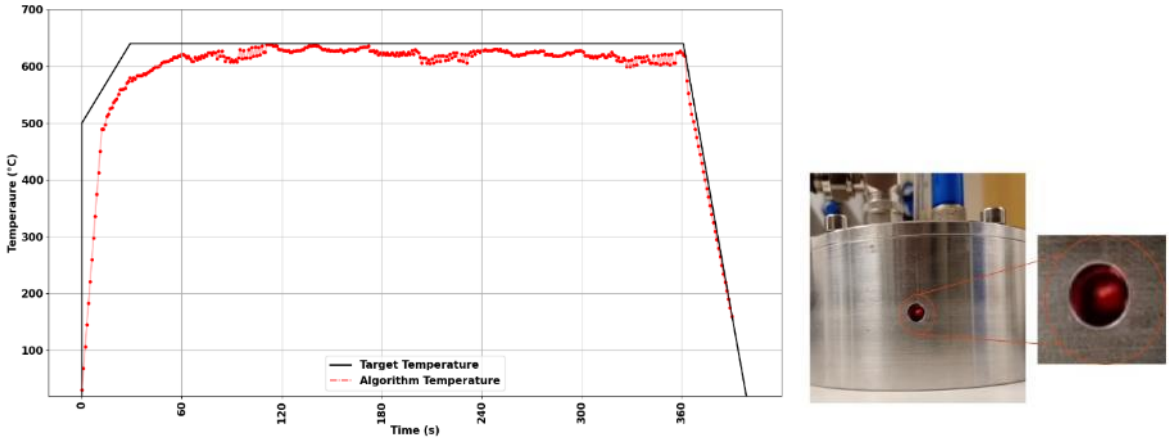

(a) (b)

Fig. 3. (a) Performance of algorithm (red) in the defined heat profile (black) for graphite. (b) Graphite glowing at 600°C.

Microwave sintering of high entropy alloy

After conducting the initial test using the designed setup and graphite sample, the adaptive algorithm utilized for the sintering process is optimized. Subsequently, the performance of the designed process and algorithm for microwave sintering is studied using the A1 HEA compound sample. The temperature profile applied and monitored for this test is illustrated in Fig. 4. In this sintering setup, the desired temperature for the sintering process has been considered around 600 degrees. In Fig. 4(a), the alloy sample is exposed to microwave radiation for 4 minutes with low microwave power and smooth heat up process. As observed, with the help of the designed setup and the temperature control algorithm, the sample's temperature reaches the targeted 600 degrees within two minutes. It will remain at this temperature based on the applied temperature and time profile.

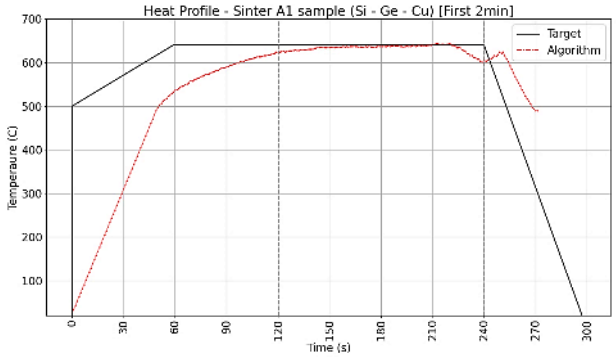

Fig. 4. Applied and monitored temperature profile with low microwave power and smooth heat up process

The sintered A1 alloy, Fig. 5(a), is studied using X-ray diffraction analysis, Fig. 5(b). X-ray analysis offers key insights into the material's composition and setup conditions. Therefore, CuO formation, indicated by minor peaks at 2theta values, could be linked to the experimental setup, while temperature adjustments might help merge certain peaks. Controlling the setup is crucial to prevent unwanted reactions and maintain product quality.

(a) (b)

Fig. 5. (a) Sintered high entropy alloy, A1 sample, (b) X-ray Diffraction Analysis of sintered sample

Additionally, the sintered samples are evaluated using Scanning Electron Microscopy (SEM). The results of this assessment are illustrated in Fig 6. This analysis shows that Ge and Si are distributed homogenously in sintered Alloy.

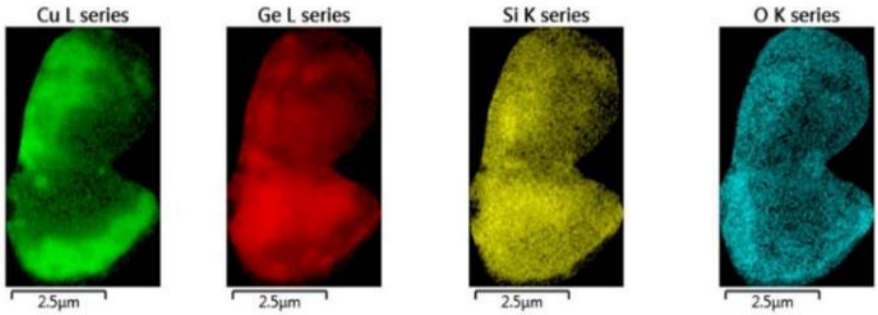

Fig. 6. Scanning Electron Microscopy (SEM) results

Conclusion

In this study, an optimized microwave sintering technique is presented using a TM010 microwave cavity resonator to precisely control the sintering of various materials. By assessing the S-parameters of the sample, the adaptive algorithm can discern changes in material properties concurrent with temperature elevations and offering energy-efficient solutions while ensuring target materials reach desired temperatures. X-ray and SEM analyses provided critical insights into the used HEA material like revealing formations of CuO during process and consistent distribution patterns of Ge and Si within the powders. So, developing of presented method provides an efficient and sustainable solution to control, monitor, and adeptly sinter high-entropy alloys (HEA).

References

[1] S. Hefford, N. Parker, J. Lees and A. Porch, "Monitoring changes in microwave absorption of Ti64 powder during microwave sintering," *2017 47th European Microwave Conference (EuMC)*, Nuremberg, Germany, 2017, pp. 927-929, doi: 10.23919/EuMC.2017.8230997.

[2] J. Cheng, D. Agrawal, Y. Zhang, R. Roy, A.K. Santra, "Synthesis of amorphous Si–Ge alloys using microwave energy," *Journal of Alloys and Compounds*, vol. 491, issues. 1–2, 2010, pp. 517-521, doi:10.1016/j.jallcom.2009.10.260

[3] S. Balaji, D. Mutharasu, N. Sankara Subramanian, et al. "A review on microwave synthesis of electrode materials for lithium-ion batteries". Ionics, Vol. 15, p 765–777, 2009.

[4] J. Cui, et al., "Recent progress in rational design of anode materials for high-performance Na-ion batteries. Energy Storage Mater., Vol 7, p 64–114, 2017.

[5] H. Xie, et al. " β -SnSb for Sodium Ion Battery Anodes: Phase Transformations Responsible for Enhanced Cycling Stability Revealed by in Situ TEM". ACS Energy Lett., Vol. 3, no. 7, p 1670–1676, 2018.

[6] } I.T. Kim, et al., "High-performance FeSb-TiC-C nanocomposite anodes for sodium-ion batteries. Phys. Chem. Chem. Phys., Vol. 16, no. 25, p. 12884–12889, 2014.

[7] E. Edison, et al., "Microstructurally engineered nanocrystalline Fe-Sn-Sb anodes: Towards stable high energy density sodium-ion batteries. J. Mater. Chem. A, Vol. 7, no. 23, p 14145–14152, 2019.

[8] H. Usui, et al, "Solid Solution Strengthening of Bismuth Antimonide as a Sodium Storage Material." Energy and Fuels, Vol. 35, no. 22, p.18833–18838, 2021.

Influence of Microwave on Polar Molecular Collision: Kinetic Mechanism of Microwave Non-thermal Effect

D. Gou[1], K. Huang[2]

[1]*School of Electronic Information Engineering, China West Normal University, Nanchong 637000, China*
[2]*College of Electronics and Information Engineering, Sichuan University, Chengdu 610064, China*
goudezhi@cwnu.edu.cn

Keywords: microwave, polar molecular collision, kinetic mechanism, non-thermal effect

The non-thermal effect of microwaves are still a controversial issue, even after much study. The polarization of polar molecules under a microwave field will inevitably lead to the change of molecular collision. Firstly, in order to give clear physical images of polar molecular collisions under microwave irradiation, the effects of a weak microwave field on the collision of water molecules was studied by molecular dynamics simulation. The spatial collision probability of water molecules increases in the direction of electric field and the proportion of high energy molecules decreases while the proportion of intermediate energy molecules increases. The results show that the microwaves change the collision orientation and kinetic energy between water molecules, that is, the microwave post-polarization effect (MWPPE).

Secondly, we have studied the spatial orientation and kinetic energy of reactive site collisions between benzyl chloride and piperidine molecules in a substitution reaction under microwave irradiation using the molecular dynamics simulation. Our results showed that microwave polarization can change the spatial orientation of reactive site collisions. Collision probability between the Cl atom of the C−Cl group of benzyl chloride and the H atom of the N−H group of piperidine increased by up to 33.5% at an effective spatial solid angle (θ, φ) of (100°~110°, 170°~190°) under microwave irradiation. Also, collision probability between the C atom of the C−Cl group of benzyl chloride and the N atom of the N−H group of piperidine also increased by up to 25.6% at an effective spatial solid angle (θ, φ) of (85°~95°, 170°~190°). Moreover, the kinetic energy of collision under microwave irradiation was also changed, that is, for the collision between the Cl atom of the C−Cl group and the H atom of the N−H group, the fraction of high-energy collisions with greater energy than 6.39×10^{-19} J increased by 45.9 times under microwave irradiation, and for the collision between the C atom of the C−Cl group and the N atom of the N−H group, the fraction of high-energy collisions greater than 6.39×10^{-19} J also increased by 29.2 times. Through simulation, the reaction rate increased by 34.4~50.3 times under microwave irradiation, which is close to the experimental increase of 46.3 times.

Thirdly, we have investigated the spatial orientation and kinetic energy of active site collisions of carnosine, a natural bioactive dipeptide, under weak microwave irradiation using the molecular dynamics simulation. The dependence of MWPPE on temperature, microwave intensity, microwave frequency, and polarization mode is very complex. In the end, the MWPPE can provide a new insight into the molecular mechanism of the microwave non-thermal effect.

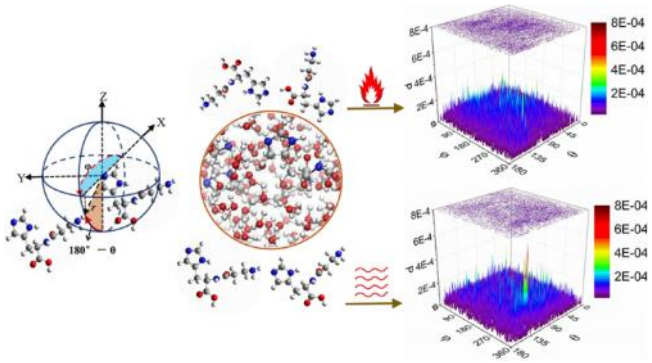

Fig. 1. Microwave post-polarization effect. Under the microwave polarization, the spatial orientation and kinetic energy of molecular collision are changed.

References

[1] D. Gou, K. Huang, Y. Liu, and H. Shi, "Influence of weak microwaves on spatial collision and energy distribution of water molecules," *Chemical Physics*, vol. 540, Sept. 2021.
[2] D. Gou, K. Huang, Y. Liu, H. Shi, and Z. Wu, "Investigation of Spatial Orientation and Kinetic Energy of Reactive Site Collision between Benzyl Chloride and Piperidine: Novel Insight into the Microwave Nonthermal Effect," *J Phys Chem A*, vol. 126, no. 17, pp. 2690-2705, Apr. 2022.
[3] D. Gou, K. Huang, Y. Liu, H. Shi, and Z. Wu, "Molecular Dynamics Research of Spatial Orientation and Kinetic Energy of Active Site Collision of Carnosine under Weak Microwave Irradiation," *J Phys Chem B*, vol. 126, no. 39, pp. 7686-7700, Sept. 2022.

Microwave Assisted Processing of Advanced Materials for Energy Applications

B. Vaidhyanathan[1], K. Annapoorani[1], H. Zhang[1], S. Saremi[1], S. Santhanam[2]

[1]*Department of Materials, Loughborough University, Loughborough, LE11 3RW, United Kingdom*
[2]*Talga Technologies Limited, Cambridge, CB24 9ZR, United Kingdom*
B.Vaidhyanathan@lboro.ac.uk

Keywords: microwave processing, batteries, energy materials, nuclear, capacitors

The merits and limitations of using microwave-assisted processing for the development of advanced materials for energy applications will be discussed in this talk using three exemplar case studies: (i) production of superior electrodes for batteries (ii) rapid manufacturing of nuclear waste disposal materials and (ii) fabrication of barium titanate based multilayer ceramic capacitors (MLCCs).

Graphene-based advanced electrodes with improved electrochemical properties have received increasing attention for use in lithium-ion batteries (LIBs). The conventional synthesis approaches involve either prolonged processing or leads to the retainment of high-concentration oxygen functional groups (OFGs). Here we report bulk synthesis of high-quality reduced graphene oxide using microwave irradiation (MWrGO). The electromagnetic interaction of GO with microwaves is elucidated at the molecular level using reactive molecular dynamic simulations. The simulation suggests that higher power microwave irradiation results in significantly less retainment of OFGs and the formation of structural voids. The synthesized MWrGO samples are thoroughly characterized in terms of structural evolution and physicochemical properties. Li-ion half-cell studies demonstrate that the MWrGO is an excellent candidate for usage as a high-capacity anode (750.0 mAh g^{-1} with near-zero capacity loss) and a high-performance cathode (high capacity retention of ~70% for LiCoO 2 at 10 C) for LIBs.

Feasibility of employing field assisted (Hybrid sintering – combination of conventional and microwave heating; Flash sintering) sintering methods for the fabrication of Ce-incorporated zirconolite ceramics was investigated for the first time. Zirconolite ceramics were produced directly from a precursor; in hybrid processing, >95% Zirconolite was obtained at 1350 °C in 2 hrs time with 1 kW microwave power. In flash processing zirconolite was obtained at ~1100 °C in < 5 mins soaking, using AC field. In comparison, conventional processing needs 1350 °C in 72 hrs for synthesis and 1450 °C in 10 hrs for sintering to achieve the desired phase/density respectively. The total time and energy savings associated with the field-assisted methods (microwave-assisted and flash) augers well for the adaptation of these energy-efficient, low-carbon manufacturing routes to produce zirconolite ceramics for nuclear waste disposal.

Interest in the fabrication of nanostructured electroceramic devices has seen exponential growth in recent years owing to the requirements of miniaturization, multifunctionality and improved reliability. Also, electronic industries tend to move towards non-Pb based electronic materials such as barium titanate (BT) for device applications. Here a detailed study was performed on the microwave-assisted processing of BT based formulations at the nano scale. >60 wt% nano BT suspensions were prepared, and screen printed, and the resultant capacitor devices were sintered using microwave, conventional and hybrid heating. With judicial selection of additives, X8R BT multilayer capacitors were fabricated, and their electrical performance evaluated against commercial capacitor components. The resultant BaTiO3 based capacitive devices exhibited high dielectric permittivity, superior X8R performance and low dissipation factor, asserting their massive potential for widespread high temperature applications.

Microwave-Sintered FeSi/Lithium-Aluminium-Borate Soft Magnetic Composite

R. Bureš[1], V. Milyutin[1], M. Fáberová[1], Z. Birčáková[1], S. Ravi[1], P. Kollár[2], J. Füzer[2]

[1]*Institute of Materials Research of Slovak Academy of Sciences, Watsonova 47, 040 01 Košice, Slovakia,* [2]*Institute of Physics, Faculty od Science, Pavol Jozef Šafárik University, Park Angelinum 9, 040 01, Košice, Slovakia*
rbures@saske.sk

Keywords: microwave sintering, soft magnetic composite, ferromagnetics/ceramics micro/nano powder, complex permeability, coercivity

Soft magnetic composites (SMC) [1] are a group of materials based on ferromagnetic powder particles surrounded by an electric insulation layer. The insulation layer as the secondary phase of the composite is created from polymeric resin or an inorganic compound with high resistivity [2]. A compact is required to create a very thin insulation layer to form a continuous network in the compacted composite to create material with high magnetic permeability and high resistivity at the same time. Currently, SMCs are in most cases produced by powder metallurgy technologies, mainly by press-and-sinter technology [3]. The ferromagnetic powder is coated or mixed with a secondary insulating component. The composite powder is pressed in a pressing die tool into the desired shape with suitable manipulation strength. Green compact is heat treated (sintered and/or annealed) to improve the physical and mechanical properties of the final composite material. In conventional iron powder metallurgy, sintering is used to achieve iron-iron bridges. The original iron particles disappear and a new grain structure with residual porosity is formed. In the case of heat treatment of SMC, it is thus not desirable to create contacts between ferromagnetic particles. Small ferromagnetic regions divided by electric insulation avoid flowing eddy currents in a large volume of material. Suppression of eddy currents reduces energy losses in alternating magnetic fields. The higher the magnetization frequency, the smaller the ferromagnetic regions needed to suppress the influence of eddy currents. SMC heat treatment results in an ideally continuous secondary phase network. This network must provide sufficient mechanical strength for the composite. On the other hand, a high proportion of the brittle secondary phase can reduce the mechanical properties and at the same time reduce the magnetic properties of the composite, especially the permeability. As the requirements for the efficiency of energy conversion devices increase, the requirements for the frequency of applied magnetically soft materials increase [4-6]. The processing of SMC is increasingly a technological challenge to solve which non-traditional technologies and progressive structure design are used for. The use of microwave (MW) heating for sintering materials can, in addition to shortening process times and providing a better energy balance, also lead to significant changes in the composition and distribution of phases in the sintered compact. The selectivity of MW heating of multiphase composite materials can affect the sintering process, structure formation, and can significantly affect the physical properties of materials such as SMCs.

In this work, we investigated the effect of microwave heating on the electrical, magnetic and structural properties of SMC prepared from powdered ferromagnetic alloy Fe6.5Si and oxide ceramics based on lithium-aluminium-borate (LAB). LAB ceramics were prepared by a mechanical milling process. Powder precursors Li_2CO_3, Al_2O_3 and H_3BO_3 in a ratio of 1:1:4 were milled in a Retsch Emax mill at 500 rpm for 4 hours at a temperature between 28-38 °C. A container and balls made of stainless steel were used for milling. Ethyl alcohol anhydride was used as a process control agent. After the first grinding, the powder material was dried and calcined at 600°C for 4 hours in air in a muffle furnace. The calcined material was dry milled at 500 rpm for 15 min. LAB ceramics (1 wt.%) prepared in this way were wet homogenized with FeSi alloy in ethanol with silane coupling agent KH550 (10 wt.%) by resonant acoustic mixing to form FeSi/LAB composite powder. In order to investigate the behaviour of FeSi powder particles in the microwave heating process, the FeSi powder was sieved into seven fractions before mixing as follows: <45, 45-63, 63-75, 75-100, 100-160, 160-212, 212-300 µm. LAB particles had a size distribution with a median d(0.5) = 7 µm. The dried composite powders were compacted by uniaxial die pressing at a pressure of 1500 MPa. The obtained green compacts in the shape of rings were sintered using MW heating. Microwave sintering (MWS) was carried out in a Synotherm Hamilab V3000 multimode sintering device. A water-cooled double-shell microwave chamber with a diameter of 500 mm and a height of 560 mm is connected by a rectangular waveguide to 3 magnetrons with a total power of 2.85 kW. The temperature is measured by an IR pyrometer Raytek. The sintered samples were placed in an alumina crucible with a diameter of 120 mm and a height of 50 mm. In the MW chamber, the crucible with the samples is enclosed in a casing made of porous alumina isolated from the stainless-steel wall of the chamber by a 20 mm layer of alumina fibers. Sintering was carried out in a protective atmosphere of nitrogen at a temperature of 725 °C with a duration at the maximum temperature of 15 and 60 min, respectively, with the use of a SiC susceptor as well as without a susceptor. The sintered composites were characterized by measuring coercivity, complex permeability and resistivity.

The temperature in the sintering process was regulated by adjusting the power of the magnetrons. In the initial stage of the experiment, we focused on achieving temperature stability, sufficient accuracy of the regulation, so that the reproducibility

of the process was as high as possible. Further experiments were realised with optimal amount and spatial distribution of SiC susceptor.

DC resistivity of FeSi/1LAB sintered for 15 and 60 min with susceptor was measured by 4-point probe method. Results in Fig.1 show a higher resistivity value of 60 min sintered composite compared to short MW sintering. SMCs with large FeSi particles show the highest resistivity. As the particle size decreases, the resistivity of the composite decreases. The coercivity of MWS FeSi-1LAB samples decreased with decreasing size of FeSi particles used for their preparation. By extending the holding time at the sintering temperature, the coercivity decreased only slightly, and only for samples with particles of 100 µm and larger, as documented in Fig.2.

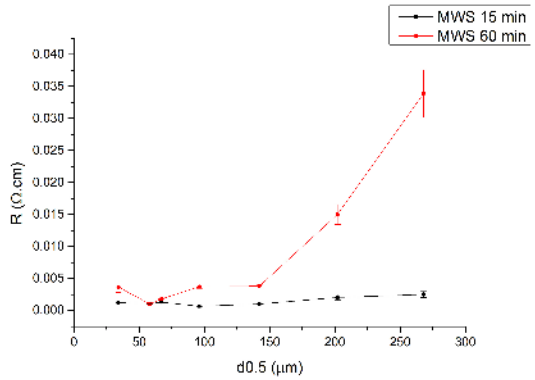

Fig. 1. Resistivity of MW sintered FeSi/LAB

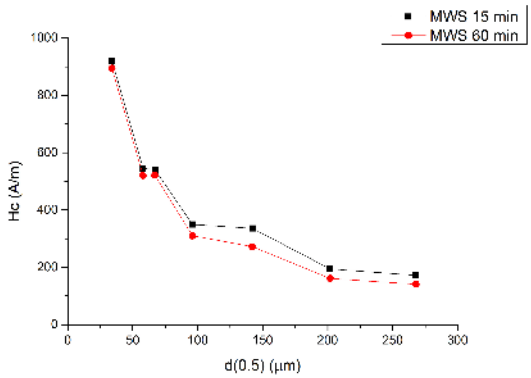

Fig. 2. Coercivity of MW sintered FeSi/LAB

The SMS based on FeSi 212-300 and 160-212 µm shows the highest permeability as well as the highest resonance frequency. The use of smaller FeSi particles (100-160 and 75-100 µm) leads to a decrease in resonance frequency and only a slight decrease in permeability. SMC with particle size 63-75 µm shows a further decrease in resonance frequency, but the permeability is close to the permeability values of the larger particles. A slight decrease in FeSi particle size to 45-63 µm leads to a slight decrease in permeability with almost no change in resonance frequency. In the case of SMC prepared from particles smaller than 45 µm, the permeability is significantly reduced, while the resonant frequency remains at a level comparable to SMC based on 75-100 µm particles.

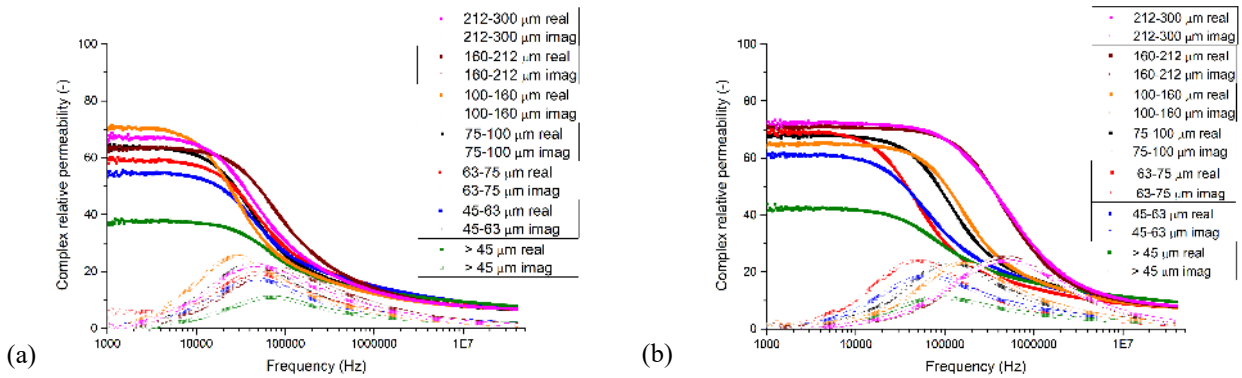

Fig. 3. Complex permeability of FeSi/LAB (a) MWS 15 min and (b) MWS 60 min

A MWS of 60 min leads to differentiation of permeability and resistivity values depending on the size of ferromagnetic FeSi particles. A shorter 15 min MWS leads to lower values of permeability and resonance frequency except for SMC based on particles below 45 µm.

Acknowledgement

This work was realized within the frame of the project financed by Slovak Research and Development Agency under the contract APVV-20-0072; and by Scientific Grant Agency of Ministry of Education of Slovak Republic and Slovak Academy of Science project VEGA 2/0029/21.

References

[1] E. A. Périgo, B. Weidenfeller, P. Kollár, and J. Füzer: Past, present, and future of soft magnetic composites, Applied Physics Reviews 5, 031301 (2018)
[2] Poškovič E., Franchini F., Ferraris L., Fracchia E., Bidulska J., Carosio F., Bidulsky R., Actis Grande M.: Recent Advances in Multi-Functional Coatings for Soft Magnetic Composites. Materials 2021, 14, 6844.
[3] Katie Jo Sunday and Mitra L. Taheri: Soft magnetic composites: recent advancements in the technology, Metal Powder Report Volume 72, Number 6 November/December 2017.
[4] A. Talaat, M.V. Suraj, K. Byerly, A. Wang, Y. Wang, J.K. Lee, P.R. Ohodnicki Jr: Review on soft magnetic metal and inorganic oxide nanocomposites for power applications, Journal of Alloys and Compounds 870 (2021) 159500

[5] Xiaowei Jin, Tong Li, Zhenlin Jia, Huigang Shi, Desheng Xue: Over 100 MHz cut-off frequency mechanism of Fe-Si soft magnetic composites, Journal of Magnetism and Magnetic Materials 556 (2022) 169366
[6] Z. Birčáková, F. Onderko, S. Dobák, P. Kollár, J. Füzer, R. Bureš, M. Fáberová, B. Weidenfeller, J. Bednarčík, M. Jakubčin, J. Szabó, M. Dilyová: Eco-friendly soft magnetic composites of iron coated by sintered ferrite via mechanofusion, Journal of Magnetism and Magnetic Materials 543 (2022) 168627

Morphology-Based Correlation Parameter for Estimating the Effective Permittivity of Anisotropic Media Composed of Non-Spherical Inclusions

J. N. Camacho Hernandez[1], G. Link[1]

[1]*Institute for Pulsed Power and Microwave Technology, Karlsruhe Institute of Technology, Eggenstein-Leopoldshafen, 76344, Germany*
jesus.hernandez@kit.edu

Keywords: effective permittivity, effective media approximation, tensor permittivity, orientation tensor, composites

The effective permittivity characterizes the response of a composite material to an electric field. The effective permittivity is a complex quantity ($\varepsilon_{\text{eff}} = \varepsilon'_{\text{eff}} - j\varepsilon''_{\text{eff}}$) in which the real part $\varepsilon'_{\text{eff}}$ is known as the effective dielectric constant and describes the ability of a dielectric medium to store electric energy in an electric field. The imaginary part $\varepsilon''_{\text{eff}}$ is the effective dielectric loss, which accounts for the energy dissipation when exposed to an electric field (i.e. microwave radiation). The effective medium approximation (EMA) is a widely used technique to estimate the effective permittivity of composite media at the macroscopic scale [1]. The EMA approach assumes that the composite material can be treated as a homogeneous medium, also known as effective media, with inclusions distributed uniformly throughout a continuum medium. Describing the effective permittivity of effective media is accomplished by using mixing relations based on the EMA approach, i.e. the Maxwell-Garnett and Bruggeman relations. However, these mixture relations are limited to microstructures consisting of spherical and quasi-spherical (i.e. ellipsoidal) inclusions [2]. Consequently, the EMA relations are inadequate for estimating the effective permittivity of media with microstructures that deviate significantly from spherical or ellipsoidal shapes. Overcoming these limitations requires an appropriate consideration of the morphology and spatial orientation of inclusions to ensure an accurate estimation of the effective permittivity. Figure 1 provides an example of a material with complex microstructure, (a) including non-spherical or non-ellipsoidal inclusions, (b) anisotropic-oriented inclusions, (c) and the corresponding general effective permittivity.

In this contribution, we present the results on an approach for estimating the effective permittivity of anisotropic-oriented inclusions by considering their morphology. The approach employs the orientation tensor [3] and a correlation parameter tensor that contains geometrical details of the inclusions to estimate the effective permittivity tensor. We have used electromagnetic wave propagation calculations on media with various geometrical-microstructures to investigate the effect of the geometrical correlation parameter on the effective permittivity. The results demonstrate that the approach can produce reliable estimates of the effective permittivity tensor of media by considering their microstructure morphology. Moreover, the approach can be used to improve the design and analysis of electromagnetic devices and systems.

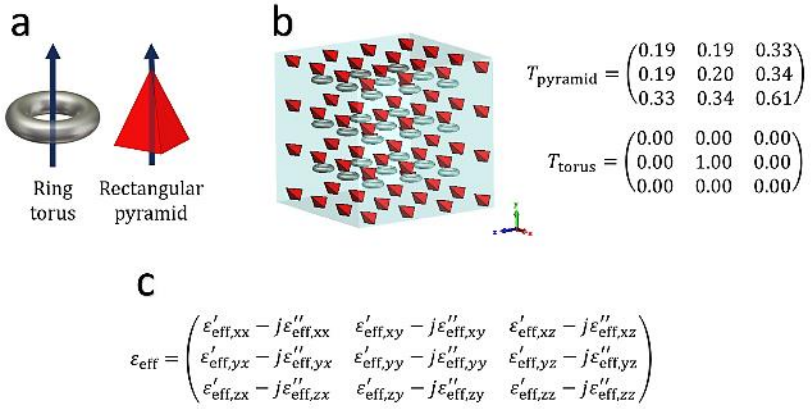

Fig. 1. (a) Examples of inclusions with non-spherical or non-ellipsoidal shapes and their basis orientation direction, (b) material with anisotropic-oriented inclusions according to their second-order orientation tensor T, (c) permittivity tensor, which describes the anisotropic behaviour of a material in response to an electric field.

References

[1] T.C. Choy, Effective Medium Theory: Principles and Applications, 2nd Ed., Oxford University Press, (2016).
[2] W. Pabst, S. Hříbalová, Describing the Effective Conductivity of Two-Phase and Multiphase Materials via Weighted Means of Bounds and General Power Means, JOM. 71 (2019) 4005–4014.
[3] W. Ogierman, G. Kokot, Generation of the representative volume elements of composite materials with misaligned inclusions, Compos. Struct. 201 (2018) 636–646

Conventional and Hybrid Sintering of 3D Printed Advanced Ceramics Filter Structures

A. Ketharam[1], P. Vasudevan[1], T. Goulas[1], A. Kundamani[1], S. Yarmadi[1], B. Vaidhyanathan[1]

[1]*Department of Materials, Loughborough University, Loughborough, LE11 3TU, UK*
k.annapoorani@lboro.ac.uk

Keywords: additive manufacturing, microwave hybrid sintering, robocasting, advanced ceramics, filters

Advanced ceramics with designed porosity have a multitude of applications in the realm of customized filters in the automotive, aerospace, space and foundry industries. Complex porous structures face design accuracy issues in conventional methods of manufacturing and could be overcome by additive manufacturing (AM) techniques. Also AM methods result in less wastage of materials compared to conventional subtractive manufacturing. While AM techniques like robocasting and stereolithography (SLA) ensure the required dimensional accuracy of the printed component, critical aspects like the structural and mechanical properties of the 3D printed ceramics are determined by its sintering process, which is also considered as the most energy intensive step in the production stages.

In this study, we have attempted to compare the processing and properties of 3D printed Yttria stabilized Zirconia (YSZ) ceramics with designed porosity, sintered using conventional sintering (radiant power heating) and hybrid (combination of microwave and radiant power) sintering methodologies. The sintered samples were analysed for density, microstructure, shrinkage, hardness and toughness. The effect of microwave power on the densification kinetics is also elucidated.

The lower processing temperature and time in hybrid processing, besides being energy efficient, resulted in finer grain structure with good densification leading to better mechanical properties.

Microwave Synthesis and Sintering of Nanostructured Lead-Free BCZT

C. P. F. Perdomo[1], B. G. Foschiani[1], A. L. F. Cardoso[2], D. N. F. Muche[2], R. F. K. Gunnewiek[2]

[1]Federal University of São Carlos, Materials Engineering Department, Rod. Washington Luiz km 235, São Carlos - SP, Brazil.
[2]Federal University of São Carlos, Graduate Program in Materials Science and Engineering, Rod. Washington Luiz km 235, São Carlos - SP, Brazil.
claudia.perdomo@ufscar.br

Keywords: microwave synthesis, lead-free piezoceramics, nanostructured BCZT, Pechini method.

The importance of ferroelectric materials with piezoelectric properties for world technological development has long been known [1]. Among such materials, the best studied and applied for this function is lead zirconate titanate. However, as it contains a heavy and toxic metal (Pb), so its use has been increasingly restricted. To meet the demand, lead-free materials have been researched [2]. Notwithstanding, it is a great challenge to find a system that does not contain lead and that presents all the characteristics essential to the application, from ease to the properties achieved. Among the lead-free materials, barium and calcium zirconate titanates have been reported as possible candidates for replacing lead-containing systems. The material is a solid solution of barium calcium titanate (BCT) and barium titanate zirconate (BZT). The best performance is at the morphotropic boundary, at 0.32 mol% of BZT (Fig. 1). However, the systems obtained present very coarse particulate matter or are more difficult to synthesize and sinter.

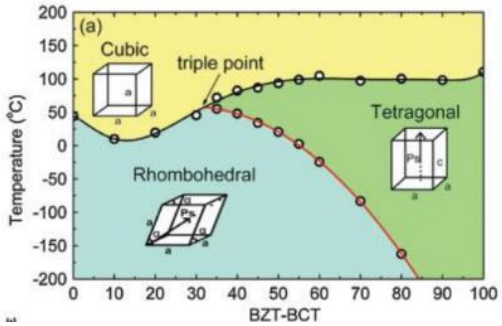

Fig. 1. Morphotropic bondary of BCT-BZT system [4-5].

In this direction, the present work aims to synthesize BCZT in different stoichiometries (0.20 and 0.32) by the microwave-assisted Pechini method. The butyl-titanate, butyl-zirconate, calcium acetate, and barium acetate precursors were solubilized in water in the proper proportions to obtain the intended stoichiometries. After, followed by the addition of ethylene-glycol and citric acid, the solution was mixed following the Pechini method protocol [2]. Microwaves were also used in the initial drying stage of the still-liquid precursor resin. The resins were thermally decomposed in a conventional muffle and were heated at 5 °C/min until 800 and 900 °C where they were held for 60 minutes, while the microwave-treated samples were heated at 50 °C/min until the same temperature, but soaked for only 20 minutes (Cober Electronics MS6K, 6 kW maximum power, operating at 2.45 GHz). Powders were characterized structurally and microstructurally by XRD and SEM. The conventional and microwave-calcined powders at 900 °C were microwave-sintered at temperatures from 1100 °C to 1300 °C, for 10 minutes. The porosity and density were calculated according to ASTM C373-88.

Pure 0.20 BZT-BCT was not obtained with the conditions of this work, even at high temperatures (Fig. 2a). Barium carbonate is one of the impurities and is recurrent when barium is a precursor. Barium reacts with CO_2 and forms carbonate. An unidentified impurity is also observed, which disappears for 0.32 BZT-BCT composition. Microwave thermal decomposition allowed pure BCZT, even at a lower temperature, where $BaCO_3$ is present for the conventional synthesis. For 0.32 BZT-BCT, the synthesis method is not relevant for crystallite size, unlike for 0.20 BZT-BCT. The Zr4+ shows a larger ionic radius, which should distort the lattice and may hinder growth. However, from Table 1 it can be seen that the lattice remains practically constant. Another explanation is that zirconium can reduce the crystallite microstrain, a hypothesis that is under investigation [6]. Microstructure is also affected by temperature and composition, but not by the method. Small particles are observed when the morphotropic precursor resin is calcined at a higher temperature. The typical aggregate derived from the polymeric precursor method is observed for all conditions. For the sintering, this condition seems to be the best and was chosen for the next step.

The morphotropic composition enabled the pure nanometric crystallites and loose particles, which is the best particulate for sintering. After sintering, evaporation was not observed, which is very common for the PZT system. Both powders were able to densify at a higher temperature.

The nanostructured morphotropic BCZT was successfully synthesized by microwave-assisted thermal decomposition. It was possible to save more than 80% in time and the pure phase was obtained at a lower temperature. The sintering allowed dense samples, and no evaporation was observed.

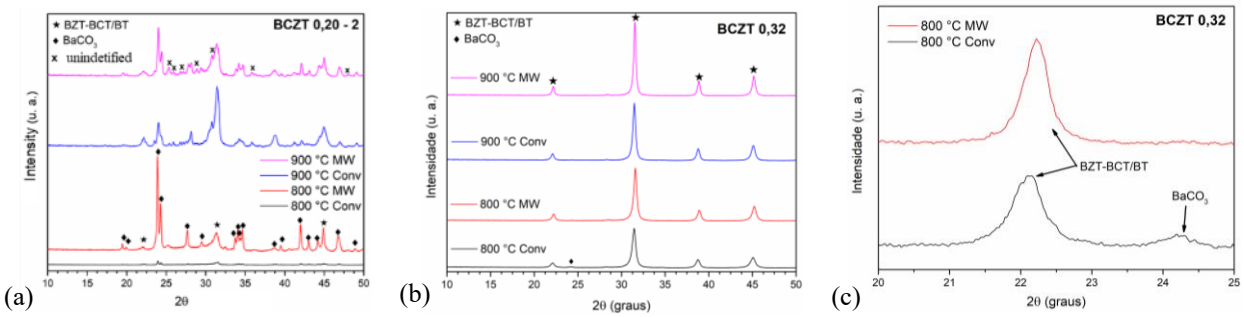

Fig. 2. XRD of all synthesis conditions (a and b) showing the impurities (c).

Table 1. Crystallite data calculated from XRD ($D_{Scherrer} = \frac{0,89\lambda}{\beta cos\theta}$).

Temperature (°C)	Sample	$D_{Scherrer}$ (nm)	d_{110} (nm)	a (nm)
800	0.20-conv	15.7	0.2846	4.9695
800	0.20-MW	7.4	0.2838	4.9824
900	0.20-conv	52.2	0.2823	5.0102
900	0.20-MW	11.1	0.2851	4.9613
800	0.32-conv	15.9	0.2851	4.9613
800	0.32-MW	18.7	0.2831	4.9949
900	0.32-conv	20.0	0.2842	4.9768
900	0.32-MW	24.8	0.2836	4.9867

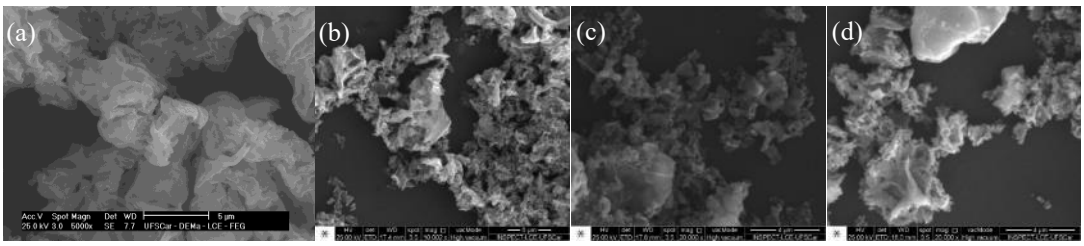

Fig. 3. SEM micrographs of 0.20 BZT-BCT (a and b) synthesized at conventional 800 and 900 °C and (c and d) MW at 800 and 900 °C.

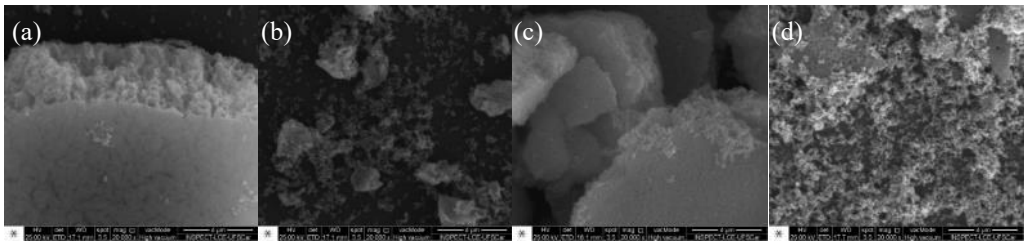

Fig. 4. SEM micrographs of 0.32 BZT-BCT (a and b) synthesized at conventional 800 and 900 °C and (c and d) MW at 800 and 900 °C.

Acknowledgements
CAPES (Finance code 001), FAPESP (grants 2017/13769-1 and 2019/25921-8) and CNPq.

References

[1] Spaldin, N. A., Cheong, S. W., Ramesh, R., Multiferroics: Past, present, and future. Physics Today, 63, p. 38-43, (2010).
[2] Perdomo, C. P. F., Zabotto, F. L., Garcia, D., Kiminami, R. H. G. A. In situ sol-gel co-synthesis at as low hydrolysis rate and microwave sintering of PZT/Fe2CoO4 magnetoelectric composite ceramics. Ceramics International, 43, p 5925-5933, (2017)
[3] Shrout, T. R., Zhang, S. J. Lead-free piezoelectric ceramics: Alternatives for PZT? Journal of Electroceramics, 19(1), 113–126., (2007).
[4] Liu X, Li Z, Wang J, Zhang R, Ali W, Wang S, Lu X, Li C, Phase equilibria and thermodynamic evaluation of BaO-TiO2-YO1.5 system, Journal of the European Ceramic Society 38, p. 5430-41(2018).
[5] Liu, W., Ren, X. Large Piezoelectric Effect in Pb-Free Ceramics. Physical review letters. (2009).
[6] Praveen, J. P., Kumar, K., James, A. R., Karthik, T., Asthana, S., & Das, D. (2014). Large piezoelectric strain observed in sol–gel derived BZT–BCT ceramics. Current Applied Physics, 14(3), 396–402

Medical and Biological Applications

Microwave-Assisted Drying Enhances Retention of Phytochemicals in the Production of Baked Vegetable Snacks

J. R. Bows[1], F. M. A. Langston[2]

[1]*PepsiCo International Ltd. 4 Leycroft Road, Leicester, England, UK*
[2]*University of Exeter, Streatham Campus, Exeter, England, UK*
john.bows@pepsico.com

Keywords: microwave, hybrid baking, phytochemical, phytonutrient, retention, vegetable snacks

Phytochemicals are bioactive compounds produced by plants, widely recognised for their potential to help in disease prevention, without being classified as essential nutrients. They therefore contribute to the functional food landscape - food that provides additional health benefits beyond its basic nutrition. Though the impact of various drying techniques on phytochemicals has been extensively studied with intact plant materials (e.g. sliced fruit or vegetables), there is limited research on plant materials contained in composite snack foods.

Common methods of processing fruit and vegetables into a snack form include convective and impingement hot-air drying, frying, and extrusion. With the exception of frying, these snacks are often formulated using fruit/ vegetable powders which are cost-effective and a practical way of achieving the taste and colour essence of the fruit and vegetable in the snack, although, often at the expense of nutrition [1]. Alternative hybrid baking methods which use technologies such as microwave or vacuum microwave, followed by hot-air drying, offer fast moisture removal rates at lower temperature and enable doughs with higher starting moisture content, removing some of the dependency on dried powders [2]. These hybrid methods could therefore provide the opportunity for the inclusion of fresh and frozen vegetables and the delivery of a higher nutritional content compared to conventional hot-air dried snacks.

This study compares the phytochemical retention of a vegetable snack following standard baking (i.e. hot air drying) or hybrid baking (microwave dehydration followed by hot air drying), as well as the impact of the pre-processing preparation of the vegetables. Five snacks were prepared from a blend of carrot, onion, parsley, and broccoli in their fresh, frozen, or freeze-dried form, and were dried by standard hot-air baking or hybrid baking. The glucosinolate, apigenin, quercetin and β-carotene content of the fresh, pre-processed, and finished products were assessed using high-performance liquid chromatography and the percentage difference between the dough and the finished product was calculated.

Apigenin glucosides were shown to be most resistant to thermal degradation followed by quercetin glucosides > glucosinolates > and β-carotene (Table 1). Hybrid baking was determined to be a less deteriorative processing technique than standard baking, due to microwave dehydration at lower temperatures than baking temperatures/times required to obtain snacks of the same moisture content. In particular, hybrid baking using fresh vegetables was the best combination for obtaining maximum phytochemical retention.

Nutrient-retentive processing of plant materials such as fruit and vegetables, starting with intact cellular structure as opposed to their dry powdered forms, and then dehydrating to dried snacks using hybrid baking processes may offer opportunities to deliver claimable additional health benefits beyond their basic nutrition.

Table 1. The percentage loss or gain of phytochemicals in the finished product compared to the starting dough.

Drying Method and pre-preparation method of the vegetables prior to blending to form the dough	Apigenin glucosides	Quercetin glucosides	β-carotene	Glucosinolates	Sulforaphane
Hybrid baked; fresh	+ 97	-21	-33	+ 147	- 99
Hybrid baked; frozen	+ 59	- 25	- 51	0	+ 987
Hybrid baked; freeze-dried	+ 70	+ 17	- 87	-100	+ 51
Standard baked; freeze-dried	+ 23	- 10	- 87	- 71	- 69
Standard baked; frozen	- 17	- 63	- 83	-48	+ 152

Acknowledgements

The authors thank PepsiCo, Inc. for funding this research. The views expressed in this abstract are those of the authors and do not necessarily reflect the position or policy of PepsiCo, Inc. Author J.R.B. is an employee of PepsiCo, Inc.

References

[1] Rezaul, M., Shishir, I., & Chen, W. (2017). Trends in Food Science & Technology Trends of spray drying : A critical review on drying of fruit and vegetable juices. Trends in Food Science & Technology, 65, 49–67. https://doi.org/10.1016/j.tifs.2017.05.006

[2] Indiarto, R., Asyifaa, A. H., Citra, F., Adiningsih, A., Aulia, G. A., & Achmad, S. R. (2021). Conventional And Advanced Food-Drying Technology : A Current Review. 10(01).

Improvement of Microwave Heating Uniformity by Moving Sliding Short Circuit: Application to 915 MHz Single-Mode Microwave Pasteurization of Solid Food

S. Curet[1], S. Nget[1,2], H. Mith[2], G. Boué[3], L. Boillereaux[1]

[1]*Oniris, Nantes Université, CNRS, GEPEA, UMR 6144, F-44000 Nantes, France*
[2]*RIC, Institute of Technology of Cambodia, Russian Federation Blvd., P.O. Box 86, Phnom Penh, Cambodia*
[3]*Oniris, INRAE, SECALIM, 44300 Nantes, France*
sebastien.curet@oniris-nantes.fr

Keywords: 915 MHz microwaves, single-mode, numerical simulation, electric field distribution, sliding short circuit, heating pattern.

Abstract
In this work, a digital twin dedicated to the 915 MHz microwave heating of a food simulant is used for prediction of both local electric fields within the microwave cavity and the temperature distribution inside the processed material. The heating strategy is based on a ramp-up heating at constant microwave input power. The strategy consists in moving back and forth the sliding short circuit (SSC) coupled with the microwave applicator to study its impact on the electric field strength and the 3D temperature distribution within the food simulant. The influence of the size of the dielectric load placed inside the microwave applicator is also evaluated. The numerical results confirm that two Tylose® samples can be heated with very similar temperature distribution at the end of processing while moving alternatively the SSC at two positions of interest where microwave reflected power is slightly modified. This procedure is also discussed for a possible extension of the methodology to reduce temperature gradient within the processed sample and improve temperature homogeneity during microwave heating.

Introduction
In the context of low carbon footprints strategies for energy use, research and development studies related to microwave heating processes for industrial applications have been increasing in the past years. Regarding this background, the food industry is particularly concerned by the development of energy-efficient microwave heating processes dedicated to tempering, drying, pasteurization or sterilization of food products.

One particular concern related to microwave heating process is the heating uniformity, which is in direct relation to the product quality, including food safety [1]. Many improvement approaches for better temperature uniformity have been recently reviewed in the literature [2-4]. To this extent, numerical simulation provides a particular advantage in the prediction of the thermal behaviour of food samples undergoing a microwave treatment since it can locally compute the electric field strength within the microwave cavity and provides information regarding the hot and cold spots locations within the product prior to the experiment. In particular, the temperature patterns within the processed sample are highly dependent on the microwave cavity configuration, product geometry and physical properties of the product (mainly thermophysical and dielectric properties).

This study focuses on the 915 MHz microwave heating process of a food-analogue matrix (Tylose®) within a single-mode microwave applicator. This work is based on a previous development of a digital-twin that enables to compute the electric field distribution inside the 915 MHz single-mode microwave cavity by taking into account all the geometrical details (waveguide transition, impedance matching elements such as iris and sliding short circuit, …) [5, 6]. This original work investigates the influence of sliding short circuit (SSC) positions on both electric field strength and temperature distribution.

Model design
The previously developed numerical model [6] includes the complete design of a waveguide transition (including the antenna), an impedance matching element (iris), a 915 MHz single-mode microwave applicator and a SSC (Figure 1). A food simulant (Tylose®) is used for experimental validation of the numerical model. The Tylose® sample is considered as a cylinder of 52 mm diameter and 65 mm height. The initial temperature of the sample is 20 °C.

For a stationary wave propagation within a microwave cavity, the SSC is used to adapt the microwave cavity by reducing as much as possible the microwave reflected power from the load. This impedance matching procedure modifies the nodes and antinodes of local electric fields along the propagation direction of microwaves. Practically, in the case of a single-mode electric field propagation within a standardized waveguide, modifying the SSC position also means that the cavity size is shortened or increased.

In the current configuration, the maximum SSC position is 990 mm from the centre of the applicator to the end part of the SSC (Figure 1). The length of the waveguide can be reduced by moving the SSC from 990 mm to 740 mm.

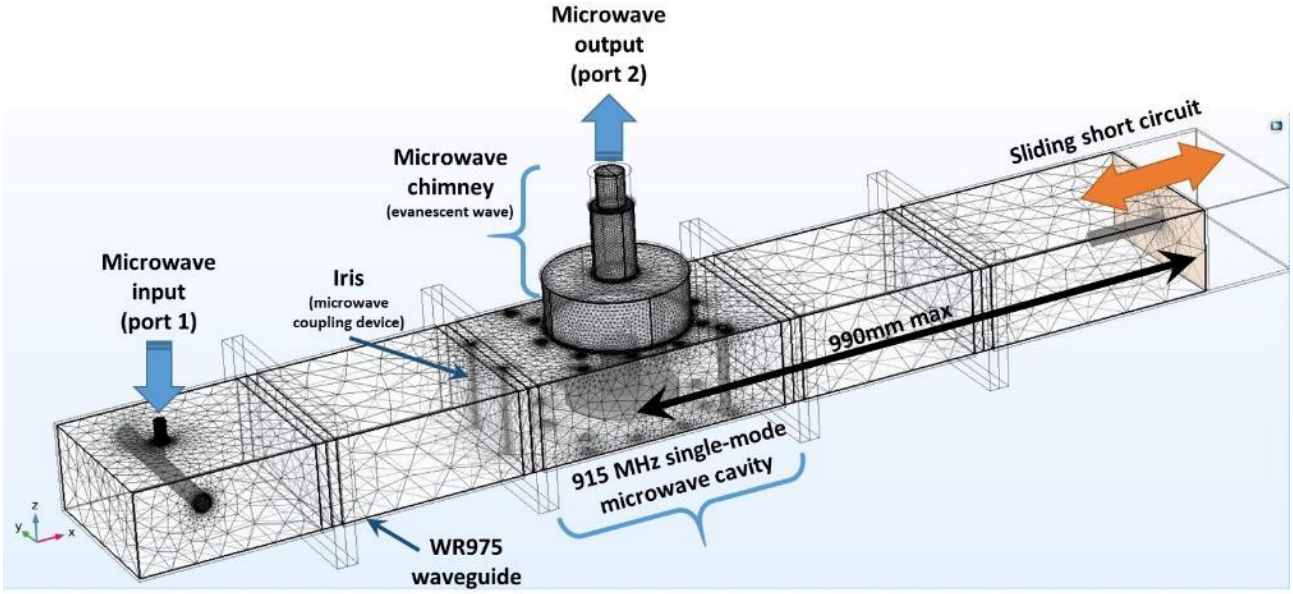

Fig. 1. Model design of the 915 MHz single-mode microwave device

For the model development, the Helmholtz equations for electric field propagation (E) is solved numerically inside the waveguide and within the dielectric medium as shown in (1)

$$\nabla^2 \vec{E} + \mu_0 \mu_r \omega^2 \varepsilon_0 (\varepsilon_r' - i\varepsilon_r'') \vec{E} = 0 \qquad (1)$$

where μ is the magnetic permeability that is considered as $\mu_0 = 4\pi \times 10^{-7}$ H/m for the vacuum and ε is the complex permittivity with $\varepsilon_0 = 8.854 \times 10^{-12}$ F/m for the vacuum. The relative complex permittivity ε_r is composed of the relative dielectric constant ε'_r and the relative dielectric loss factor ε''_r with the complex notation "i" and ω is the angular frequency (rad/s).

The electric field strength is linked to the microwave heat generation term as shown in (2).

$$Q_M = \pi f \varepsilon_0 \varepsilon_r'' E^2 = \frac{1}{2} \omega \varepsilon_0 \varepsilon_r'' E^2 \qquad (2)$$

COMSOL® Multiphysics 6.1 is used to build the 3D model and solves the electric field propagation within the microwave cavity and heat transfer inside the processed sample. Thermophysical and dielectric properties of Tylose® are either extracted from literature or measured from room temperature to 60 °C. Based on the temperature range for investigation, we consider that the thermophysical and dielectric properties are constant [6].

Tylose® sample is placed within a PET plastic container and located at the centre of the Teflon® plate. The dielectric properties of PET, Teflon® are also considered as constant.

The model is solved with a two steps approach: the electromagnetic field is first solved in the frequency domain (time-harmonic propagation of electric field) then the heat transfer is solved as a time-dependent study by taking into account the microwave volumetric heat source calculated in the first step as shown in (3)

$$\rho_s C_p \frac{\partial T}{\partial t} = \nabla \cdot (k \nabla T) + Q_M \qquad (3)$$

where ρ_s, C_p and k are density, specific heat and thermal conductivity of the Tylose® sample respectively [6]. The boundary condition for the side surface of the PET sample cell is assuming a natural convective heat flux (4)

$$k \frac{\partial T}{\partial n} = hc(T_{ext} - T_s), \quad \forall t > 0 \qquad (4)$$

where h_c is the natural heat transfer coefficient (5 W.m^{-2}.K^{-1} in this work)

The model is solved with a Dell® Precision™ Workstation computer equipped with 2 × Intel® Xeon processors (8 cores), at 2.5 GHz, with 256 GB RAM, running on Windows® 10 Professional, 64 bits.

Results and discussions

Microwave cavity filled with one cylindrical sample

The first configuration considers that the cavity is filled with one Tylose® sample placed at the centre of the Teflon® plate [6]. In this configuration, the iris aperture is fixed at 94 mm to ensure optimum microwave coupling with the load.

At 915 MHz, the guided wavelength for an empty WR975 waveguide is 437 mm. First, a parametric numerical study is performed where the SSC position is moved following ¼ guided-wavelength (109 mm) starting from 857 mm (optimum SSC position to obtain the minimum reflected power when the Tylose® sample is placed at the centre of the plate [6]). Both microwave reflected power and local electric field strength along the propagation direction are analysed in terms of amplitude and phase.

Table 1. Microwave reflected signals following ¼ guided wavelength SSC displacements (iris aperture = 94 mm)

SSC position (mm)	P_{ref}/P_{in} (%)	S11 (dB)
857	11.7%	-9.33
747.78	91.8%	-0.37
638.56	11.7%	-9.34
529.33	91.8%	-0.37
420.11	11.6%	-9.34
310.89	91.8%	-0.37

Table 1 indicates that peak and valleys of microwave reflected powers are separated by ¼ guided wavelength. This result validates the propagation of the standing wave pattern within the WR975 waveguide. The minimum reflected power is 11.6% (- 9.3 dB) for a maximum value of 91.8% (-0.37 dB).

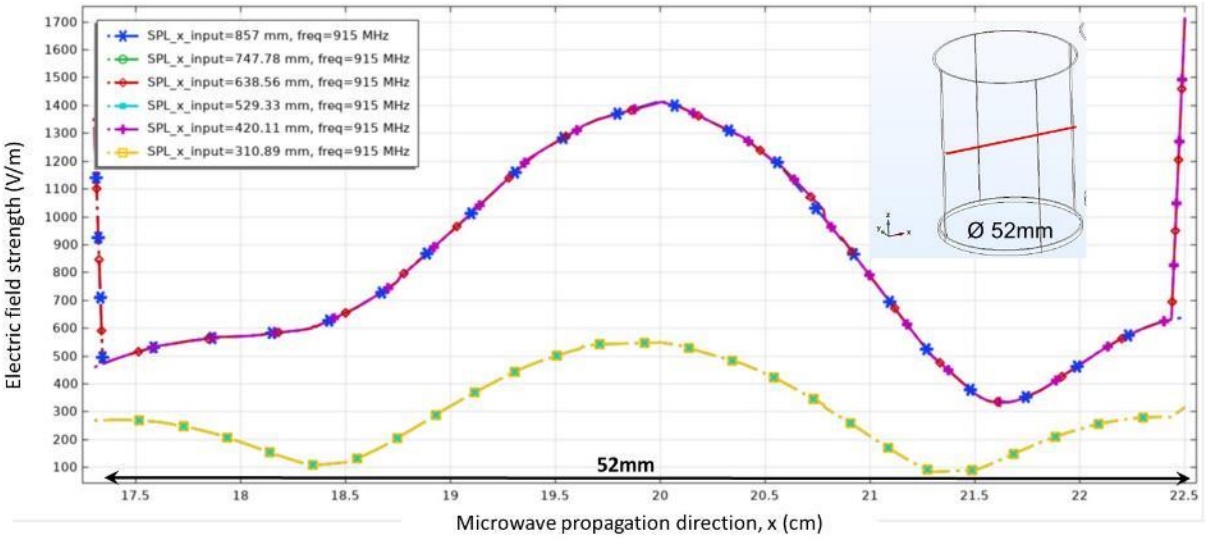

Fig. 2. Electric field strength along a central horizontal line within the Tylose® sample

Figure 2 depicts the electric field strength along a central horizontal line inside the Tylose® sample. Minimum and maximum amplitudes of the electric field are noticed following the various SSC positions. On one hand, for each data associated with minimum and maximum reflected powers, the local electric fields are superimposed between each other. On the other hand, the different amplitudes of the electric fields are considered in phase regarding the position of the extremums of electric fields following *x*-axis.

From this configuration with one sample placed in the microwave cavity, there is no effect of the SSC displacements to modify local positions of electric field within the sample following *x*-axis. The SSC will only affect the amplitude of the local electric field strength at one geometrical position.

Microwave cavity filled with two cylindrical samples

In the second configuration, two Tylose® samples with the same characteristics (geometrical and physical properties) are placed within the cavity following the microwave propagation direction (Figure 3).

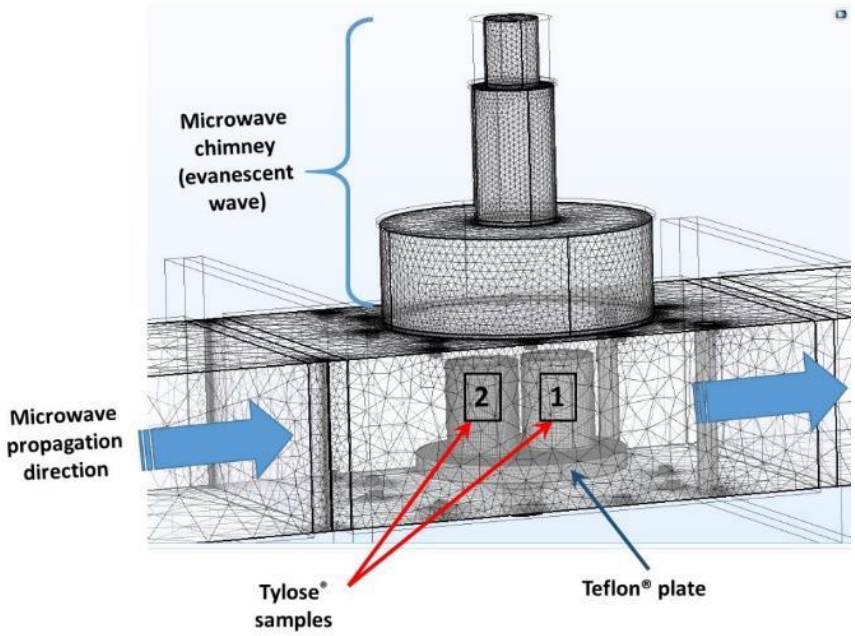

Fig. 3. 915 MHz single-mode applicator with 2 Tylose® samples

In this configuration, the iris is completely open due to the larger size of the dielectric load placed in the cavity (better impedance matching than the configuration with one sample). The electric field distribution is computed within the cavity with SSC positions starting from 990 mm to 840 mm every 50 mm. The electric field strength is analysed for every SSC positions along a central horizontal line following microwave propagation direction.

Table 2. Microwave reflected signals following displacements of the SSC (full iris aperture)

SSC position (mm)	P_{ref}/P_{in} (%)	S11 (dB)
990	6.3%	-12.0
940	17.3%	-7.6
890	9.3%	-10.3
840	6.8%	-11.7

Table 2 indicates that microwave reflected powers do not exceed 17% (-7.6 dB) for the different SSC positions which indicate quite a good impedance matching for every SSC position. Extremums of microwave reflected powers are found for 990 mm and 940 mm SSC positions.

Figure 4A depicts the electric field strength along the full waveguide length following a central horizontal line starting from the antenna to the SSC. The figure indicates that electric field strength within air are highly modified depending on the SSC position. Nevertheless, within the microwave applicator, the electric fields strength inside Tylose® are globally in-phase signals with a very high electric field gradient at the interface between the two samples (9 kV/m maximum value).

Figure 4B focuses on the electric field strength within the two Tylose® samples following two SSC positions of interest (990 mm and 940 mm). For these two locations, the amplitudes of electric fields are not in phase and local values for sample 1 and 2 are symmetric following the central axis where maximum electric field is 9 kV/m.

From this observation, it remains possible to alternate between both SSC positions during the microwave heating of the Tylose® samples placed in the cavity. The alternative low and high electric fields can affect the heat generation due to microwaves and thus modify the temperature gradients within the processed samples.

The second step of this numerical study consists in solving the heat transfer equation within both samples with two alternative SSC positions (990 mm and 940 mm). Several scenarios are proposed to investigate the influence of the electric field pattern on the temperature profiles within the samples for each SSC position.

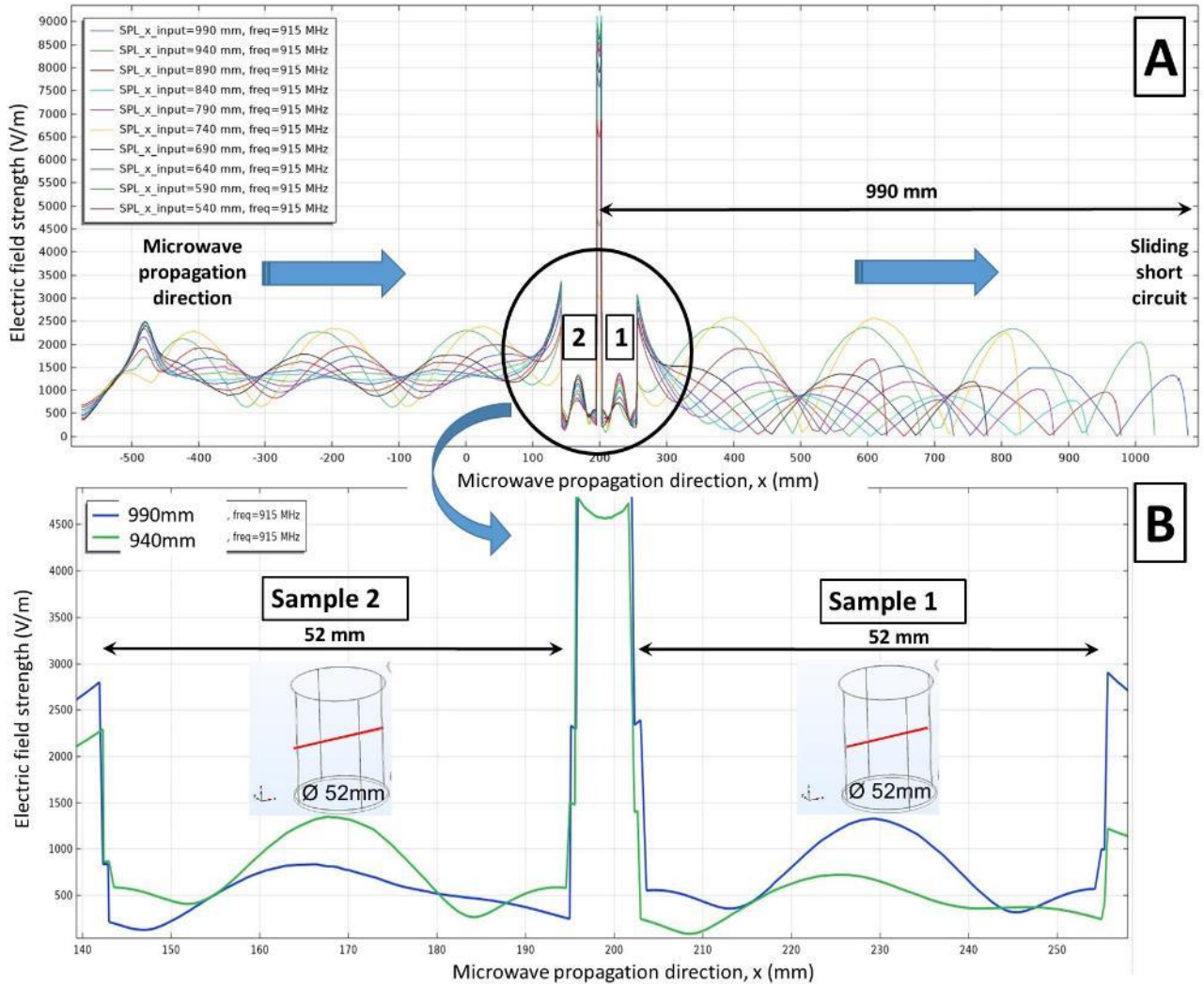

Fig. 4. Electric field distribution along the microwave propagation direction

Numerical simulations are performed with 27 W constant microwave input power during 650s (17.55 kJ of total energy supply). Table 3 indicates the different heating scenarios where both SSC positions and time of exposure are modified (total microwave heating time is 650s). The absorbed microwave energy during the whole process is also evaluated for each sample.

Table 3. Heating scenarios following various SSC positions and exposure times associated with the absorbed energy

Phase 1	Phase 2	Phase 3	Phase 4	Phase 5	Absorbed energy sample 1 (kJ)	Absorbed energy sample 2 (kJ)	Total absorbed energy (kJ)
990mm/ 650s	-	-	-	-	9.2	7.2	16.4
990mm/ 300s	940mm/ 350s	-	-	-	6.6	8.8	15.4
990mm/ 200s	940mm/ 150s	930mm/ 300s	-	-	8.1	7.9	15.9
990mm/ 150s	940mm/ 250s	990mm/ 250s	-	-	7.3	8.3	15.6
990mm/ 200s	940mm/ 250s	990mm/ 200s	-	-	7.3	8.3	15.6
990mm/ 100s	940mm/ 100s	990mm/ 100s	940mm/ 100s	990mm/250s	7.7	8.1	15.8

For all heating scenarios, the average total absorbed energy is 15.78 ± 0.34 kJ (Table 3). Heating phases with modification of SSC positions and time of exposure slightly reduce the microwave absorbed power within both samples comparing to the reference treatment with SSC position at 990 mm during 650s (6.3% microwave reflected power).

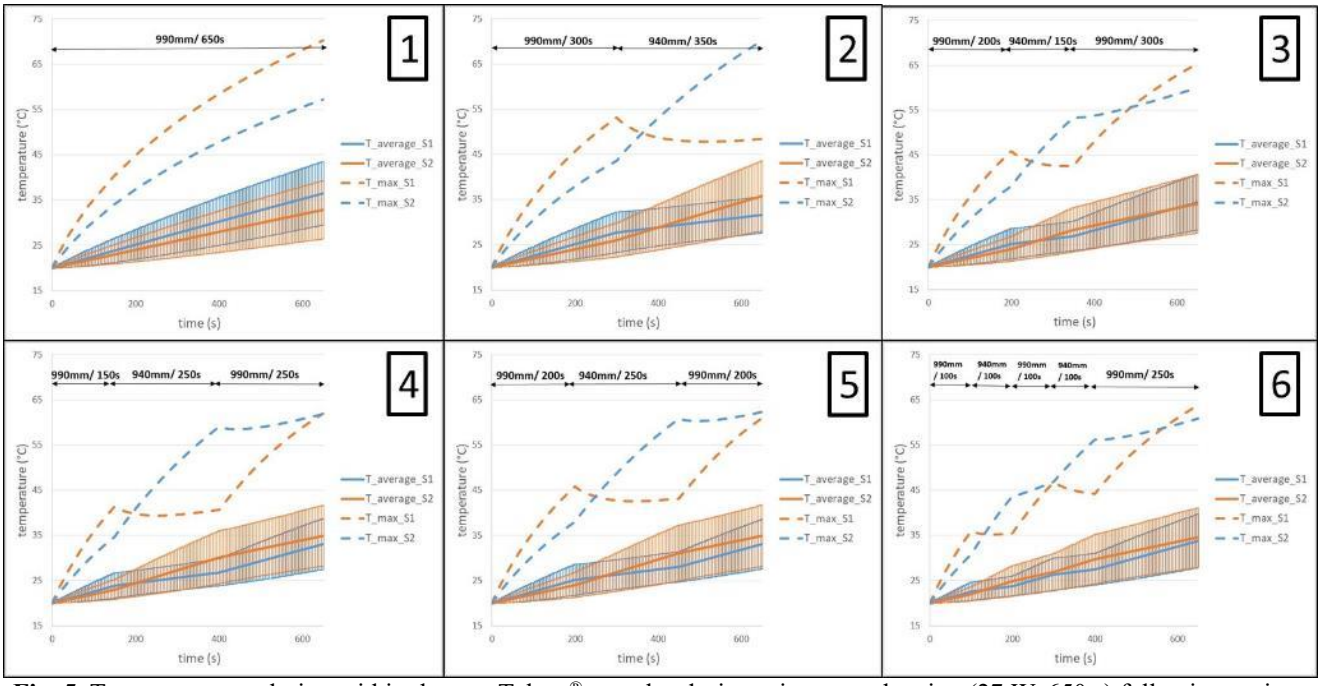

Fig. 5. Temperature evolution within the two Tylose® samples during microwave heating (27 W, 650 s) following various heating scenarios with different SSC positions and exposure times.

Figure 5 displays the mean temperatures within sample 1 and 2 associated with their standard deviations. The evolution of the max temperature of both samples is also analysed. The highest temperature gradients are obtained for the heating scenario 1 and 2 (first two lines of Table 3). For these two heating treatments, the max temperature can reach local values up to 65°C for both samples.

For the heating scenarios 3 to 6 (lines 3 to 6 in Table 3), the mean temperatures associated with their standard deviations are globally lower than the first heating treatments. The local max temperatures for sample 1 and 2 are strongly affected by the change in both SSC position and time of exposure. Heating scenario 4 and 5 exhibits very close local max temperatures (around 62°C) and similar microwave absorbed energy for sample 1 and 2 at the end of the thermal treatment. This result is also confirmed with the 3D temperature distribution (Figure 6) at the end of processing time for scenarios 4 and 5.

Figure 6 clearly illustrates the influence of the different SSC positions on the local temperature distribution within each sample during the microwave heating. In any case, the hot spot is always located at the centre for each sample whatever the SSC positions and exposure times. The back and forth motion of the SSC enables to modify the local electric field strength at different location of samples 1 and 2 so that temperature distribution is varying within both samples depending on the dynamic position of the SSC.

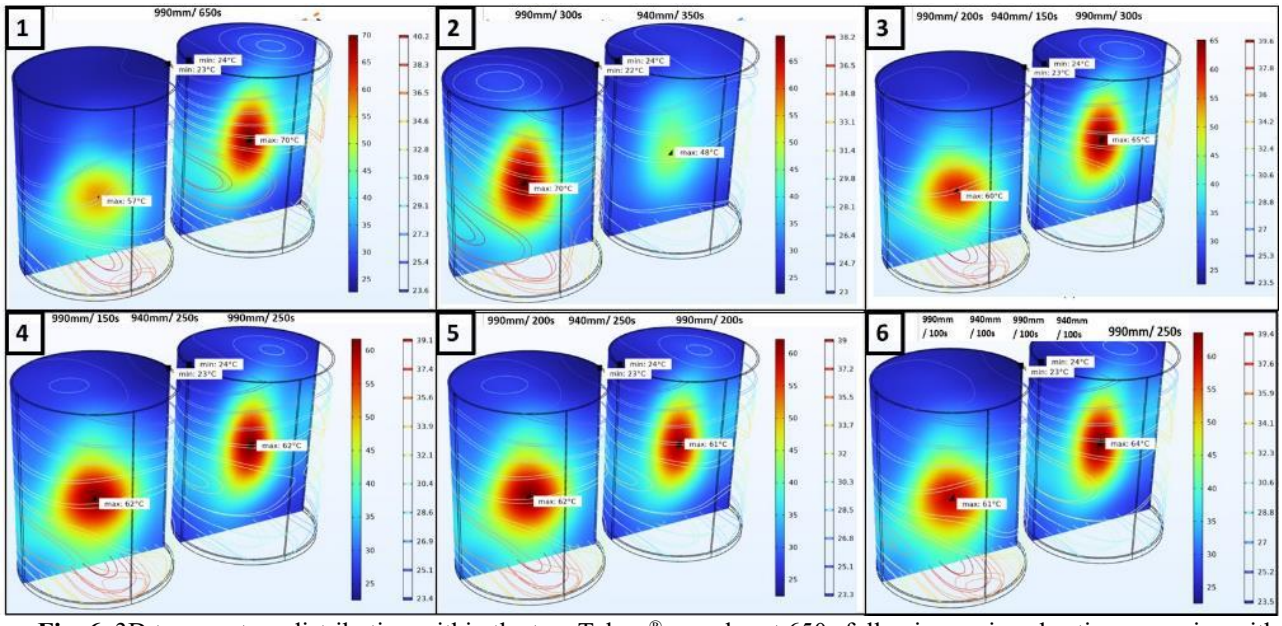

Fig. 6. 3D temperature distribution within the two Tylose® samples at 650s following various heating scenarios with different SSC positions and exposure times.

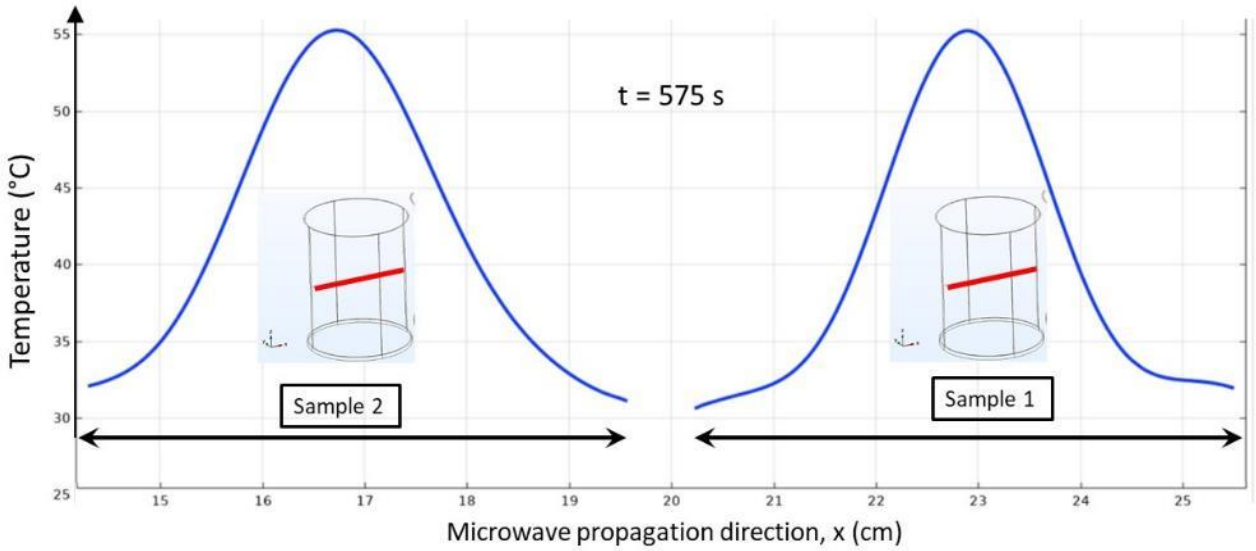

Fig. 7. Temperature distribution within the two Tylose® samples at 575s following two horizontal lines based on heating scenario n°5.

Based on heating scenario n°5 (990mm/200s, 940mm/250s and 990mm/200s), Figure 7 depicts the temperature distribution along a central horizontal line for the two samples at time 575 s. One can notice that similar temperature curves are obtained for both samples with 55°C maximum temperature reached at the centre of both cylinders.

Conclusion/ Perspectives

This work is dedicated to the numerical modelling of the 915 MHz microwave heating of a food simulant placed inside a single mode applicator (static mode without rotation of the Teflon® plate). The main findings can be resumed in two main bullet points. First, with the placement of one dielectric sample inside the microwave applicator in static mode, it is not possible to modify the position of nodes and anti nodes of the electric field inside the sample by the only motion of the SSC position. So far this strategy is not able to improve temperature uniformity inside the processed sample as it can only affect the local amplitudes of the electric field at specified locations.

The addition of one similar dielectric sample inside the microwave applicator leads to a completely different behavior so that mutual interactions are encountered between both samples that can modify the local electric field strength at specific locations. In particular, this numerical study highlights some scenario of interest to ensure optimal microwave heating of both samples to reach the same end temperature distribution. This heating strategy enables us to overcome the common problems of heterogeneous temperature distribution between different samples placed in a microwave cavity.
Perspectives of such a work would be to applied the same strategy with a reference sample and an additional one with different dielectric properties and different geometry. The challenge would be to find the optimal dielectric properties values and topology of the additional dielectric sample to reduce hot spots formation within the reference sample without losing too much microwave power when heating the additional dielectric load (need to find an additional sample able to interact with the electric field with a very low heat dissipation). To this extent, the SSC could act as an additional impedance matching element to insure the optimum microwave coupling with the cavity.

References

[1] C. D. Albuquerque, S. Curet, L. Boillereaux (2021). Influence of heating rate during microwave pasteurization of ground beef products: experimental and numerical study, J. Food Process Eng. 2022, e13722. https://doi.org/10.1111/jfpe.13722.
[2] Klinbun, W.; Rattanadecho, P. Numerical study of initially frozen rice congee with thin film resonators package in microwave domestic oven. J. Food Process Eng. 2022, 45, e13924. https://doi.org/10.1111/jfpe.13924.
[3] Shen, L.; Gao, M.; Feng, S.; Ma, W.; Zhang, Y.; Liu, C.; Liu, C.; Zheng, X. Analysis of heating uniformity considering microwave transmission in stacked bulk of granular materials on a turntable in microwave ovens. J. Food Eng. 2022, 319, 110903. https://doi.org/10.1016/j.jfoodeng.2021.110903.
[4] Wipawee, T.; Witchuda, D.; Pitiya, K. Simulation of Thermal and Electric Field Distribution in Packaged Sausages Heated in a Stationary Versus a Rotating Microwave Oven. Foods 2021, 10, 1622. https://doi.org/10.3390/foods10071622.
[5] Nget, S.; Mith, H.; Curet, S.; Boillereaux, L. Reflection Coefficient-Based Validation of Electromagnetic Model: Application to Model Food at 915 MHz. In Proceedings of the 36th Annual European Simulation and Modelling Conference (ESM® 2022), Porto, Portugal, 26–28 October 2022; pp. 165–169.
[6] Nget, S.; Mith, H.; Boué G., Curet S., L. Boillereaux. The Development of a Digital Twin to Improve the Quality and Safety Issues of Cambodian Pâté: The Application of 915 MHz Microwave Cooking, Foods 2023 12(6), 1187, https://doi.org/10.3390/foods12061187

Personalized Haemostatic Agents with Increased Bioactivity Obtained under Microwave-Assisted Conditions

J. Radwan-Pragłowska[1], Ł. Janus[1], A. Sierakowska[1], T. Galek[2], K. Łysiak[2], P. Bąk[1], J. Śmietana[1], M. Tupaj[2], D. Bogdał[1]

[1]Department of Biotechnology and Physical Chemistry, Faculty of Chemical Engineering and Technology, Cracow University of Technology, Warszawska 24 Street, 31-155 Cracow, Poland
[2]Faculty of Mechanics and Technology, Rzeszow University of Technology, Kwiatkowskiego 4 Street, 37-450 Stalowa Wola, Poland
Julia.radwan-praglowska@pk.edu.pl, t.galek@prz.edu.pl

Keywords: microwave, haemostatic agents, chitozan, biomaterials

Nowadays, an extremely dynamic development of the health care sector is observed, which directly translates into an increase in demand for innovative medical devices with advanced properties [1-4]. The most modern biomaterials are based on synthetic and natural polymers and composites. One of the most promising raw materials to produce medical devices is chitosan - a deacetylated derivative of chitin, the main source of which are the exoskeletons of crustaceans [5-9], insects, arachnids, cell walls of some fungi and algae are made [10-13].

The production method consists in the deacetylation of chitin using a concentrated solution of sodium hydroxide or appropriate enzymes [9,14]. Chitosan is built of two randomly occurring types of units, i.e. glucosamine and N-acetylglucosamine linked by β-1,4-glycosidic bonds. Its chemical structure resembles substances from the group of glycosaminoglycans, constituting an element of the extracellular matrix, e.g. chondroitin sulphate. Chitosan is characterized by many interesting biological properties, such as biocompatibility, biodegradability, antipyrogenicity and mucoadhesiveness. In addition, it has antibacterial, antioxidant and haemostatic properties [15-19]. The bioactivity of chitosan is attributed to free amino groups in its chemical structure.

The presence of active functional groups and their polycationic nature mean that the polymer can interact with various proteins, which translates into the ability to enter various interactions with cells or the ability to influence their differentiation processes. All this makes it attract the attention of not only scientists, but also manufacturers of medical devices around the world [4,20-21].

Maintaining adequate haemostasis after injury and during surgery, is one of the greatest challenges of modern medicine [22–24]. As many as 1.5 million blood transfusions are performed annually. Approximately 40% of trauma deaths and over 90% of fatalities occurred in the pre-hospital setting, and 50% of these deaths were reported massive blood loss as a causal factor. Moreover, 80% of fatal injuries in the United States alone resulted from uncontrolled haemorrhage. Haemorrhage in trauma patients is also the leading cause of reoperation [25-27]. Thus, development of novel biomaterials which would help to prevent the outflow of blood from blood vessels is a great challenge. Most of the haemorrhages appear under non-sterile conditions. Therefore, effective haemostatic agent should not only be able to stop the bleeding but also prevent from microbial infections.

The aim of the following work was to develop novel, advanced haemostatic agents which would be characterized by superior biological activity. The goal was achieved by preparing chemically crosslinked chitosan-based biomaterials with the possibility of personalization via shaping using 3D techniques. Firstly, fungal-derived chitosan was mixed with NH_2 rich crosslinking agents (amino acids) and high-boiling-point solvent. For this reason, a 3D printed mould was prepared which was further filled with semi-product and freeze-dried. The products were obtained under microwave-assisted conditions which resulted in the increase of free amino groups responsible for electrostatic interactions with biomolecules responsible for the blood coagulation cascade process and further modified with the enzyme lysozyme to improve its antibacterial performance.

Final products were tested over chemical structure using FT-IR spectroscopy. Morphology was evaluated by scanning electron microscope (SEM). To verify their potential as haemostatic agents, the samples' ability to absorb simulated body fluid and human blood was investigated. Also, their susceptibility to biodegradation has been verified. Moreover, their antimicrobial activity has been studied on two different strains, namely e. *coli* and s. *aureus*. Finally, the samples were confirmed to be non-toxic to mouse fibroblasts L929 cell line as well as osteosarcoma MG 63 cell line. Additionally, they exhibited positive impact on cells proliferation.

The results clearly demonstrated that newly developed chitosan-based 3D shaped aerogels can be successfully applied as modern haemostatic agents.

Acknowledgement
This research was funded by National Centre for Research and Development, grant number LIDER/21/0120/L-10/18/NCBR/2019.

References

[1] Ravi Kumar, M. N. V. A Review of Chitin and Chitosan Applications. Reactive and Functional Polymers. 2000.
[2] Seidi, F.; Khodadadi Yazdi, M.; Jouyandeh, M.; Dominic, M.; Naeim, H.; Nezhad, M. N.; Bagheri, B.; Habibzadeh, S.; Zarrintaj, P.; Saeb, M. R.; Mozafari, M. *Chitosan-Based Blends for Biomedical Applications.* International Journal of Biological Macromolecules. 2021.
[3] Swain, S.; Kumar Ghosh, S.; Roy, A. *Application of Chitosan and Chitosan Derivatives: A Review*. ~ 150 ~ The Pharma Innovation Journal 2021, 10 (7).
[4] Wang, W.; Meng, Q.; Li, Q.; Liu, J.; Zhou, M.; Jin, Z.; Zhao, K. *Chitosan Derivatives and Their Application in Biomedicine.* International Journal of Molecular Sciences. 2020.
[5] Cheung, R. C. F.; Ng, T. B.; Wong, J. H.; Chan, W. Y. *Chitosan: An Update on Potential Biomedical and Pharmaceutical Applications*. Marine Drugs. 2015. https://doi.org/10.3390/md13085156.
[6] Bakshi, P. S.; Selvakumar, D.; Kadirvelu, K.; Kumar, N. S. *Chitosan as an Environment Friendly Biomaterial – a Review on Recent Modifications and Applications.* International Journal of Biological Macromolecules. 2020.
[7] Muthu, M.; Gopal, J.; Chun, S.; Devadoss, A. J. P.; Hasan, N.; Sivanesan, I. *Crustacean Waste-Derived Chitosan: Antioxidant Properties and Future Perspective*. Antioxidants. 2021. https://doi.org/10.3390/antiox10020228.
[8] Younes, I.; Rinaudo, M. *Chitin and Chitosan Preparation from Marine Sources. Structure, Properties and Applications*. Marine Drugs. 2015.
[9] Santos, V. P.; Marques, N. S. S.; Maia, P. C. S. V.; de Lima, M. A. B.; Franco, L. de O.; de Campos-Takaki, G. M. *Seafood Waste as Attractive Source of Chitin and Chitosan Production and Their Applications*. International Journal of Molecular Sciences. 2020. https://doi.org/10.3390/ijms21124290.
[10] Ghormade, V.; Pathan, E. K.; Deshpande, M. v. *Can Fungi Compete with Marine Sources for Chitosan Production?* International Journal of Biological Macromolecules. 2017. https://doi.org/10.1016/j.ijbiomac.2017.01.112.
[11] Dhillon, G. S.; Kaur, S.; Brar, S. K.; Verma, M. *Green Synthesis Approach: Extraction of Chitosan from Fungus Mycelia.* Critical Reviews in Biotechnology. 2013.
[12] Hoover, D. G. Production of Chitosan by Fungi. Food Biotechnology 1993, 7 (1).
[13] Rahman, M. A.; Halfar, J. *First Evidence of Chitin in Calcified Coralline Algae: New Insights into the Calcification Process of Clathromorphum Compactum.* Scientific Reports 2014, 4.
[14] Kou, S. (Gabriel); Peters, L. M.; Mucalo, M. R. *Chitosan: A Review of Sources and Preparation Methods*. International Journal of Biological Macromolecules. 2021.
[15] Vázquez, J. A.; Rodríguez-Amado, I.; Montemayor, M. I.; Fraguas, J.; del González, M. P.; Murado, M. A. *Chondroitin Sulfate, Hyaluronic Acid and Chitin/Chitosan Production Using Marine Waste Sources: Characteristics, Applications and Eco-Friendly Processes: A Review*. Marine Drugs. 2013.
[16] Huang, M.; Khor, E.; Lim, L. Y. *Uptake and Cytotoxicity of Chitosan Molecules and Nanoparticles: Effects of Molecular Weight and Degree of Deacetylation.* Pharmaceutical Research 2004, 21 (2).
[17] Ways, T. M. M.; Lau, W. M.; Khutoryanskiy, V. v. *Chitosan and Its Derivatives for Application in Mucoadhesive Drug Delivery Systems*. Polymers. 2018.
[18] Abd El-Hack, M. E.; El-Saadony, M. T.; Shafi, M. E.; Zabermawi, N. M.; Arif, M.; Batiha, G. E.; Khafaga, A. F.; Abd El-Hakim, Y. M.; Al-Sagheer, A. A. *Antimicrobial and Antioxidant Properties of Chitosan and Its Derivatives and Their Applications: A Review*. International Journal of Biological Macromolecules. 2020.
[19] Huang, L.; Liu, G. L.; Kaye, A. D.; Liu, H. *Advances in Topical Hemostatic Agent Therapies: A Comprehensive Update.* Advances in Therapy. 2020.
[20] Negm, N. A.; Hefni, H. H. H.; Abd-Elaal, A. A. A.; Badr, E. A.; Abou Kana, M. T. H. *Advancement on Modification of Chitosan Biopolymer and Its Potential Applications.* International Journal of Biological Macromolecules. 2020.
[21] Aranaz, I.; Alcántara, A. R.; Civera, M. C.; Arias, C.; Elorza, B.; Caballero, A. H.; Acosta, N. *Chitosan: An Overview of Its Properties and Applications.* Polymers. 2021.
[22] Peng, H. T. *Hemostatic Agents for Prehospital Hemorrhage Control: A Narrative Review. Military Medical Research*. 2020.
[23] Yu, P.; Zhong, W. *Hemostatic Materials in Wound Care*. Burns and Trauma. 2021.
[24] Pereira, B. M.; Bortoto, J. B.; Fraga, G. P. *Topical Hemostatic Agents in Surgery: Review and Prospects*. Revista do Colegio Brasileiro de Cirurgioes. 2018.
[25] Wedmore, I.; McManus, J. G.; Pusateri, A. E.; Holcomb, J. B. *A Special Report on the Chitosan-Based Hemostatic Dressing: Experience in Current Combat Operations.* Journal of Trauma - Injury, Infection and Critical Care 2006, 60 (3).
[26] Hirshberg, A.; Wall, M. J.; Ramchandani, M. K.; Mattox, K. L. *Reoperation for Bleeding in Trauma*. Archives of Surgery 1993, 128 (10).
[27] Kaynak, M. F.; Yilmaz, O.; Rodoplu, U.; Maltepe, F.; Gokmen, N. *Hemostatic Effects of Microporous Polysaccharide Hemosphere® in a Rat Model with Severe Femoral Artery Bleeding.* Advances in Therapy 2007, 24 (3).
[28] (Achneck, H. E.; Sileshi, B.; Jamiolkowski, R. M.; Albala, D. M.; Shapiro, M. L.; Lawson, J. H. *A Comprehensive Review of Topical Hemostatic Agents: Efficacy and Recommendations for Use.* Annals of Surgery. 2010.

Microwave and Radiofrequency Ablation: A Comparative Study Between Technologies in Ex-Vivo Tissues

F. Lobascio[1], M. Fiore[1], N. Di Modugno[1], C. Bruno[1], T. De Nicolo[1], R. Di Modugno[1]

[1]Leanfa s.r.l., Via C. A. Dalla Chiesa 6, Ruvo di Puglia, Italy
fabio.lobascio@leanfa.com, marco.fiore@leanfa.com, nicola.dimodugno@leanfa.com, cristian.bruno@leanfa.com, thomas.denicolo@leanfa.com, rocco.dimodugno@leanfa.com

Keywords: microwave, radiofrequency, medical applications, medical equipment, solid-state, tissue ablation, cancer, temperature control, ex-vivo

Introduction

Microwave (MW) and Radiofrequency (RF) ablation are minimally invasive technologies that use a local temperature increase to induce the denaturation of the cellular membrane proteins and kill cells. These procedures can be used for cancer treatments [1], pain management [2], heart rhythm disorders [3], benign tumours [4] and so on [5][6].

The large variety of applications makes the market of RFA and MWA devices extremely thriving, with strong growth prospects over the next few years. One of the focal points of the development of these technologies and their diffusion is the introduction of solid-state generators, that are smaller, lighter, more robust and have a much longer lifespan than magnetron-based or tube-based ones.

There are several differences between the two technologies which do not lead one of them to be always more effective than the other [7]. RFA is a well-established treatment that can count on a long track of records of success since ‘90s [8], while MWA has only been adopted in ‘00s [9] and on a large scale in the last decade. Despite this, MWA is a faster technique that can be more efficient to treat larger tumours [10].

Due to the absence of a standard procedure [11] and to the continuous technology and applications improvements [12], the skill and the experience of the doctor play a fundamental role in the choice the procedure type, although this means a greater load of responsibility and less repeatability of the results.

To facilitate the work of the operator in choosing the most suitable set of parameters for each clinical case, Leanfa performed several experimentations about the dimensions and issues related to RFA and MWA. By observing the size of the ablated areas in ex-vivo tissues (i.e., chicken breast and bovine liver) and correlating it to the used power and intervention time, an ablation reference matrix was obtained which can guide the choice of the clinician, after having scaled the dimensions based on the type of tissue and the expected blood perfusion.

The experimental setup (Fig. 1) included a Hybrid Generator for scientific purpose, with a microwave or radiofrequency water cooled laboratory probe. During testing, the ablation temperature was controlled by closed-loop algorithms that tailored the delivered power in relation to the desired temperature profile, measured by a thermocouple sensor embedded in the probe. Very accurate and repetitive results were obtained thanks to the extreme flexibility and reliability of solid-state technology, used for both RFA and MWA tests.

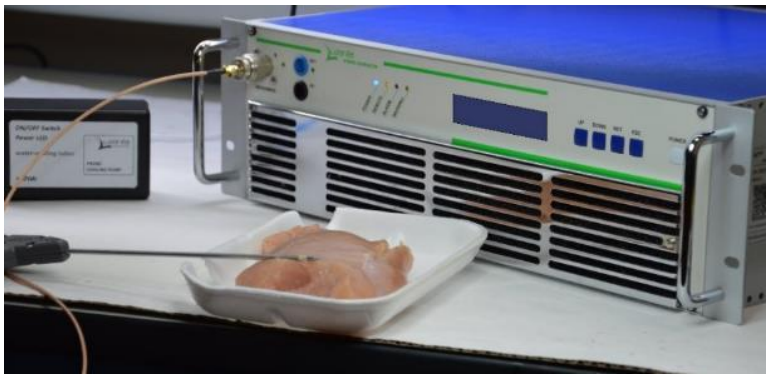

Fig. 1. Leanfa Hybrid Generator in an experimental setup (MWA on chicken breast).

State of the art

Considering the data of various national registers [13][14], the treatment of pathologies through RFA or MWA counts from several thousand to several tens of thousands of patients per country. The average cost of disposable equipment for each procedure ranges from a few thousand dollars to several thousand [15]. Furthermore, more and more patients are candidates

for non-pharmacological therapies, especially when it comes to diseases related to the cardiovascular system such as atrial fibrillation. In addition, the cost of each ablation system can range from several tens to several hundred thousand dollars. Therefore, the medical ablation market appears to be booming and certainly has not yet reached its peak.

Thermal ablation aims to bring the tissues to a temperature >60°C to denature their proteins and induce a coagulative necrosis of the cells. The technological challenge consists in covering the entire volume occupied by the lesion, in the shortest possible time and trying to preserve the surrounding healthy tissues. For this reason, the most typical application of this therapy uses needle or catheter probes which are introduced into the target tissue via minimally invasive surgery [16].

Even if the principle that makes the therapy effective is the same, there are substantial differences between the two technologies which must be taken into consideration in order to make a rational choice based on the specific clinical case. The heating of RFA is due to the Joule related to the current flow, relied to the presence of dissolved ions in the fluids that perfuse the tissues. This means that, as it dries, the tissue conducts less and less current, until it carbonises (Fig. 2). For this reason, radiofrequency ablation should be supported by impedance control algorithms, to avoid tissue dehydration too rapidly, before the target reaches the desired temperature and necrosis. MWA transfers electromagnetic energy to the polar molecules of the tissue (mainly water), raising its temperature. This makes the technique less affected by drying phenomena and allows uniform heating of a larger volume in less time [17].

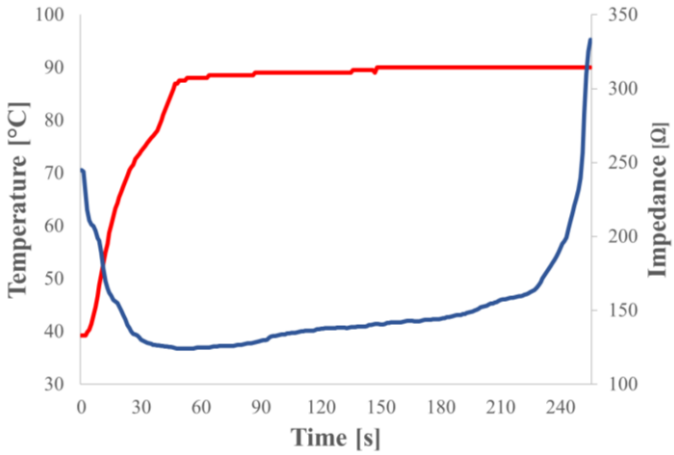

Fig. 2. Impedance and temperature trend in RFA.

While it seems that MWA is always more effective than RFA, there are some details that shouldn't be overlooked. First of all, the costs of an intervention with RFA are lower, thanks to the greater simplicity and larger adoption of the technology. Also, RF conductive coupling is very useful when it is desired to ablate heterogeneous tissue selectively, as the current will always follow the path with the lowest impedance (very effective in ablations of bone or spine metastases) [18]. Another advantage of RFA is the possibility to create applicators of very different shapes, to better customize the ablation pattern according to the application, as well as the possibility to strongly reduce the probe size since it is not necessary to use coaxial cables.

Overall, RFA is less expensive and is very effective for performing controlled ablations with minimally invasive probes (cardiac pathologies, small lesions, tissues with particular composition), while MWA is optimal for performing large ablations in highly vascularized tissues (liver cancers) where there is a need to reach higher temperatures.

Materials and methods

In order to obtain an ablation matrix that can guide the doctor in choosing the right set of parameters based on the clinical case, it is necessary to use equipment that have the ability to provide reliable and repeatable results. Leanfa has been working for years to improve the performance of its devices to make them more and more accurate through the development of hardware that integrates the most modern technologies and power and temperature profile control algorithms. Thanks to control systems based on impedance or reflected power readings, the Leanfa hybrid RF and MW generator can carry out controlled ablation, without causing unwanted carbonization and without involving areas where the tissue is not expected to be damaged.

Hybrid Generator

The Leanfa Hybrid Generator can deliver up to 250 W on 50 Ω of MW power at the frequency of 2450 MHz and up to 50 W on 100 Ω of RF power at the frequency of 480 kHz. The main feature of the device in RF mode is management of the output power as a function of the measured tissue impedance and temperature profile. In MW mode the generator can use a low power RF tone to measure the impedance without increasing the tissue temperature. The equipment includes a peristaltic pump (Fig. 3a) for catheter cooling with saline solution of water. The energy is delivered to the tissue in Continuous Wave mode (CW), and the temperature of the ablation volume and of the cooled zone is measured and used to drive the power output stage.

Probes

The radiofrequency probe is composed of two cables that run through the applicator until they connect to two electrodes, whose size and distance determine the shape of the ablation volume. The microwave probe is composed of a coaxial cable and a coaxial termination that performs as an antenna. Due to the unbalanced nature of coaxial cables, current could flow along the surface of the outer conductor, causing unwanted heating along the cable [19]. Therefore, the antenna must be properly matched to the load to have the maximum energy transfer and must have a suppression system of current flow along the outer conductor. Both probes integrate a micro-hydraulic circuit (Fig. 3b) for the shaft cooling to prevent unwanted heating of tissue portions outside the target volume caused by the Joule effect related to conductor losses. The probes also feature two thermocouples (Fig. 3c), one near the tip for ablation temperature monitoring and one immediately behind the ablation zone, where the tissue temperature must not increase for any reason, to spare those tissues that are not in the target volume.

Tissues under test

The chosen ex-vivo tissues on which the procedures have been performed are chicken breast and bovine liver. These tissues have been previously heated to start each procedure at the temperature of about 37°C, to simulate as much as possible the environment inside a living body.

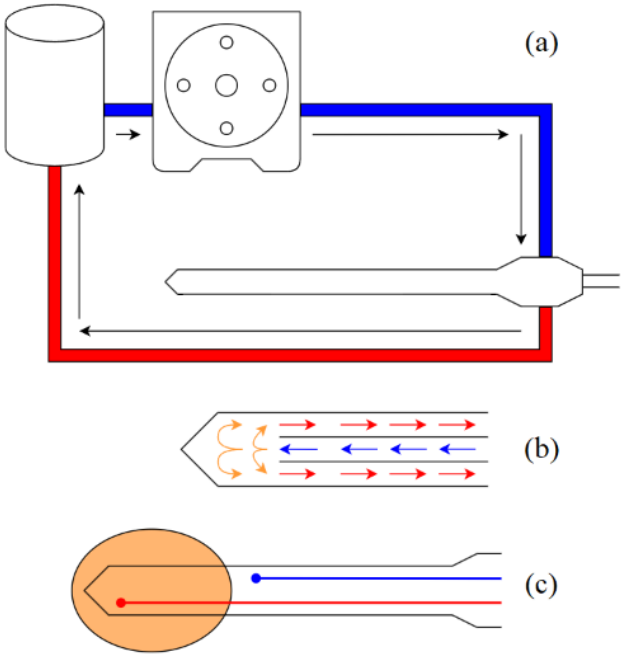

Fig. 3. Leanfa system features: (a) peristaltic pump for shaft cooling, (b) micro-hydraulic circuit, (c) embedded thermocouples for temperature profile monitoring.

Discussion

The experience of Leanfa with various applications, on various organs and tissues, has led to the aim of carrying out ablations as largest as possible and with the highest roundness index. This is because the uniform size of a sphere lends itself very well to the operations that aim to hit only the target tissue, sparing as much as possible the nearby healthy ones. This does not happen easily due to the tail effect related to unwanted heating of the catheter part closest to the emission zone or even to a variation of the electrical properties of the ablated tissue, which no longer make the shortest path between the poles coincide with the preferential signal path.

The Roundness Index is a value between 0 and 1, a high value of this index represents the tendency of the shape to be spherical and can be calculated as ratio between two ablation diameters. Assuming the tissue to be homogeneous and given the difficulty of measuring both the transverse and longitudinal diameters due to the incision that must be made on the ablated tissue, the two will reasonably be considered equal (Fig. 4). This leads to consider the planar Roundness Index as in (1) as the most representative of the ablation sphericity.

$$RI = Size\ B\ /\ Size\ A \qquad (1)$$

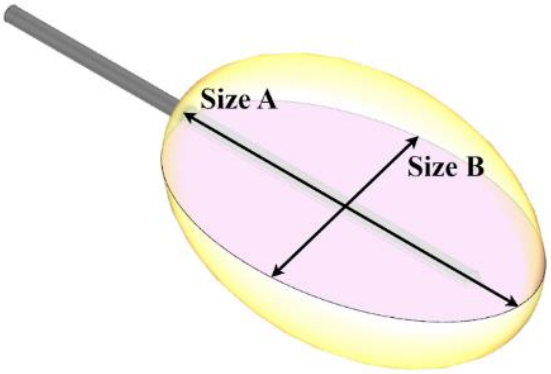

Fig. 4. Ablation sizes considered for Roundness Index calculation.

The procedures have been performed using a temperature closed loop drive algorithm, setting the maximum output power and the procedure duration (fixed at 10 min). The algorithm performs a constant temperature ramp until the target is reached. Since protein denaturation starts at around 60°C and the water boiling temperature is around 100°C, a good target to set is 95°C to heat the tissue as much as possible without generating bubbles that can mismatch the load in MWA mode or can reduce the contact surface with RFA electrodes.

As predicted by theory, results (Table 1) show higher Roundness Index and size in MWA. Generally, all sizes of the ablated tissue with RFA are smaller due to the occlusive effect that the dried tissue produces with its high impedance at radiofrequency. The dimensional difference can also be observed between the results obtained on chicken breast and bovine liver (Fig. 5), due to the different electrical proprieties and the less homogenous composition of bovine liver, which has a denser vascularization which limits the heat propagation.

The results obtained are consistent with those documented by literature [20] and data provided by the main players in the metastasis ablation market using MWA and RFA. Certainly, the procedures performances can be significantly increased if the generator, with its thermal profile and power control algorithms, is associated with probes designed with advanced technologies and simulation systems. A good combination of this technology with state-of-the-art probes could significantly reduce surgery times, subjecting the patient to less risk, and maximally safeguarding healthy tissues.

Fig. 5. Example of ablation in bovine liver (left) and chicken breast (right).

Table 1. Ablation dimensions measurements and calculated Roundness Index.

MW energy on chicken breast			
Max Power [W]	Size A [mm]	Size B [mm]	Roundness Index
50	20	18	0,90
100	33	30	0,91
150	37	32	0,86
200	48	43	0,89
250	50	45	0,90
MW energy on bovine liver			
Max Power [W]	Size A [mm]	Size B [mm]	Roundness Index
50	18	15	0,83
100	32	25	0,78
150	35	28	0,8
200	40	33	0,83
250	42	35	0,83
RF energy on chicken breast			
Max Power [W]	Size A [mm]	Size B [mm]	Roundness Index
10	22	12	0,55
20	24	13	0,54
30	25	15	0,60
40	30	17	0,57
50	32	19	0,59
RF energy on bovine liver			
Max Power [W]	Size A [mm]	Size B [mm]	Roundness Index
10	20	12	0,60
20	22	12	0,55
30	24	14	0,58
40	27	15	0,55
50	30	17	0,57

Conclusions

Once the effectiveness of RFA and MWA technologies has been verified and given the increase in the number of operations over the years, it is important that the medical industry sector takes care of increasingly improving the performance of these procedures. For RFA it is necessary to invest in delivery algorithms according to the electrical parameters linked to the tissue hydration. Furthermore, multi-probe applications can be a good way to increase the volume to be treated with the same intervention time. For MWA it is necessary to invest in antennas that can allow greater customization of the ablation shapes, as well as control of the high temperatures that can be reached with this technology. The problem of higher costs, on the other hand, could be offset over time with a reduction in hospitalization times and the probability of metastasis recurrence. These improvements can be combined to get the best out of each of the two technologies, thanks to the use of hybrid generators that allow, depending on the case, providing a specific therapy.

References

[1] G. Carrafiello, D. Laganà, M. Mangini, et al. “Microwave tumors ablation: principles, clinical applications and review of preliminary experiences.”, International journal of surgery, London, England, vol. 6, Suppl 1, p. 65-69, Dec. 2008.
[2] D.K. Filippiadis, S. Yevich, F. Deschamps, J.W. Jennings, S. Tutton, A. Kelekis “The Role of Ablation in Cancer Pain Relief.”, Current oncology reports, vol. 21(12), p. 105, Nov. 2019.
[3] W. Wisser, C. Khanzen, E. Deviatko, et al. “Microwave and radiofrequency ablation yield similar success rates for treatment of chronic atrial fibrillation.”, European journal of cardio-thoracic surgery: official journal of the European Association for Cardio-thoracic Surgery, vol. 25(6), p.p. 1011-1017, Jun. 2004.
[4] J. Reis, Y. Chang, A.K. Sharma “Radiofrequency ablation vs microwave ablation for osteoid osteomas: long-term results.”, Skeletal radiology, vol. 49(12), p.p. 1995-2000, Dec. 2020.
[5] L. Bennardo, I. Fusco, C. Cuciti, et al. “Microwave Therapy for Cellulite: An Effective Non-Invasive Treatment.”, Journal of clinical medicine, vol. 11(3), p. 515, Jan. 2022.
[6] S.J. Goodyear, I.K. Nyamekye “Radiofrequency ablation of varicose veins: Best practice techniques and evidence.”, Phlebology, vol. 30, Suppl 2, p.p. 9-17, Nov. 2015.
[7] F. Izzo, V. Granata, R. Grassi, et al. “Radiofrequency Ablation and Microwave Ablation in Liver Tumors: An Update.”, The oncologist, vol. 24(10), 990–1005, Oct. 2019.
[8] D.I. Rosenthal, A. Alexander, A.E. Rosenberg, A.D. Springfield “Ablation of osteoid osteomas with a percutaneously placed electrode: a new procedure.”, Radiology, vol. 183(1), p.p. 29-33, Apr. 1992.
[9] D.E. Dupuy, R.J. Zagoria, W. Akerley, W.W. Mayo-Smith, P.V. Kavanagh, H. Safran “Percutaneous radiofrequency ablation of malignancies in the lung.”, AJR. American journal of roentgenology, vol. 174(1), p.p. 57-59, Jan. 2000.
[10] K. Suwa, T. Seki, K. Aoi, et al. “Efficacy of microwave ablation versus radiofrequency ablation for hepatocellular carcinoma: a propensity score analysis.”, Abdominal radiology, New York, vol. 46(8), p.p. 3790-3797, Aug. 2021.
[11] H. Rathke, B. Hamm, F. Güttler, et al. “Comparison of four radiofrequency ablation systems at two target volumes in an ex vivo bovine liver model.”, Diagnostic and interventional radiology, Ankara, Turkey, vol. 20(3), p.p. 251-258, May-Jun. 2014.

[12] A. Pfannenstiel, J. Iannuccilli, F.H. Cornelis, D.E. Dupuy, W.L. Beard, P. Prakash "Shaping the future of microwave tumor ablation: a new direction in precision and control of device performance.", International journal of hyperthermia: the official journal of European Society for Hyperthermic Oncology, North American Hyperthermia Group, vol. 39(1), p.p. 664–674, Apr. 2022.
[13] N. Molitor, E. Yalcinkaya,A. Auricchio, et al. "Swiss National Registry on Catheter Ablation Procedures: Changing Trends over the Last 20 Years.", Journal of clinical medicine, Basel, Switzerland, vol. 10(14), 3021, Jul. 2021.
[14] J. Criado, A. Quesada, R. Cózar, "18th Official Report of the Spanish Society of Cardiology Working Group on Electrophysiology and Arrhythmias (2018).", Revista Española de Cardiología, Alicante, Spain, vol. 72(12), p.p. 1031-1042, Dec. 2019.
[15] T. Hunter, S. Palli, J. Rizzo, "Cost comparison of radiofrequency catheter ablation versus cryoablation for atrial fibrillation in hospitals using both technologies.", Journal of medical economics, vol. 19(10), p.p. 959-964, May 2016.
[16] H. Takahashi, B. Kahramangil, E. Berber, "Local recurrence after microwave thermosphere ablation of malignant liver tumors: results of a surgical series.", Surgery, vol. 163(4), p.p. 709-713, Dec. 2017.
[17] P. Donlon, M. Dennedy, "Thermal ablation in adrenal disorders: a discussion of the technology, the clinical evidence and the future.", Current Opinion in endocrinology, diabetes and obesity, vol. 28(3), p.p. 291-302, Jun. 2021.
[18] M. Eckmann, M. Martinez, S. Lindauer, et al., "Radiofrequency ablation near the bone-muscle interface alters soft tissue lesion dimensions.", Regional Anesthesia & Pain Medicine, vol. 40(3), p.p. 270-275, May-Jun 2015.
[19] Y. Mohtashami, H. Luyen, J. F. Sawicki, et al., "Tools for Attacking Tumors: Performance Comparison of Triaxial, Choke Dipole, and Balun-Free Base-Fed Monopole Antennas for Microwave Ablation," IEEE Antennas and Propagation Magazine, vol. 60(6), p.p. 52-57, Dec. 2018.
[20] P. Afaghi, M. Lapolla, K. Ghandi, "Percutaneous microwave ablation applications for liver tumors: recommendations for COVID-19 patients." Heliyon, Vol. 7(3), Mar. 2021.

Effect of Microwave Drying on Antioxidant Capacity of Agricultural By-Products

A. Valle-Gómez[1], R. C. Viramontes-Bocanegra[1], G. Dávila-Hernández[2], M. E. Sánchez-Pardo[1], A. Ortiz-Moreno[1]

[1]Instituto Politécnico Nacional, Escuela Nacional de Ciencias Biológicas, Av. Wilfrido Massieu 399, 07738, Mexico City, Mexico
[2]Universidad Autónoma de Guerrero, Facultad de Enfermería, 2. P°. de la Cañada s/n, Alta Progreso 39610, Acapulco de Juárez, Mexico
ortizalicia@hotmail.com

Keywords: antioxidant capacity, HPLC, carrot pomace, tamarind pericarp, coconut husk, drying.

Abstract
Food waste has been relevant in recent years because it contains nutrients and bioactive compounds; thus, it has become necessary to look for alternatives for its preservation. One of the most employed process techniques is drying. Microwave drying, has been proposed to reduce the moisture content of these residues and extend their shelf life. Residues from coconut mesocarp, as well as carrot and tamarind pericarp were studied. Microwave drying increased the antioxidant capacity of coconut by 5%, carrots by approximately 1%, and tamarind pericarp by around 26%. The antioxidant capacity of these agricultural residues showed correlation with the content of phenolic compounds. Microwave drying, as compared to convective drying, increased the concentration of catechin for coconut, epicatechin for carrot, and chlorogenic acid for tamarind pericarp.

Introduction

Food industry generates high amounts of agricultural waste [1], it has been reported that one-third of the foodstuff is lost or wasted around the world, which is about 1.3 billion tons per year. The losses in the food industry are mainly at the production, postharvest, and processing stages in the food supply chain [2]. Agricultural by-products are an important source of nutrients, such as biopolymers (polysaccharides and fibers) and bioactive compounds (phenolic compounds, organic acids, and carotenoids). Mexico, for instance, generates approximately 76 million tons of residues per year, only respect to fruits and vegetables [3].

Coconut husk represents one of the most important crops in Mexico; however, 83% of the fruit is waste and 17% is employed industrially, which constitutes an environmental problem. Coconut husk gained importance for its high content of phenolic compounds and antioxidant capacity [4]. It is possible to manufacture several food products from coconuts, such as oil, coconut milk, coconut flour, and water of coconut, which have health benefits [5]; moreover, coconut husk can be employed as a raw material to make food products and give them added value given the presence of bioactive compounds of interest. Besides, coconut husk has many uses in different industries, in the construction industry serving as material for cement [6].

Mexico is a megadiverse country; hence, it is possible to find many crops throughout the year, such as carrots and tamarind. Both crops are present in the daily meals of Mexican people in juices, fruit water, candies, and salads. The carrot bagasse represents 50% of the fruit and has a high content of carotenoids, fiber, and antioxidants [7]. In recent studies, carrot bagasse has been employed as ingredient for functional yogurt [8] and a substrate to produce β-fructofuranosidase by batch culture using *A. niger* [9], among others.

Tamarind contains 30% pulp, 40% seed, and 30% pericarp [10]. Tamarind pericarp contains polyphenols, flavonoids, anthocyanins, carotenoids, and vitamin C [11]. Tamarind has antibacterial, antioxidant activities, and pharmacological activities. These activities have been ascribed to bioactive compounds present in the tamarind [12].

On the other hand, there are different treatments for extending the shelf life of foodstuff and preserving their composition, and thermal processing is one of these treatments. Microwave drying is a thermal process that has shown to preserve the antioxidant capacity of vegetables, improve the taste, and extend the shelf life of fruits and vegetables [13]. The aim of the present project was to determine the impact of drying by two different techniques on the antioxidant capacity of three agricultural by-products, coconut husk, carrot bagasse, and tamarind pericarp.

Materials and methods

Carrots were purchased from a local market in Mexico City. Carrot pomace was obtained from juice extraction (Moulinex 753, Mexico). It was 51.6% juice and 48.4% carrot pomace. The coconuts (3–4 months old) were purchased from the Guerrero coast in Mexico and weighed approximately 1.6 kg. Tamarind (native, big pod) was provided by the largest producer of tamarind in Mexico. The fruits were washed, sanitized, and rinsed with distilled water.

Microwave drying
Samples of 100 g were treated by microwave drying using a microwave oven (LG, MJ1481BP, China). Table 1 summarizes the operating conditions.

Table 1. Operating conditions used for microwave drying.

Sample	Power (W)	Time (min)
Coconut husk	720	10
Carrot pomace	700	15
Tamarind pericarp	224.9	2.6

Conventional drying
Convective drying was conducted in a cabinet drying oven (Lindberg, Blue M, USA), and the operating conditions for each sample are detailed in Table 2.

Table 2. Operating conditions used for convective drying.

Sample	Temperature (°C)	Time (min)
Coconut husk	60	120
Carrot pomace	55	300
Tamarind Pericarp	60	120

Extraction of bioactive compounds
Each sample (1 g) was homogenized by using a plate stirrer (Thermo Scientific mod. 135935, China) with 5 mL of methanol–water mixture (80:20, v/v) for 30 min. The extracts were sonicated (Ultrasonic cleaner SB-5200 DTN) for 30 min at 25 °C. The samples were centrifuged (Hermle Z326, Germany) at 8000 g for 15 min at 4 °C. Antioxidant capacity and total phenolic compounds were determined to the supernatant.

Total phenolics
The total phenolic content was estimated by the Folin-Ciocalteu method [14]. The reaction mixture contained 100 µL of sample extract, 900 µL of Folin-Ciocalteu reagent, and 750 µL of 7% sodium bicarbonate solution. After 90 min at room temperature, the absorbance at 725 nm was measured by means of a Jenway 6705/UV–Vis spectrophotometer (Staffordshire, UK) and used to calculate the phenolic content using a calibration curve of gallic acid as the standard. The results were expressed as mg gallic acid equivalent (GAE) per gram of dry weight (DW) sample.

Chromatography
An Agilent 1200 liquid chromatograph with a UV-Vis detector and a reverse phase C18 column (250 mm × 4.6 mm, 5 µm particle size) was used. The elution gradient consisted of a mobile phase A (water-acetonitrile-acetic in a ratio 93:5:2 v/v/v) and phase B (water-acetonitrile-acetic 58:40:2) from 0 to 100% of B, 1 mL/min flow rate, 20 µL injection, 50 min run time for each sample, and absorbance reading at 280, 320, and 360 nm. Calibration curves were prepared from commercial standards of the phenolic compounds *p*-coumaric acid, vanillic acid, syringic acid, caffeic acid, gallic acid, ascorbic acid, chlorogenic acid, quercetin, rutin, ferulic acid, resveratrol, citric acid, in order to calculate concentrations from the quantification of the areas under the curves.

Antioxidant capacity
The antioxidant capacity was determined by two different methods: 2,2-diphenyl-1-picrylhydrazyl (DPPH), and ferric reducing antioxidant power (FRAP). For the DPPH method [15], the extracts of each sample (50 µL) were mixed with 1950 µL of DPPH solution and incubated in the dark at room temperature for 30 min. The absorbance was read at 515 nm. The FRAP method [15] was conducted by preparing a solution of 10 mM TPTZ and 20 mM ferric chloride, diluted in 300 mM sodium acetate buffer (pH 3.6) at a ratio of 1:1:10. Samples (50 µL) were added to 1.5 mL of the TPTZ solution, and the absorbance at 595 nm was determined after the samples were incubated for 20 min at 37°C. The results of the three methods were expressed as µmol Trolox (6-hydroxy-2,5,7,8-tetramethylchroman-2-carboxylic acid) equivalents/g DW.

Statistical analysis
The experiments were performed in triplicate. The mean values, standard deviations, and analyses of variance (ANOVA) were calculated by GraphPad Prism 8. The significant differences between the means were determined using the Tukey test ($p \leq 0.05$).

Results and discussion

Effect of drying on phenolic compounds content
The total phenolics in fresh coconut husk was 42.10 mg/GAE g DW. The drying by microwave and conventional oven had no significant difference ($p \leq 0.05$). The samples dried by microwave showed a better retention of phenolic compounds.

Carrot pomace was more affected by conventional drying given the 91.7% decrease observed in the content of phenolic compounds. The convective drying process could affect phenolic compounds differently, according to the group of phenolic compounds and their location in the vegetable cells [4,16]. In the case of tamarind pericarp, there was an increase in the extraction of phenolic compounds. The results for each agricultural by-product are shown in Table 3.

Table 3. Comparison of total phenolics content (TCP) of carrot pomace, coconut husk, and tamarind pericarp before and after microwave (MD) and convective (CD) drying.

Sample	TCP (mg GAE/g DW) Fresh	TCP (mg GAE/g DW) MD	TCP (mg GAE/g DW) CD
Coconut Husk	42.10 ± 0.001^{a}	45.5 ± 0.04^{a}	45.0 ± 0.023^{a}
Carrot Pomace	18.42 ± 0.36^{a}	14.12 ± 0.03^{b}	1.52 ± 0.016^{c}
Tamarind Pericarp	37.75 ± 0.13^{a}	51.83 ± 0.33^{b}	40.77 ± 0.04^{c}

Values with different superscript letters in the same arrow are significantly different ($p < 0.05$. Mean ±SD).

The increase in the extraction of phenolic compounds was reported also for blueberry pomace processed by microwave freeze vacuum drying. Low-temperature drying treatment could further concentrate the phenolic compounds. However, the most employed drying technique for fruits and vegetables is the convective one, though it was reported that this processing affects the colour, aroma, taste, and nutritional components of the samples dried [17]. The increase in phenolic compounds by microwave drying was also reported in apples. The decrease in moisture content and consequent increase in concentrations are probably responsible for this effect [18].

It was possible to identify ten phenolic compounds in the coconut husk such as gallic, 4-hydroxybenzoic, vanillic, ferulic, and syringic acids, vanillin, catechin, kaempferol, epicatechin, and rutin. In the case of carrot pomace, the phenolic compounds with the highest concentration were chlorogenic acid, catechin, piacetannol, and gallic acid. And for the tamarind pericarp, epicatechin, catechin, vanillic acid, and luteolin were identified. Microwave drying increased the concentrations of gallic acid in coconut husk [4], probably due to the thermal degradation of compounds of the kind of gallotannins, which have been reported to be the esters of gallic acid and sugars [4,19]. The microwave energy may disrupt the cell wall and enhance the release of bioactive compounds from cell walls [10,20]. Therefore, the increase in the concentration of some phenolic compounds after microwave drying on agricultural by-products may be due to this cellular disruption and the breakdown of certain compounds.

Effect of drying on antioxidant capacity

Coconut husk reported a higher increase in antioxidant capacity after microwave drying by the FRAP assay with 782.88 µmol TE/g DW. Carrot pomace was the most affected by microwave drying with 21.2% loss in antioxidant capacity. In general, conventional drying decreased the antioxidant capacity, and the loss could be attributed to the operating conditions, namely, time and temperature. Consequently, the cell matrix could open and facilitate the extractability and bioaccessibility of total phytochemicals, which promotes the release of bound phenols in soluble forms of low molecular weight that can be easily degraded by browning and oxidative reactions due to the heating process. [21]. Table 4 presents the results of antioxidant capacity for the three samples by the two assays (DPPH and FRAP).

Table 4. Comparison of antioxidant capacity by two methods (DPPH and FRAP) of coconut husk, tamarind pericarp, and carrot bagasse between microwave (MD) and convective drying (CD).

Sample	DPPH (µmol TE/g DW) Fresh	DPPH (µmol TE/g DW) MD	DPPH (µmol TE/g DW) CD	FRAP (µmol TE/g DW) Fresh	FRAP (µmol TE/g DW) MD	FRAP (µmol TE/g DW) CD
Coconut Husk	73.5 ± 0.053^{a}	77.22 ± 0.04^{a}	75.77 ± 0.05^{a}	358.56 ± 2.26^{a}	782.88 ± 1.10^{b}	473.52 ± 2.29^{c}
Carrot Pomace	30.00 ± 0.10^{a}	27.00 ± 0.05^{a}	19.61 ± 0.57^{b}	145.68 ± 2.29^{a}	125.60 ± 1.14^{b}	26.72 ± 0.75^{c}
Tamarind Pericarp	45.44 ± 2.6^{a}	61.88 ± 2.3^{b}	46.93 ± 0.09^{a}	472.04 ± 6.3^{a}	560.13 ± 2.13^{b}	549.10 ± 2.2^{c}

Values with different superscript letters in the same arrow are significantly different ($p<.05$. Mean ±SD).

The increase in the antioxidant capacity measured by the DPPH method after microwave drying occurred in a higher proportion in the tamarind pericarp, and this may be due not only to its content of phenolic compounds but also to the presence of other types of compounds such as ascorbic acid, citric acid, among others. Similar increases in antioxidant capacity by microwave drying were observed in brocade orange peels, due to having the highest retention of ascorbic acid and phenols after the process [22].

Conclusions

Microwave drying is a new thermal process that improves the antioxidant capacity of fruits and vegetables. The process is more efficient than conventional hot air drying, reducing the processing time by more than 90%. The microwave drying improves the antioxidant capacity of coconut husk, carrot bagasse, and tamarind pericarp and makes them useful to be included in functional food formulations. This can contribute to mitigate environmental problems if the agricultural by-products could be employed as raw material for different products, not only in the food industry, given their significant content of bioactive compounds.

References

[1] T. de Aquino Gondim *et al.*, "Assessment of metabolic, mineral, and cytotoxic profile in pineapple leaves of different commercial varieties: A new eco-friendly and inexpensive source of bioactive compounds," *Food Res. Int.*, vol. 164, no. October 2022, 2023, doi: 10.1016/j.foodres.2022.112439.
[2] FAO, *Food loss and food waste: Causes and solutions*. Rome: Food and Agriculture Organization of the United Nations (FAO), 2011.
[3] M. Vargas-Ortiz, G. Rodríguez-Jimenes, M. Salgado-Cervantes, and D. Pallet, "Minimally Processed Avocado Through Flash Vacuum-Expansion: Its Effect in Major Physicochemical Aspects of the Puree and Stability on Storage," *J. Food Process. Preserv.*, vol. 41, no. 3, pp. 1–10, 2017, doi: 10.1111/jfpp.12988.
[4] L. Valadez-Carmona, R. M. Cortez-García, C. P. Plazola-Jacinto, H. Necoechea-Mondragón, and A. Ortiz-Moreno, "Effect of microwave drying and oven drying on the water activity, color, phenolic compounds content and antioxidant activity of coconut husk (Cocos nucifera L.)," *J. Food Sci. Technol.*, vol. 53, no. 9, pp. 3495–3501, 2016, doi: 10.1007/s13197-016-2324-7.
[5] P. M. Divya, B. S. Roopa, C. Manusha, and P. Balannara, "A concise review on oil extraction methods, nutritional and therapeutic role of coconut products," *J. Food Sci. Technol.*, vol. 60, no. 2, pp. 441–452, 2023, doi: 10.1007/s13197-022-05352-0.
[6] F. R. B. Martinelli, F. R. C. Ribeiro, M. T. Marvila, S. N. Monteiro, F. da C. G. Filho, and A. R. G. de Azevedo, "A Review of the Use of Coconut Fiber in Cement Composites," *Polymers (Basel).*, vol. 15, no. 5, pp. 1–15, 2023, doi: 10.3390/polym15051309.
[7] M. Hernández-Ortega, G. Kissangou, H. Necoechea-Mondragón, M. E. Sánchez-Pardo, and A. Ortiz-Moreno, "Microwave Dried Carrot Pomace as a Source of Fiber and Carotenoids," *Food Nutr. Sci.*, vol. 04, no. 10, pp. 1037–1046, 2013, doi: 10.4236/fns.2013.410135.
[8] Z. Sharifi, A. Jebelli Javan, M. A. Hesarinejad, and M. Parsaeimehr, "Application of carrot waste extract and Lactobacillus plantarum in Alyssum homalocarpum seed gum-alginate beads to create a functional synbiotic yogurt," *Chem. Biol. Technol. Agric.*, vol. 10, no. 1, pp. 1–18, 2023, doi: 10.1186/s40538-022-00377-1.
[9] L. Guerra, D. Romanini, S. López, V. Castelli, and A. Clementz, "Upcycling of carrot discards into prebiotics (fructooligosaccharides) as high value food ingredients," *Food Bioprod. Process.*, vol. 138, pp. 172–180, 2023, doi: 10.1016/j.fbp.2023.01.011.
[10] G. Dávila-Hernández, C. S. Delgadillo-Arévalo, M. E. Sánchez-Pardo, H. Necoechea-Mondragon, and A. Ortiz-Moreno, "Pretreatment of tamarind pericarp to increase antioxidant availability and its application in a functional food," *J. Food Sci. Technol.*, vol. 58, no. 6, pp. 2385–2394, 2021, doi: 10.1007/s13197-020-04751-5.
[11] S. C. Han *et al.*, "Antialcohol and Hepatoprotective Effects of Tamarind Shell Extract on Ethanol-Induced Damage to HepG2 Cells and Animal Models," *Foods*, vol. 12, no. 5, 2023, doi: 10.3390/foods12051078.
[12] K. O. Fagbemi, D. A. Aina, M. O. Adeoye-Isijola, K. K. Naidoo, R. M. Coopoosamy, and O. O. Olajuyigbe, "Bioactive compounds, antibacterial and antioxidant activities of methanol extract of Tamarindus indica Linn.," *Sci. Rep.*, vol. 12, no. 1, pp. 1–12, 2022, doi: 10.1038/s41598-022-13716-x.
[13] J. Liu, Y. Liu, and X. Wang, "Effects of bioactive compounds and pharmacological activities in medicinal fruits and vegetables by thermal processing," *J. Futur. Foods*, vol. 3, no. 3, pp. 252–262, 2023, doi: 10.1016/j.jfutfo.2023.02.009.
[14] R. M. Cortez-García, A. Ortiz-Moreno, L. G. Zepeda-Vallejo, and H. Necoechea-Mondragón, "Effects of Cooking Methods on Phenolic Compounds in Xoconostle (Opuntia joconostle)," *Plant Foods Hum. Nutr.*, vol. 70, no. 1, pp. 85–90, 2015, doi: 10.1007/s11130-014-0465-2.
[15] M. Chakraborty and A. Mitra, "The antioxidant and antimicrobial properties of the methanolic extract from Cocos nucifera mesocarp," *Food Chem.*, vol. 107, no. 3, pp. 994–999, 2008, doi: 10.1016/j.foodchem.2007.08.083.
[16] C. Kirszberg, D. Esquenazi, C. S. Alviano, and V. M. Rumjanek, "The Effect of a Catechin-rich Extract of Cocos nucifera on Lymphocytes Proliferation," *Phyther. Res.*, vol. 17, no. 9, pp. 1054–1058, 2003, doi: 10.1002/ptr.1297.
[17] L. Zhang *et al.*, "Effects of four drying methods on the quality, antioxidant activity and anthocyanin components of blueberry pomace," *Food Prod. Process. Nutr.*, vol. 5, no. 1, 2023, doi: 10.1186/s43014-023-00150-3.
[18] V. D. Soproni *et al.*, "Phenolic Content, Antioxidant Capacity, and Browning Impact of Apple Slices during Microwave Drying: A Chemometric Approach," *Processes*, vol. 11, no. 6, p. 1601, 2023, doi: 10.3390/pr11061601.
[19] N. Miletić, O. Mitrović, B. Popović, V. Nedović, B. Zlatković, and M. Kandić, "Polyphenolic Content and Antioxidant Capacity in Fruits of Plum (Prunus domesticaL.) Cultivars 'Valjevka' and 'Mildora' as Influenced by Air Drying," *J. Food Qual.*, vol. 36, no. 4, pp. 229–237, 2013, doi: 10.1111/jfq.12035.
[20] C. Castro-López *et al.*, "Impact of extraction techniques on antioxidant capacities and phytochemical composition of polyphenol-rich extracts," *Food Chem.*, vol. 237, pp. 1139–1148, 2017, doi: 10.1016/j.foodchem.2017.06.032.
[21] J. Tian *et al.*, "Domestic cooking methods affect the phytochemical composition and antioxidant activity of purple-fleshed potatoes," *Food Chem.*, vol. 197, pp. 1264–1270, 2016, doi: 10.1016/j.foodchem.2015.11.049.
[22] Z. Wang *et al.*, "Comparison of different drying technologies for brocade orange (Citrus sinensis) peels: Changes in color, phytochemical profile, volatile, and biological availability and activity of bioactive compounds," *Food Chem.*, vol. 425, p. 136539, 2023, doi: 10.1016/j.foodchem.2023.136539.

Potential Applications of Microwave Drilling in Surgery Based on Frequency-Adaptive Solid-State Sources

T. Zheng[1], Q. Yang[1], Z. Liu[1], J. Liu[1], B. Zeng[1]

[1]*University of Electronic Science and Technology of China, Chengdu, China*
bqzeng@uestc.edu.cn

Keywords: microwave drill, medical surgery, solid-state sources, frequency adaptive

Since the first application of microwaves to drilling by E. Jerby [1] and others, it has received wide attention due to its advantages such as no noise, no dust debris, and no need for vibration, and the local heat-affected area of the microwave drill is smaller than the wavelength of electromagnetic waves, which makes it suitable for more minute and delicate operations such as silicon heating and doping, surgery, biological tissue ablation, and other fields [2].

With the development of semiconductor technology, the feed source of the microwave drill has also been converted from a magnetron to a solid-state source, which makes the whole experimental setup more convenient and efficient to build [3]. However, what has been overlooked is that as the drilling process advances, changes in the tip of the drill and the internal morphology of the workpiece can lead to an impedance mismatch, and the increase in dielectric loss or decrease in conductivity of the workpiece material as the temperature rises can also have an impact on the microwave reflection. Based on solving the above impedance mismatch problem [4], this paper explores the potential application of microwave drilling in surgery.

The realization mechanism of microwave drilling (shown in Fig. 1 (a)) is the strong electric field generated around the tip of the drill, i.e., the highest energy deposition rate, through direct contact with non-conductive materials such as glass, bioceramics, concrete, etc. to transfer microwave energy to the workpiece, so that it absorbs microwaves to generate heat. Hotter materials are more likely to absorb microwaves, so based on this non-linear positive feedback local hot spots are generated so that the workpiece softens or even melts, and eventually the drill enters into the hot spot.

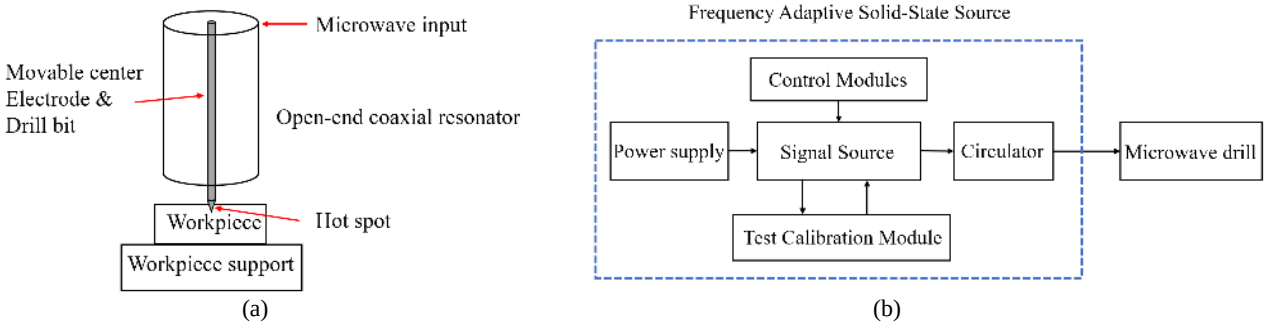

Fig. 1. (a) Schematic diagram of the microwave drill. (b) Structure diagram of the experimental setup.

The micro-zone heating processing device constructed in this paper contains an open-ended coaxial antenna model with uniform loss, and the energy feed efficiency, cavity size and center electrode geometry are optimized in COMSOL Multiphysics v5.5 where the electromagnetic thermal phenomena of the microwave drilling process are simulated. Fig. 2 shows the numerical simulation results of the open-ended coaxial antenna resonator (30 mm long and 1.2 and 14 mm inner and outer diameters, respectively) by 30 W microwave power at 2.45 GHz. The load is 6 mm(Φ) × 0.55 mm soda lime glass, and the maximum electric field at the tip of the drill can reach ~10^6 V/m. The simulation uses the perfectly matched layer (PML) to absorb the scattered waves and imposes perfect electric conductor (PEC) boundary conditions on the metal.

In order to explore the potential application of microwave drilling in surgery, we perform preliminary simulation of electromagnetic radiation. The simulation was performed using the human head geometry provided by HFSS software and the previously designed coaxial cavity, the model and Poynting vector distribution (the square faces distributed vertically at 0.5 mm intervals) are shown in Fig. 3. Simulation results show that the Poynting vector near the local hot spot is the largest (~10^9 W/m^2) and decays rapidly to a range (<50 W/m^2) after 6 mm longitudinal depth. This steep decline in electromagnetic radiation reveals that the electromagnetic shock and temperature radiation range will be small. On the other hand, for the user, it is impossible for it to be hand-held, at least 50 mm radially and 20 mm axially from the drill.

In terms of experiments, considering the possible resonant frequency point shift phenomenon during the drilling process, a frequency adaptive solid-state microwave source is introduced, and the schematic diagram is shown in Fig. 1(b). Among them, the control module includes the control of time and power, and the test calibration module completes the monitoring and feedback of the voltage-frequency change curve in the signal source. In addition, the applicable range of solid-state source frequency is 2-3GHz, which meets the experimental requirements.

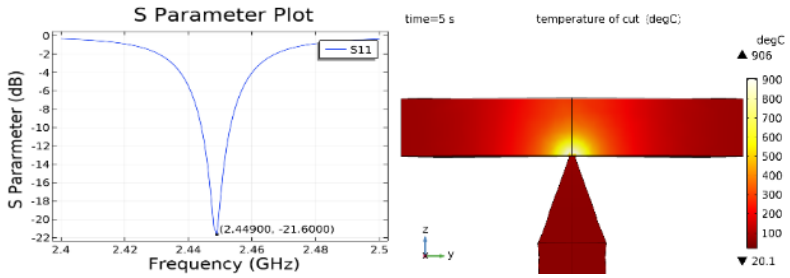

(a) (b)

Fig. 2. Numerical simulation results of open-end coaxial antenna resonator by 30 W microwave power at 2.45 GHz. (a) S_{11} Parameter. (b) Distribution of temperature at 5s.

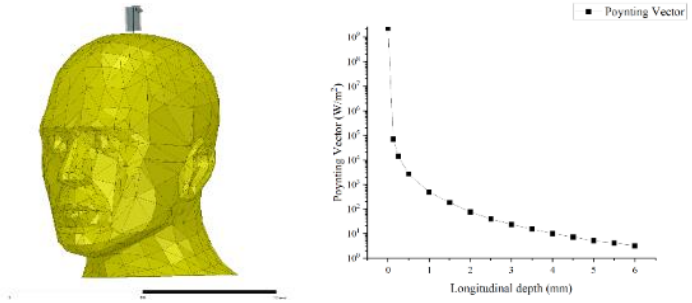

Fig. 3. The diagram of the Poynting vector distribution at different positions.

We first conducted experiments on edible animal bones to demonstrate its effectiveness. Fig. 4(a) shows the results of drilling the duck head using different powers and times, which caused different degrees of carbonization. In clockwise order from the top left are 100 W 5s, 100 W 2s, 100 W 1s, 50 W 3s, 50 W 1s and 30 W 1s. Fig. 4(b) shows an array of a 5 cm × 7 cm leg bone piece drilled every 3s using a frequency-adaptive solid-source. The experimental procedure is efficient and convenient, and the results are more stable and controllable.

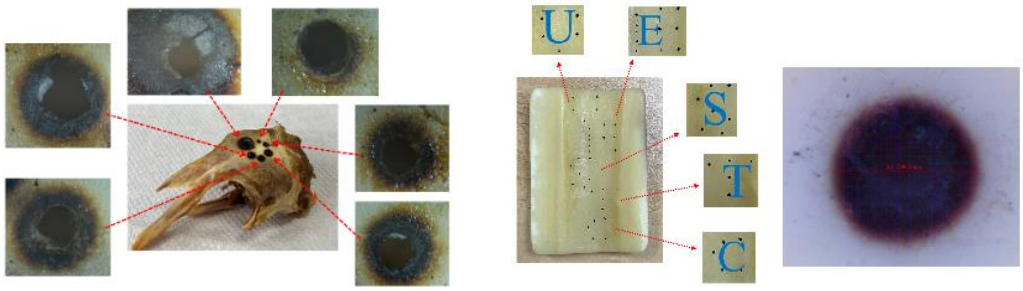

(a) (b)

Fig. 4. (a) Microwave drilling based on duck head. (b) Array drilling of the leg bone and its detailed view.

Theoretically, microwave drills are capable of drilling diameters from 0.5 mm to 10 mm. With the help of frequency-adapted solid-sources, we can perform fine drilling operations with a minimum diameter of 0.6 mm. In addition, between the skull and the brain is the meninges, which consists of three layers of tissue that cover and protect the brain and spinal cord [5]. This small gap between the skull and brain tissue, as well as radiation simulations and temperature estimates of human head tissues, suggest that microwave drill has great potential for surgery. However, this still requires extensive simulations and experimental exploration, such as the possible hazardous impacts of thermal effects caused by the microwave drill and other experimental issues that have not been predicted yet.

Acknowledgment

This work was partially supported by the National Nature Science Foundation of China (No. 61921002, 9216304).

References

[1] E. Jerby, V. Dikhtyar, O. Aktushev, and U. Grosglick, “The microwave drill,” Science, vol. 298, pp. 587–589, 2002.
[2] Y. Eshet, R. R. Mann, A. Anaton, T. Yacoby, A. Gefen and E. Jerby, "Microwave drilling of bones," in IEEE Transactions on Biomedical Engineering, vol. 53, no. 6, pp. 1174-1182, June 2006, DOI: 10.1109/TBME.2006.873562.
[3] Meir and E. Jerby, "Localized Rapid Heating by Low-Power Solid-State Microwave Drill," in IEEE Transactions on Microwave Theory and Techniques, vol. 60, no. 8, pp. 2665-2672, Aug. 2012, DOI: 10.1109/TMTT.2012.2198233.
[4] Y. Shoshani, T. Levin and E. Jerby, "Concrete Cutting by a Solid-State, Localized Microwave-Heating Applicator," in IEEE Transactions on Microwave Theory and Techniques, vol. 69, no. 9, pp. 4237-4245, Sept. 2021, DOI: 10.1109/TMTT.2021.3081098.
[5] A Neurosurgeon’s Overview the Brain’s Anatomy. https://www.aans.org/en/Patients/Neurosurgical-Conditions-and-Treatments/Anatomy-of-the-Brain

The Far-Infrared Microwave and Radio Wave Rays of the Sun Induce Plant Growth

S. Yanagida[1], T. Matsumura[2]

[1]*Osaka University, ISIR, Ibaraki, Osaka, Japan*
[2]*Minerva Light Laboratory, Kyoto, Japan*
yanangida@mls.eng.osaka-u.ac.jp

Keywords: molecular modeloing, triplet oxygen ($^3O_2$), singlet oxygen ($^1O_2$), thermal effect of microwave energy, dielectric loss, magnetic loss, van der Waals force aggregation, mitochondria

The Sun's far-infrared (FIR) radiation includes energy with wavelengths in the region of 500~0 $cm^{-1,}$ i.e., frequency region of 10 THz, GHz and radio waves. We considered that FIR energy from sunlight is essential for the growth of plants as shown by recent literature [1]. In other words, FIR is closely related to the activation of mitochondria, the engine of plant cells. The role of mitochondria is to generate superoxide anion radicals (O_2^{-*}) for the production of chemical energy from oxygen. The contribution of solar FIR to plant growth is predicted due to the magnetic loss of triplet oxygen ($^3O_2$) to singlet oxygen ($^1O_2$). The singlet oxygen ($^1O_2$) has higher oxidation power than triplet oxygen ($^3O_2$), leading to quick formation of superoxide anion radicals (O_2^{-*}) and growth of plants.

As we reported [2][3], molecular modeling based on density functional theory (DFT/MM) verifies the theory that the IR and FIR spectra of equilibrium geometries of molecular van der Waal force aggregates. Equilibrium structures of triplet oxygen ($^3O_2$) agglomerates which contain water (H_2O) molecules, and their theoretical IR/FIR spectra are verified by DFT/MM. Formation of highly active singlet oxygen ($^1O_2$) is verified by analyzing absorption peaks and the intensity of the DFT/MM-based IR/FIR spectra of both $^3O_2$ and $^1O_2$.

We predict that oxygen molecules form van der Waals aggregates in mitochondria in plant cells [4]. We assume the formation of trimer van der Waals aggregates of triplet oxygen $(^3O_2)_3$, and van der Waals aggregates, $[(^3O_2)_2H_2O)]$ and $[(^3O_2(H_2O)_2]$ as hydrated triplet oxygens. Their equilibrium conformations (EQG) were determined by DFT/MM using *Spartan* (B3LYP, 6-31G*) software. The EQG structures are shown with spin density, confirming that they are produced exothermically. When compared with their theoretical IR/FIR spectra (Figs. 1, 2 and 3), the hydrated $[(^3O_2)_2H_2O)]$ and $[(^3O_2(H_2O)_2]$ structures undergo significant absorptions in the 500-0 cm^{-1} wavelength region. The absorptions are verified by the intermolecular motion of $^3O_2$ and H_2O molecules [5]. It is interesting to note that at a glance, □max of absorption in 500-0 cm^{-1} region, and the absorption and dissipation in 4000-500 cm^{-1} region can be seen. Then, the thermo-upconversion mechanism-based thermal effect is understandable especially for $[^3O_2(H_2O)_2]$. Strictly speaking, however, the absorption intensity in the 4000-500 cm^{-1} region does not balance well with absorption intensity in the 500-0 cm^{-1} region.

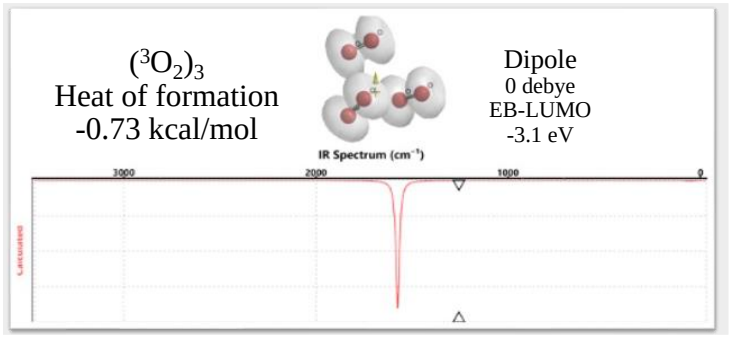

Fig. 1. Theoretical IR/FIR spectra obtained for equilibrium geometry of triplet oxygen trimer $(^3O_2)_3$

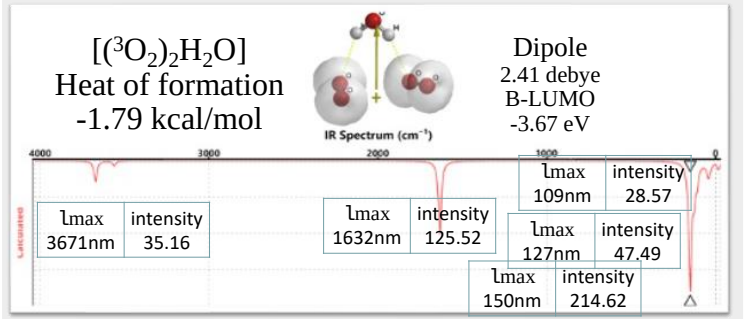

Fig. 2. Theoretical IR/FIR spectra obtained for equilibrium geometry of hydrated triplet oxygen dimer $[(^3O_2)_2H_2O]$

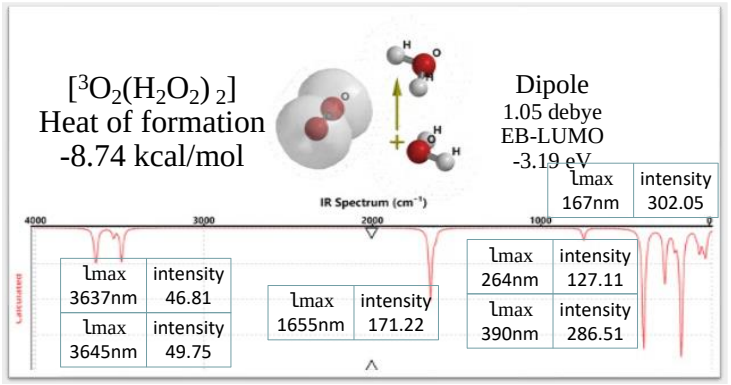

Fig. 3. Theoretical IR/FIR spectra obtained for equilibrium geometry of di-hydrated triplet oxygen $[^3O_2(H_2O_2)_2]$

We now come to consider that this will aid in the prediction and verification of not only up-conversion of the 500-0 cm^{-1} energy, but also the magnetic loss of $^3O_2$ to $^1O_2$.

This prediction of FIR magnetic loss for $[(^3O_2)_2H_2O]$ is verified by comparing its IR/FIR spectrum with the IR/FIR spectrum of dihydrated singlet oxygen aggregate, $[^1O_2(H_2O)_2]$.

Fig. 4 shows the theoretical IR/FIR spectrum for EQG of the dihydrate $^1O_2$ van der Waals aggregate of $[^1O_2(H_2O)_2]$ with its heat of formation, its dipole, and its ELUMO as an oxidation poteintial measurement. The heat of formation indicates the higher probability of formation than that of $[^3O_2(H_2O)_2]$. Interestingly, the ELUMO, -4.16 eV is much lower than the EBLUMO of $[(^3O_2(H_2O)_2]$, -3.16 eV. This verifies a significant increase in oxidizing power of oxygen in mitochondria under the 500-0 cm^{-1} wavelngth energy irradiation. We now understand that FIR irradiation of mitochondria converts the triplet oxygen aggregates $[(^3O_2(H_2O)_2]$ to the singlet oxygen aggregate $[^1O_2(H_2O)_2]$.

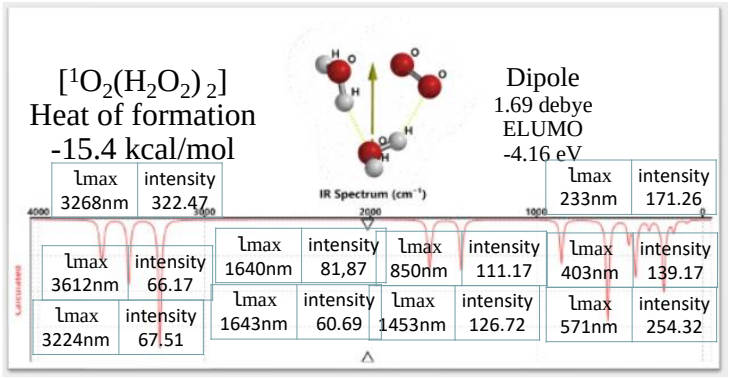

Fig. 4. Theoretical IR/FIR spectra obtained for equilibrium geometry of di-hydrated single oxygen $[^1O_2(H_2O_2)_2]$

Furthermore, The IR/FIR spectrum shows that the absorption intensity in the 4000-500 cm^{-1} region balances well with absorption intensity in the 500-0 cm^{-1} region. Thermo-upconversion of FIR-irradiated $[^1O_2(H_2O)_2]$ and subsequent thermal effects thermally drive the production of O_2^{-*} in mitochondria, leading to plant growth.

Sunlight FIR promotes plant growth by inducing hydrated triplet oxygen $[(^3O_2(H_2O)_2]$ in mitochondria to hydrated singlet oxygen $[^1O_2(H_2O)_2]$ with excellent oxidizing power. That is, mitochondrial production of energetic substances, superoxide anion radicals $[O_2^{-*}(H_2O)]$, is accelerated. The budding of trees in early spring makes us realize this.

References

[1] NAOJ Nobeyama Radio Observatory, About Nobeyama. Available from: https://www.nro.nao.ac.jp/en/public/teles.html#rp
[2] S. Yanagida and T. Matsumura, Computational Verification of Heating Mechanisms at Radio and Microwave Frequencies Using Density Functional Theory, AMPERE Newsletter Issue 95, March 12, 2018
[3] S. Yanagida and T. Matsumura, Quantum chemistry molecular modeling for radio-frequency and microwave-frequency thermo-upconversion heating of metal oxides of NiO and Fe_2O_3, Conference: **Ampere** 2019, DOI: 10.4995/AMPERE2019.2019.10234
[4] Shozo Yanagida, Kenji Osabe, Takeharu Nagai and Nobuyuki Murakami, Quantum chemistry molecular modeling for longevity:Importance of antioxidative effects in mitochondria as battery of cells, Integr Mol Med, 2019 doi: 10.15761/IMM.10003803
[5] IMPI home page. Available from: https://impi.org/members-only/

Disruptive Effect of Quorum Sensing on Microbial Cultivation under Microwave Irradiation

R. Baba[1], M. Hirano[1], T. Hitasaka[1], A. Watanabe[1], S. Ohuchi[2]

[1]Graduate School of Computer Science and Systems Engineering, Kyushu Institute of Technology, 680-4 Kawazu, Iizuka, Japan
[2]Department of Bioscience and Bioinformatics, Kyushu Institute of Technology, 680-4 Kawazu, Iizuka, Japan
ohuchi@bio.kyutech.ac.jp

Keywords: Escherichia coli, microbial cultivation, quorum sensing system

We have clarified that microwave heating promotes the growth of bacteria such as Escherichia coli and Bacillus subtilis. The growth curve of microorganisms reaches the stationary phase through the logarithmic phase, and it was found that the number of bacteria in the stationary phase increased by about 1.5 times under microwave irradiation. At first, we understood this phenomenon to be a reaction promotion effect by microwave heating. However, a different interpretation is possible when considering the process of microbial growth. In other words, it was thought that it was the influence on the quorum sensing system of microorganisms. Conventionally, it has been understood that the stationary phase in the process of microbial growth is due to the balance between new microbial cells and dead sterilized cells. However, recent studies have demonstrated that the quorum-sensing system functions to control the number of cells, which is the essence of the stationary phase of the growth process. In other words, in the quorum sensing system, microorganisms express a certain amount of signal molecules called autoinducers and communicate between cells. If the number of bacteria increases, the number of autoinducers also increases, so the growth of the bacteria stops and the number of bacteria is kept constant. The reason for this is thought to be that the number of cells is kept from increasing more than necessary in order to adapt to the shortage of nutrients and sudden changes in the environment.

On the other hand, in our study, the quorum sensing system may have been destroyed because the number of bacteria increased in culture under microwave irradiation compared to normal culture. To test this hypothesis, we conducted a study to observe the growth of Escherichia coli in a culture medium containing autoinducer signal molecules involved in the quorum sensing system.

Escherichia coli culture under normal conditions was centrifuged, and assuming that the supernatant contained autoinducers, a new nutrient source was added to the supernatant, and the cells were cultured under microwave irradiation as a medium. As a specific experimental procedure, Escherichia coli was added to lysogeny broth (LB) liquid medium, stirred, and cultured at 37°C. Sampling was performed every 2 hours and turbidity was measured at a wavelength of 600 nm. The culture solution cultured to the stationary phase was centrifuged at 5000 rpm for 5 minutes to separate the cells. The supernatant of the culture solution was removed, transferred to a new sterilized test tube, fresh LB liquid medium and Escherichia coli were added, stirred, and normal culture and a culture under microwave irradiation were performed. Both experiments were performed at the optimum temperature of 37°C for Escherichia coli. For normal culture, we used a water bath, and for culture under microwave irradiation, we used a precisely temperature-controlled microwave irradiation device manufactured in our laboratory. Samples were taken every 2 hours, and the turbidity was measured at a wavelength of 600 nm and compared. Turbidity decreased in both the normal culture and the culture under microwave irradiation because the autoinducer was included, but the decrease was 7% in the normal culture and 3% under the microwave irradiation. As a result, proliferation was confirmed despite the presence of a large amount of autoinducer. Since the molecular structures of peptide analogues of Escherichia coli autoinducers have been clarified, it is necessary to conduct quantitative experiments using those signal molecules in the future. This experiment demonstrates the disruptive effect of quorum sensing on microbial cultures under microwave irradiation.

Modelling and Numerical Techniques

Numerical Simulations on Uniform Microwave Heating using Waveguide-type Zeroth-Order Resonator

B. Takahara[1], T. Mitani[1], N. Shinohara[1]

[1]*Research Institute for Sustainable Humanosphere, Kyoto University, Gokasho, Uji, Kyoto 611-0011 Japan*
baku_takahara@rish.kyoto-u.ac.jp

Keywords: microwave heating, metamaterial, zeroth-order resonator, waveguide

We propose the use of a waveguide-type Zeroth-Order Resonator (ZOR) as a microwave heating apparatus. The use of a waveguide-type ZOR is expected to prevent uneven heating, which is a drawback in microwave heating, and to achieve uniform microwave heating over a wide area.

When waveguides are used for microwave heating apparatus, we can heat with high power because of the reduced risk of power leakage, but uneven heating is caused because of the difference in the intensity of the electric and magnetic fields at the nodes and antinodes of the standing waves [1]. When considering heating only by the electric field, the uniform area, in which the power loss is more than 50% of the peak value, $\lambda/4$ is centered at the antinode of the standing wave, where λ is the guide wavelength.

In order to extend the range of uniform heating, we focused on the zeroth-order resonator [2][3][4], in which the wavelength in the resonator is infinite. In the zeroth-order resonant state, the wave number at the resonant frequency is zero, so the amplitude and phase are the same regardless of the position in the resonator. This characteristic is expected to enable uniform microwave heating over a wide area. We have studied electromagnetic coupled type uniform microwave heating using ZORs mounted on a dielectric substrate [5]. However, heating efficiency was less than 20% due to the large loss in the resonator. Therefore, in this study, we investigate the use of a waveguide-type ZOR that has low loss in the resonator and can handle higher power.

Figure 1 shows the ZOR used in this study. The model shown in Fig.1 consists of eight cascaded unit cells. The standard waveguides (WRI-22) are connected at both ends to excite TE_{10}-mode. The unit cell consists of a square waveguide with metal cylinders arranged alternately. The metal cylinders behave as capacitors and inductors to realize the zeroth-order resonance. The zeroth-order resonant frequency of the designed waveguide is adjusted to 2.45 GHz without a dielectric as a heated object. Figure 2 is the comparison of the electric field distribution between a standard waveguide and the waveguide proposed in this study. It can be seen that the wavelength in the z-direction is extended by the metal cylinders, and the electric fields have the same amplitude and phase in the designed waveguide.

In this study, a dielectric material is placed in the waveguide as a heated object. The dielectric material affects the zeroth-order resonance condition, so the zeroth-order mode does not propagate with parameters designed without the heated object. Therefore, it is necessary to adjust the parameters to satisfy the zeroth-order resonance condition by considering the dielectric material effect. We focused on h, which is the length of the metal cylinder, as the parameter to be adjusted. Table 1 shows h and resonant frequency that satisfies the zeroth-order resonance condition when the thickness of the heated object t and dielectric constant ε_r of the hated object varied. It can be seen that the larger ε_r, and the larger t, which is the principal direction of the electric field, the lower the resonant frequency due to the wavelength-shortening effect.

Finally, in order to achieve faster heating, one of the ports at both ends of the resonator was shorted, and simulations were conducted. Since the phase of the reflected wave changes depending on the length of L_{p2}, we adjusted L_{p2} so that the electric field distribution in the waveguide becomes uniform. Figure 3 shows a comparison of the power loss density distribution divided by the maximum values between the standard waveguide and the waveguide-type ZOR. It can be confirmed that the power loss density distribution of the heated object becomes uniform by using the zeroth-order resonator. This indicates that the waveguide-type ZOR proposed in this study is effective in extending the uniform heating range.

Table 1. Relations between heated objects, h and the zeroth-order resonant frequencies.

Frequency	ε_r	tanδ	Width	t	h
2.43 GHz	12	0.01	10 mm	2 mm	31.1 mm
2.27 GHz	12	0.01	10 mm	10 mm	32.3 mm
1.98 GHz	12	0.01	10 mm	20 mm	33.8 mm
2.43 GHz	24	0.01	10 mm	2 mm	31.1 mm
2.26 GHz	24	0.01	10 mm	10 mm	32.4 mm
1.93 GHz	24	0.01	10 mm	20 mm	34.0 mm

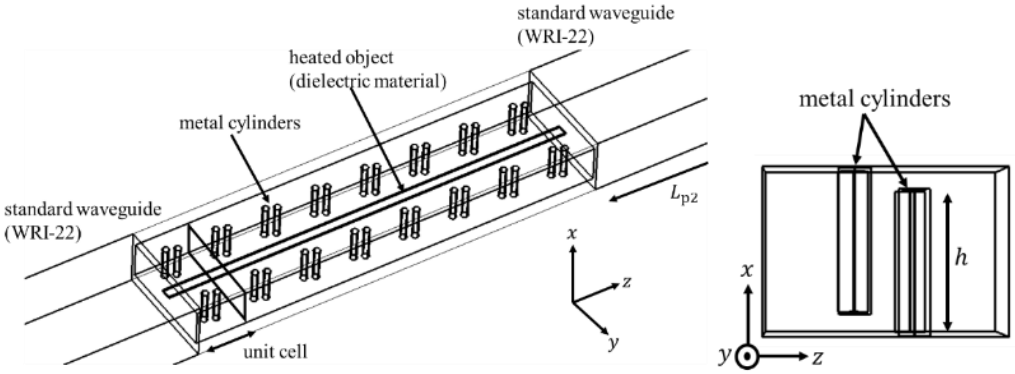

Fig. 1. The model of waveguide-type ZOR.

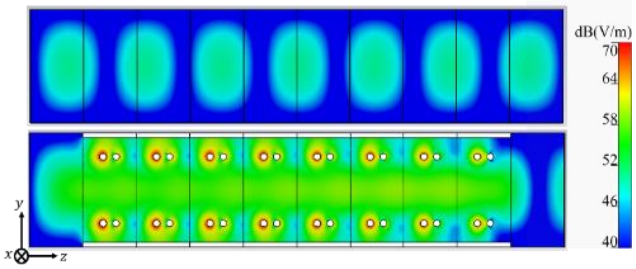

Fig. 2. Comparison of E-field distribution.

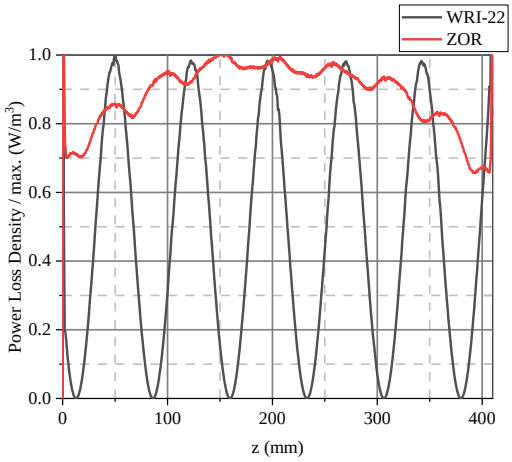

Fig. 3. Comparison of power loss density distribution.

Acknowledgment

This work was supported by JSPS KAKENHI Grant Number JP21K04175.

References

[1] Li, Z. Y., R. F. Wang, and T. J. D. T. Kudra. "Uniformity issue in microwave drying." Drying Technology 29.6 (2011): 652-660.
[2] A. Sanada, C. Christophe, and T. Itoh. "Novel zeroth-order resonance in composite right/left-handed transmission line resonators." Proc. Asia-Pacific Microwave Conf. Vol. 3. 2003.
[3] Shimizu, Kenta, Hiroshi Kubo, and Atsushi Sanada. "Radiation characteristics of waveguide-type zeroth-order resonator." 2010 Asia-Pacific Microwave Conference. IEEE, 2010.
[4] T. Yamamoto, H. Kubo, and S. Sadamasu. "Waveguide-Type CRLH Transmission Line Composed of Metallic Cylinder-Pairs Arranged in Two Lines and Its Radiation Characteristics as a Leaky-Wave Antenna." 2018 Progress in Electromagnetics Research Symposium (PIERS-Toyama). IEEE, 2018.
[5] Takahara, Baku, Tomohiko Mitani, and Naoki Shinohara. "Feasibility Study on Electromagnetic Coupled Type Uniform Microwave Heating Using a Zeroth-Order Resonator." 2022 Asia-Pacific Microwave Conference (APMC). IEEE, 2022.

Multiphysics Modelling of an Intermittent Microwave Pultrusion Process

M. Engler[1], G. Link[1], J. Jelonnek[1]

[1]*Institute for Pulsed Power and Microwave Technology (IHM), Karlsruhe Institute of Technology (KIT), Karlsruhe, Germany*
Moritz.Engler@kit.edu

Keywords: microwave, material processing, carbon fiber, power applications

Pultrusion is one of the most important manufacturing processes for the production of fiber reinforced plastics. In pultrusion the reinforcing fibers are impregnated with a thermoset matrix material and then pulled through a heated forming die. The thermoset cures while moving through the die and solidifies with the cross section imposed by the tool [1]. As this is a continuous process it is suited very well to large scale production and therefore very economical compared to other production processes for fiber reinforced composites [2]. However, the process is limited to the production of profiles with constant cross section which are straight or of constant radius [3]. Microwave assisted pultrusion offers large potential for improvement of the process as the selective heating properties of microwaves can be used to only heat the pultrusion profile in an otherwise cold tool. Turning the microwave on and off during the process allows alternate application to cured and uncured sections. The uncured sections can then be reshaped in a following processing step e.g. by folding them into a more complex space frame structure [4].

In this work a microwave assisted intermittent pultrusion process using carbon fibers as reinforcement is investigated via finite element modelling in COMSOL Multiphysics. The microwave pultrusion tool is designed to keep the heating zone as short as possible which will also lead to sharp transitions between the cured and uncured profile sections. This was achieved by using a coaxial microwave applicator which is shown in Figure 1, where the profile is pulled through the center conductor. The center conductor is then interrupted by a ceramic window and the conducting carbon fibers will act as the center conductor from this point on. Due to the low conductivity of carbon fibers they will be effectively heated as soon as they exit the previous tool section. The ceramic window is kept short to minimize the heat loss of the pultrusion profile to the tool. The last section of the tool consists of a microwave filter to prevent leakage of radiation. The microwave is fed using a T intersection and three tuning stubs are included between the T and the window to achieve optimal heating of the profile. The profile is an elliptical cross section with a minor axis of 1.8 mm and a major axis of 5.8 mm.

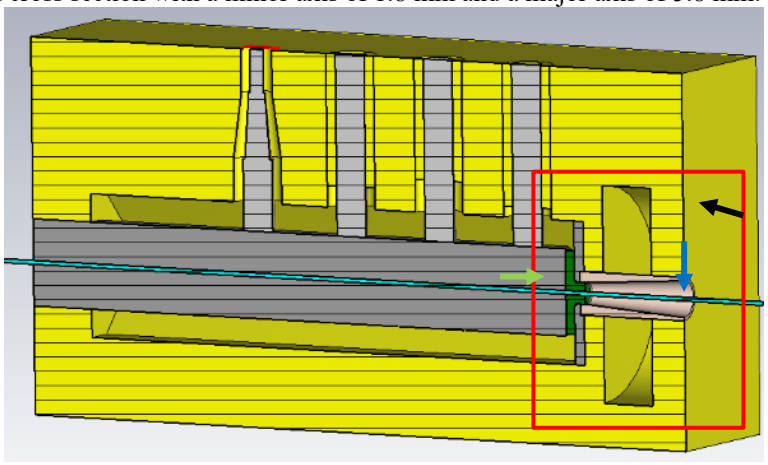

Fig. 1. 3D Model of the coaxial microwave applicator. The red box shows the parts of the tool which are used for the Multiphysics simulation. The arrows mark the points which are used for temperature measurements.

To simulate the curing of the resin, the profile needs to be modeled with a moving mesh, however the moving mesh in COMSOL is not supported by the electromagnetic wave solver. The simulation must therefore be split into two steps. First the electromagnetic model is solved by itself. The resulting power loss distribution can then be used as a heat source for the thermal model. This approach is valid, as the microwave behavior of the profile is dominated by the carbon fibers which do not change during the curing. The contribution of the resin can be neglected. To keep the solving duration of the thermal model within a reasonable time frame the model needs to be built as efficiently as possible. As the interaction of the microwave with the profile occurs only after the profile leaves the center conductor, only the tool area marked in red in Figure 1 needs to be considered for the simulation. While the exclusion of the matching elements and the T intersection might change the simulated efficiency the general interactions of the process will not be affected. Another measure to reduce the model size is to exploit the two axes of symmetry of the model reducing the model to a quarter of its original size. For the thermal model symmetry boundary conditions need to be applied to the cut surfaces, whereas the electromagnetic model

requires the use of perfect magnetic conducting boundaries to allow the existence of the coaxial mode. The biggest contribution for increasing the simulation performance is by reducing the length of the profile as much as possible. Due to the small size of the profile cross section compared with the tool the mesh resolution of the profile needs to be very fine. The length of the profile is determined by the pultrusion speed and the process duration. To achieve results close to the steady state, several on-off cycles of microwave power should be included in this duration. Instead of simulating this duration entirely it is beneficial to only simulate a single on-off cycle. After this cycle the profile can be moved back to its original position and the temperature distribution of the last timestep can be used as the initial values for the next simulation cycle. This way the length of the simulated profile is kept as short as possible.

With this model the influence of several process parameters such as microwave power, pultrusion speed or tool temperature on the curing of the profiles and especially on the transitions between cured and uncured profile segments has been investigated. For the simulations a microwave power of 50 W and a pultrusion speed of 16 cm/min was used. The profile was modeled with an effective conductivity of 40 kS/m and the reaction kinetics of the fast-curing polyurethane resin system described in [5].

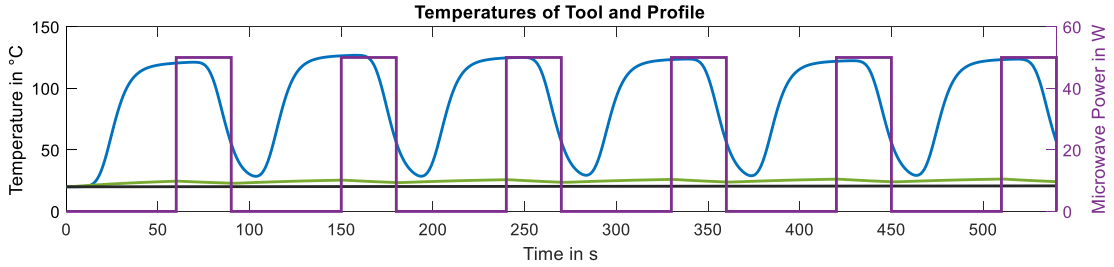

Fig. 2. Simulated temperatures at the profile surface directly after exiting the tool (blue), at the ceramic window(green) and on the tools outside wall (black, according to the arrows in Figure 1 and microwave power at the port (purple)

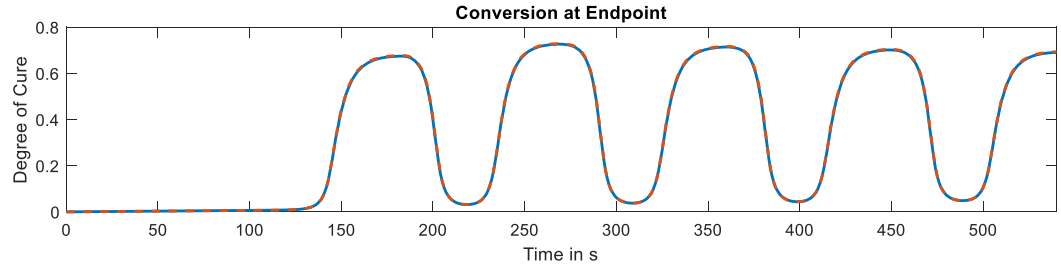

Fig. 3. Achieved degree of conversion after reaction has stopped at the center of the profile (blue, solid) and at the surface (red, dashed).

Figures 2 and 3 show the temperature and conversion at specific points over the course of six on-off cycles with 60 s on time and 30 s off time. It can be seen that the short contact region in the ceramic window serves its purpose and does not take too much heat out of the profile, as the second on cycle already achieves the maximum temperature and conversion. From Figure 3 the average transition lengths can be found. The average transition lengths from 20 % to 60 % degree of cure are 3 cm when turning the power on and 2.1 cm for turning the power off. This is a result of the profile transferring some of its thermal energy to the tool. Overall, this energy loss is still small as the ceramic disk only shows minimal heating and the outside wall of the tool does not show any temperature change. The homogeneity of the microwave heating is also sufficient, as no difference in cure can be observed between the profile center and profile surface in Figure 3.

Acknowledgement

The authors acknowledge the financial support by the Federal Ministry for Economic Affairs and Energy of Germany in the project IMPULS (ZF4204604).

References

[1] H. C. Gray, “Method of and apparatus for continuously forming shapes of resin impregnated fabric,” U.S. Patent 2 526 945, Oct. 24, 1950
[2] M. B. Renato, “Modelling and Simulation of the Closed Injection Pultrusion Process,” PhD thesis, Karlsruher Institut für Technologie, Karlsruhe, Germany, Oct. 2017
[3] G. Struzziero, G.M. Maistros, J. Hartley and A.A. Skordos, “Materials modelling and process simulation of the pultrusion of curved parts,” *Composites Part A: Applied Science and Manufacturing*, vol. 144, May 2021
[4] J. M. Methven, S.R. Ghaffariyan and A.Z. Abidin, “Manufacture of Fiber-Reinforced Composites by Microwave Assisted Pultrusion,” *Polymer Composites*, vol. 21, pp. 493 – 644, Aug 2000
[5] R. B. Prime, C. Michalski and C.M. Neag, “Kinetic analysis of a fast reacting thermoset system,” *Thermochimica Acta*, vol. 429, pp. 213 – 217, May 2005

A Slotted Waveguide Antenna for High Temperature Homogeneous Heating Systems

M. Juttu[1], R. Behrend[1], H. Krause[1]

[1]*TU Bergakademie Freiberg, Institute of Thermal Engineering, Gustav-Zeuner-Straße 7, 09599 Freiberg, Germany*
Muralimohan.Juttu-Vidyasagar@iwtt.tu-freiberg.de

Keywords: microwave, antenna, high-power, slotted waveguides, uniform heating

Introduction

A slotted waveguide antenna radiates energy through the slots present on the surface of the waveguide [1]. It offers the possibility to distribute large amounts of input microwave power through its slots, which are spread along the length of the waveguide. Due to its small volume and low weight, a slotted waveguide antenna is often used in radar and telecommunication applications. Industrial heating applications requiring homogenized temperature conditions during the heating process can also use the slotted waveguide antenna. By optimizing the position and size of slots, it is possible to generate a nearly homogenized electric field distribution above the surface of the waveguides.

Stevenson [2] and Elliot [3] have provided design procedures for positioning and sizing longitudinal slots. In their design rules, the length of rectangular slots should be around half the free space wavelength. The terminating slot is located at a distance of quarter-guide wavelength from the waveguide shorting wall. The inter-slot distance is equal to the half-guide wavelength.

Rueggeberg has proposed a method through which each slot pair distributes nearly equal amounts of power over the distribution of slots [4]. According to his design, the inter-slot distance equals the three-quarter-guide wavelength. The terminating slot is located at a distance of 60.2 mm from the waveguide shorting wall. The rounded longitudinal slots are 65.1 mm long and 6 mm wide.

The guide wavelength λ_g is the distance between two equal-phase planes along the waveguide. It is calculated by the following equation.

$$\lambda_g = \frac{\lambda_f}{\sqrt{1-\frac{\lambda_f}{\lambda_{cutoff}}}} = \frac{c}{f} \times \frac{1}{\sqrt{1-\left(\frac{c}{2a\,.f}\right)}} \quad (1)$$

where λ_f is the free-space wavelength, f is the operating frequency, c is the speed of light, a is the size of the waveguide's broader face, and λ_{cutoff} is the cutoff wavelength.

This paper concentrates on developing a slotted waveguide antenna to heat a thin polymer tape along its width uniformly. The heating of the polymer tape is a continuously operated process. The objective is to find an optimum set of waveguide parameters that can offer a homogenized electric field distribution throughout the covering length of the slots. The design procedures of Stevenson, Elliot, and Rueggeberg were considered during this process. Several geometric configurations have been simulated using the RF Module of the commercial software suite COMSOL. The influence of parameters such as the number of slots, inter-slot distance, terminal slot distance, slot length, slot displacement, and waveguide length was studied during the simulation. A representative longitudinal slotted waveguide has been designed, manufactured, and integrated with a test setup for experimental validation. Experimental data show good resemblances with the simulated ones.

Physical Model and Dimensions

The longitudinal slotted waveguide antenna illustrated in Figure 1 is adopted as the physical model. A WR340 S-band waveguide with the size of the broader face a= 86.36 mm and the size of the narrower face b= 43.18 mm is considered for the simulation. The guide space wavelength for such dimensions operating at a 2.45 GHz frequency is 173.38 mm. The free space wavelength is 122.36 mm. Rounded slots are considered over the sharp-cornered rectangular slots to prevent electrical breakdown problems. Uniform slot displacement is considered for this model.

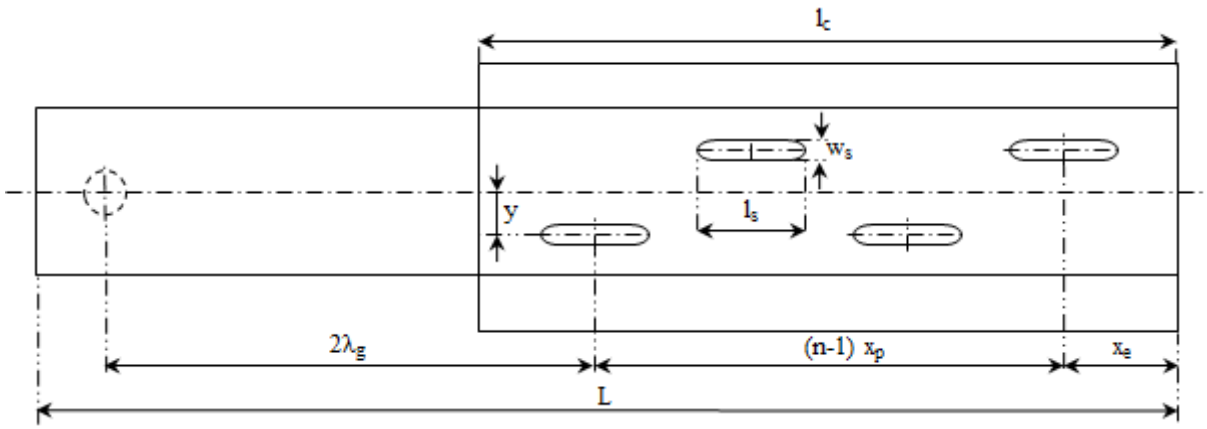

Fig. 1. A WR340 S-band longitudinal rounded slotted waveguide antenna, enclosed in a microwave chamber.

The input microwave power is fed into the bottom of the waveguide through a coaxial cable. The inner wire of the cable, made of copper, continues to run into the waveguide and introduces microwaves into the waveguide. The cable's center is 25 mm from the front wall of the waveguide. The first slot is located at a distance of twice the guide space wavelength. The width of the slot is fixed at 6 mm [4]. By varying parameters such as inter-slot distance (xp), number of slots (n), terminating slot distance (xe), slot length (ls), and slot displacement (y), several configurations are modeled in the Solidworks program. The polymer tape, which has to be heated uniformly along its width, enters the microwave chamber, as shown in Figure 2, at 50 mm from the outer surface of the waveguide. From now onwards, this is known as the reference plane.

Governing Equation

The RF module frequency domain interface in the commercial software suite COMSOL has been chosen to solve the electromagnetic wave propagation through the slotted waveguide antenna. The frequency domain solves numerically Maxwell's equation to obtain the electromagnetic field distribution at the desired reference plane. The following equation is solved for the electric field vector E inside the waveguide:

$$\nabla \times (\mu_r^{-1} \nabla \times \mathrm{E}) - k_0^2 \left(\varepsilon_r - \frac{\mathrm{j}\sigma}{\omega \varepsilon_0}\right) \mathrm{E} = 0 \qquad (2)$$

where μ_r denotes the relative permeability tensor, ω is the angular frequency, σ is the conductivity tensor, ε_0 is the relative permittivity of vacuum, ε_r is the relative permittivity tensor, and k_0 is the free space wave number.

Initial and Boundary condition

Initial conditions: There is no external electric field applied to the model. The air domain inside the waveguide is maintained at a pressure of 0.1 atm (abs) and a temperature of 293.15 K.

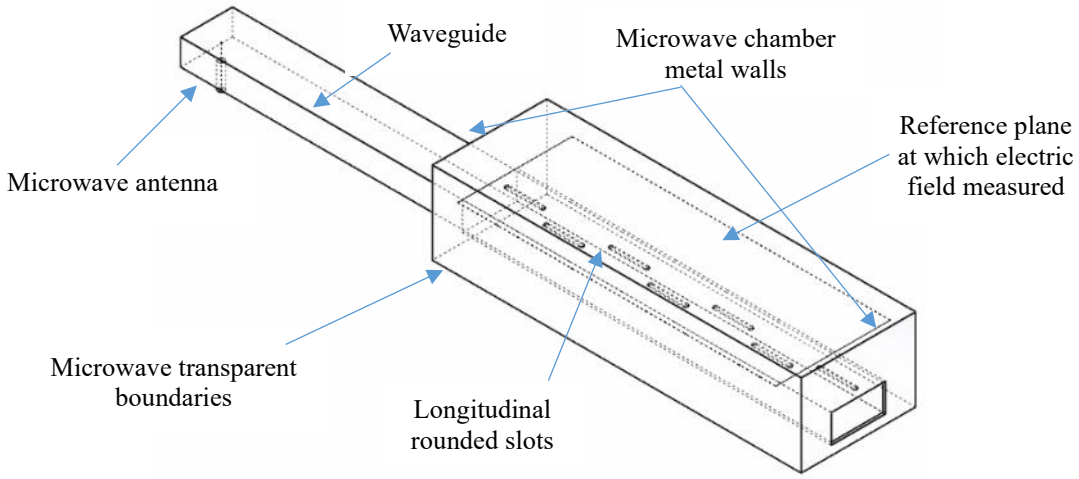

Fig. 2. Model of the slotted waveguide antenna

Boundary conditions

The input microwave power is fed through the coaxial cable and is set up using a Port boundary condition, with a 100 W power. Wave excitation is switched on at this port. An impedance boundary condition is set for the metal surfaces of the waveguide, made of aluminum, and for the inner wire of the coaxial cable, made of copper. The slotted zone of the waveguide antenna is enclosed in a microwave chamber enclosure, where the longitudinal metal walls are chosen as the perfect electric

conductor boundary condition. The other walls of the microwave chamber are considered microwave transparent walls. Scattering boundary conditions are set to these walls.

Mesh and Numerical Parameters

The physics-controlled mesh option has been chosen for the mesh generation. The linear solver solves the governing equation automatically for a frequency of 2.45 GHz. The electric field's convergence criterion is 1x10 -4.

Results and Discussion

The following section compares the simulation results by varying the waveguide parameters such as inter-slot distance (xp), terminal slot distance (xe), slot length (ls), and displacement (y). Figure 3 shows the electric field distribution (2D) at the reference plane above the outer surface of the waveguide for one such set of waveguide parameters.

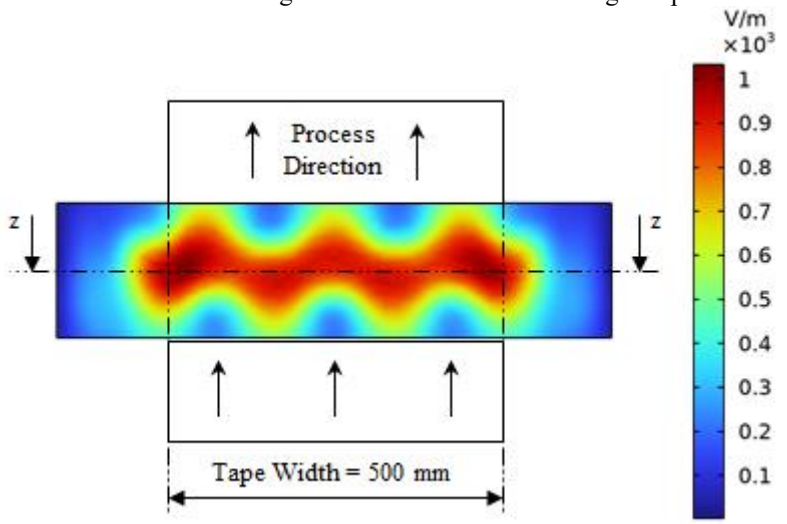

Fig. 3. Electric field distribution at the reference plane for waveguide parameter xp=86.7 mm, n=7, y=10.8 mm, lc=780.1 mm, ls=65 mm and L=1021.9 mm (Case 6)

Converting 2D to 1D solution

Considering the continuous mode of the application, the tape enters the microwave chamber, is heated uniformly along its width, and exits the chamber. Also, the electric field strength reaches a maximum value at the line z-z on the reference plane, which is directly above the center line of the waveguide. Considering both points, comparing the electric field distribution (1D) at the line z-z for different waveguide parameters is easy and simplifies the problem. Figure 6 contains the 1D electric field distribution of the waveguide parameter set (Case 6) discussed in Figure 3.

Selection Criteria

The coefficient of variation (COV) is a statistical measure of the relative dispersion of data points in a data series around the mean. It is represented as the ratio of the standard deviation to the mean, usually expressed in percentages. Here, COV is the ratio of the standard deviation of the electric field distribution at the line z-z to the mean electric field. Lower COV means that the electric field is homogenously distributed throughout the width of the tape.

$$COV = \frac{Standard\ Deviation}{Mean} * 100\ \%$$

The S11 Parameter is the input reflection coefficient with the network output terminated by a matched load. It is usually expressed in decibels (dB). If S11 = 0 dB, all the power is reflected from the antenna, and nothing is radiated. In the simulation, the S11 parameter is evaluated for each set of waveguide parameters.

Waveguide Parameters

Inter-slot distance (xp) is the distance between two consecutive longitudinal slots. The optimum inter-slot distance to generate a homogenous electric field distribution throughout the width of the sample was found by carrying out simulations at values 43.4 mm (quarter-guide wavelength), 86.7 mm (half-guide wavelength), and 130 mm (three-quarter-guide wavelength). The other waveguide parameters were kept fixed during these simulations and are mentioned in Table 1.

Table 1. Comparison based on inter-slot distance.

Case	x_p	n	x_e	y	l_s	l_c	L	E_{mean}	COV	S_{11}
	mm	-	mm	mm	mm	mm	mm	V/m	%	dB
1	86.7	7						921.7	10.9	-5.2
2	43.4	13	43.4	10.8	65	600	935.3	953.4	43.1	-5.3
3	130.0	5						679.3	50.1	-2.8

For xp = 43.4 mm and 130 mm, the electric field distribution, as shown in Figure 4, varied like a sinusoidal wave throughout the width of the sample. The COV was more than 40% for both of these cases. For xp = 86.7 mm, the electric field distribution was comparatively better than in the other cases, with only 10 % COV throughout the tape width and a reasonable S11 parameter equal to -5.2. Based on the above results, xp = 86.7 mm (half-guide wavelength) is chosen as the optimum inter-slot distance.

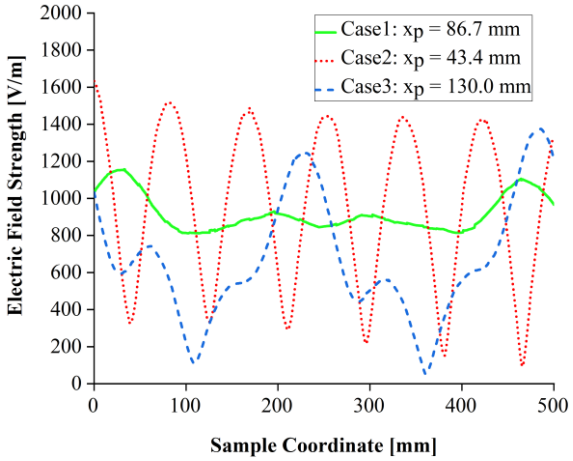

Fig. 4. Electric field distribution at the line z-z on the reference plane for different inter-slot distance (xp) values

Terminating slot distance (xe) is the distance between the last slot's center and the waveguide's wall. Similar to the above condition, simulations were conducted at values 43.4 mm, 86.7 mm, and 130 mm and the results were shown in Figure 5. The other waveguide parameters were kept fixed and are mentioned in Table 2.

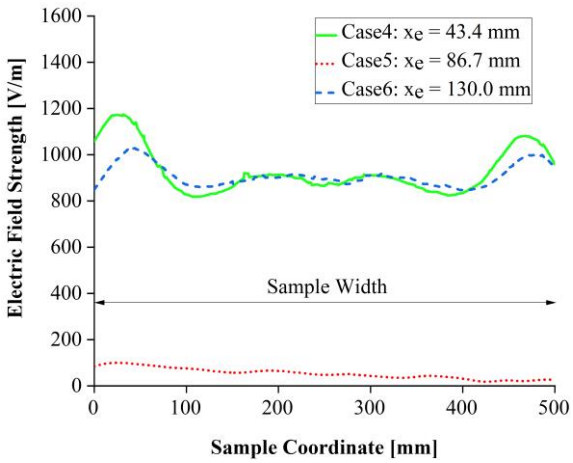

Fig. 5. Electric field distribution at the line z-z on the reference plane for different terminal-slot distance (xe) values

When xe = 86.7 mm, the S11 parameter was evaluated as -0.1 dB. It indicates that almost all the input power was reflected, generating a weak electric field strength throughout the tape width. When xe = 43.4 mm, the electric field strength was reasonably distributed throughout the sample width with a COV of 10.5 %. When xe = 130 mm, nearly a homogeneous electric field distribution was achieved with a COV of 5.3 %. Based on the above results, xe = 130 mm (three-quarter-guide wavelength) is the optimum terminating slot distance.

Table 2. Comparison based on terminating slot distance.

Case	x_p	n	x_e	y	l_s	l_c	L	E_{mean}	COV	S_{11}
	mm	-	mm	mm	mm	mm	mm	V/m	%	dB
4			43.4			600.0	935.3	925.1	10.5	-5.1
5	86.7	7	86.7	14.4	65	693.5	978.6	54.1	41.8	-0.1
6			130.0			780.1	1021.9	911.0	5.3	-5.2

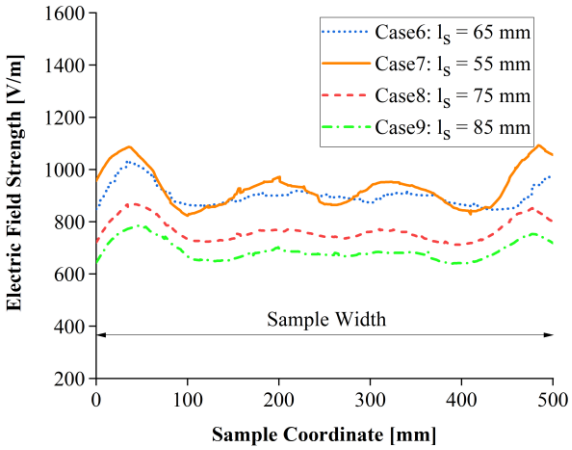

Fig. 6. Electric field distribution at the line z-z on the reference plane for different slot distance (ls) values.

Table 3. Comparison based on length of slot.

Case	x_p	n	x_e	y	l_s	l_c	L	E_{mean}	COV	S_{11}
	mm	-	mm	mm	mm	mm	mm	V/m	%	dB
6					65			911.0	5.3	-5.2
7	86.7	7	130.0	14.4	55	780.1	1021.9	931.7	7.6	-6.2
8					75			771.1	5.7	-3.1
9					85			692.6	5.7	-2.3

In order to find the optimum slot length (ls), simulations were conducted at different slot length values 55, 65, 75, and 85 mm and the results were shown in Figure 6. The other waveguide parameters were kept fixed and are mentioned in Table 3. For ls = 75 and 85 mm, the S11 parameter was evaluated as -3.1 and -2.3 dB, indicating a considerable portion of the input power was reflected, resulting in a lower average electric field strength. For ls = 65 mm, nearly a homogeneous electric field distribution was achieved with a COV of 5.3 %, chosen as the optimum slot length.

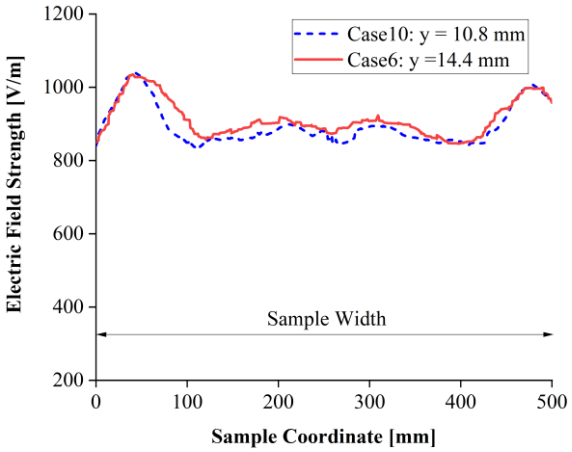

Fig. 7. Electric field distribution at the line z-z on the reference plane for different slot displacement (y) values

Table 4. Comparison based on slot displacement.

Case	x_p	n	x_e	y	l_s	l_c	L	E_{mean}	COV	S_{11}
	mm	-	mm	mm	mm	mm	mm	V/m	%	dB
6	86.7	7	130.0	14.4	65	780.1	1021.9	911.0	5.3	-5.2
10				10.8				893.5	5.9	-5.3

Slot displacement (y) is the distance between a slot's center and the waveguide's centerline. Simulations were conducted at slot displacement (y) values of 10.8 mm and 14.4 mm and the results were shown in Figure 7. For y = 14.4 mm, nearly a homogeneous electric field distribution was achieved with a COV of 5.3 %, chosen as the optimum slot displacement.

Based on the above simulation, it has been evaluated that the optimized waveguide has seven slots, with an inter-slot distance of 86.7 mm (half-guide space). The terminal slot distance is 130.0 mm (three-quarter-guide space), and the slot length is 65 mm. The slot displacement was chosen as 14.4 mm. The total length of the waveguide is 1021.9 mm, with a chamber length of 780.1 mm.

Experimental Verification

As illustrated in Figure 5, a test setup was constructed to validate the distribution of the electromagnetic radiation through the rounded slots. The test setup mainly consists of a waveguide, a test chamber, and a vacuum pump. The waveguide was welded tangentially on the top of the test chamber. A microwave power source was connected to one end of the waveguide and a short circuit slider to the other. The distribution of the electric field inside the chamber was measured by heating water samples. For this purpose, several trays filled with water were located on the longitudinal axis of the chamber.

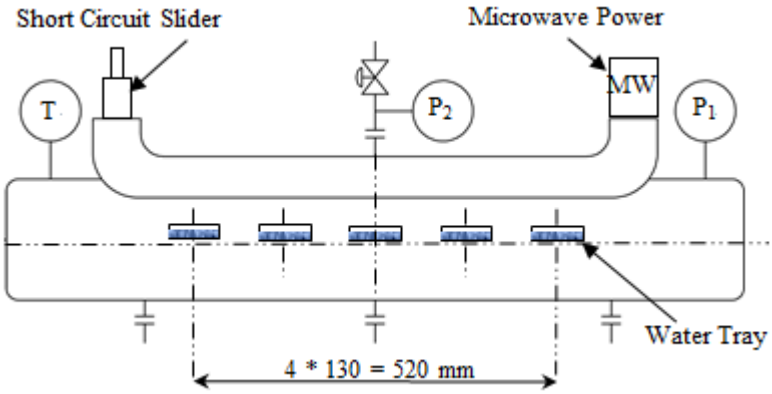

Fig. 8. Schematic of the test setup

A WR340 waveguide with dimensions a=86.36 mm and b=43.18 mm with seven rounded slots positioned on the broader side of the waveguide at 86.7 mm inter-slot distance was used in the setup. The slots are uniformly displaced at a distance of 14.4 mm from the centerline of the waveguide. The slot is 65 mm in length and 6 mm in width. Considering the above dimensions, the slots cover a length of 585 mm in the waveguide. As shown in Figure 5, five water trays were placed in the chamber. The middle water tray is located precisely in the center of the chamber, and the other trays are positioned symmetrically on both sides, at a distance of 130 mm between each other. The water tray has a width of 110 mm , covering a total length of 630 mm . The test chamber has an inner diameter of 150 mm and a length of 985 mm . 200 g of water is added to each tray before starting the experiment.

The experiments were conducted at power levels 500 W, 750 W, 1000 W, and 1200 W. Before starting the experiment, the initial temperature of the water present in each tray was measured. The temperature was measured by dipping a thermocouple into each water tray. The chamber was closed before commencing the experiment. The microwave power was switched on in steps of 2 minutes. After 2 minutes, the power was switched off, the chamber was opened, and the water temperature in each tray was measured. This process is continued for a total active period of 20 minutes (excluding the measurement time).

The measured temperatures of each water tray at various power levels were plotted graphically in Figure 6. The graph illustrates that the water temperatures were almost similar at tray positions 2, 3, and 4. It indicates that the electric field distribution did not vary much in those zones. The water temperatures were lower at tray positions 1 and 5. It indicates that the electric field strength was lower in the corner. It is due to the reason that the slots did not fully cover the trays. Increasing the slot covering distance or decreasing the covering distance of the water trays makes it possible to generate a closer to homogenous electric field strength above the center line of the waveguide.

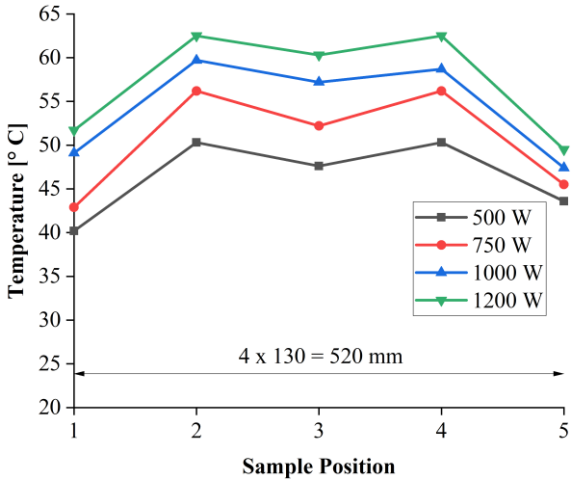

Fig. 9. Temperature distribution of water trays at various power levels

Conclusions

By adopting the design principles of Stevenson, Elliot, and Rueggeberg, this paper has investigated several geometric configurations of a longitudinal, rounded-slotted waveguide antenna using the RF Module of the commercial software suite COMSOL. The influence of waveguide parameters such as the number of slots, inter-slot distance, terminal slot distance, slot length, slot displacement, and waveguide length in generating homogenized electric field distribution was studied during the simulation. An optimum set of waveguide parameters was selected by comparing the electric field strength distribution and S11 parameters for various geometric configurations. The chosen data set was mainly from Stevenson's design principles. As a proof of concept, a representative longitudinal slotted waveguide has been designed, manufactured, and integrated with a test setup, and the results were presented.

Acknowledgement

We sincerely thank Mr. Maximilian Linn for building the test setup and conducting experiments on the same.

References

[1] Gilbert, R. A., Antenna Engineering Handbook, Chapter: Waveguide Slot Antenna Arrays, McGraw-Hill, 2007.
[2] Stevenson, A. F., “Theory of slots in rectangular waveguides,” Journal of Applied Physics, Vol. 19, 24–38, 1948.
[3] Elliott, R. S. and L. A. Kurtz, “The design of small slot arrays,” IEEE Trans. Antennas Propagat., Vol. 26, 214–219, March 1978.
[4] Rueggeberg, W., “A multislotted waveguide antenna for high-powered microwave heating systems” IEEE Trans. Ind. Applicat., Vol. 16, No. 6, 809–813, 1980.

Modelling Microwave Plasmas in NIRIM-Style Tube Reactors for Diamond and Hafnium Carbide Growth

J. A. Cuenca[1], J. Stritt[1], E. L. H. Thomas[1], S. Mandal[1], O. A. Williams[1]

[1]*School of Physics and Astronomy, Cardiff University, Cardiff, CF24 3AA, Wales, UK*
cuencaj@cardiff.ac.uk

Keywords: microwave, plasma, chemical vapour deposition, diamond

Microwave plasma chemical vapour deposition (MPCVD) is a well-established approach for the epitaxial growth of single crystal diamond (SCD) and polycrystalline diamond (PCD). The quartz tube waveguide reactor, pioneered and developed by the National Institute for Research in Inorganic Materials (NIRIM) [1], is a simple MPCVD system that enables diamond growth with relatively low impurities [2]. It is also a potential technology for growing ultra-high temperature ceramics (UHTCs). UHTCs can be defined as non-metallic, inorganic solids with melting points higher than 3000℃, examples including hafnium carbide (HfC) and hafnium carbonitride (HfCN) with melting points at much higher than 4000 K [3]. Deposition of HfC and potentially HfCN can be achieved using radio frequency CVD at low pressures, however, the rate is very slow at several angstroms a minute [4]. MPCVD offers much higher electron density plasmas, potentially enabling faster growth of HfC and HfCN.

In this work, we investigate the potential of using the MPCVD NIRIM reactor for producing HfC and HfCN. We use diamond deposition as a preliminary means of understanding; first modelling using COMSOL Multiphysics® to understand the typical electron densities and initial operating conditions for igniting the microwave plasma [5], and secondly through experimental diamond growth. This study specifically looks at the effect of susceptor/holder height and how this affects deposition.

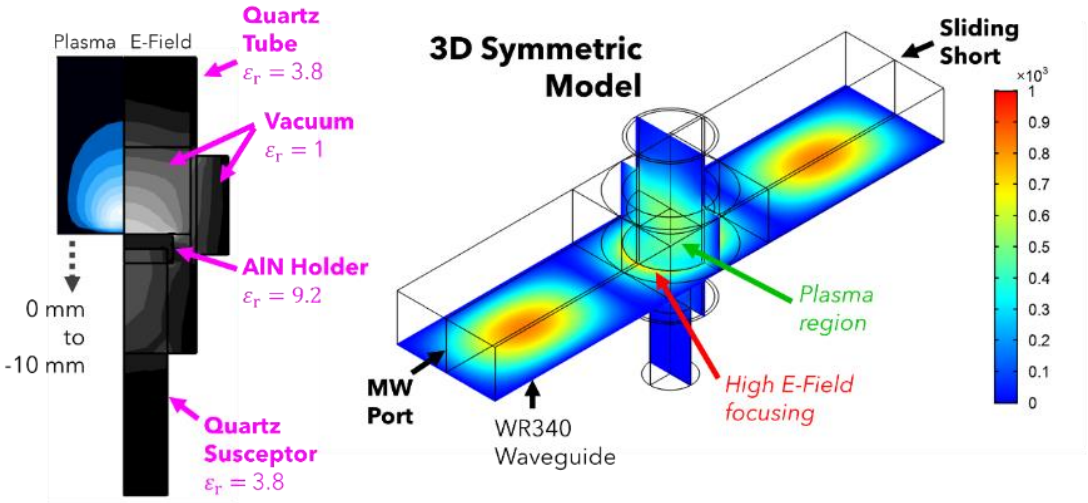

Fig. 1. Finite Element model of electron density (plasma) and electromagnetic (E-Field) distributions of the NIRIM style tube reactor.

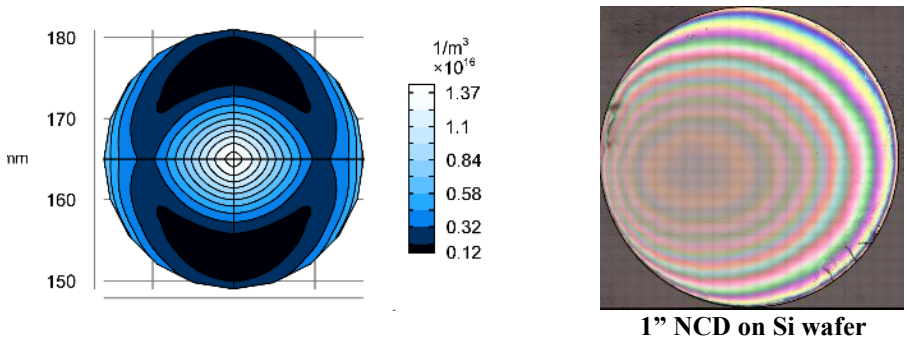

Fig. 2. Surface profiles from modelling and experimentally deposited nanocrystalline diamond (NCD) on Si (right). Surface profile photo shows a 1" diameter Si wafer with NCD (<1 μm), demonstrating elliptical non-uniformity

References

[1] S. Koizumi, Phys. Status Solidi Appl. Res. 172, 71 (1999).
[2] E.L.H. Thomas, L. Ginés, S. Mandal, G.M. Klemencic, and O.A. Williams, AIP Adv. 8, (2018).
[3] W.G. Fahrenholtz, G.E. Hilmas, I.G. Talmy, and J.A. Zaykoski, J. Am. Ceram. Soc. 90, 1347 (2007).
[4] P. Špatenka, H. Suhr, G. Erker, and M. Rump, Appl. Phys. A Mater. Sci. Process. 60, 285 (1995).
[5] J.A. Cuenca, S. Mandal, E.L.H. Thomas, and O.A. Williams, Diam. Relat. Mater. 124, 108917 (2022).

Fast and Rigorous BoR FDTD Algorithm for the Modelling of Coupled EM-Thermal Processes in Axisymmetrical Devices

L. Nowicki[1], M. Celuch[1], M. Olszewska–Placha[1], J. Rudnicki[1]

[1]*QWED Sp. z o. o., Krzywickiego 12, 02078 Warsaw, Poland,*
lukasznowicki@qwed.eu

Keywords: microwave heating, electromagnetic heating, multiphysics modelling, numerical techniques, computational electromagnetics, heat flow, batteries, computer aided design.

Motivation and background

Computational modelling has been gaining increasing interest of the microwave heating community and as such, it has become a regular topic of AMPERE conferences. While this paper is not meant as a review, let us refer the reader to two papers of AMPERE 2001, subsequently archived [1][2], for more historical references including relevant background and perspectives for further developments. In particular, it can be seen that the works on microwave power modelling follow two paths: identification and re-use of pre-existing computational tools [1] originally developed for other microwave technologies such as telecommunication and radar, and development of dedicated modelling workflows [2], which take the nonlinear processes as the focus. Additionally, benchmark examples have been defined [3], which allow meaningful verification and comparison of commercial and in-house modelling tools without revealing industrial secrets of the reference microwave applicator designs [1][3][4]. A review chapter [4] summarises the state-of-the-art in the use and development of the currently leading FDTD (Finite-Difference Time-Domain) and FEM (Finite Element) Methods, including accuracy and efficiency comparison of four popular commercial software packages (QuickWave and CST – for FDTD, COMSOL and HFSS – for FEM) for an open benchmark after [3] as well as a commercial domestic microwave oven.

The starting point for our work reported herein is an observation that the works as in [1-4] consider microwave heating problems in their full 3D (three-dimensional) representation. While such an approach is always correct, it is not always computationally efficient. If the structure of interest contains geometrical symmetries, exploiting such symmetries in the computer model accelerates the simulation by several orders of magnitude, without any loss of accuracy or physical information, which is incorporated analytically [5]. Of specific interest in microwave technologies are axially symmetrical problems, such as coaxial components [6] and satellite communication antennas [5]. Also in the area of microwave heating, axisymmetrical applicators are relevant to, e.g., timber drying [7]. In our H2020 NanoBat project [8], the specific interest was on the modelling of electromagnetic (EM) heating in batteries, many of which are in practice cylindrical. This has stimulated our work to couple the Bodies-of-Revolution (BoR) formulation of the FDTD method for Maxwell equations [5][6] with an analogous BoR FDTD for heat flow equations. Let us note that this requires casting the equations into the cylindrical coordinate system. While the operation appears in principle straightforward, its practical implementation it requires solving specific mathematical problems due to e.g., on-axis singularities [9], which influence stability and efficiency of the algorithm. In the available literature on thermal modelling, this has been obviated by either ignoring the cylindricity of the system and keeping the differential operators in their Cartesian forms (which approximates the reality far away from the axis but is unacceptable for small-radius problems and effects e.g., in batteries) or by requiring manual coordinate transformations by the user [10]. In our work, a rigorous BoR FDTD formulation for coupled EM-heat flow equations has been developed based on the approach of [6][9]. The transformation of coordinates is included in the code and therefore transparent to the user. The achieved computational efficiency improvements, with respect to the brute-force 3D modelling, are by over a factor of 100, as shown by the examples below. No physical information is lost, no mathematical pre-processing is required on the user's side.

Coupled electromagnetic and thermal simulation of axisymmetrical microwave process

Heat transfer refers to the exchange of energy in the form of heat between bodies or environments that are at different temperatures. This transfer can occur through conduction, convection, or radiation. The second laws of thermodynamics dictate that over time, temperature differences within a closed system will become more uniform as heat is transferred from hotter areas to cooler ones. This homogenisation process is accompanied by the movement of heat flux from high-temperature areas to low-temperature areas, with the rate of heat flux increasing as the temperature difference between the two points becomes larger. Using heat transfer theory, the differential equation for heat transfer shows how temperature is distributed continuously with respect to both spatial and time coordinates, allowing for the solution of heat conduction problems. Process of conducting FDTD analysis starts with sinusoidal excitation to obtain the electromagnetic steady-state. The analysis is then used to produce a 3D pattern of average dissipated power in lossy material. The enthalpy per cell is then upgraded using the average power and a-defined time of heating in seconds, resulting in an updated enthalpy density. Next, the temperature distribution in each FDTD cell is updated.

As an implementation example, a model imitating a popular AAA battery [11] is chosen. Thus, the model is a cylinder with a length of 49.5 mm and a radius of 9.5 mm filled with lossy material through the centre of which passes a cathode rod of

1.25 radius (Fig. 1). A common electrolyte is chosen as the loss material; Lithium hexafluorophosphate (LiPF6) salt with a concentration of 0.5 mol/kg dissolved in dimethyl carbonate (DMC). At this concentration, as shown in [12], conductivity hardly increases with temperature. For this reason, it has been assumed that it is constant and its value has been set to 2 S/m. The relative permittivity also does not change and is equal to 3.1075. In order to take advantage of the capabilities of the heating module, we also enter thermodynamic material parameters such as: density of 1.29 g/cm3, specific heat of 0.1339 J/(g°C) and thermal conductivity equal to 0.0045 W/(cm°C). These values are taken from [13].

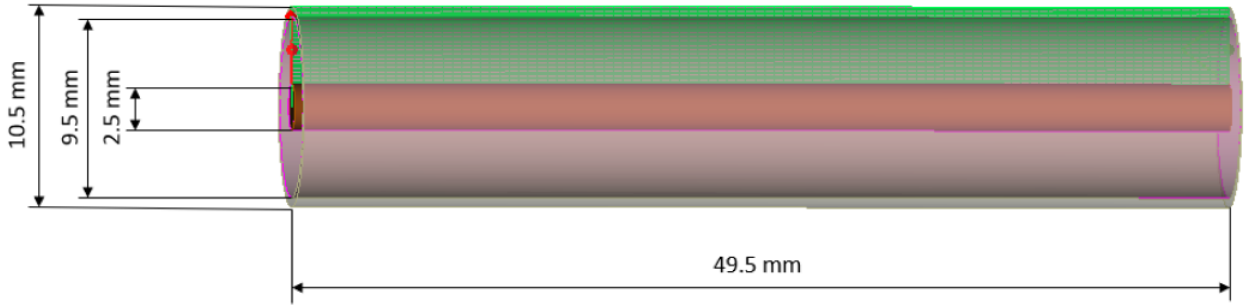

Fig. 1. Dimensions of the considered model of the popular AAA battery.

Two models are considered, for which accuracy and efficiency will be compared: classical full 3D and BoR developed in this work. In both models, the meshing in the axial direction is set to 0.5 mm while 0.1 mm is used in the cross-section (of which only the radial direction is discretised in the BoR model) (Table 1). To generate a steady state, the models are bounded by a source and a load and excited by a sinusoidal TEM field. Here, the frequency of 2.45 GHz is used for compatibility with ISM microwave applications and in the range of GHz technologies explored in [8] for battery materials' testing. The simulation begins with an FDTD EM analysis of the battery model up to the EM steady-state. Based on this, a template of average power dissipation values is calculated. The enthalpy value in each FDTD cell is then updated. All the material parameters defined above are used to obtain the temperature distribution. These results are provided to the heat transfer module HFM, where FDTD thermal calculations are run by solving the heat flow equations with adiabatic boundary conditions. After its completion, it returns the final temperature, enthalpy, and dissipated power distributions.

Table 1. The final parameters of the electromagnetic and heat flow simulation procedure performed for the battery model.

Calculations method	BoR FDTD			3D		
	Simulation time (min:sec)	Iterations	Number of cells	Simulation time (min:sec)	Iterations	Number of cells
EM	0:04	17647	11948	0:54	20504	1212516
HFM	0:08	1764		1:36	2050	

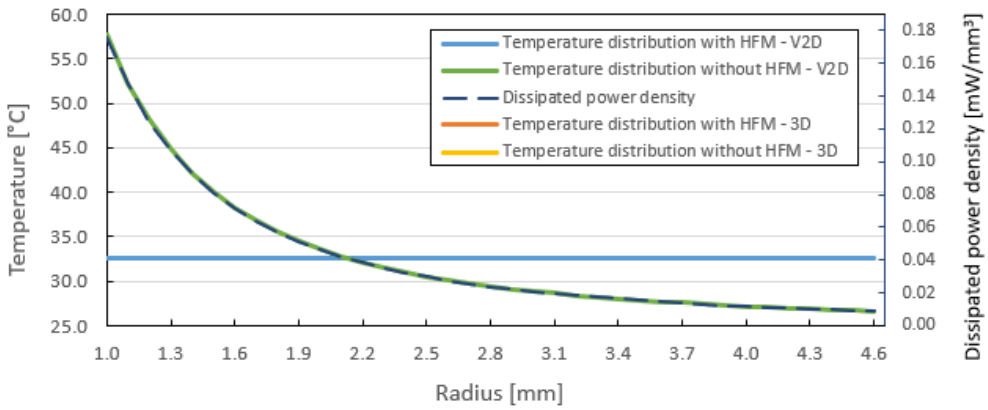

Fig. 2. Temperature distribution for heating simulations without and with flow with adiabatic boundary conditions in the radial direction (on the inner and outer conducting electrode) at an initial temperature of 25 °C – BoR and 3D results overlap.

To study the speed of the thermal calculations and their influence on the overall computing effort, nonzero electrical losses and thermal conductivity are set only over a section of the electrolyte, of increasing thickness. An increase in the thickness increases the simulation time although for the BoR FDTD model it is only a few seconds (Table 2). The dissipated power density is the same for both cases, BoR and 3D (Fig. 2), and as analytically expected, in the radial direction it is inversely proportional to radius squared. In the pure EM model, without heat flow, the temperature distribution follows the dissipated power distribution pattern. When heat flow is included, after the HFM stage, the temperature distribution is uniform in the radial direction, as shown in Fig. 2. All curves resulting from BoR simulations coincide with those from 3D (Fig. 2) but are

obtained after much shorter simulation times - economies are by an order of magnitude for this small model and increase with model size (Table 1).

Table 2. Simulation times obtained after the heating procedure with the heat flow module for different electrolyte thicknesses of the BoR FDTD and 3D model with adiabatic boundary conditions.

Thickness of electrolyte [mm]	Simulation time (min:sec)	
	BoR FDTD	3D
1	0:08	0:59
10	0:10	1:06
20	0:10	1:39
30	0:11	2:03
40	0:12	2:21

Extension to a nonlinear microwave process in axisymmetrical resonators

In this section, the previous BoR FDTD algorithm with a heat flow module will be extended with an algorithm for automatic updating of material parameters as a function of temperature, following the methodology proposed for 3D simulations in [2]. Additionally, we shall explain how an FDTD algorithm, which is deterministic by nature, is applied to solving eigenvalue problems in microwave resonators.

For illustration, a microwave heating device model based on the patent of [16] will be presented. The device of [16] is designed to heat disk-shaped objects containing different amounts of water. The device is shown in Fig. 3. It uses an antenna connected to a coaxial cable to introduce energy into the load. The device itself is designed to produce TM_{011} wave patterns, TM_{010} wave patterns, or a combination of the two, depending on the object's dielectric constant. The applicator's dimensions are carefully selected to meet two conditions: to create cylindrical TM_{011} resonance and to generate a TM_{010} field pattern when not in resonance. Figure 2 shows the dimensions of the considered applicator calculated based on the recommendations in [16] and assuming its operation close to the ISM frequency of 2.45 GHz. Then from equation (1) for the obtained radius, the frequencies for TM_{010} and TM_{011} modes are analytically calculated as 2.13 GHz and 2.44 GHz. The TM_{01} mode is the second mode (of the second lowest cutoff frequency) to propagate in a circular waveguide, with the TE_{11} mode being the fundamental mode (of the lowest cutoff frequency). Each mode is evanescent below its cutoff frequency, while above the cutoff frequency it propagates with a well-defined propagation constant. The cutoff frequency is dictated by the waveguide radius r and modal numbers m, n:

$$f_{c,TMmn} = \frac{c}{2\pi}\frac{\chi_{m,n}}{r}, \qquad (1)$$

where f_c is the cutoff frequency [Hz], c is the speed of light in vacuum [m/s], r is the radius of the waveguide [mm] and $\chi'_{m,n}$ is n-th root of m-th Bessel function. For TE modes, the root $\chi_{m,n}$ of the Bessel function is replaced by the root $\chi'_{m,n}$ of the function's derivative.

We first create a pure EM model and simulate it with BoR FDTD. We aim to solve an eigenvalue problem in the cylindrical applicator, confirming the analytically pre-calculated eigenfrequencies. To this end, we eliminate the feeding structure (coaxial line in Fig. 2a) and simulate only the cylindrical. Since FDTD is in itself a deterministic method, we need to approximate the eigenvalue problem by a resonant deterministic problem. We do so by inserting a virtual point source connected to a longitudinal E-field node close to the axis of rotation. Fig. 4 shows the Fourier transform of the current flowing through such a virtual point source – the minima indicate the resonances (in accordance with the physical sense of the resonance). Both resonances seen in Fig. 4 (2.13 GHz and 2.44 GHz) well approximate the analytically calculated ones – the discrepancy is caused by numerical dispersion and decreases with refined FDTD discretization.

The resonator is then modelled together with the feeding coaxial line. Now, minima of abs(S11) indicate the resonances of the actual heating device. Since the coupling is small, they are similar to the resonant frequencies calculated with the virtual point source. Then a lossy material with a thickness of 5 mm is placed in the applicator (as indicated in Fig. 3a). As a consequence, the resonant frequencies are shifted downward.

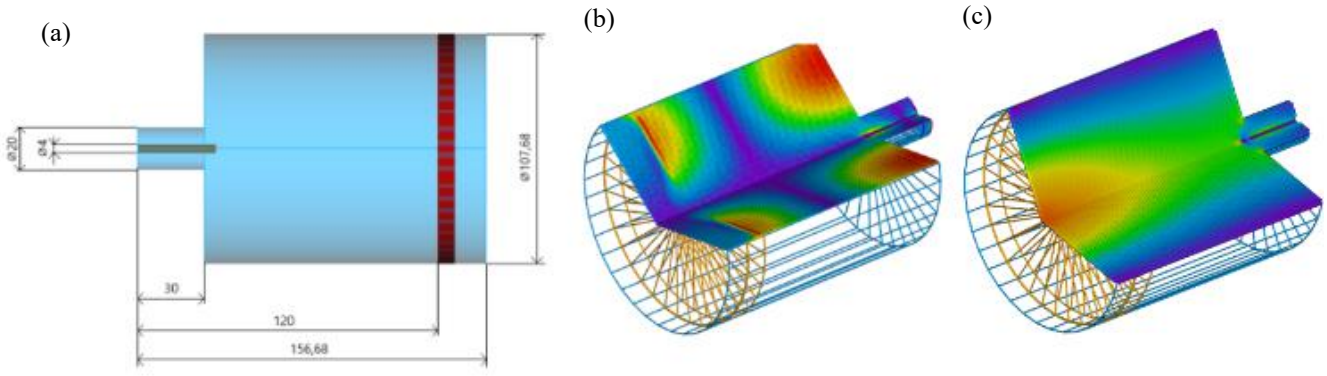

Fig. 3. Considered microwave applicator, its (a) dimensions after [16] and distribution of the (b) magnetic field and (c) electric field of the TM_{011} mode, in a 270 degree view of the cylinder.

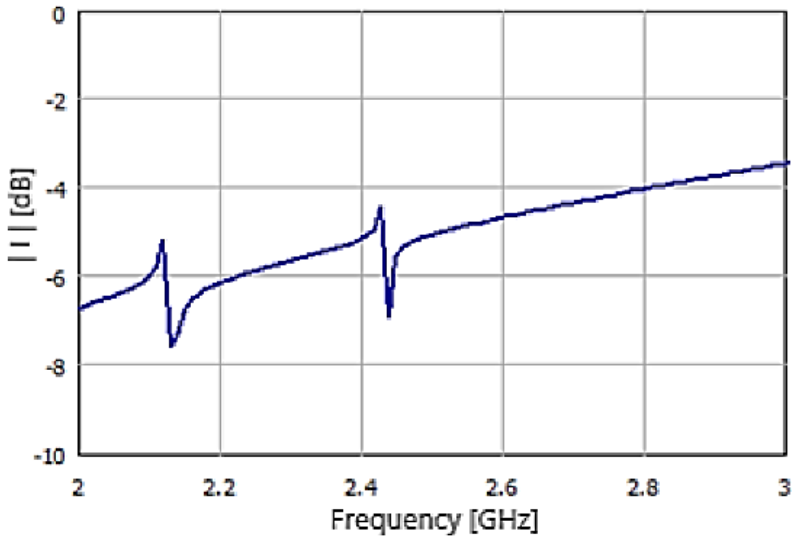

Fig. 4. Current flowing between the auxiliary point source and the resonator.

Apart from the frequency response, another crucial factor to consider a model of microwave oven is uniformity of heating of the materials being processed. The lossy material placed in the applicator has temperature-dependent material parameters defined. These are updated at the end of the heating step.

The simulations use a source with a sinusoidal TEM excitation at 2.13 GHz. The meshing is uniform in both directions and is 1 mm. One of the heated objects is bread, whose parameters are defined as temperature-independent constants. The electrical conductivity is equal 0.221 S/m and the effective permittivity is 4.17 after [7]. The final heating time is 120 seconds with different time steps as in the legend in Fig.6. The simulation assumes an initial temperature of -20 °C. Using BoR FDTD when calculating EM steady in each case simulation takes only one second. What it can be notice at Fig. 6 is that when we increase the number of steps during heating the bread including the heat flow module, the temperature doesn't go up so quickly. This happens because we are splitting the total power delivered over 120 seconds into smaller parts. That means there are more instances of heat flow during the simulation. If you focus on the differences in temperature distributions of different heating steps (Fig. 5). It can be noticed that the temperature across the bread doesn't change significantly anymore. This means that the temperature distribution becomes more stable. This information helps us figure out the best balance between simulation time and the accuracy final results. This is also confirmed by the Fig. 6, where for steps of 5 and 10 seconds they begin to converge. However, it should be taken into account that linear interpolation is used to draw the lines between successive heating steps. Note that the number of steps is really important when the material undergoes dynamic changes in its properties.

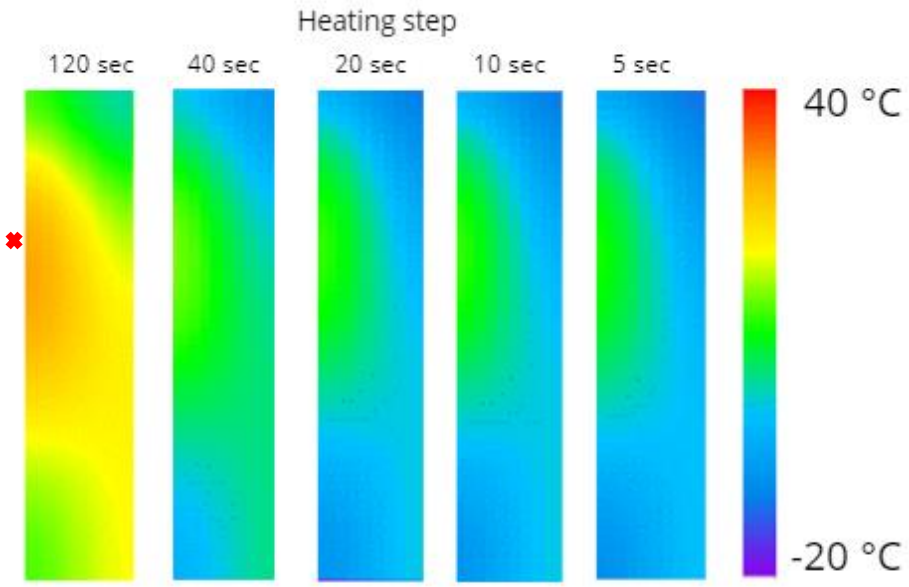

Fig. 5. Distribution of final temperature in bread after heating for 120 seconds, including heat flow phenomenon – parameterised simulations using different heating steps. Red spot means hot spot in bread.

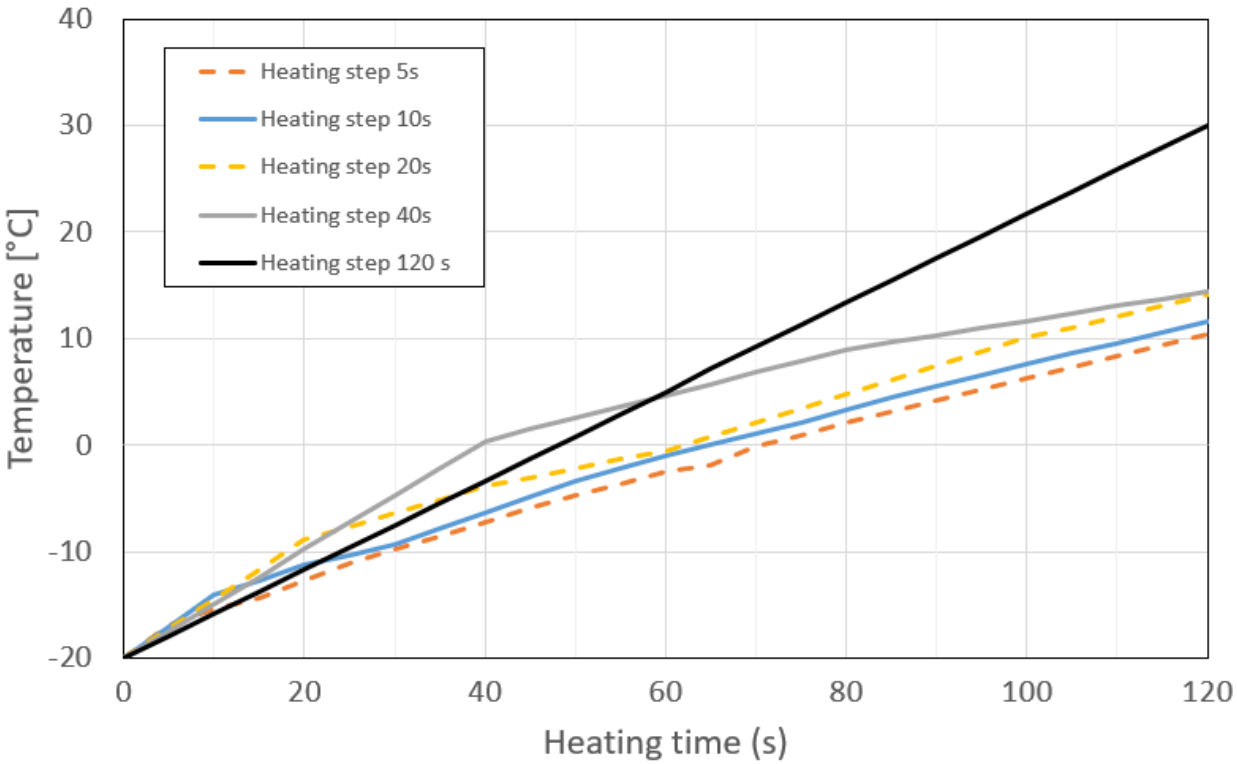

Fig. 6. Comparison of temperature evolution in simulated bread hot spot in heating simulations including heat flow.

The second material considered is beef whose parameters depend significantly on temperature. Parameters are also as in [17]. The relative permittivity changes from 4.9 to 41.7 in the temperature range from -20 to 80 °C. In the same range, its conductivity changes from 0.064 to 2.426 S/m maximum conductivity, which occurs in the -1 °C. Consequently, the power dissipated is most effectively absorbed by the beef causing an increase in temperature. However, an interesting relationship can be seen when the hot spot is examined, in these cases the maximum temperature at each step was taken into account. For beef, the temperature distributions are shown after heating (120 seconds) taking into account the heat flow phenomenon (Fig. 7) and with this step of the heating procedure like in Fig. 5. The increase in temperature in the beef causes significant changes in conductivity. If we set a step of 120 seconds, so one step is taken, all the power lost in the beef will be calculated on the initial parameters. Reducing the heating step of the simulation causes a hot spot to appear. It was marked with a red cross and the maximum temperature values were taken from there. Based on them, lists of such values were created for heating mode with and without flow calculations (Fig. 8) for beef.

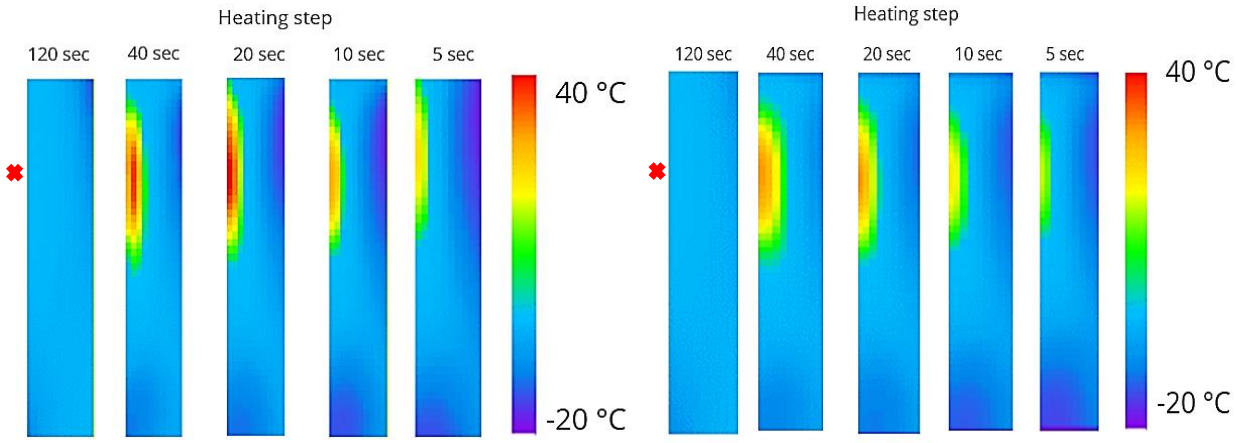

Fig. 7. Distribution of final temperature in beef after heating for 120 seconds (a) heat flow neglected (b) including heat flow phenomenon. Parameterised simulations using different heating steps. Red spot means hot spot in beef.

When the beef gets to around -1 C its properties start changing significantly. It is important to mention that Fig. 8 shows that after 120 seconds, the values for BHM and BHM+HF are a bit different by 2 hundredths of a degree. The curves that come together at the 60-second mark for all steps are because of how much the material properties matter. See, between -2.2 and -1 degrees, there are 5 different temperatures where the material's permeability and conductivity change. Conductivity goes up by about 1 S/m, and permeability increases by a significant 19 points. This means there's some uncertainty in choosing the right step.

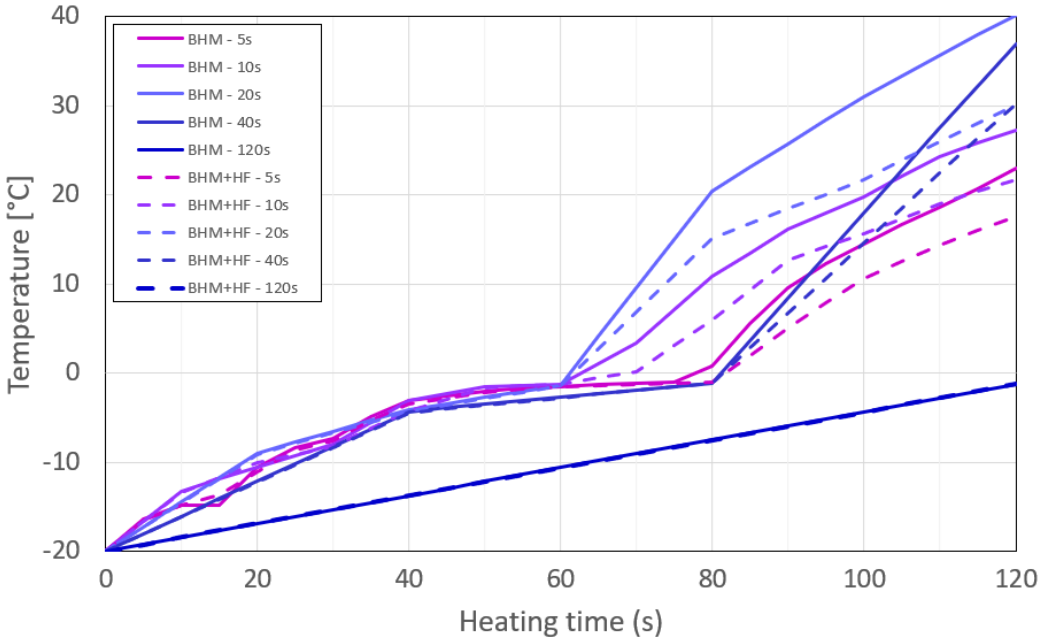

Fig. 8. Comparison of temperature evolution in simulated beef hot spot in with and without considering heat flow with different simulation time step.

Conclusions and future work

The Bodies-of-Revolution FDTD algorithm has been extended from pure electromagnetic to coupled nonlinear EM-thermal problems including heat flow phenomena. Compared with 3D modelling, significantly lower simulation times have been demonstrated for the BoR approach. For more complex models, the difference will definitely be more noticeable. A cylindrical microwave heating applicator has been considered as an EM eigenvalue and deterministic problem, and then as a multiphysics problem. Based on the AAA battery model, the algorithm was verified for a linear problem with adiabatic boundary conditions. The nonlinear problem is parameterised by dividing the microwave heating time into heating steps, with EM parameters of all materials assumed constant during each such step, but changed automatically by the software in each FDTD cell separately, between each two heating steps, in accordance to the local temperature of each cell.

Further work is ongoing on including charge transport mechanisms in the multiphysics problem. In the realm of battery industries, incorporating charge transport mechanisms and coupled electrochemical models into electromagnetic testing tools is crucial for accurate characterization and understanding of energy materials, such as those used in Li-ion batteries, facilitating advancements in battery research and technology. The developed solvers as well as a representative examples

are made available on the Open Platform of NanoBat [8] and I4Bags [17] projects, which aims develop processing and characterisation of battery applications.More results will be presented at the conference.

Acknowledgement
The reported work received funding from the European Union's Horizon 2020 research and innovation programme under grant agreement NanoBat No 861962. Currently the work of QWED team receives funding from the Polish National Centre for Research and Development under M-ERA.NET3/2021/83/I4BAGS/2022.

References

[1] V.V. Yakovlev, "Examination of contemporary electromagnetic software capable of modeling problems of microwave heating", in: Advances in Microwave and Radio Frequency Processing: Report from 8th International Conference on Microwave and High-Frequency Heating (Bayreuth, 2001), ed. M. Willert-Porada, Springer, Berlin, 2006, pp. 178-190.
[2] M. Celuch-Marcysiak, W.K. Gwarek, and M. Sypniewski, „A novel FDTD system for microwave heating and thawing analysis with automatic time-variation of enthalpy-dependent media parameters", in: Advances in Microwave and Radio Frequency Processing: Report from 8th International Conference on Microwave and High-Frequency Heating (Bayreuth, 2001), ed. M. Willert-Porada, Springer, Berlin, 2006, pp. 199-209.
[3] P.O.Risman, "A microwave oven model - examples of microwave heating computations", Microwave World, vol.19, No.1, Summer 1998, pp.20-23.
[4] M. Celuch, P. Kopyt, and M. Olszewska-Placha, "Modeling of cavities and loads with FDTD and FEM methods", Ch. 18 in: Development of packaging and products for use in microwampereave ovens" , eds. U. Erle, P. Pesheck, and M. Lorence, Elsevier, 2020, pp. 459-511.
[5] M. Celuch and W. K. Gwarek, "Industrial design of axisymmetrical devices using a customized FDTD solver from RF to optical frequency bands", IEEE Microwave Mag., vol. 9, No. 6, pp. 150-159, Dec. 2008.
[6] W.K. Gwarek, "Computer-aided analysis of arbitrarily-shaped coaxial discontinuities", IEEE Trans. Microwave Theory Tech., vol.36, pp. 337-342, Feb. 1988.
[7] P.O.Risman and M.Celuch-Marcysiak, "Electromagnetic modelling for microwave heating applications", invited paper, Proc. 13th Intl.Conf. on Microwaves, Radar and Wireless Communications MIKON-2000, Wroclaw, May 2000, vol.3, pp.167-182.
[8] (2023) H2020 NanoBat Open Modelling Platform [Online]. Available: https://www.qwed.eu/nanobat2.php
[9] M. Celuch-Marcysiak and W.K. Gwarek, "Improved and simpler FDTD formulation for axisymmetrical problems", Proc.2000 IEEE-AP-S International Symp. and USNC/URSI National Radio Science Meeting, Salt Lake City, Utah, US, July 2000, vol.1, pp.228-231.
[10] T. Kindo, "Guidelines for Equation-Based Modeling in Axisymmetric Components", (2023) COMSOL Blog. [Online]. Available: https://www.comsol.com/blogs/guidelines-for-equation-based-modeling-in-axisymmetric-components/
[11] Energizer product datasheet, https://data.energizer.com/pdfs/e92.pdf
[12] E. R. Logan,1 Erin M. Tonita, K. L. Gering, Lin Ma,Michael, K. G. Bauer, Jing Li, L. Y. Beaulieu and J. R. Dahn "A Study of the Transport Properties of Ethylene Carbonate-Free Li Electrolytes" " Journal of The Electrochemical Society, 165 (3) A705-A716 (2018), March 2018
[13] David R. Lide, ed., CRC Handbook of Chemistry and Physics, Internet Version 2005, <http://www.hbcpnetbase.com>, CRC Press, Boca Raton, FL, 2005. If a specific table is cited, use the format: "Physical Constants of Organic Compounds", in CRC Handbook of Chemistry and Physics, Internet Version 2005, David R. Lide, ed., <http://www.hbcpnetbase.com>, CRC Press, Boca Raton, FL, 2005.
[14] W. J. R. Hoefer and P. P. M. So, The Electromagnetic Wave Simulator: A Dynamic Visual Electromagnetics Laboratory based on the Two-dimensional TLM Method, J.W.Wiley Software, 1991.
[15] A.Z. Elsherbeni and V. Demir, The Finite-Difference Time-Domain Method for Electromagnetics with MATLAB (R) Simulations, SciTech Publishing Inc., New York, 2016.
[16] Per O. Risman, Huskvarna, Sweden, Microwave Heating Apparatus, United States Patent, Appl. No.: 974,606,1981
[17] I4Bags Open Modelling Platform [Online] Available: https://qwed.eu/i4bags.html

Towards Temperature Uniformity Control: A Process Conditions Selection Chart

E. Colombini[1], C. Leonelli[1], P. Veronesi[1]

[1]*Department of Engineering "Enzo Ferrari", University of Modena and Reggio Emilia, Via P. Vivarelli 10, 41125 Modena, Italy*
paolo.veronesi@unimore.it

Keywords: dielectric heating, multiphysics modelling, thermal model, temperature homogeneity index

Numerical simulation is a powerful tool to gather deeper knowledge on the temperature distribution in microwave (MW) heated reactors for chemical synthesis. This can be particularly useful when comparing conventional and microwave heating. Being aware of the major effects of temperature profile upon several chemical processes, such as the production of nanoparticles from solution with nucleation and growth mechanism, we have realized that very few published papers are dedicated to possible methods to identify experimental conditions leading to a specific temperature homogeneity distribution inside the reaction volume [1,2].

In this contribution we present the development of a process conditions selection chart, which can be used as a guideline to perform microwave synthesis with temperature-related objectives, like reaching the conditions of maximum or minimum temperature distribution homogeneity or minimum/maximum temperature gradients in the load. Numerical simulation was conducted by FEM using COMSOL Multiphysics software, setting the coupling of pre-defined application modes of RF and heat transfer and convection, when applicable. This allows a two-way coupling of the electromagnetic field and the thermal field, as their effects superimposed and affected each other.

We present two completely different cases, namely the dielectric heating at 2.45 GHz of a liquid reaction media [3] and the dielectric heating of a distribution of solid parts arranged in the reaction volume.

In order to develop processing maps addressing the maximum homogeneity of temperature distribution, we defined a temperature homogeneity index, as the ratio between the average temperature and its standard deviation at a certain heating time. This value is used to compare alternative microwave heating conditions (power density, stirring, load shape factor) and to compare them to conventional heating as well.

A second index, namely the variance of the temperature gradient existing within the load volume has been defined to address possible problems in solid state processing of materials deriving from local differences of temperature, leading to breakage of the parts under processing.

Based on such indexes, a method to obtain a selection chart of the more advantageous heating process is defined and can be used to select the experimental conditions expected to lead to the desired results as defined by the objective function.

A dedicated single-mode MW applicator (WR340 waveguide) operating at 2.45 GHz with a cylindrical load in regions of predominant E-field was used and three optical fibres (Neoptix, Canada) were implemented for experimental validation purposes. A LEANGEN-2450M-250-E solid state source (LEANFA Srl, Italy) was chosen for its capabilities of careful control of the emitted power in 1 W steps, measurement the reflected power, and its narrow bandwidth which is much more similar to the simulated source than a conventional magnetron-based source is.

Figure 1 qualitatively depicts the model used in this study and the power density in the cylindrical load investigated, equipped with the three optical fibres.

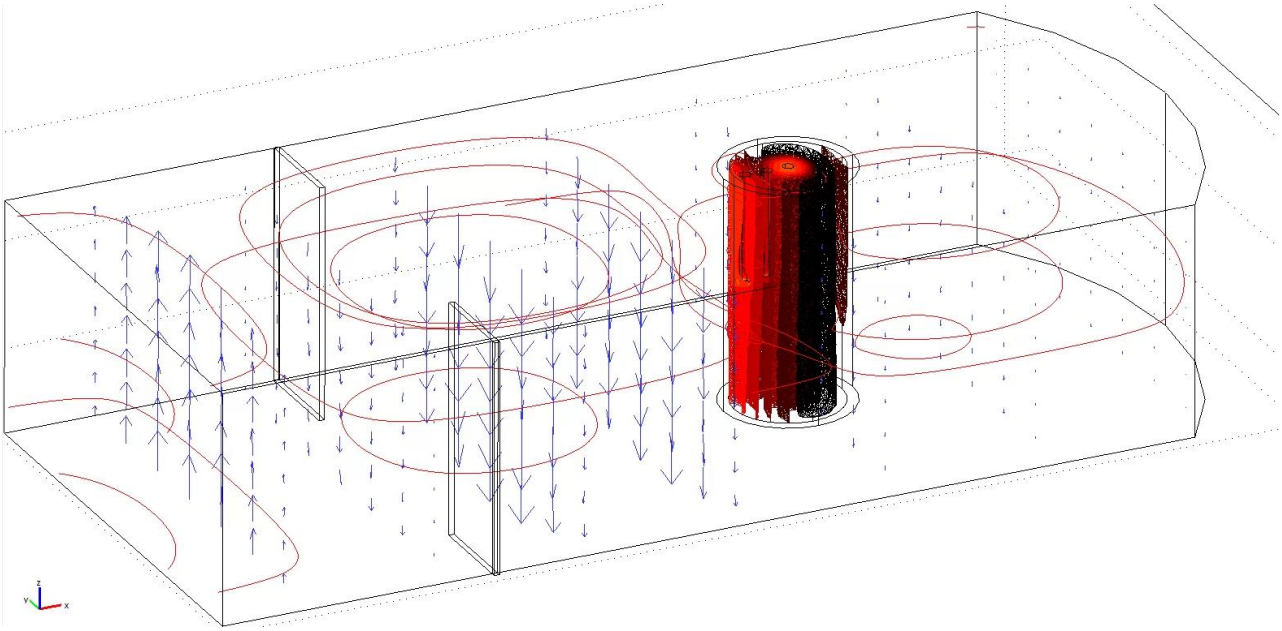

Fig. 1. Model geometry and cylindrical load position.

The result is a significant contribution to the amelioration of the MW-assisted processes that are often addressed as poorly reproducible processes and it can serve also to identify the conditions which result in favourable dielectric heating compared to conventional heating.

References

[1] A. Malhotra, W. Chen, H. Goyal, P. J. Plaza-Gonzalez, I. Julian, J. M. Catala-Civera, and D. G. Vlachos, "Temperature homogeneity under selective and localized microwave heating in structured flow reactors", *Ind. Eng. Chem. Res.* vol. 60, issue 18, pp. 6835–6847, Jan. 2021.

[2] P. Veronesi, E. Colombini, O. S. Canarslan, G. Baldi, and C. Leonelli, "Procedure to generate a selection chart for microwave sol-gel synthesis of nanoparticles", *Chem. Engineer. Process. - Process Intensification*, in press, March 2023.

[3] E. Paradisi, R. Rosa, G. Baldi, V. Dami, A. Cioni, G. Lorenzi, and C. Leonelli, "Effect of isopropanol co-product on the long-term stability of TiO_2 nanoparticle suspensions produced by microwave-assisted synthesis", *Chem. Engineer. Process. - Process Intensification*, vol. 159, n. 108242, Jan. 2021.

Modelling of Measurement Scenarios to Determine the Dielectric Properties of Spherically Shaped Semi-Conducting Microwave Absorption Ceramic Objects

B. Wäppling Raaholt[1], P. Ankarson[2]

[1]*Research Institutes of Sweden, Lindholmspiren 3A, Göteborg, Sweden*
[2]*Research Institutes of Sweden, Brinellgatan 4, Borås, Sweden*
Birgitta.Raaholt@ri.se

Keywords: microwave, complex permittivity, dielectric properties, inhomogeneous loads, simulation, modelling, measurement

The dielectric properties of materials are commonly described either for a bulk geometry consisting of small particulates (e.g. stacked wheat grains) that facilitate the use of mixture formulae or for a state where the materials are ground and mixed into very small pieces or tiny particulates (e.g. crushed lentils). However, many materials occur as larger particulates, e.g. spherically shaped objects). Spherically shaped objects of microwave absorption ceramics are used as an example of how the individual particulate as well as the bulk dielectric properties in a microwave field, for example a microwave heating process, can be analyzed by a model of effective permittivity. Such a model can describe the dielectric properties of stacked spherically shaped absorption ceramic objects surrounded by air pockets.

With the extensive research on additive manufacturing and microwave absorption ceramics, great possibilities are opened for microwave manufacturing of arbitrarily shaped absorption ceramics in a faster, cheaper, and more flexible way. Microwave modelling provides a tool to design and optimize the microwave melting and molding process, that is combined with additive manufacturing in terms of e.g. 3D printing [1]. However, accurate modelling of the microwave process requires access to dielectric properties that realistically describe the objects to be heated. In this paper, a method is discussed where modelling of measurement scenarios is used to determine the effective dielectric properties of spherically shaped absorption ceramic objects.

The permittivity of stacked spherically shaped microwave absorption ceramic objects were determined by modelling the resulting S11 parameters for a degenerate mode cavity, similar to the method described in [2, 3]. Representative examples of the dielectric properties are e.g., a silicon carbide foam (C-SiC foam) of density 400 kg/m^2: 12.5-j4.5 at 20 °C [4].

The results will be presented as illustrative examples of how modelling of measurement scenarios can be used to determine the dielectric properties for microwave absorption ceramic objects. The application of the suggested method will be discussed at the conference.

Modelling tools can serve to better describe measurement scenarios and save time. In the presented case, it will facilitate accurate determination of dielectric properties, complex permittivity, for microwave absorption ceramics, a semiconductor for wide industrial use.

References

[1] A review: 3D printing of microwave absorption ceramics - Wang - 2020 - International Journal of Applied Ceramic Technology - Wiley Online Library https://ceramics.onlinelibrary.wiley.com/doi/full/10.1111/ijac.13604
[2] B. Wäppling Raaholt, B and P.O. Risman. *Permittivity of inhomogeneous food items by retro-modelling with a degenerate mode cavity*. The 9th International Conference on Microwave and High-Frequency Heating, AMPERE. September 2003, Loughborough, UK.
[3] P.O. Risman, and B. Wäppling Raaholt. *Effective microwave dielectric properties of food materials consisting of large particulates*, ISEMA conference, Weimar, 2005.
[4] Q. Li et al (2020) *Experimental study on dielectric properties of SiC material and temperature distribution of rubber materials containing silicon carbide coated metal via microwave heating*, IOP Conf. Series, Material Sci. Eng. 772 012012 https://iopscience.iop.org/article/10.1088/1757-899X/772/1/012012/pdf
[5] Quickwave™ software, by QWED sp. z o.o, Poland, 1997–2005; www.qwed.com.pl

Machine-Learning Efficiency Optimization of Microwave Applicators with Plasma

C. E. Williams[1], E. K. Murphy[2], V. V. Yakovlev[1]

[1]*Center for Industrial Mathematics and Statistics, Department of Mathematical Sciences, Worcester Polytechnic Institute, Worcester, MA 01609, USA*
[2]*Thayer School of Engineering, Dartmouth College, Hanover, NH 03755, USA*
vadim@wpi.edu

Keywords: electric conductivity, decomposed neural network, FDTD modelling, frequency of electron collision, optimization, plasma frequency

Microwave (MW) plasma has shown a significant contribution to applications in processing technology [1] with demonstrable impact on the efficiency and quality of various processes. Examples include production of synthetic diamonds [1]-[3], surface processing for semiconductor manufacturing (deposition, etching, cleaning) [1], [4], plasma-based decomposition of CO_2 [5], etc. However, advancement of these applications is constrained by the challenges associated with development of efficient and controllable MW applicators for industrial use [1].

While sample computer simulations aiding in the design of such applicators have been reported in [2], [4], [6], [7], the use of advanced electromagnetic (EM) modeling and CAD remains limited due to the absence of adequate input data for the models of the system with plasma medium. The direct measurement of complex permittivity of plasma is challenging [8], [9] and, moreover, parameters of plasma are usually specific to the MW system in which it is ignited and maintained. Therefore, the complex permittivity of plasma is mostly estimated by theoretical calculation [8]. Recently, a simple physics-driven approach to characterization of MW plasma for EM modeling using the FDTD technique was proposed in [10]. In this model, the complex permittivity of plasma is represented by the electric conductivity, which is conditioned by the plasma frequency f_p, and the frequency of electron collisions, γ. Using this approach, EM modeling of a conventional MW applicator displayed well-known behavior of the electric field in presence of plasma [10].

Presently developing this work, we propose a machine-learning (ML) technique in which an FDTD model of a MW applicator with plasma is employed in an optimization loop. This technique allows one to find the optimum geometry of the applicator and determine the neutral gas required for optimal performance. Optimality here means energy efficiency; the objective function is defined as a minimum value of the reflection coefficient $|S_{11}|$ at an operating frequency f_0. The procedure is based on the neural network technique featuring constrained optimization response surface sampling in the dynamic training of the decomposed radial-basis-function (RBF) network [11]. To demonstrate functionality of the optimization technique, we use a model of a conventional MW applicator, like that which was used in the study [10]. The model consists of a cylindrical cavity with a coaxial thin-wall quartz vessel containing uniformly distributed plasma (Fig. 1); the model is built in the 3D FDTD EM simulator QuickWave [12]. The ML procedure identifies the geometry of the applicator and the plasma parameters f_p and γ which satisfy the objective function.

In accordance with [10], plasma frequency f_p, is conditioned by electron density which, in turn, depends on the neutral gas density and the degree of ionization [4]. It is difficult to determine the specific value of electron density, however, it can be assumed within a certain plausible range. As such, we specify f_p as the design variable in our optimization procedure. Furthermore, following [10], the frequency of electron collision g, depends on the neutral gas density, the average electron velocity, and the electron collision cross-section. Per the approach [4], the first two parameters can be assumed constants. To estimate the latter, one can use the calculated atomic radius of the neutral gas in which the plasma is excited and maintained. Then γ can be seen as dependent on the gas, therefore, constituting a set of typical gases as a discrete design variable in our optimization.

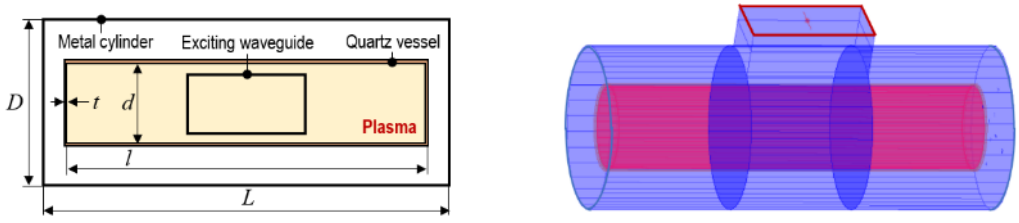

(a) (b)

Fig. 1. 2D (a) and 3D (b) views of the modelled cylindrical cavity with a coaxial quartz vessel (containing plasma); contrary to [10], the cavity is excited by a longitudinally oriented rectangular waveguide.

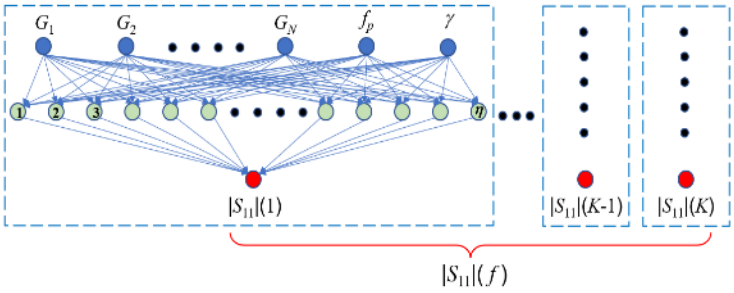

Fig. 2. Architecture of a decomposed RBF network with *h* hidden neurons.

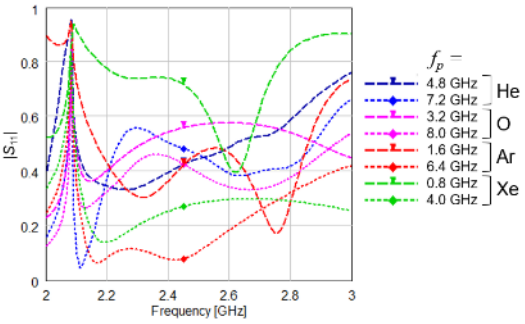

Fig. 3. Examples of non-optimal characteristics of $|S_{11}|$ for different neutral gases (γ) and plasma frequencies f_p as well as random D and d; optimized characteristic is found for Ar, f_p = 6.4 GHz, D = 95 mm, and d = 46 mm.

The RBF network used in the proposed machine-learning procedure (Fig. 2) follows the concept and methodology of the neural network optimization of microwave systems that is described in [11]. It works with input vectors of design variables $X_i = [G_1, G_2, \ldots, G_N, f_p, \gamma]$, where G_j (j = 1, …, N) are geometrical parameters of the modeled applicator, and i = 1, …, P, where P is the number of points (input-output pairs) of modeling data. The network output vectors are obtained by taking K equally spaced values of frequency characteristics of $|S_{11}|$ over a specified frequency range. The procedure implemented in MATLAB includes the dynamic network training and testing performed with the use of the input data for the FDTD model and its output results.

In the illustrative optimization, the applicator in Fig. 1 is characterized by constant parameters t = 1.5 mm, l = 220 mm, L = 240 mm and excited by WR284. The CAD goal is to find the values of four design variables, two geometrical parameters $G_1 = D$ and $G_2 = d$ as well as f_p and g corresponding to a minimum value of $|S_{11}| \leq 0.1$ at f_0 = 2.45 GHz. The following specifications are applied: $90 \leq D \leq 130$ mm, $40 \leq d \leq 80$ mm, $0.4 \leq f_p \leq 8.0$ GHz, and γ = [0.248 (He), 0.373 (Ne), 0.456 (F), 0.595 (O), 0.810 (N), 1.303 (Ar), 2.001 (Kr), 3.014 (Xe)]. The procedure starts with an initial database of 50 randomly chosen points generated in the specified domain, and the stopping criterion is set for the database size reaching 500 points. The FDTD model features a fine non-uniform mesh with 2 mm cells in air and 1.5 mm cells in quartz and plasma. When run on a regular Windows PC, the steady state is reached within a few minutes.

An optimized frequency response of $|S_{11}|$ is shown in Fig. 3 along with seven examples of typical non-optimized characteristics. The curve with the lowest value (0.75) of the reflection coefficient at 2.45 GHz corresponds to the specific geometry, neutral gas, and plasma frequency. The optimal design is found with 102 points in the database.

The described ML procedure employing the decomposed RBF network with three continuous (D, d, f_p) and one discrete (γ) input parameters (design variables) demonstrates its robustness and computational efficiency. The underlying FDTD model, however, relies on the simplified characterization of complex permittivity of plasma that, in particular, assumes that plasma frequency is a controllable/known parameter. With the uncertainties in input data of the EM models, our optimization procedure can be instructive in determining the operational bounds of applicators with MW plasma.

References

[1] L. Bardos and H. Barankova, *Microwave Plasma Sources and Methods in Processing Technology*, Hoboken, NJ: IEEE Press/Wiley, 2022.
[2] F. Silva, K. Hassouni, X. Bonnin, and A. Gicquel, Microwave Engineering of plasma-assisted CVD reactors for diamond deposition, *J. of Physics: Condensed Matter*, vol. 21, no. 36, 364202, 2009.
[3] E.L.H. Thomas, L. Gines, S. Mandal, G.M. Klemencic, and O.A. Williams, A simple, space constrained NIRIM type reactor for chemical vapour deposition of diamond, *AIP Advances*, vol. 8, 035325, 2018.
[4] S. Pauly, A. Schulz, M. Walker, M. Gorath, K. Baumgärtner, and G. Tovar, "Modeling and experimental study of remote microwave plasma source for high-rate etching," *Chemie Ingenieur Technik*, vol. 94, pp. 410-416, 2022.
[5] M.Y. Ong, S. Nomanbhay, F. Kusumo, and P.L. Show, Application of microwave plasma technology to convert carbon dioxide (CO_2) into high value products: A review, *J. of Cleaner Production*, vol. 336, 130447, 2022.
[6] G. Shivkumar, S.S. Tholeti, M.A. Alrefae, T.S. Fisher, and A.A. Alexeenko, "Analysis of hydrogen plasma in a microwave plasma chemical vapor deposition reactor," *J. of Applied Physics*, vol. 119, 113301, 2016.
[7] L. Latrasse, M. Radoiu, T. Nelis, and O. Antonin, "Self-matching plasma sources using 2.45 GHz solid-state generators: microwave design and operating performance," *J. Microwave Power and Electromag. Energy*, vol. 51, pp. 237-258, 2017.
[8] G. Wang, H. Pan, S. Lai, Y. Zhou, L. Wu, H. Zhu, and Y. Yang, "Dynamic measurement of relative complex permittivity of microwave plasma at atmospheric pressure," *Processes*, vol. 9, 1812, 2021.
[9] L. Li, H. Hu, P. Tang, B. Chen, and Z. He, "A microwave reflection method to determine the complex permittivity of time-varying plasma," *Proc. 2018 IEEE Intern. Symp. on Antennas and Propagation, Boston, MA, 2018*, 978-1-5386-7102-3.
[10] C.E. Williams and V.V. Yakovlev, "Characterization of microwave plasma in electromagnetic modeling for processing applications," *Proc. 57th IMPI's Microwave Power Symp., Denver, CO, June 2023*, pp. 51-53.
[11] E.K. Murphy and V.V. Yakovlev, "Neural network optimization of complex microwave structures with a reduced number of full-wave analyses," *Intern. J. of RF & Microwave Computer-Aided Engng*, vol. 21, no 2, pp. 279-287, 2011.
[12] *QuickWave*, QWED Sp. z o.o., 1998-2023, http://www.qwer.eu.

Metamaterial Solution for Homogeneous Curing of Carbon Fiber Reinforced Polymer

Y. Alekajbaf[1], S. Murali[2], D. Dancila[1, 2, 3]

[1]*FREIA, Department of Physics and Astronomy, Uppsala University, Sweden*
[2]*Percy Roc AB, Uppsala, Sweden*
[3]*Microwave Group, Department of Electrical Engineering, Uppsala University, Sweden*
Yasin.alekajbaf@Physics.uu.se

Keywords: microwave, carbon fiber reinforced polymer, microwave curing, patch array, dielectric resonators

Introduction

Carbon Fiber Reinforced Polymer (CFRP) is known as a high-demand material in many industries such as aerospace, wind power, marine, and automotive due to its mechanical properties like high strength-to-weight ratio, lightweight composition, and corrosion resistance. The curing process is a critical step in the manufacturing of CFRP composites because this process determines the final properties of the composite. Traditional curing methods for CFRP, including conduction heating and oven curing, suffer from notable disadvantages such as excessive energy consumption, lengthy processing periods, and restricted scalability [1], [2]. To overcome these challenges, microwave heating solutions for CFRP curing is studied as a promising solution with the potential to significantly reduce processing times and energy consumption. Microwave curing involves using microwaves to heat and cure materials, particularly thermosetting polymers. Therefore, to reach an efficient and homogenous curing process of CFRP, studied of CFRP's properties and its electromagnetic behavior are important [3]-[5]. The dielectric properties of a material, such as the dielectric constant and loss factor, determine its ability to absorb microwaves. However, CFRP, being a highly reflective material, impedes efficient microwave absorption. The high dielectric loss factor of CFRP causes it to behave as a reflector in the electromagnetic field. This property, along with its low penetration depth, renders microwave curing alone inefficient for CFRP [6]-[8].

Presently, curing techniques predominantly utilizing ovens or autoclaves with conductive heating face challenges like inconsistent temperature regulation. Additionally, these approaches typically consume more time and energy. However, in recent times, microwave heating has presented benefits including quick heating, uniform thermal properties, and the capability to produce high quality, efficiently processed composite products [9].

Although microwave curing of CFRP composites is attractive due to its control and energy efficiency. However, its adoption is constrained by the shielding effect in multidirectional CFRP laminates commonly used in aerospace. Indirect microwave heating methods using sensitive mediums or susceptive molds have been explored but present efficiency and flexibility challenges [3], [7], [10]. Various strategies, such as specialized cavity designs and lossy medium heating, have been investigated [11], [12]. Notably, patch resonators as a matching layer have shown success in curing specific CFRP configurations [8], [13]. Yet, challenges like uneven heating persist, emphasizing the need for further innovations in microwave-based CFRP curing processes.

In this paper, we present a solution for microwave curing of CFRP including a metamaterial array on the epoxy (dielectric) layer that is placed on the surface of the CFRP. An array of square patches are used as a resonator at 2.45 GHz. The coated CFRP component is placed in a multi-mode cavity, and the curing process is controlled using an advanced algorithm to achieve a homogeneous thermal distribution.

Microwave based CFRP curing

Microwave heating is a developing technique for curing carbon fiber reinforced polymer (CFRP) composites, offering several benefits and addressing certain limitations of conventional curing methods. One important parameter for successful microwave heating is the dielectric properties of the CFRP material, including the dielectric constant and loss factor, which determine its ability to absorb microwaves. The benefits of microwave heating for CFRP curing include reduced processing times, energy savings, improved control over temperature distribution, and the ability to switch the curing reaction on and off. The controllability of microwave heating enables uniform volumetric processing, which can lead to improved mechanical properties of cured composites. Additionally, microwave heating offers the potential for scalability and faster production rates. However, there are some limitations to consider, such as equipment issues, high costs of microwave systems, potential lack of penetration in thick laminates, non-uniform curing, void formation, and safety concerns [10].

The main challenges of microwave-based CFRP curing are non-uniform heating and weak microwave absorption issues, stemming from complex interactions between microwave radiation and the conductive nature of the carbon fiber material. As a result, based on previous research, using a multi-mode microwave cavity can provide a more uniform distribution of microwave energy, thereby reducing the occurrence of hot spots and improving overall heating uniformity. Additionally, incorporating microwave susceptors into the CFRP composite, such as metamaterial components and patch resonators that

enhance microwave absorption, can increase the efficiency of the curing process. This can be achieved by combining microwave and conduction heating methods [8], [12], [13].

Based on previous research and the approaches discussed, we propose an effective hybrid method to achieve homogeneous heating in CFRP curing. In this method, the CFRP composite is coated with dielectric epoxy, and small resonator parts are strategically placed on it. The coated CFRP is then placed in a multi-mode cavity. Additionally, to achieve a high-performance solution for CFRP curing and optimize homogeneity in this process, a control loop is implemented in the proposed system.

The proposed microwave based CFRP curing system

The presented system for CFRP curing integrates a coated CFRP sample, a multi-mode cavity, microwave heat sources, and a control loop for optimal heat distribution, as depicted in Fig. 1. This approach ensures effective microwave-based curing of the CFRP material.

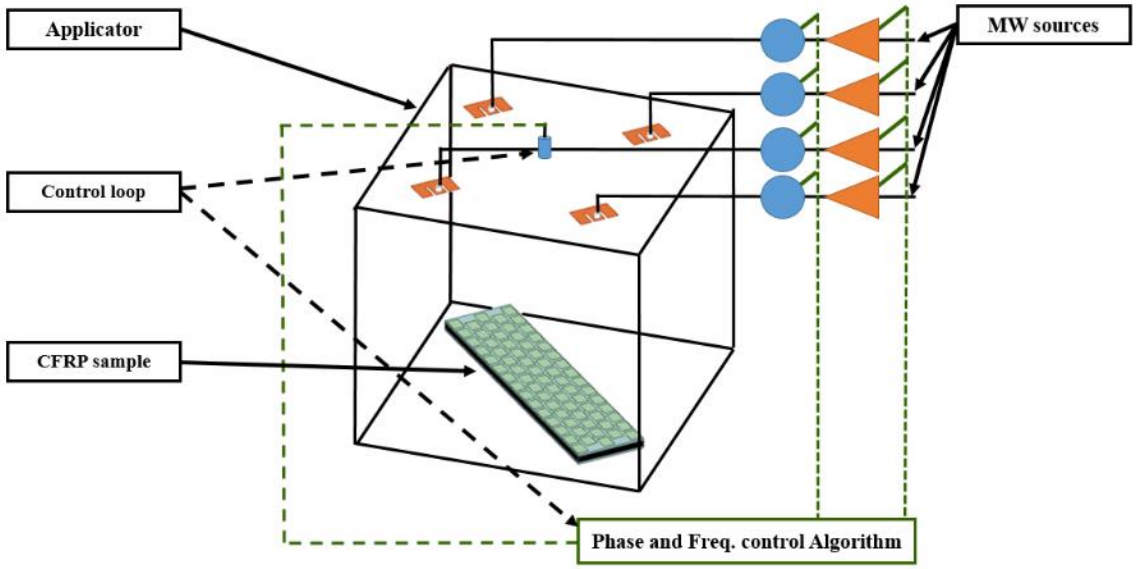

Fig. 1. Implemented system for microwave-based CFRP curing, including the coated CFRP composite with the resonance patches, applicator, MW sources, and phase and frequency control.

CFRP composite

Carbon Fiber Reinforced Polymer (CFRP) is a composite material integrating carbon fibers within a polymer matrix, primarily epoxy. This multilayered structure with varied orientations is integral for microwave-based curing, necessitating a deep understanding of its electromagnetic properties. Unlike homogeneous substances, CFRP's electrical characteristics are influenced by its orientation and lamination, with configurations like unidirectional (UD) layers imparting maximum stiffness in the fiber direction and multi-directional layers providing omni-directional strength [14]. For our study, we employed a 2.8 mm thick, four-layered HexPly® 8552 (AS4 fiber) CFRP composite. Analyzing the permittivity of CFRP is pivotal for its electromagnetic simulation and consistent curing. Our investigations, utilizing HFSS software and models from the Ansys Granta library, revealed CFRP's low absorption coefficient, classifying it as a conductor with minimal resistance or a magnetic reflector.

Microwave Source

Fig. 1 shows a system for CFRP curing with four ports, each linked to an E-shaped antenna. They operate between 2.3 and 2.7 GHz via 250 W amplifiers. Phase shifters at each end enable precise electric field distribution, ensuring uniform carbon absorption.

Exposure Chamber

The designed heating system in Fig. 1 uses a 500 × 500 × 500 mm multi-mode cavity at 2.45 GHz. Four E-shaped antennas, connected to individual amplifiers, propagate waves. Positioned centrally on the cavity's top, they control heat, enabling homogeneous curing. The simulated and fabricated and applicator are shown in Fig. 2.

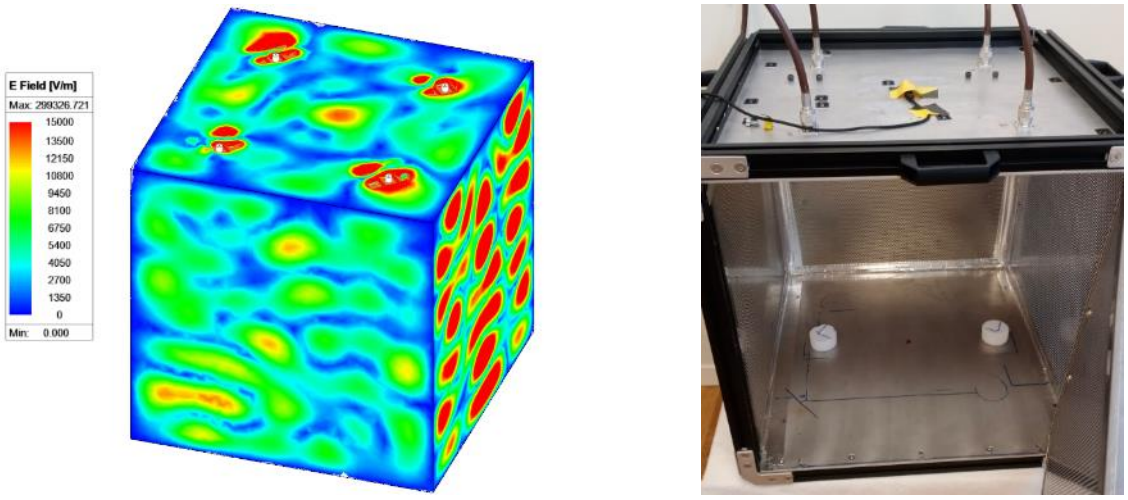

(a) (b)

Fig. 2. (a) E-field distribution in the designed multi-mode cavity powered by four MW ports with the ability to adjust phase and frequency, separately, (b) fabricated applicator.

Metamaterial matching design

Microwave-based CFRP curing faces challenges like non-uniform heating and weak absorption due to interactions with carbon fiber. A multi-mode cavity and optimization control loop offer uniform energy distribution, reducing hot spots. Incorporating microwave susceptors enhances absorption, combining microwave and conduction heating. Our proposed hybrid method involves coating CFRP with dielectric epoxy and resonators, then placing it in a controlled multi-mode cavity, as shown in Fig. 3.

(a)

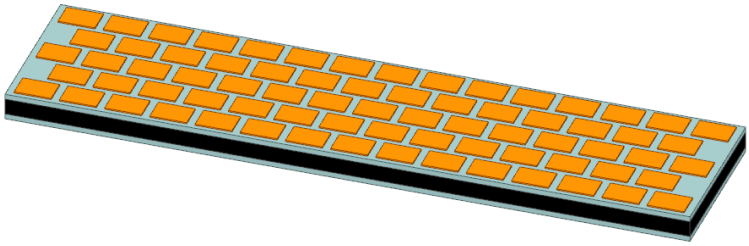

(b)

Fig. 3. (a) Coated CFRP component by metamaterial patch resonators, (b) Metamaterial patch resonators arrangement

Rectangular resonance patches, designed for 2.45 GHz, are simulated in HFSS using periodic boundary conditions. These patches resonate with incident microwaves in a controllable multi-mode cavity, enabling efficient CFRP heating. The simulation structure and its transmission line model are depicted in Fig. 4.

The analytical equivalent model of square patches is illustrated in Fig. 4b. The equivalent impedance of patches for different incident wave angles is calculated by (1), (2) [13].

$$Z_{P,inp}^{TE} = \frac{jw\mu\frac{\tan(\beta d)}{\beta}}{1-2k_{eff}\alpha\frac{\tan(\beta d)}{\beta}(1-\frac{1}{\varepsilon_{r+1}}sin^2\theta)} \quad (1)$$

$$\alpha = \frac{K_{eff}D}{\pi}\ln\left(\frac{1}{sin\frac{\pi\omega}{2D}}\right) \quad (2)$$

where θ is the angle of incidence and K, D, and d, are the wave number, patch width, and dielectric height, respectively. A comparison of the analytical model with HFSS simulations is shown in Fig. 5, with the patches' dimensions: D=22.6 mm, w (patches space) = 2 mm, d=4 mm, ε_r (dielectric constant) = 4.4 (FR4).

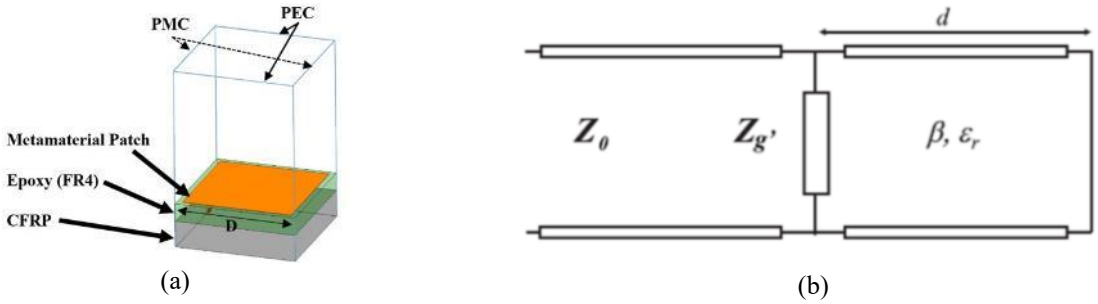

(a) (b)

Fig. 4. (a) Presented structure for CFRP covered by square patch array resonator (b) Equivalent transmission line model

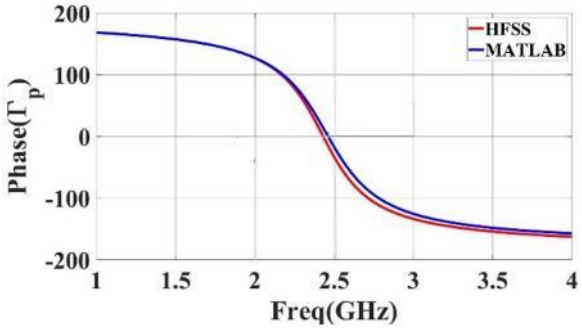

Fig. 5. Comparison of the analytical model with HFSS simulations

Optimization control unit

Utilizing the phase and frequency adjustments offered by the power amplifiers, a sophisticated optimization control loop ensures even heating across the CFRP. The IR sensor actively observes temperature fluctuations, while an IR camera provides visual feedback on the CFRP's heating dynamics. This complex system, surpassing typical SISO feedback loops, heavily relies on AI methodologies for precision.

Simulation and experimental results

Utilizing HFSS and Icepack software, we simulated the electromagnetic and thermal responses of the setup depicted in Fig. 1. The experimental setup for the proposed microwave curing system is shown in Fig. 6(a). In the 2.4 to 2.7 GHz range, Fig. 6(b) illustrates the heat distribution on CFRP under varied phase and frequency scenarios. These outcomes underscore the system's efficacy, particularly given the harmonious wave distribution observed experimentally.

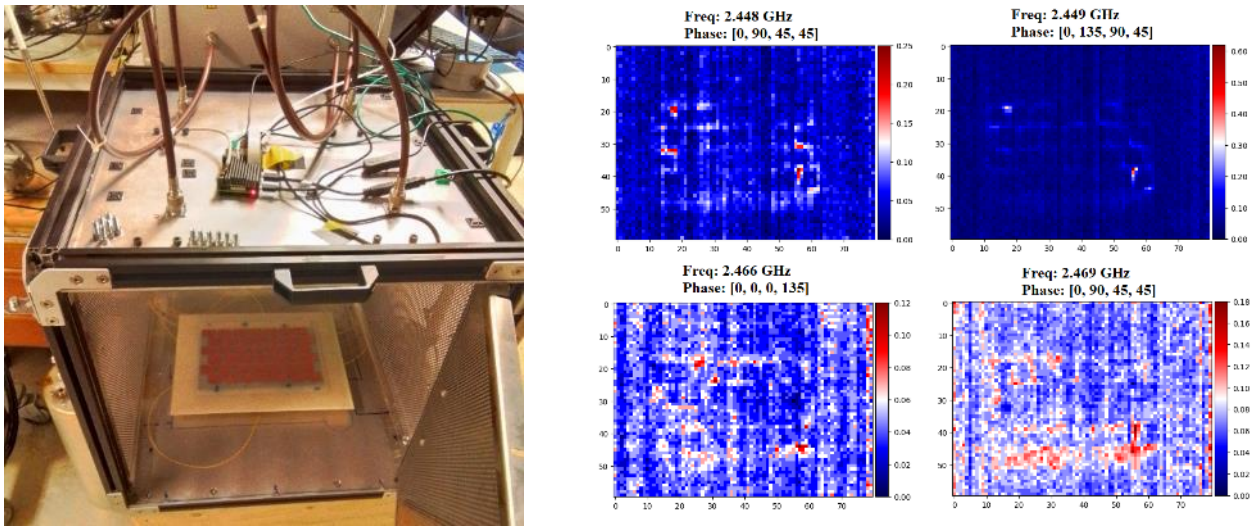

(a) (b)

Fig. 6. (a) Experimental setup for microwave curing of CFRP covered by patch array (b) Initial experimental test results

Conclusion

In conclusion, our research introduces an advanced and sustainable method for curing carbon fiber reinforced polymers (CFRP) with microwaves. By leveraging a metallic resonance coating and strategically placing the coated CFRP in a multi-mode cavity powered by four 250-Watt amplifiers, we ensure even heating patterns. These amplifiers, adjustable in power, frequency, and phase, are governed by a sophisticated control loop, achieving consistent absorption across the presented array. This method ensures maximum absorption in dielectric materials, culminating in a controlled and efficient CFRP curing process. Experimental evidence underscores the success of this pioneering approach in managing the microwave-based curing of CFRP.

References

[1] S.W. Kim, et al., "Cure behaviors and mechanical properties of carbon fiber-reinforced nylon6/epoxy blended matrix composites," Composites Part B: Engineering, Vol 112, p 15-21, 2017.
[2] R. Kumar, S. Zafar, "Comparative study of microwave and thermal curing processes in terms of temperature characteristics and mechanical performance of carbon fibre composites," Proceedings of the Institution of Mechanical Engineers, Part E: Journal of Process Mechanical Engineering, 2023.
[3] C.O. Mgbemena, et al., "Accelerated microwave curing of fibre-reinforced thermoset polymer composites for structural applications: A review of scientific challenges," Composites Part A: Applied Science and Manufacturing,
[4] Vol. 115, p 88-103, 2018.
[5] J. Galos, "Microwave processing of carbon fibre polymer composites: a review," Polymers and Polymer Composites. Vol. 29, no. 6, pp. 151-162, 2021.
[6] J. Galos, "Microwave processing of carbon fibre polymer composites: a review," *Polymers and Polymer Composites*. Vol. 29, no. 6, pp. 151-162, 2021. doi:10.1177/0967391120903894
[7] D. Abliz, et al., "Curing Methods for Advanced Polymer Composites - A Review" Polymers and Polymer Composites, 21, 6, pp. 341-348, 2013.
[8] J. Zhou, et al., "Dielectric properties of continuous fiber reinforced polymer composites: Modeling, validation, and application." Polym. Compos., Vol 39, p 4646-4655, 2018.
[9] J. Zhou, Y. Li, Z. Zhu, E. Xu, S. Li, and S. Sui, "Microwave heating and curing of metal-like CFRP laminates through ultrathin and flexible resonance structures," Compos. Sci. Technol., vol. 218, no. August 2021, p. 109200, 2022.
[10] R. Kumar, S. Zafar, "Comparative study of microwave and thermal curing processes in terms of temperature characteristics and mechanical performance of carbon fibre composites," Proceedings of the Institution of Mechanical Engineers, Part E: Journal of Process Mechanical Engineering, 2023.
[11] N. Li, et al.,"A new process control method for microwave curing of carbon fibre reinforced composites in aerospace applications," Composites Part B: Engineering, Vol. 122, p 61-70, 2017.
[12] B. Nuhiji, et al., "Simulation of carbon fibre composites in an industrial microwave," Materials Today: Proceedings, Vol 34, no. 1, p 82-92, 2021.
[13] K. Chen, et al., "Improvements in Temperature Uniformity in Carbon Fiber Composites during Microwave-Curing Processes via a Recently Developed Microwave Equipped with a Three-Dimensional Motion System," Materials, vol. 16, no. 2, p 705, 2023.
[14] O. Luukkonen et al., "Simple and Accurate Analytical Model of Planar Grids and High-Impedance Surfaces Comprising Metal Strips or Patches," IEEE Transactions on Antennas and Propagation, vol. 56, no. 6, pp. 1624-1632, 2008.
[15] A. Galehdar, et al., "The Effect of Ply Orientation on the Performance of Antennas in OR on Carbon Fiber Composites," Progress In Electromagnetics Research, Vol. 116, 123-136, 2011.

Measurements and Metrology

Improvement of the Perturbation Technique in Microwave Characterization of Lossy Materials in a Cylindrical Cavity

K. Ghorab[1], R.Thabet[1], J. Tao[2], M. Riabi[1]

[1]*Laboratory of Electromagnetic and Telecommunications,University Frères Mentouri Constantine 1, Constantine, Algeria.*
[2]*LAPLACE, Toulouse University, CNRS, INPT, UPS, Toulouse, France*
khawla.ghorab@umc.edu.dz
tao@laplace.univ-tlse.fr

Keywords: cavity perturbation technique, maximum volume, dielectric resonators, depolarizing factor

The perturbation method is very widely used in the microwave characterization of the electromagnetic properties of materials in resonant cavities [1-4]. However, the classical formulation of small perturbation finds its validity restricted by the shape, the small size and also the nature of the sample to be characterized. In a recent publication [2], a new formulation of the rectangular resonant cavity perturbation technique (CPT) has been proposed. In this formulation, the limits on the size, shape and location of the sample to be measured, have been improved and validated by fairly accurate measurements on samples of different geometries. This formulation is based on the introduction of depolarized fields inside the sample under test and the separation of depolarized and initial fields. By this improvement in the formulation, the maximum sample to cavity volume ratio is found to increase by more than 30% in some cases. Estimating the maximum sample volume is important to accurately assess the complex properties of materials using CPT without exceeding the limits of validity of the method.

In this work, we have extended the formulation mentioned above to the case of a perturbed circular cylindrical cavity using a new set of formulas. The measurement theory of the maximum volume ratio of the sample to cylindrical cavity $\left(\frac{Vs}{Vc}\right)_{max}$ has been investigated in order to guarantee a precise estimation of the complex permittivity. A TM_{010} cylindrical cavity was proposed. Fig. 1. and Fig. 2. illustrate the variation of $\left(\frac{Vs}{Vc}\right)_{max}$ as a function of permittivity when the sample is a dielectric bar and a dielectric thin-disk, respectively. In the first case, the volume ratio is only related to the relative dielectric constant and, in the second case, it depends on the dielectric constant and the relative dielectric loss factor. As expected, the sample volume is affected by the shape and the nature of the material. Table 1 shows the estimated value of the volume ratio for the low-loss sample Al_2O_3, proposed with some geometries. The results are improved by more than 8% in the proposed approach compared to the results in [2].

We have also investigated the area, distance from the center of the cavity, in which the sample can be placed without affecting the field lines using formulas and experimental measurement of the quality factor and the resonance frequency. This study is necessary because the placement of the sample in the center of the cavity is not always the best alternative and can cause excessive perturbation of the mode to be excited.

Based on the results determined from experimental and numerical measuring regarding the maximum volume, we investigate the improved CPT to measure the complex permittivity more accurately than in its classical form.

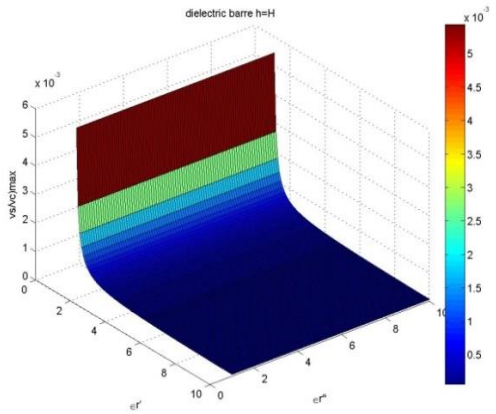

Fig. 1. $\left(\frac{Vs}{Vc}\right)_{max}$ as a function of the permittivity for a dielectric bar

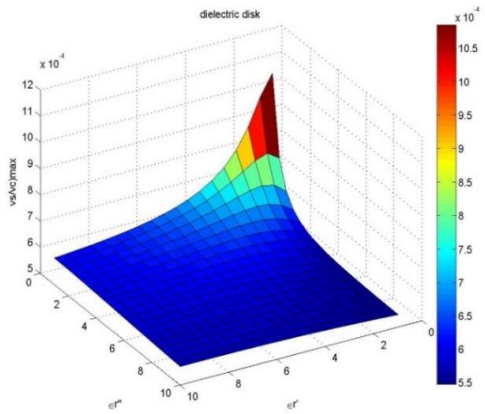

Fig. 2. $\left(\frac{Vs}{Vc}\right)_{max}$ as a function of the permittivity for a dielectric thin disk

Table 1. Comparison between the maximum volume ratios of sample to circular cavity and sample to rectangular cavity

The shape of the sample	Material - Al_2O_3		
	Cylindrical Cavity (improved)	Rectangular cavity [2]	Rate of increase
Sphere	0.000249317	0.000230	+8.4%
Bar	0.0000686189	0.0000719	-4.56%
Disk	0.00061071298	0.000563	+8.48%

References

[1] Z. Peng, J. Y. Hwang, and M. Andriese, "Maximum sample volume for permittivity measurements by cavity perturbation technique," IEEE Trans. Instrum. Meas., vol. 63, no. 2, pp. 450–455, 2014, doi: 10.1109/TIM.2013.2279496.
[2] C. Kim, L. Minz, and S. Park, "Improved Measurement Method of Material Properties Using Continuous Cavity Perturbation Without Relocation," IEEE Trans. Instrum. Meas., vol. 69, no. 8, pp. 5702–5716, Aug. 2020, doi: 10.1109/TIM.2020.2966358.
[3] S. B. Jones and S. P. Friedman, "Particle shape effects on the effective permittivity of anisotropic or isotropic media consisting of aligned or randomly oriented ellipsoidal particles," Water Resour. Res., vol. 36, no. 10, pp. 2821–2833, 2000, doi: 10.1029/2000WR900198.
[4] A. K. Jha, N. K. Tiwari, and M. J. Akhtar, "Accurate Microwave Cavity Sensing Technique for Dielectric Testing of Arbitrary Length samples," IEEE Trans. Instrum. Meas., vol. 70, 2021, doi: 10.1109/TIM.2021.3073438.

A Robust Dielectric Properties Measurement System for High Temperatures

R. Behrend[1], H. Krause[1]

[1]*TU Bergakademie Freiberg, Institute of Thermal Engineering, Gustav-Zeuner-Straße 7, 09599 Freiberg, Germany*
Ralph.Behrend@iwtt.tu-freiberg.de

Keywords: microwave, dielectric properties, measurement system, high temperatures

Abstract
Within this paper, the development and verification of a simple, robust measurement system for dielectric properties at higher temperatures up to 950 °C will be described. Necessary modifications in microwave apparatus design for high temperature applications will be shown, including radiation shielding and flange cooling, and influences on measurement will be analysed. Initial measurements are shown to benchmark results against known material properties. These measurements show acceptable agreement with literature data for Al_2O_3 and capture the trends sufficiently well.

Introduction
Knowing dielectric properties is a key element for design and operation of microwave heating systems. This holds even more true, when considering microwave heating processes with temperatures above 500 °C. Above this temperature, many oxidic materials tend to exhibit a nonlinear change in dielectric properties [1]. Recent developments in high temperature microwave applications demonstrate the increasing need for appropriate measurement systems to provide the required data. [2]. Refractory materials for high temperature applications are often oxide based and made from naturally occurring resources and are typically sintered or cast. Even cast materials can be inhomogeneous on a macroscopic scale. Determination of dielectric properties therefore requires a sufficiently large sample size in order to capture these inhomogeneities.

Since the 1950s [3] a plethora of high temperature dielectric measurement systems and methods have been developed. They rely on very different approaches such as cavity perturbation techniques, coaxial probe techniques and free field approaches. All methods have distinctive advantages and disadvantages when considering e.g., sample size, sample heating, robustness (meaning repeatability) and technological effort. Especially sample size and heating become relevant factors when non-homogeneous samples need to be investigated. In more recent years several groups have presented research within this field, e.g. [4-8], and several new approaches for high temperature dielectric measurement have been presented. Furthermore, dielectric data for inhomogeneous oxidic materials at high temperature was reported by several groups, e.g. [9-11], including some few measurements for ceramic fibres. However, data on refractory materials remains sparse and current measurement systems may not capture all aspects of the materials well.

Development of the measurement system
Measurement principle
From literature a wide range of measurement systems application has been analysed and ranked in several categories for the application at high temperatures with inhomogeneous samples. Usable sample size, microwave measurement range and temperature range have been considered as the most relevant factors. Robustness of the measurement, size of the measurement system, ease of implementation and usability for bulk materials have also been taken into account. The most common measurement systems (cavity perturbation method (CPM), transmission line method (TLM), free space method (FSM), and open-ended coaxial probe method (OCM) have been assessed and compared. All considered criterions have been given points ranging from 1 to 5 with 1 being a poor fit and 5 being a perfect fit. The results from the assessment are given in Table 1. Sample size refers to the material under test – for inhomogeneous materials a larger sample will produce a more reliable average of material properties – therefore a larger sample size was deemed advantageous. Further important criterions are temperature range and permittivity range (ε_r measurement range), especially the imaginary part of permittivity ε_r'', since it might change over several orders of magnitude during measurement. The ability to reproduce measurements was evaluated under the term “robustness”. Since some refractories or oxidic materials may be bulk products the usability of containers was considered an important criterion. Here, for example, the evaluation of OCM is difficult. While OCM can handle bulk materials very well, the consideration of container materials requires significant effort. A compact setup was considered advantageous for later transfer into production settings. From experience, some measurement setups can easily be influenced by environmental factors like temperature or other microwave devices. A system with comparatively low influenceability was considered as better.

Overall, all criterions are at least to a minor degree subjective and depend on the experience and equipment of the operator. The last criterion “ease of implementation” is highly subjective and may differ greatly from user to user. It should also be

noted that for nearly every shortcoming in a criterion (e. g. sample size, temperature range) solutions have been proposed in literature. These solutions tend to affect other criterions.

Table 1. Rating matrix for several dielectric measurement methods with 1 being a poor fit and 5 being a perfect fit.

Criterion	Weight	CPM	TLM	FSM	OCM
Sample Size	2	2	4	5	2
ε_r Measurement Range	2	2	3	2	3
Temperature Range	2	3	3	3	2
Robustness	1	5	4	3	2
Bulk Materials	1	2	3	4	1
Compactness	1	4	4	2	5
Interaction with surroundings	1	5	5	1	2
Ease of Implementation	1	5	2	2	2
Sum		**27**	**35**	**30**	**24**

Considering the intended purpose of the measurement system the waveguide reflection dielectric resonator approach was chosen as a basis for the new system. Especially, an approach document by Sheen [12] was identified as suitable candidate for the system due to its technological simplicity and applicability for comparatively large material samples.

Design

The setup is based on WR340 waveguides to use as many off-the-shelf components as possible. Indeed, the moving short and the coax-waveguide transition are off the shelf components. Given by the dimensions, the usable measurement range is between 2.17-3.30 GHz, in accordance with DIN 47302 and depending on the material under test (MUT). Flanges are adapted IEC-PDR 26 flanges. To reduce edges between the components levelling pieces were precision milled and fixed to the flanges with dowel pins. The measurement waveguide was built from high temperature resistant steel (1.4841) and equipped with water-cooled flanges. The flanges prevent heat transfer to other components and minimized thermal expansion, thus preventing the formation of edges. The measurement waveguide has an overall length of 750 mm, 250 mm of which are heated by two 950 W electric heaters Kanthal HAS 150/250/57.5. Some details regarding construction and setup can be found in Fig. 1, displaying a cross-section of the measurement apparatus. The apparatus has an overall length of about 1000 mm. The sample is placed on low absorbing material of known dielectric properties (Rath KVS 174/400, measurement data from [15]).

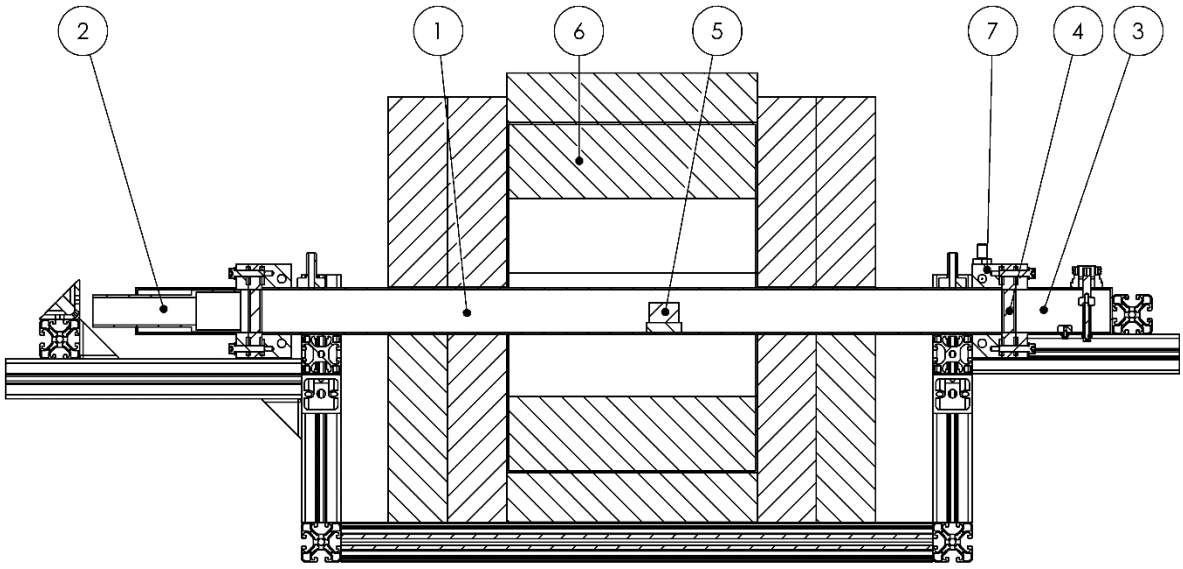

1: Measurement Waveguide
2: Moving short
3: Coax-Waveguide-transition
4: Levelling piece with PTFE window
5: Sample and sample holder
6: Electric heaters and insulation
7: Water-cooled flanges

Fig. 1. Cross-sectional view of the measurement apparatus. Key features are indicated and named. The apparatus has an overall length of about 1000 mm.

Temperature was controlled using an Omega CN7500. Temperature data was measured using a type K thermocouple and data acquisition was performed by an Omega OMB-DAQ-3001 system. The material of the waveguide allows a maximum temperature of 1150 °C. In order to prevent deformation of the waveguide a maximum temperature of 950 °C was chosen.

To protect the coax-waveguide transition antenna from high temperature radiation a PTFE insert was placed at the levelling piece.

Microwave measurements were carried out using an Agilent E5071C vector network analyser (VNA) with a measurement range from 100 kHz to 8.5 GHz. Measurement signals were transmitted to the measurement apparatus using a 1.5 m SS 402 Harbor coaxial cable with 50 Ohm impedance and type N-adapters at both ends. The cable was measured with an attenuation of 1.04 dB by the manufacturer. The setup was calibrated before every measurement using an Agilent 85092C HF-ECal calibration device. For calculation of the dielectric properties the S_{11} measurements of the VNA were used. A detailed explanation on the calculation can be found elsewhere [12]. For measurement the system is tuned to resonance using the moving short. Resonance frequency f_x, the S_{11}-value at resonance frequency (P_{min}) and the S_{11}-value at peak half-width (P_x) and the peak half width frequency range (Δf_x) are then used for calculation. Fig. 2 illustrates the measured values.

The dielectric properties of the sample can be calculated as functions of geometric properties of sample and waveguide as well as the indicated measurements from the VNA. In broad terms the real part of permittivity ε_r' can be calculated using

$$\varepsilon_r' = f(D, L_1, L_2, h, f_0) \qquad (1)$$

with D beeing the diameter of the sample, L_1 being the distance of the sample from the sample to the bottom of the waveguide, L_2 beeing the distance from the sample to the top of the waveguide and h beeing the inner height of the waveguide. The imaginary part of permittivity, ε_r'', can be calculated as a function as indicated in equation (2):

$$\varepsilon_r'' = f(\varepsilon_r', f_0, P_{max}, P_{min}, \Delta f_x) \qquad (2)$$

Details of the calculation can be found elsewhere [12-14]. Since dimensions of the waveguide have to be considered in calculation, the thermal expansion of the materials was considered for calculation as well.

Determination of heating curve

The system allows for variable sample sizes. For initial tests cylindrical samples with a diameter of 36 mm and a height of 20 mm was chosen. Since these samples are rather large for an accurate measurement the samples have to dwell at measurement temperature for a certain time in order to reach uniform temperature within the sample. The dwell time was calculated for several materials with different material properties (high heat capacity and low thermal conductivity, low thermal conductivity and low heat capacity and so on). A one-dimensional difference equation scheme was employed to calculate temperature distribution within the sample for a given temperature curve. It was determined, that for temperatures above 200 °C a dwell time of 30 minutes is sufficient to achieve a temperature difference between core and surface of the sample < 5 K for all samples, except the case of high heat capacity and high thermal conductivity, where 400°C have to be reached. Due to the needed dwell times, the overall time for measurement can easily exceed 12 hours, when aiming for small temperature steps.

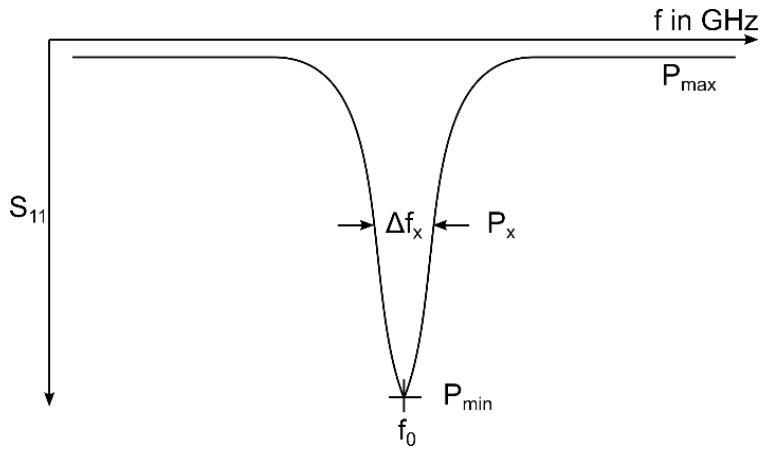

Fig. 2. Data to be acquired from the VNA. Sketch, adapted from Sheen [12].

Determination of influence factors on measurement accuracy

Several influence factors that could influence measurement accuracy have been analysed. In a first step the needed measurement resolution was determined. The VNA can measure up to 1601 datapoints over a given frequency range. The frequency range was varied from 300 kHz to 1 GHz in six steps, resulting in a measurement resolution ranging from 187 Hz/pt to 625 kHz/pt. Resonance frequency f_0 and P_{min} were measured and compared using the best resolution as base for comparison. Once reaching a measurement resolution larger than 125 kHz/pt the deviation of P_{min} becomes larger than 1%, severely effecting measurement accuracy. However, no such effect could be measured for f_x, where the deviation is below 0.1% for the whole analysed range.

Drift of the measurement systems was analysed. It was found that the measurement system is highly stable (within fractions of a percent drift in S_{11} and f_0) over long periods of time (24h), but highly susceptible to temperature variation within the room.

For measurement the moving short is moved to achieve a resonant state with a high quality-factor Q, indicated by $|P_{min}| \rightarrow \infty$ and $\Delta f_x \rightarrow 0$. While the influence on f_0 is negligible, the influence on P_{min}, P_x and Δf_x is not. Deviations of about 35% can occur, if the system is not brought to a resonance point.

Due to the use of a moving short the positioning of the sample material has no significant influence on the measurement of P_{min}. However, f_0 depends weakly on the position of the sample.

As described above, a PTFE insert was used in order to protect the antenna of the waveguide-coax-transition from heat radiation. A test with Al_2O_3 samples revealed a measurement deviation may be as high as 144% for ε_r'' at room temperature, while it becomes less than 1% for 750°C and higher. Further testing with high absorbing materials showed a diminishing influence of PTFE the higher absorbing the sample material becomes.

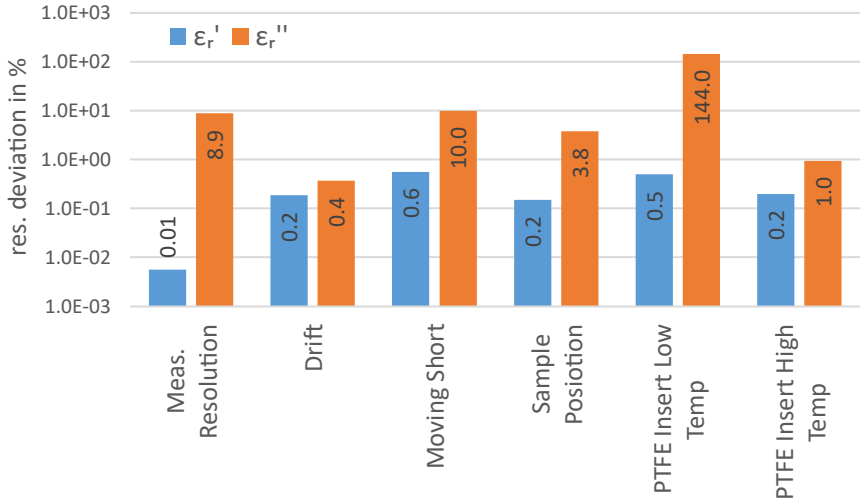

Fig. 3. Influence factors on measurement accuracy. Displayed as relative deviation in % from a base scenario with close to optimal conditions.

Fig. 3 shows a comparison of the analysed influence factors and highlights the influence of the PTFE insert as well as the position of the moving short. It is clear, that the influence on ε_r'' is much higher in each category than on ε_r'. The figure also highlights the impact of the PTFE insert at low temperature in comparison to all other influence factors.

Measurement of Al_2O_3-Samples and comparison with literature data

Al_2O_3 is on of the most researched materials in terms of dielectric properties. Due to its relevance in many applications regarding high temperature high frequency applications a wide range of research regarding its dielectric properties has been published over the years. For this reason, Al_2O_3 is used as a benchmark case for dielectric properties measurement systems. Al_2O_3 samples with a diameter of 30 mm and a hight of 20 mm and a purity of 99.9% were measured in the temperature range from 25 °C to 900 °C. Measurements were taken at 25 °C and in 50 K steps beginning from 200 °C up to 900 °C. The system was calibrated before the measurement.

Fig. 4 shows the results of the measurement in comparison to literature values derived from [1]. Four data sets are displayed together with the measurement frequency, density and purity. The datasets were chosen as close as possible to the current measurements with the new apparatus. The data shown spans a temperature range from 25 °C to 1200 °C with ε_r' ranging from 9.01 at room temperature to 11.7 at about 1100 °C and ε_r'' ranging from 0.0045 to 0.12. Own measurements are displayed in red as average of three measurements for temperatures from 25 °C to 900 °C.

Fig 4. highlights the difficulties of precise dielectric properties measurement and need for it. The displayed very similar materials differ widely, especially when comparing ε_r''. While sample Al_2O_3 06 shows a sharp increase in dielectric properties at temperatures as low as 200 °C and reaches $\varepsilon_r'' = 0.11$ at 365 °C, sample Al_2O_3 05 shows a similar behaviour when reaching temperatures above 1000 °C. However, the real part of permittivity is similar for both samples. Our own results show acceptable agreement with literature values. In the temperature range from room temperature up to 400 °C ε_r'' values are a little higher than literature values. This can be attributed to the measurement deviation introduced by the PTFE insert, as described above. Considering the calculated deviation, the results are very close to the average of the literature values. From 400 °C to 500 °C the measurements show a steep increase in ε_r'' from 0.015 to 0.042, followed by a decline to 0.023 at 650 °C. This happened in all measurements and can be attributed to the moving short being moved over a small step

between moving short waveguide and levelling piece. This in turn changed the S_{11}-peak- width and resulted in the shown behaviour. For higher temperatures the measured dielectric properties follow the trend of the literature data. Further tests with materials with higher ε_r'' have not shown any sign of the aforementioned measurement deviation which is in accordance with the presumed cause of the deviation.

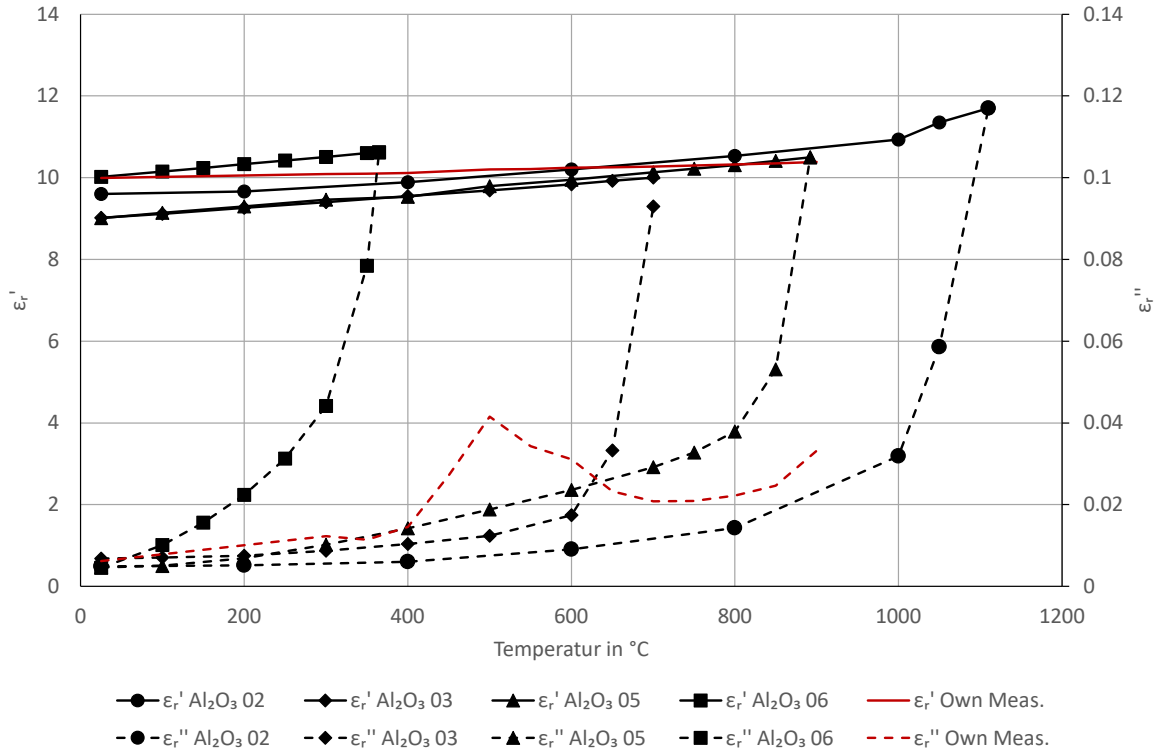

	Frequency [GHz]	Density [g/cm³]	Purity [%]	Source
Al_2O_3 02	3.55-3.79	3.765	97.0	P.36, [1]
Al_2O_3 03	3.61-3.80	3.649	94.0	P.29, [1]
Al_2O_3 05	3.61-3.89	3.663	95.0	P.5, [1]
Al_2O_3 06	3.05-3.00	3.963	n.A.	P.24, [1]
Own Meas.	3.32-3.39	3.8	99.9	[-]

Fig. 4. Literature data of ε_r' and ε_r'' for Al_2O_3 and average of own measurements of of ε_r' and ε_r'' for Al_2O_3 over a temperature range from 20 °C to 1200 °C. Purity, density and measurement frequency were given to the best knowledge from the source data [1].

Summary and Conclusion

In this paper we have shown the development of a new high temperature measurement system for dielectric permittivity for large material samples. A waveguide reflection dielectric resonator approach was adapted due to its technological simplicity and adaptability for high temperature measurements. These adaptions, aimed at reducing influence of high temperature on the test setup, were analysed among other factors regarding their influence on measurement accuracy. A first set of measurements for Al_2O_3 was presented and compared to literature data. The new measurement system captures the trends fairly well but also exhibits some deviations from the expected values. Some explanation on possible reasons have been given and discussed. Due to the relatively large sample size the measurement system is well suited for measurements on refractory materials. Since especially refractories from the glass industry typically exhibit very high values of ε_r'', the mentioned deviations caused by PTFE insert will diminish. Future work will concentrate on an improved moving short and increased accuracy at low ε_r''.

Acknowledgement

The authors would like to thank the German Federal Ministry of Education and Research as well as the European Union and Projektträger Jülich (PTJ) for funding the project “MiGWa” under PTJ Grant Agreement Number 01LJ2001B within the KlimPro funding scheme.

References

[1] W. B. Westphal and A. Sils, *Dielectric Constant and Loss Data*, Technical Report AFML-TR-72-39, 1972
[2] (2015) Development of adaptive ProductioN systems for Eco-efficient firing processes. [Online]. Available: https://cordis.europa.eu/project/id/314636

[3] W. B. Westphal, *High-Temperature Dielectric Measurements on Radome Ceramics in the Microwave Region*, Technical Report 113, 1957, Available: https://apps.dtic.mil/sti/pdfs/AD0122938.pdf
[4] M. K. Park, H. N. Kim, S. S. Baek, E. S. Kang, Y. K. Baek, K. Yong Kee; Do Kyung: *Dielectric Properties of Alumina Ceramics in the Microwave Frequency at High Temperature*. In: SSP 124-126, S. 743–746, 2007. DOI: 10.4028/www.scientific.net/SSP.124-126.743.2
[5] M. Reichmann, S. Hahn, G. Walter, K. Dornich: *Verfahren zur temperaturabhängigen Erfassung von Dielektrizitätsparametern zur Hochtemperatur-Mikrowellenprozessierung von keramischen Werkstoffen*. In: cfi - ceramic forum international 87 (5), D9-D14.4, 2010
[6] J. M. Catala-Civera, A. J. Canos, P. Plaza-Gonzalez, J. D. Gutierrez, B. Garcia-Banos, F. L. Penaranda-Foix *Dynamic Measurement of Dielectric Properties of Materials at High Temperature During Microwave Heating in a Dual Mode Cylindrical Cavity*. In: IEEE Trans. Microwave Theory Techn. 63 (9), S. 2905–2914, 2015 DOI: 10.1109/TMTT.2015.2453263.7
[7] B. Garcia-Baños, J. M. Catalá-Civera, F. Peñaranda-Foix, P. Plaza-González, G. Llorens-Vallés *In Situ Monitoring of Microwave Processing of Materials at High Temperatures through Dielectric Properties Measurement*. Materials 9 (5), S. 349, 2016 DOI: 10.3390/ma9050349.1
[8] Y. Wu, L. Wu, H. Zhu, T. Hong *Design of High Temperature Complex Dielectric Properties Measuring System Based on XGBoost Algorithm*. Materials 13 (6), 2020 DOI: 10.3390/ma13061419.
[9] B. García-Baños, A. M. Lopez Buendia, C. Suesta, J. M. Catalá-Civera, J.F. Reinosa, J. F. Fernández *Dynamic Study of microwave heating of quartz sand up to 1100°C and effects of particle size*. In: 15th International Conference on Microwave and High Frequency Heating. Krakow, S. 107, 2015
[10] Z. Di Zhai; F. Zhang, C. Wei, Y. Bai, L. Zhu, G. Li, *Dielectric properties and electromagnetic wave transmission performance of polycrystalline mullite fiberboard at 2.45 GHz.* In: Ceramics International 46 (6), S. 7362–7373, 2020. DOI: 10.1016/j.ceramint.2019.11.232.
[11] X. Shang, L. Di Zhai, M. Liu, J. Chen, F. Zhang, C. Wei *Dielectric properties and electromagnetic wave transmission performance of aluminium silicate fibreboard at 915 MHz and 2450 MHz.* Ceramics International 47 (6), S. 7539–7557, 2020. DOI: 10.1016/j.ceramint.2020.11.092.
[12] J. Sheen, *Microwave Dielectric Properties Measurements Using the Waveguide Reflection Dielectric Resonator*, 2007 IEEE Instrumentation & Measurement Technology Conference IMTC 2007, Warsaw, 2007
[13] J. Sheen, *Study of microwave dielectric properties measurements by various resonance techniques*. In: Measurement 37 (2), 123–130, 2005
[14] J. Sheen, *Comparisons of microwave dielectric property measurements by transmission/reflection techniques and resonance techniques*. In: *Measurement Science and Technology* 20 (4), P. 42001, 2009
[15] M. Buryan, *Entwicklung von Auslegungsprinzipien für mikrowellen- und gasbeheizte Hybrid-Sinteröfen*, Dissertation, TU Bergakademie Freiberg, Freiberg 2004

A Calibration Approach for the Bulk Temperature Estimation from Container Surface Temperature during Microwave Heating Processes

R. Pérez-Campos[1], J. Fayos-Fernández[1], J. Monzó-Cabrera[1]

[1]*Departamento de Tecnologías de la Información y las Comunicaciones, Universidad Politécnica de Cartagena, 30202 Cartagena, Spain*
juan.monzo@upct.es, jose.fayos@upct.es, rafael.perez@upct.com

Keywords: microwave heating, multimode cavity, pyrometer, temperature calibration, granular materials

Introduction

The advantages of employing microwaves to heat materials are well known and have gained widespread acceptance in recent decades. Microwave dielectric heating has been found in several cases to significantly reduce processing times, enhance physical and/or mechanical properties, and increase product yields when compared to conventional heating processes [1, 2]. In microwave processing, energy is rapidly converted into heat inside the materials by electromagnetic radiation, whereas thermal energy is simply transported throughout the volume of the sample by an external heating source in conventional heating [3].

Although many microwave heating studies have been conducted in modified domestic microwave ovens, the present trend strongly favors the use of specialized instruments for chemical synthesis [4]. Today's commercially available microwave reactors incorporate, among other things, direct temperature control of the reaction mixture and software that allows temperature control via microwave power output adjustment. The main reason for that is the need to continuously monitor the reaction temperature during the microwave irradiation process.

Unfortunately, traditional direct temperature sensors, such as thermometers or thermocouples, are difficult to use because they may couple with the electromagnetic field. A more accurate method of monitoring temperature is to use fiber-optic (FO) sensors. Unlike thermocouples, FO measuring instruments are immune to electromagnetic interference and do not require shielding. Nonetheless, FO probes offer significant drawbacks, including that they are highly fragile, have a high price, and also have a limited temperature measurement range.

The sample temperature is usually acquired using a calibrated external sensor integrated into the cavity, which is able to monitor the surface temperature of the sample container from a predefined distance [5]. It is expected that the temperature measured on the sample container's exterior will correspond to the temperature of the material within. However, utmost caution must be taken when relying on this fact. Given that the sample containers are commonly composed of a thermal insulator (e.g., borosilicate glass), a certain time is required for the temperature sensor to reflect the sample temperature [6, 7]. Hence, the reliable monitoring of reaction temperature becomes nontrivial in spite of being critical to the proper development of the microwave-assisted process [8].

Kappe studied the accurate measurement of reaction temperature in a single-mode microwave cavity [7]. The conclusion was that no differences between FO and infrared temperature sensors will be observed, with the latter being able to accurately reflect the internal reaction temperature provided that: the infrared thermometer is properly calibrated; the reaction mixture is both quite homogeneous and low microwave absorbing; and the reaction is not exothermic. García-Baños et al. developed a temperature calibration method to obtain the bulk temperature under microwave irradiation from the surface temperature measurements [9].

Nonetheless, when the mixture becomes heterogeneous and difficult to stir, some disparities in the recorded FO and infrared temperatures may occur. In addition to that, some temperature gradients can be formed within the microwave-heated sample if efficient stirring is not provided during the microwave heating process as a result of heterogeneous electromagnetic field distribution [10]. Despite the strong interest in adequately monitoring the sample temperature during microwave processes, to the best of the authors' knowledge, there is no contribution in the literature that estimates the thermal parameters affecting the pyrometer temperature records in a practical way in order to predict the sample temperature by means of that of the sample container in a multimode cavity.

In this paper, we provide a case study on a calibration approach describing the sample temperature estimation from the pyrometer records during microwave-heating processes in a multimode cavity. The sample temperature's mean value is estimated as a function of the container's surface temperature as detected by the pyrometer. Various thermal parameters have been considered to explain the errors that usually result from measuring the temperature of the container surface instead of that of the sample.

Materials and Methods

The materials under test (MUT) for the calibration tests were tap water and Peruvian quinoa (Chenopodium quinoa Willd) seeds, produced by Laboratorios Almond S.L. and commercially accessible at a well-known Spanish supermarket chain. The quinoa seeds had an apparent bulk density of 750 kg/m^3, with seed sizes ranging from 1 to 2 mm. Its moisture content was about 10%. In addition to their shape being quite homogenous, their properties have been widely studied: physical [11], thermal [12], and dielectric [13]. Hence, the drawbacks of monitoring temperature during microwave-heating processes of heterogeneous mixtures or high-microwave-absorbing materials are avoided.

Finally, ground-tire rubber (GTR) was the MUT for the evaluation of the calibration approach. It was kindly provided by Synthelast (Spain). Its bulk density is about 0.4 g/cm3, with granule sizes ranging from 0.5 to 1 mm. Its main components are those described in [4]: natural rubber (36%), carbon black (27%), synthetic rubber (22%), inorganic components (8.5%), additives and oil (6.5%). Due to its complex chemical composition, heterogeneous particle size, and temperature-dependent dielectric properties (thermal runaway may occur) [4], GTR is primarily used. In this way, the calibration approach can be evaluated using this worst-case scenario.

Microwave Processing Setup

Three metallic tubes (whose hollow diameters were 1.6 cm) were welded to the upper wall of the microwave cavity to act as by-passes for the connection of accessories and sensors. The lengths of the tubes (i.e., 14.5 cm) ensured a cut-off cylindrical waveguide, serving as microwave filters and preventing radiation leakage outward.

A motorized PTFE stirrer was used to provide a MUT's time-averaged temperature pattern as uniform as possible. As depicted in Figure 1, the stirrer shaft was passed through the central by-pass tube at a rotational speed of 5 rpm. An axial fan (Nidec Beta SL, D07R-12T2S4, Japan) with a maximum flowrate of 33.6 m^3/hour was used to extract the generated gases from the cavity through a drilled area (with holes of 2.5 mm in width) at the left side wall. The drilled cavity wall's flow rate rating was significantly decreased since the fan intake was attached to the outside of the wall.

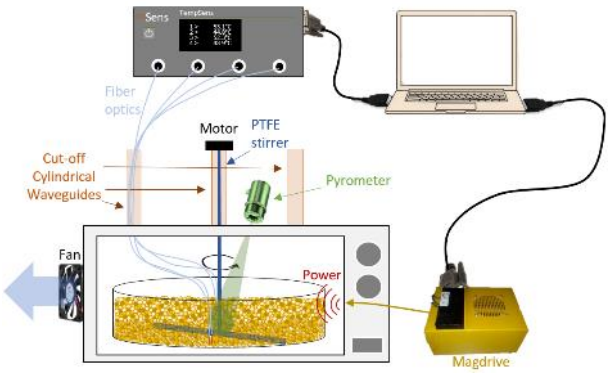

Fig. 1. Schematic diagram of the experimental system

A programmable power source (Dipolar AB, MagDrive 1000, Sweden) generated the microwave energy and supplied power to a 2.45 GHz, 1 kW-rated magnetron.

Temperature Monitoring

The MUT temperature was monitored using two OF sensors (OpSens, OTG-A, Canada) connected to a signal conditioner (OpSens, TempSens, Canada). The measurement accuracy for temperatures below and above 45°C is 0.3°C and 0.8°C, respectively. As shown in Figure 2, the sensor tips were positioned in contact with the MUT in diametrically opposed positions on the inside walls of the quartz container. This arrangement prevented measurement points from floating out of control and minimized the chance of damaging the sensors because of the twisting of the OF.

When gases arise from the sample, the use of pyrometers or infrared cameras to measure the MUT temperature from above is unreliable, as detailed in [14]. Hence, the pyrometer (CTLaser LT, Optris, Germany) was located behind the microwave oven. The pyrometer offers a measurement accuracy of 1°C or 1% for temperatures below and above 100°C, respectively. Its emissivity was set to 0.92 [15]. The pyrometer was pointing at the container through a by-pass tube with a diameter and a length of 1.6 cm and 4.5 cm, respectively. The container temperature was also registered by two OFs.

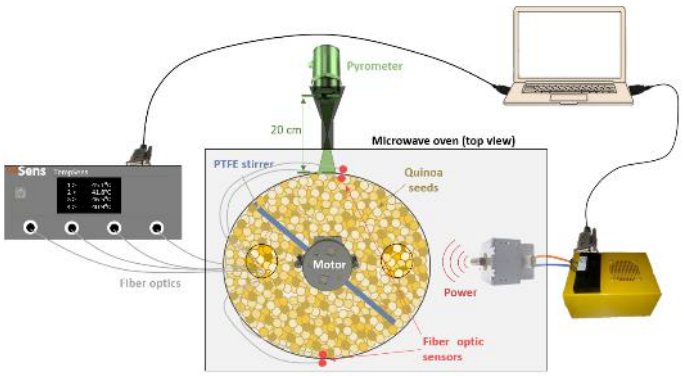

Fig. 2. Schematic diagram of the pyrometer and the fiber optic sensors positioning

The distance between the pyrometer and the container wall was 20 cm, and therefore, the surface of the container seen by the pyrometer had a diameter of 9 mm, according to the manufacturer's specifications.

Bulk Temperature Estimation

The data taken into consideration for the determination of the involved parameters corresponds to the cooling period, thus avoiding any data alteration due to the microwave irradiation.

Despite the fact that the pyrometer is pointing at the pyrex container, its temperature values can be different from those of the container. There are several reasons for that, the most important of which are misalignment, an imperfect emissivity value, error drift caused by ageing, and a partial obstruction of the pyrometer's vision. Thus, a parameter relating the pyrometer records and the temperature of the container wall was defined. It has been called the "vision level" (VL) and it is described in (1):

$$T_{pyro} - T_{env} = (T_{out} - T_{env}) \cdot VL \qquad (1)$$

where T_{pyro} is the temperature registered by the pyrometer, T_{env} is the environmental temperature (i.e., 24°C), T_{out} is the temperature of the container's outside wall, and VL is the vision level. The latter parameter was defined as a number comprised between 0 (the pyrometer is completely obstructed) and 1 (the pyrometer is registering the container temperature adequately) in order to rectify any type of error.

As a result of the sample heating, a heat flux (Q_T) is generated from the container's outer walls to its surroundings. The heat flux value can be mathematically determined by applying (2):

$$Q_T = h_T \cdot \Delta T_{out-env} = h_T(T_{out} - T_{env}) \qquad (2)$$

where Q_T is the heat flux from the sample outwards through the container wall ($W \cdot m^{-2}$), h_T is the convection factor ($W \cdot m^{-2} \cdot K^{-1}$), and $\Delta T_{out-env}$ is the temperature gradient between the container outside wall and the room temperature.

Some temperature differences are found between the container's inner and outer temperatures, given the heat flux generated as a consequence of the sample heating. This heat flux value can be determined by means of (3):

$$Q_T = k_{pyrex} \frac{\Delta T_{in-out}}{x} = k_{pyrex} \frac{(T_{in} - T_{out})}{x} \qquad (3)$$

where k_{pyrex} is the container's thermal conductivity (k_{pyrex} = 1.15 $W \cdot m^{-1} \cdot K^{-1}$) [16], ΔT_{in-out} is the temperature gradient between the container's inside (T_{in}) and outside (T_{out}) wall temperatures, and x is the thickness of the container wall (3.1 mm).

When heating water by applying electromagnetic energy, convection currents occur due to a difference in temperature (or density) between different regions within the same material, and therefore, the fluid is continuously moving. Energy is transferred from hotter areas to colder areas, and this process continues until total equilibrium is reached. Hence, convection currents are helpful to achieve a more homogenous temperature distribution.

However, convection current requires the presence of a fluid (liquid or gas). When working with granular material such as quinoa seeds, the solid's internal particles are fixed and immobile, making it impossible to detect a flow by variations in temperature or density. Hence, convection currents cannot be formed and the distance from the OF sensors to the container inner wall (x') needs to be known.

This distance is not easy to determine. Adhesive tape cannot be placed over the sensor tip, as it would not be consequently measuring the temperature of the MUT but that of the adhesive tape. In addition to that, the adhesive tape might be damaged as a consequence of the high temperatures, and therefore, the sensor tip will not be fixed. As a solution for that, the adhesive

tape was placed above the sample, as shown in Figure 3. Despite the fact that the OF sensors are well fixed, the exact location of the sensor tip is not yet determined.

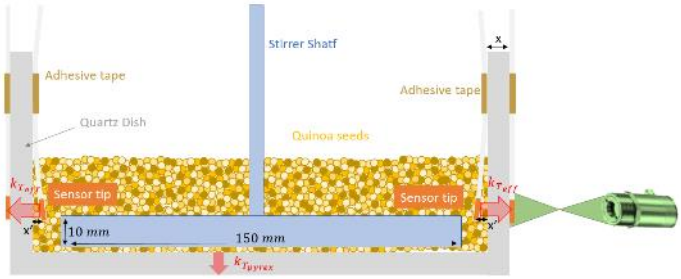

Fig. 3. Schematic diagram for the explanation of the influence of the OF sensors on the temperature measurements

From the MUT temperature measurement point to the outside, there are various layers of dielectrics (e.g., quinoa and pyrex) of different thermal conductivity. Thus, x' can be determined by considering that the heat flux must be equal in quinoa seeds and in pyrex at the interface between the layers, as shown in (4):

$$Q_T = k_{pyrex}\frac{\Delta T_{in-out}}{x} = k_{quinoa}\frac{\Delta T_{quinoa-in}}{x'} \qquad (4)$$

where k_{quinoa} is the thermal conductivity of quinoa (W·m^{-1}·K^{-1}), $\Delta T_{quinoa\text{-}in}$ is the temperature gradient between the quinoa and the inside container wall temperatures, and x' is the distance from the OF sensor to the container inside wall.
The thermal conductivity of quinoa (k_{quinoa}) was calculated as described by (5):

$$k_{quinoa} = \alpha \cdot \rho \cdot C_s \qquad (5)$$

where α is the thermal diffusivity of quinoa seed ($8\cdot10^{-8}$ m^2·s^{-1}) [17], ρ is its true density (1058 kg·m^{-3}) [11], and C_s is its specific heat capacity (J·kg^{-1}·K^{-1}), which is strongly influenced by temperature. In this contribution, a linear relation between the specific heat capacity of quinoa and its temperature is used, as described in [12] and shown in (6):

$$C_s = 20.9 \cdot T + 1046.3 \qquad (6)$$

where T is the quinoa temperature (°C). Regarding the GTR thermal conductivity, it is 0.15 W·m^{-1}·K^{-1} [18].

Transmitted Power Regimes

In all calibration testing, the power transmitted from the Magdrive power source to the magnetron was 900 W. Table 1 describes the microwave testing parameters: material used, objective parameter (i.e., parameter value to determine), power level employed, temperature reached, and sample mass. Independently of the material employed, some water vapour emanated during the tests.

Table 1. Parameters for the calibration tests.

Material	Objective parameter	Number of tests	Power (W)	Temperature reached (°C)	Mass (g)
Water	VL and h_T	3	900	90	1000
Quinoa	x'	3	900	110	600

As the gases can hinder the pyrometer, the maximum temperature during the test was adjusted to minimize the appearance of water vapour. Another restriction was the sample mass, as the sample must cover at least the height required for the pyrometer to adequately monitor the container temperature.

Regarding the test conducted for the evaluation, different power levels were transmitted to the magnetron, as described in Table 2. It must be noted that very long tests (longer than 20 minutes) were avoided as some power transmission troubles were found. Consequently, the maximum temperature for tests employing water varies.

Table 2. Parameters for the evaluation tests.

Material	Number of tests	Power (W)	Temperature reached (°C)	Mass (g)
Water	1	300	72	1000
	1	600	87	1000
	1	900	94	1000
Quinoa	1	300	110	600
	1	600	110	600
	1	900	110	600
GTR	1	300	110	300
	1	600	110	300
	1	900	110	300

Results and Discussion

Calibration Procedure

The data employed for the determination of the VL and the convection coefficient corresponds to the cooling period during the tests with water.

The container wall outside temperature versus the pyrometer-registered temperature of water are shown in Figure 4 (left) for a temperature range comprised between 27 and 90°C, as well as the data fit from equation (1). In Figure 4 (right), one can see both the container wall's inside and outside temperatures. The optimum value for the convection factor (h_T) was obtained by employing equations (2) and (3).

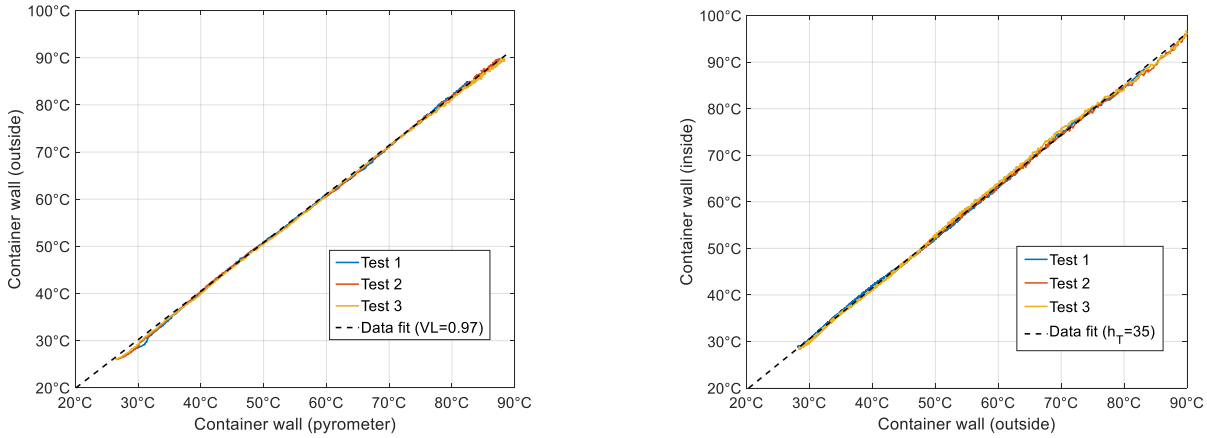

(a) (b)

Fig. 4. Temperature data for the convection factor determination.

The optimum values used to fit the experimental data as well as the root mean square error (RMSE) and the coefficient of determination (R^2) are detailed in Table 3.

Table 3. RMSE and R^2 for the VL and the convection coefficient estimations.

From	To	Parameter	Value	Test	RMSE	R^2
Pyrometer	Container wall (outside)	VL	0.97	1	0.55	0.9990
				2	0.40	0.9996
				3	0.48	0.9993
Container wall (outside)	Container wall (inside)	h_T	35	1	0.29	0.9995
				2	0.37	0.9993
				3	0.45	0.9991

The next step consists of the determination of the x' value. For that purpose, the data corresponding to the cooling period during the tests with quinoa seeds was taken into consideration. Figure 5 shows the container's inside wall temperature dependence on the bulk temperature of quinoa. The data fitting obtained using equation (4) is also shown.

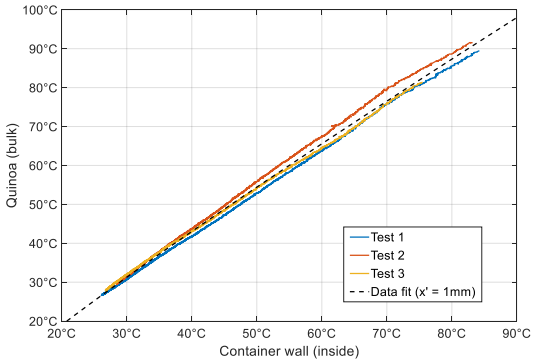

Fig 5. Quinoa bulk temperature versus container inside wall temperature.

Despite the fact that some differences between the data from different tests are observed (mainly due to a not completely homogenous temperature distribution), the data fitting shows a good agreement for the work temperature range. Table 4 describes the value for *x'* employed for the experimental data fitting, the RMSE, and the R^2 values obtained.

Table 2. *RMSE and R^2 values for the x' estimation.*

From	To	x' (mm)	Test	RMSE	R^2
Container wall (inside)	Bulk	1.0	1	1.06	0.9958
			2	1.37	0.9937
			3	0.65	0.9979

Evaluation

Three tests employing water were conducted to evaluate the optimum values determined for VL and the convection coefficient. The water temperature monitored by the OF sensors over time is shown in Figure 6. The temperature corrections obtained after applying equations (1) and (2) are also shown. The 900 W-powered test length is shorter than expected (1200 s), as steam hindered the pyrometer.

Small differences are observed between the experimental data and the values after the correction. As a general trend, estimated values tend to be a bit lower than experimental ones. Despite the fact that an anomalous behaviour is found for the test transmitting 300 W during heating (i.e., in the initial stage, the temperature increment velocity is lower than that at the heating final stage), the pyrometer seems to be useful for the temperature estimation.

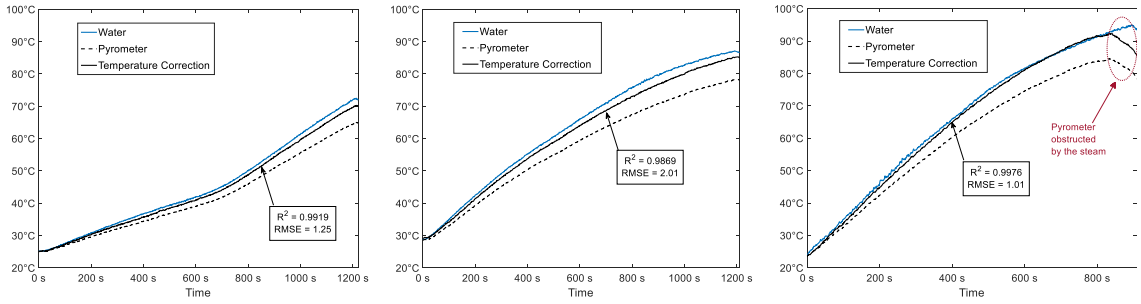

(a) (b) (c)

Fig. 6. Water temperature over time for the evaluation tests at different power levels: (a) 300 W; (b) 600 W; (c) 900 W

For a better understanding of the error committed when estimating the temperature, the error is shown in Figure 7, as are both the actual and estimated heat fluxes. The error strongly increased at the beginning of the tests, as can be easily observed in the 900W-rated test. Regarding the heat fluxes, the estimated values are lower than the actual ones. The actual heat flux continues growing until the water begins to evaporate, that is, until the pyrometer temperature reaches near 70°C. Thus, the estimated values are approaching those of the actual heat flux as a consequence of its decline.

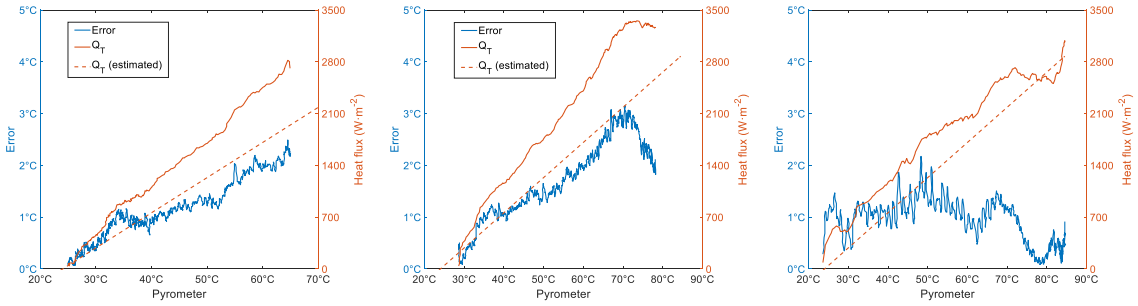

(a) (b) (c)

Fig. 7. Temperature estimation error and heat flux versus pyrometer temperature for the evaluation tests with water at: (a) 300 W; (b) 600 W; (c) 900 W

There are two main reasons to explain the error. First, the fact that the pyrex offers a low thermal conductivity can delay the measurement of thermal effects in the sample. The other significant limitation is due to the air inside the cavity, which remains cool (at room temperature), thereby causing a decrease in the surface temperature of the sample container and resulting in temperature gradients during microwave heating. As a result, the pyrometer's measurement of the surface temperature of the pyrex container cannot be considered representative of the sample temperature, at least, at the beginning of the heating process. A different situation is found later, when evaporation starts, as both estimated and actual heat fluxes offer similar values, and therefore, the temperature error is close to zero.

Figure 8 shows the bulk temperature of the quinoa seeds, as well as both the pyrometer records and its temperature correction. In this case, temperature values after the correction were much lower than those of the MUT. It must be noted that the estimated temperature was very near the MUT temperature during the final stage of the tests, with the exception of the 900W-rated test. It seems that a higher amount of water vapour emanated during that test.

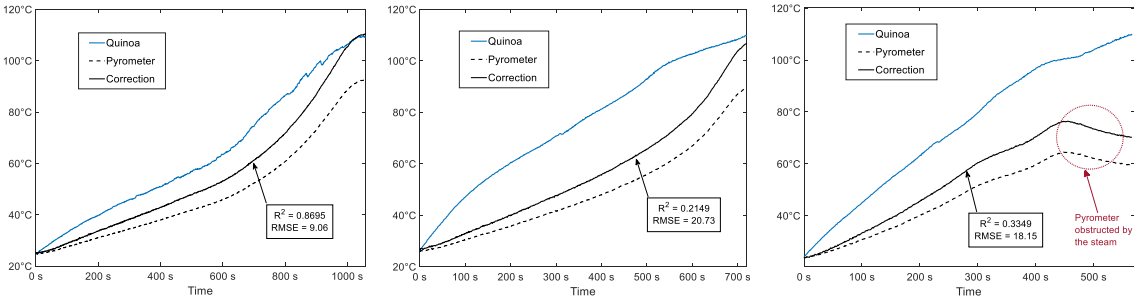

(a) (b) (c)

Fig. 8. Quinoa temperature during the evaluation tests: (a) 300 W; (b) 600 W; (c) 900 W

Despite the fact that both the thermal conductivity of quinoa and the distance from the temperature measurement point to the container inner wall were considered, the differences between the quinoa temperature values and those estimated are quite higher than those observed when employing water. Thus, the RMSE and R^2 values are quite poor for the temperature corrections during the heating period.

The error committed due to the temperature estimation using quinoa seeds, the actual heat flux, and the estimated heat flux can be observed in Figure 9. The error increment was significant at the beginning of the test, especially in the tests transmitting higher power levels (i.e., 600 W and 900 W). The estimated heat flux values are much lower than the actual ones. From about 60°C for the pyrometer, the fact that moisture content in quinoa seeds begins to evaporate can be seen in the heat flux behaviour; it starts to decline. From that moment on, the values of the estimated and actual heat fluxes are consequently more similar.

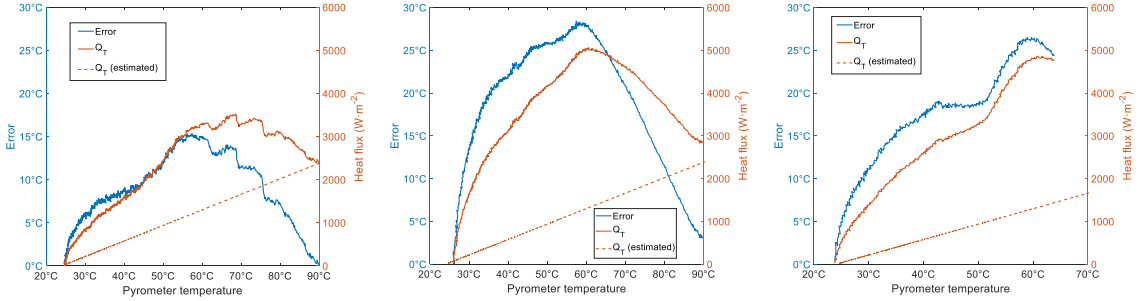

(a) (b) (c)

Fig. 9. Temperature estimation error and heat flux versus pyrometer temperature for the evaluation tests with quinoa seeds at: (a) 300 W; (b) 600 W; (c) 900 W

The delay in the bulk temperature measurement leads to a significant error when estimating the temperature, as explained before. However, this error was rather low for the 300 W test. Despite the fact that the pyrometer's records are not representative of the sample temperature at the beginning of the heating process, smaller temperature errors were observed once evaporation started. Nevertheless, the appearance of water vapour can partially blind the pyrometer, as occurred for the test with the highest power level.

The GTR temperature, the pyrometer records, and the temperature correction can be seen in Figure 10. One can observe that, after the correction, the estimated temperature is still lower than that of the GTR. Nonetheless, these values were near the MUT ones at the final stage of the test employing the lowest power level. Regarding the 600 W and 900 W-rated tests, a larger GTR temperature increase as well as a decrease in the pyrometer temperature records are observed at the end. It seems that some hotspots were generated, thereby emanating some gases that hindered the pyrometer.

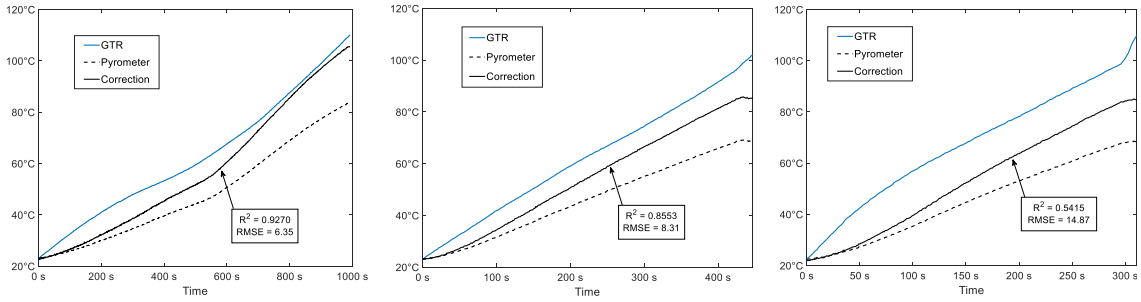

(a) (b) (c)

Fig. 10. GTR temperature during the evaluation tests: (a) 300 W; (b) 600 W; (c) 900 W

There is a significant difference between the GTR and the estimated temperature values. Furthermore, this difference seems to be higher with higher power levels, as indicated by the RMSE and R^2 values.

The difference in value between the GTR and the estimated temperatures (i.e., error) when using the GTR, as well as the heat flux and the estimated one, are depicted in Figure 11. As seen before with quinoa seeds, the error increments significantly at the beginning of the tests, and the actual heat flux values are significantly higher than the estimated ones. From the tests delivering 600 W and 900 W, a strong increase in the temperature error can be observed at the end of the experiments. Allegedly, the fact that some hotspots in the GTR sample appear can lead to thermal runaway and the appearance of gases, i.e., the GTR temperature strongly increases [4] while the pyrometer readings start to degrade [14].

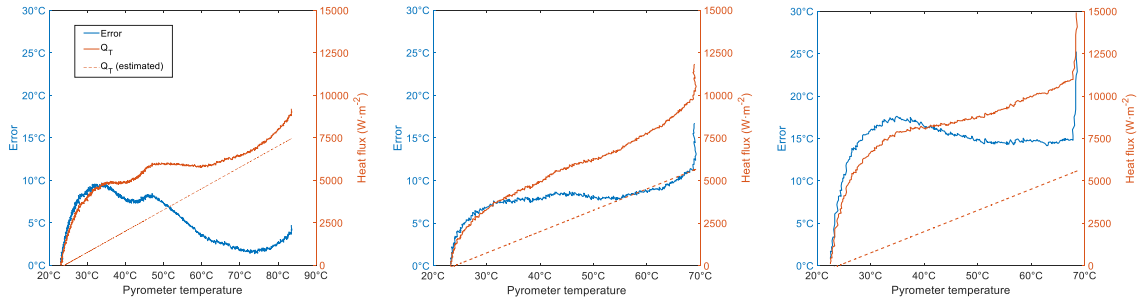

(a) (b) (c)

Fig. 11. Temperature estimation error and heat flux versus pyrometer temperature for the evaluation tests with quinoa seeds at: (a) 300 W; (b) 600 W; (c) 900 W

The error when estimating the temperature, mainly due to the delay in the bulk temperature measurement, was higher as higher power levels were employed. If some chemical processes happen, the temperature estimation is seriously affected, as seen at the end of the tests using GTR. Although similar GTR temperatures were reached, the temperature estimation was not affected during the 300 W test. A possible reason is that a homogeneous temperature distribution is achieved when using lower power levels, thereby avoiding hot spots.

Conclusions

In this study, a calibration approach for the microwave processing in a multimode oven was presented by measuring the sample temperature with two OF sensors and the container temperature with another two OF sensors and a pyrometer. During the process, the quinoa seeds were continuously agitated with a PTFE stirrer. Although only one power level was used for the calibration tests, three power levels were employed for the evaluation experiments.

In the initial stage of the experiments, the estimation of the bulk temperature became inaccurate, especially for high relative power levels, due to the delay time for the sample temperature increment to be reflected by the container surface and consequently acquired by the pyrometer. Nonetheless, the bulk temperature estimation becomes appropriate for single bulk

temperatures, or even for a certain bulk temperature range, provided that the heat flux increment with respect to the pyrometer temperature is linear.

Some water vapour was emanated during the experiments. Although the steam was extracted from the cavity, it hindered the pyrometer's vision for the test with the highest power level, as easily observed in the evaluation tests with quinoa seeds. The more power is transmitted, the more cold and hot spots are generated. As a result, the amount of water vapour (or other gases) will increase, even obstructing the pyrometer readings if the gas extraction level is not high enough. Thus, in order to achieve better temperature uniformity and avoid the pyrometer obstruction, it seems advisable to employ low relative power levels.

It must be emphasized that the discussion on appropriate temperature monitoring herein has been restricted to determining the bulk temperature. Some complications may arise if the sample is strongly microwave-absorbing [7], if its complex permittivity values vary significantly with increasing temperatures (e.g., ground-tire rubber [4]), or when the chemical reactions occurring during the microwave processing are endothermic, thus requiring an extensive calibration procedure [19].

Special attention should be paid if some chemical processes take place during the microwave-heating process, as observed during the experiments using GTR. Chemical changes in the material may imply meaningful variation in its temperature, and therefore the estimation error might be inaccurate. Furthermore, some gases may emanate and partially obstruct the pyrometer. As a result, the pyrometer temperature would be decreasing whereas the bulk temperature would be rapidly increasing.

This research will contribute to a better understanding of bulk temperature estimation during microwave treatment of liquids or granular materials with mechanical stirring. Furthermore, the calibration approach presented in this paper can help determine some thermal parameter values affecting the heating performance, thereby enhancing further simulation of dielectric heating.

References

[1] E. T. Thostenson and T. W. Chou, Microwave processing: fundamentals and applications, Compos. Part A Appl. Sci. Manuf., vol. 30, no. 9, pp. 1055–1071, 1999. DOI: 10.1016/S1359-835X(99)00020-2.
[2] D. E. Clark, D. C. Folz, and J. K. West, Processing materials with microwave energy, MSEng.: A, 287(2), 153-158, 2000. DOI: 10.1016/S0921-5093(00)00768-1
[3] S. Singh, D. Gupta, V. Jain, and A. K. Sharma, Microwave processing of materials and applications in manufacturing industries: A Review, Mater. Manuf. Process., vol. 30, no. 1, pp. 1–29, 2015. DOI: 10.1080/10426914.2014.952028.
[4] R. Pérez-Campos, et al., Dynamic Permittivity Measurement of Ground-Tire Rubber (GTR) during Microwave-Assisted Devulcanization, Polym. J., vol. 14, no. 17, pp. 3543, 2022. DOI: 10.3390/polym14173543
[5] J. M. Catalá-Civera, et al., Dynamic measurement of dielectric properties of materials at high temperature during microwave heating in a dual mode cylindrical cavity, IEEE Trans. Microw. Theory Tech., vol. 63, no. 9, pp. 2905-2914, 2015. DOI: 10.1109/TMTT.2015.2453263
[6] D. Obermayer, and C. O. Kappe, On the importance of simultaneous infrared/fiber-optic temperature monitoring in the microwave-assisted synthesis of ionic liquids, Org. Biomol. Chem., vol. 8, no. 1, pp. 114-121, 2010. DOI: 10.1039/B918407D
[7] C. O. Kappe, C. O. How to measure reaction temperature in microwave-heated transformations, Chem. Soc. Rev., vol. 42, no. 12, pp. 4977-4990, 2013. DOI: 10.1039/C3CS00010A
[8] C. O. Kappe, B.Pieber, and D. Dallinger, Microwave effects in organic synthesis: myth or reality?, Angew. Chem. Int. Ed., vol. 52, no. 4, pp. 1088-1094, 2013. DOI: 10.1002/anie.201204103
[9] B. García-Baños, et al., Temperature assessment of microwave-enhanced heating processes, Sci. Rep., vol. 9, no. 1, pp. 1-10, 2019. DOI: 10.1038/s41598-019-47296-0
[10] T. Durka, et al., On the accuracy and reproducibility of fiber optic (FO) and infrared (IR) temperature measurements of solid materials in microwave applications, Meas. Sci. Technol., vol. 21, no. 4, pp. 045108, 2010. DOI: 10.1088/0957-0233/21/4/045108
[11] C. Vilche, M. Gely, and E. Santalla, Physical properties of quinoa seeds, Biosyst. Eng., vol. 86, no. 1, pp. 59-65, 2003. DOI: 10.1016/S1537-5110(03)00114-4
[12] O. Uncu, O. S. Jolayemi, and S. Unluturk, Evaluation of rheological, textural and thermal properties of quinoa (Chenopodium quinoa Willd) based breakfast puree, Int. J. of Food Process. Technol., vol. 4, no. 2, 2017. DOI: 10.15379/2408-9826.2017.04.02.01
[13] R. Pérez-Campos, J. Fayos-Fernández, and J. Monzó-Cabrera, Permittivity measurements for raw and boiled quinoa seeds versus temperature, bulk density, and moisture content, CRFS, vol. 6, pp. 100528, 2023. DOI: 10.1016/j.crfs.2023.100528
[14] R. Pérez-Campos, et al., "Improved control on the microwave devulcanizing of ground tire rubber by means of sulphur gas sensors," AMPERE 2021, 2021, pp. 146-153. DOI: 10.5281/zenodo.5378213
[15] The Engineering Toolbox (2003) Emissivity Coefficients common Products. [Online]. Available: https://www.engineeringtoolbox.com/emissivity-coefficients-d_447.html
[16] D. Muñoz Codorníu, "Medida de la conductividad térmica de materiales porosos (grafeno/cerámicas) usando una cámara termográfica," 2019, Universidad Politécnica de Madrid, Madrid, Spain, Jun. 2019.
[17] N. L. Huamán Castilla, et al., Efecto del contenido de humedad y temperatura sobre la difusividad térmica en granos andino, Revista SQP, vol. 82, no. 3, pp. 259-271, 2016.
[18] M. Gschwandl, et al., "Thermal conductivity measurement of industrial rubber compounds using laser flash analysis: Applicability, comparison and evaluation," In Proc. AIP, 2019, vol. 2065, no. 1, pp. 030041. DOI: 10.1063/1.5088299
[19] J. M. Serra, et al., Hydrogen production via microwave-induced water splitting at low temperature, Nat. Energy, vol. 5, no. 11, pp. 910-919, 2020. DOI: 10.1038/s41560-020-00720-6

Measurement of Dielectric and Thermal Properties of Materials under Microwave Heating

J. R. Sánchez[1], B. Garcia-Baños[1], J. D. Gutiérrez-Cano[1], P. J. Plaza-González[1]

[1]*ITACA Institute, Universitat Politècnica de València, Camino de Vera, 46022, Valencia, Spain. juasncm1@upv.es*

Keywords: dielectric properties, thermal properties, microwave heating, calorimetry.

Microwave heating has emerged as an important technology given its ability to provide sustainable and efficient electrification of the industry [1]. Compared to traditional fossil fuel based heating methods, microwaves present rapid heating, reduce energy consumption, and produce no greenhouse gas emissions. The successful implementation of microwave heating processes requires the investigation of the thermal behaviour of the materials under intense microwave fields to predict the actual amount of heat released or absorbed by the samples.

Thermal analysis (TA) is a technique used to study the physical and chemical properties of materials as a function of temperature. There are different methods of thermal analysis, including differential scanning calorimetry (DSC), thermogravimetric analysis (TGA), and differential thermal analysis (DTA).

Microwave Thermal Analysis (MWTA) employs microwaves to rapidly heat and measure the thermal properties of materials. MWTA offers several advantages over traditional TA methods such as faster heating rates, accuracy, and the ability to analyze the interaction of microwaves with materials under study [2,3]. This is of particular interest since microwaves can enhance reaction rates and thermal transformation in materials. While these methods have proven to be effective in several applications, they are limited to provide differential measurements, which involve comparing the thermal properties of different materials to identify differences in their thermal behavior.

To address these limitations, a new method for simultaneous quantitative measurement of temperature-dependent dielectric and thermal properties (MW-DETA) through microwave processing is described in this work. Quantitative results require an accurate analysis of the power balance within the cavity. This information is critical for determining the material's specific heat and to provide the efficiency and effectiveness of the thermal process.

The measurement of the dielectric properties is crucial for discerning the power balance in the cavity. Specifically, the proposed method, based on the cylindrical microwave reactor proposed by [4], is able to measure the dielectric properties of the samples under study as a function of the temperature, assessing the fraction of the input microwave power absorbed by the sample, as well as the portion that is dissipated in the metallic walls of the reactor.

The diagram displayed in Fig. 1 illustrates the power balance of the entire process of microwave heating, necessary to ensure accurate thermal measurements. The microwave power fed into the cavity (absorbed power) is divided into dielectric power and metallic wall losses depending on the dielectric properties of the material. The net power is the difference between the dielectric power and the power lost through conduction, convection, and radiation (thermal losses). The combination of wall losses and thermal losses determines the total losses experienced within the cavity (total losses).

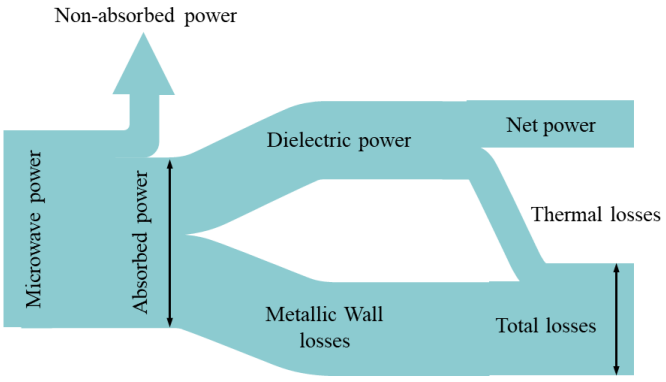

Fig. 1. Power distribution during the heating process.

As an illustrative example of the efficacy of the MW-DETA method, microwave heating experiments were conducted on ceramic materials. In this regard, Macor was selected as the Material Under Test (MUT) due to its ability to withstand temperatures above 400°C without undergoing any significant alterations in its properties. MW-DETA capabilities are assessed by comparing the specific heat of Macor obtained using the described method and conventional DSC. The results

presented in Fig. 2 demonstrate a good agreement between the two methods, indicating that MW-DETA provides highly satisfactory results of quantitative measurements of thermal parameters.

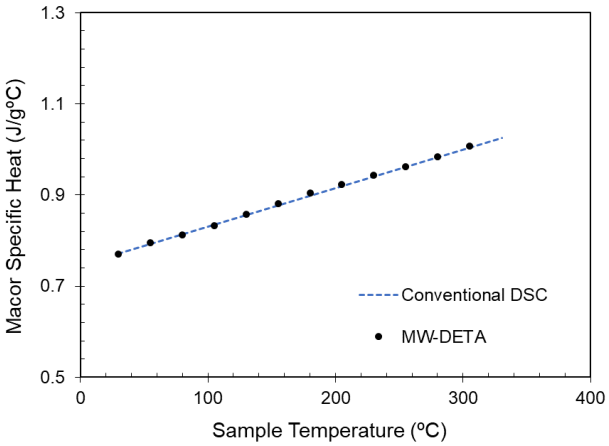

Fig. 2. Evaluation of the developed Microwave Method.

In conclusion, a fast method for determining the dielectric and thermal properties of a material sample as a function of temperature by microwave heating has been described. This approach offers a powerful and versatile tool for analyzing how the energy is distributed, enabling the assessment of the efficiency of microwave systems. This can unlock the full potential of microwave heating technology in industrial applications, from food processing to materials science.

References

[1] J. M. Serra et al., "Hydrogen production via microwave-induced water splitting at low temperature," Nature Energy, vol. 5, no. 11, pp. 910–919, 2020.
[2] P. K. Gallagher, Handbook of Thermal Analysis and Calorimetry, 1st ed. Amsterdam: Elseiver, 2008.
[3] E. Karmazsin, R. Barhoumi, P. Satre, and F. Gaillard, "Use of Microwaves in Thermal Analysis," Journal of Thermal Analysis, vol. 30, pp. 43-47, 1985.
[4] J. M. Catalá-Civera, A. J. Canós, P. Plaza-González, J. D. Gutiérrez, B. García-Baños, and F. L. Peñaranda-Foix, "Dynamic Measurement of Dielectric Properties of Materials at High Temperature during Microwave Heating in a Dual Mode Cylindrical Cavity," IEEE Trans Microw Theory Tech, vol. 63, no. 9, pp. 2905–2914, Sep. 2015, doi: 10.1109/TMTT.2015.2453263.

Novel Test Fixture for the Temperature-Dependent Dielectric Characterization of Lossy Food Products at RF

J. D. Gutiérrez-Cano[1], J. R. Sánchez[1], B. García-Baños[1], J. M. Catalá-Civera[1]

[1]*Instituto ITACA, Universitat Politècnica de València, Camino de Vera s/n, 46022, Valencia, Spain*
jdgutierrez@itaca.upv.es

Keywords: radiofrequency, coaxial probe, dielectric measurements, food products, lossy materials.

Radiofrequency (RF) and microwave energy are becoming increasingly popular in industrial processes such as drying, curing, and material processing. These technologies have demonstrated the ability to improve efficiency, reduce processing times, lower operational costs, and enhance product quality [1]. Their potential to deliver these benefits makes them promising and appealing candidates for future industrial applications, paving the way for a more sustainable and efficient industry. In particular, food science and industries have been early adopters of RF and microwave technologies due to their ability to provide rapid, high-quality food products while maintaining their nutritional and sensory properties [2][3].

Permittivity is a physical property that describes how a food material responds to electromagnetic radiation [4], and it plays a crucial role in developing RF and microwave heating applications. Permittivity is a variable quantity that is primarily influenced by frequency and temperature. To ensure the trustworthiness of permittivity data, it is essential to choose a measurement method that considers the dependencies of permittivity and the material's state. While permittivity data for food products at microwave frequencies is extensive, data at RF is still scarce. Given the unique properties of lossy food materials at RF, developing new measurement cells is still needed to advance our understanding of food behaviour at these frequencies.

This work presents a measurement setup for the temperature-dependent dielectric characterization of food products at RF frequencies. The proposed design employs an open coaxial cell of suitable dimensions to enhance measurement accuracy at RF. The cell is placed at the bottom of a pressure-proof stainless-steel cylindrical vessel that houses the food material.

To guarantee a consistent operation within the temperature range of up to 120ºC, specific components of the test fixture necessitated a tailored design. The coaxial bead was made of a material with a stable dielectric response and negligible coefficient of linear thermal expansion. The coaxial cell was connected to a coaxial line with a built-in heat sink to cool and protect the connection to the VNA, thereby reducing calibration drifts. The setup includes a metallic piston to seal the cylindrical vessel able to withstand the pressure at elevated temperatures and prevent the formation of air bubbles. Additionally, the vessel was covered with rock wool to provide thermal insulation and mitigate potential hazard risks associated with the setup operation.

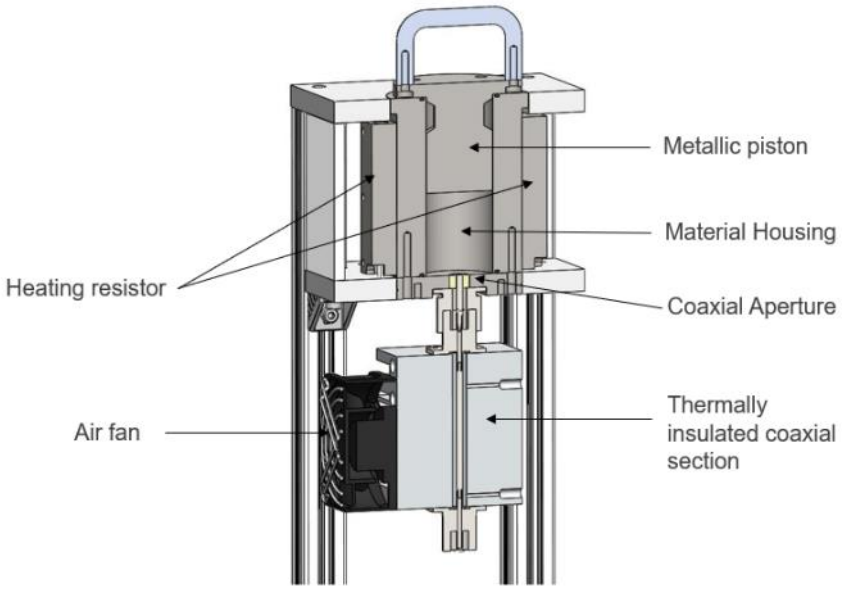

Fig. 1. Schematic view of the test fixture.

Circuit analysis and mode-matching techniques [5] were employed to model the cell's response, optimize its dimensions for maximum sensitivity, and calculate permittivity from the reflection coefficient measurements. Unlike conventional methods

that rely on calibration with known materials, this analysis accounted for the complete measurement setup, avoiding the need for such calibration measurements. At RF, the probe covered an area of the Smith chart six times larger than the smaller coaxial cells typically used to perform permittivity measurements at these frequencies in the literature [6][7]. This result demonstrates the accuracy enhancement provided with this approach for permittivity characterization at RF, also rigorously evaluated and confirmed with a comparative uncertainty study.

The test fixture was employed to determine the temperature-dependent permittivity of commercial food samples at the ISM frequency of 40.68 MHz. The results proved the significant influence of the ionic content and temperature on the permittivity results at these frequencies.

These findings suggest that the use of larger probes has the potential to improve the overall accuracy and reliability of permittivity measurements of lossy food products at RF, which could also have practical applications in other scientific and industrial fields.

References

[1] Komarov, V. V., "A review of radio frequency and microwave sustainability-oriented technologies," *Sustainable Materials and Technologies*, 2021, vol. 28, p. e00234.
[2] Rincon, Angela M., Singh, Rakesh K., and Stelzleni, A. M.. "Effects of endpoint temperature and thickness on quality of whole muscle non-intact steaks cooked in a radio frequency oven," *LWT-Food Science and Technology*, 2015, vol. 64, no 2, p. 1323-1328.
[3] Li, R., Kou, X., Cheng, T., Zheng, A., & Wang, S.. "Verification of radio frequency pasteurization process for in-shell almonds," *Journal of Food Engineering*, 2017, vol. 192, p. 103-110.
[4] Piyasena, P., Dussault, C., Koutchma, T., Ramaswamy, H. S., and Awuah, G. B., "Radio frequency heating of foods: principles, applications and related properties—a review," *Critical reviews in food science and nutrition*, 2003. vol. 43, no 6, p. 587-606.
[5] Penaranda-Foix, F. L. and Catala-Civera, J. M., "Circuital analysis of cylindrical structures applied to the electromagnetic resolution of resonant cavities," in *Passive Microwave Components and Antennas*, Vitaliy Zhurbenko, Ed., IntechOpen, 2010, p. 141-168.
[6] Guo, W., Wu, X., Zhu, X., & Wang, S., "Temperature-dependent dielectric properties of chestnut and chestnut weevil from 10 to 4500 MHz," *Biosystems Engineering*, 2011, vol. 110, no 3, p. 340-347.
[7] Zhu, Z., & Guo, W.. "Frequency, moisture content, and temperature dependent dielectric properties of potato starch related to drying with radio-frequency/microwave energy," *Scientific reports*, 2017, vol. 7, no 1, p. 9311.

Measuring of Process-Dependent Temperature Distribution in Bricks During Drying with Intermittent Microwaves Using Distributed Fibre-Optical Sensors

M. Ganß[1], R. Wagner[1], A. Tretau[1], N. Vorhauer-Huget[2], L. Briest[2], E. Tsotsas[2]

[1]*Materials Research and Testing Institute at the Bauhaus-University Weimar, Coudraystr.9, 99423 Weimar, Germany*
[2]*Thermal Process Engineering, Otto von Guericke University Magdeburg, Magdeburg, Germany*
ralf.wagner@mfpa.de

Keywords: microwave, brick, distributed fibre-optical sensors, temperature profile

Microwave technology is an important building block for electrifying drying processes for building materials like bricks. In former studies [1, 2] we showed that bricks with smaller geometry could be successfully dried without geometry deformations and cracks using an intermittent microwave process. For bricks with geometric dimensions larger than the penetration depth of the microwave, it becomes difficult to reach the core of the brick and to achieve a uniform energy input for the drying process due to shielding. In the present contribution, we discuss the influence of different power inputs on the temperature and drying behaviour of larger vertically perforated bricks using distributed fibre-optical sensors.

For the investigation of the effect of different power inputs on the temperature and drying behaviour, two experiments with constant and intermittent settings were carried out. A stepwise increase of the power input was carried out in test S. One intermittent cycle always remained the same duration at 95 s. The microwave energy during drying was varied by increasing or decreasing the pulse duration within the cycle. In experiment K - constant, the pulse duration was always 15 s, while in experiment H more microwave energy was irradiated by a pulse duration of 40 s. The microwave energy was then reduced by decreasing the pulse duration.

The temperature evaluations in the bricks were carried out using distributed, fibre-optic sensors in combination with a coherent frequency-domain reflectometer (ODiSI B, LUNA Innovations Incorporated, USA). The optical glass fibres with polyimide coating had a length of approx. 3 m and a diameter of 150 µm. A thin Teflon capillary served as a guiding aid and decoupling mechanism.

The samples used in the tests were vertically perforated bricks (HLZ), which were freshly extruded in a factory. When wet, the width of the HLZ was 52 cm and the depth 15 cm. For installation in the test chamber, the height of the HLZ was shortened to about 20 cm. At an initial moisture content of about 26.5 % (ATRO), the mass of the samples was between 15.3 kg and 16.0 kg.

The sensor fibres were placed in different measuring sections through the HLZ. The fibres were applied in four horizontal profiles, each passing through a continuous bar and the adjacent chambers. Details can be seen in Figure 1. Table 1 lists the respective measuring sections of the experiments.

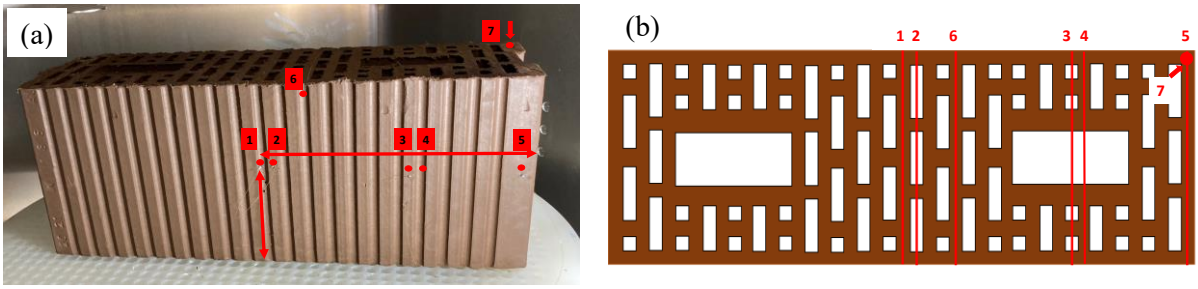

Fig. 2. (a) HLZ sample of experiment was placed in the microwave with the openings facing upwards. The numbers show the placement of the measuring sections. (b) Sketch of the measuring sections as seen from above.

Table 1. Position of the temperature profiles and which ones were realised in the respective experiments (yes = x).

Line	1	2	3	4	5	6	7
Label	Middle	Bar			Side	Top	Edge
Height [cm]	11.2	11.2	10.5	10.5	10.5	19.0	
Width [cm]	26.7	25.2	11.5	10.0	1.0	22.0	

Exp. K- konstant	X	X	X		X	X	
Exp. S - steigend	X	X	X	X	X		
Exp. H - hoch	X	X	X	X			X

The temperature profiles i.e. temperature versus sensor position for different process times measured with the fibre-optical sensors in Figure 2 reveal that with this sensor technique, it was possible to measure temperatures in the bricks with a spatially resolution of approx. 0.65 mm and with acquisition rate of 5 Hz.

The temperature profiles show almost constant temperatures in both measuring sections (line 1, middle and line 5, side) in the beginning of drying with even higher moisture contents in the material (compare the temperature profiles at time t = 60 min and t = 150 min in Figure 2a and b). The extension of the pulse duration after t = 150 min and the associated higher energy input leads to the formation of an inhomogeneous temperature profile in the outer part of the brick (line 5), as shown by comparison of the temperature profile at of t = 205 min. In the temperature profile of 'line 5-side', the higher values are in the area around 2 cm distance from the side. In contrast, higher temperature values are found in the measurement section 'line 1-middle' in the centre of the profile. In general, the temperatures in the process increase with the process time. With advanced drying, temperatures above 110 °C could be observed in the HLZ without destroying the brick or even forming significant cracks.

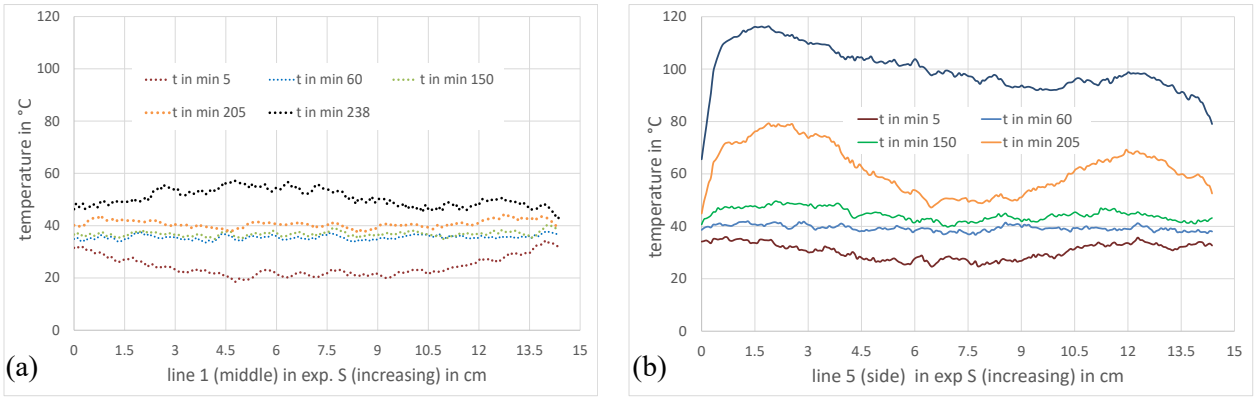

Fig. 3. Temperature profiles at different times in the measuring sections (a) 1-middle and (b) 5-side in the experiment S (increasing)

In summary, the investigations clearly illustrate the advantages of using distributed fibre-optical sensors for measuring the temperature profiles during intermittent microwave processes. A better temperature evaluation can be realized using spatial resolved sensor data for this new drying process technology, which allows a better understanding, and therefore better control of the process. The sensor data can be further used for the validation and development of numerical models for the process design. For the first time a complete temperature profile was measured and a shielding process was proven during the microwave drying of bricks with complex geometries.

References

[1] L. Briest, N. Vorhauer, A. Tretau, R. Wagner, E. Tsotsas (2022) "Microwave drying of wet clay in pilot-scale plant" 22nd International Drying Synposium
[2] L. Briest, A. Tretau, R. Wagner, E. Tsotsas, N. Vorhauer (2022) "Microwave-assisted drying of clay roof tiles" *Drying Technology* vol. 40 (9)
[3] D. Samiec (2011) "Verteilte faseroptische Temperatur- und Dehnungsmessung mit sehr hoher Ortsauflösung" *Photonik*, vol.6 (34)
[4] D. Wada, J-I. Sugiyama, H. Zushi, H. Murayama (2015) "An optical fiber sensing technique for temperature distribution measurements in microwave heating" *Measurement Science and Technology*, vol 26, p. 5105-5112

Precipitation and Fog Monitoring Based on Microwave Link

B. H. Kwon[1], D. I. Seo[2], Z. Seo[1], G. M. Lee[1], H. Bae[1]

[1]*Depatment of Environmental Atmospheric Sciences, 45 Yongso-ro Nam-gu, Busan, Korea*
[2]*Nature Info, 05838 Y-7116 Chungmin-ro 66, Songpa-gu, Seoul, Korea*
bhkwon@pknu.ac.kr

Keywords: microwave, attenuation, quantitative precipitation estimation, mean path average, noise level

Rainfall monitoring is commonly conducted using rain gauge networks in conjunction with weather radar networks. It is hard to install and maintain a number of rain gauges, and weather radar is an expensive alternative. On the other hand, as the number of microwave network links for communication are increasing, the rainfall estimation based on the microwave link will be a very useful alternative technology in many countries.

Novel methods for detecting rainfall, estimating near-ground level rainfall and improving the accuracy of near-ground rainfall with X-band radar attenuation correction were developed over commercial microwave links operated by Korea Telecom. The commercial microwave links (ML) with relatively low frequencies from 6 to 8 GHz were operated along path lengths ranging from 5.7 to 37.4 km traversing the city of Seoul, Korea in urban areas, one of the rainfall observation blind spots [1,2].

Rainfall detection using rain-induced attenuation was validated by rain detectors, and the results confirmed that microwave links can be used to detect rainfall with an accuracy of ≥ 90%. The mean bias of the path-averaged rainfall rate, as compared to the rainfall rate from ground rain gauges, was between -3 and 1 mmh^{-1}. We confirmed that microwave links operating at frequencies of 6-8 GHz have the potential to provide an alternative rainfall monitoring technique that can be useful in undeveloped nations that need economical surveillance of rainfall.

The correlation coefficient between microwave-link-based rainfall rate and rain gauge rainfall rate was more than 0.9 and mean error was 0.7 mmh^{-1}. The correlation coefficient between radar-based rainfall rate and rain gauge measurement was 0.5 to 0.7 and the mean error was 4.1 to 5.1 mmh^{-1}. Microwave-link-based rainfall rate yield significantly improved quantitative estimation compared to radar-based rainfall rate.

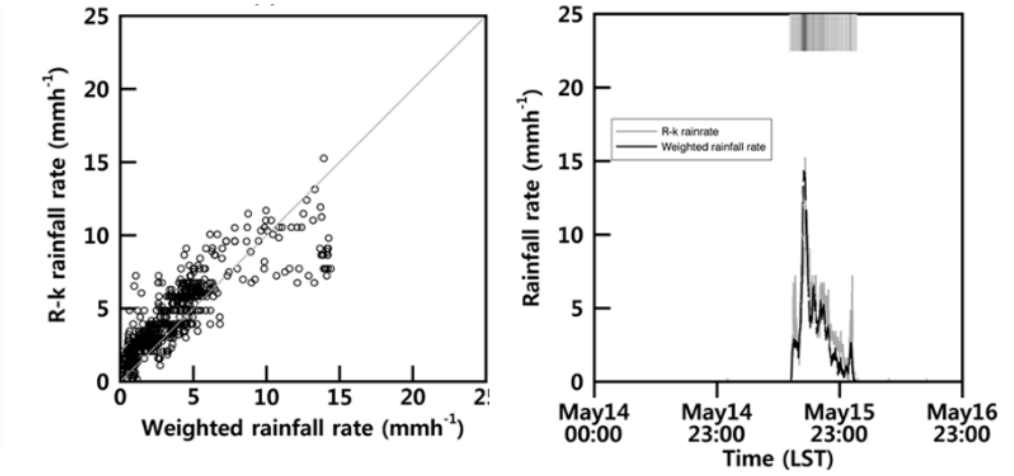

Fig. 1. Comparison of the R-k rainfall rate with the weighted rainfall rate for the ML.

Although ML is useful, the use of commercial ML for precipitation monitoring requires the development of data collection equipment as well as negotiations and agreements with companies. In order to develop a simple ML system, it is necessary to solve restrictions such as frequency use permission. Therefore, we decided to develop a new meteorological instrument for monitoring precipitation using a freely available 24 GHz transceiver. The test bed is a flat area with paddy fields around the Boseong standard weather station. It is regarded as the best place for experiments to study the attenuation effect depending on the distance between the transmitter and the receiver. This area is situated where sea fog often flows in due to the sea and the valley. We plan to present observation results showing whether the higher-frequency sensor detects the fog.

References

[1] M. Kim and B. H. Kwon, "Attenuation Correction of X-Band Radar Reflectivity Using Adjacent Multiple Microwave Links," *Atmosphere,* Vol 9, 287; doi:10.3390/atmos9080287, 2018.
[2] M. Kim and B. H. Kwon, "Attenuation Correction of X-Band Radar Reflectivity Using Adjacent Multiple Microwave Links," *Remote sensing*, Vol 12, 2133; doi:10.3390/rs12132133, 2020.

Microwave Dielectric Characterization of High-Loss Samples

A. Cintio[1], R. D'Ambrosio[1], G. Annino[1]

[1]*Istituto per i Processi Chimico-Fisici, IPCF-CNR, Via G. Moruzzi 1, Pisa, Italy*
geannino@ipcf.cnr.it

Keywords: microwaves, dielectric characterization, microwave-assisted processes, high-loss samples, Si, SiC

The determination of the dielectric properties plays an essential role in all those applications where a controlled and predictable interaction between electromagnetic waves and materials of interest is crucial. In particular, dielectric measurements at high temperatures have gained considerable attention in relation to the development of microwave-assisted processes, which hold the promise to enable processing routes that are intrinsically more efficient, both in terms of energy balance and processing time.

For many materials, the dielectric permittivity $\varepsilon(T)=\varepsilon'(T)-i*\varepsilon''(T)$ is strongly dependent on the temperature, T. Moreover, at sufficiently high temperatures these properties are often characterized by high dielectric losses. In these conditions, the determination of the dielectric properties cannot be based on perturbative techniques which can lead to very inaccurate results, sometimes so inaccurate as to be unphysical [1].

Recently, a setup for the dielectric characterization of samples at a frequency around 2.45 GHz and temperature T up to 1200 °C was built and employed for ceramic materials. The system is based on a resonant cavity and employs a rigorous data analysis procedure enabling the characterization of materials with dielectric properties largely variable with the temperature, without the need for any calibration procedure [2].

This approach makes it possible to characterize, in a single measurement session, materials whose dielectric behaviour changes continuously with T from a low-loss one ($\varepsilon'>>\varepsilon''$) to a very high-loss one ($\varepsilon''>\varepsilon'$) [3]. However, this transition is often associated with high values of ε and to a strong rearrangement of the electric field in the sample, which makes the control over the measurement errors critical. This contribution focuses on the analysis of the experimental data and of the related measurement error for materials exhibiting a continuous transition with T from low losses to very high losses, such as single-crystal Si and SiC. The most relevant quantities affecting the errors and the conditions in which the dielectric permittivity of high-loss samples can be determined with reasonable accuracy will be discussed.

References

[1] G. Annino, M. Cassettari, "Comment on "On the negative value of dielectric permittivity of the water surface layer" [Appl. Phys. Lett. 83, 4506 (2003)]", *Appl. Phys. Lett.*, vol. 85, p. 1301, 2004.
[2] G. Annino, A. Cintio, R. D'Ambrosio, A. Lazzeri, "Dielectric characterization of Si, SiC, SiC/SiC, and C/SiC samples", Oral presentation, 17th International Conference on Microwave and High Frequency Heating, 9-12 September 2019, Valencia, Spain
[3] F. Wooten, *Optical poperies of solids*, Chap. 3. New York, USA: Academic Press, 1972.

Localized Microwave Heating with Temperature Measurement using Magnetic Resonance

Y. Nikawa[1]

[1]*School of Science and Engineering, Kokushikan University, 4-28-1 Setagaya, Setagaya-ku, Tokyo 154-8515, Japan*
nikawa@kokushikan.ac.jp

Keywords: ferrimagnetic resonance, microwave magnetic heating, magnetic resonance imaging, temperature mapping

Microwave heating modality is studied using ferrimagnetic resonance which can be applied in the microwave frequency region. By using ferrimagnetic resonance, the subject heating area and heating efficiency can be controlled. For the magnetic field of the electromagnetic (EM) wave that excites the spin and the EM field emitted from the excited spin at the position *(x, y, z)*, as the direction of position is defined as x, the linear gradient magnetic field $G_x x$ is superimposed on the static magnetic field B_0. By placing the measuring object in a magnetic field, the nuclear magnetic resonant frequency $\omega_0(x, y, z)$ in the targeting object is obtained as in (1).

$$\omega_0(x, y, z) = \gamma(B_0 + G_x x) \tag{1}$$

By multiplying the linear gradient magnetic field in the x direction, the nuclear magnetic resonant frequency changes in proportion to position x, so that position can be identified, and *y* and *z* can be identified by the same process. On the other hand, excluding the region of $\omega = \omega_0$, which is a resonant region, (2) and (3) can be obtained for the permeability $\mu^* = \mu' - j\mu''$ when the magnetostatic field intensity B_0 is the positive condition.

$$\mu' = 1 + \frac{|\gamma| M_0}{|\gamma| B_0 - \omega} \tag{2}$$

$$\mu'' = 1 + \frac{|\gamma| M_0 \omega \alpha}{(|\gamma| B_0 - \omega)^2} \tag{3}$$

Where M_0 is magnetization, γ is the gyromagnetic ratio, and α is the coefficient.

Also, the heating modality can be installed in Magnetic Resonance Imaging (MRI) equipment which can scan the heating medium inside. A three-directional end view of the medium can be obtained using MRI. The MRI equipment applies an external DC magnetic field and EM waves with non-ionizing radiation, while diagnostic imaging apparatus such as X-ray computed tomography (CT) uses high-energy ionizing radiation.

Typical images are obtained by MRI equipment by weighting dissipation time of longitudinal relaxation of hydrogen atom which is represented by T_1 and that of horizontal relaxation which is represented by T_2. The dissipation time of longitudinal relaxation and that of horizontal relaxation in an atom is independent. Therefore, it is necessary to obtain the image to represent T_1 and T_2, respectively. The starting time to measure dissipation time of longitudinal M_z and that of horizontal M_{xy}, of atomic spin in the stage of nuclear magnetic resonance are shown in (4) and (5) which are equivalent to the elapsed time after stopping RF pulse;

$$M_z = M_0(1 - e^{-k_1 t}), \tag{4}$$

$$M_{xy} = M_0 e^{-k_2 t}. \tag{5}$$

The temperature change in the cross-section of the targeted material can be obtained by measuring phase shift of time sequential T_1 enhanced signal, because the longitudinal relaxation time T_1 includes the temperature information of material. By using this phase shift, $\Delta\phi$, temperature change inside the sample material is obtained as shown in (6).

$$\Delta T(i, j) = \frac{\Delta\phi(i, j)}{2\pi\gamma B_0 C T_e} \tag{6}$$

Where, ΔT is the difference in temperature, C(-0.01 ppm/°C) is the temperature coefficient, and T_e is the echo time. The phase measuring procedure shown in (6) will be one of the promising techniques to nondestructively obtain temperature data inside the sample. To enhance the sensitivity of temperature change, the material includes ionized manganese which has strong T_1 enhanced signal, and has been the focus of studies [1], [2].

Cross sectional temperature mappings using MRI are shown in Figs. 1 and 2. In Fig. 1, the heating applicator is coaxial and the tip of it is set at the center of the heating target [3]. From the result, the temperature change is observed nondestructively and the maximum temperature is located at the center of the medium. In Fig. 2, the heating applicator is a waveguide and the aperture of it is set on the top of the heating medium. From the result, the temperature elevation is observed nondestructively and the maximum temperature is distributed around the top surface of the medium. Fig. 3 shows the experimental setup of microwave heating using magnetic resonance [4-6]. To realize localized heating by ferrimagnetic resonance, ferrite powder is dispersed in the heating target. The center frequency of heating is 2.45 GHz. Fig. 4 shows the experimental result of SAR distribution by microwave heating with an external DC magnetic field. The results also show the SAR distribution without an external magnetostatic field. The absorbed power in the resonant area is controlled by the external magnetic field strength and irradiated microwave frequency. It can be found that the localized microwave heating by ferrimagnetic resonance can be controlled by external magnetic field strength. The results shown here are useful to control localized microwave heating with nondestructive temperature measurement.

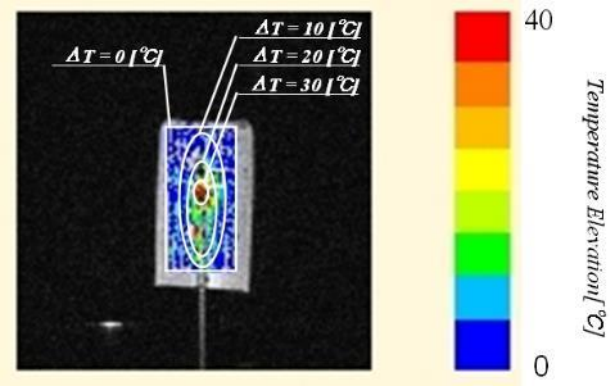

Fig. 1. Cross sectional temperature mapping using MRI by coaxial applicator.

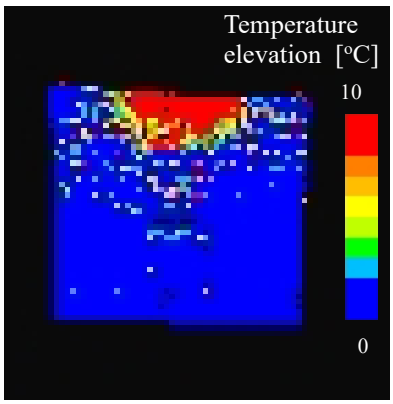

Fig. 2. Cross sectional temperature mapping using MRI by waveguide applicator.

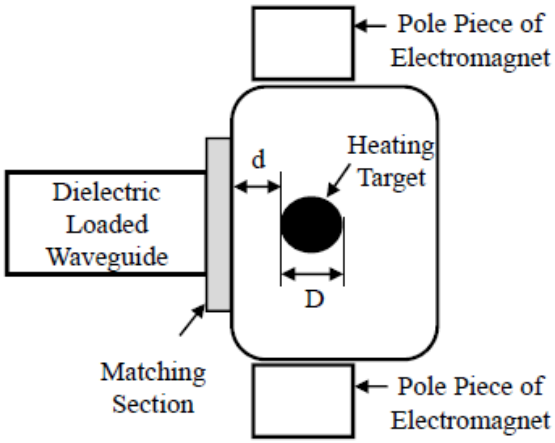

Fig. 3. Experimental setup of microwave heating using magnetic resonance.

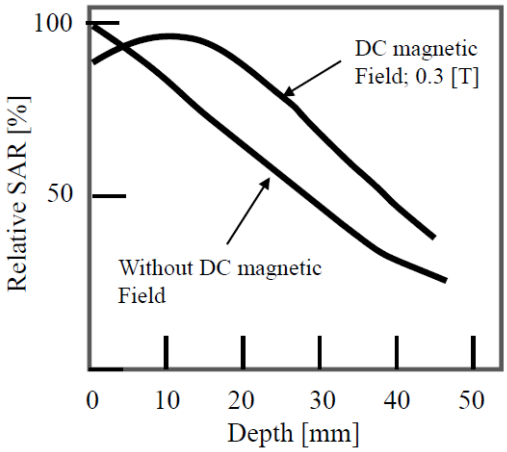

Fig. 4. Experimental result of microwave heating with/without external DC magnetic field.

References

[1] Y. Nikawa, M. Nishioka, "Microwave Diagnosis Based on MRI Imaging", *GCMEA 2008 / MAJIC 1st*, pp.799-802, 2008.
[2] S. Nakamura, M. Nakamura, E. Maeda and Y. Nikawa, "Noninvasive Internal Temperature Measurement During Moxa-Needle Treatment Using MRI", Proceedings of GCMEA 2012 / MAJIC 2nd, 2012.
[3] Y. Nikawa, " Study on Dry Phantom Model to Evaluate SAR Distribution in Human Tissue," *Book of Proceedings of 7th International Conference on Microwave and High Frequency Heating*, pp. 383-386, 1999.
[4] Y. Nikawa and S. Nakamura, "Dynamic Measurement of Permittivity and Permeability Using Ferrite Loaded Cavity," *2013 IEEE MTT-S International Microwave Symposium Digest*, 2013, 4 pages in CD-ROM.
[5] Y. Nikawa and T. Takase, " Microwave Visualizing Equipment Using Miniature Loop Array," *Proceedings of GCMEA 2008 / MAJIC 1st*, 2008, pp. 823-826, 2008.
[6] Y. Nikawa and T. Takase, "Visualization of EM Field Considering Magnetic-Field Orientations," *The First Symposium of Japan Society of Electromagnetic Wave Energy Applications, Proceedings*, pp. 160-161, 2007.

Multivariate Calibration Approach to Dielectric Spectroscopy for Continuous Online Monitoring of Chemical Synthesis

D. Dalligos[1], L. T. Ball[1], M. Pilling[3]. G. Dimitrakis[2]

[1]*School of Chemistry, University of Nottingham, University Park, Nottingham, NG7 2RD, UK*
[2]*Department of Chemical and Environmental Engineering, University of Nottingham, University Park, Nottingham, NG7 2RD, UK*
[3]*AstraZeneca, Macclesfield, UK*
georgios.dimitrakis@nottingham.ac.uk

Keywords: microwave, sensor technology, chemistry, dielectric properties, reaction monitoring

Off-line monitoring is commonly used to determine the progress of a reaction/process in research and industry. However, it is time consuming, inefficient and challenging for reactions that use toxic reagents and high temperature/pressure. Furthermore, there are also potential safety risks to the operators. To minimise or eliminate these issues, continuous in-situ monitoring is an alternative approach by employing process analytical techniques (PAT) that are available. Nevertheless, there is no single analytical technique that can be applied to every system. Dielectric spectroscopy (DS) is a technique that measures the dielectric properties of a material as a function of frequency. It has a wide range of applications in biological systems [1], agriculture [2] and polymers [3]. The advantages of DS are that it is relatively cheap, fast, non-destructive and easy to operate and maintain. It has been previously used successfully to monitor polymerisation reaction in real time [4].

The present study demonstrates the potential of DS as a PAT tool for monitoring chemical synthesis when there is a change in the dielectric properties of the reaction medium, as a result of a chemical transformation. The experiments revealed that DS can follow the conversion of the starting material to the product with good comparability to off-line Nuclear Magnetic Resonance (NMR) spectroscopic data. To enhance the performance of DS as an in-situ monitoring technique, a multivariate calibration approach (Partial Least Squares regression) was used to process the data and the robustness of the predictive model was evaluated at 5 °C intervals. Finally, a simple test for deciding quickly the suitability of DS as an analytical tool for any new process is also being presented.

References

[1] A. L. Gioia, E. Porter, I. Merunka, A. Shahzad, S. Salahudden, M. Jones and M. O'Halloran, "Open-ended coaxial probe technique for dielectric measurement of biological tissues: challenges and common practices", *Diagnostics*, vol. 8, pp. 40, Jun. 2018.
[2] D. E. Khaled, N. N. Castellano, J. A. Gasquez, A. Perea-Moreno, F. Manzano-Agugliaro, "Dielectric spectroscopy in biomaterials: agrophysics", *Materials*, vol. 9, pp. 310, Apr. 2016.
[3] J. W. Schultz, "Dielectric spectroscopy in analysis of polymers", *Encyclopedia of Analytical Chemistry: Applications, Theory and Instrumentation*, Sep. 2006.
[4] A. Kalamiotis, A. Ilchev, D. J. Irvine, G. Dimitrakis, "Optimised use of dielectric spectroscopy at microwave frequencies for direct online monitoring of polymerisaton reactions", *Sensors and Actuators B: Chemical*, vol. 290, pp. 34-40, Jul. 2019.

Thank you to all of our sponsors